



High-Energy Neutrino Emission from Astrophysical Transients

DOCTORAL THESIS

by

TETYANA PITIK

Supervisor: Prof. Irene Tamborra

This thesis has been submitted to the PhD School of The Faculty of
Science, University of Copenhagen
7th October 2023

Introduction

The high-energy Universe remains enigmatic, with many astrophysical events still requiring complete understanding. Investigating these phenomena solely through electromagnetic radiation can pose significant challenges. Photons interact with matter and radiation during their journey from the sources to Earth, resulting in a degradation of the information they carry. Furthermore, even if the electromagnetic signal manages to reach Earth, its information can be ambiguous, making it difficult to decipher the underlying source physics. In contrast, neutrinos can be abundantly produced in these sources as a byproduct of particle acceleration. Due to their weakly interacting nature, they can travel undisturbed through space, giving access to environments that cannot be tested otherwise. This thesis aims to harness the potential of high-energy neutrinos to shed light on the enigmatic nature of some poorly understood transient events.

Our first focus is on long gamma-ray bursts originating from relativistic collimated jets born in the cataclysmic deaths of massive stars. They are the most powerful phenomena observed in the Cosmos with their exceptionally intense flashes in gamma rays, which can outshine entire galaxies for a fleeting period. Despite being discovered more than five decades ago, fundamental questions on the gamma-ray burst jet composition, energy dissipation, particle acceleration, and radiation mechanisms remain unanswered. Different models exist, but no single model can explain the electromagnetic observations and multiple mechanisms may be at play across different gamma-ray bursts or even within a single burst event. The limited number of gamma-ray photons and the associated statistical challenges allow flexibility in fitting the same dataset with various input models. Hence, the information carried solely by electromagnetic emission has been insufficient to address all the open questions about jet workings. In this thesis, we investigate the potential of neutrinos in addressing these questions.

We then consider a class of extremely luminous supernovae that defy conventional emission mechanisms that describe core-collapse supernova emission: superluminous supernovae. One possible explanation for these exceptionally bright events invokes the interaction between energetic supernova ejecta and a very dense circumstellar medium formed by the progenitor star through intense winds and violent eruptions before the final supernova explosion. The mechanisms responsible for the substantial modification in the progenitor envelopes, which lead to significant loss of stellar mass, remain a

challenging and active area of research. The neutrino signal, combined with the photon one, carries information about this ejected material structure, geometry, mass, and composition, which is crucial to pinpoint the type of progenitor involved and, ultimately, the underlying operating mechanisms.

Today, neutrino astronomy stands at a critical crossroads. The IceCube Neutrino Observatory has successfully confirmed the existence of a flux of high-energy cosmic neutrinos, and we have started seeing some significant associations with steady sources. However, determining the origin of the bulk of these neutrinos has proven challenging because of the detector's limited sensitivity. With the advent of new neutrino telescopes, such as IceCube Gen-2 and KM3Net, along with advancements in technology and data analysis techniques, we expect to significantly improve neutrinos' detection capabilities. Given the positive premises, we believe that in the forthcoming years, these facilities will allow us to gain deeper insights into the transient sources investigated in this thesis.

In the following chapters, we introduce the mechanisms behind the acceleration of energetic particles in astrophysical environments and the production of high-energy neutrinos and electromagnetic radiation. Our primary focus is initially directed to the prompt emission phase of long-gamma ray bursts, aiming to improve our understanding of the nature of relativistic jets responsible for the gamma-ray emission. To this aim, we investigate neutrino production for various proposed models associated with prompt emission. To compare the different models, we employ up-to-date observations and simulation results. We then concentrate on some peculiar features observed during the afterglow emission of certain gamma-ray bursts, known as "optical jumps." Assuming that these jumps arise from collisions between relativistic shells emitted due to late activity of the central engine, we investigate the prospects of detecting neutrinos and examine whether their detection can provide insights into the nature of these jumps. In the second part of the thesis, we shift our attention to interaction-powered supernovae. Initially, we explore the interpretation of the transient event AT2019fdr as a superluminous supernova, aiming to determine whether the observed neutrino event IC200530A can be explained as originating from this superluminous supernova as opposed to the tidal disruption event interpretation. Motivated by our positive findings and the ever-growing detection rate of these rare transients, in the final part of the thesis, we explore the relation between high-energy neutrino production and photometric properties of interaction-powered supernovae, such as their optical peak luminosity and lightcurve rise time. The outcome of this investigation is crucial to guide and optimize upcoming targeted multimessenger searches of neutrinos from this class of transients.

Introduktion

Det højenergetiske univers bliver ved med at være gådefuldt, med mange astrofysiske fænomener, der stadig ikke forstås til fulde. At undersøge disse fænomener udelukkende gennem elektromagnetisk stråling kan indebære betydelige udfordringer. Fotoner interagerer med materie og stråling under deres rejse fra deres kilder og frem til Jorden, hvilket resulterer i en forringelse af den information, de bringer med sig. Selvfølgelig hvis det elektromagnetiske signal når Jorden, kan dets information derudover være svært at tyde, hvilket gør det vanskeligt at afkode den bagvedliggende kildes fysik. I modsætning hertil kan neutrinoer produceres i rigelige mængder i selvsamme kilder som en biprodukt af partikelacceleration. På grund af deres svagt interagerende karakter kan de rejse uforstyrret gennem rummet og give adgang til miljøer, der ikke kan undersøges på anden vis. Denne afhandling har til formål at udnytte potentialet af højenergi-neutrinoer til at kaste lys over den gådefulde karakter af nogle af de transiente begivenheder, vi har sværest ved at forstå. Vores første fokus er langvarige gammaglimt (gamma-ray bursts), der stammer fra relativistiske koncentrerede jetstråler, der skabes, når tunge stjerner kolliderer. De er de mest kraftfulde fænomener observeret i kosmos med deres exceptionelt intense glimt af gammastråler, der kan overstråle hele galakser i en flygtig periode. På trods af at de blev opdaget for mere end fem årtier siden, forbliver grundlæggende spørgsmål om sammensætningen af gammaglimtets jetstråler, deres energidissipation, partikelacceleration og strålingsmekanismer ubesvarede. Der findes forskellige modeller, men ingen enkeltstående model kan forklare de elektromagnetiske observationer, og flere mekanismer kan være involverede på tværs af forskellige gammaglimt eller endda inden for en enkelt gammaglimt-begivenhed. Det begrænsede antal gammastrålefotoner og de tilknyttede statistiske udfordringer tillader fleksibilitet i at tilpasse det samme datasæt med forskellige inputmodeller. Derfor har den information, der udelukkende tilvejebringes af elektromagnetisk emission, været utilstrækkelig til at besvare alle de åbne spørgsmål om, hvordan jetstråler virker. I denne afhandling undersøger vi neutrinoers potentiale for at besvare disse spørgsmål. Vi betragter dernæst en klasse af ekstremt lysstærke supernovaer, der trods de konventionelle emissionsmekanismer, der beskriver emissionen fra kernekollaps-supernovaer: superluminøse supernovaer. En mulig forklaring på disse exceptionelt lysstærke begivenheder involverer interaktionen mellem det energirige stof, der bliver slynget ud fra su-

pernovaer, og det meget tætte circumstellære medium, der dannes af den oprindelige stjerne (progenitor star) gennem intense vinde og voldelige udbrud før den endelige supernovaeksplosion. Mekanismerne, der er ansvarlige for den betydelige ændring i de oprindelige stjernes skaller (envelopes), som fører til betydeligt tab af stjernemasse, forbliver et udfordrende og aktivt forskningsområde. Neutrinosignalet, kombineret med fotonsignalet, indeholder information om dette udstødte materiales struktur, geometri, masse og sammensætning, hvilket er afgørende for at fastlægge hvilken type af oprindelig stjerne, der var involveret, og i sidste ende de underliggende mekanismer. Til dato står neutrinoastronomi ved en kritisk skillevej. IceCube neutrinoobservatoriet har med succes bekræftet eksistensen af en flux af højenergetiske kosmiske neutrinoer, og vi er begyndt at se nogle betydelige forbindelser mellem dem og stabile kilder (steady sources). Det har imidlertid vist sig udfordrende at bestemme oprindelsen af hovedparten af disse neutrinoer på grund af detektorens begrænsede sensitivitet. Med fremkomsten af nye neutrinoteleskoper såsom IceCube Gen-2 og KM3NeT, sammen med fremskridt inden for teknologi- og dataanalyseteknikker, forventer vi at forbedre neutrinoernes detektionsmuligheder markant. Ud fra de positive forudsætninger tror vi, at disse faciliteter i de kommende år vil give os mulighed for at få dybere indsigt i de transiente kilder, som denne afhandling undersøger. I de følgende kapitler introducerer vi mekanismerne bag accelerationen af energirige partikler i astrofysiske miljøer og produktionen af højenergi-neutrinoer og elektromagnetisk stråling. Vores primære fokus er i begyndelsen rettet mod den indledende emissionsfase (prompt emission phase) af lange gammaglimt med det formål at forbedre vores forståelse af relativistiske jetstrålers natur, der er ansvarlige for gammastrålingen. Til dette formål undersøger vi neutrinoproduktionen for forskellige foreslåede modeller forbundet med prompt-emissionsfasen. For at sammenligne de forskellige modeller anvender vi opdaterede observationer og simuleringresultater. Vi koncentrerer os derefter om nogle bemærkelsesværdige træk observeret under eftergløds-emissionen (afterglow emission) af visse gammaglimt kendt som ”optiske spring” (optical jumps). Under forudsætning af, at disse spring opstår som følge af sammenstød mellem relativistiske skaller, der udsendes på grund af sen aktivitet i den centrale kraftkilde, undersøger vi mulighederne for at detektere neutrinoer og undersøger, om deres detektion kan give indsigt i disse springs natur. I den anden del af afhandlingen skifter vi vores opmærksomhed til interaktionsdrevne supernovaer. Indledningsvist udforsker vi fortolkningen af den transiente begivenhed AT2019fdr som en superluminøs supernova med det formål at bestemme, om den observerede neutrino-begivenhed IC200530A kan forklares som stammende fra denne superluminøse supernova i modsætning til en fortolkning baseret på en tidal disruption event. Motiveret af vores positive resultater og den stadigt voksende detektionsrate af disse sjældne transiente begivenheder, udforsker vi i den sidste del af afhandlingen forholdet mellem produktionen af højenergi-neutrinoer og de fotometriske egenskaber ved interaktionsdrevne supernovaer, såsom

deres optiske maksimale luminositet og lyskurvens stigningstid (lightcurve rise time). Resultatet af denne undersøgelse er afgørende for at vejlede og optimere kommende målrettede multimessenger-søgninger efter neutrinoer fra denne klasse af transiente begivenheder.

Publication list

This thesis is based on the following published journal articles:

1. **Paper I:** **Tetyana Pitik**, Irene Tamborra, Maria Petropoulou
Neutrino signal dependence on gamma-ray burst emission mechanism
[JCAP 05\(2021\) 034](#), [arXiv:2102.02223](#)
2. **Paper II:** Ersilia Guarini, Irene Tamborra, Damien Begue, **Tetyana Pitik**, Jochen Greiner
Multi-messenger detection prospects of gamma-ray burst afterglows with optical jumps
[JCAP 06 \(2022\) 06, 034](#), [arXiv:2112.07690](#)
3. **Paper III:** **Tetyana Pitik**, Irene Tamborra, Charlotte R. Angus, Katie Auchettl
Is the high-energy neutrino event IceCube-200530A associated with a hydrogen-rich superluminous supernova?
[ApJ 929 \(2022\) 2, 163](#), [arXiv:2110.06944](#)
4. **Paper IV:** **Tetyana Pitik**, Irene Tamborra, Massimiliano Lincetto, Anna Franckowiak
Optically Informed Searches of High-Energy Neutrinos from Interaction-Powered Supernovae
[MNRAS](#), [arXiv:2306.01833](#)

Publications not included in the thesis:

1. **Tetyana Pitik**, Daniel J. Heimsoth, Anna M. Suliga, A. Baha Balantekin
Exploiting stellar explosion induced by the QCD phase transition in large-scale neutrino detectors
[Phys. Rev. D 106 \(2022\), 103007](#), [arXiv:2208.14469](#)

Thesis outline

This thesis is structured in twelve chapters:

In Chapter 1, we begin with an introduction to neutrinos, providing a concise historical overview of discoveries and key experiments that have shaped our understanding of their properties. We then present the natural and human-made sources that produce neutrinos over more than twenty decades in energy and intensity. Finally, we cover the primary interaction channels between neutrinos and matter, focusing in particular on the detection technique of high-energy neutrinos.

In Chapter 2, we explore the concept of multi-messenger astronomy, which combines observations from various cosmic messengers, including neutrinos, photons, and cosmic rays, to gain a comprehensive understanding of astrophysical phenomena. The chapter delves into the mechanisms responsible for high-energy neutrino production in astrophysical contexts, such as hadronic and photo-hadronic interactions involving accelerated charged particles and surrounding matter or radiation. We also examine the correlations between neutrinos, cosmic rays, and photons, highlighting their intricate interplay, and conclude by mentioning some of the interesting transient sources expected to be sources of high-energy neutrinos.

In Chapter 3, we walk the reader through the main processes that give rise to high-energy charged particles in astrophysical environments. We start from the original idea of Fermi acceleration, pass to the diffusive shock acceleration at relativistic and non-relativistic shocks, and conclude by describing the acceleration in the context of magnetic reconnection.

In Chapter 4, we give a brief summary of the most important energy-loss mechanisms that particles undergo in extreme astrophysical contexts and are pertinent to the subjects discussed in this thesis. These mechanisms encompass energy losses from radiative processes as well as particle interactions.

In Chapter 5, we provide an overview of the evolution of massive stars, emphasizing

the mechanisms leading to substantial stellar mass losses and the ejection of stellar envelopes before they end their life through a supernova explosion. We then describe the emission mechanisms powering standard supernovae, which is important for understanding their difference from interaction-powered supernovae.

In Chapter 6, we present a comprehensive overview of the two transient sources that are the key focus of this thesis: interaction-powered supernovae and long gamma-ray bursts. We delve into the observational aspects and provide the essential theoretical framework to understand the observational properties characterizing both phenomena.

In Chapter 7, we summarize the projects carried out in Paper I and Paper II on the high-energy neutrino emission from the prompt and afterglow phase of the long-gamma-ray burst. We provide the motivation underlying the projects and discuss the main results of these studies.

Chapter 8 is a reprint of Paper I.

Chapter 9 is a reprint of Paper II.

In Chapter 10, we summarize the projects carried out in Paper III and Paper IV on the high-energy neutrino emission from interaction-powered supernovae. We provide the motivation underlying the projects and discuss the main results of these studies.

Chapter 11 is a reprint of Paper III.

Chapter 12 is a reprint of Paper IV.

Contents

1	Neutrino physics	1
1.1	Historical overview	1
1.2	Neutrino sources and fluxes	5
1.3	Neutrino oscillations	8
1.4	Neutrino interaction with matter	11
1.5	Neutrino detection	13
1.5.1	Cherenkov detectors	13
1.5.2	Detection of neutrinos with IceCube	15
1.5.2.1	IceCube properties	15
1.5.2.2	Event topologies	15
1.5.2.3	IceCube data	17
2	Neutrinos as cosmic messengers	18
2.1	Multi-messenger astronomy	18
2.2	High-energy neutrino production	20
2.2.1	The hadronic mechanism	22
2.2.2	The photo-hadronic mechanism	23
2.2.3	Difference between hadronic and photo-hadronic mechanisms	25
2.2.4	Connecting neutrinos with γ -rays and cosmic rays	26
2.3	Transient source candidates of high-energy neutrinos	28
3	Particle acceleration	32
3.1	Acceleration principle	32
3.2	Fermi acceleration mechanism	34
3.2.1	Energy gain in the particle-cloud encounter	35
3.3	Shock hydrodynamics	37
3.3.1	Jump conditions	38
3.4	Diffusive Shock Acceleration	39
3.4.1	Principle of Diffusive Shock Acceleration	39
3.4.2	Magnetic field amplification	41

3.4.3	Energy gain after a cycle upstream-downstream-upstream . . .	42
3.4.4	Power-law particle distribution	43
3.4.5	Relativistic shocks	45
3.4.6	Particle acceleration in relativistic shocks	47
3.4.7	Shock parametrization	48
3.5	Magnetic reconnection	48
3.5.1	Particle acceleration through magnetic reconnection	51
4	Energy-loss processes	53
4.1	Leptonic processes	53
4.1.1	Synchrotron radiation	53
4.1.1.1	Physics of synchrotron radiation	53
4.1.1.2	Synchrotron spectrum	54
4.1.2	Inverse-Compton scattering	56
4.1.2.1	Physics of Inverse-Compton emission	56
4.1.2.2	Inverse-Compton spectrum	57
4.1.3	Bremsstrahlung	58
4.2	Hadronic processes	58
4.2.1	Photo-pair production (Bethe-Heitler)	59
4.2.2	Photo-hadronic interaction	59
4.2.3	Hadronic interaction	60
5	Stellar evolution and supernova explosion	61
5.1	Stellar evolution in a nutshell	61
5.2	Core-collapse supernovae	63
5.3	Mass loss in massive stars	66
5.4	Classification of supernovae	69
5.5	Emission from “standard” supernovae	70
5.5.1	Power sources of supernovae lightcurves	71
6	Selected transient sources	74
6.1	Interaction-powered supernovae	74
6.1.1	Interaction of supernova ejecta with circumstellar medium	75
6.1.2	Emission from interaction-powered supernovae	78
6.2	Long Gamma-Ray Bursts	85
6.2.1	Observational facts on Long Gamma-Ray Bursts	87
6.2.1.1	Prompt emission	87
6.2.1.2	Afterglow emission	90
6.2.2	Theoretical framework of Long Gamma-Ray Bursts	92
6.2.2.1	Central engine	92
6.2.2.2	Relativistic motion	95

6.2.2.3	Frames of reference and Doppler boost	96
6.2.2.4	Initial conditions at the central engine	98
6.2.3	Matter-dominated jets	99
6.2.3.1	Fireball dynamics	100
6.2.3.2	Prompt emission models in the fireball scenario . . .	102
6.2.4	Poynting flux-dominated jets	104
6.2.4.1	Magnetic jet dynamics	105
6.2.4.2	Prompt emission models for magnetic jets	106
7	Paper I and II: description and summary of the main results	109
7.1	Paper I	109
7.1.1	Context and motivation	109
7.1.2	Summary of the main results	112
7.1.3	Critical outlook	113
7.2	Paper II	114
7.2.1	Context and motivation	114
7.2.2	Summary of the main results	115
8	Paper I: Neutrino signal dependence on gamma-ray burst emission mechanism	116
8.1	Introduction	117
8.2	Dynamical evolution of gamma-ray burst jets	119
8.2.1	Kinetic dominated jets	120
8.2.1.1	Jet model with internal shocks	122
8.2.1.2	Jet model with a dissipative photosphere and internal shocks	123
8.2.1.3	Jet model with three emission components	124
8.2.2	Poynting flux dominated jets	125
8.2.2.1	ICMART model	126
8.2.2.2	Magnetized jet model with gradual dissipation	127
8.2.3	Proton synchrotron model	128
8.3	Main model ingredients	129
8.3.1	Reference model parameters	129
8.3.2	Spectral energy distribution of protons	131
8.4	Neutrino production in the gamma-ray burst jet	132
8.5	Results: Gamma-ray burst neutrino emission	134
8.5.1	Kinetic dominated jets	135
8.5.1.1	Jet model with internal shocks	135
8.5.1.2	Jet model with a dissipative photosphere and internal shocks	136
8.5.1.3	Jet model with three emission components	139

8.5.2	Poynting flux dominated jets	142
8.5.2.1	ICMART model	142
8.5.2.2	Magnetized jet model with gradual dissipation	143
8.5.3	Proton synchrotron model	146
8.6	Discussion	149
8.6.1	Energetics	150
8.6.2	Detection perspectives	151
8.6.3	Uncertainties in the jet parameters	153
8.7	Conclusions	155
9	Paper II: High-energy neutrinos from afterglow optical-bumps	157
9.1	Introduction	158
9.2	Modelling of the merger of two relativistic shells	161
9.2.1	Physics of the blastwave	161
9.2.2	Merger of two relativistic shells	163
9.3	Photon energy distribution and light curve	166
9.3.1	Photon energy distribution during the afterglow	166
9.3.2	Photon energy distribution during the shell merger	169
9.3.3	Light curve	170
9.4	Energy distributions of protons and neutrinos	171
9.4.1	Proton energy distribution	171
9.4.2	Neutrino energy distribution and flux expected at Earth	173
9.5	Afterglow signals	175
9.5.1	Particle emission in the absence of a late shell collision	175
9.5.2	Particle emission in the presence of a late shell collision	179
9.6	Neutrino detection perspectives	181
9.6.1	All-sky quasi-diffuse flux	182
9.6.2	Point source searches	185
9.6.3	Detection prospects for GRB 100621A and a GRB 130427A-like burst	186
9.7	Conclusions	188
10	Paper III and IV: description and summary of the main results	189
10.1	Paper III	189
10.1.1	Context and motivation	189
10.1.2	Summary of the main results	191
10.1.3	Critical outlook	192
10.2	Paper IV	193
10.2.1	Context and motivation	193
10.2.2	Summary of the main results	193
10.2.3	Critical outlook	195

11 Paper III: IceCube event from a hydrogen-rich superluminous supernova?	196
11.1 Introduction	197
11.2 AT2019fdr: A type II _n superluminous supernova	198
11.3 Model setup	200
11.3.1 Spectral energy distributions of protons and neutrinos	201
11.3.2 Parameters characteristic of AT 2019fdr	205
11.3.3 Neutrino flux and event rate at Earth	207
11.4 Forecast of the neutrino signal	208
11.4.1 Energy fluence and temporal evolution of the neutrino event rate	209
11.4.2 Dependence of the neutrino signal on the parameters of AT2019fdr	212
11.5 Discussion	217
11.6 Conclusions	220
12 Paper IV: High-energy neutrinos from interaction-powered supernovae	221
12.1 Introduction	222
12.2 Model for interaction-powered supernovae	223
12.2.1 Modeling of the circumstellar medium	224
12.2.2 Shock dynamics	224
12.2.3 Interaction-powered supernova emission	227
12.2.4 Supernova model parameters	229
12.3 Scaling relations for the photometric supernova properties	230
12.4 Maximum proton energy	233
12.5 Expected neutrino emission from interaction-powered supernovae	236
12.5.1 Spectral energy distribution of neutrinos	236
12.5.2 Energy emitted in neutrinos	237
12.6 Neutrino detection prospects	240
12.6.1 Expected number of neutrino events at Earth	240
12.6.2 Expected number of neutrino events for SN 2020usa and SN 2020in	241
12.6.3 Characteristics of the detectable neutrino signal	246
12.6.4 Follow-up strategy for neutrino searches	249
12.6.5 Multi-messenger follow-up programs	251
12.7 Conclusions	252
Summary and conclusions	254
A Appendix Paper I	256
A.1 Spectral energy distributions of photons: fitting functions	256
A.1.1 Band function	256
A.1.2 Cut-off power-law	257
A.1.3 Power law	257

A.1.4	Double broken power law	258
A.2	Magnetized jet model with gradual dissipation: dependence of the neutrino emission on the input parameters	259
A.3	Quasi-diffuse neutrino flux for standard internal shock parameters	261
B	Appendix Paper II	263
B.1	A model for the late collision and merger of two relativistic shells	263
B.2	Degeneracies among the parameters characteristic of the merging shells	269
B.3	Cooling timescales of protons and mesons	270
C	Appendix Paper III	274
C.1	Parameter space adopted in the modeling of AT2019fdr	274
C.2	Maximum proton energy	276
D	Appendix Paper IV	278
D.1	Dependence of the supernova lightcurve properties on the model parameters	278
D.2	Dependence of the maximum proton energy on the supernova model parameters	279
D.3	Constant density scenario	284
	References	287

Neutrino physics

In this Chapter, we introduce the reader to the realm of neutrinos. We start by providing a concise historical overview, touching upon the key experiments that have shaped our understanding of neutrino properties. Subsequently, we present the most important known sources of neutrinos, highlighting their distinct fluxes and energies. Following this, we illustrate the primary interaction channels through which neutrinos interact with matter. In particular, we concentrate on the detection methodology and the current data of high-energy neutrinos, which represent the central focus of this thesis.

1.1 Historical overview

Neutrinos are elementary particles with a spin of $1/2$, representing the neutral leptons in the Standard Model. Since they have no electric charge, they do not interact electromagnetically. Furthermore, neutrinos are colorless, meaning they cannot interact via the strong force. Hence, in the framework of the Standard Model, they interact with matter only via the weak force.

The history of neutrinos is a tale of persistence and paradigm-shifting discoveries. It all began in 1930 when Wolfgang Pauli postulated the existence of an electrically neutral half-spin particle as a "desperate remedy" to preserve the conservation of energy and momentum in β -decay¹. This process is a form of radioactivity where a

¹Wolfgang Pauli hypothesized the existence of the neutrino in an open letter to a group of nuclear physicists [381]: *Dear Radioactive Ladies and Gentlemen! I have hit upon a desperate remedy to save [...] the law of conservation of energy. [...] there could exist electrically neutral particles, which I will call neutrons, in the nuclei [...] The continuous β spectrum would then make sense with the assumption that in β -decay, in addition to the electron, a neutron is emitted such that the sum of the energies of the neutron and electron is constant. But so far, I do not dare to publish anything about this idea, and trustfully turn first to you, dear*

primary nucleus (A, Z) decays into a lighter secondary one of the same mass number, an electron (or positron), and nothing else visible:

$$(A, Z) \rightarrow (A, Z \pm 1) + e^\mp + \text{nothing else visible} \quad (1.1)$$

In the absence of invisible particles in the final state, the energy of e^\mp should have a well-defined value, $E_e \simeq Q \equiv M_i - M_f$, namely be equal to the mass difference of the initial and final nuclei. Contrary to the expectations, experimentalists observed a continuum spectrum ranging from m_e up to the maximum allowed energy Q . Several explanations were proposed to account for this puzzling anomaly (Niels Bohr even speculated about the possibility of a violation of energy conservation). However, in December 1930, Wolfgang Pauli conjectured the existence of a non-observed particle emitted during the reaction. This unobserved particle had to be neutral (to conserve electric charge), very light (since $E_{e,\max} \simeq Q$), and with spin 1/2 (to satisfy angular momentum conservation and statistics). In modern notation, β -decays are now considered as the processes:

$$A(Z, N) \rightarrow A(Z + 1, N - 1) + e^- + \bar{\nu}_e \quad [\beta^- \text{ decay}] \quad (1.2)$$

$$A(Z, N) \rightarrow A(Z - 1, N + 1) + e^+ + \nu_e \quad [\beta^+ \text{ decay}] \quad (1.3)$$

where Z and N are the number of protons and neutrons in a nucleus, respectively.

In 1934, Enrico Fermi named the particle *neutrino*, within the formulation of his theory of β -decay (the first theory of one of the four fundamental forces, the weak force). He explained the β -decay in terms of a 4-fermion interaction with strength G_F . This interaction would also predict the scattering of neutrinos off matter via $\bar{\nu}_e + p \rightarrow n + e^+$ process. In 1934 Bethe and Peierls estimated the cross section for this process [90]. The obtained value was so tiny that they wrote "... one can conclude that there is no practically possible way of observing the neutrino". Indeed, the actual value for this cross section is $\sigma \sim 10^{-44} \text{ cm}^2$ in the MeV energy range, and for a neutrino of energy of a few MeV, this corresponds to a probability of 10^{-11} to interact inside the Earth when following a trajectory passing through its center.

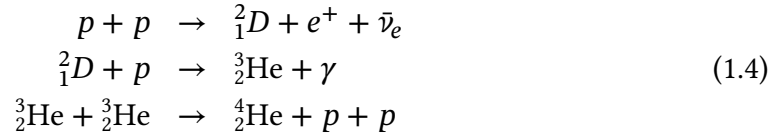
Therefore, neutrino detection remained elusive for more than 20 years until the results of Reines and Cowan [137] in 1956. They used the Savannah River in South Carolina nuclear reactor as an antineutrino source and a water detector with dissolved cadmium chloride. The detection method consisted of observing the two gamma rays created by the annihilation of the positron from $\bar{\nu}_e + p \rightarrow n + e^+$ with a background electron, followed, with a few μs delay, by the gamma ray emitted in the deexcitation of cadmium after the neutron capture: $n + {}^{112}\text{Cd} \rightarrow {}^{113}\text{Cd} + \gamma$. This discovery earned Fred Reines the 1995 Nobel Prize in Physics.

radioactive ones, with the question of how likely it is to find experimental evidence for such a neutron [...] I admit that my remedy may seem almost improbable because one probably would have seen those neutrons, if they exist, for a long time. But nothing ventured, nothing gained [...] Thus, dear radioactive ones, scrutinize and judge.

Another important chapter in understanding neutrinos revolves around the concept of families or generations. The year 1937 marked a significant milestone with the discovery of the muon. Being a heavier version of the electron, it also enters the Fermi interactions accompanied by a neutrino. An important question arose: Was this neutrino identical to the one observed in β -decays, or was it of a different type? Following a suggestion by Pontecorvo, this problem was solved in 1962 by L. M. Lederman, M. Schwartz, and J. Steinberger [145], who performed the first experiment with accelerator neutrinos. A beam of pions was created by bombarding a Beryllium target with a proton beam. These pions would subsequently decay and produce neutrinos. They studied the interaction with nucleons of type $\nu_\mu + N \rightarrow \mu^- + X$ or $\nu_\mu + N \rightarrow e^- + X$. Only the first type of interaction was found, demonstrating that ν_e and ν_μ are different particles. They participate separately in weak interactions with their corresponding charged leptons. This result earned Lederman, Schwartz, and Steinberger the Nobel Prize in 1988.

The third charged lepton, the tau, was discovered in 1975 at SLAC. Being just a heavier copy of the electron and the muon, it was concluded that a third neutrino flavor had to exist. The direct detection of the ν_τ was achieved only in 2000 by the DONUT experiment at Fermilab [274]. Once different neutrino families were established, the question of whether there could be mixing and transitions between them was open.

It was known at the time that there should be a neutrino flux from our Sun. The existence of this flux had been predicted when it was understood that the primary energy source of stars comes from nuclear fusion reactions in their cores. In particular, for a star of the mass of the Sun, the primary channel that converts hydrogen to helium, and that accounts for $\sim 82\%$ of the total produced energy, is the following *p-p I chain*:



The complete chain releases a net energy of 26.732 MeV but only 2.2% of this energy goes to the neutrino ($E_\nu \sim 0.6$ MeV). Other branches of the p-p chain can produce electron neutrinos with energies up to 15 MeV. The latter had been the target of the Homestake experiment that, led by Raymond Davis, measured the solar neutrino flux for almost thirty years [146]. The radiochemical detector was a tank filled with chlorine (the less toxic C_2Cl_4). Interactions of electron neutrinos with chlorine atoms in the tank produced radioactive isotopes of argon via inverse β -decay:



The radioactive ${}^{37}_{18}\text{Ar}$ nuclei were extracted and counted. However, only around one-third of the predicted neutrino flux by J. Bahcall and collaborators' [71] Standard Solar

Model was detected. Many subsequent radiochemical and water Cherenkov detectors confirmed the deficit, including the Kamioka Observatory [185]. The results of these experiments were fundamental in establishing the presence of a deficit of solar neutrinos, which became known as the "solar neutrino problem".

The solar neutrino problem remained unsolved for about three decades: it needed to be clarified whether neutrinos oscillated into a flavor that could not be detected or whether the theoretical predictions of the flux were severely flawed. The first idea of neutrino oscillations had been already put forward by B. Pontecorvo in 1957 [398], subsequently addressed by him and Gribov in [217]. It was known that oscillations could explain the deficit in electron neutrinos. However, it was a solution that would have required a modification of the accepted Standard Model of particle physics, which formerly assumed that neutrinos were massless and so could not change flavor. However, if neutrinos had mass, the "missing" solar neutrinos could be electron neutrinos, which changed into other flavors as they propagated to Earth, rendering them invisible to the detectors that were sensitive only to electron neutrinos.

The definitive answer came in 2001 thanks to the Sudbury Neutrino Observatory (SNO) experiment [44]. It was able to measure two separate reactions on deuteron (D): the charged current (CC) interaction $\nu_e + D \rightarrow p + p + e^-$ (sensitive only to electron neutrinos) and the neutral current (NC) $\nu_x + D \rightarrow p + n + \nu_x$ (sensitive to all neutrino types), for $x = e, \mu, \tau$. By comparing the ν_e and ν_x fluxes deduced from the data, the SNO experiment was able to prove that ν_e flux constitutes only roughly a third of the overall solar neutrino flux and that the observed total flux is in good agreement with the theoretical predictions.

In 1985, the Kamiokande experiment in Japan and the IMB (Irvine, Michigan, and Brookhaven) collaboration in the USA reported a deficit in the atmospheric muon neutrinos for the first time. These neutrinos come from the decay of pions and kaons produced when cosmic rays (CRs) interact with nuclei in the atmosphere. Echoing the solar neutrino problem, the deficit of muon neutrinos became the "atmospheric neutrino anomaly". In 1998, the Super-Kamiokande experiment discovered that it was zenith-angle dependent, and this was consistent with two flavors $\nu_\mu \leftrightarrow \nu_\tau$ oscillation [184]. In 2015, T. Kajita for the Super-Kamiokande collaboration and A.B. McDonald for the SNO collaboration received the Nobel Prize in Physics for "the discovery of neutrino oscillations, which shows that neutrinos have a mass." This was the first particle physics evidence that the Standard Model is incomplete.

On 23 February 1987, three neutrino detectors (Super Kamiokande, IMB, and Baksan) registered 24 neutrinos within less than 13 seconds from SN 1987A, a nearby supernova in the Large Magellanic Cloud, approximately 168 000 light years away.

Another significant achievement was obtained on 23 February 1987, when three neutrino detectors (Super Kamiokande, IMB, and Baksan) registered altogether 24 neutrinos within less than 13 seconds from SN 1987A, a nearby supernova in the Large

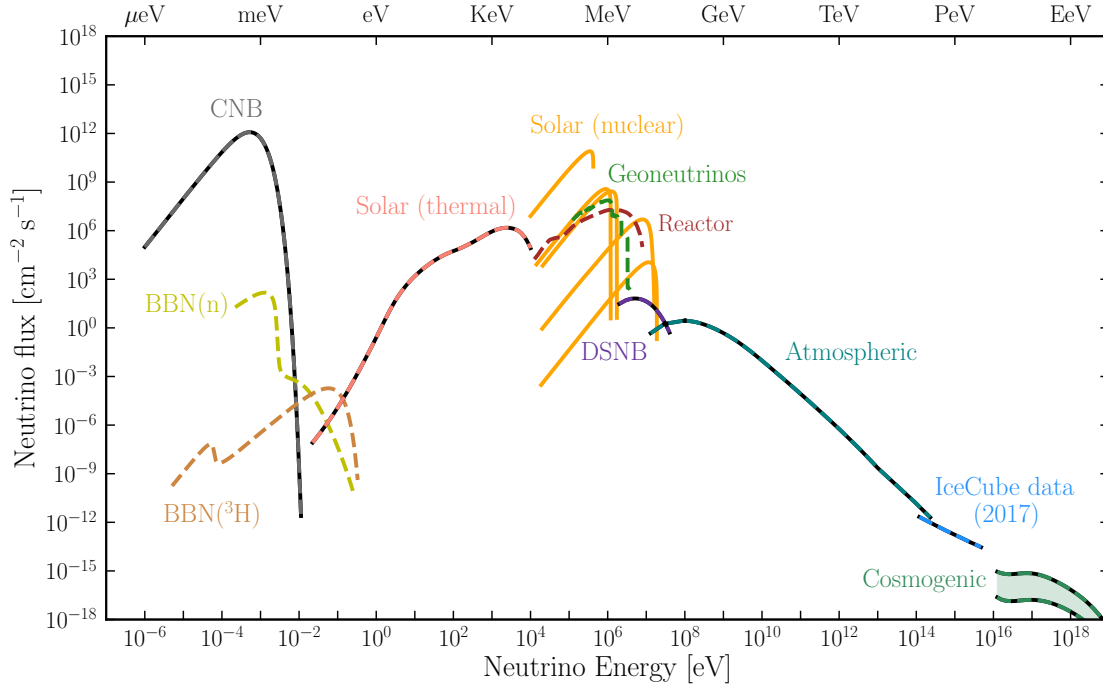


Figure 1.1: The total neutrino spectrum at Earth, integrated over directions and summed over flavors. Solid lines are for neutrinos, dashed or dotted lines for antineutrinos, superimposed dashed and solid lines for sources of both ν and $\bar{\nu}$. Figure adapted from [482].

Magellanic Cloud, approximately 168 000 light-years away [239]. This revealed the first neutrino source ever observed beyond our solar system and represented a step toward resolving the supernova explosion mechanism.

The second breakthrough for neutrino astronomy arrived in December 2012, when the most energetic neutrino ever discovered ($E_\nu \sim 10^{15}$ eV) smacked into the IceCube detector in Antarctica [8]. This event marked a significant milestone by opening a new window into the Universe and triggering a new era of exploration into the mysteries of high-energy cosmic phenomena.

1.2 Neutrino sources and fluxes

Today, we know that neutrinos are overwhelmingly present in the Cosmos. They are the second most common particle in the Universe, after photons. The various sources of neutrinos around us may be broadly divided into two groups: natural and human-made sources. Figure 1.1 shows the total neutrino flux as a function of neutrino energy from various neutrino sources, spanning more than 20 decades in energy and 30 decades in flux. Starting from the lowest energies, we find [482]:

- **Cosmic neutrino background (CNB):** are neutrinos that have been produced in the early Universe and represent today a remnant background somewhat analogous to the cosmic microwave background (CMB) photons (grey line in Fig. 1.1). When the Universe was very young and hot, all the fundamental particles composed a hot plasma in which the reaction rates of various particles were in thermal equilibrium. As the Universe expanded and cooled down, such equilibrium could not be maintained. After it was ~ 1 s old, and the temperature fell below a few MeV, the neutrinos decoupled from the thermal bath. As a result, a relic background of very low energy neutrinos was left, with a present-day temperature of $\simeq 1.945$ K $\simeq 0.17$ meV. The current density of neutrinos plus antineutrinos for each mass eigenstate is predicted to be $n_{\nu_i} + n_{\bar{\nu}_i} = 112$ cm $^{-3}$, which summed over the three species is comparable to the density of photons in the CMB ~ 410 cm $^{-3}$.
- **Solar neutrinos:** are primarily neutrinos produced in the nuclear fusion reactions that fuel the Sun (orange lines in Fig. 1.1). The Sun generates energy via two fusion chains, the p-p and the CNO chains. We have shown in Eq. (1.4) the p-p I chain. There are two other branches of the p-p chain, as well as a *pep-reaction*, which are much less likely to occur compared to the main channel. Roughly 3% of the total solar power is emitted in neutrinos with energies ranging below ~ 0.4 MeV to almost 19 MeV. The total flux reaching the Earth is about 6×10^{10} cm $^{-2}$ s $^{-1}$. In addition to producing neutrinos through fusion reactions, several other mechanisms can create neutrinos with typical thermal energies in the core of the stars (pink line in Fig. 1.1). These processes involve the production of neutrino pairs in Compton-like interactions ($\gamma e \rightarrow e \nu \bar{\nu}$), Bremsstrahlung from nuclei ($Ae \rightarrow Ae \nu \bar{\nu}$), plasmon decay ($\gamma^* \rightarrow \nu \bar{\nu}$) and pair annihilation ($e^- e^+ \rightarrow \nu \bar{\nu}$). In the case of the Sun, which has a central temperature of $T_{\text{core}} \simeq 1.3$ keV, the luminosity associated with these thermal neutrinos is negligible. However, these processes become increasingly important and can even determine the later stages of the evolution in the case of more massive stars.
- **Geoneutrinos:** are neutrinos produced in the decays of unstable, radioactive elements – mostly uranium ^{238}U , thorium ^{232}Th , and potassium ^{40}K —inside the Earth, with a flux exceeding 10^{25} s $^{-1}$. These same decays also generate heat, which makes up some portion (thought to be about 60%) of the geothermal heat flow. The amount of geoneutrinos produced depends upon the abundance of radioactive materials present within the Earth. While we know their amount and distribution within the Earth’s crust, direct information from its interior is limited to depths of approximately 10 km. These uncertainties about the Earth’s radioactive content translate into uncertainties about the amount of geothermal heat and geoneutrinos generated by radioactive decay. As a result, measurements of geoneutrinos hold the potential to offer insights into the nature of Earth’s radio-

activity.

- **Reactor neutrinos:** are neutrinos produced in nuclear reactors. These are the strongest sources of terrestrial antineutrinos, with $\bar{\nu}_e$ coming from the β -decay of the fission products. The neutrino energies peak at around 3 MeV and extend to about 8 MeV. Unlike other human-made sources, like accelerators, the neutrino flux from reactors is isotropic.
- **Supernova neutrinos:** are neutrinos produced when a star with a mass larger than about $8 M_{\odot}$ at the end of its life explodes like a supernova. A considerable amount of energy, of the order of 3×10^{53} erg, is released when the star's core collapses. Almost 99% of this is emitted in neutrinos that escape in a burst lasting several seconds and with typical energies of about 10 to 30 MeV. In these spectacular processes, neutrinos have a predominant role. In addition to endeavors aimed at detecting neutrinos that will be emitted during the next nearby supernova explosion, such as the one that occurred in 1987 within the nearby Large Magellanic Cloud galaxy, it is also important to try to detect the cumulative neutrino background resulting from all the past supernovae that exploded in the Universe. This represents the diffuse supernovae neutrino background (DSNB, purple line in Fig. 1.1).
- **Atmospheric neutrinos:** are neutrinos that originate from the decay of hadrons produced when energetic CRs hit the nuclei in the atmosphere of the Earth. In general, the spectrum of these neutrinos peaks at 1 GeV and extends up to about a few hundred GeV.
- **High-energy astrophysical neutrinos:** are neutrinos in the TeV-PeV energy range that have been detected by the IceCube neutrino observatory since 2013 in the form of a diffuse and isotropic flux (blue line in Fig. 1.1). The origin of these neutrinos has not been pinpointed yet. However, we know they must be produced as secondaries in the interactions of CRs in violent and explosive events occurring in the Universe. We will discuss better their production mechanisms in Sec. 2.2 and the candidate sources of this flux in Sec. 2.3.
- **Cosmogenic neutrinos:** are neutrinos expected to be created in the interactions of ultra-energetic CRs ($E \sim 10^{20}$ eV) with the radiation or with the gas that they encounter while they exit from the sources of production, as well as with the background radiations of the Universe (CMB and extra-galactic background light) that they travel through when they propagate from the sources up to us. Given the very low predicted flux, detecting these neutrinos necessitates much larger detectors than those currently available. This goal should be achieved with the next generation of radio facilities, such as the Giant Radio Array for Neutrino

Detection (GRAND) [54], or the Antarctic Ross Ice-Shelf ANtenna Neutrino Array (ARIANNA) [76], and the detector from space POEMMA (Probe of Extreme Multi-Messenger Astrophysics) [371].

1.3 Neutrino oscillations

As we have seen, active neutrinos come in three families. This was determined with great accuracy in 1989 at the LEP collider at CERN through studies of Z_0 boson decay: $Z_0 \rightarrow \nu_\alpha + \bar{\nu}_\alpha$ [510]. A fourth active neutrino is not allowed by the invisible width of the Z boson, to which it would contribute as much as one active neutrino. The present best value for this quantity is $N_\nu = \Gamma_{\text{inv}}/\Gamma_{Z \rightarrow \nu\bar{\nu}} = 2.9963 \pm 0.0074$, where $\Gamma_{Z \rightarrow \nu\bar{\nu}} = 167$ MeV is the theoretically expected rate for decay into a given neutrino flavor and is accurately calculable in the Standard Model.

Since neutrinos have masses, two bases can be used to describe them: the flavor basis, ν_α , $\alpha = e, \mu, \tau$, in which each neutrino is associated with the corresponding charged lepton and the mass basis, ν_i , $i = 1, 2, 3$, in which each neutrino has a definite mass. The two bases, as required by probability conservation, are related by a unitary matrix U , the so-called Pontecorvo-Maki-Nakagawa-Sakata (PMNS) matrix:

$$|\nu_\alpha\rangle = \sum_{i=1}^3 U_{\alpha i}^* |\nu_i\rangle \quad (1.6)$$

which can be parametrized in terms of three mixing angles θ_{12} , θ_{13} , θ_{23} and a CP-violating phase δ , $U = U(\theta_1, \theta_2, \theta_3, \delta)$. In the presence of this mixing and non-degenerate neutrino masses, neutrino oscillations can occur. If, for example, we assume that neutrinos are produced with the same momentum \vec{p} , then it is clear that different neutrino mass states will have slightly different energies $E_i = \sqrt{m_i^2 + p^2}$. The basic picture is that, in production and detection, neutrinos are described by flavor states, which are eigenstates of weak interaction. These represent a coherent superposition of massive states which have slightly different masses. The coherence is a key condition that needs to be satisfied at production, detection, and during the propagation to have neutrino oscillations. This means that the uncertainty on the neutrino energy σ_E and momentum σ_p at production and detection must be much larger than the difference between the energies of neutrino mass states: $\sigma_E \gg \Delta E = E_i - E_j$, or $\sigma_p \gg \Delta p = p_i - p_j$ (in case neutrinos were produced with the same energy, for example). If E and p were measured very accurately, one could tell which physical neutrino mass state is emitted, and oscillations would disappear. The latter can also be understood by invoking the Heisenberg uncertainty principle: a very small uncertainty on the measurement of the momentum $\sigma_p \ll \Delta p$ implies a very large uncertainty σ_x of the spatial coordinate

where the neutrino is created. When such σ_x becomes larger than the typical oscillation length, it becomes impossible to observe any oscillation pattern [260].

Another source of decoherence is given by the wave packet separation during the propagation. The wave packets associated with each mass state propagate with different group velocities $v_i = p_i/E$. In the ultra-relativistic limit, the difference between these velocities is $|\Delta v_{ij}| \simeq c|\Delta m_{ij}|/2E^2$. This implies that the wave packets of the different mass components will tend to separate from each other as they propagate. Their wave functions will no longer significantly overlap after they travel a distance l_{coh} such that $|\Delta v_{ij}|l_{\text{coh}}/c = \sigma_x$. When this happens, the different ν_i cannot interfere to produce neutrino oscillations, which become averaged out. The associated coherence length is:

$$l_{\text{coh}} = \frac{c\sigma_x}{|\Delta v_{ij}|} \simeq 2 \times 10^9 \text{ km} \frac{\sigma_x}{10^{-10} \text{ m}} \left(\frac{E_\nu}{\text{GeV}} \right)^2 \frac{10^{-4} \text{ eV}^2}{\Delta m_{ij}^2}. \quad (1.7)$$

The size of the wave packet σ_x must be determined by the coherence size of the production process, which is a general property of the wave packets of all particles created in some process.

Let us now calculate the probability of finding a neutrino created in a given flavor state ν_α to be in another flavor state ν_β . Each neutrino mass state evolves in time according to the following equation:

$$|\nu(t)\rangle = \sum_{i=1}^3 U_{\alpha i}^* e^{-iE_i t} |\nu_i\rangle. \quad (1.8)$$

The probability of transition from ν_α to ν_β at time t is then obtained by projecting the state $|\nu(t)\rangle$ in the ν_β direction as:

$$P_{\nu_\alpha \rightarrow \nu_\beta}(t) = |\langle \nu_\beta | \nu(t) \rangle|^2 = \left| \sum_{i=1}^3 U_{\beta i} U_{\alpha i}^* e^{-E_i t} \right|^2 \quad (1.9)$$

where we have used the fact that $\langle \nu_i | \nu_j \rangle = \delta_{ij}$. In all experimentally relevant situations, neutrinos are highly relativistic ($m_i \ll E_i$), so we can make the following approximations:

$$E_i = p + \frac{m_i^2}{2p} \Rightarrow \Delta E_{ij} = E_i - E_j = \frac{\Delta m_{ij}^2}{2p} \simeq \frac{\Delta m_{ij}^2}{2E} \quad (1.10)$$

and write the neutrino flavor oscillations as ²

$$P_{\nu_\alpha \rightarrow \nu_\beta}(L, E) = \sum_{ij} U_{\alpha i}^* U_{\beta i} U_{\alpha j} U_{\beta j}^* e^{-i \frac{\Delta m_{ij}^2 L}{2E}}, \quad (1.11)$$

where we have defined $\Delta m_{ij}^2 = m_i^2 - m_j^2$, and approximated $p \simeq E$ and $t = L$. It is apparent from this formula that oscillations between one flavor and another are possible only if there is leptonic mixing ($U \neq I$) and at least two neutrinos have masses. One substitutes U with its complex conjugate U^* for antineutrinos.

It is important to stress that the coherence at production and detection of neutrinos is usually satisfied extremely well due to the tininess of neutrino masses. On the other hand, the coherence propagation condition is satisfied very well for all but astrophysical and cosmological neutrinos that travel long distances. This means that for astrophysical neutrinos, the oscillatory behavior does not hold for distances longer than the coherence length l_{coh} , which is usually $l_{\text{coh}} \ll L$. In this case, the oscillations get averaged out in Eq. (1.11), leading to an effectively constant measurable probability:

$$\langle P_{\nu_\alpha \rightarrow \nu_\beta} \rangle = \sum_i |U_{\alpha i}|^2 |U_{\beta i}|^2. \quad (1.12)$$

From this, it follows immediately that if the flux of the neutrino flavor β emitted at the surface of the source is $\phi_{\nu_\beta}^0$, the flux at Earth will be:

$$\phi_{\nu_\beta} = \sum_\alpha \langle P_{\nu_\alpha \rightarrow \nu_\beta} \rangle \phi_{\nu_\alpha}^0. \quad (1.13)$$

The values of elements of the U matrix are known with certain accuracy and continue to be refined in new experiments; see, e.g., Ref. [167]. From Eq. (1.12), it is clear that the experiments looking for astrophysical neutrinos from sources at large distances are sensitive to the mixing parameters but are not sensitive to the neutrino mass differences. Furthermore, we can use Eq. (1.13) to determine the neutrino flavor ratios on Earth, provided the ratio at the source is known. If, for example, neutrinos and antineutrinos are leaving the source with the following fractions: $f_{\nu_\tau} = 0$, $f_{\nu_\mu} = 1 - f_{\nu_e}$, then their flavor ratio at Earth is given by Eq. (1.13):

$$\begin{cases} f_{\nu_e} \simeq 0.18 + 0.36 f_{\nu_e}^0 \\ f_{\nu_\mu} \simeq 0.44 - 0.25 f_{\nu_e}^0 \\ f_{\nu_\tau} \simeq 0.38 - 0.11 f_{\nu_e}^0 \end{cases} \quad (1.14)$$

²We note that in deriving Eq. (1.11) we assumed that the mass states are described by plane waves, which extend with the same amplitude over the whole space-time, and are not appropriate to describe localized particles. However, it can be shown that performing a more accurate analysis using wave packets instead of plane waves to allow for a spread in the values of momenta and energies describing the neutrino state would lead to the same expression of the probability, as long as the coherence of the superposition between different mass eigenstates is not lost. See, e.g., Ref [260].

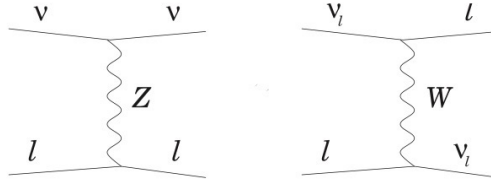


Figure 1.2: Neutral and charged-current interactions.

For the value $f_{\nu_e}^0 = 1/3$ expected from pion decays in the source, we obtain an approximate equality of the detection probabilities of the three neutrino flavors at the detection point, $(f_{\nu_e} : f_{\nu_\mu} : f_{\nu_\tau}) \simeq (1 : 1 : 1)$.

1.4 Neutrino interaction with matter

Neutrinos can interact in two ways: through charged current (CC) and neutral current (NC) interactions, mediated by the charged W^\pm and neutral Z^0 bosons, respectively (Fig. 1.2). In the NC case, the initial and final states coincide, and only a momentum transfer between the neutrino and the target particle is possible. At the same time, for CC interactions, there is also the appearance of a charged lepton in the final state. Neutrinos interact with both leptons and nucleons, but since this thesis centers on very energetic neutrinos, we will focus only on neutrino-nuclei interactions, whose cross-section is much larger than that of neutrino-lepton interactions.

In general, we must consider both CC and NC interactions of neutrinos and anti-neutrinos hitting free nucleons or nucleons bounded in nuclei. Because of lepton flavor conservation, CC neutrino interaction will produce a negatively charged lepton in the final state, while antineutrino interactions will produce positively charged leptons. To produce the lepton in the final state, neutrinos must possess energy above a threshold which, in the laboratory system, is:

$$s = (E_\nu + M)^2 \gtrsim (m_l + M)^2 \quad \Rightarrow \quad E_\nu > E_{\text{th}} = \frac{m_l^2 + 2Mm_l}{2M} \quad (1.15)$$

where M and m_l are the nucleon and lepton masses, respectively. For ν_e , $E_{\text{th}} \sim 0$, while for ν_μ and ν_τ , it is $E_{\text{th}} \sim 0.11$ GeV and ~ 3.5 GeV, respectively.

All the interaction processes that the neutrinos can undergo can be categorized in general as: *elastic*, where the final state contains the same number and type of particles as the initial state, *quasi-elastic*, where the final state contains particles different from the initial ones but with the same number, and *inelastic*, where energy is converted to create new particles. See Ref. [179] for an exhaustive discussion of all possible channels for neutrino interactions. Here, we briefly present the three different interaction

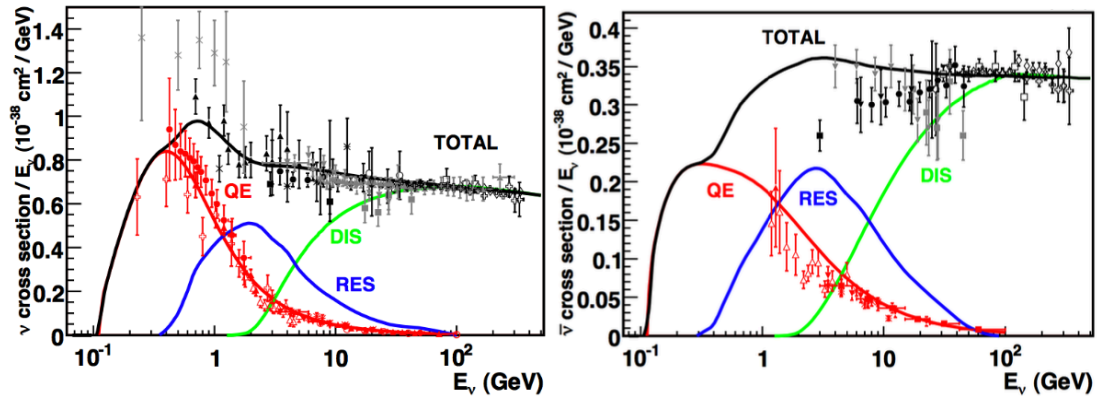


Figure 1.3: The plots show the neutrino (left) and antineutrino (right) cross-section as a function of the neutrino energy for the CC interaction. Both the total and the individual contributions from the different processes, quasi-elastic (QE), resonant production (RES), and deep inelastic scattering (DIS), are shown. Figure from [422].

subtypes that dominate in different kinematical regimes for $E_\nu \gtrsim 100$ MeV, where the nucleons do not look like point-like objects for the neutrinos (see Fig. 1.3):

- For $E_\nu \lesssim 1$ GeV we are in the *quasi-elastic scattering* (QE) regime, where the cross-section is dominated by the following CC interactions with nucleons: $\nu_e + n \rightarrow e^- + p$ and $\bar{\nu}_e + p \rightarrow e^+ + n$. In this case, the nucleon is not broken up. The relevant energies of the incoming neutrino go from a few hundred MeV to a few GeV. The process is denoted as *elastic scattering* for NC interactions at low energies since the exchanged Z_0 boson leaves the initial nucleus intact.
- For $1 \text{ GeV} \lesssim E_\nu \lesssim 10 \text{ GeV}$, the neutrino energy is still not enough to break up the nucleon, and the cross-section is dominated by *resonant* (RES) processes. In this regime, neutrinos can excite the target nucleon to a resonance state. The resultant baryonic resonance (e.g., Δ^+) decays to various possible mesonic final states, producing combinations of nucleons and mesons.
- For $E_\nu \gtrsim 5 \text{ GeV}$, neutrinos undergo *deep inelastic scattering* (DIS) with the nucleon. Given enough energy, the neutrino can resolve the individual quark constituents of the nucleon, and the scattering breaks the nucleon up, producing a bunch of hadronic debris. In an NC DIS interaction, a neutrino of the same flavor as the incoming neutrino is emitted, while for CC DIS, a charged lepton with the same flavor as the initial neutrino leaves the interaction vertex.

Even though interactions with hadrons generally have a larger cross-section than with leptons, there is one peculiar situation in which the neutrino interactions can be

largely enhanced: in the presence of an s-channel resonance by a W boson exchange. This is called *Glashow resonance* and it describes an anti-electron neutrino scattering with an electron by the exchange of an on-shell W boson, i.e. when $s = (p_{\bar{\nu}_e} + p_e)^2 \simeq M_W^2$ [206]. Considering that the target electron is at rest, this corresponds to an electron neutrino energy $E_{\bar{\nu}_e}^{\text{WR}} = M_W^2/2m_e \simeq 6.3$ PeV. This process can provide an interesting channel for detecting PeV electron antineutrinos of astrophysical origin, and indeed an event of this type has recently been observed in the IceCube detector [4].

1.5 Neutrino detection

After a neutrino undergoes an interaction process, one needs to detect some of the particles produced in the interaction. The approach to achieve this detection varies depending on factors such as the energy of the neutrinos and the neutrino flavor that one is aiming to detect. Other factors include the level of radioactivity in the detector materials, which must be minimized to reduce the background, the desired precision in measuring the energy or direction of the detected particles, and the intensity of the neutrino flux that needs to be measured. These factors collectively determine the optimal design and size of the neutrino detector. As we have seen in Sec. 1.1, the *radiochemical technique* was the first method used to study low-energy solar neutrinos. However, such detectors are only helpful in measuring the total neutrino rate. There is no information on the energy (just that it needs to be above the threshold), the direction of the original neutrino, or the interaction time. Other types of detectors exploit *liquid scintillators*, which allow for precise determination of location and energy, but only for low-energy neutrinos, e.g., those coming from reactors.

1.5.1 Cherenkov detectors

In this thesis, we are interested in neutrinos with energies $E_\nu \gtrsim 100$ GeV, and of astrophysical origin. Currently, large volume ice and water Cherenkov detectors are employed to observe them since transparent media are crucial to reconstruct the direction of the neutrino sources. The exploited detection technique consists of collecting photons from *Cherenkov radiation*. Such radiation is produced by charged particles that travel faster than light in a medium, namely when the particle velocity is $v > c/n$, where n is the refractive index of the medium. This condition corresponds to the particle having energy larger than the threshold $E_{\text{th}} = m/\sqrt{1 - 1/n^2}$, where m is the mass of the particle (in water, where $n = 1.33$ this threshold is $E_{\text{th}} \simeq 0.78$ MeV for an electron, and $E_{\text{th}} \simeq 160$ MeV for a muon). Particles exceeding their respective threshold energies emit Cherenkov radiation, forming a blue/UV light cone. The angle of this cone is $\theta_{\text{Ch}} = \arccos(c/vn)$ (it is $\theta_{\text{Ch}} \simeq 41^\circ$ in the ultra-relativistic limit). The points where

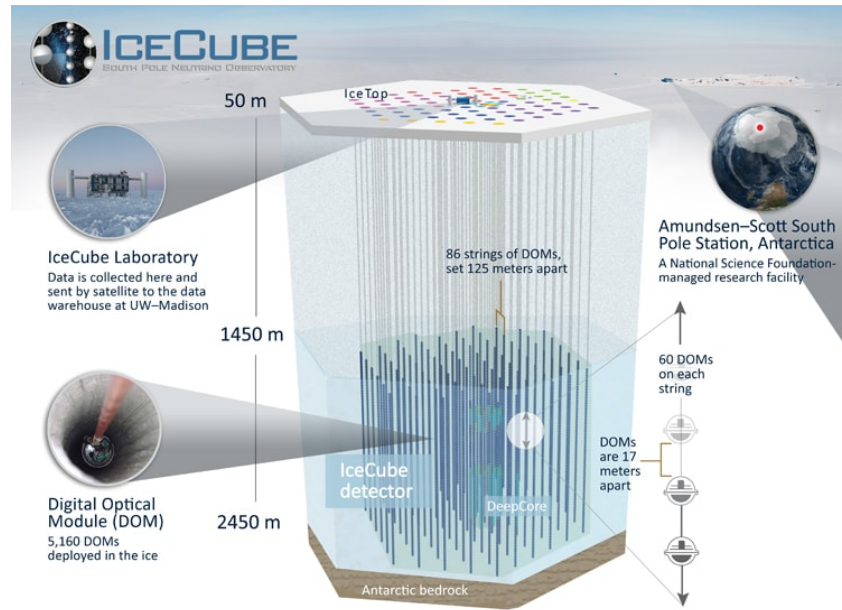


Figure 1.4: A schematic view of the IceCube Neutrino Observatory. Credit: IceCube/NSF

these cones intersect the walls of a detector create Cherenkov rings. By measuring the light captured in photo-multiplier tubes (PMTs) placed around the detector, one can reconstruct the motion's direction of the charged particle and estimate its energy. This information is beneficial when the direction of the particle is correlated with the direction of the neutrino that produced it. The water Cherenkov technique allows observing electron scattering events, inverse β -decays, and tracks of muons produced in ν_{μ} CC interactions.

The cross-section for neutrino-nucleon interactions for neutrino energies in the TeV-PeV range is found to be $\sigma_{\nu N} \sim 10^{-36} - 10^{-33} \text{ cm}^2$ [25]. From this one can roughly estimate the probability for a PeV neutrino to interact when crossing a nucleon column density N of one km of water to be of order $P \sim N\sigma_{\nu N} \simeq N_A \text{ cm}^{-3} 1\text{km} \sigma_{\nu N} \simeq 6 \times 10^{-5}$, where $N_A = 6.022 \times 10^{23}$ is the Avogadro number. Hence, one can see that to observe a few to a few tens of neutrino events per year above 100 TeV, detector volumes of $\sim \text{km}^3$ size are necessary. To this purpose, giant detectors exploiting the Cherenkov technique have been built using deep sea water (ANTARES Observatory [41] and KM3NeT-ARCA [40] in the Mediterranean), deep lakes (GVD detector in Lake Baikal in Siberia) [66] and the Antarctic ice (the IceCube detector in the South Pole) [14].

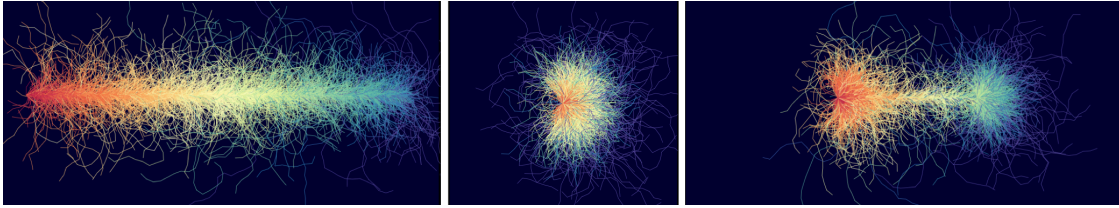


Figure 1.5: The typical signatures of interaction observable inside the IceCube detector. The images have been obtained from a simulation of Cherenkov light propagation in the ice from [2]. There is a track-like event (left), a shower-like event (middle), and a double-bang event (right). The color scheme refers to arrival times: red denotes earlier photons, and blue denotes those registered later.

1.5.2 Detection of neutrinos with IceCube

In this section, we focus, in particular, on the IceCube Observatory and describe the detector properties and the signatures that various flavors of neutrinos leave upon interaction. The detection principle is very similar to the other water detectors we have mentioned and are currently taking data.

1.5.2.1 IceCube properties

IceCube is a large-scale detector consisting of 1 cubic kilometer of instrumented ice located near the geographic South Pole in Antarctica. It has been operating in full configuration since 2011. It consists of 5160 digital optical modules (DOMs) deployed in the transparent ice at depths between 1450 m and 2450 m below the surface. The primary in-ice array consists of 78 strings with a vertical separation of the DOMs of 17 m and a horizontal spacing of 125 m [14]. The strings are mostly distributed in a hexagonal shape. Such a design was chosen to fulfill the scientific goal of detecting astrophysical neutrinos in the energy range of $\mathcal{O}(\text{TeV})$ – $\mathcal{O}(\text{PeV})$.

Additionally, there is a denser instrumented volume, the *DeepCore*, whose design is optimized for detecting neutrinos with energies from 10 GeV to 100 GeV. Finally, located on the surface of the ice, we find *IceTop*. This consists of 81 stations with 162 ice-filled tanks instrumented with PMTs that detect Cherenkov radiation from CRs air showers. It is sensitive to CRs with energies in the PeV–EeV range. Furthermore, it is also used as a partial veto for detecting downward-going neutrinos with IceCube. An illustration of the detector is shown in Figure 1.4.

1.5.2.2 Event topologies

An observed neutrino at IceCube is called an *event*. The topology of neutrino events can vary depending on the neutrino flavor, its energy, and the type of interaction in the

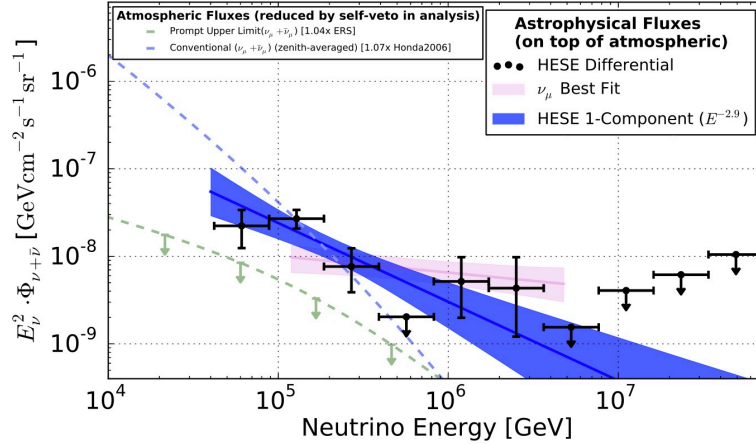


Figure 1.6: Summary of diffuse neutrino observations (per flavor) by IceCube. The black points show IceCube’s measurement of the cosmic $\nu + \bar{\nu}$ flux. The pink line and area indicate the best-fit and 1σ uncertainty range of a power-law fit to the $\nu_\mu + \bar{\nu}_\mu$ data. The blue band shows the 1σ uncertainties on the result of a single power-law fit to the HESE data. Figure taken from [13].

ice. The light deposition patterns generally fall into two sub-groups: track-like events and shower-like events. The names refer to the shape of the events, i.e., a track has a long track-like shape, while a shower is shorter and has a more round shape. We can summarize the various interactions as follows [2] (see Fig. 1.5):

- *Track-like events:* are generated by muons produced in CC ν_μ interactions. These muons can travel very long distances through the water or ice, producing Cherenkov light along their tracks, besides losing energy by ionization or collisions with nuclei. They can even be detected when they are produced outside the detector and then cross it, in which case they are referred to as *through-going muons*. These muon tracks allow to achieve a good angular resolution, even better than 1° , but the energy reconstruction may be poor if only part of the track is observed, in which case just a lower bound on it can be set.
- *Shower-like events:* are generated in NC interactions of all neutrino flavors, as well as in CC interactions of ν_e (all energies) and ν_τ ($E_\nu \lesssim 100$ TeV). These showers typically extend a few meters inside the detector, and their observation provides a good energy reconstruction. Nevertheless, they have a very poor directionality, with the typical shower angular resolution for IceCube being about 10° for energies above 100 TeV.
- *Double bang events:* This is a peculiar signature that can be obtained with very high energy ν_τ . Here, the ν_τ CC interaction produces a τ lepton, and the recoiling nucleus produces a hadronic cascade, leading to the first bang. If the energy of the

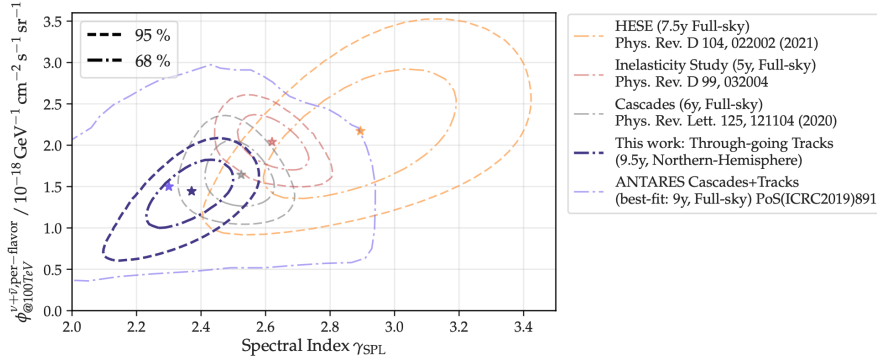


Figure 1.7: Summary of astrophysical neutrino-flux measurements. Figure taken from [21].

τ is high enough, it may travel a significant distance before it decays to produce the second bang, the latter originating from the shower produced by the τ decays into hadrons (or an electron). The decay length of a τ is 50 m (E_τ/PeV) so that the two showers can be separated in space already for energies $E_\tau \gtrsim 100 \text{ TeV}$.

1.5.2.3 IceCube data

Using multiple years of operation, IceCube has detected a diffuse flux of astrophysical neutrinos in the energy range from $\sim 100 \text{ TeV}$ to $\sim 10 \text{ PeV}$ (see Fig. 1.6). IceCube records events at a 2.5–2.9 kHz rate. Most of these events are muons originating from CR air showers, traversing the ice, and reaching the IceCube’s depth. Approximately one in a million recorded events originates from a neutrino interaction. Despite this seemingly low rate, it allows the accumulation of a huge sample of high-energy neutrinos (10^5 yr^{-1}), mainly of atmospheric origin. Out of these, roughly $\sim 30 \text{ yr}^{-1}$ are identified with high confidence as having astrophysical origin [10]. Indeed, above $\sim 300 \text{ TeV}$, the atmospheric neutrino flux reduces to less than one event per year, and thus events in that energy are identified as cosmic in origin.

By measuring the high-energy astrophysical neutrinos in various detection channels, high-energy starting events (HESE, the neutrino interactions that occur within the instrumented volume), shower-type events, and track-like events, different models have been fitted to the data. Currently, the observed flux is well described by a single power law parametrization [21, 3, 23]:

$$\Phi_{\text{astro}}^{\nu+\bar{\nu}}(E_\nu) = \phi_{\text{astro}} \left(\frac{E_\nu}{100 \text{ TeV}} \right)^{-\gamma_{\text{SPL}}} \quad (1.16)$$

where ϕ_{astro} is the normalization for each neutrino flavor at $E_\nu = 100 \text{ TeV}$ and γ_{SPL} the spectral index of the single power-law. The best-fit parameters for different analyses can be visualized in Fig. 1.7.

Neutrinos as cosmic messengers

In this Chapter, we provide an overview of multimessenger astronomy, specifically focusing on high-energy neutrinos as cosmic messengers. We delineate the primary mechanisms responsible for neutrino production in astrophysical contexts, particularly the hadronic and photo-hadronic interactions involving accelerated charged particles and surrounding matter or radiation. Additionally, we explore the correlations between neutrinos, cosmic rays, and photons, highlighting their intricate interplay. We conclude by identifying key transient sources that hold promise for high-energy neutrino observations, forming the foundation for our subsequent studies of specific sources.

2.1 Multi-messenger astronomy

Soon after the 1956 discovery of the neutrino, the idea emerged that it would represent an ideal astronomical messenger. Having essentially no mass and no electric charge, neutrinos are very similar to photons, except for one rather important attribute: their extremely feeble interactions with matter. Such property is at the same time a blessing and a curse: on the one hand, it allows neutrinos to travel from the edge of the Universe without absorption and with no deflection by magnetic fields and reach us unscathed from cosmic distances; on the other hand, their weak interactions make them very difficult to detect, and requires enormous detectors, as we have already seen in the previous Chapter.

Since Galileo invented the telescope, over the last four hundred years, our knowledge of the Universe has been acquired mainly via the detection of *optical* photons from different astronomical objects. In the 20th century, the observational window on the Universe extended to the *radio*, *infrared*, *ultra-violet*, *X-ray* and *γ -ray* astronomy, thanks to the invention of more advanced ground-based telescopes and the launch of

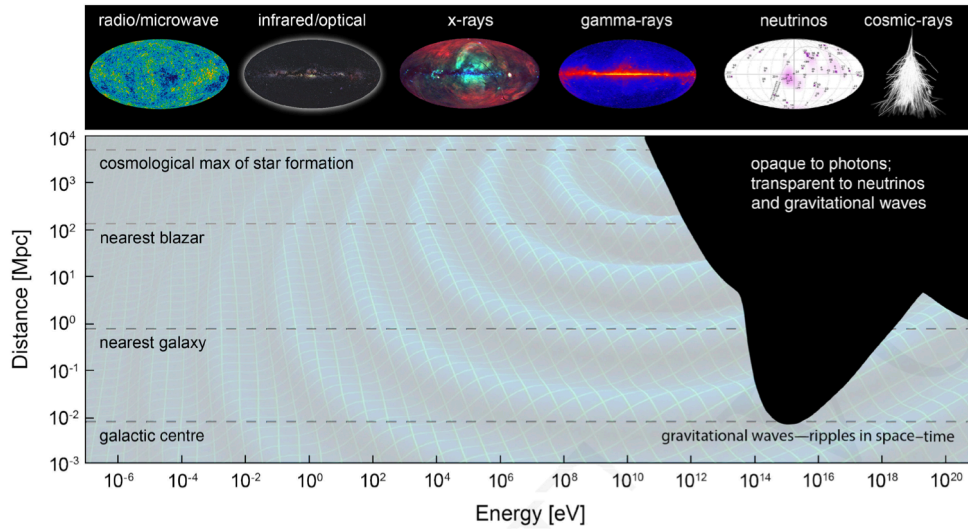


Figure 2.1: Distance horizon at which the Universe becomes opaque to electromagnetic radiation. Photons of the highest energy and CRs get absorbed over short distances, limiting our view of the most violent cosmic phenomena. However, gravitational waves and neutrinos can traverse the Universe unimpeded, rendering them appropriate tools for exploring the high-energy aspects of the Cosmos. Figure taken from [75].

satellites equipped with X-rays and γ -rays detectors outside the atmosphere, in orbit around the Earth.

However, if we try to observe the Universe even at higher energies, there is an insurmountable problem we face: our visible horizon is limited to typical distances of our galactic center. Indeed, as can be seen in Fig. 2.1, the Universe is opaque to electromagnetic radiation with energies $E_\gamma \gtrsim 10^{15}$ eV coming from sources farther than a few tens of kiloparsec. Such radiation becomes completely absorbed during its long journey through space due to the pair-production process $\gamma\gamma \rightarrow e^+e^-$ on the CMB and the extragalactic background light (EBL). This absorption limits our ability to receive direct information from distant or densely populated regions of the Cosmos where the most violent astrophysical phenomena occur. Also, CRs are an unusable messenger if we are interested in obtaining prompt information about the source producing them due to deflection by intergalactic magnetic fields they experience during the propagation to Earth.

The era in which photons were the only messenger particles exploited to learn about the Universe outside our Solar system ended in 2013, with the discovery of an astrophysical flux of high-energy neutrinos [6]. A further breakthrough occurred in 2015 when another element was added to the roster of cosmic messengers: gravitational waves (GWs), which were directly detected from the merger of two black holes by the Laser

Interferometer Gravitational-Wave Observatory (LIGO) [31]. These events marked the birth of *multimessenger astronomy*, which has the great potential of providing complementary information carried by all four messengers about the structure of astrophysical objects and physical processes in their interiors.

The viability of time-domain multimessenger astronomy was successfully demonstrated through coordinated observation campaigns in 2017 and 2018. These efforts resulted in the discovery of GWs arising from the neutron star merger event GW170817, associated with a short GRB (GRB 170817A) and a kilonova event (AT 2017gfo) [29, 30]. The detection of electromagnetic counterparts across various wavelengths confirmed the correlation between neutron star mergers, short GRBs, and kilonova emissions. Another significant achievement in 2017 was the joint detection of the high-energy neutrino event IceCube-170922A and the flaring blazar TXS 0506+056 [11], being the first time that a known source was shown to be associated with high significance (at the $\sim 3\sigma$ level) to an astrophysical high-energy neutrino (see Fig. 2.2 for a timeline of significant milestones in the neutrino astronomy).

Both these events showcase the immense potential inherent in multimessenger approaches, which hopefully will enable us to address many of the key questions still open in astrophysics. One of these questions concerns the origin of CRs. Identifying their sources and understanding the mechanism responsible for their acceleration is one of the most intriguing puzzles that has continued to engage the scientific community since their discovery in 1912. In what follows, we discuss the production of IceCube neutrinos, the connection that it is believed to exist with ultra-high energy CRs, and the isotropic gamma-ray background detected by the Fermi satellite.

2.2 High-energy neutrino production

There is a widely accepted hypothesis that neutrinos currently detected by IceCube are produced in the astrophysical sources responsible for the acceleration of high-energy CRs (see Chapter 3). A simple reason for this is that we constantly observe the atmospheric neutrinos, which stem from interactions between CRs and the atmosphere of the Earth. Similarly, if the sites where CRs are accelerated, or the surrounding environment have sufficient target material to make CR interaction more efficient, they could represent potentially observable sources of high-energy neutrinos. Atmospheric neutrinos mainly originate from meson decays, like pions and kaons. These mesons are strongly suppressed at very high energies because of their interaction with the highly dense atmosphere, which reduces the atmospheric neutrino flux. On the other hand, if the densities inside the astrophysical sources producing neutrinos are low enough to give the mesons sufficient time to decay, then it is natural to expect that the flux of these neutrinos for energies $\gtrsim 10$ TeV would become observable at Earth.

In the following sections, we discuss the two main mechanisms via which we believe



Figure 2.2: A timeline of the main breakthroughs in neutrino astronomy, from Pauli’s neutrino prediction to the IceCube detection of high-energy neutrinos associated with three known sources: the blazar TXS 0506056, the Seyfert II galaxy NGC 1068, and the Galactic plane of the Milky Way. Credit: NASA/ESA/A.Van Der Hoeven/Nick Risinger.

high-energy neutrinos are produced: the hadronic mechanism (or pp interaction) when CRs interact with the gas and the photo-hadronic mechanism (or $p\gamma$ interaction) when they interact with the electromagnetic radiation.

2.2.1 The hadronic mechanism

The pp interaction takes place when a high-energy CR proton or, more in general, a nucleon in a CR nucleus collides with a proton at rest (or with a nucleus of mass number A , which may be approximately described as an ensemble of A nucleons) in the acceleration region or the surrounding medium. This collision produces a large number of pions (π) and, to a smaller extent, also to some heavier mesons (e.g. kaons K). The subsequent decay of these mesons will eventually lead to high-energy γ -rays and neutrinos. For pions, we have for example:

$$\begin{aligned} p + p &\rightarrow X + N_\pi(\pi^+ + \pi^- + \pi^0) \\ \pi^\pm &\rightarrow \mu^\pm + \nu_\mu/\bar{\nu}_\mu \\ \mu^\pm &\rightarrow e^\pm + \nu_e/\bar{\nu}_e + \bar{\nu}_\mu/\nu_\mu \\ \pi^0 &\rightarrow \gamma + \gamma, \end{aligned} \quad (2.1)$$

where N_π is the pion multiplicity, and X represents all the other hadrons produced in the interaction. When considering very high energies, the experimental observations show that the three types of pions, π^+ , π^- , π^0 , are produced in similar amounts (so that their multiplicities are similar) and that they carry a small fraction of the primary proton energy.

The kinematics governing these decay processes are such that in the pion's rest frame, each gamma ray originating from the π^0 decay carries 1/2 of the initial energy. Similarly, in the decay sequence of charged pions, each of the four light (anti)leptons carries away approximately 1/4 of the initial pion energy. For the neutrino production rate, one needs to treat separately the muon neutrinos resulting from the two-body pion decays, $\nu_\mu^{(1)}$, and the electron and muon neutrinos from the three-body muon decay, ν_e and $\nu_\mu^{(2)}$ (see Eq. (2.1)). For neutrinos produced by proton CRs we have [262]:

$$Q_{\nu_\alpha + \bar{\nu}_\alpha}(E_\nu) = \frac{dN_\nu}{dE_\nu dt} = N_N \int_{E_\nu}^{\infty} \frac{dE_p}{E_p} \sigma_{pp,inel}(E_p) Q_p(E_p) F_{\nu_\alpha}\left(\frac{E_\nu}{E_p}, E_p\right) [E^{-1} T^{-1}] \quad (2.2)$$

where $Q_p(E_p)$ is the proton differential rate (in units of $E^{-1}T^{-1}$), N_N is the column density of nucleons traversed by the emitted CRs as they exit from the source (in units of L^{-2}), and $\sigma_{pp,inel}$ is the inelastic cross section for the pp interaction, which is found to have a mild logarithmic energy dependence $\sigma_{pp,inel} \simeq (34.9 + 1.98L + 0.18L^2)$ mb, with $L = \ln(E_p/\text{TeV})$ [262]. The adimensional functions F_{ν_α} describe the yield of neutrinos

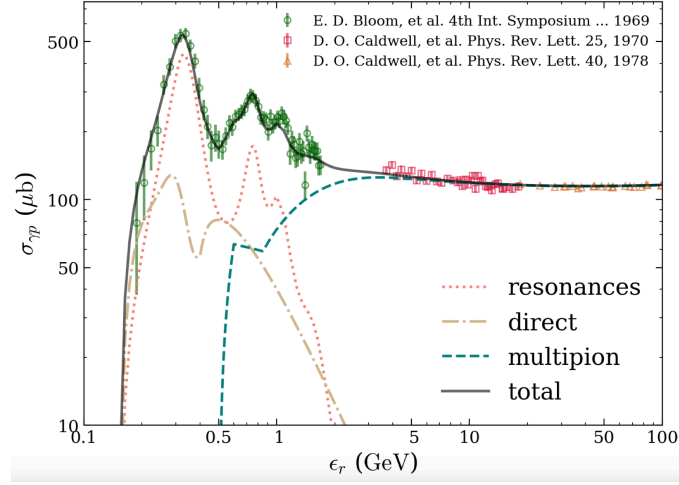


Figure 2.3: The cross section for inelastic scattering of photons by protons as a function of their relative energy ϵ_r . Figure from [153]

with energies E_γ from the interaction of a proton with energy E_p with the gas target. These functions have been parameterized in [262] from the results of simulations of pp interactions. For photons, there is an expression analogous to the one in Eq. (2.2) but in terms of a distribution F_γ . It is generally assumed that the typical pion energy is $E_\pi \simeq E_p/5$, and since the four particles resulting from the pion decays share similar amounts of energy, we have that $E_\gamma \simeq E_\pi/4 \simeq E_p/20$. One would similarly have $E_\gamma \simeq E_p/10$ for the neutral pions. But one needs to be careful with these simplistic estimates, since, as we have written above, the neutrinos resulting from the interaction of a proton with a given energy, are expected to have a quite broad distribution of energies. We point the reader to Ref. [423] for a discussion on the implications of such an assumption.

As a final remark, we want to highlight that Eq. (2.2) holds only if pions and muons do not lose energy before decaying, either by synchrotron emission in the presence of magnetic fields or by interactions with the medium. Should this assumption not hold, one would need to account for the modification of the pion spectra due to such cooling processes.

2.2.2 The photo-hadronic mechanism

In the py scenario, an energetic proton interacts with a photon of a large enough energy (UV, X-rays, or γ -rays) and produces mesons. The simplest example is the following:



The threshold for this process is

$$s = (p_p + p_\gamma)^2 \geq (m_{p(n)}c^2 + m_\pi c^2)^2 \rightarrow \varepsilon_{\text{tr}} = m_\pi + m_\pi^2/2m_{p(n)} \quad (2.4)$$

The neutral pion has mass $m_{\pi^0} = 135$ MeV, so the threshold is ~ 145 MeV, while for charged pions with mass $m_\pi = 139.6$ MeV, the threshold is ~ 150 MeV. There are several contributions to the total $p\gamma$ cross-section, as shown in Fig. 2.3.

1. *Resonance production*: the most likely channel that produces pions around the threshold (at $\varepsilon_r = 340$ MeV) is the Δ^+ resonance channel, where the cross-section is enhanced (see Fig. 2.3). In this case, a proton turns into the higher energy equivalent particle Δ^+ ($m_{\Delta^+} = 1.232$ GeV) with spin 3/2, which subsequently decays to mesons:

$$p + \gamma \longrightarrow \Delta^+ \longrightarrow \begin{cases} n + \pi^+ & 1/3 \text{ of all cases} \\ p + \pi^0 & 2/3 \text{ of all cases} \end{cases} \quad (2.5)$$

This is then followed by the decay of pions into leptons and neutrinos, as in Eq. (2.1). More massive resonances also contribute.

2. *Direct production*: processes with the same initial and final states as in Eq. (2.5) can also take place in the t -channel, where the initial γ and nucleon exchange a meson instead of creating a (virtual) baryon resonance in the s -channel, which again decays. $p\gamma \rightarrow n\pi^+$ entirely dominates this channel for $0.25 \lesssim \varepsilon_r \lesssim 1$ GeV.
3. *Multi-pion production*: For $\varepsilon_r \gtrsim 1$ GeV, the dominant channel is statistical multi-pion production leading to two or more pions.

In the resonant Δ production process, as in the pp scenario, the pions carry on average about 1/5 of the proton energy, and hence one expects that the average energy of the photons produced in the π^0 decays satisfies $E_\gamma \simeq E_p/10$. In contrast, the neutrinos from the charged pion decays would have $E_\nu \simeq E_p/20$. This time, the total energy distributions for neutrinos and photons depend on the spectrum of the CR protons and the target photon spectrum. Similarly to what we saw for the pp case, these distributions can be obtained from the yields derived from Monte Carlo simulations using codes such as SOPHIA [336] and making the convolution with the proton and photon spectra. By assuming that the photon field is isotropic and that the muons and pions do not suffer energy losses before they decay, one obtains [261]:

$$Q_{\nu_\alpha + \bar{\nu}_\alpha}(E_\nu) = \frac{dN_\nu}{dE_\nu dt} = \int d\varepsilon_\gamma \frac{dE_p}{E_p} Q_p(E_p) \frac{dn_{\text{ph}}(\varepsilon_\gamma)}{d\varepsilon_\gamma} \Phi_{\nu_\alpha}\left(\frac{E_\nu}{E_p}, \eta\right) [E^{-1} T^{-1}] \quad (2.6)$$

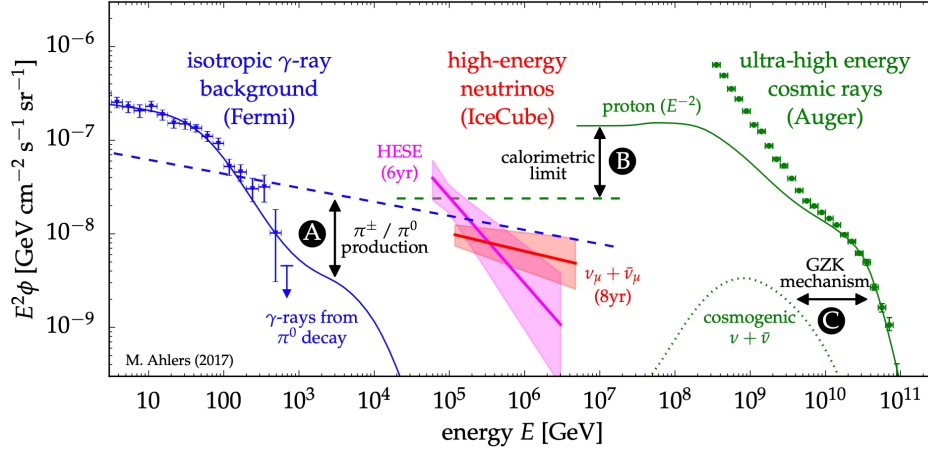


Figure 2.4: The spectral flux of IceCube neutrinos (red line for upgoing track analysis, and magenta line for HESE analysis), diffuse extragalactic γ -ray background (blue data), and ultra-high-energy CRs (green data). The multimessenger connection is established as follows: **A)** the joined production of charged pions (π^\pm) and neutral pions (π^0) in cosmic-ray interactions leads to the emission of neutrinos (dashed blue) and γ -rays (solid blue), respectively. **B):** cosmic ray emission models (solid green) of the most energetic CRs imply an upper limit (calorimetric limit) on the neutrino flux from the same sources (green dashed). **C)** the same cosmic ray model predicts the emission of cosmogenic neutrinos from the interaction with CMB photons (GZK mechanism). Figure from [46].

where ε_γ is the energy of the isotropic target photons, n_{ph} the photon density (in units of L^{-3}), and $\eta = 4\varepsilon_\gamma E_p / m_p^2$. The different functions $\Phi_{\nu_\alpha} \left(\frac{E_\nu}{E_p}, \eta \right)$, which represent the secondary particle distributions for a given proton and photon energy, were conveniently parameterized in [261]. However, in the GRB environments considered in this thesis (Sec. 6.2) where $p\gamma$ interactions are the dominant neutrino production channel, the cooling that pions and muons undergo before decaying is strong and cannot be ignored when computing the final neutrino spectra. To this aim, we will follow the work done in Refs. [296, 241], which allows us to predict the intermediate particles (pions, muons, kaons) spectra separately and to not integrate them out.

2.2.3 Difference between hadronic and photo-hadronic mechanisms

The main difference between the two scenarios concerns the spectra of the secondaries produced in the interaction. The $p\gamma$ mechanism has a significantly high threshold for the proton energy. Indeed, to produce the resonance Δ^+ , the proton energy needs to

satisfy the condition:

$$E_{p,\text{th}} > \frac{m_{\Delta}^2 - m_p^2}{4\varepsilon_{\gamma}} = 160 \left(\frac{1\text{MeV}}{\varepsilon_{\gamma}} \right) \text{GeV}. \quad (2.7)$$

The resulting neutrino spectrum is then highly suppressed for $E_{\nu} \lesssim E_{p,\text{th}}/20$. In contrast, given its extremely low threshold, for the pp mechanism, the neutrino fluxes can extend to much lower energies without any suppression. Furthermore, for the $p\gamma$ process, the resulting neutrino and gamma spectra will strongly mirror the shape of the target photon spectrum, while in the pp case, the secondary particles closely mimic the distribution of the primary protons, as previously explained (see Eqs. 2.2 and 2.6). So, if a power-law describes the parent proton spectrum, the daughter particles will also exhibit a distribution that closely resembles a power-law with nearly the same slope.

Other differences concern the relative proportion of the neutrino and γ -ray fluxes and the production of electron antineutrinos. Both are related to the amount of neutral/charged pions and the type of charged pions produced in the interaction, as we will see in the next section.

2.2.4 Connecting neutrinos with γ -rays and cosmic rays

In this section, we want to briefly outline the relation between neutrino, photon, and ultra-high energy CRs fluxes from a generic source where pp or $p\gamma$ interactions are at play. Let us introduce the variable $K_{\pi} = N_{\pi^{+}+\pi^{-}}/N_{\pi^0}$, denoting the ratio of charged-to-neutral pions produced in CR interactions. If the proton energies in the $p\gamma$ scenario are such that the production of secondaries occurs mainly at the Δ resonance, then we would have $K_{\pi} = 0.5$. If, however, one considers energies beyond the Δ resonance, where the multipion production becomes relevant, this ratio increases and typically tends to become $K_{\pi} \simeq 1$. On the other hand, for the pp mechanism, one has that $K_{\pi} = 2$ since the three types of pions are all produced in similar amounts. As previously mentioned, neutrinos and γ -rays are expected to carry 1/4 and 1/2 of their parent pion energy, respectively. With this information, we can relate their production rate to the one for pions as [46]:

$$\sum_{\alpha} E_{\nu} Q_{\nu_{\alpha}+\bar{\nu}_{\alpha}}(E_{\nu}) \simeq 3[E_{\pi} Q_{\pi^{+}+\pi^{-}}(E_{\pi})]_{E_{\pi} \simeq 4E_{\nu}}, \quad (2.8)$$

$$E_{\gamma} Q_{\gamma}(E_{\gamma}) \simeq 2[E_{\pi} Q_{\pi^0}(E_{\pi})]_{E_{\pi} \simeq 2E_{\gamma}} \quad (2.9)$$

which, combined, lead to a relation between the total fluxes emitted in neutrinos and photons:

$$\frac{1}{3} \sum_{\alpha} E_{\nu}^2 Q_{\nu_{\alpha}+\bar{\nu}_{\alpha}}(E_{\nu}) \simeq \frac{K_{\pi}}{4} [E_{\gamma}^2 Q_{\gamma}(E_{\gamma})]_{E_{\gamma}=2E_{\nu}}. \quad (2.10)$$

Note that this relation holds as long as the muons are not damped, so that the neutrino plus antineutrino flavor ratio at the source is approximately that from the pion-decay chain ($\nu_e : \nu_\mu : \nu_\tau$) $\simeq (1 : 2 : 0)$, which after taking into account the oscillations 1.13, it is approximately $(1 : 1 : 1)$ at Earth.

There are several caveats one should keep in mind before using the above relation to extract some meaningful information about a source producing γ -rays and neutrinos:

- γ -rays might be produced by leptonic processes (involving only leptons, see Chapter 4) such as synchrotron or inverse Compton. In this case, there would be no associated neutrinos.
- γ -rays might be absorbed in the source if it is thick enough, while neutrinos are not. No direct relation between the two fluxes can be established in this case.
- γ -rays might be absorbed in their route to Earth by CMB and EBL. This would degrade the emitted radiation through electromagnetic cascades down to energies below a TeV. As we have seen, at PeV energies, no photons can reach us from outside the Milky Way; at TeV energies, no photons can reach us from sources beyond a few hundred Mpc (Fig. 2.1). In this case, the connection between the high-energy neutrino and γ -ray fluxes becomes quite indirect.

Aware of the caveats, one can analyze the observation of the two messenger fluxes to infer information about the mechanisms operating inside single astrophysical sources and understand the origin of observed diffuse fluxes. Indeed, it is clear that, if there is a connection, the overall IceCube flux with energies between ~ 10 TeV and 10 PeV can only be related to a contribution to the diffuse fluxes of γ -rays below a few TeV since their sources are expected to be extragalactic and far away. Under the assumption that these sources are not opaque to photons, one could use the upper bounds on the diffuse fluxes of GeV to TeV γ -rays obtained by the Fermi satellite (see, e.g. [37]) to constrain the astrophysical neutrino sources [342]. By doing so, a strong tension arises with neutrino data at energies $E_\nu \lesssim 100$ TeV in the pp scenarios involving CR source spectra with slope > 2.3 extending below 100 TeV (Fig. 2.4). The high intensity of the neutrino flux below 100 TeV compared to the Fermi data can be explained if considering cosmic-ray accelerators optically thick in GeV-TeV γ -rays [344]. Some sources complying with these requirements are represented by choked GRB jets and active galactic nuclei (AGN) cores. The data at energies $\gtrsim 100$ TeV, on the other hand, may be accounted for by invoking CR reservoirs, with galaxy clusters and starburst galaxies representing an example [339].

As far as neutrino-CRs relation is concerned, this would be naturally expected, since neutrinos result from CRs interaction with a target material (be it gas or radiation), but it turned out not to be so straightforward. By assuming that CRs below the spectral ankle ($E \lesssim 5 \times 10^{19}$ eV, see Fig. 3.1) were of Galactic origin, and that CRs above \sim

10^{19} eV were protons of extragalactic origin the extrapolation of the ultra-high-energy CR flux to lower energies with a power-law E^{-2} allowed to derive the Waxman-Bahcall limit on the high-energy neutrino flux [499]. This limit was obtained by considering an efficient interaction for intermediate-energy CRs (probability of interacting ~ 1) and free escape for the most energetic ones. Everything below such neutrino flux implies that the system is “optically thin” for the CR interaction. Remarkably, this limit was very close to the observed IceCube flux (see calorimetric limit in Fig. 2.4) and suggested a connection between the two messengers could hold. Nevertheless, we know today that some assumptions made to compute this upper bound are no longer valid. In particular, measurements from the Pierre Auger Observatory [1] indicate that cosmic ray composition becomes heavier beyond the ankle, and it is still not clear at which exact energy the detected flux of CRs starts to be of astrophysical origin. More refined unified models of all three messengers have been put forward [350, 171], but these still need to be tested by next-generation neutrino detectors such as IceCube-Gen2 as well as gamma-ray telescopes such as CTA.

2.3 Transient source candidates of high-energy neutrinos

We have already mentioned some of the candidate sources proposed to explain the neutrino flux observed by IceCube, like starburst galaxies, clusters of galaxies, or the cores of AGN. These are all examples of steady sources, which emit for very long times compared to the human lifetime. Indeed, as of today, after TXS 0506+056, the second most significant association of high-energy neutrinos with an astrophysical object has been reported for the Seyfert II starburst galaxy NGC 1068 (a starburst galaxy with a central AGN obscured by a dusty torus) [18]. In addition, recently, an emission of neutrinos with energies $\lesssim 100$ TeV has been identified from the Milky Way at the 4.5σ level of significance [22]. This signal is consistent with modeled diffuse emission expected from CRs interacting with the interstellar medium in the Galactic plane of the galaxy. However, the focus of this thesis, as the title suggests, is on transient astrophysical objects, which hold significant promise for neutrino detection using the current and future IceCube-like facilities. There are several reasons for this:

- *Enhanced neutrino emission:* Transient events are often characterized by intense and short-lived bursts of particle acceleration and energy release. This results in a higher likelihood of producing high-energy neutrinos through various mechanisms, such as photohadronic and hadronic interactions. These energetic neutrinos are more easily detectable due to their higher flux and distinct energy spectrum.

- *Reduced background:* Transient events have a well-defined time window during which the neutrino emission occurs. The focused and rapid emission can significantly reduce the atmospheric background and make it easier to identify neutrino signals.
- *Localization:* Transient events can often be localized in the sky with relatively high precision, especially if they are also observed through electromagnetic or gravitational wave observations. This allows IceCube and other neutrino observatories to narrow down the search region for potential neutrino sources, improving the chances of detection.
- *Multimessenger approach:* Transient events are excellent for multimessenger studies, where data from various observations (neutrinos, electromagnetic radiation, gravitational waves) are combined. This holistic approach provides complementary information about the astrophysical processes involved, aiding in source identification and a more detailed understanding of their physics. Indeed, IceCube developed a real-time alert system that rapidly sends astronomical coordinates of the detected neutrinos to the Gamma-ray Coordinate Network (GCN) for potential follow-up by different astronomical telescopes. This is a powerful way to identify the sources of high-energy neutrinos.

Having hopefully conveyed the potential inherent in transient sources, let us now briefly present some of the transient candidates expected to be sources of high-energy neutrinos [317, 343] (see Fig. 2.5):

- **Flaring blazars:** blazars are a subclass of AGN with bright relativistic jets emanating from the nucleus and pointing close to the observer's line of sight. Given the favorable conditions for particle acceleration in their strong jets, they were one of the first sources to be proposed as CR factories. Their spectra, which extend from radio to γ -ray band, present two bumps, one at low and one at high energies. In lepto-hadronic models, the second bump can stem from the electromagnetic cascades of the hadronic secondaries produced in the interaction of the co-accelerated protons with the jet environment. Neutrinos are thus a by-product of this interaction. It is known that blazars are highly variable objects, so it is natural to search for correlations between neutrino detections and the fluctuating states observed across a broad spectrum of wavelengths (especially radio, X-rays, and γ -rays).
- **Tidal disruption events:** a tidal disruption event (TDE) occurs when a star following a Keplerian orbit gets too close to a supermassive black hole (SMBH), leading to its complete disintegration due to the tidal forces exerted by the SMBH. Subsequently, the fragmented stellar material is accreted towards the SMBH at

a super-Eddington rate, resulting in a distinct flare lasting for several months to years [414]. TDEs are among the brightest transients occurring in the Universe. By emitting radiation across a wide range of wavelengths from optical to X-rays, they serve as exceptional tools for investigating quiescent SMBHs located at the cores of distant inactive galaxies. Several regions around the SMBH-like relativistic jets, disks, disk coronae, or the wind/outflows launched as a consequence of strong accretion [234] - have been proposed as sites of acceleration of CRs and thus the production of high-energy neutrinos.

- **Neutron star mergers:** During the merger of two neutron stars, a portion of their mass undergoes tidal disruption, creating a disk around the newly formed, central compact object. The central object eventually collapses into a black hole. The accretion of the surrounding material into the black hole can drive relativistic jets and outflows. These jets are responsible for the observed short GRBs (sGRBs), as confirmed by the detection of GRB 170817A in coincidence with the GW event GW170817 [31]. Neutrinos are expected to be produced inside the relativistic jet via photo-hadronic interactions [467].
- **Interaction-powered supernovae:** stars with a mass greater than $8 M_{\odot}$ at the end of their lives explode as a supernova (SN). In the explosion, a fraction of the SN ejecta's gravitational binding energy is converted into kinetic energy. A strong shock between the ejecta and the circumstellar medium is expected to develop and accelerate protons to relativistic energies if a very dense ambient material surrounds the SN. Such protons then collide with the ambient particles and can lead to the production of GeV-TeV neutrinos via pp interaction, as we will better see in Sec. 6.1.
- **Choked jets:** If the progenitor star has enough angular momentum, the central compact object that forms after the final collapse can produce a relativistic jet. If such a jet is not energetic enough to make its way through the dense stellar envelope, it gets choked inside the star. Here, if the conditions for efficient acceleration of particles are fulfilled, 10-100 TeV neutrinos can be produced.
- **Long γ -ray bursts:** if the jet produced by the collapsing star is powerful enough, it can get out of the stellar envelope and manifest itself through the production of an extremely energetic long γ -ray burst (LGRB) event. Again, the accelerated particles inside the jet can produce quite energetic neutrinos mainly via $p\gamma$ interactions, as we will see in Sec. 6.2.

In Chapter 6, we will, in particular, focus on interaction-powered supernovae and LGRBs.

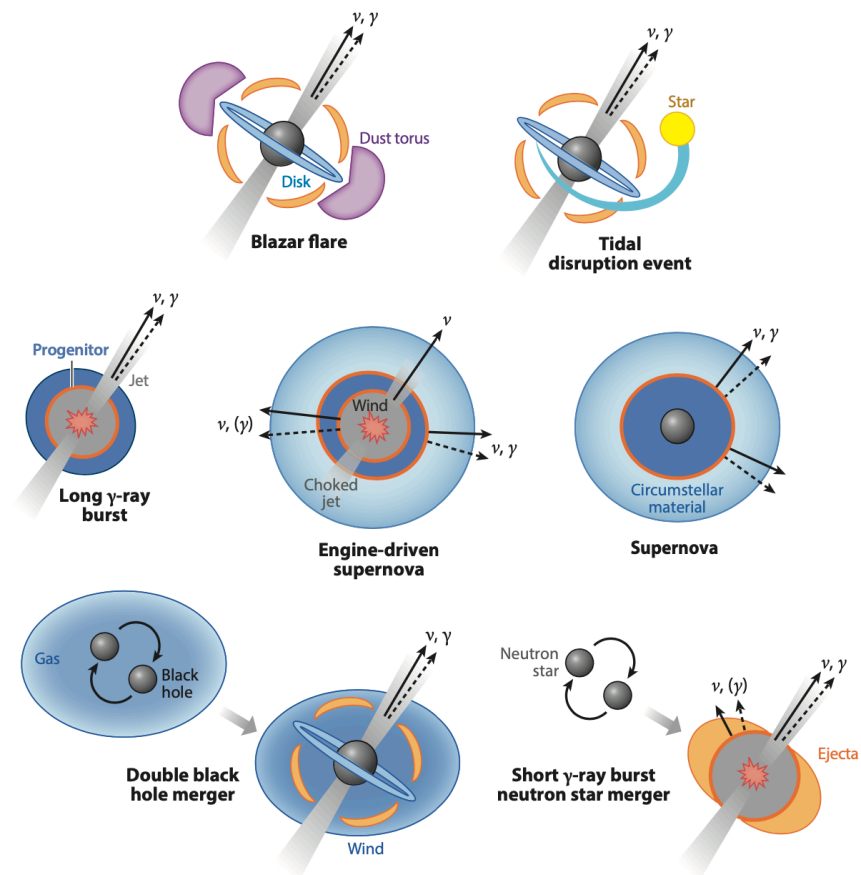


Figure 2.5: Illustrative picture of the most interesting high-energy multimessenger transient sources. Figure from [46].

Particle acceleration

In the previous chapters, we have seen that charged particles of very high energies are necessary to explain the origin of neutrinos routinely detected by the IceCube Observatory. It is clear that the extraordinary energies in CRs that we observe on Earth (Fig. 3.1), covering approximately 11 orders of magnitude from a few GeV up to a few times 10^{20} eV, and the almost perfect power-law behavior of their spectrum, cannot be explained by thermal phenomena. Hence, these CRs must have undergone some form of acceleration, and in this Chapter, we delve into the mechanisms that allow such acceleration. We first introduce the reader to the original idea of particle acceleration presented by Fermi, which relies on stochastic collisions of particles with some scatterer centers. Then, we describe its modern application in the context of non-relativistic and relativistic shocks produced by supersonic hydrodynamic outflows. Finally, we conclude by briefly presenting the phenomenon of magnetic reconnection, which, analogously to shocks, can produce non-thermal relativistic particles. The acquired knowledge will be exploited in the Chapter of our results.

3.1 Acceleration principle

The mechanism of acceleration of charged particles is believed to be connected to electromagnetic fields present in astrophysical sources or within the interstellar medium (ISM). In general, the average electric field equals zero since the motion of free particles makes it difficult to maintain large electrostatic fields in the mostly ionized media common in astrophysical systems. Nevertheless, transient electric fields can be produced due to localized time-varying magnetic fields, and notably, strong and enduring electric fields are predominantly observed in the proximity of fast-rotating magnetized objects like pulsars.

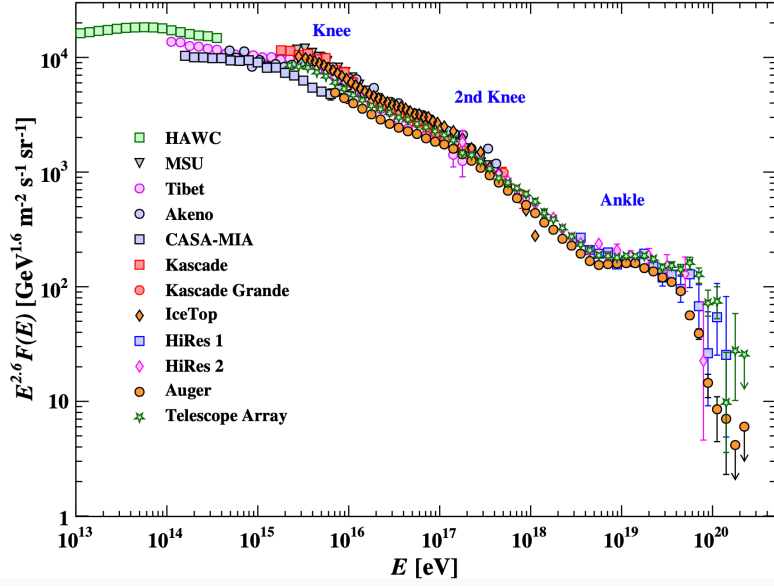


Figure 3.1: Cosmic-ray spectrum measured by different experiments from 10^{14} eV up to beyond 10^{20} eV. From PDG.

On the contrary, magnetic fields are ubiquitous in all astrophysical sources with high-energy phenomena, including the ISM. These fields are commonly invoked in almost all theoretical models of cosmic-ray acceleration. At first glance, this statement may appear perplexing since the Lorentz force $\vec{F} = q\vec{v} \times \vec{B}$ does not perform work and thus should not be directly invoked to accelerate particles. However, a time-varying magnetic field generates an electric field, as expressed by Maxwell's equation, $\vec{\nabla} \times \vec{E} = -\partial\vec{B}/\partial t$. Furthermore, a magnetic field \vec{B}' in a given reference becomes a combination of a magnetic field \vec{B} and an electric field \vec{E} in another reference frame moving relative to it, due to Lorentz transformation of the electromagnetic tensor $F_{\mu\nu}$.

Therefore, it is important to highlight that what we will present primarily relies on describing the electromagnetic field in a specific astrophysical medium using a pure magnetic field. This choice is solely for practical convenience since it makes calculations easier. In principle, it is always possible to describe the same process using electric fields, which are physically responsible for the acceleration of charged particles. Given the magnetic nature of the acceleration, it is useful to define here the Larmor radius (or gyroradius) of the particle, $r_L = p/(ZeB)$, where Ze is the charge of the particle, p the momentum, and we assumed that particle velocity and magnetic field are perpendicular. For relativistic particles with energy $E = pc$, it becomes

$$r_L = \frac{E}{ZecB}. \quad (3.1)$$

This gives the first constraint on acceleration mechanisms: the acceleration site must have a size R larger than r_L .

3.2 Fermi acceleration mechanism

The Fermi mechanism is historically the first discovered acceleration process. It was first proposed by Fermi in 1949 and was based on the fact that the ISM is filled with “clouds” of ionized gas in random movement with respect to the “Galactic frame”. These clouds carry a magnetic field and can in principle, reflect the incoming charged particles, acting as “magnetic mirrors”¹, accelerating them to high energies [175] (see Sec. 3.4.2 for more details on the role of the magnetic field as a scatterer center of charged particles).

Let us assume that a charged particle, with a velocity v , “hits” a steady cloud, as shown in Fig. 3.2. The particle is reflected with the same velocity and no net energy gain as it would be on a wall. Let us now assume that the cloud is moving with a velocity V toward the particle (which still has a velocity v with respect to the Galactic frame). In the cloud frame, the particle has a velocity $v + V$, and, assuming a perfectly elastic collision, the particle is reflected with the same (but opposite) velocity. Back to the Galactic frame (adding V to the particle velocity in the cloud frame), due to the head-on collision between the particle and the cloud, the particle has been accelerated to a velocity $v + 2V$. Let us now consider the cloud going away from the particle with a velocity V with respect to the Galactic frame. With the same calculation, we conclude that in the Galactic frame, the particle has been decelerated to a velocity $v - 2V$ after the collision.

The essential idea behind Fermi’s acceleration mechanism is thus clear: particles will be accelerated by each encounter with a magnetic cloud coming toward them and decelerated by the encounters with magnetic clouds going away from them. The energy gain (or loss) for each encounter can be calculated by a double change of reference frame, Galactic frame \rightarrow cloud frame \rightarrow Galactic frame. Note that in this representation, the only role of the magnetic field is to function as a reflection agent. In its absence, the particles would go through the moving cloud without any energy change (ignoring the interaction with the cloud particles). This means also that the energy gain should be independent of the magnetic field, as we will see later.

¹When a magnetic field remains relatively constant over one Larmor gyration, a particle conserves its magnetic moment, denoted as $\mu = p_{\perp}^2/B$, where p_{\perp} represents the momentum component perpendicular to the magnetic field. Since magnetic fields do not perform work, the total momentum, $p^2 = p_{\perp}^2 + p_{\parallel}^2$, remains constant as well. Consequently, when a particle encounters a region with a stronger magnetic field, its p_{\perp} must increase, leading to a decrease in p_{\parallel} . If the magnetic gradient is sufficiently pronounced, the particle may eventually halt before reversing its motion. This phenomenon, known as *magnetic mirroring*, can be considered an effective mechanism for scattering particles within non-uniform magnetic fields.

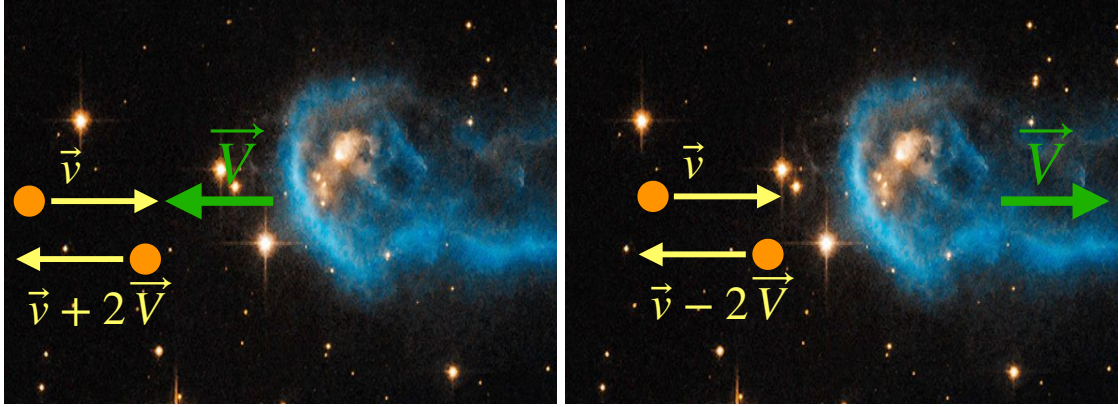


Figure 3.2: *Left:* The particle and the cloud velocities are opposite in direction. The particle gains energy in head-on elastic scattering. *Right:* The particle and the cloud velocities are in the same direction. The particle loses energy in the elastic scattering.

3.2.1 Energy gain in the particle-cloud encounter

We assume that inside the cloud, the scattering of particles is due to magnetic irregularities, which can only change the direction of the particle and perform no work on it (see Sec. 3.4.2), meaning that in the cloud frame, the scattering is purely elastic. Furthermore, we consider that particles are ultra-relativistic (i.e., $E \simeq pc$). Our system is described in 2D and is shown in Fig. 3.3: the particle enters the cloud with angle θ_i with respect to the cloud velocity \vec{V} and is isotropized by the magnetic turbulence so that the angle of the particle escaping from the cloud θ_o is random. By using the primed quantities for the cloud frame and the unprimed ones for the Galactic frame, we have that energy of the particle in the double change of reference frame transforms as:

$$E'_i = \Gamma E_i (1 - \beta \cos \theta_i) \quad (3.2)$$

$$E_o = \Gamma E'_o (1 + \beta \cos \theta'_o). \quad (3.3)$$

where $\beta = V/c$, $\Gamma = (1 - V^2/c^2)^{-1/2}$ is the Lorentz boost factor of the cloud in the Galactic frame, i and o refer to the properties of the incoming and outgoing particle, respectively. Since the particle does not gain or lose energy, we have that $E'_o = E'_i$, and we get:

$$E_o = \Gamma^2 E_i (1 - \beta \cos \theta_i) (1 + \beta \cos \theta'_o) \quad (3.4)$$

$$\Rightarrow \frac{\Delta E}{E} = \frac{E_o - E_i}{E_i} = \frac{\beta^2 - \beta \cos \theta_i + \beta \cos \theta'_o - \beta^2 \cos \theta_i \cos \theta'_o}{1 - \beta^2} \quad (3.5)$$

We need to average the above equation over the incoming and outgoing directions to get the mean energy change. For gas clouds, the outgoing angle is uniformly distributed in

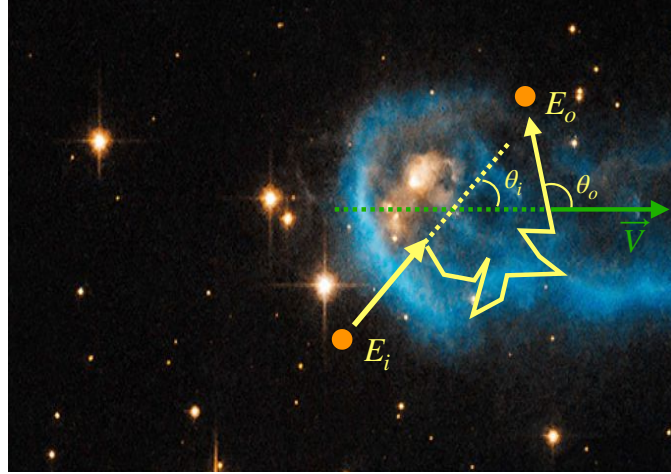


Figure 3.3: Schematic view of the “interaction” of a charged particle with a magnetic cloud. The particle enters the cloud and is isotropized by the magnetic turbulence.

the cloud frame since there is no preferred direction at all, which means that $\langle \cos \theta'_o \rangle = 0$. Hence, it remains to calculate $\langle \cos \theta_i \rangle$. If the clouds are uniformly distributed, the probability of having an encounter with incidence angle θ_i should be proportional to the relative velocity between the particles and the cloud: $P(\theta_i) \propto c - V \cos \theta_i$. We then have:

$$\langle \cos \theta \rangle = \frac{\int_{-1}^1 \cos \theta_i (1 - \beta \cos \theta_i) d(\cos \theta_i)}{\int_{-1}^1 (1 - \beta \cos \theta_i) d(\cos \theta_i)} = -\frac{2/3\beta}{2} = -\frac{\beta}{3} \quad (3.6)$$

By substituting this result in 3.5, we finally get:

$$\left\langle \frac{\Delta E}{E} \right\rangle = \frac{\beta^2 + \beta^2/3}{1 - \beta^2} \simeq \frac{4\beta^2}{3}. \quad (3.7)$$

This result shows that the average gain in energy is indeed positive and demonstrates that the famous Fermi’s mechanism is truly an acceleration mechanism for charged particles. All the point (which might seem counter-intuitive at first sight) is that head-on collisions are *on average* more frequent, leading to an average gain rather than loss of energy². Nevertheless, the increase in energy is only *second order* in β , and this

²What is the reason behind the higher occurrence of head-on collisions? To grasp this concept, let us draw a simple and familiar analogy. Imagine a bustling marketplace with people moving in various directions. Now, consider a person walking through the crowd. It becomes apparent that they are more likely to come across individuals approaching from the opposite direction than those moving in the same direction. It is all about the relative velocities involved, and a similar reasoning applies to magnetic clouds. Moreover, in the marketplace scenario, if the surrounding individuals are walking slower, the number of people encountered and those overtaken will be smaller. This parallel holds for magnetic

is why this mechanism is also often called *second order Fermi mechanism*, or *stochastic acceleration*. It is not very efficient, as typically $V \ll c$. Although Fermi's original discussion considers clouds, subsequent elaborations have instead considered scattering off magnetohydrodynamic waves, in which case the relevant velocity becomes the Alfvén speed, $V = V_A = B/\sqrt{4\pi\rho}$, where B is the magnetic field and ρ the particle density. For interstellar magnetic fluctuations $V \sim 1 - 10$ km/s, so that $\sim 10^{10}$ collisions would be needed just to double the particle's energy. This is where Fermi's original idea of accelerating CRs in interstellar turbulence *quantitatively* fails: it is just too slow.

However, one could show that if all the collisions were head-on, the average over $P(\theta_i)$ would be only on values $\cos\theta_i < 0$, and the energy gain would be dominated by the second term in Eq. (3.5), which is proportional to β (first-order Fermi mechanism), rather than β^2 . A mechanism providing only head-on collisions is likely a good candidate for cosmic-ray acceleration.

During the late 1970s, multiple authors independently recognized that the “astrophysical shocks” provide in principle such a mechanism, known as *Diffusive Shock Acceleration* (DSA). This process relies on the repeated scattering of particles across the shock, which, through multiple head-on collisions, can gain energy with exceptional efficiency. Before delving into the details of particle acceleration, we provide a concise overview of the main properties of shocks in the next section.

3.3 Shock hydrodynamics

We know that shocks are ubiquitous in the Universe, from our Solar system to more extreme environments like supernova remnants, AGN, or GRBs. These shocks exhibit particle acceleration, as evidenced by radiation detection across a wide spectrum, from radio frequencies to gamma rays. Such radiation is commonly attributed to the energy losses of accelerated electrons.

Astrophysical shock waves adhere to the same macroscopic principles as their terrestrial counterparts. They originate from outflows that propagate with velocities exceeding the local speed of sound³. However, unlike “terrestrial shocks,” the key distinction lies in the predominantly *collisionless* nature of astrophysical shock waves.

clouds as well.

³In general, any perturbation in a fluid (like an aircraft) causes a wave to propagate at the speed of sound in the medium. This ensures that the disturbance information spreads throughout the fluid so that it can react to it promptly and appropriately. This means that alterations in macroscopic quantities, such as pressure and temperature, occur in an adiabatic manner. However, if the source of the disturbance moves faster than the sound speed, it can outpace the sound wave. In this scenario, the fluid can no longer react adiabatically and undergoes a sudden change, a shock. This shockwave forms a transitional zone between the already shocked fluid and the fluid that has yet received no information about the disturbance.

Indeed, the shock formation and energy dissipation processes do not occur through particle collisions or Coulomb interactions but rather through the interaction between particles and the ambient magnetic field. In the absence of these fields, supersonic outflows would effortlessly pass through the ambient medium without any noticeable shock formation.

3.3.1 Jump conditions

When a shock wave propagates through a medium, such as the ISM, it is important to distinguish between the downstream region (the region that has already been shocked) and the upstream region (the region of space ahead of the shock that has not been shocked yet). The hydrodynamics of a stationary, non-viscous, and non-relativistic fluid is described by classical equations for the conservation of mass, momentum, and energy. In the case of a one-dimensional shock, these equations yield a solution where physical quantities exhibit a discontinuity across a surface, accompanied by an increase in entropy.

Let us consider the frame of reference within the shock front to analyze the shock dynamics. We assign the subscript “1” to denote upstream physical quantities and subscript “2” to denote downstream physical quantities in the shock frame (see Fig. 3.4). The density, pressure, temperature, and flow velocity in both media (ρ_i, P_i, T_i, V_i) are determined by the conservation relation at the shock. Shocks that satisfy the conservation of mass, momentum, and energy are said to be adiabatic. For stationary shocks, the three thermodynamic conservation equations, which establish the relationship between downstream and upstream quantities, read as [374]:

- mass conservation: $\rho_2 V_2 = \rho_1 V_1$
- momentum conservation: $P_2 + \rho_2 V_2^2 = P_1 + \rho_1 V_1^2$
- energy conservation: $\frac{1}{2} V_2^2 + e_2 + \frac{P_2}{\rho_2} = \frac{1}{2} V_1^2 + e_1 + \frac{P_1}{\rho_1}$

and can be expressed by the so-called *Rankine-Hugoniot jump conditions*:

$$\chi \equiv \frac{\rho_2}{\rho_1} = \frac{V_1}{V_2} = \frac{(\gamma + 1)M^2}{(\gamma - 1)M^2 + 2} \rightarrow \frac{\gamma + 1}{\gamma - 1} \quad (3.8)$$

$$\frac{P_2}{P_1} = \frac{2\gamma M^2 - \gamma + 1}{\gamma + 1} \rightarrow \frac{2\gamma M^2}{\gamma + 1} \quad (3.9)$$

$$\frac{T_2}{T_1} = \frac{[2\gamma M^2 - \gamma + 1][(\gamma - 1)M^2 + 2]}{(\gamma + 1)^2 M^2} \rightarrow \frac{2\gamma(\gamma - 1)}{(\gamma + 1)^2 M^2} \quad (3.10)$$

where for an ideal gas, the pressure is $P_i = (\gamma - 1)\rho_i e_i$, T_i is the temperature⁴, and e_i is the energy density given by $e_i = \frac{1}{\gamma - 1} \frac{P_i}{\rho_i}$. We have introduced the compression factor between the downstream and upstream density $\chi \equiv \rho_2/\rho_1$ and the sonic Mach number $M \equiv V_1/c_{s,1}$, where the sound speed is defined as $c_s = \sqrt{\gamma P/\rho}$. The asymptotic values for $M^2 \gg 1$ are also reported after the \rightarrow symbol. $\gamma = c_p/c_v$ is the adiabatic index of the gas, and the typical values are $\gamma = 5/2$ for an ideal, monoatomic gas, and $\gamma = 7/5$ for an ideal diatomic gas. Generally, $\chi = 4$ for any strong shock, and both the pressure and temperature jumps are proportional to M^2 , meaning that a strong shock can heat the downstream plasma very efficiently. Astrophysical shocks are often very strong, so we expect shock dynamics to often be in such a regime.

3.4 Diffusive Shock Acceleration

As previously mentioned, despite its shortcomings, the Fermi mechanism is the foundation for many modern acceleration mechanisms that have been proposed following Fermi's groundbreaking work. Around the same time, several authors introduced DSA as a way to achieve a first-order Fermi acceleration, which offered the additional advantage of enabling the "cloud" velocity to reach substantial values (e.g., $V \approx$ thousands of km/s for supernova remnant shocks). This elegant process effectively overcomes most of the challenges the original Fermi mechanism faces.

3.4.1 Principle of Diffusive Shock Acceleration

Let us assume for the moment that the shock is non-relativistic. Concentrating only on the velocity discontinuity, we can easily understand the interest of shock waves for particle acceleration. In the shock frame, the upstream medium is coming toward the shock with a velocity V_1 (note, of course, that $V_1 = V_{\text{sh}}$ where V_{sh} is the shock velocity). Passing through the shock, the gas slows down, and the downstream medium moves away from the shock with a velocity $V_2 = V_{\text{sh}}/\chi$ (see Fig. 3.4).

Let us now consider an observer at rest in the upstream frame. He sees the shock and the downstream medium approaching with velocities $V_1 = V_{\text{sh}}$, and $\Delta V = V_1 - V_2 = \left(\frac{\chi-1}{\chi}\right)V_{\text{sh}}$, respectively. For an observer at rest with respect to the downstream fluid, the shock is going away with the velocity V_2 , but the upstream medium is coming toward the observer, again with velocity $\Delta V = V_1 - V_2 = \left(\frac{\chi-1}{\chi}\right)V_{\text{sh}}$.

⁴Since particles are accelerated at the shock front, both upstream and downstream are not in strict thermal equilibrium. So T_i introduced can be understood as effective temperatures that define the mean internal specific energy density in the two streams.

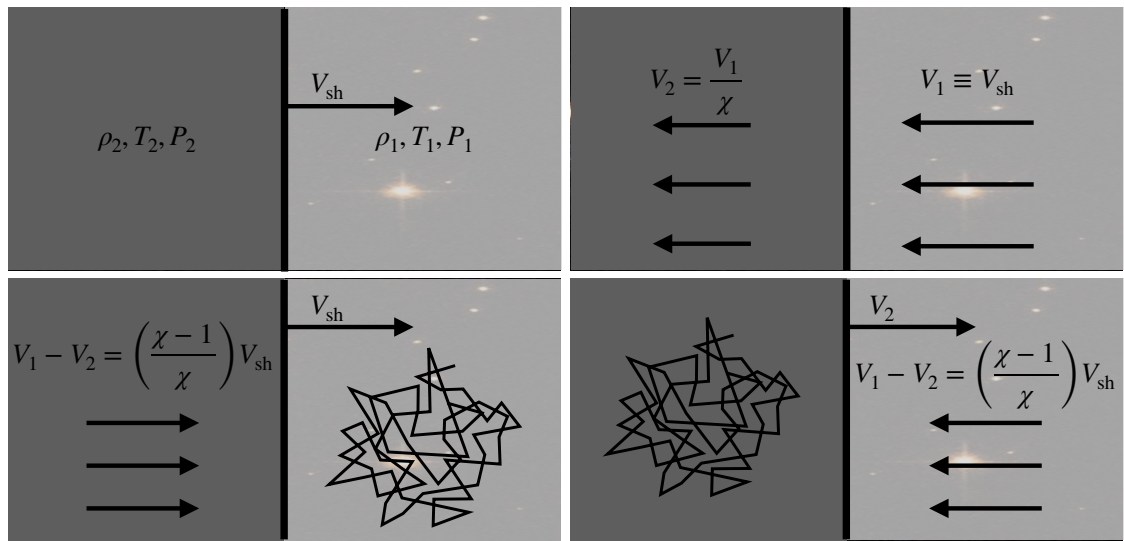


Figure 3.4: *Upper left:* A strong shock wave propagating at a supersonic velocity V_{sh} through stationary interstellar gas with density ρ_1 , pressure P_1 , and temperature T_1 . The density, pressure, and temperature behind the shock are ρ_2 , P_2 , and T_2 , respectively. *Upper right:* The same situation is seen in the reference frame where the shock front is at rest. In this frame of reference, the upstream-to-downstream velocity ratio is $V_1/V_2 = \chi$. For a fully ionized plasma, $\chi = 4$. *Lower left:* The gas flow is observed in the frame of reference in which the upstream gas is stationary, and the velocity distribution of the high-energy particles is isotropic. *Lower right:* The gas flow as observed in the frame of reference in which the downstream gas is stationary and the velocity distribution of high energy particles is isotropic.

In a situation where both the upstream and downstream media are magnetized, a particle arriving from the upstream medium and passing through the shock would perceive the downstream medium as a “magnetic cloud” moving towards it (a cloud with a velocity ΔV relative to the upstream fluid’s rest frame). Similarly, a particle from the downstream medium passing through the shock would view the upstream medium as a “magnetic cloud” approaching it (with a velocity ΔV relative to the downstream fluid’s rest frame). Consequently, a particle that crosses the shock multiple times, such as moving from upstream to downstream and back upstream, can gain energy by interacting with these moving “magnetic clouds.” The crucial distinction from Fermi’s original mechanism is that all the collisions occur head-on in this configuration. In addition, the Alfvén wave velocity $V_A \sim 10\text{km/s}$ is now replaced with $\Delta V \sim 10^4\text{km/s}$. This suggests that the process involving charged particles cycling across a shock front could be significantly more efficient than Fermi’s original proposal. To validate this assertion, we must calculate the energy variation experienced by a charged particle during a cycle *upstream* \rightarrow *downstream* \rightarrow *upstream*.

3.4.2 Magnetic field amplification

Before proceeding, let us briefly summarize the role of the magnetic field in the acceleration process at shocks (see reviews [306, 313, 111] for details and references):

1. *Shock formation*: The shock formation itself generates magnetic turbulence and instabilities in the surrounding plasma.
2. *Plasma instabilities*: The diffusive flux of energetic particles upstream of the shock is expected to drive plasma instabilities. Such *streaming instabilities* may lead to rapid growth of different modes, either resonant (or Alfvén instability), so-called because it grows at wavenumbers resonant with the Larmor radius of the streaming CRs (saturating at $\delta B/B \sim 1$, where δB is the turbulent magnetic field), or non-resonant (Bell instability), which grows faster than the resonant instability at wavenumbers non-resonant with the Larmor radius. The basic physics of the Bell instability is that a return current $-\vec{j}_{\text{cr}}$ produced in reaction to streaming CRs stretches and distorts the magnetic field via a $-\vec{j}_{\text{cr}} \times \vec{B}$ force.
3. *Magnetic field amplification*: the turbulence and instabilities generated by the above processes stretch and twist the magnetic field lines, causing a change in the topology and an amplification of any pre-existing magnetic field. For example, numerical simulations have shown that the non-resonant instability can grow exponentially and amplify the magnetic field up to $\delta B/B \sim 10 - 100$.
4. *Particle scattering*: The amplified turbulent magnetic fields act as magnetic scatterers. The scattering process randomizes particle trajectories and enables them

to cross the shock front multiple times, gaining energy with each crossing through diffusive shock acceleration.

It is important to note that the generation of magnetic turbulence and instabilities in shocks is a highly complex and nonlinear process. The details can vary depending on the specific astrophysical environment, the shock properties, and the plasma conditions. Understanding these processes requires sophisticated theoretical models, numerical simulations, and observations in various astrophysical contexts.

3.4.3 Energy gain after a cycle upstream-downstream-upstream

To calculate the mean energy gain experienced by a charged particle during a cycle *upstream* \rightarrow *downstream* \rightarrow *upstream*, we need to make the following assumptions to define the framework of our calculation:

- The shock is an infinite plane.
- The upstream and downstream media have an infinite spatial extension.
- The relevant physical quantities are in a steady state.
- The energetic charged particles are *isotropized* upstream and downstream of the shock reference frames.
- The shock is non-relativistic ($V_{\text{sh}} \ll c$), whilst the charged particles are relativistic ($v \approx c$).

For this calculation, we use unprimed quantities for the upstream frame and primed quantities for the downstream frame. Let θ_1 be the angle between the particle velocity v and the shock normal at the initial shock crossing in the upstream frame, and θ'_2 the angle of the particle with the shock normal in the downstream frame, when crossing the shock back to the upstream medium, as depicted in Fig. 3.5 On a cycle *upstream* \rightarrow *downstream* \rightarrow *upstream*, the fractional gain corresponds to (see Sec. 3.2.1)

$$\frac{\Delta E}{E} = \frac{E_2 - E_1}{E_1} = \frac{\beta^2 - \beta \cos \theta_1 + \beta \cos \theta'_2 - \beta^2 \cos \theta_1 \cos \theta'_2}{1 - \beta^2} \quad (3.11)$$

with $\beta = \Delta V/c$ this time. To get the mean fractional gain, we need to average again on $\cos \theta_1$ and $\cos \theta'_2$, so we need to know the probability of crossing the shock with an angle between θ and $\theta + d\theta$. Assuming a particle density n_0 , the number of particles crossing the shock with velocity $c \cos \theta$, an angle between θ and $\theta + d\theta$, through a surface dS during a time dt is $d^4N = n_0 c \cos \theta d\Omega dS dt = (n_0/2) c \cos \theta \sin \theta d\theta dS dt$.

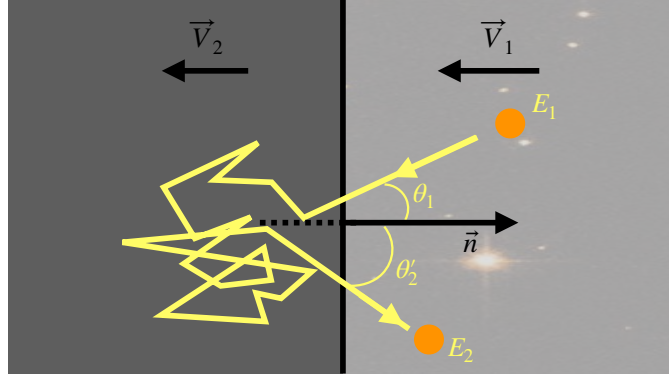


Figure 3.5: Schematic view of a cycle as seen in the shock rest frame: the particle initially in the ISM (upstream medium) enters the shocked medium (downstream medium) with an angle θ_1 with respect to the shock normal \vec{n} , it is then isotropized by the magnetic turbulence in the downstream medium and reflected back to the upstream medium with an angle θ'_2 . Here, the particle will eventually be isotropized and scattered back across the shock to start a new cycle.

The probability of crossing the shock with an angle between θ and $\theta + d\theta$ is thus proportional to $\cos \theta \sin \theta d\theta$. We then have:

$$\langle \cos \theta \rangle = \frac{\int_{\theta_{\min}}^{\theta_{\max}} \cos^2 \theta \sin \theta d\theta}{\int_{\theta_{\min}}^{\theta_{\max}} \cos \theta \sin \theta d\theta} = \frac{\left[\frac{1}{3} \cos^3 \theta \right]_{\theta_{\min}}^{\theta_{\max}}}{\left[\frac{1}{2} \cos^2 \theta \right]_{\theta_{\min}}^{\theta_{\max}}}. \quad (3.12)$$

For the particle to cross from upstream to downstream, one needs $\theta_{\min} = \pi/2$ and $\theta_{\max} = \pi$ (the shock and particle velocities are antiparallel), leading to $\langle \cos \theta_1 \rangle = -2/3$, while for the crossing from downstream to upstream, it is necessary that $\theta_{\min} = 0$ and $\theta_{\max} = \pi/2$, which gives $\langle \cos \theta'_2 \rangle = 2/3$. Since $\Delta V \ll c$ ($V_{\text{sh}} \ll c$), we neglect terms in β^2 in Eq. (3.11), and finally get the fractional energy gain for one cycle:

$$\left\langle \frac{\Delta E}{E} \right\rangle = \frac{4}{3} \frac{V_1 - V_2}{c} = \frac{4}{3} \beta_{\text{sh}} \left(\frac{\chi - 1}{\chi} \right) \equiv \alpha. \quad (3.13)$$

As anticipated, DSA proves to be an acceleration mechanism ($\langle \Delta E/E \rangle > 0$) that results in an energy gain proportional to β , marking a significant step forward compared to the original Fermi mechanism. Consequently, DSA is commonly referred to as the *first-order Fermi mechanism* for obvious reasons.

3.4.4 Power-law particle distribution

Once the mean energy gain from a single cycle *upstream* \rightarrow *downstream* \rightarrow *upstream* is computed, the next step involves estimating the number of cycles that particles can

undergo before “leaving the system.” It is crucial to identify the mechanism that limits the number of cycles a particle can achieve and thus estimate the probability of escape from the “acceleration region.”

In the context of our assumptions (infinite media upstream and downstream, and steady state), particles lack any means of escaping upstream of the shock. Due to the isotropization of the accelerated particles by ambient magnetic fields, the fluid of accelerated particles exhibits no net velocity with respect to the rest frame of the medium (either downstream or upstream). Consequently, in the upstream medium frame, the shock ‘chases’ the particles, leading to a return probability of 1 and an escape probability of 0, while in the downstream medium, the shock moves away with a velocity of $V_2 = V_{\text{sh}}/\chi$. This means that the accelerated particles are slowly advected away from the shock on average. To estimate the escape probability, one can compare the flux of particles being advected far away from the shock with the flux of particles entering the downstream medium by crossing the shock from the upstream medium.

The key characteristic of DSA lies in its ability to accelerate particles with a spectrum that remains entirely independent of the specific details of particle scattering. This property has been elegantly demonstrated through Bell’s insightful approach [79]. Let us consider N_0 test particles with an initial energy E_0 injected into a generic acceleration mechanism, denote $E = GE_0 = (1 + \alpha)E_0$ and $1 - P$ as the average energy of the particle and the probability that the particle leaves the accelerator after one round trip, respectively. After one cycle, there will be N_0P particles with a mean energy of GE_0 . Similarly, after k steps, there will be $N = N_0P^k$ particles with energy $\geq E = E_0G^k$. By eliminating $k = \ln(N/N_0)/\ln P = \ln(E/E_0)/\ln G$, we obtain

$$\ln\left(\frac{N}{N_0}\right) = Q \ln \frac{E}{E_0} \rightarrow N = N_0\left(\frac{E}{E_0}\right)^Q \quad Q \equiv \frac{\ln P}{\ln G} \quad (3.14)$$

We need to calculate P . Let us focus on the escape probability $P_{\text{esc}} = 1 - P$ and consider the accelerated particle density n_0 . Due to the global advection of the downstream fluid away from the shock front with a velocity V_2 , the flux of accelerated particles passing through a unit surface very far away from the shock is $\phi_{\text{esc}} = n_0V_2$. On the other hand, for an isotropic flux, the number of particles per unit surface and unit time crossing the shock from upstream to downstream is $\phi_{\text{up} \rightarrow \text{down}} = \frac{n_0}{4}c$. The escape probability is then simply the ratio $P_{\text{esc}} = \phi_{\text{esc}}/\phi_{\text{up} \rightarrow \text{down}} \simeq \frac{4}{R}\beta_{\text{sh}}$. We now have everything we need to predict the slope of the accelerated particle spectrum:

$$Q = \frac{\ln(1 - P_{\text{esc}})}{\ln(1 + \alpha)}. \quad (3.15)$$

Since the shock is non-relativistic, $\beta_{\text{sh}} \ll 1 \Rightarrow P_{\text{esc}} \ll 1$ and $\alpha \ll 1$, which leads to

$Q = -P_{\text{esc}}/\alpha = 3/(\chi - 1)$. Note that Q corresponds to the spectral index of the integral energy spectrum (i.e., the total number of particles with energy larger than E). Hence we have that

$$N(\geq E) = \int_E^\infty n(E)dE \Rightarrow n(E) = \frac{dN(\geq E)}{dE} = (k - 1) \frac{N_0}{E_0} \left(\frac{E}{E_0}\right)^{-k} \quad k = \frac{\chi + 2}{\chi - 1}. \quad (3.16)$$

The spectral index k we obtained depends only on the compression ratio $\chi = V_1/V_2$. This means that for a monoatomic gas and any strong shock (i.e., a shock for which $V/c_s \gg 1$), one always gets $\chi = 4$, and the slope of the power-law is $k = 2$. Namely, it is “universal”. We stress that our derivation holds for relativistic particles and non-relativistic shocks. When the shocks are relativistic [96, 335], or when shocks are strongly magnetized and the magnetic field is quasi-perpendicular to the shock normal [267, 81], instead, the assumptions that the CR distribution is isotropic in the fluid frame should be relaxed, in general leading to spectra that deviate from the universal one and depend on the details of the scattering process.

3.4.5 Relativistic shocks

So far, we have outlined the acceleration of particles at non-relativistic shocks. Since in this thesis, we will talk about relativistic jets in the context of GRBs, in this section, we introduce the formalism necessary to describe shocks with velocities in the relativistic regime. The general expression for sound speed can still be expressed as $c_s = \sqrt{\frac{\gamma P}{\rho}}$, except that the “effective” density now includes all the internal energy and pressure, i.e.

$$\rho = \frac{h}{c^2} = \rho_0 + \frac{e + P}{c^2} = \rho_0 + \frac{1}{c^2} \frac{\gamma}{\gamma - 1} P \quad (3.17)$$

Hence, we get:

$$c_s = c \sqrt{\frac{\gamma P}{\rho_0 c^2 + \frac{\gamma}{\gamma - 1} P}} = \begin{cases} \sqrt{\gamma P / \rho_0} & P \ll \rho_0 c^2 \text{ (non relativistic)} \\ c \sqrt{\gamma - 1} \simeq \frac{c}{\sqrt{3}} & P \gg \rho_0 c^2 \text{ (relativistic)}, \end{cases} \quad (3.18)$$

where $\gamma = 4/3$ has been used in the relativistic regime. If the fluid speed exceeds this relativistic sound speed, i.e., $\Gamma > \sqrt{3/2} \simeq 1.225$, a relativistic shock will develop. If we now define the specific enthalpy density (enthalpy density per particle):

$$h_* = \frac{h}{n} = \frac{nmc^2 + e + P}{n} = mc^2 + \frac{\gamma}{\gamma - 1} \frac{P}{n} \quad (3.19)$$

with m being the mass of the particles constituting the fluid, we can write the revised Rankine-Hugoniot conditions for a hydrodynamic relativistic shock in the rest frame

of the shock as follows [520]:

$$n_1 V_{1s} = n_2 V_{2s} \quad (3.20)$$

$$\Gamma_{1s} h_{*1} = \Gamma_{2s} h_{*2} \quad (3.21)$$

$$h_{*1} V_{1s} + \frac{P_1}{n_1 h_{*1}} = h_{*2} V_{2s} + \frac{P_2}{n_2 h_{*2}}. \quad (3.22)$$

Here, we again adopt three reference frames: the upstream frame “1”, the downstream frame “2”, and the shock front frame “s”. So, for example, Γ_{12} stands for the relative Lorentz factor between the upstream and downstream, and Γ_{1s} stands for the relative Lorentz factor between the upstream and the shock front.

In many problems (e.g., the afterglow problem in GRBs), the unshocked upstream is cold so that $e_1 = P_1 = 0$, $h_* = mc^2$. The jump conditions then become:

$$\frac{e_2}{n_2} = (\Gamma_{21} - 1)mc^2 \quad (3.23)$$

$$\frac{n_2}{n_1} = \frac{\gamma\Gamma_{21} + 1}{\gamma - 1} \quad (3.24)$$

$$\Gamma_{1s}^2 = \frac{(\Gamma_{21} + 1)[\gamma(\Gamma_{21} - 1) + 1]^2}{\gamma(2 - \gamma)(\Gamma_{21} - 1) + 2}. \quad (3.25)$$

For strong relativistic shocks, where $\Gamma_{21} \gg 1$, one has:

$$e_2 = (\Gamma_{21} - 1)n_2 m^2 \simeq \Gamma_{21} n_2 mc^2 \quad (3.26)$$

$$n_2 = 4\Gamma_{21} n_1 \quad (3.27)$$

$$\Gamma_{1s} \simeq \sqrt{2}\Gamma_{21} \quad \text{and} \quad \Gamma_{2s} \simeq \frac{3}{4}\sqrt{2}, \quad (3.28)$$

where we have used that $\gamma = (4\Gamma_{21} + 1)/(3\Gamma_{21})$ ⁵. We thus see that a relativistic shock is much stronger than a non-relativistic one, with downstream relativistic “temperature” of the order of $\Gamma_{21} mc^2$, and a compression ratio of $\chi = 4\Gamma_{21}$. We can interpret what we have just found in the following way: a downstream (region 2) observer sees a cold upstream (region 1) moving towards the observer with a bulk Lorentz factor Γ_{21} . After passing the shock, this bulk motion is converted to a *random* motion of the particles in the downstream rest frame with the Lorentz factor of the same order. From the above equations, we also have that $e_2 \simeq 4\Gamma_{21}^2 n_1 mc^2$, which is about $4\Gamma_{21}^2$ times the upstream rest mass energy density.

⁵It can be shown that in general one may write $P = \kappa e$, with $\kappa \simeq \frac{\bar{\Gamma} + 1}{3\bar{\Gamma}}$, where $\bar{\Gamma}$ is the average Lorentz factor of the gas particles.

From this we have $\gamma = \frac{c_p}{c_v} = \frac{e+P}{e} = \kappa + 1 \simeq \frac{4\bar{\Gamma} + 1}{3\bar{\Gamma}} \simeq \begin{cases} \frac{5}{3}, & \bar{\Gamma} \sim 1 \text{ (non relativistic)} \\ \frac{4}{3}, & \bar{\Gamma} \gg 1 \text{ (relativistic)} \end{cases}$

3.4.6 Particle acceleration in relativistic shocks

As pointed out in Sec. 3.4.2, there is an interdependence between the shock structure, the generation of energetic particles, and the generation of turbulence. The penetration of energetic particles in the shock precursor generates magnetic turbulence, providing the scattering process needed for particle acceleration through the Fermi process. This successful development first elaborated on non-relativistic shocks and inspired similar investigations for the relativistic ones. Since the particles gain much more energy for each crossing, efficient acceleration was expected. However, in ultra-relativistic shocks, there are some difficulties. Indeed, as we have seen, the particle drift downstream of the shock implies that more particles are moving downstream than upstream ($P_{\text{esc}} \propto \beta_{\text{sh}}$), and this anisotropy is of the order of β_{sh} when measured in the downstream frame [263]. Thus, while particle anisotropy is negligible for non-relativistic shocks, the distribution becomes highly anisotropic in the relativistic case, implying that one must simultaneously determine the spectrum and the angular distribution of the particles, which is the main difficulty underlying the analysis of test particle acceleration when the shock is relativistic. Semi-analytical studies of relativistic shock kinetic theory suggest that particles can be accelerated to a power law and that the derived power slope is quite “universal”. Assuming isotropy in the downstream, [263] found a generalization of the non-relativistic $k = (\chi + 2)/(\chi - 1)$ (see Eq. (3.16)):

$$k = \frac{\beta_{1s} - 2\beta_{1s}\beta_{2s}^2 + 2\beta_{2s} + \beta_{2s}^3}{\beta_{1s} - \beta_{2s}}, \quad (3.29)$$

which reduces to the non-relativistic expression, once $\beta_{1s}, \beta_{2s} \ll 1$ are assumed. For ultra-relativistic shocks, $\beta_{1s} \simeq 1$ and $\beta_{2s} \simeq 1/3$, implying $k \simeq 20/9 \simeq 2.22$. We see that the primary distinction in the relativistic scenario is that the energy spectrum becomes steeper compared to the non-relativistic case. Various studies have found different values for the spectral index. For example, [36] derived $k \simeq 2.2 - 2.3$ for various input parameters. $k \simeq 2.3$ was found for *parallel* (where the upstream magnetic field direction is parallel to the shock normal direction) relativistic shocks through Monte Carlo simulations [165]. Even steeper spectral indices $k \simeq 2.4$ resulted from particle-in-cell simulations [445].

The steeper spectral index is attributed to a combination of factors, including anisotropy in the particle distribution function and the available time for scattering. Particles in the upstream region do not diffuse significantly upstream; instead, they are rapidly overtaken by the shock before the particle’s direction has been significantly altered. Similarly, particles in the downstream region are rapidly advected downstream. As a consequence, both in the upstream and downstream regions, CRs have limited time to generate turbulent magnetic fields. The ability of CRs to generate turbulence is critical, and at very high bulk Lorentz factors, this effect can entirely prevent DSA from occurring. At an ultra-relativistic shock, the combination of quasi-perpendicular magnetic

fields, steep cosmic ray spectra, and reduced time available before the shock overtakes or advects away the CRs severely limits both the scale-size and magnetic field amplification associated with the turbulence generated by streaming or drifting CRs. Consequently, diffusion occurs well above the Bohm regime, and the maximum particle energy is accordingly lowered (see [111] and references therein).

3.4.7 Shock parametrization

To fully characterize non-relativistic and relativistic shocks from first principles, expensive numerical simulations of considerable computational cost are necessary. However, due to the complexity of the plasma physics at the microscopic level, a common approach is to parametrize the shocks using empirical parameters. These parameters account for our limited knowledge of the detailed microscopic processes while establishing a direct link with the observed properties. This simplification significantly reduces the complexity of the problems and serves as a bridge between the macroscopic and microscopic worlds. Some widely employed microphysical parameters include the following:

- k_e : the power-law index of the non-thermal electrons. Similarly, one can define an index for the non-thermal proton, k_p .
- ε_B : the fraction of the shock internal energy that goes into magnetic fields
- ε_e : the fraction of the shock internal energy that goes into accelerated electrons
- ε_p : the fraction of the shock internal energy that goes into accelerated protons

By definition, one has

$$\varepsilon_B + \varepsilon_e + \varepsilon_p = 1. \quad (3.30)$$

It is observed from several astrophysical environments that ε_e and ε_B can vary across orders of magnitudes, and also k_e is not universal, but dependent on the strength of the self-generated fields.

3.5 Magnetic reconnection

Magnetic reconnection is widely recognized in high-energy astrophysics as a mechanism that rapidly generates high-energy particles and radiation during flare-like events. This phenomenon is observed in various astrophysical objects, including pulsar wind nebulae, extragalactic jets, microquasars, GRBs, and coronae's heating above dense objects like accretion disks in X-ray binaries and AGN. It is also associated with the launch of transient large-scale outflows, potentially occurring in microquasars and GRBs.

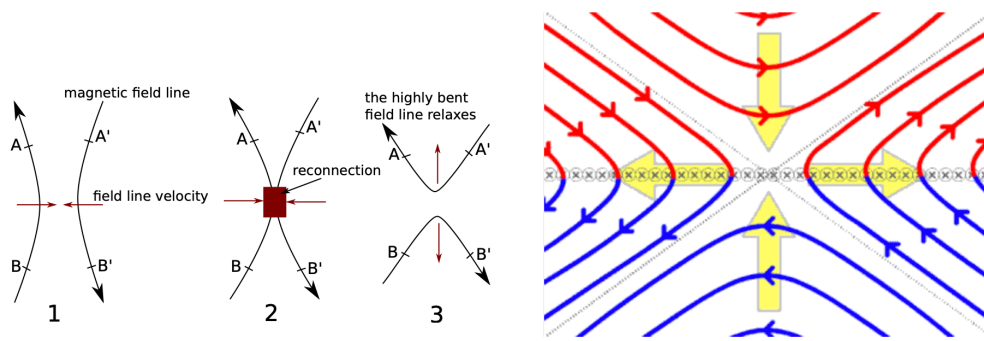


Figure 3.6: *Left:* In a 2D model of magnetic reconnection, the field topology can undergo a re-arrangement. Before the event (Image 1), points A and B (A' and B') lie on the same field line. However, after the event (Image 3), field lines connect points A and A' (B and B' respectively). This reconfiguration drives a strongly accelerated outflow in the directions where the highly bent magnetic field lines are relaxing. Figure from [316] *Right:* Yellow arrows: plasma motion, and also the motion of the field lines, which are drawn in red and blue. Reconnection occurs at the center. Figure taken from the Wikipedia article on magnetic reconnection.

The mechanism that triggers magnetic reconnection involves magnetic flux variations that induce, via Faraday's equation, electric fields. These induced electric fields imply a response from the plasma that tries to screen it. An ideal plasma (where the electrons are massless and never collide) does so perfectly, and the currents arising from charges set in motion by these electric fields produce magnetic fields that cancel the former magnetic flux variations: reconnection cannot occur, magnetic field lines cannot break apart. It is thus clear that non-ideal effects are needed for reconnection to initiate. Once initiated, these same non-ideal processes sustain the finite reconnection electric field and allow reconnection to go on. The system relaxes its energy during explosive reconnection events where two magnetic field lines are pushed together, cut at their intersection point, and subsequently reconnected with one another (see Refs. [313, 307, 316]). This is what happens in the left panel of Fig. 3.6, which presents a simple schematic of a reconnection site, depicting converging field lines of opposite polarity that undergo resistive dissipation. The central region of reconnection, characterized by the field lines' distinctive shape, is often referred to as an "X-point" or "X-line". In the right panel of Fig. 3.6, we can see how a convergent flow from above and below forces the field lines to reconnect, and the flow is then ejected to the right and left sides by magnetic tension (because the newly created red-and-blue field lines are highly bent and, due to the MHD force $\vec{j} \times \vec{B} \propto [\vec{V} \times \vec{B}] \times \vec{B}$ acting on the plasma, they tend to straighten). Even though magnetic reconnection is a local process, it dramatically affects the large-scale dynamics. We can quote some important effects [316]:

- It alters the magnetic structure significantly. Macroscopic regions initially not connected by any field line can become connected. As a result, the paths of ac-

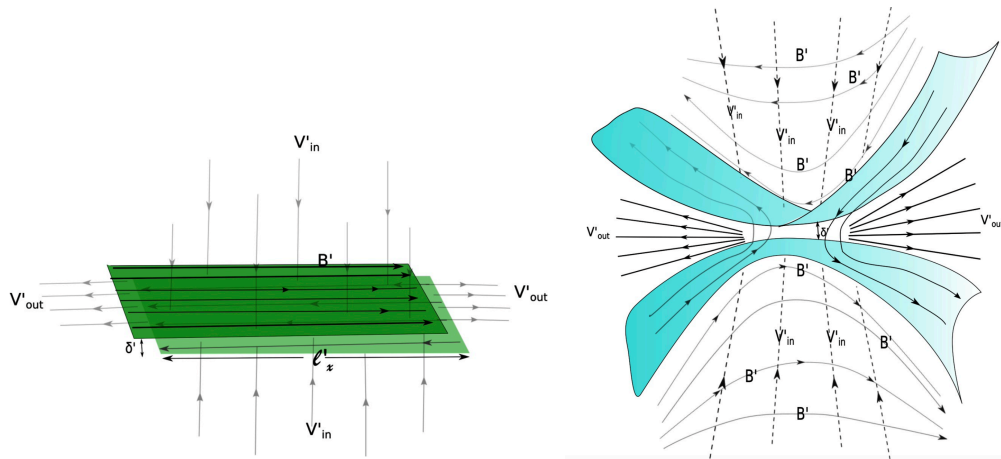


Figure 3.7: Configurations of magnetic reconnections: *Left:* A schematic sketch of the current sheet and plasma from outside the sheet flowing toward it, for *Sweet-Parker magnetic reconnection*. *Right:* A schematic sketch of plasma inflow and current-sheet, for *Petschek magnetic reconnection*. Much of the plasma flowing toward the current sheet does not pass through it but is redirected by standing shock waves; stationary slow mode shocks separate the inflow and outflow regions. Figures from [281].

celerated particles and heat are influenced, with both tending to flow more easily along the field lines than perpendicularly to them. Another noteworthy instance of large-scale topological change is the growth of magnetic islands up to the system's size. Such islands concentrate electric currents and induce profound changes in the overall system dynamics. This transformation in topology also permits the magnetic field to relax to a lower energy state, a change that was previously forbidden due to the conservation of field line identity in an ideal plasma, where it cannot break. Newly reconnected field lines can experience substantial tension forces and drive motion within the plasma.

- It converts magnetic energy into kinetic energy. This kinetic energy can be:
 - an increase of the bulk flow velocity: the flow is accelerated.
 - thermal: the plasma is heated.
 - non-thermal: high-energy particles are produced. The kinetic energy of the particles can be partly converted into radiation.

The distribution of energy among these components, the rate of energy transfer, the characteristics of the non-thermal component's spectrum, the velocity of the ejected bulk flows, the conditions that permit reconnection, especially in 3D geometries, and the back-coupling of reconnection events to large scales, are all active areas of ongoing research and investigation.

- It creates areas where the plasma is not ideal, either in the central dissipation region where the field lines reconnect or further away. These are places where strong electric fields, currents, waves, and instabilities are present. They can produce non-thermal high-energy particle populations.
- It can create turbulence

Magnetic reconnection is often described using two main non-relativistic frameworks: Sweet-Parker reconnection, where a long current sheet forms between the converging field lines, in a planar geometry, or Petschek reconnection, where rapid reconnection proceeds at the X-point in an X-shaped geometry, as shown in Fig. 3.7. Another way of having a rapid reconnection is in the presence of turbulence, which allows multiple reconnection events to occur simultaneously. Also, the relativistic reconnection, defined as the regime where the magnetic energy density exceeds the rest mass energy density of the plasma, which is relevant to jets, is now under simulation and shows much greater promise as an agent for extreme particle acceleration.

3.5.1 Particle acceleration through magnetic reconnection

Various acceleration mechanisms and multiple acceleration sites have been identified within a reconnection event, but which one dominates depends on the magnetic field geometry and plasma parameters, and it is still an open question. The efficiency of each process and the resulting particle spectrum are other key issues. Understanding these aspects is challenging due to the highly nonlinear nature of acceleration physics, necessitating simulations that span very long times and large domains to accurately capture the relaxed particle distributions, particularly in three dimensions when applicable. The principal known acceleration mechanisms are the following (see Ref. [316] for a more detailed description):

- **Acceleration by the reconnection electric field:** The reconnection electric field, resulting from magnetic flux variations and sustained by non-ideal processes in a steady state, can accelerate particles around the central dissipation region. However, this acceleration does not necessarily lead to a population of non-thermal high-energy particles capable of emitting high-energy photons. In 2D setups, reconnection outflows leave the central region with speeds close to the Alfvén speed, forming Alfvénic jets. These jets primarily undergo bulk flow acceleration. However, the reconnection electric field can produce high-energy tails in the particle distribution under certain conditions. PIC simulation studies have shown the creation of power-law tails of high-energy electrons using this mechanism, with power-law indexes potentially harder than those generated by collisionless shocks and shorter acceleration times. This mechanism can also produce power laws for ions.

- **Acceleration by contracting magnetic islands:** Magnetic islands, represented by closed field lines, undergo a contraction phase when they merge. During this phase, energetic particles within the islands become trapped by the magnetic structure. As the island contracts, these particles rebound between the converging sides of the island. This sets the stage for the first-order Fermi mechanism to come into play and accelerate these particles. The energy gain of the particles is primarily attributed to the electric field generated by the motion of the island sides within the magnetic field.
- **Acceleration between the two converging inflows:** Another acceleration mechanism, also relying on the first-order Fermi process and stochasticity, is the bouncing motion of particles between the two inflows converging from both sides of the current sheet. Energy is gained when the particle turns around and is transferred by the motional electric field present in the inflow. [159] derives the power-law spectral index that tends towards $k = 1$ for maximally compressive cases, namely when the compression ratio $\chi = \rho_{\text{out}}/\rho_{\text{in}}$ is maximized. Note that χ is not restricted to low values as in the case of shocks. Reconnection achieves its highest compression when effectively transforming magnetic energy into kinetic energy, potentially facilitating the transition from a Poynting flux-dominated jet to a kinetically dominant one. This means that a Fermi process within a reconnection zone establishes an inherent connection between magnetic energy release and particle acceleration.
- **Acceleration in contracting current sheets:** The contraction of current sheets, whether triggered by instability or large-scale dynamics, can make the first-order Fermi mechanism operate.

The ones we described above are just some of the main processes invoked to explain particle acceleration in magnetic reconnection events. Other acceleration mechanisms exist, such as stochastic acceleration in the turbulence associated with reconnection.

Energy-loss processes

In this Chapter, we briefly review the main particle energy-loss processes at play in many astrophysical environments and relevant to the topics covered in this thesis. These comprise the energy losses due to radiative processes and particle interactions. Here, we provide the most important formulas useful to understand the physics underlying the various emission mechanisms, and we point the interest readers to the references [153, 301, 199] for more detailed discussions and derivations.

4.1 Leptonic processes

4.1.1 Synchrotron radiation

Synchrotron emission is a fundamental process in astrophysics that is crucial in understanding a wide range of astrophysical phenomena. In this brief overview, we will introduce the key aspects of synchrotron emission, exploring the underlying physics of the emission mechanism and the spectral properties.

4.1.1.1 Physics of synchrotron radiation

We have seen in Chapter 3 that shocks are ubiquitous in the high-energy Universe and that these can accelerate charged particles - electrons, protons, and heavier nuclei - to ultra-relativistic energies. The magnetic field responsible for the acceleration is also a source of energy loss processes for the charged particles. In particular, magnetic fields induce the particles that are accelerated along a curved path or orbit to emit *synchrotron radiation*. For an electron with Lorentz boost factor $\gamma = 1/\sqrt{1 - \beta^2}$, with velocity \vec{v} making a pitch angle θ with the direction of the magnetic field \vec{B} , the relativistic Larmor formula gives the total radiated power, $P_{\text{syn}}(\theta) = 2\sigma_T\beta^2\gamma^2cU_B \sin^2 \theta$, where $\beta = v/c$,

$\sigma_T = 6.65 \times 10^{-25} \text{cm}^2$ is the Thomson scattering cross section, and $U_B = B^2/(8\pi)$ is the magnetic energy density. If now we average on an isotropic pitch-angle distribution and consider a generic relativistic particle of mass m , charge Z , Lorentz factor γ , the Larmor formula becomes:

$$P_{\text{syn}} = \frac{4}{3} \sigma_T \left(\frac{m_e}{m} \right)^2 Z^4 \gamma^2 c U_B. \quad (4.1)$$

where $\beta \sim 1$ has been adopted. It is clear already from this expression that light particles are the ones that most efficiently cool by synchrotron radiation. By taking, for example, electrons and protons, we have that $m_e/m_p \sim 5.4 \times 10^{-4}$, a proton with the same Lorentz factor of an electron, radiates $\sim 10^{-7}$ less power, making the contribution of particles heavier than electrons completely negligible in most astrophysical environments. For particles with an isotropic pitch angle distribution and that radiate via synchrotron, the lifetime (or *cooling time*) is:

$$t_{\text{sync}}(\gamma) = \frac{\gamma m c^2}{P_{\text{syn}}} = \frac{6\pi m^3 c}{\sigma_T m_e^2 Z^4 \gamma B^2}. \quad (4.2)$$

One can see that more energetic particles have shorter cooling times. Unless otherwise specified, since the emitting particles are essentially electrons and positrons, we assume $m = m_e$ and $Z = 1$. The formulae will be re-scaled when needed by the particle mass of interest.

At a time t after the acceleration of a population of electrons with a power-law distribution, the *cooling Lorentz factor* γ_c above which they have lost most of their energy (so that $t = t_{\text{sync}}(\gamma_c)$) is given by:

$$\gamma_c(t) = \frac{6\pi m_e c}{\sigma_T B^2 t}. \quad (4.3)$$

For an impulsively accelerated particle ensemble, as time progresses, the cooling energy at the moment t defines the maximum energy of the population so that $\gamma_{\text{max}} \simeq \gamma_c$.

4.1.1.2 Synchrotron spectrum

There is a characteristic frequency associated with the synchrotron process that corresponds to the inverse of a specific time interval. In cases of relativistic electrons, this time interval is not the orbital revolution period. Rather, it represents the portion of time within each orbit during which the observer detects radiation (the emission is observed only during the fraction of the orbit within the beaming angle $1/\gamma$). It can be shown that such frequency is given by

$$\nu_s(\gamma) = \gamma^2 \nu_L = \frac{\gamma^2 e B}{2\pi m_e c} \quad (4.4)$$

where ν_L is the Larmor frequency, defined as the gyration frequency for sub-relativistic particles. Most of the power is emitted at $\nu_* \simeq 0.29\nu_c$, where $\nu_c = \frac{3}{2}\nu_s(\gamma) \sin \theta$ is the *critical frequency*. The spectrum emitted from a single electron has the following frequency dependence:

$$P(\nu, \gamma, \theta) \propto \begin{cases} \nu^{1/3} & \nu \ll \nu_c \\ \nu^{1/2} e^{-\nu/\nu_c} & \nu \gg \nu_c, \end{cases} \quad (4.5)$$

where $P(\nu, \gamma, \theta) = dE/(dtd\nu)$ is the emitted power per unit frequency.

We now consider a population of particles described by a power law distribution and emitting in a magnetic field. We have already seen in Chapter 3 how shocks and magnetic reconnection can accelerate particles to power-law distributions with a certain spectral index k . So, we introduce the following:

$$N(\gamma) = A_\gamma \gamma^{-k} \text{ for } \gamma_{\min} < \gamma < \gamma_{\max} \quad \text{or} \quad N(E) = A_E E^{-k} \text{ for } E_{\min} < E < E_{\max}, \quad (4.6)$$

where $A_\gamma = A_E(m_e c^2)^{(1-k)}$, and γ_{\min} and γ_{\max} are the maximum and minimum Lorentz factors of the electron energy distributions, respectively.

To get the total photon spectrum emitted by such an electron distribution, one would need to integrate over γ the power produced by a single electron with a given γ times $P(\nu, \gamma, \theta)$ (namely $\int_{\gamma_{\min}}^{\gamma_{\max}} N(\gamma) P(\nu, \gamma, \theta) d\gamma$). By doing so, we obtain the following synchrotron spectrum:

$$F_\nu \propto \begin{cases} \nu^{1/3} & \nu < \nu_{\min} \\ \nu^{-(k-1)/2} & \nu_{\min} < \nu < \nu_{\max} \\ \nu^{1/2} e^{-(\nu/\nu_{\max})} & \nu > \nu_{\max}, \end{cases} \quad (4.7)$$

where $\nu_{\min[\max]} = \frac{3}{2}\nu_s(\gamma_{\min[\max]}) \sin \theta$. It can be shown that if instead of being uniform, the magnetic field in the emission region is randomized (as is the case of magnetic fields generated in shocks and in regions of magnetic reconnection events), one obtains 4.7 for the emitted synchrotron radiation, but dropping the $\sin \theta$ term in ν_{\min} and ν_{\max} expressions.¹

One important aspect that must be considered at this point is that, analogously to all other emission processes, an absorption counterpart exists also for synchrotron radiation. Indeed, the emitted synchrotron photons can interact with a charge in a magnetic field and transfer their energy to the charge. The separation between the

¹This is true in the regime where $\gamma\lambda_B/r_L \gg 1$, where λ_B is the correlation scale of the random magnetic field, and r_L the Larmor radius of a particle with Lorentz factor γ , as defined in Eq. (3.1). Particle-in-cell simulations suggest that the random magnetic field configuration in collisionless shocks is consistent with being in this regime.

thick and thin regime happens at the *self-absorption frequency* ν_a , below which the synchrotron flux is self-absorbed (the synchrotron spectrum peaks very close to ν_a). Moreover, the spectrum in Eq. (4.7) has been derived for the radiation emitted from an ensemble of electrons that have undergone an *impulsive* acceleration to a power-law distribution. However, we know that in many astrophysical environments, new particles can be continuously injected in the acceleration process (think of a shock sweeping fresh particles from the medium is propagating through).

In summary, when considering an ensemble of electrons characterized by a continuously injected power-law distribution and subject to synchrotron cooling and self-absorption, the resulting synchrotron radiation spectrum can be represented as a multi-segment broken power law. The specific form of these spectra depends upon the relative sequencing of ν_a , ν_{\min} , and ν_c , and results in six different orderings. When $\nu_m < \nu_c$ ($\nu_m > \nu_c$), the particles are said to be in a *slow cooling* (*fast cooling*) regime. When $\nu_a < \nu_c$ ($\nu_a > \nu_c$), we are in the presence of *weak absorption* (*strong absorption*). Here, we show as an example only one of the six different orderings that will be relevant when treating gamma-ray bursts, namely the case $\nu_a < \nu_c < \nu_{\min} < \nu_{\max}$ (fast cooling, weak absorption):

$$F_\nu = F_{\nu, \max} \begin{cases} \left(\frac{\nu_a}{\nu_c}\right)^{\frac{1}{3}} \left(\frac{\nu}{\nu_a}\right)^2 & \nu \leq \nu_a \\ \left(\frac{\nu}{\nu_c}\right)^{\frac{1}{3}} & \nu_a < \nu \leq \nu_c \\ \left(\frac{\nu}{\nu_c}\right)^{-\frac{1}{2}} & \nu_c < \nu \leq \nu_{\min} \\ \left(\frac{\nu_{\min}}{\nu_c}\right)^{-\frac{1}{2}} \left(\frac{\nu}{\nu_{\min}}\right)^{-\frac{k}{2}} & \nu_{\min} < \nu \leq \nu_{\max}. \end{cases} \quad (4.8)$$

4.1.2 Inverse-Compton scattering

4.1.2.1 Physics of Inverse-Compton emission

Inverse Compton (IC) scattering is the process in which ultra-relativistic electrons scatter low-energy photons so that the photons gain energy at the expense of the kinetic energy of the electrons. It must be distinguished from the direct Compton scattering, in which the electron is at rest, and it is the photon that gives part of its energy to the electron. This interaction can occur in two different regimes, the Thomson and the Klein–Nishina regimes. In the Thomson regime, the photon's energy in the electron rest frame is much smaller than $m_e c^2$. In this case, the recoil of the electron, even if it always exists, is small and can be neglected. In the opposite case (photon energies

larger than $m_e c^2$), we are in the Klein–Nishina regime, and we cannot neglect the recoil. It can be shown that the maximum (minimum) energy of the scattered photon can be achieved in a head-on (tail-on) collision (the photon would be scattered in the direction of the electron velocity vector or the opposite direction, respectively). If ε_0 is the energy of the photon before collision, and the electron has Lorentz factor γ , the final photon energy becomes $\varepsilon_1 = 4\gamma^2\varepsilon_0$ for head-on collisions, and $\varepsilon_1 = 1/(4\gamma^2)\varepsilon_0$ for tail-on collisions. Averaging over all relative photon-electron directions, the average energy of the scattered photons is $\langle\varepsilon_1\rangle = (4/3)\gamma^2\varepsilon_0$. The IC scattering process is thus an effective means of creating very high-energy photons and is highly efficient in reducing the energy of high-energy electrons whenever large fluxes of photons and relativistic electrons occupy the same volume.

Let us now consider an isotropically distributed incoming photon distribution. It can be shown that the total energy loss rate of a generic particle of mass m , charge Z , and Lorentz factor γ in the Thomson regime is:

$$P_{\text{IC}} = \frac{4}{3}\sigma_T\left(\frac{m_e}{m}\right)^2 Z^4\gamma^2 c U_{\text{ph}}, \quad (4.9)$$

where U_{ph} is the energy density of the target photons, and $\beta \sim 1$ has been adopted. Notice the similarity with the synchrotron energy loss. The energy loss rates for both processes are the same once the radiation energy density is replaced by the magnetic energy density U_B . Consequently, when relativistic particles exist within a region with some radiation and magnetic energy densities, they emit radiation through the synchrotron and IC scattering mechanisms. The ratio of the two luminosities will be:

$$\frac{P_{\text{IC}}}{P_{\text{syn}}} = \frac{U_{\text{ph}}}{U_B}. \quad (4.10)$$

The relative importance of the two energy densities determines which mechanism is the dominant cooling mechanism for the particles. Finally, the cooling time due to the IC process is:

$$t_{\text{IC}}(\gamma) = \frac{\gamma m c^2}{P_{\text{IC}}} = \frac{3m^3 c^2}{4\sigma_T m_e^2 Z^4 \gamma c U_{\text{ph}}}. \quad (4.11)$$

As already pointed out for the synchrotron radiation, the IC loss rate is strongly suppressed for all particles heavier than electrons. So, in the following, we discuss only electrons.

4.1.2.2 Inverse-Compton spectrum

The resultant spectrum of IC scattering should, in principle, depend on the characteristics of both the incident photon spectrum and the energy distribution of the electrons.

However, in practice, it is only necessary to determine the spectrum produced by one single electron of a given energy γmc^2 , scattering photons of a given energy ε_0 . The final photon spectrum is then obtained by averaging over the actual distributions of photons and electrons. It can be shown that for an electron power-law distribution $N(\gamma) \propto \gamma^{-k}$, the resulting IC spectrum is $F_\gamma \propto \nu^{-(k-1)/2}$, regardless of the detailed spectrum of incident photons. Note that this energy dependence is identical to the case of synchrotron emission (Sec. 4.1.1.2), which is not a coincidence. Indeed, it is because both the IC and the synchrotron single electron spectra are peaked at a typical frequency that is a factor γ^2 greater than the starting energy seed.

4.1.3 Bremsstrahlung

Bremsstrahlung, or also *free-free radiation*, is the emission produced from unbound electrons interacting with the Coulomb electric field of atomic ionized nuclei. The electrostatic interaction decelerates the electron, which emits photons, bringing away part of its kinetic energy. It is an important electron emission mechanism in dense plasma, as might be the case of the heated ionized material in the downstream region of a shock. It becomes the primary cooling process for temperatures $T > 10^7$ K. For a plasma of electrons with number density n_e , ions of charge Z_i with number density n_i , the total emitted energy per unit time and volume can be demonstrated to be:

$$J_{\text{br}} = \frac{dE}{dt dV} = g n_e n_i Z_i^2 T^{1/2} \quad [E L^{-3} T^{-1}] \quad (4.12)$$

with g being a numerical factor that depends on the specifics of the interaction. Hence, for an overall neutral plasma ($n_e = n_i$), the cooling time for bremsstrahlung energy loss can be estimated by dividing the total thermal energy density of the plasma by J_{br} :

$$t_{\text{br}}(T) = \frac{3}{2} \frac{n_e k_B T}{J_{\text{br}}} \propto \frac{T^{1/2}}{Z_i n_e}. \quad (4.13)$$

We do not provide details of the photon spectrum that results from this kind of emission since we do not directly use it in the context of this thesis.

4.2 Hadronic processes

As charged particles, protons (and more generally ions) can emit radiation similarly to electrons via synchrotron and IC mechanisms. We have already derived the formulae of the total emitted power (see Eq. (4.1)- (4.9)), and we have seen that because of the significant difference in mass, the radiation power of particles heavier than electrons is much lower. This means that unless the total energy carried by protons is much

larger than that carried by electrons, proton synchrotron and IC emissions are much weaker than those of electrons in a typical astrophysical environment and thus can be neglected.

4.2.1 Photo-pair production (Bethe-Heitler)

The photo-pair production, commonly referred to as the *Bethe-Heitler mechanism*, is a fundamental process in high-energy astrophysics where a high-energy photon interacts with the electromagnetic field of a nucleus, resulting in the creation of an electron-positron pair:

$$p + \gamma \rightarrow p + e^+ e^-. \quad (4.14)$$

For a proton of energy E_p , the threshold for this process can be determined by the condition:

$$s = (p_p + p_\gamma)^2 \geq (m_p c^2 + 2m_e c^2)^2 \rightarrow E_p \geq \frac{m_p m_e}{\varepsilon_\gamma}, \quad (4.15)$$

where ε_γ is the energy of the target photon, and we assumed head-on collisions. By considering only relativistic protons, the photon energy in the proton rest frame becomes $\varepsilon_r = \gamma_p \varepsilon_\gamma (1 - \cos \theta)$, with $\gamma_p = E_p / m_p c^2$. The cross-section $\sigma_{\phi e}(\varepsilon_r)$ for photo-pair production in the regime $\varepsilon_r \gg m_e c^2$ is [153]:

$$\sigma_{\phi e}(\varepsilon_r) \simeq \frac{7}{6\pi} \alpha_f \sigma_T \ln \left(\frac{\varepsilon_r}{m_e c^2 k_{\phi e}} \right), \quad (4.16)$$

where $k_{\phi e}$ is a constant in the range $2 \lesssim k_{\phi e} \lesssim 6.7$, and $\alpha_f \simeq 1/137$ is the fine structure constant. Finally, one can show that the timescale for photo-pair energy loss is given by:

$$t_{\text{BH}}(\gamma_p) \simeq \left[\frac{7m_e \alpha \sigma_T c}{9\sqrt{2}\pi m_p \gamma_p^2} \int_{\gamma_p^{-1}}^{\infty} d\varepsilon \frac{n_{\text{ph}}(\varepsilon)}{\varepsilon^2} \left\{ (2\gamma_p \varepsilon)^{3/2} \left[\ln \left(\frac{2\gamma_p \varepsilon}{k_{\phi e}} \right) - \frac{2}{3} \right] + \frac{2}{3} k_{\phi e}^{3/2} \right\} \right]^{-1} \quad (4.17)$$

where $n_{\text{ph}}(\varepsilon)$ is the target photon density field (in units of $E^{-1}L^{-3}$), and we have defined $\varepsilon = \varepsilon_\gamma / (m_e c^2)$.

4.2.2 Photo-hadronic interaction

We have discussed in detail the $p\gamma$ mechanism in Sec. 2.2.2. The energy-loss timescale for this process is [153]:

$$t_{p\gamma}(\gamma_p) = \left[\frac{c}{2\gamma_p} \int_{\frac{\varepsilon_{\text{th}}}{2\gamma_p}}^{\infty} d\varepsilon \frac{n_{\text{ph}}(\varepsilon)}{\varepsilon^2} \int_{\varepsilon_{\text{th}}}^{2\gamma_p \varepsilon} d\varepsilon_r \varepsilon_r \sigma_{p\gamma}(\varepsilon_r) K_{p\gamma}(\varepsilon_r) \right]^{-1}, \quad (4.18)$$

where $\epsilon = \epsilon_\gamma/m_e c^2$. The inelasticity is found to be $K_{p\gamma} \simeq 0.2$ for $0.39 \lesssim \epsilon_r \lesssim 0.98$ GeV, and $\simeq 0.6$ for $\epsilon_r \gtrsim 0.98$ GeV. Depending on the type of source environment, the photon spectrum can extend from sub-eV up to TeV energies, and its shape can contain peaked (thermal) or power-law (non-thermal) components.

4.2.3 Hadronic interaction

The pp mechanism was discussed in Sec. 2.2.1. We have also seen that the cross-section varies very slowly with energy. For many practical purposes, it is enough to consider the mean total *cross section for pp* in the TeV-PeV energy range,

$$\langle\sigma_{pp}\rangle \simeq 6 \times 10^{-26} \text{cm}^2, \quad (4.19)$$

which is about two orders of magnitude higher than that of the $p\gamma$ process. The cooling time of a relativistic accelerated proton due to inelastic pp collisions is roughly given by:

$$t_{pp} = \frac{1}{c\langle\sigma_{pp}\rangle n_p K_{pp}} \quad (4.20)$$

where $K_{pp} \sim 0.5$ is the pp interaction inelasticity. This high value tells us that only a few interactions are required for energetic protons to lose a large fraction of their initial energy.

Stellar evolution and supernova explosion

In Chapter 6, we introduce the two astrophysical transient sources that are the focal points of investigation in this thesis: interaction-powered supernovae and long gamma-ray bursts. To provide a comprehensive context and facilitate the understanding of the progenitors responsible for these phenomena, both of which are linked to massive stars reaching the end of their lifecycle through a supernova explosion, in this chapter, we offer a concise overview of the evolution of massive stars. Interaction-powered supernovae necessitate a dense medium surrounding the progenitor star. Thus, we outline the mechanisms governing stellar mass losses, which culminate in a substantial ejection of the stellar envelope during the pre-supernova phase. We also present the classification and describe the standard emission mechanisms of core-collapse supernovae (CCSNe). This knowledge will be necessary for interpreting and distinguishing the emission mechanisms inherent to interaction-powered supernovae compared to standard supernovae.

5.1 Stellar evolution in a nutshell

Stellar evolution follows a series of distinct stages that can eventually lead to supernova (SN) explosions. A star can be initially approximated as a uniform sphere with mass M_* and radius R_* that is held together by its self-gravity and is balanced against collapse by pressure gradients, with pressure dropping sharply at its surface. Integrating hydrostatic balance equations for the entire star

$$\frac{dP}{dr} = -\frac{GM_r\rho}{r^2} \quad \text{and} \quad \frac{dM_r}{dr} = 4\pi\rho r^2, \quad (5.1)$$

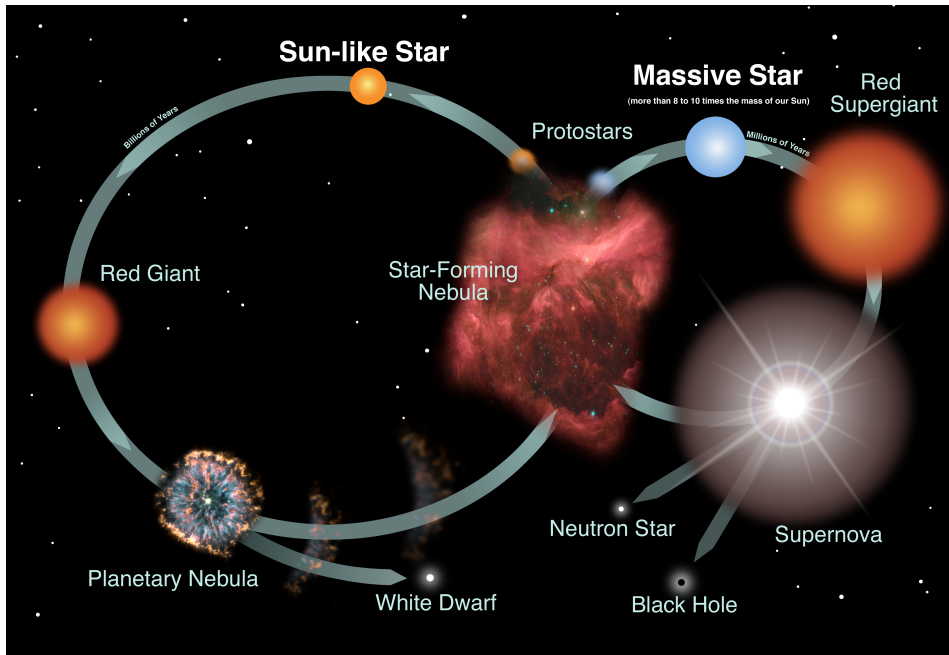


Figure 5.1: Diagram showing the lifecycles of Sun-like and massive stars. Credit: NASA and the Night Sky Network.

where M_r is the enclosed mass below a given radius r within the star and ρ the density, the central pressure becomes $\bar{P} \propto M_* \bar{\rho} / R_*$ (where the bar indicates the averaged quantities over the entire star), which captures the balance between internal energy and gravitational energy. If we consider an ideal gas ($\bar{P} \propto \bar{\rho} \bar{T}$), we can derive the relation between central temperature and density, $\bar{T} \propto \bar{\rho}^{1/3} M_*^{2/3}$. The latter implies that when a star contracts and releases energy at the expense of its gravitational binding energy, not only the density but also the temperature increases. This relation holds for the ideal gas Equation-of-State (EOS) and is a consequence of the Virial theorem for an object bound by self-gravity.

If, instead, the pressure is provided by non-relativistic degenerate electrons, we have that $P_e \propto \rho^{5/3}$ (the pressure does not depend on the temperature), and the thermal energy does no longer play a role in supporting the star against gravity. The boundary between these two regimes is defined by equating degenerate pressure at zero temperature with thermal pressure. Given these premises, we can summarize the typical phases of the evolution of all stars as follows [305] (see also Fig. 5.1):

- **Protostar formation:** a region of a molecular cloud contracts to higher density and temperature under its gravity, forming a dense core known as a protostar.
- **Main Sequence Phase:** When the central temperature of the protostar reaches $T \sim 10^7$ K, hydrogen fusion begins in the core, producing helium through nuc-

lear reactions. The star enters a stable phase known as the Main Sequence (MS), where the outward pressure from fusion balances the gravitational collapse. This is where the stars spend most of their lives.

- **Red Giant/Supergiant phase:** When hydrogen in the core is completely consumed, the star is described as a He core plus an H-rich envelope. The lack of radiation pressure from nuclear burning makes the core contract and the inner temperature rise. As a result, H in the regions outside the core starts to burn in a shell surrounding the core. Stellar models consistently predict that, at this stage, there is a huge expansion of the outer layers of the star, which becomes a Red Giant or Supergiant, depending on the zero-age main sequence mass (M_{ZAMS}). As the red giant phase progresses, the He core continues to contract and heat up, while the hydrogen-burning shell deposits additional helium “ash” on it. Eventually, when temperatures $T \sim 10^8$ K are reached, the fusion of He nuclei into heavier elements is ignited.
- **Post-He burning phases:** in the subsequent evolution, the star initiates a series of successive stages, each consisting of the contraction and heating of its inner regions, leading to the ignition of new nuclear reactions that can be summarized as follows: $\text{H} \rightarrow \text{He}, \text{He} \rightarrow \text{C}, \text{C} \rightarrow \text{O}, \text{O} \rightarrow \text{Ne}, \text{Ne} \rightarrow \text{Si}, \text{Si} \rightarrow \text{Fe}$. The last burning stage stops with the formation of an iron core.

The electron degenerate pressure and when it dominates mainly determines a star’s fate. Less massive stars, with $M_{\text{ZAMS}} \lesssim 10 M_{\odot}$ (M_{\odot} being the mass of the Sun), become degenerate before forming an iron core. In these cases, the electron degenerate pressure can halt the contraction and the ignition of subsequent nuclear reactions. The resulting object is a dense and hot star called a white dwarf (WD) (see the left branch in Fig. 5.1).

More massive stars, with $M_{\text{ZAMS}} \gtrsim 10 M_{\odot}$, undergo all the stages of nuclear burning up to the production of elements in the “iron group” with an atomic mass number around $A = 56$. At this stage, the star’s outer envelope has expanded to about $1000 R_{\odot}$ (where R_{\odot} is the radius of the Sun), and it has a dense core of radius $\sim 10^4$ km with an onion-like layered structure. The iron group elements are a “dead end” in nuclear energy production since their fusion into heavier elements consumes, rather than release, thermal energy. This fact is at the root of the “iron catastrophe” that follows.

5.2 Core-collapse supernovae

When in the contraction, the mass of the iron core reaches the Chandrasekar limit for the electron degenerate gas, $M \sim M_{\text{ch}} \sim 1.4 M_{\odot}$, the degenerate electrons become relativistic. Their EOS softens, transitioning from $P_e \propto \rho^{5/3}$ to $P_e \propto \rho^{4/3}$ [305]. For increasing masses, the electron pressure becomes incapable of supporting the core against

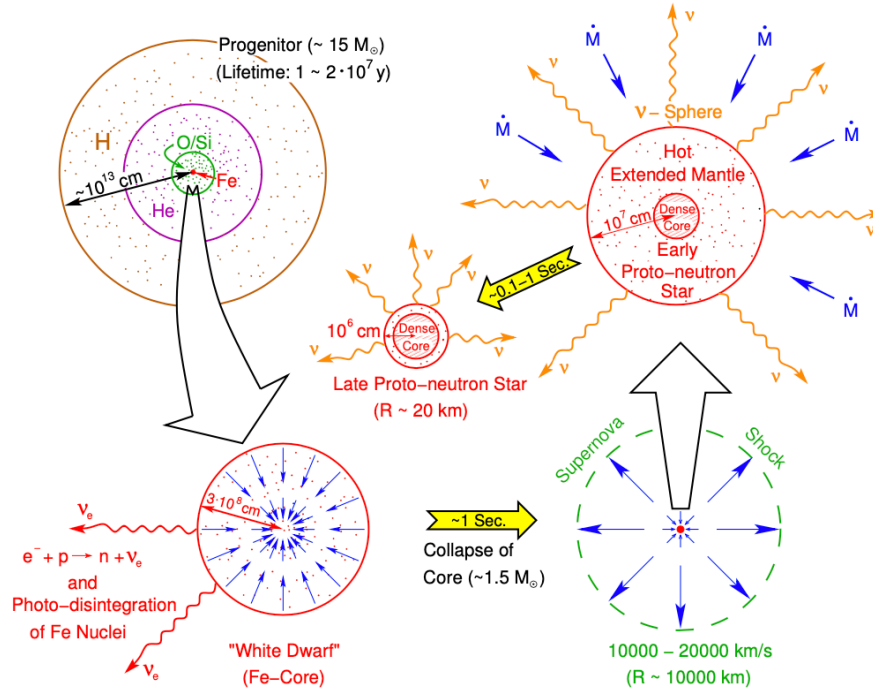
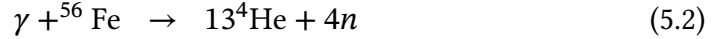


Figure 5.2: Evolution of a massive star from the onset of iron-core collapse to a neutron star. The progenitor star at the moment of collapse (upper left corner) exhibits a typical onion-like structure, with concentric layers of progressively heavier elements towards the nucleus. The iron core in the center (lower left corner) is primarily supported by the fermion pressure of the nearly degenerate electrons. However, this stability is disrupted when rising temperatures permit the partial photo-disintegration of iron nuclei. As a result, the core starts to contract, and the contraction becomes a collapse over a free-fall timescale when electron pressure is further removed by their captures on both bound and free protons. This process releases electron neutrinos, which initially escape freely. A fraction of a second later, the catastrophic inward collapse halts as nuclear-matter density is reached, and a proto-neutron star begins to form. At this point, a powerful shock wave is launched and propagates outward, leading to the star's disruption in a SN explosion (lower right corner). The nascent neutron star (upper right corner) gradually contracts into a more compact form while accreting additional matter within its first second of existence. This phase, along with the subsequent cooling and neutronization of the compact remnant, is governed by the emission of neutrinos and antineutrinos of all flavors, which diffuse outward from the dense core over a period of tens of seconds. Figure from [249].

gravity, and the core collapses. As the density and temperature continue to increase, two processes begin:

1. **Nuclear Photodisintegration:** the energetic photons get absorbed in the endothermic (i.e., energy-consuming) nuclear reactions:



Given the need of 124 MeV and 28.3 MeV for unbinding the nuclei in the two reactions, approximately 10^{52} erg of the core thermal energy is extracted already in this process.

2. **Neutronization:** as the core density gets higher, for $\rho \gtrsim 10^{11} \text{ g cm}^{-3}$, electron capture starts playing an important role, due to the increasing electron Fermi energy that forbids the neutron decay:



This process reduces the number of free electrons in the core and their supporting degeneracy pressure. Furthermore, the neutrinos produced in the reaction can leave the star. These neutrinos carry kinetic energy (usually of a few MeV), which is lost for the core.

As a consequence of these processes, which lead to an almost total loss of thermal pressure support, the core evolves toward an increasingly dense and neutron-rich structure as the collapse proceeds on a free-fall timescale. Neutrino losses cool the star until the core matter reaches densities of about $\sim 4 \times 10^{11} \text{ g cm}^{-3}$. At such high densities, neutrinos cannot diffuse out of the core and are “trapped”. The collapse continues until the core reaches nuclear matter densities ($\rho \sim 10^{14} \text{ g cm}^{-3}$). At such extreme densities, characterized by tightly packed nucleons, the repulsive nature of the strong nuclear force kicks in, effectively stiffening the EOS dramatically. As a result, the collapse of the inner core experiences an abrupt halt, setting off a strong shock wave that propagates into the still collapsing outer core. This sequence of events is commonly called the “core bounce” [136].

Initially, the shock moves rapidly outward through the outer core. However, strong neutrino cooling behind the shock and the photodissociation of iron-group nuclei cause the shock to come to a standstill at a radius of approximately ~ 100 kilometers. In the meantime, the inner core, consisting of the original core and additional mass that has fallen through the shock, has regained quasi-hydrostatic equilibrium and is made mainly of neutrons: a newborn hot proto-neutron star (PNS), which cools very fast via emission of neutrinos. How the stalled shock is “revived”, i.e., made to propagate out dynamically to expel the outer layers of the star, remains the subject of active research

(see reviews [326, 250, 106]). There are several proposed mechanisms, and some examples of these include magnetorotational supernova mechanism [287], the acoustic mechanism [107], sterile neutrino decays [186] and conversions [402], and the quark-hadron phase transition mechanism [426]. However, the most promising scenario for most CCSNe is the *delayed neutrino-heating mechanism* [91]. In this model, the shock's revival occurs through the reabsorption of a portion of the neutrinos emitted from the surface of the PNS surface in the region behind the shock. If the neutrino heating is sufficiently strong, the resulting increase in thermal pressure pushes the shock outwards. This reinvigorated shock then blows off the star's outer shells in what is observed as a SN explosion.

The explosion expels the matter outside a certain distance from the PNS into the stellar surrounding medium. The remnant central object consists mainly of neutrons. Because of the high density, the neutrons are partially degenerate; the degeneracy becomes complete as the core cools, primarily through the emission of neutrinos, and it settles down as a neutron star (see right branch in Fig. 5.1). A schematic representation of the evolution of a massive star from the onset of iron-core collapse to a neutron star is shown in Fig. 5.2. We note that only for stars in a specific mass range ($\sim 8 - 30 M_{\odot}$ on the MS), the explosion from a CCSN results in the formation of a neutron star. More massive stars can still end their lives as CCSNe, but instead likely generating a black hole in the center due to the fallback of material onto the neutron star, or directly forming a black hole, without SN explosion [236].

The whole process of the collapse, beginning with a Chandrasekhar mass iron core with radius $R_{\text{core}} \sim 1000$ km and ending with a PNS with radius $R_{\text{PNS}} \sim 10$ km, takes a fraction of a second. The gravitational collapse liberates an enormous amount of gravitational binding energy:

$$\Delta E_{\text{gr}} = \frac{3}{5} G M_{\text{core}}^2 \left(\frac{1}{R_{\text{PNS}}} - \frac{1}{R_{\text{core}}} \right) \simeq \frac{3}{5} \frac{G M_{\text{core}}^2}{R_{\text{PNS}}} = 3.1 \times 10^{53} \left(\frac{M_{\text{core}}}{1.4 M_{\odot}} \right)^2 \left(\frac{R_{\text{PNS}}}{10 \text{ km}} \right)^{-1} \text{ erg.} \quad (5.5)$$

The bulk of this energy (about 99%) is carried away by neutrinos of all flavors, as confirmed by the detection of neutrinos from SN 1987A [239]. About $\sim 10^{51}$ erg is carried away by the ejected mass (M_{ej}) as kinetic energy, and at most $\sim 10^{49}$ erg is emitted in radiation. The energy per unit mass sets the scale of the associated explosion velocity: it is $v_{\text{ej}} = \sqrt{2GM_{\text{core}}/R_{\text{core}}} \sim 10^4$ km s⁻¹, essentially the escape velocity from the core.

5.3 Mass loss in massive stars

Before describing the characteristic emission from SNe, we need to discuss the phenomenon of stellar mass loss. We know from observations that during their pre-SN

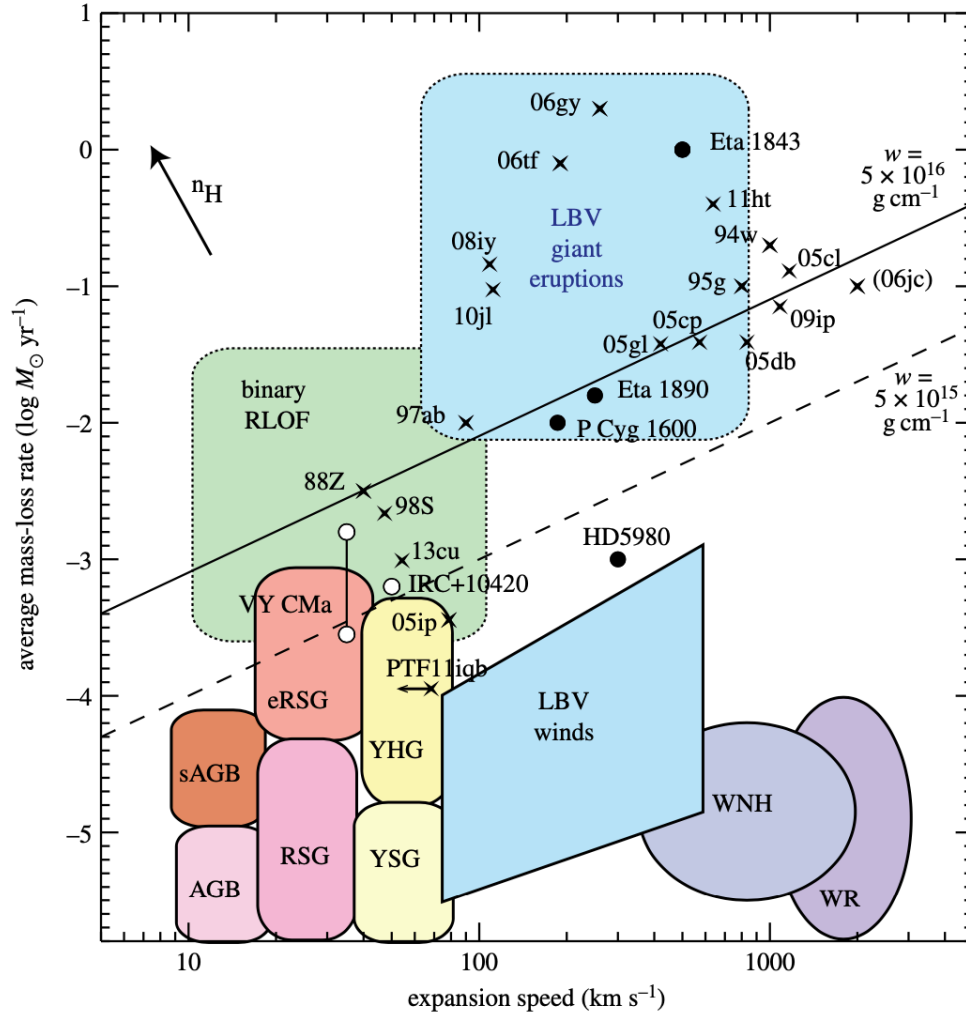


Figure 5.3: Plot of mass-loss rate as a function of wind velocity. The solid colored regions correspond to values for various types of evolved massive stars, corresponding to asymptotic giant branch (AGB) and super-AGB stars, red supergiants (RSGs) and extreme RSGs (eRSG), yellow supergiants (YSG), yellow hypergiants (YHG), luminous blue variables (LBV) winds and LBV giant eruptions, binary Roche-lobe overflow (RLOF), luminous WN stars with hydrogen (WNH) and WC Wolf–Rayet (WR) stars. A few individual stars with well-determined, very high mass-loss rates are shown with circles (e.g., η Car’s eruptions and P Cyg’s eruption). Also shown with ‘X’s are some representative examples of SNe II_n (and one SN Ib_n). Figure from [53].

evolution, many stars must have undergone significant mass loss episodes and lost part of their envelope. The strength of the mass loss strongly affects the stellar evolution and the final fate of the star, with a significant impact on the type of SN that ultimately occurs.

There are two ways in which stars can lose part of their envelope:

- via **steady winds**, that occur due to the intense radiation pressure generated in high-luminous stars with high metallicities. We have seen that massive stars emit enormous energy through nuclear fusion in their cores. This energy is radiated outward as intense UV and optical radiation. Photons carry momentum, and as they interact with atoms and ions in the star's outer layers, they exert a force on these particles: the radiation pressure. Stars with higher metallicity have line-absorption processes, which enhance the radiation pressure and can trigger mass loss more easily. As massive stars evolve, they go through stages where their luminosity can increase, causing an increase in mass-loss rates.

A rough estimate of the mass-loss rate in a radiatively driven wind can be computed by assuming that each photon emitted by the star transfers its momentum of $h\nu/c$ to a gas particle in the wind. The star loses momentum at a rate of L/c , where L is the radiative luminosity. The rate at which the wind carries away such momentum is $\dot{M}_w v_w$, where v_w is the asymptotic wind velocity that is constant in time and space and is on the order of the escape velocity from the star's photosphere. By setting the two rates equal to each other, we estimate the mass loss rate of the star:

$$\dot{M}_w = \frac{L}{c v_w}. \quad (5.6)$$

The mass-loss rate and the velocity of these winds strongly depend on the progenitor stars' type, luminosity, and temperature. In Fig. 5.3, the expected mass loss and wind velocities from observed classes of stars are shown.

- via **episodic winds**: these are sporadic, short-lived episodes of mass loss, often associated with eruptive events in massive stars. While the exact mechanism behind these eruptions remains unknown, there are clear historical examples of them occurring, with η Carinae being the most famous. In the mid-nineteenth century, η Car experienced a remarkable outburst that lasted a decade, during which it expelled roughly $10 M_\odot$ of material [450]. Typically, super-Eddington winds, instabilities in the later stages of nuclear burning, explosive shell ignition, or mass transfer in binaries are invoked to provide the necessary energy observed in the outbursts. Luminous Blue Variables (LBVs, see Fig. 5.3) provide an example of stars in this category. When these stars eventually explode, the interaction with the surrounding material can result in a Type IIn SN.

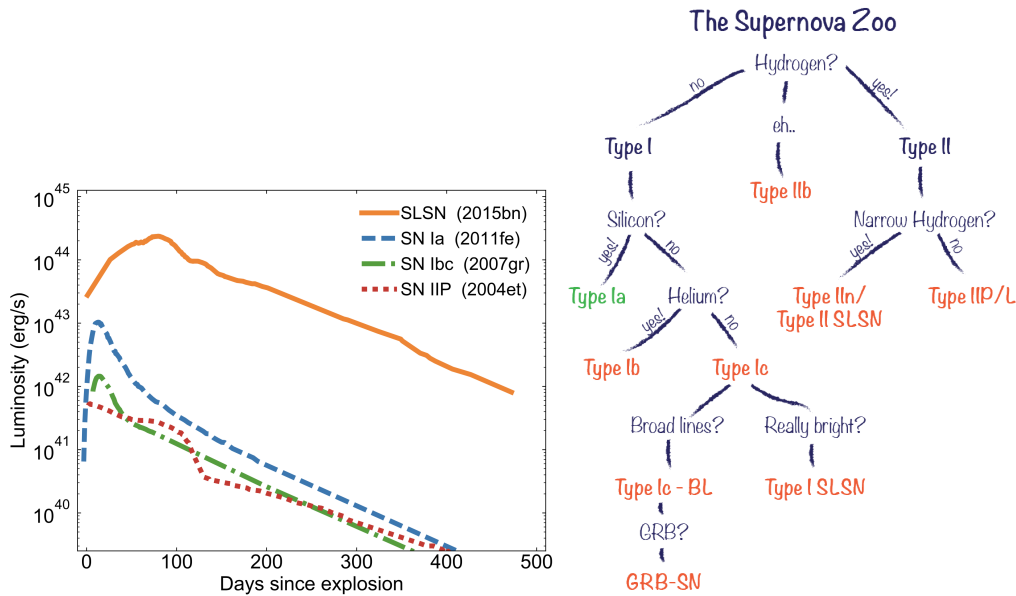


Figure 5.4: *Left panel:* Examples of optical lightcurves of SNe of different types. Credit: M. Nicholl. *Right panel:* Classification of all types of observed SNe. Figure from Web.

5.4 Classification of supernovae

The main physical parameters that determine the observed properties of a typical CCSN whose progenitor did not undergo strong mass loss during its evolution are M_{ej} , the kinetic energy of the explosion E_k (as well as the mass of synthesized radioactive material), and the composition and structure of the star's envelope at the time of the explosion. This leads to the vast diversity in observed types of normal ejecta-dominated CCSNe, whose classification and typical lightcurves can be seen in Fig. 5.4. CCSNe are broadly categorized into two main groups based on the presence or absence of hydrogen (H) lines in their spectra. These sub-types can be classified as follows:

1. **Type I SNe:** are SNe that either have weak or no H lines in their spectra. There are further sub-divisions within Type I SNe:
 - **SNe Ia:** exhibit strong silicon (Si) lines in their spectra and are not CCSNe. Instead, they result from thermonuclear explosions of white dwarf stars.
 - **SNe Ib:** if Si lines are not present but strong He lines are observed, the SN is classified as Type Ib.
 - **SNe Ic:** when neither Si nor He lines are detected in the spectra of a Type I SN, it is categorized as Type Ic.

2. **Type II SNe:** these SNe have prominent hydrogen-rich spectra. Type II SNe are further characterized as:

- **SNe IIb:** in cases where the H lines gradually disappear at later times, the SN is similar to Type Ib.
- **SNe IIn:** these SNe display H narrow spectral lines. They are a subset of interaction-powered SNe, which will be discussed in detail in Sec. 6.1.

Additionally, Type II SNe can be classified based on their lightcurve behavior:

- **SNe IIL:** if the luminosity decreases linearly after reaching its peak.
- **SN IIP:** if the luminosity remains relatively constant or plateaus for several months after reaching its peak.

5.5 Emission from “standard” supernovae

Having explored the various subtypes of SNe lightcurves along with their distinctive spectral features, in this section, we provide a brief overview of the basic physics governing the emission mechanism from the majority of SNe. However, before delving into this, it is necessary to mention one important phenomenon inherent to exploding stars – the synthesis of heavy nuclei.

After the core bounce, in accordance with the neutrino-driven explosion paradigm, the revived shock wave propagates outward through the stratified layers of the star. The shock is incredibly hot and energetic, with temperatures reaching billions of degrees Kelvin. Nuclear reactions can occur at very high rates within such a hot and dense environment. Besides photodisintegration, where high-energy photons disintegrate atomic nuclei into their constituent protons and neutrons, the extreme temperatures within the shock wave also allow the fusion of nuclei, resulting in the synthesis of heavier elements. This process, known as “explosive nucleosynthesis,” depends on the maximum temperature attainable behind the shock wave, as well as neutrino interactions and electron capture that can affect the neutron-to-proton ratio in the shock environment. The outcome of nucleosynthesis is a substantial change in the composition of materials in the innermost ejecta, with the formation of a wide range of elements [59]. For materials with roughly equal numbers of protons and neutrons (which is ^{26}Si), the most abundant produced isotope turns out to be ^{56}Ni (due to the combination of its being at the peak in the binding energy and the equal numbers of protons and neutrons in it), followed by He and other Fe-peak elements. So, upon the complete disruption of the progenitor star, we can visualize the resulting SN as an outburst of metal-rich ejecta with a layered composition structure that expands into the surrounding interstellar medium (ISM) or circumstellar matter (CSM). The dynamic evolution of this

ejected material is quite complex. The shock’s propagation determines the distribution of explosion energy within the progenitor star’s envelope. Although the star undergoes mixing, it does not achieve homogenization. The post-shock material’s velocity, density, and heavy element distributions influence the SN lightcurve. The outermost part of the star, typically encompassing only a small fraction of the envelope’s mass (around 1%), develops a steep power-law density structure, significantly impacting the lightcurve during shock breakout and the initial 10 to 20 days thereafter. However, to get a basic physical understanding of the broad-scale evolution of SN ejecta in the aftermath of several tens of days post-shock passage, in what follows, we neglect this complex phase and adopt idealized initial conditions that provide an approximate representation of the ejected material.

5.5.1 Power sources of supernovae lightcurves

Multiple sources can contribute to the luminosity observed in SNe. One primary source is the *thermal energy* deposited by the shock wave’s propagation through the progenitor star. The total energy of the ejecta can be written as the sum of the kinetic and thermal energies, $E_{\text{tot}} = E_{\text{k}} + E_{\text{th}}$. We anticipate that the thermal energy immediately after the shock breakout (i.e., at the initial radius R_0 for the expanding ejecta, where R_0 is the progenitor’s radius) is $E_{\text{th}}(R_0) \sim E_{\text{k}}$, so the equipartition is realized [256].

Initially, the ejecta are optically thick, and we can reasonably neglect energy loss through radiation. Therefore, the internal thermal energy decreases because of the adiabatic expansion, which translates to $E_{\text{th}}(R) = E_{\text{th},0}(R/R_0)^{-1}$, where $E_{\text{th},0} = E_{\text{tot}}/2$. In realistic explosion calculations, most of the ejected envelope has an approximately homologous velocity profile and uniform density a few days after shock passage. The velocity distribution results from the innermost layers pushing the overlying layers and transferring most of their kinetic energy and momentum to them. Within these approximations, it is possible to model the ejecta in spherical symmetry as a hot, freely expanding ionized material with initial radius R_0 and density $\rho_0 = (3/4\pi)M_{\text{ej}}/R_0^3$. The velocity v of each ejecta shell is approximately constant in time and proportional to its position within the ejecta (homologous expansion). At t_0 it is $v = v_0(r(t_0)/R_0)$, where $v_0 = v_{\text{ej}}$ is the (constant) velocity of the outermost shell of the ejecta initially at R_0 . The radius of each gas shell increases linearly with time as:

$$r(t) = r(t_0) + v(t - t_0) \simeq v(t - t_0) \quad \text{for } t - t_0 \gg t_{e,0}, \quad (5.7)$$

where $t_{e,0} = R_0/v_0$ is the initial expansion timescale of the ejecta. For the outermost shell: $R(t) = R_0 + v_0(t - t_0) \simeq v_0(t - t_0)$. Mass conservation then gives:

$$\rho(t) = \rho_0 \left(\frac{R_0}{R(t)} \right)^3 \simeq \frac{\rho_0 t_{e,0}^3}{(t - t_0)^3}. \quad (5.8)$$

For homologous expansion, we can write the evolution of the internal energy as $E_{\text{th}}(t) = E_{\text{th},0}(t/t_{e,0})^{-1}$.

In general, we can express the luminosity of the SN lightcurve as:

$$L_{\text{SN}} = \frac{E_{\text{SN}}(t_{\text{SN}})}{t_{\text{SN}}}, \quad (5.9)$$

where t_{SN} is the appropriate timescale for the duration of the lightcurve, and E_{SN} is the appropriate energy. Therefore, L_{SN} and t_{SN} depend on the specific power source. If the only source is the thermal energy stored in the ejecta, then t_{SN} would be set by the effective diffusion time through the ejecta, given by [60]:

$$t_{\text{diff}} \simeq \frac{\kappa M_{\text{ej}}}{\zeta c R} \quad (5.10)$$

where ζ is a scaling constant that depends on the opacity distribution, κ , and density. With $\zeta \sim 13.8$, applicable to a range of the density/opacity distribution, the diffusion time is described as follows:

$$t_{\text{diff}}(t) \simeq 130 \text{ days} \left(\frac{\kappa}{0.2 \text{ cm}^2 \text{ g}^{-1}} \right) \left(\frac{M_{\text{ej}}}{M_{\odot}} \right)^{3/2} \left(\frac{E_{\text{tot}}}{10^{51} \text{ erg}} \right)^{-1/2} \left(\frac{t}{\text{day}} \right)^{-1} \quad (5.11)$$

where we have used $R = v_0 t$. As the ejecta expand and the density drops, the diffusion timescale decreases. Therefore, at some point, it becomes shorter than the characteristic expansion timescale $t = R/v_0$. The moment at which this happens defines the time of the luminosity peak, $t_{\text{diff}}(t_{\text{peak}}) = t_{\text{peak}}$, which thus reads as:

$$t_{\text{peak}} \simeq 11 \text{ days} \left(\frac{\kappa}{0.2 \text{ cm}^2 \text{ g}^{-1}} \right)^{1/2} \left(\frac{M_{\text{ej}}}{M_{\odot}} \right)^{3/4} \left(\frac{E_{\text{tot}}}{10^{51} \text{ erg}} \right)^{-1/4}. \quad (5.12)$$

One can easily check, by rewriting the diffusion time in terms of the optical depth of the ejecta as $t_{\text{diff}} = \tau R/3c$, that this occurs when $\tau \sim 3c/v_0$, meaning that the maximum light is not when the ejecta turn transparent, as one might naively expect [99]. This is, roughly speaking, the basic mechanism that determines the characteristic timescale in the rise and decay of standard SNe, as shown in the lightcurves of Fig. 5.4. The characteristic luminosity due only to internal thermal energy becomes then:

$$L_{\text{SN,th}} = \frac{E_{\text{th}}(t_{\text{peak}})}{t_{\text{peak}}}. \quad (5.13)$$

By using Eq. (5.12), it reduces to

$$L_{\text{SN,th}} \simeq 10^{41} \text{ ergs}^{-1} \left(\frac{\kappa}{0.2 \text{ cm}^2 \text{ g}^{-1}} \right)^{-1} \left(\frac{M_{\text{ej}}}{M_{\odot}} \right)^{-1} \left(\frac{E_{\text{tot}}}{10^{51} \text{ erg}} \right) \left(\frac{R_0}{10^6 \text{ km}} \right). \quad (5.14)$$

Given that the typical observed luminosity of SNe is $\gtrsim 10^{42}$ ergs $^{-1}$, it is evident that this energy source is important for a RSG progenitor (SNe II), for example, but not for more compact stars like SNe Ia or SNe Ib/c, for which the initial thermal energy is essentially depleted by the epoch of maximum light and an alternative source of luminosity is needed. This alternative is well known, and it is provided by *radioactive decay*, especially the chain: $^{56}\text{Ni} \rightarrow ^{56}\text{Co} \rightarrow ^{56}\text{Fe}$.

^{56}Ni is unstable, $^{56}\text{Ni} + e^- \rightarrow ^{56}\text{Co} + \gamma + \nu_e$, with a half-life of 6.1 days (e-folding lifetime $\tau_{\text{Ni}} = 6.1/\ln 2$ days = 8.8 days). In turn, ^{56}Co decays to stable ^{56}Fe , 81% of the time by electron capture: $^{56}\text{Co} + e^- \rightarrow ^{56}\text{Fe} + \gamma + \nu_e$, and 19% by positron decay, $^{56}\text{Co} \rightarrow ^{56}\text{Fe} + e^+ + \gamma + \nu_e$, with half-life 77 days ($\tau_{\text{Co}} = 111.3$ days) [99]. The important aspect to consider here is that the energy emitted via radioactivity cannot be converted into the adiabatic expansion of the ejecta until the decay starts occurring. So the fact that the radioactive energy is deposited at later times, in the form of γ -rays and positrons (with neutrinos escaping without energy deposition), makes it possible to avoid most of the adiabatic conversion into kinetic energy to heat the ejected material, and emit the thermal emission in ultraviolet, optical, and infrared (UVOIR) bands¹. The fact that the decay times of ^{56}Ni and ^{56}Co are roughly the same as the timescale on which a solar mass of material exploded with 10^{51} erg of energy becomes nearly optically thin, is a coincidence of physics, one that allows SN Ia to shine so brightly.

All the decay energy of ^{56}Ni and about 97% of the decay energy of ^{56}Co are released in the form of γ -rays. The total available energy from the nuclear decay is [99]:

$$L_{\text{Rad}} = (6.45 \times 10^{43} e^{-t/8.8 \text{ days}} + 1.45 \times 10^{43} e^{-t/111.3 \text{ days}}) \frac{M_{\text{Ni}}}{M_{\odot}} \text{ erg s}^{-1}. \quad (5.15)$$

Not all this energy is necessarily absorbed by the SN ejecta to heat them. This is the case only during the early phases when the ejecta are dense, but at later times, when the ejecta are optically thin, proper treatment of the γ -ray transport is needed to estimate the expected luminosity. However, it can be shown that around the peak time, Eq.(5.12), the optical depth for γ -ray absorption is still high, so that the peak luminosity is roughly determined by the decay power (usually dominated by the ^{56}Co decay for most of SNe); this is $10^{41} - 10^{43}$ erg s $^{-1}$ for $M_{\text{Ni}} = 0.01 - 1 M_{\odot}$.

¹The γ -ray heating happens as follows: γ -rays are initially trapped in the SN’s optically thick and dense ejecta through Compton scattering and pair production interactions. These interactions result in the gradual redistribution of γ -ray energy among the particles in the ejecta, increasing the kinetic energy of the ejecta’s constituents (atoms, ions, and electrons). This, in turn, raises the temperature of the ejecta. The increased temperature leads to a rise in thermal pressure. This pressure gradient can drive the overall expansion of the SN remnant. As the ejecta expand, they cool, and the temperature of the emitted radiation drops. The degraded γ -rays through the Compton scattering create a continuum down to ~ 100 keV below which the photons are absorbed through the photoelectric absorptions.

Selected transient sources

In this Chapter, we present a comprehensive overview of the two transient sources addressed in this thesis: interaction-powered supernovae and long gamma-ray bursts. We delve into the observational aspects and provide the essential theoretical framework that will help the reader understand the observational properties characterizing both phenomena.

6.1 Interaction-powered supernovae

An energy source alternative to the thermal and radioactive ones discussed in the previous Chapter, and of significant interest for the work in this thesis, is provided by the interaction of the SN ejecta with the circumstellar medium (CSM), which we will call *ejecta-CSM interaction*. In this case, the main power would come from converting the ejecta kinetic energy into radiation.

All SNe must interact with interstellar material at some stage. If the density of this material is not high enough, then the interaction becomes observable only some decades after the explosion as X-rays from a young SN remnant. Here, we concentrate on cases when the density in the vicinity of the exploding star is much higher than average due to much more powerful winds in the pre-SN stage or other hydrodynamic events such as pulsations, eruptions, and violent mass transfer in a binary star, as discussed in. Sec. 5.3

There are strong arguments to believe that Type IIn SNe and their extreme version, represented by Type IIn Superluminous SNe (SLSN IIn), are mainly powered by ejecta-CSM interaction. This is particularly due to their distinctive characteristics, like the slow-evolving, long-lived, and relatively bright lightcurves, as well as the presence of narrow H lines in their spectra. It is difficult to explain the very high peaks ($\sim 10^{43} - 10^{44} \text{ ergs}^{-1}$) and luminosities observed in SLSN IIn (see Fig. 5.4) without

invoking interaction with a very dense CSM ¹. By looking at Eq. (5.15), we see that a power input provided by the radioactive decay of ⁵⁶Ni would require the production of up to $10 M_{\odot}$ of ⁵⁶Ni in the ejecta. Masses like this are extremely hard to synthesize unless invoking very special and highly massive progenitors, which die as pair-instability SNe ² [331].

There is one crucial thing we need to remember: in general, one should not identify SNe IIn and related categories as a supernova type (or, more accurately, not an intrinsic explosion type) but as an external phenomenon associated with CSM interaction. It is crucial to understand that any CCSNe, thermonuclear SNe, or even non-SN explosive outflows can manifest as a SN IIn. All that is required is fast ejecta with sufficient energy crashing into slower ejecta with sufficient density.

In this section, we describe the basic physical picture of the dynamics of the ejecta-CSM interaction. Then, we provide a brief observational perspective, discussing the expected emission due to the interaction. We consider the idealized case of spherical supernova ejecta interacting with a spherical CSM, as sketched in Fig. 6.2. We note that our description applies in particular to CCSNe.

6.1.1 Interaction of supernova ejecta with circumstellar medium

Let us consider a spherical CSM density profile with total CSM mass M_{CSM} contained within an outer radius R_{CSM} and described by a power-law function of the radius:

$$\rho_{\text{CSM}}(R) = \frac{(3-s)M_{\text{CSM}}}{4\pi R_{\text{CSM}}^3} \left(\frac{R}{R_{\text{CSM}}} \right)^{-s} = BR^{-s}. \quad (6.1)$$

We note that $B = \dot{M}_w/4\pi v_w R^2$ for the case of a wind-density profile, with $s = 2$. When the star explodes, the SN ejecta expand inside the CSM and interact with it. Since the velocity of the outer layers of the supernova ejecta ($\sim 10^4 \text{ km s}^{-1}$) is much higher than the velocity of the CSM medium, v_w , we can consider the CSM to be stationary. Given the supersonic velocities of the ejecta, the interaction results in the formation of a forward shock (FS) propagating outwards, heating the CSM, and a reverse shock (RS)

¹We note that luminous blue variables (LBV) have been suggested [453] as possible progenitors of SNe and SLSNe IIn, given the large periodic mass loss rates observed in some cases (see Fig. 5.3), but several complications exist [160].

²The most massive stars, typically those with mass $M \gtrsim 140 M_{\odot}$, can undergo a unique type of SN known as a pair-instability SN (PISN) [236]. This phenomenon is driven by a critical temperature in the star's core, where high-energy photons convert into e^-e^+ pairs, reducing the core's radiation pressure and initiating the core collapse. However, before the core can entirely collapse, the explosive burning of oxygen reverses the process, resulting in a powerful explosion that completely disrupts the entire star. These PISNe are exceptionally energetic, with an estimated energy release of about 10^{52} ergs.

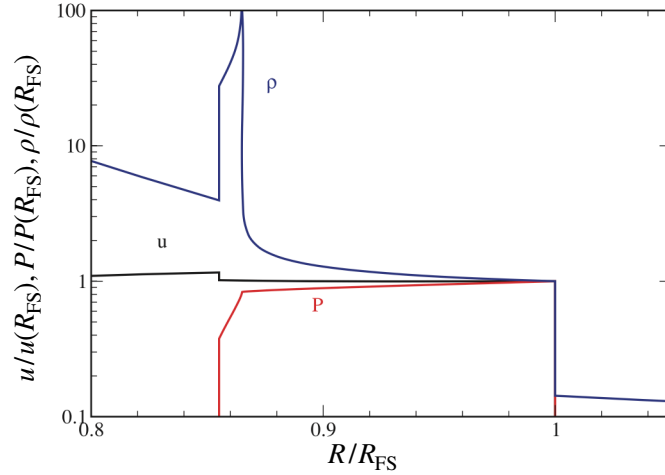


Figure 6.1: The velocity (black), pressure (red), and density (blue) profiles of the self-similar solution for SN ejecta (from the left) with $n = 10$ propagating through a CSM (at the right) with $s = 2$. The radial coordinate is normalized to the radius of the FS, and the physical quantities are normalized to their post-shock values at the FS front. The contact discontinuity corresponds to the radius at which the density peaks, while the RS is located where there is a jump in the ejecta density. Adapted from [72].

propagating inwards (in mass), reheating the outer layers of the ejecta (see Fig. 6.2). The forward-shocked CSM and the reverse-shocked ejecta are separated by a contact discontinuity (CD), R_{CD} , where the density peaks, as shown in Fig. 6.1.

Before interaction with the wind, the radial density profile of the outer layers of the ejecta can usually be described by a steep power law. Relying on numerical simulations [314], it is found that during the homologous expansion, the density profile is [130, 332]:

$$\rho_{ej}(R, t) = g_n t^{n-3} R^{-n}, \quad (6.2)$$

with

$$g_n = \frac{1}{4\pi(n-\delta)} \frac{[2(5-\delta)(n-5)E_k]^{(n-3)/2}}{[(3-\delta)(n-3)M_{ej}]^{(n-5)/2}}, \quad (6.3)$$

where E_k is the total SN kinetic energy, M_{ej} is the total mass of the SN ejecta, n is the density slope of the outer part of the ejecta and δ the slope of the inner one. The parameter n depends on the nature and properties of the progenitor's envelope (it can be convective or radiative); $n \simeq 12$ is typical of RSGs [314], while lower values are expected for more compact progenitors (e.g., a value of $n \simeq 10$ is predicted for SN Ib/Ic and SN Ia progenitors).

When the interaction region between the two shocks can be treated in a thin-shell approximation, namely when the radial distance between the two shocks is small compared to R_{CD} , the evolution of the shell can be described by a self-similar solution with

adiabatic index $\gamma = 4/3$, appropriate for a radiation dominated gas [126]. Let us assume that the shocked gas is concentrated in a shell with mass M_s , velocity v_{sh} , and radius $R_{\text{sh}} \equiv R_{\text{CD}}$. Balancing the ram pressure from the CSM and the impacting ejecta, the momentum equation for the shocked material becomes [131]:

$$M_s \frac{dv_{\text{sh}}}{dt} = 4\pi R_{\text{sh}}^2 [\rho_{\text{ej}}(v_{\text{ej}} - v_{\text{sh}})^2 - \rho_{\text{CSM}} v_{\text{sh}}^2]. \quad (6.4)$$

The mass of the shocked shell M_s is given by the sum of the swept up ejecta mass behind the RS, $M_{\text{RS}} = 4\pi \int_{R_{\text{sh}}}^{\infty} \rho_{\text{ej}}(r)r^2 dr$, and that of the CSM behind the FS, $M_{\text{FS}} = 4\pi \int_0^{R_{\text{sh}}} \rho_{\text{CSM}}(r)r^2 dr$. With $v_{\text{ej}} = R_{\text{sh}}/t$ the maximum ejecta velocity close to the RS, one finds that the shell radius evolves as a power law in time [126]:

$$R_{\text{sh}}(t) = \left[\frac{Ag_n}{B} \right]^{\frac{1}{n-s}} t^{\frac{n-3}{n-s}} \equiv \alpha t^{\frac{n-3}{n-s}}, \quad (6.5)$$

with B defined as in Eq. (6.1), and A a constant. The solution applies after a few expansion times. The velocity of the FS is:

$$v_{\text{sh}} = \frac{dR_{\text{sh}}}{dt} = \frac{(n-3)R_{\text{sh}}}{(n-s)t} = \frac{(n-3)}{(n-s)} v_{\text{ej}}, \quad (6.6)$$

while the RS velocity is

$$v_{\text{RS}} = v_{\text{ej}} - v_{\text{sh}} = \frac{(3-s)}{(n-s)} v_{\text{ej}}. \quad (6.7)$$

The radii of the FS and the RS are given by

$$R_{\text{FS(RS)}} = \beta_{\text{FS(RS)}} R_{\text{sh}}, \quad (6.8)$$

where β_{FS} and β_{RS} are constants representing the ratio of the shock radii to the contact-discontinuity radius R_{sh} (see also Fig. 6.2). The width of the shocked shell is consequently $\Delta R = R_{\text{FS}} - R_{\text{RS}}$. The values of β_{FS} and β_{RS} are determined by the values of n and the slope of the CSM density profile, and are given in Table 1 of Ref. [126]. The self-similar solution describes the normalized profiles of the density, velocity, and pressure profiles and depends on the values of n , s , and the adiabatic index of the shocked materials, γ . An example of such a profile for $n = 10$, $s = 2$, and $\gamma = 4/3$ is shown in Fig. 6.1.

We note that no self-similar solution exists for the general case and that the solution above holds only for the cases where $M_{\text{ej}} \gg M_{\text{CSM}}$. In the opposite regime, $M_{\text{ej}} \ll M_{\text{CSM}}$, also called *blastwave-regime*, the situation is similar to a point explosion in a power-law medium. In this case, the whole ejecta are immediately swept by the RS, and the energy of the ejecta is promptly dissipated in a small region at the center of the CSM. The FS propagation in a power-law atmosphere has been well studied in the literature (e.g., [517]).

6.1.2 Emission from interaction-powered supernovae

Based on the scalings we provided in the previous section, we can derive the properties of the emission we expect to see from interaction-powered SNe. As sketched in Fig. 6.2, the structure created by the FS and RS shocks consists of four different zones where heated material can radiate and contribute to the observed spectrum:

- Zone 1 represents the unshocked CSM outside the FS.
- Zone 2 represents the CSM already swept up and heated by the FS.
- Zone 3 represents the decelerated SN ejecta already shocked by the RS.
- Zone 4 represents the freely expanding SN ejecta.

The kinetic luminosity of the FS is [481]:

$$L_{\text{FS}} = \frac{d}{dt} \left(\frac{1}{2} M_{\text{FS}} v_{\text{sh}}^2 \right) = M_{\text{FS}} v_{\text{sh}} \frac{dv_{\text{sh}}}{dt} + \frac{1}{2} \frac{dM_{\text{FS}}}{dt} v_{\text{sh}}^2 = 2\pi\rho_{\text{CSM}} R_{\text{sh}}^2 v_{\text{sh}}^3 \quad (6.9)$$

where we have ignored the small deceleration of the shell ($dv_{\text{sh}}/dt \simeq 0$). Analogously, one can find the luminosity of the RS as:

$$L_{\text{RS}} \simeq 2\pi\rho_{\text{ej}} R_{\text{sh}}^2 v_{\text{RS}}^3. \quad (6.10)$$

We expect that a fraction ϵ_{FS} of L_{FS} and a ϵ_{RS} of L_{RS} will be converted into radiation. The efficiencies ϵ_{FS} and ϵ_{RS} will depend on SN and CSM parameters. From the above two expressions, one can also show that $L_{\text{FS}}/L_{\text{RS}} = (n-s)/(3-s)$ [462], so for steep ejecta profile the RS would only insignificantly contribute to the total energy dissipation rate. For this reason, in what follows and in the Chapter on our results, we will only focus on the FS.

Now, we can infer the typical wavebands in which this radiation should be observed. Let us derive the temperature T_i of a species with mass m_i right behind a shock of velocity v_{sh} by requiring that $3/2k_B T_i = 1/2m_i v_{\text{ud}}^2$, where k_B is the Boltzmann constant, and v_{ud} the upstream speed in the downstream frame. Using Eq. (3.8), we have that $v_{\text{ud}} = (1 - 1/\chi)v_{\text{sh}} = [2/(\gamma + 1)]v_{\text{sh}}$, and thus

$$k_B T_i = \frac{4}{3(\gamma + 1)^2} m_i v_{\text{sh}}^2. \quad (6.11)$$

If the plasma is in full thermal equilibrium, we can use a single temperature to describe it. Assuming solar abundances and equipartition between ions and electrons, the above expression tells us that the temperature of the shocked CSM is

$$T_{\text{FS}} \sim 1.2 \times 10^9 \text{ K} \left(\frac{n-3}{n-s} \right)^2 \left(\frac{v_{\text{ej}}}{10^4 \text{ kms}^{-1}} \right)^2. \quad (6.12)$$

Here we have adopted a mean atomic weight $\mu \sim 0.6$ for a fully ionized plasma of solar abundance and replaced $m_p \rightarrow \mu m_p$. The temperature at the RS would be instead $T_{\text{RS}} = T_{\text{FS}}/(n-3)^2$ [131]. We see that for typical parameters, the temperatures of the two shocks are very different, $\sim (1-3) \times 10^9$ K for the FS and $\sim 10^7 - 5 \times 10^8$ K for the RS, depending on n .

If L_{FS} could be directly released and observed at Earth, the spectrum would be expected to be hard, peaking in the X-ray band and with emission lines. Nevertheless, spectra with these characteristics are rarely observed in SNe IIn and have not been seen in SLSNe II. So, it is natural to conclude that the CSM must be optically thick to radiation, and the effects of radiative diffusion of the shock-generated luminosity must be significant in explaining the currently observed optical LCs and spectra of these events. Let us indeed describe more carefully the different conditions in which the FS can emit radiation.

First of all, we note that the expression for T written in Eq. (6.11) holds only for collisionless shocks, and thus for radii R such that $\tau_{\text{CSM}}(R) < c/v_{\text{sh}}(R)$, where $\tau_{\text{CSM}}(R) = \int_R^\infty \kappa_{\text{es}} \rho_{\text{CSM}}(r) dr$ is the optical depth of the CSM between R and the observer, c the speed of light, and κ_{es} the electron scattering opacity of the CSM medium³. As discussed in Chapter 3, a collisionless shock is mediated by plasma instabilities, which can accelerate particles to relativistic energies.

When $\tau_{\text{CSM}} > c/v_{\text{sh}}$, the shock is instead said to be a radiation-mediated shock (RMS), which means that the shocked plasma's thermal energy density is dominated by radiation. In such shocks, the photons generated in the downstream shock region diffuse upstream and decelerate the incoming plasma by Compton scattering off the electrons, which in turn stop the nuclei through collective plasma interactions (e.g., an electrostatic field).

The condition $\tau_{\text{CSM}} > c/v_{\text{sh}}$ can be intuitively understood as follows: a shock with velocity v_{sh} produces radiation; the diffusion of energy carried by radiation causes the shock to develop a finite width with optical depth $\delta\tau \sim c/v_{\text{sh}}$ [502]. This optical depth can be inferred by equating the hydrodynamical timescale and the diffusion timescale over the shock front. At large optical depths $\tau_{\text{CSM}} \gg c/v_{\text{sh}}$ ($\delta\tau \ll \tau_{\text{CSM}}$), the shock wave can still be treated as an ideal discontinuity, and diffusion can be neglected. Once the shock approaches a radius where $\tau_{\text{CSM}} \sim \delta\tau$, radiation starts leaking by diffusion since the escape velocity becomes larger than the shock velocity. When this happens, the shock dissolves and is said to “breakout” or “breakdown”. The radius at which $\tau_{\text{CSM}} = c/v_{\text{sh}}$ is called the breakout radius, R_{bo} . At R_{bo} , all the thermal energy accumulated

³The opacity κ_{es} is, of course, composition dependent, and its value typically ranges from $\sim 0.2 \text{ cm}^2 \text{ g}^{-1}$ for hydrogen-free matter to $\sim 0.4 \text{ cm}^2 \text{ g}^{-1}$ for a pure hydrogen composition. For a solar composition, one has $\kappa_{\text{es}} = 0.2(1 + X_{\text{H}}) \simeq 0.34 \text{ cm}^2 \text{ g}^{-1}$ [425], where $X_{\text{H}} = 0.73$ is the hydrogen mass fraction [300].

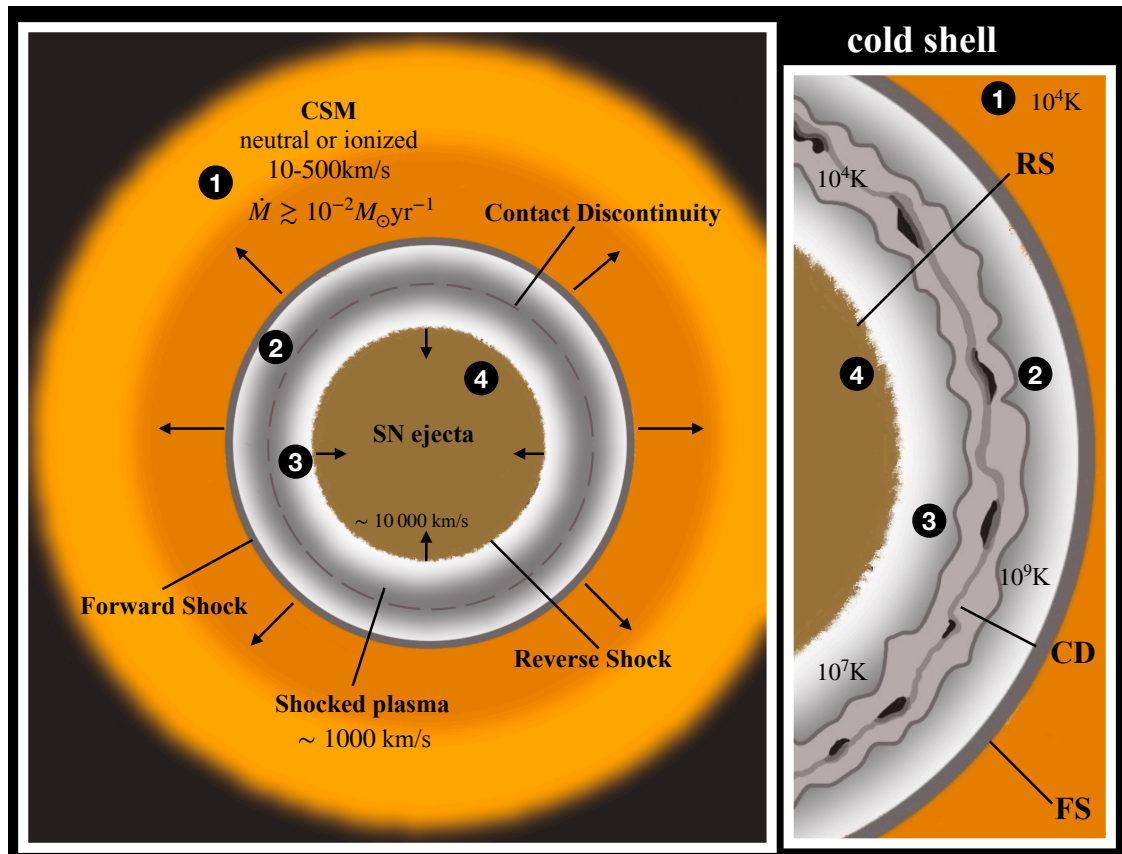


Figure 6.2: Sketch of the basic picture of a SN interacting with a CSM. Four different zones are noted with numbers: (1) the pre-shock CSM, (2) the shocked CSM, (3) the shocked SN ejecta, and (4) the freely expanding SN ejecta. These zones are divided by boundaries corresponding to the FS, the RS, and the CD between the shocked CSM and shocked ejecta, where material cools and piles up. This is often called the cold, dense shell (CDS) in SNe II_n. Each zone's typical temperatures are displayed, indicating what kind of emission is expected to be produced in these events. Adapted from [99].

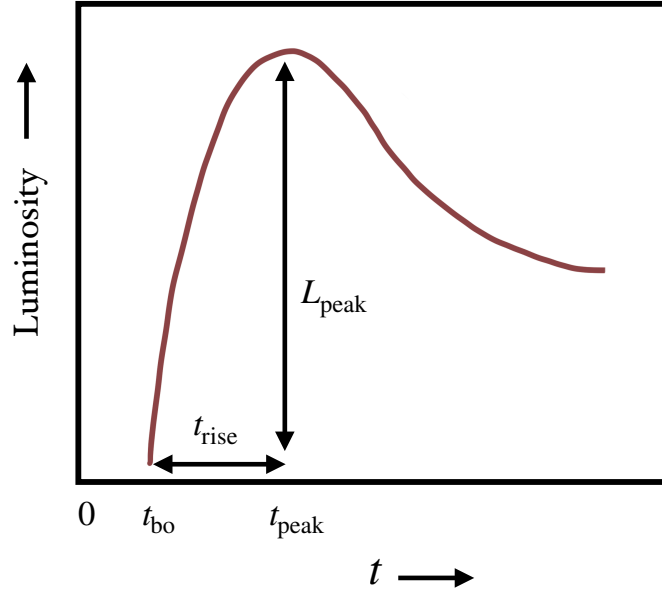


Figure 6.3: Sketch of the SN luminosity evolution (in arbitrary units) resulting from the interaction of the SN shock with the dense CSM. The origin ($t = 0$) coincides with the SN explosion time. The LC starts rising to the peak at the breakout time t_{bo} . The rise time is given by the photon diffusion time in the optically thick CSM.

until that point can be released. In general, the amount of energy in the interaction shell above some velocity v_* can be estimated as [132]:

$$E_{\text{diss}} = \int_{v_*}^{\infty} \frac{1}{2} \rho_{\text{ej}}(t, r) v^2 4\pi r^2 dr = 2\pi \int_{v_*}^{\infty} \rho_{\text{ej}}(t, r) \frac{r^4}{t^2} dr = \frac{4}{3} \frac{E_{\text{k}}^2}{M_{\text{ej}} v_*^2}. \quad (6.13)$$

So, if we want to know how much kinetic energy of the ejecta component has been swept up by the shell before R_{bo} , we should substitute $v_* = R_{\text{bo}}/t_{\text{bo}}$ (where t_{bo} is the breakout time, so that $R_{\text{sh}}(t_{\text{bo}}) = R_{\text{bo}}$), and consider that the energy in radiation is $E_{\text{rad}} = \epsilon_{\text{rad}} E_{\text{diss}}$. This energy will be released to the observer over a diffusion time scale t_{diff} , namely the time it takes for photons to propagate through the CSM mass comprised between R_{bo} and the photosphere R_{PH} (defined as the radius where $\tau_{\text{CSM}} = 1$). The characteristic post-shock temperature for a radiation-mediated shock is (e.g., [465]):

$$T_{\text{RMS}} = \left(\frac{18 \rho_{\text{CSM}} v_{\text{sh}}^2}{7 a_{\text{BB}}} \right)^{1/4}, \quad (6.14)$$

where a_{BB} is the Stefan–Boltzmann energy density coefficient⁴. We see that T_{RMS} increases proportionally to the square root of the shock velocity, and it is significantly

⁴We obtained this temperature by comparing the radiation pressure in the post-shock region (assum-

lower than that of a collisionless shock. Consequently, the resulting thermal transient should fall into the UV/optical range.

With the above information, we can finally summarize the properties of expected radiation from interaction-powered transients. We identify three different phases: a pre-shock breakout, a shock breakout, and a post-shock breakout phase:

- While the shock is in the optically thick part of the CSM, where $\tau_{\text{CSM}} > c/v_{\text{sh}}$, no radiation can escape to the observer because the shock propagates faster than the photons can diffuse.
- When the shock reaches R_{bo} , the accumulated radiation during the interaction with the wind before the breakout is released over a diffusion time scale, t_{diff} . As the breakout occurs, these photons start leaking toward the observer, and their observed temperature is set by their interaction with the unshocked CSM through which they diffuse. The temperature of this radiation is indeed expected to peak in the optical, and in general to be lower than the temperature of the radiation at the breakout, $\sim T_{\text{RMS}}(R_{\text{bo}})$ ⁵. This is the breakout radiation, and in the optical lightcurve, it should represent the bulk of the luminosity before the peak and at the peak. The rise time to the peak, t_{rise} , would then be given by the photon diffusion time (see Fig. 6.3).
- Following the breakout, the shock may transition into a collisional or collisionless shock if the wind density does not fall abruptly. Since for these kinds of systems, it can be shown that the plasma ion frequency, $\omega_p = (4\pi\rho_{\text{CSM}}e/m_p)^{1/2}$, is many orders of magnitude larger than the ion Coulomb collision rate per particle, $\nu_C = \rho_{\text{CSM}}\sigma_C v_{\text{sh}}/m_p$, the FS will become collisionless, mediated by plasma instabilities [258]. The internal energy in the post-breakout phase will thus be dominated by the CSM material heated by the FS.

The bulk of the FS kinetic luminosity (see Eq. (6.9)) should, in principle, be observed in the UV/X-ray region of the spectrum and not optical (Eq. (6.12)). Nevertheless, the statistics present a contradiction. Only a mere $\sim 3\%$ of SNe IIn have been observed emitting in the X-ray bands [119], and most of them have

ing blackbody radiation) with the ram pressure from the CSM. Another way would be estimating T from the radiation energy density at breakout, namely from $E_{\text{rad}}(R_{\text{bo}})$ and the volume of the shocked shell $4\pi(R_{\text{FS}}^3 - R_{\text{RS}}^3)/3$ at time t_{bo} .

⁵The observed temperature depends strongly on whether or not there is thermal equilibrium between the diffusing radiation and the radiation produced in the unshocked CSM. In the case of thermal equilibrium preserved up to large radii, the observed temperature is expected to be lower than the breakout temperature since it would be set by the external parts of the wind where the radiation energy density is lower. Vice versa, if the photons at the shock are out of thermal equilibrium, then the observed temperature can be much higher (see [465]).

X-ray emission after around a year. Moreover, SLSNe are generally known to be weak X-ray emitters. This can be explained once considering the severe inhibition of X-rays produced at the shock by photoelectric absorption and Compton down-scattering in the unshocked upstream CSM (see, e.g., [465, 308]).

Generally speaking, there should always be two different components contributing to the lightcurve in this post-breakout phase: one soft component in the optical/UV band, generated by the unshocked gas ahead of the shock, and one hard component in the X-ray band, generated by the hot shocked electrons via free-free emission and IC of the soft photons. If thermal equilibrium is maintained ahead of the shock, it has been shown that the X-ray emission is strongly suppressed and should represent a small fraction ($\sim 10^{-4}$) of the UV-optical energy at earlier times. It would then become visible only at later times (at $10 - 50 t_{\text{rise}}$, which can be up to ~ 500 days after the breakout) [465].

- The unshocked CSM, (1) in Fig. 6.2, is heated by the breakout radiation, as well as the shock hard radiation. It can be ionized, and the subsequent recombination would produce narrow emission lines in the optical, especially $H\alpha$, and in the UV, e.g., Lyman- α . The width of these narrow lines could provide a measure of the wind velocity.
- Together with the thermal soft and hard radiation, non-thermal radiation is expected to be produced by the accelerated electrons at the shock. The most important emission mechanism is usually synchrotron emission. Nevertheless, the radio emission of electrons is expected to be significantly affected by either the external free-free absorption process of the surrounding ionized medium or the internal synchrotron self-absorption by the same electrons responsible for the emission. The dominant absorption mechanism depends upon the mass loss rate, magnetic field in the shocked shells, shock velocity, and ejecta density. Only $\sim 10\%$ of SNe IIn have been observed in radio bands, and they typically exhibit delayed and not very bright emissions. This is indeed often attributed to absorption effects [119].
- Also, infrared (IR) emission can be observed from SNe IIn or their superluminous version. There are two ways in which IR radiation can be produced:
 1. The first one requires the presence of dust in the CSM. After a SN occurs, the temperature of a CSM dust grain will be determined by a balance between heating by absorption of SN radiation and cooling by IR emission. Because typical dust grains evaporate at about 1500 K, a CCSN will evaporate dust out to a certain radius R_{dust} dictated by the maximum SN luminosity; this maximum probably occurs at shock breakout. For $R > R_{\text{dust}}$, the dust survives and subsequently cools. Dust that manages to survive the SN event and maintains a temperature T emits IR radiation, with a peak wavelength

at around $\lambda_{\max} \sim 6(T/500\text{ K})\mu\text{m}$, according to the blackbody Wien law. When the optical depth for dust absorption in the UV region is significant, this can lead to the phenomenon of an *infrared echo* [99];

2. The second way of producing IR is by direct dust formation by the SN itself. SNe involving strong interaction with CSM offer a unique and potentially more efficient mechanism for dust creation than standard SNe. In classical SNe, dust forms within the expanding ejecta, where there is competition between cooling and the rapidly diminishing density. Indeed, the two necessary ingredients for efficient dust formation are a high density and a low temperature so solid condensation can occur and grain nucleation can begin. Even if dust could form efficiently in normal SNe, it might get destroyed when the RS crosses the ejecta. Conversely, in interacting SNe, evidence indicates rapid dust formation within the highly dense post-shock cooling shell (Zones 2 and 3 in Fig. 6.2). Furthermore, this dust is situated behind the two shock fronts, increasing its likelihood of survival and potential contribution to the interstellar medium's dust budget.
- In addition to electrons, protons (or heavier nuclei, if present) are expected to be accelerated at both FS and RS. If the CSM is dense enough, the interaction of these relativistic particles with the cold medium leads to the production of high-energy γ -rays and neutrinos, as we have shown in Chapter 2. We discuss the production of neutrinos in Sec. 10.1.
 - Finally, once the wind density drops abruptly, at R_{CSM} , the FS becomes inefficient and the luminosity fades quickly. If it is still bright enough to be detected at this stage, one could finally observe the standard emission from the SN ejecta, whose primary power source would be radioactive decay.

6.2 Long Gamma-Ray Bursts

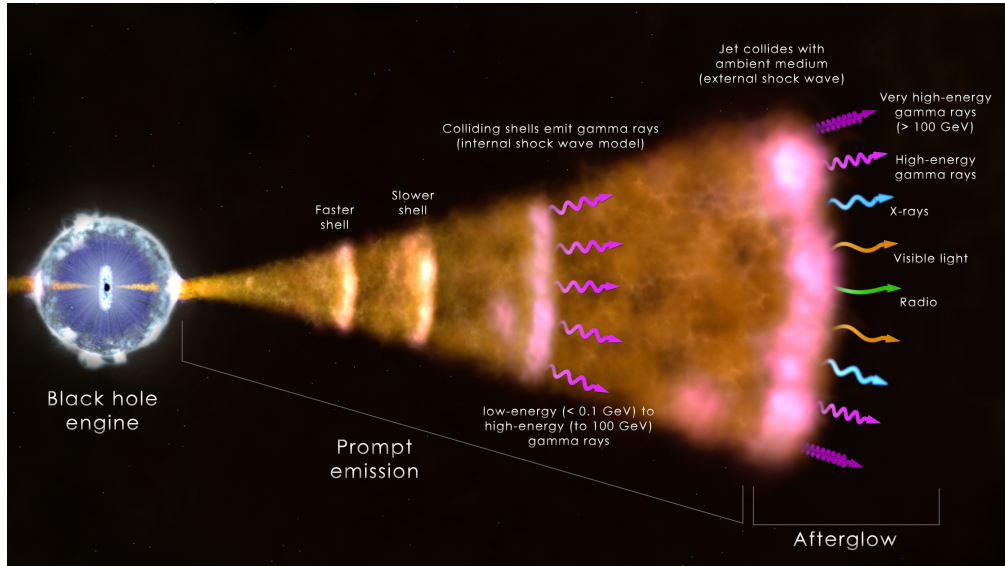


Figure 6.4: Schematic representation of a relativistic collimated jet responsible for the prompt γ -ray emission, having an internal origin to the jet, and the afterglow emission, resulting from the interaction of the jet with the surrounding medium. Credit: NASA/Goddard Space Flight Center/ICRAR.

Long Gamma-Ray Bursts (LGRBs) are the most powerful phenomena in the Cosmos. They represent extraordinarily intense flashes of γ -ray radiation, which can outshine entire galaxies for a brief moment and are believed to originate from relativistic collimated jets born in the cataclysmic deaths of massive stars. They exhibit a bursty emission pattern, lasting from milliseconds to thousands of seconds. Their energy normally peaks in the sub-MeV to MeV range. After the initial γ -ray pulse, the late emission from LGRBs, also known as *afterglow*, can extend from minutes to months or even years and is observable across various wavelengths, including radio, millimeter, infrared, optical, ultraviolet, X-rays, and γ -rays. LGRBs emit isotropic γ -ray luminosities ranging from $\sim 10^{50}$ to 10^{54} erg s $^{-1}$. This energy output is staggering, surpassing the Sun's lifetime energy emission in less than one second.

This section presents the observational properties of both prompt and afterglow emissions. To follow, we introduce the theoretical framework of LGRBs and present the models proposed in the literature to explain the bright prompt emission. The prompt and the afterglow phases are schematically shown in Fig. 6.4 and will be our main focus of investigation in Sec.7.1.

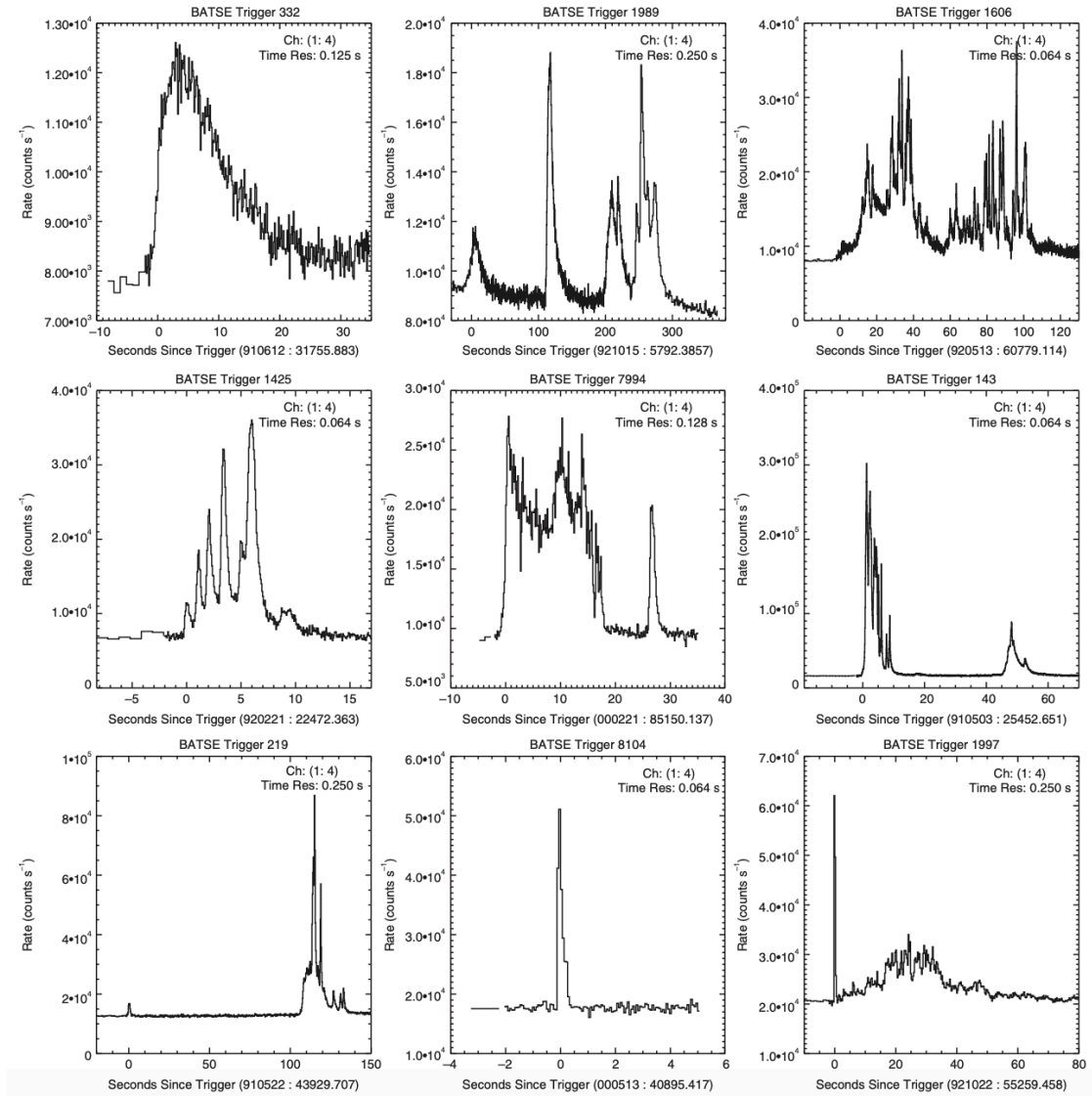


Figure 6.5: Sample lightcurves of BATSE LGRBs. Figure from [520].

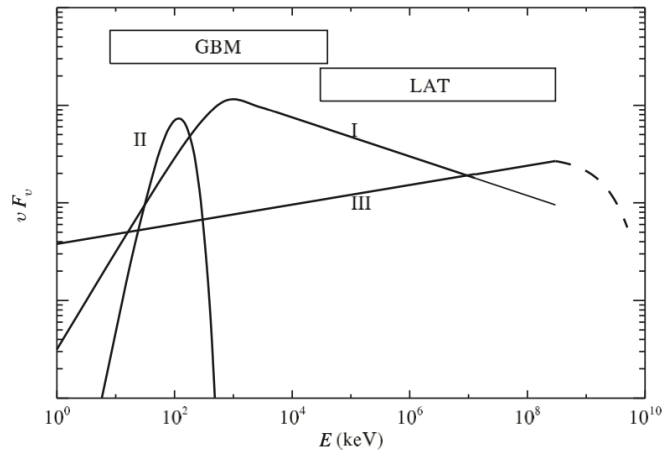


Figure 6.6: The three possible spectral components that shape the observed time-resolved spectra of LGRBs. The most common observed component is I. Some components can be suppressed in some LGRBs. Figure from [520].

6.2.1 Observational facts on Long Gamma-Ray Bursts

In what follows, we summarize the main observed properties of LGRB lightcurves and spectra. The interested reader can find a more complete and detailed overview in the thorough reviews [320, 281, 520]. We divide our discussion into prompt emission and afterglow emission.

6.2.1.1 Prompt emission

- **Temporal properties**

1. **Duration T_{90} :** is the time interval within which 90% of the burst fluence is detected. For LGRBs, it spans three orders of magnitude, from a few to thousands of seconds, and peaks at 20 – 30 s.
2. **Lightcurves:** are extremely irregular, as can be seen in Figure (6.5). Some bursts consist of very erratic, spiky components, while others are smooth with one or a few pulses. Some bursts contain distinct, well-separated by quiescent gaps emission episodes, while others present pulses that follow one another with brief temporal separations.
3. **Pulses:** have widths δt varying in a wide range. The shortest spikes can have millisecond widths, and $\delta t/T_{90}$ can reach values as low as 10^{-3} .

- **Spectral properties**

The continuum LGRB spectrum is non-thermal. Thermal (Planck-like) spectra are ruled out for the vast majority of bursts. Instead, for most cases, the spectrum can be effectively described by a smoothly-joining broken power law, commonly referred to as *Band-function* (see Fig. 6.6). The main components that have been identified in the spectral analyses of LGRBs are the following:

1. **Band function** (I in Fig. 6.6) This spectral model involves three independent parameters: a low-energy photon spectral index (α_γ), a high-energy photon spectral index (β_γ), and the break energy in the spectrum ($\varepsilon_{\gamma,0}$). It is important to note that this spectral shape holds for the integrated emission over the entire burst duration and for emission observed during specific time intervals within the burst. The photon number spectrum (in units of photons $\cdot L^{-2} \cdot T^{-1} \cdot E^{-1}$) in this model reads as [73]:

$$n_\gamma^{\text{Band}}(\varepsilon_\gamma) = C \begin{cases} \left(\frac{\varepsilon_\gamma}{100 \text{ keV}}\right)^{\alpha_\gamma} e^{-\frac{\varepsilon_\gamma}{\varepsilon_{\gamma,0}}} & \varepsilon_\gamma < (\alpha_\gamma - \beta_\gamma)\varepsilon_{\gamma,0} \\ \left(\frac{(\alpha_\gamma - \beta_\gamma)\varepsilon_{\gamma,0}}{100 \text{ keV}}\right)^{\alpha_\gamma - \beta_\gamma} e^{\beta_\gamma - \alpha_\gamma} \left(\frac{\varepsilon_\gamma}{100 \text{ KeV}}\right)^{\beta_\gamma} & \varepsilon_\gamma \geq (\alpha_\gamma - \beta_\gamma)\varepsilon_{\gamma,0} \end{cases} \quad (6.15)$$

where ε_γ is the photon energy and C the normalization constant of the spectrum. The peak energy in the $\varepsilon_\gamma^2 n_\gamma^{\text{Band}}$ spectrum, $\varepsilon_{\gamma,p}$, is related to $\varepsilon_{\gamma,0}$ through $\varepsilon_{\gamma,p} = (2 + \alpha_\gamma)\varepsilon_{\gamma,0}$. The typical spectral parameters inferred from observations are: $\alpha_\gamma \simeq -1.1$ and $\beta_\gamma \simeq -2.2$. The distribution of the peak seems to form a continuum from several keV to multi-MeV and is centered around $\varepsilon_{\gamma,p} \simeq 300 \text{ keV}$ [218].

2. **Thermal component** (II in Fig. 6.6) or quasi-thermal, is found to contribute to the observed spectra of a fraction of bursts.
3. **High-energy component** (III in Fig. 6.6) Most of the detections at high energies are consistent with an extended Band spectrum without further breaks. However, there are several examples in which this is not the case, and a power-law component is found extending to the Fermi LAT band to high energies (above 100 MeV) but sometimes also to low energies (in the X-ray band).

Generally, one may consider a prompt emission spectrum, which includes all three spectral components. Their significance may vary among the population of LGRBs. Usually, I is the dominant component. The superposition between the different components has been seen in a handful of LGRBs. Component III seems to evolve independently and typically emerges later than the other two. The exact physical origins of the three components remain partially elusive. One plausible

hypothesis associates the thermal component with the emission from the photosphere of relativistic ejecta while attributing the Band component to non-thermal synchrotron radiation within the optically thin region. Alternatively, there is ongoing debate regarding whether both components represent quasi-thermal emissions from the photosphere. Component III is mysterious. Its rapid variability, not unambiguously linked to the afterglow phase, suggests that it might not arise from there. The precise physical mechanisms responsible for Component III remain debatable, although some form of inverse Compton scattering process is likely involved.

- **Energetics** The total *isotropic* energy emitted during the prompt phase is found to be $E_{\gamma, \text{iso}} \sim 10^{50} - 10^{54}$ erg. To infer the total *intrinsic* energy, one needs to consider the collimation of LGRB jets. The beaming factor of a GRB is defined as $f_b \equiv \Delta\Omega/4\pi$, where $\Delta\Omega$ is the solid angle of the jet. Considering a bipolar, conical jet with a half-opening angle θ_j , one has $\Delta\Omega = 4\pi(1 - \cos \theta_j)$, so that

$$f_b \equiv 1 - \cos \theta_j \simeq \frac{\theta_j^2}{2} \quad (6.16)$$

where the second approximation applies when $\theta_j \ll 1$. For high-luminosity LGRBs, data suggest $f_b^{-1} \sim 500$, which corresponds to a mean *jet opening angle* $\theta_j \sim 3^\circ$. With this information, the estimate of the *true* emission energy E_γ becomes straightforward: $E_\gamma = f_b E_{\gamma, \text{iso}}$. The latter is found to have a narrower distribution, clustered around $5 \times 10^{50} - 10^{51}$ erg, suggesting a “standard” energy reservoir for LGRBs [520].

- **Supernova connection** It turns out that at least some LGRBs are associated with some (not all) broad-line Type Ic SNe (see Sec. 5.4 and Fig. 5.4). The progenitors of these SNe are Wolf-Rayet stars that, due to powerful winds, have also been stripped of their external He layer. During a supernova event, the greater the velocity of the ejected material, the more significant the dispersion in radial velocity, consequently causing the spectral lines to appear broader. The presence of broad spectral lines in these events thus suggests that they are associated with highly energetic explosions. Remarkably, only a fraction of these broad-line SNe are observed to be linked with LGRBs. The precise reason why certain massive stars become LGRB progenitors remains uncertain. However, the angular momentum present in the star’s core could be a critical factor in determining whether a collimated and relativistic jet can be launched during the stellar collapse, leading to the formation of a GRB.

6.2.1.2 Afterglow emission

Observationally, the afterglow phase of a LGRB represents the temporal phase after the end of the prompt sub-MeV emission, and it was predicted before its discovery. Regardless of the nature of the central engine, we know that the GRB phenomenon is connected to an extremely energetic outflow. Irrespective of their location in the Universe, there exists a surrounding medium (even if its density is low) that will decelerate this outflow. Typically, this deceleration occurs through a strong forward shock (FS) propagation into the surrounding medium. However, in the early stages, there is also a reverse shock (RS) that penetrates the ejected material itself (analogously to what we have seen for interaction-powered SNe). The shocked decelerating material constitutes what is typically called a “blastwave shell”. These shocks facilitate the acceleration of electrons (and protons), ultimately leading to the generation of intense, broad-spectrum, non-thermal radiation via the synchrotron process (and also synchrotron self-Compton (SSC) emission in the high-energy band). Hence, from a theoretical perspective, an afterglow can be defined as the broad-spectrum radiation released during the interaction between the fireball ejecta and the surrounding medium. This emission is supposed to originate either from the external FS or from the external RS when it crosses the ejecta. However, observations conducted by Swift have indicated that not all forms of observationally defined afterglow emission can be attributed to emissions from external shocks. For instance, X-ray flares and “internal” plateaus likely stem from an “internal” region within the jet, driven by late-stage central engine activities. In this thesis, we will use the observational definition for the afterglow, and in what follows, we mainly focus on the observational properties of the afterglow phase that we need to know for our study in Sec. 7.1.

- **General properties**

1. Afterglows are (quite) broad-band, having been detected in the X-ray, the optical/infrared, and the radio bands. In each band, the lightcurve generally displays a power-law decay behavior. Indeed, the afterglow flux density can typically be characterized by

$$F_{\nu}(t, \nu) \propto t^{-a} \nu^{-b}, \quad (6.17)$$

with ν being the frequency of the observed radiation, and a and b are usually positive indices.

2. The X-ray afterglow can be described by a canonical lightcurve composed of different components, even if not every LGRB has all these components. On top of the normal decay phase predicted in the standard external FS model, the other observed temporal behaviors in the X-ray band can be explained

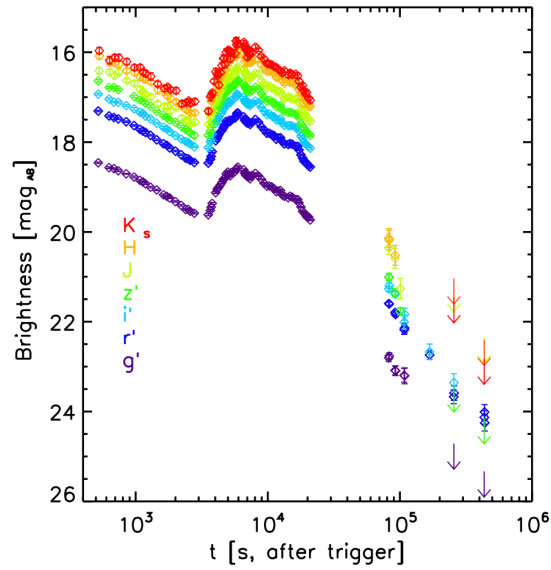


Figure 6.7: Re-brightening feature in multiple optical bands observed during the afterglow phase of GRB 081029. Figure from [359].

either by invoking a “tail” of the prompt emission or a prolonged continuous energy injection into the blastwave or some late activity of the LGRB central engine which produces X-ray flares, suggesting that the duration of a LGRBs is usually (much) longer than what T_{90} records.

3. Our attention in Sec. 7.2 will be directed toward the optical afterglow emission. It is observed that the *late-time optical afterglow* lightcurves (later than a couple of hours after the GRB trigger) are relatively “regular”, typically having a single power-law decay with a decay index of $a \sim 1$. Richer features other than power-law decays have been discovered for bursts with high-quality data. Figure 6.7 shows an example of an optical *re-brightening feature*, which is not expected from the simplest afterglow models. The proposed models for interpreting these features include density bumps or voids in the circumburst medium, multiple episodes of energy injection into the blastwave, angular fluctuations in energy per unit solid angle, or the existence of multiple jet components. We will discuss better the optical bumps in Sec. 7.2.

6.2.2 Theoretical framework of Long Gamma-Ray Bursts

In this section, following Ref. [520], we lay out the basic theoretical concepts necessary to grasp the physics behind LGRBs. We briefly describe the central engines capable of producing relativistic jets associated with GRBs. Then, we show the importance of the various reference frames for relativistically moving ejecta to correctly interpret the observations on Earth.

6.2.2.1 Central engine

Following the progenitor system's catastrophic destruction, a central engine formation becomes necessary to fuel the high-energy jet in a GRB. A good central engine candidate must be able to account for the different observational properties observed in GRBs. Therefore, it should be able to 1) release isotropic energies in the range of $E_{\gamma,\text{iso}} \sim 10^{49} - 10^{55}$ erg, 2) produce an outflow with very large Lorentz factors ($\gtrsim 100$), 3) operate intermittently, so to explain the wide range of temporal LGRB features, 4) reactivate itself at late times, to explain the X-ray or optical flares observed after the prompt emission, 5) launch jets with a variety of compositions, ranging from matter-dominated fireballs to Poynting-flux-dominated outflows, as indicated by prompt emission observations by Fermi.

While the primary candidate has long been a hyper-accreting black hole (BH), recent observations have introduced the possibility of an alternative engine, at least in the case of certain GRBs. This alternative engine is believed to be a rapidly rotating, intensely magnetized neutron star, often referred to as a millisecond magnetar. See Ref [355] for a comprehensive review of the central engines of LGRBs.

Hyper-Accreting Black Holes

If LGRBs owe their power to an accretion process onto a stellar-mass BH, a relatively high accretion rate becomes necessary. The primary source of the jet's power can be either the gravitational potential energy stored within the accreted matter or the rotational energy of the BH itself. The accretion rate is important even in the second scenario since it impacts the rate at which the BH spin energy is extracted. In general, we can write the luminosity due to accretion as

$$L_{\text{GRB}} = \zeta \dot{M} c^2 = 1.8 \times 10^{51} \text{ erg s}^{-1} \left(\frac{\zeta}{10^{-3}} \right) \left(\frac{\dot{M}}{1 M_{\odot} \text{ s}^{-1}} \right), \quad (6.18)$$

where \dot{M} is the mass accretion rate into the BH. Given a reasonable efficiency ($\zeta \sim 10^{-3}$) in converting matter into energy, the required accretion rate for a typical LGRB is $0.1 - 1 M_{\odot} \text{ s}^{-1}$. With such a high accretion rate, the accretion flow becomes hot

enough to make efficient the e^+/e^- capture processes:

$$e^- + p \rightarrow n + \nu_e, \quad e^+ + n \rightarrow p + \bar{\nu}_e. \quad (6.19)$$

Abundant neutrinos are generated within the disk, which escape and cool the disk. The accretion flow in this regime is called a neutrino-dominated accretion flow (NDAF).

On the other hand, from the collapse of the progenitor star, a rapidly spinning BH can be formed, and the efficient accretion would further increase its angular momentum. If the disk has strong poloidal magnetic fields, the energy and angular momentum of the rotating BH can be extracted through the *Blandford-Znajek mechanism*. In such a case, the spin energy of the BH would be the ultimate power source of the jet.

Let us now briefly describe the two well-established mechanisms for the launch of a jet:

- **Neutrino-driven mechanism:** neutrinos and antineutrinos produced in a NDAF would annihilate just above the accretion disk, resulting in the production of photons and e^-e^+ pairs. Neutrinos can also strip baryonic matter from the disk. Consequently, this process would form a hot fireball with minimal baryon contamination above the disk. Neutrino annihilations exhibit substantial optical depths, especially near the BH's spin axis, facilitating the creation of a wide, relativistic outflow in the polar region. For LGRB jets originating from a BH at the core of a massive star, the surrounding stellar envelope would further collimate the outflow, resulting in relatively narrow jets, as observed for LGRBs. In general, the $\nu\bar{\nu}$ annihilation luminosity depends on the mass accretion rate \dot{M} , BH mass, and the spin of the BH, and there is no simple analytical derivation of these dependencies. Baryon loading in the fireball is achieved through neutrino–nucleon weak interaction via CC interactions to strip protons or NC interactions to strip neutrons. Neutrinos can transfer momentum to protons/neutrons, giving rise to a neutrino-driven baryon wind.
- **Blandford-Znajek mechanism:** when a highly magnetized accretion disk coexists with a rapidly spinning BH, with magnetic field lines that thread the BH's event horizon and are connected to a distant astrophysical load, the field lines become twisted due to the BH spin and exert a torque on the BH to slow it down. In this way, the BH's spin energy gets extracted via the BZ mechanism, giving rise to a jet dominated by Poynting flux. For a BH with magnetic field strength B near the horizon, the total Poynting flux power from the BZ process may be estimated as:

$$L_{\text{BZ}} = (1.7 \times 10^{50} \text{ erg s}^{-1}) a_*^2 \left(\frac{M_{\text{BH}}}{M_{\odot}} \right)^2 \left(\frac{B}{10^{15} \text{ G}} \right)^2 F(a_*) \quad (6.20)$$

where $a_* = Jc/GM_{\text{BH}}^2$ is the dimensionless BH spin parameter, J being the BH angular momentum, and

$$F(a_*) = \left[\frac{1+q^2}{q^2} \right] \left[q + \left(\frac{1}{q} \right) \arctan q - 1 \right], \quad q = \frac{a_*}{1 + \sqrt{1 - a_*^2}}. \quad (6.21)$$

A small amount of baryons is expected to be entrained in the Poynting flux dominated jet. A neutrino-driven baryon wind should still originate from the NDAF accretion disk. Protons, however, cannot penetrate the magnetically dominated outflow due to their small gyration radius. Baryon loading is achieved through neutrons that can penetrate the jet freely. Neutrons may decay into protons to load baryons in the jet, but neutron decay is a relatively slow process. So, the BZ jets have much lower baryon loading than $\nu\bar{\nu}$ -annihilation jets, which means that the maximum achievable Lorentz factors of the jet should be larger.

Based on what we have written so far, here we list the main differences between the two mechanisms that we need to remember for later discussions:

- for high B and high a_* , the BZ power exceeds the $\nu\bar{\nu}$ -annihilation power significantly;
- for high B and low a_* , the $\nu\bar{\nu}$ -annihilation power exceeds the BZ power if the mass accretion rate \dot{M} is sufficiently large, and becomes negligible for low \dot{M} ;
- for low B and low a_* , the $\nu\bar{\nu}$ -annihilation power dominates;
- the BZ mechanism launches a Poynting-flux-dominated jet, whereas the $\nu\bar{\nu}$ -annihilation mechanism launches a hot fireball;
- the baryonic loading in the BZ jet is much lower than in a $\nu\bar{\nu}$ -annihilation jet.

Millisecond magnetars

If in the collapse of the massive progenitor star, a neutron star (NS) with a very short rotational period P and very high magnetic field is formed, then it can have the right parameters to be the engine powering a LGRB jet. The total spin energy of a millisecond magnetar with an initial spin period $P_0 \sim 1$ ms is

$$E_{\text{rot}} \simeq \frac{1}{2} I \Omega^2 \simeq (2.2 \times 10^{52} \text{ erg}) \left(\frac{M_{\text{NS}}}{1.4 M_{\odot}} \right) \left(\frac{R_{\text{NS}}}{10^6 \text{ cm}} \right)^2 \left(\frac{P_0}{1 \text{ ms}} \right)^{-2} \quad (6.22)$$

where $I \simeq 2/5 M_{\text{NS}} R_{\text{NS}}^2$ is the moment of inertia of a NS with mass M_{NS} and radius R_{NS} . E_{rot} represents an upper limit on the total energy budget of a LGRB within the magnetar

model if the spin energy of the magnetar powers the emission. There are a few energy extraction mechanisms proposed in the literature. The most famous one invokes the extraction of the millisecond magnetar rotational energy via magnetic dipole and relativistic wind spindown, or gravitational wave radiation. We point the reader to [520] and references therein to learn more about the other possible mechanisms. What is important to know is that magnetar models are typically invoked for very special GRBs, like the ones that display plateaus in their X-ray afterglow lightcurves. On the other hand, from the prompt emission data, there is no smoking gun evidence for a magnetar central engine, and several aspects are still under ongoing research.

6.2.2.2 Relativistic motion

One significant observational evidence about GRB ejecta is that they must move towards Earth with a relativistic speed. This is a consensus of all cosmological GRB models. The first robust argument that required a relativistic motion for GRB is related to the *compactness problem*. This problem can be briefly described as follows: we observe photons from GRBs with energies surpassing the rest mass energy of electrons, so in principle, they have the potential to interact with each other inside the source to produce e^-e^+ pairs. This means that to be able to escape from the GRB environment, the optical depth $\tau_{\gamma\gamma}$ for the process $\gamma\gamma \rightarrow e^+e^-$ must be $\tau_{\gamma\gamma} < 1$. However, this is never the case for GRBs. Indeed, let us consider the typical total isotropic gamma-ray energy, $E_{\gamma,\text{iso}} \sim 10^{51}$ erg and naively take the size of the emission region to be $R \sim c\delta t \sim 3 \times 10^8$ cm ($\delta t/10$ ms), where δt is the observed variability timescale in the GRB lightcurves. Assuming that a fraction f of the emitted energy is above the two-photon pair production threshold (let us take for the moment both photons close to the threshold, so with $\varepsilon_\gamma \gtrsim m_e c^2$), the number density of pair producing photons and the $\gamma\gamma$ optical depth can be written as

$$n_{\text{ph}} \sim \frac{E_{\gamma,\text{iso}} f}{4/3\pi R^3 \varepsilon_\gamma}, \quad \tau_{\gamma\gamma} \simeq \sigma_T n_{\text{ph}} R \sim \frac{E_{\gamma,\text{iso}} \sigma_T f}{4/3\pi R^2 \varepsilon_\gamma} \sim 10^{15} f \gg 1. \quad (6.23)$$

Therefore, the γ -rays should have been attenuated before escaping the source and reaching the Earth. The only way to eliminate this apparent paradox is by invoking relativistic bulk motion, i.e., the GRB emitting region moves towards us observer with a high Lorentz factor. The relativistic motion eases the compactness problem in two ways. First, there is the *de-boost* of the photon energy in the comoving frame, so that the pair production threshold condition for two photons of energy ε'_1 and ε'_2 in the comoving frame $\varepsilon'_1 \varepsilon'_2 \geq (m_e c^2)^2$, becomes $\varepsilon_1 \varepsilon_2 \geq \Gamma^2 (m_e c^2)^2$ in the observer frame. This means all the previous γ -rays above the pair production threshold are now X-rays in the comoving frame and below the threshold. The second effect of the relativistic motion is the increase of the emitting region size by a factor Γ^2 , as we will illustrate in the next

section. By using a photon spectrum above the peak $n_\gamma(\varepsilon_\gamma) \propto \varepsilon_\gamma^{\beta_\gamma}$, with $\beta_\gamma \sim -2.2$ (typical of Band-function spectrum, see Sec. 6.2.1.1), it can be shown that the pair optical depth drops by a factor of Γ^6 . The Γ required to satisfy the observations is of order ~ 100 . Hence, GRBs involve the fastest bulk motions known so far in the Universe. Measuring the Lorentz factor of GRBs is extremely difficult, so one needs to infer it through theoretical modeling using several techniques. Although with large uncertainties, Γ of a good sample of LGRBs has been estimated, and it is confirmed to have values $100 \lesssim \Gamma \lesssim 1000$.

6.2.2.3 Frames of reference and Doppler boost

When considering a relativistic GRB jet, there are three frames of reference of special importance:

- the rest frame of the central engine (the *lab frame*), where the jet is moving with speed β and Lorentz factor Γ ;
- the rest frame of the jet, or the *comoving frame*;
- the rest frame of the observer at Earth, or simply the *observer frame*.

The lab frame is, except for the cosmological expansion factor $(1 + z)$, the same as the observer's frame of reference, and we will refer to them also as *fixed frame*. All the physical processes occurring in the outflow (i.e., radiative processes) are most easily described in the comoving frame. Comoving properties and lab frame properties are related through special relativistic Lorentz transformations. We denote quantities characteristic of the jet as X , \tilde{X} , and X' in the observer, lab, and comoving frames, respectively.

With the three reference frames defined, there are four times relevant for the GRB problem. Indeed, there is a complication that comes from the propagation effect, as we will shortly see. The four times are:

- the central engine time \tilde{t}_{eng} measured in the lab frame;
- the jet *emission* time \tilde{t}_e measured in the lab frame;
- the comoving jet *emission* time t'_e measured in the comoving frame;
- the *observation* time t_{obs} measured in the observer frame.

In general, we can consider a shell emitter moving with a dimensionless speed β , at an angle θ with respect to the observer's line of sight (Fig. 6.8). Let us suppose that the central engine sends two light signals at $\tilde{t}_{\text{eng},1}$ and $\tilde{t}_{\text{eng},2} > \tilde{t}_{\text{eng},1}$ towards the relativistically moving (spherical) ejecta. The ejecta emits two light signals at $\tilde{t}_{e,1}$ and

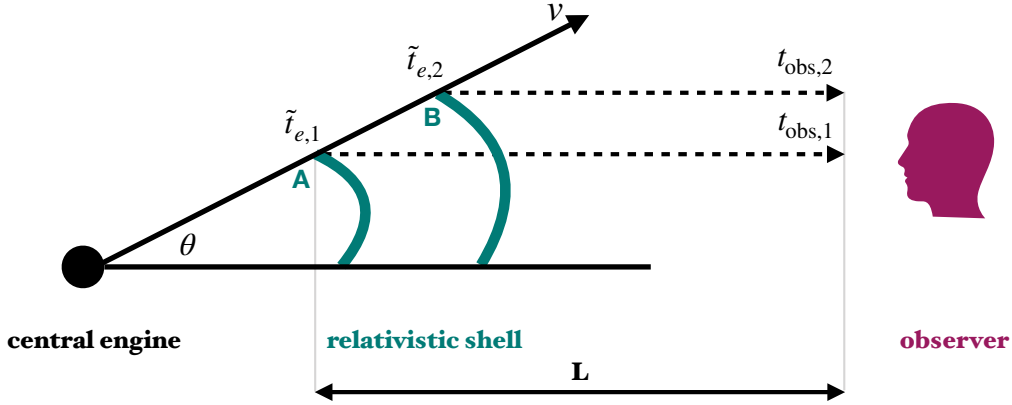


Figure 6.8: The geometric configuration of the GRB central engine, the relativistic emitting shell, and the observer.

$\tilde{t}_{e,2} > \tilde{t}_{e,1}$ towards an observer immediately after it receives the signal from the central engine. The observer receives the two light signals emitted by the ejecta at $t_{\text{obs},1}$ and $t_{\text{obs},2} > t_{\text{obs},1}$.

We want to find out the relationship among the engine time interval $\Delta\tilde{t}_{\text{eng}} = \tilde{t}_{\text{eng},2} - \tilde{t}_{\text{eng},1}$, the ejecta emission time interval $\Delta\tilde{t}_e = \tilde{t}_{e,2} - \tilde{t}_{e,1}$, and the observer time interval $\Delta t_{\text{obs}} = t_{\text{obs},2} - t_{\text{obs},1}$. We will neglect the cosmological expansion factor $(1+z)$ in our discussion.

For the relationship between $\Delta\tilde{t}_{\text{eng}}$ and $\Delta\tilde{t}_e$ we consider the fact that after receiving the first signal and before receiving the second signal, the shell has traveled a distance $v\Delta\tilde{t}_e$. So, the distance that signal 2 travels is equal to the distance signal 1 travels plus the distance the ejecta travels during the interval between receiving the two signals, i.e., $c(\tilde{t}_{e,2} - \tilde{t}_{\text{eng},2}) = c(\tilde{t}_{e,1} - \tilde{t}_{\text{eng},1}) + v\Delta\tilde{t}_e$, which re-arranged gives $c\Delta\tilde{t}_{\text{eng}} = (c-v)\Delta\tilde{t}_e = (1-\beta)\Delta\tilde{t}_e$. For $\beta \lesssim 1$, we can approximate:

$$1 - \beta = \frac{(1 + \beta)(1 - \beta)}{1 + \beta} \simeq \frac{1 - \beta^2}{2} = \frac{1}{2\Gamma^2}, \quad (6.24)$$

which means that

$$\Delta\tilde{t}_e \sim 2\Gamma^2\Delta\tilde{t}_{\text{eng}}. \quad (6.25)$$

The interpretation of this is intuitive: since the ejecta is moving away from the engine at a relativistic speed, it takes a very long time for the signal to catch up with it. Analogous geometric relation can be used to link Δt_{obs} and $\Delta\tilde{t}_e$. Referring to Fig. 6.8, let us assume that the distance between the observer and location A is L . The first photon arrives to the observer at $t_{\text{obs},1} = \tilde{t}_{e,1} + L/c$, while the second photon arrives to the observer at $t_{\text{obs},2} = \tilde{t}_{e,2} + (L/c - \beta \cos \theta \Delta\tilde{t}_e)$. Re-arranging, one gets $\Delta t_{\text{obs}} = (1 - \beta \cos \theta)\Delta\tilde{t}_e$. For

$\beta \gtrsim 1$ and a small opening angle, $\theta \ll 1$, one obtains:

$$\Delta t_{\text{obs}} = \frac{\Delta \tilde{t}_e}{2\Gamma^2}. \quad (6.26)$$

We see that the observed time is significantly reduced. This is the propagation effect we were talking about earlier, and it is due to the fact that the ejecta is moving towards the observer at relativistic speed, which makes the temporal separation between the two emitted signals very brief. This is one of the fundamental arguments used to solve the ‘‘compactness problem’’ discussed in the previous chapter. Indeed, to infer the emitting region size from the observed variability δt in the GRB lightcurve, one should multiply δt by a factor $\sim 2\Gamma^2$, resulting in $R \sim 2\Gamma^2 c \delta t$ instead of $R \sim c \delta t$ used above.

Finally, comparing Eqs. (6.25) and (6.26), we obtain the relation:

$$\Delta t_{\text{obs}} = \frac{1 - \beta \cos \theta}{1 - \beta} \Delta \tilde{t}_{\text{eng}} \quad (6.27)$$

When $\theta = 0$, one has $\Delta t_{\text{obs}} = \Delta \tilde{t}_{\text{eng}}$, which makes sense since the central engine and the observer are at rest with respect to one another. For $\theta \neq 0$, typically Δt_{obs} is much longer than $\Delta \tilde{t}_{\text{eng}}$. Finally, we conclude by relating the time interval between the two emitted signals in the engine, comoving, and observer frames:

$$\Delta t'_e = \frac{\Delta \tilde{t}_e}{\Gamma}, \quad \Delta t'_e = \frac{\Delta t_{\text{obs}}}{\Gamma(1 - \beta \cos \theta)} \quad (6.28)$$

where $\mathcal{D} = 1/\Gamma(1 - \beta \cos \theta)$ is the *Doppler factor*. Some of the most important quantities that we will need later (time, energy, length, volume, and solid angle) have the following Doppler transformations between the observer-frame and the comoving-frame:

$$dt = \mathcal{D}^{-1} dt', \quad E = \mathcal{D} E' \quad dr = \mathcal{D} dr' \quad dV = \mathcal{D} dV' \quad d\Omega = \mathcal{D}^{-2} d\Omega'. \quad (6.29)$$

6.2.2.4 Initial conditions at the central engine

We introduce here some parameters characterizing the dynamical evolution of relativistic outflows that we will study in the next sections. For a pure fireball, when the magnetic field can be completely neglected, the key parameter defining the jet dynamics is the *energy per baryon*, defined as

$$\eta \equiv \frac{L_{\text{m},0}}{\dot{M}_b c^2} = \frac{E_{\text{m},0}}{M_b c^2} = \frac{M_b c^2 + E_{\text{th},0}}{M_b c^2} \quad (6.30)$$

where $E_{\text{m},0}(L_{\text{m},0})$ is the total jet energy (luminosity), $M_b(\dot{M}_b)$ is the total baryon loading (baryon loading rate), and $E_{\text{th},0}$ is the initial fireball thermal energy at the central

engine.

If the central engine also carries a strong magnetic field, then we introduce the *generalized magnetization parameter* defined as:

$$\sigma_0 \equiv \frac{L_{\text{p},0}}{L_{\text{m},0}} = \frac{E_{\text{p},0}}{\eta M_b c^2}, \quad (6.31)$$

where $L_{\text{p},0}$ is the average Poynting luminosity, and $E_{\text{p},0}$ is the total initial Poynting flux. For a “cold” central engine (no fireball component), one has $\eta \sim 1$ and $\sigma_0 \gg 1$.

Including both the hot (fireball) and cold (Poynting flux) components, the central engine can be defined by the parameter

$$\mu_0 = \frac{E_0}{M_b c^2} = \frac{M_b c^2 + E_{\text{th},0} + E_{\text{p},0}}{M_b c^2} = \eta(1 + \sigma_0), \quad (6.32)$$

where E_0 is the initial total energy of the ejecta. During the evolution of the jet, some energy could be radiated away while the rest is conserved and can be converted from one form to another. At a generic radius, for a slice of outflow ejected, one can define:

$$\mu(R) = \frac{E(R)}{M_b c^2} = \Gamma(R)\Theta(R)(1 + \sigma(R)), \quad (6.33)$$

where $\Gamma(R)$ is the bulk Lorentz factor, $\Theta(R)$ is the total comoving energy per baryon ($\Theta - 1$ is the internal energy), and $\sigma(R) = L_{\text{p}}(R)/L_{\text{m}}(R)$ is the generalized magnetization parameter, all at the radius R . Neglecting radiative losses, the conservation of energy requires that $\mu = \mu_0$, or

$$\mu_0 = \eta(1 + \sigma_0) = \Gamma\Theta(1 + \sigma) \quad (6.34)$$

As we will see, the magnetization parameter σ drops with time, and Γ increases with time. So we can see that the maximum Lorentz factor achievable is:

$$\Gamma_{\text{max}} = \mu_0 \simeq \begin{cases} \eta & \sigma_0 \ll 1 \\ 1 + \sigma_0 & \eta \sim 1. \end{cases} \quad (6.35)$$

6.2.3 Matter-dominated jets

In this section, we assume that the LGRB jet is produced by a neutrino-driven-like mechanism, with magnetic fields playing no role in the dynamics of the jet. First, we describe the evolution of the resulting fireball in the jet’s ambient medium (see Refs. [395, 318, 272]). To follow, we present the most invoked dissipative mechanisms in this theoretical framework for interpreting LGRB observations.

6.2.3.1 Fireball dynamics

Let us consider a fireball with the baryon mass load M_b and the total energy E . The fireball is composed of photons, electron/positron pairs, and a small amount of baryons. In the simplest toy model, we have the following picture: the engine injects an average constant luminosity L of duration T so that $E = LT$ and the initial width of the whole fireball shell is $\Delta_0 = cT$; due to the intermittent nature of the central engine, the luminosity will be characterized by a variability time scale $t_v \ll T$, which is reflected by the spiky and irregular LGRB lightcurves (therefore, the fireball shell consists of many mini-shells); the particle (usually hydrogen) number density of the ambient medium, also called circumburst medium (CBM), is n_{CBM} . The dynamical evolution of a fireball includes three phases: *acceleration*, *coasting*, and *deceleration*. We can summarize these three phases as follows (see Refs. [522, 320, 281, 520]):

- **Acceleration phase:** solving the three (mass, energy, momentum) conservation equations for the free expansion of an isotropic fireball leads to the following scalings in the radiation-dominated phase (early acceleration phase, where $e \propto T^4 \gg n$):

$$\Gamma \propto R, \quad n \propto R^{-3}, \quad e \propto R^{-4} \quad T \simeq \Gamma T' \sim \text{const.} \quad (6.36)$$

Here, n and e are the particle density and the thermal energy density of the fireball, respectively. T and T' represent the observed and the comoving temperature of the fireball. The expansion occurs at the expense of the comoving frame's internal energy, given the initial high optical depth.

- **Coasting phase:** in the matter-dominated regime ($e \ll n$) there is the following set of scalings:

$$\Gamma \propto \text{const}, \quad n \propto R^{-2}, \quad e \propto R^{-8/3}, \quad T \propto R^{-2/3}. \quad (6.37)$$

Since the bulk Lorentz factor per particle cannot increase beyond the initial value of random internal energy per particle, η , it only grows until it reaches $\Gamma_{\text{max}} \sim \eta$ (see Eq. 6.35), which is achieved at what is called *saturation radius*, R_{sat} . For an impulsive injection, such that $\Delta_0 < R_0$, R_0 being the initial radius of the fireball, the saturation radius is $R_{\text{sat}} = \eta R_0$ ⁶. For a long duration shell ($\Delta_0 \gg R_0$), the entire shell reaches the maximum Lorentz factor at $R_{\text{sat}} \sim \eta \Delta_0$. In the case of

⁶We have assumed that at $t = 0$, when the fireball is created, particles have an isotropical distribution of velocities, and no net bulk motion, hence $\Gamma_0 \sim 1$. This is not always the case. Indeed, if the fireball is not “naked” but needs to propagate through a stellar envelope before being released in space, one would need to consider the initial condition right at the emergence from the progenitor star surface with radius R_* (see Fig. 8.1). As we will see in Sec. 7.1, in that case numerical simulations show that $\Gamma_0 \sim 1 - 10$, and the saturation radius would be rescaled to $R_{\text{sat}} \sim \eta R_0 / \Gamma_0$, where R_0 is the new appropriate initial size of the fireball.

a BH of mass M_{BH} , this initial radius would be of the order of the Schwarzschild radius of the BH, $R_0 \sim 2GM_{\text{BH}}/c^2$. This is the coasting phase. It is important to mention that during the acceleration phase and a good portion of the coasting phase since all the materials essentially move with the speed of light, the shell width in the fixed frame remains constant, $\Delta \sim \Delta_0$ (the spread of the fixed frame radial width is very small, $\delta R/R \sim \Gamma^{-2}$). The comoving shell width $\Delta' = \Gamma\Delta_0$, on the other hand, increases with radius linearly. The radius at which the shell starts to spread significantly is $\sim \eta R_{\text{sat}}$. The above conclusions hold, assuming the fireball shell evolves as a whole. However, if there is an intermittent injection of many mini-shells, these are likely to evolve independently, and coast at a smaller radius $\sim \eta_s \delta_0$, where η_s is the Lorentz factor of that particular mini-shell, and δ_0 is the width of the mini-shells.

Let us consider two mini-shells with different Lorentz factors and injected with a spatial separation δ_0 . In particular, we assume that a slower shell with Γ_s leads a faster one with Γ_f . As shown in Eq. (6.41), the two shells catch up at the radius $R_{\text{IS}} \simeq 2\Gamma_s^2 \delta_0$. This is called the *internal shock radius* and is the site of the prompt γ -ray emission within the framework of the internal shock model, as we will see in Sec. 6.2.3.2.

Another important radius we need to mention here is the *photospheric radius*, R_{PH} . As the fireball shell expands, it cools, and the photon number density drops. When it reaches R_{PH} , namely when the photons become optically thin to both pair production and to Compton scattering off the free electrons/positrons, the thermal energy that has not been converted to kinetic energy is radiated away with an approximate blackbody spectrum. This is the first electromagnetic signal that should be detected from the fireball, and that is sometimes observed in the LGRB spectra, as we have seen in Sec. 6.2.1.1. R_{PH} is usually above the coasting radius R_{sat} , with a temperature $T \sim T_0 (R_{\text{PH}}/R_{\text{sat}})^{-2/3}$, but could be below R_{sat} if the initial fireball is clean enough (i.e. with a large enough η), in which case $T = T_0$, where T_0 is the initial temperature of the fireball.

- **Decelerating phase:** the fireball shell is eventually decelerated by the CBM. During the initial fireball-medium interaction, a RS propagates into the fireball to stop it. Usually, the deceleration radius (R_{dec}) is defined as the radius where the RS has crossed the whole fireball shell. For an impulsive isotropic fireball (of short duration), it can be shown that R_{dec} is the radius where the CBM mass collected by the fireball is equal to $1/\Gamma_{\text{max}}$ of the fireball rest mass, i.e., $M_{\text{CBM}} \sim M_b/\Gamma_{\text{max}}$. This is usually termed the “thin shell” case. On the other hand, if the shell is thick enough, the deceleration radius moves further out. As the fireball decelerates, a strong FS forms and propagates into the medium. So, the deceleration radius is essentially the initial forward shock radius and should mark the beginning of the

afterglow emission.

All the relevant radii in the fireball problem are shown in Fig. 8.1.

6.2.3.2 Prompt emission models in the fireball scenario

In the previous section, we have presented the basics for the evolution of an energetic fireball produced by a central compact engine. We have mentioned that the first light expected to be detected from a LGRB jet is the photospheric radiation, released when the fireball becomes optically thin. This is guaranteed radiation, which should always be present and can be more or less bright depending on the initial conditions at the central engine. However, as we have seen in Sec. 6.2.1.1, the observational data tell us that the spectra from most GRBs are non-thermal, suggesting the presence of dissipative processes inside the jets. This section presents two of the most invoked mechanisms to explain the observed LGRB lightcurve and spectral properties: the internal shock model and the dissipative photosphere model.

Internal Shock Model

Let us consider a relativistic baryonic jet in which the Lorentz factor varies with time, as naturally expected for an erratic central engine that launches an unsteady outflow. In such a scenario, the faster part of the outflow catches up with a slower-moving part ahead of it. This collision results in a dissipation of the kinetic energy of the jet and in the formation of a pair of shock waves that propagate into both the fast and slow shells. The shocks can amplify turbulent magnetic fields through plasma or fluid instabilities. Scattering of electrons (and protons) by magnetic irregularities upstream and downstream can lead to a Fermi acceleration process resulting in relativistic power law distributions, as we have thoroughly discussed in Chapter 3. Electrons can cool efficiently and radiate their energy away through processes like synchrotron and inverse-Compton emission (as shown in Chapter 4), producing the γ -ray emission observed in LGRBs. The model is commonly called the “internal shock model” because shocks occur within the jet due to a non-zero velocity gradient. One of the primary strengths of this model is its simplicity, allowing it to account for the rapid variability observed in the prompt LGRB lightcurves, which can occur on timescales as short as milliseconds. For the sake of simplicity, let us consider two shells of Lorentz factors Γ_s and Γ_f , with the subscripts denoting the slow and the fast shell, respectively. The fast shell is ejected from the central engine after the slow one with a delay δt_0 . In what follows, we calculate the distance where the two shells collide. If we call t_{IS} and R_{IS} the time and the radius at which the collision happens, we have that:

$$(\beta_f - \beta_s)t_{\text{IS}} = \beta_s \delta t_0 \quad \Rightarrow \quad t_{\text{IS}} = \frac{\beta_s \delta t_0}{\beta_f - \beta_s}. \quad (6.38)$$

The collision radius is then:

$$R_{\text{IS}} = v_2 t_{\text{IS}} = \frac{\beta_s \beta_f c \delta t_0}{\beta_f - \beta_s} = \frac{c \delta t_0}{\beta_s^{-1} - \beta_f^{-1}}. \quad (6.39)$$

For $\Gamma_s, \Gamma_f \gg 1$, we have that:

$$R_{\text{IS}} \simeq \frac{c \delta t_0}{(2\Gamma_s^2)^{-1} - (2\Gamma_f^2)^{-1}}. \quad (6.40)$$

If we take $\Gamma_f = k\Gamma_s$, with $k > 1$, then we get:

$$R_{\text{IS}} \simeq \frac{2k^2}{k^2 - 1} \Gamma_s^2 c \delta t_0 \gtrsim 2\Gamma_s^2 c \delta t_0. \quad (6.41)$$

The last approximate expression is what is commonly used as an estimate of the internal shock radius. We conclude by pointing out that while the internal shock model offers many compelling aspects for understanding GRB prompt emission, it also presents several challenges that are not easy to overcome. Among these are the efficiency, peak energy, and fast cooling problems (see [520] for a more detailed discussion). It is found that 1) the collisions are not very efficient in producing the observed energy in γ -rays, 2) the simplest synchrotron model cannot reproduce the typical spectral peak observed in LGRBs in the sub-MeV range ($\epsilon_{\gamma,p}$ introduced in Sec. 6.2.1.1) unless requiring that an extremely small fraction of electrons are accelerated, and 3) the deep fast cooling regime in which the electron should radiate to match the observed peak, would lead to a spectral index $\alpha_\gamma \sim -1.5$, inconsistent with the typically observed $\alpha_\gamma \sim -1$. Several solutions have been proposed to alleviate these problems, but it remains difficult to solve them all. This motivated the development of the photosphere models and the optically thin magnetic dissipation models, which we discuss next.

Dissipative photosphere model

In the dissipative photosphere model, the observed main emission component (the Band component) of LGRBs comes from the photosphere, instead of being produced at larger radii in an optically thin region, as is the case for the internal shock model. The photosphere emission of a pure fireball discussed earlier can be precisely predicted from the theory [319]. Nevertheless, the need to explain the observed non-thermal spectra has led to considering several possible mechanisms to dissipate energy below the photosphere to allow sub-photosphere electrons to have a different temperature from the seed photons and thus distort the seed thermal photon spectrum via Comptonization. These photons should be generated at not too-high optical depths for Thompson scattering to prevent them from undergoing rapid thermalization with electrons. The proposed sub-photosphere dissipative processes include small-radii internal shocks, nuclear and Coulomb collisions in a neutron-rich outflow, and magnetic dissipation. All of

them have advantages and drawbacks. We will not delve into the specificity of these mechanisms since it is out of the scope of this thesis and not necessary for our later discussion. The interested reader can find the relevant references in Sec. 8. Here, we want to stress that the dissipative photosphere model presents an appealing framework for understanding the prompt emission of certain LGRBs, particularly those characterized by a hard α_γ and a “narrow” Band-function spectrum. However, a significant and ongoing debate within the scientific community revolves around whether this model can be applied universally to account for the main Band-function component observed in the spectra of *all* GRBs. The arguments in favor of the dissipative photosphere models include the following: 1) the observed energy peak values in LGRBs typically fall in proximity to the temperature of the GRB central engine, and in general, it relies on fewer independent parameters when compared to the synchrotron model; 2) it has been argued that the shape of the Band function is too narrow for synchrotron radiation, while the thermal peak is narrow enough to fit the Band spectrum; 3) dissipative photosphere emission has a much higher radiative efficiency compared, for example, to the internal shock model, and naturally interprets the observations. Among the arguments against the model there is the fact that the observed typical low-energy photon index α_γ of the Band function is much softer for the photosphere models (which typically predict $\alpha_\gamma \sim 0.4$), and the proposals to soften α_γ have to make some ad hoc assumptions. So, while the synchrotron models predict a spectrum that is too soft, the photosphere models predict a spectrum that is too hard. Indeed, a debate between the two models persisted for many years, which may be coined as a “battle of α ” [519].

6.2.4 Poynting flux-dominated jets

In this section, we consider Poynting-flux-dominated outflows, those expected to be launched via the BZ mechanism that taps the BH spin energy or due to magnetic dipole radiation that causes the spindown of a millisecond magnetar (see Sec. 6.2.2.1). The dynamics of such outflows is significantly different from the fireball case. The key parameter defining the evolution of the jet is determined by the initial magnetization at the central engine, introduced in Eq. 6.31, and that can be written as

$$\sigma_0 = \frac{B^2}{4\pi\Gamma\rho c^2} = \frac{B'^2}{4\pi\rho'c^2}, \quad (6.42)$$

where B and ρ are the jet’s magnetic field strength and matter density in the fixed frame, and B' and ρ' are the corresponding quantities in the comoving frame.

In contrast to the fireball scenario, where isotropy is a suitable approximation, a Poynting-flux-dominated outflow features a globally ordered magnetic field, rendering the problem intrinsically anisotropic. The evolution of a Poynting-flux-dominated jet depends on the configuration of the magnetic field. Since both hyper-accreting BHs or milli-

second magnetars should be rapidly spinning, a strong toroidal magnetic field component can be generated. The specific field arrangement depends on whether the magnetic axis aligns with the spin axis. Among the possible magnetic field configurations are helical and striped wind [454] configurations. The *helical* configuration may be achieved when an axisymmetric poloidal field is wrapped around the jet axis into an azimuthal field configuration and is relevant for a hyper-accreting BH with a prograde accretion disk. Given the typically short duration of the GRB central engine, when the emission occurs, the “jet” can be already at a considerable distance from the central engine and can look like a “flying pancake” with wrapped wires (see right panel of Fig. 6.9). The second configuration corresponds to a *striped-wind* arrangement (see left panel of Fig. 6.9). This configuration emerges when the magnetic field axis is not aligned with the spin axis, akin to the configuration found in pulsars, so it could be pertinent in the context of a central engine featuring a millisecond magnetar. Detailed numerical simulations have demonstrated that the outflow from the magnetar tends to exhibit collimation along the rotational axis of the collapsing star [103]. This results in the launch of a collimated jet that shares similarities with the helical configuration but has a striped-wind geometry characterized by alternating directions of magnetic field lines. Magnetic jets with such a configuration are more prone to dissipation compared to the ones with a helical geometry since reconnection events are facilitated in a geometry where field lines have an alternating polarity (see Sec. 3.5).

6.2.4.1 Magnetic jet dynamics

Analogously to the case of a fireball, also in the case of a magnetic jet, we can identify three stages in the dynamical evolution: acceleration, coasting, and deceleration. It is known that magnetic jets can be self-accelerated even within the ideal MHD framework, thanks to the presence of a non-zero magnetic pressure gradient within the outflow. However, it can be shown that the strong tension stored in the twisted magnetic fields can accelerate the ejecta only to at most a Lorentz factor $\Gamma_{\text{ra}} = (1 + \sigma_0)^{1/3}$. This limit comes from the requirement that in order for the front part of the jet to receive a push from the back, the fast magneto-sonic waves should have the time to propagate across the ejecta and reach the front. This condition, known as the *sonic condition*, has been derived rigorously within various contexts [281]. Other mechanisms are thus needed to accelerate the outflow at even higher velocities. One possible and widely used mechanism has been introduced in Refs. [158, 157], and is the *continuous magnetic dissipation* scenario. Within this scenario, magnetic dissipation continuously occurs at all radii, likely through magnetic reconnection. Indeed, when magnetic fields within the outflow undergo dissipation via processes like magnetic reconnection, part of the magnetic energy is converted into thermal energy, which in turn can be converted into kinetic energy, providing the needed acceleration of the outflow (see Sec. 3.5). It has been shown that in this scenario the Lorentz factor evolves as $\Gamma \propto R^{1/3}$. This way, at

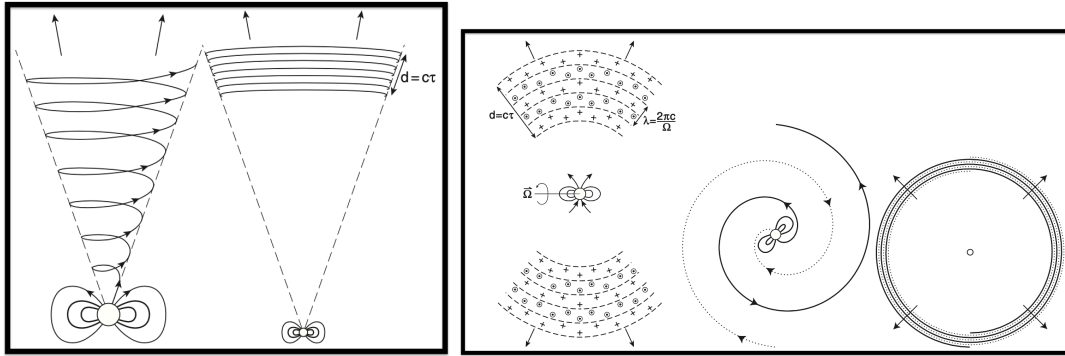


Figure 6.9: *Left panel:* The helical magnetic configuration in GRB jets is relevant for hyper-accreting BH. *Right:* The striped-wind magnetic configuration, relevant for millisecond magnetars. The outflow has a quasi-spherical shape. When observed from an equatorial viewpoint (first sketch), one can see a striped wind with layers of alternating magnetic polarity of a characteristic width $\sim cP$, where P is the period of the millisecond rotator. This pattern arises because the field lines stemming from opposite poles either enter or exit the paper plane due to the rapid rotation. When observed from the pole of rotation (middle sketch), one can see two wrapped spiral field lines with opposite orientations, forming “stripes.” At greater distances where emission should occur (third sketch), the field lines tend to concentrate within a thin spherical shell. Figures from [454].

least in principle, it should become possible to achieve the maximum Lorentz factor $\Gamma_{\max} \sim 1 + \sigma_0$ (Eq. 6.31). As for the fireball case, the radius at which Γ becomes Γ_{\max} is called the saturation radius. For the interaction phase with the CBM, which determines the dynamics of a magnetic jet in the deceleration regime, we refer the interested reader to Ref. [211].

6.2.4.2 Prompt emission models for magnetic jets

Within a Poynting-flux-dominated jet, the bulk of energy is contained in the Poynting flux. To make the GRB prompt emission efficient, it is necessary to convert part of the Poynting flux energy into other forms of energy. Some scenarios have been discussed in the literature.

One possibility is that significant magnetic dissipation occurs already below the jet photosphere. Most of the magnetic energy would be converted to particle and radiation energy at small radii, so a relatively bright photosphere emission would be observable. The magnetization parameter σ should be relatively low at the photosphere radius. This is the case that could be used in the dissipative photosphere model.

Another possibility is to have continuous magnetic dissipation until larger radii, to produce other than photospheric emission also synchrotron emission by the accelerated electrons in the optically thin region above the photosphere. This is what we will call

the **magnetized jet model with gradual dissipation** in Sec. 8, and a sketch of this scenario is displayed in Fig. 8.3.

A third possibility is to keep the magnetic energy from dissipating until the jet reaches a large enough radius. Within this scenario, $\sigma(R_{\text{PH}}) \gg 1$, so that the photosphere emission is greatly suppressed (by a factor of $[1 + \sigma(R_{\text{PH}})]^{-1}$). One scenario for dissipating magnetic energy at a large distance from the central engine has been proposed in [523]. The model is called **ICMART** (Internal-Collision-induced Magnetic Reconnection and Turbulence). The key ingredients of this model are the following [520]:

- The GRB central engine needs to have a large σ_0 ($\gtrsim 100$), but a moderate fireball parameter η is possible.
- The jet remains Poynting flux dominated and undissipated until reaching a large enough distance, e.g., $\sim 10^{15}$. At such distance, the magnetization parameter σ remains above unity. This is in contrast to the internal shock model, which necessitates $\sigma < 1$. The kinetic energy available for internal shocks is reduced by $(1 + \sigma)$ compared to the already small internal energy available in traditional internal shock models, so internal shock contribution is completely negligible.
- The central engine is not steady and intermittently ejects Poynting-flux-dominated “shells”. Internal collisions among these highly magnetized shells would trigger the dissipation of magnetic energy in the outflow through rapid turbulent reconnections. Such collisions may happen at $R \sim 10^{15}$ cm.
- For a helical magnetic configuration, repeated collisions may be needed to destroy the ordered magnetic fields and eventually trigger an ICMART event.
- In this model, the magnetic energy is not dissipated until an ICMART event is triggered. At the photosphere, the outflow is Poynting flux dominated so that the photosphere emission is suppressed. The model predicts a bright, non-thermal emission component and a weak or non-detectable thermal emission component.
- An ICMART event would proceed in a runaway manner. Seed rapid reconnections would trigger turbulence, which would facilitate more reconnections until most of the magnetic energy is dissipated. See Fig. 8.2 for a cartoon picture of the ICMART model showing various distance scales.

Among the appealing properties of the ICMART model there is a very high energy dissipation efficiency. It has been shown by numerical simulations that it can be as high as 35% [149]. It may account for the existence of the fast and slow components observed in LGRB lightcurves: the fast variability component could be explained by the presence of mini-jets due to multiple reconnection sites in the emission region created by the turbulent reconnections, whereas the slow variability component would be related to

central engine activity. It can reproduce the right observed photon peak, and alleviate the fast cooling problem (see [520] for a more detailed discussion). However, it remains a model that relies on many qualitative speculations and clearly requires proof from numerical simulations.

Paper I and II: description and summary of the main results

In this Chapter, we summarize the projects carried out in Paper I and Paper II, whose reprints are reproduced in Chapters 8 and 9, respectively. Both articles are related to LGRB jets we introduced in Sec. 6.2. Here, we summarize the motivation underlying the projects and discuss the main results.

7.1 Paper I

7.1.1 Context and motivation

In Chapter 2, we have presented the landscape of high-energy phenomena in the Universe observable through CRs, γ -rays, and neutrinos. In particular, in Sec. 6.2, we have focused on and extensively described LGRBs. We have seen how rich the LGRB phenomenology is and how intricate the theory of prompt emission is. Five decades after their discovery, the fundamental questions related to GRB jets have not yet found a decisive answer. We still do not know 1) if they are predominantly composed of baryonic matter or a Poynting flux, 2) at which distance from the central engine the emission is generated, 3) what is the mechanism responsible for the dissipation of energy, 4) how the particles are accelerated, and 5) what is the mechanism through which the photons are radiated. Assuming a specific jet composition and a particular model relevant to that composition, the GRB emission can occur anywhere between the photospheric radius $R_{\text{PH}} \sim 10^{11} - 10^{12}$ cm and the deceleration radius $R_{\text{dec}} \sim 10^{16} - 10^{17}$ cm. Energy dissipation can occur via shocks or magnetic reconnection; the particles can be accelerated in shocks (via first or second-order Fermi acceleration) or magnetic reconnection sites. The photons can be radiated in optically thin regions, more likely by leptons

via synchrotron or SSC (but a hadronic origin is also possible), or be produced in the optically thick region below the photosphere.

Given the richness of observational data and the inherent uncertainties within the different models, no single model can explain all the observations related to prompt emission. Furthermore, each of the existing models, also the ones we did not cover in Sec. 6.2, relies on a single mechanism at a particular emission site. However, various mechanisms are probably at play across different emission sites, varying between GRBs or even within a single GRB event. Precious as it may be, the information carried only by electromagnetic emission has not been enough so far to answer all the open questions regarding these objects.

In Chapter 2, we stressed the importance of multimessenger detection from astrophysical sources to get a complete picture of their underlying workings. We know GWs can be associated with short GRBs originating from compact binary mergers. There could be GW emissions also linked to LGRBs. Indeed, GWs are expected to be generated in the collapse of very massive and rapidly spinning stars in the case of an asymmetrical collapse to a BH and instabilities in the disk surrounding the central compact object. Nevertheless, these predictions are very uncertain (e.g., [270]). In our work, we focus on high-energy neutrinos, the only other possible messenger that can be produced and promptly observed in association with γ -rays.

In 1995, three papers, with different arguments, proposed that typical LGRBs can be the dominant sources of UHECRs [495, 480, 327]¹. Obviously, neutrinos represent a natural byproduct of the interaction between CRs trapped in the acceleration region and the guaranteed target photon field of the prompt emission². The threshold condition for Δ -resonance (Eq. 2.7), assuming $E_\nu \sim 0.05 E_p$, and considering the Lorentz transformation between the comoving and observer frame, can be rewritten as:

$$E_\nu \gtrsim 8 \text{ GeV} \left(\frac{\Gamma}{1+z} \right)^2 \left(\frac{\varepsilon_\gamma}{\text{MeV}} \right)^{-1}. \quad (7.1)$$

For different models, one has different emission sites and thus different Γ and ε_γ values. During the prompt emission, if we take a typical $\Gamma^2 \sim 10^5$, $\varepsilon_\gamma \sim 300 \text{ keV}$, and $z \sim 1$, from Eq. 7.1 one gets $E_\nu \sim \text{PeV}$, as long as protons can be accelerated to an energy

¹Among the strong motivations, there was the similarity between the UHECR energy density and GRB photon energy density on Earth. One can show that, for example, the internal shocks that we introduced in the internal shock model for prompt LGRBs fulfill the requirements necessary to accelerate protons to UHE, while the condition for the external shocks (FS and RS in the afterglow phase) is more stringent [520].

²We do not consider pp interactions, since compared to $p\gamma$ interactions, they are typically less efficient due to the requirement of low density in the jet for relativistic motion. However, these interactions can be significant at smaller radii when the jet is highly compact or when the jet is still within the star, allowing jet protons to interact with nucleons within the stellar envelope.

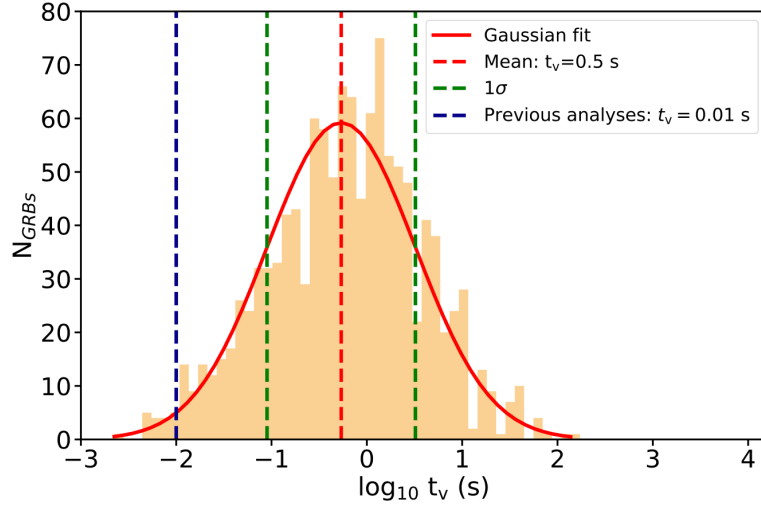


Figure 7.1: Distribution of minimum variability timescales obtained by analyzing 1213 GRB light curves. The solid red line indicates the Gaussian fit of the distribution. The dashed red line is the mean of the distribution, from which a mean value of $t_v = 0.5$ s is obtained. The dashed green lines indicate the 1σ level. The default value, $t_v = 10$ ms, is indicated in dashed blue, typically adopted in stacked searches. Figure from [50].

greater than a few 10^{16} eV. This requirement is not stringent since various models predict a proton energy up to 10^{20} eV and higher. Ref. [500] first discussed and predicted the neutrino flux from LGRBs in the context of the internal shock model, and over the years, many other authors have calculated the PeV neutrino flux from LGRBs using both analytical and numerical methods [500, 408, 409, 152, 347, 230, 235].

From the observational side, all the searches of high-energy neutrinos coincident with LGRBs, both in spatial direction and in time by the IceCube collaboration, have consistently obtained null results. Stacked searches have constrained their contribution to the high-energy neutrino diffuse isotropic flux to less than 1% (e.g., [7]). These non-detections were used to put limits on the internal shock, photospheric, and ICMART models by constraining model parameters like baryonic load (i.e., the ratio between the luminosity in relativistic protons to the luminosity in radiated photons, $f_p = L_p/L_\gamma$) and Lorentz factor of the jet. As a result, most of the parameter space for the internal and photospheric model was excluded, leaving only small baryonic loads and large bulk Lorentz factors unconstrained. Nevertheless, several assumptions are made in these kinds of studies. Let us mention just some of them. All models assume that proton acceleration occurs at a single location, where γ -rays are also produced and emitted. This must not be necessarily the case. For example, already in the framework of internal shocks, we know that multi-zone internal shock models predict lower neutrino

fluxes (see, e.g. [109]) that remain beyond the current detector sensitivity and thus are unconstrained. The variability timescale is always assumed to be $t_v \sim 10$ ms for all GRBs, one of the lowest observed in the LGRB lightcurves. However, if we look at the distribution of known values of t_v in Fig. 7.1, obtained from Fourier analyses on LGRB light curves, we see that the default value adopted is located in the tail of the measured distribution, and is not representative of the overall GRB population. Finally, all LGRBs in the analyzed samples are typically assumed to have identical values for f_p and Γ . Given all these assumptions, the conclusions that firmly exclude some models should be relaxed.

In this context, the aim of Paper I was to 1) use the most up-to-date parameters from observations and simulations that would be more suitable to describe a representative LGRB, 2) investigate the production of neutrinos for different jet composition and dissipation mechanisms, and make a fair comparison of the different models proposed in the literature, also considering models not previously explored for neutrinos, 3) determine whether the produced high-energy neutrinos could be within reach of IceCube-Gen2 [10], and thus if they have the potential of unraveling the nature of LGRB jets.

7.1.2 Summary of the main results

In the work presented in Chapter 8, with updated parameters, we re-consider the internal shock model, the ICMART model, introduced in Sec. 6.2, and the PH-IS model. The latter is a two-zone model with the main emission coming from a dissipative photosphere and neutrinos produced at the internal shocks that develop later during the fireball evolution. In addition to these, we investigate for the first time from the neutrino perspective, the jet model with three emission components, which also includes an early afterglow emission, the magnetized jet model with gradual dissipation (presented in Sec. 6.2), and proton synchrotron emission model, where protons are considered to be the particles which radiate the observed emission in a marginally fast-cooling regime. To compare them, instead of assuming the same properties of the observed radiation and then case by case tuning the jet parameters to reproduce them, we choose to adopt, for both investigated types of jets, the same initial total energetics and the saturation Lorentz factor, with the microphysical parameters suited for the specific acceleration region, and specific jet composition. Each model offers different predictions for the production of high-energy neutrinos, which depend on factors such as the magnetic field strength, jet density, the location of the proton acceleration region, the fraction of the total kinetic energy going into protons and electrons, and the details of the particle spectra (e.g., the power slope describing the proton and photon spectra).

To visualize the differences among the models, we choose to adopt the average values of the observed parameters to be representative of the whole LGRB population, with a typical γ -ray flux produced from a GRB at redshift $z = 2$ (the redshift at which the

LGRB distribution peaks). We then converted the total neutrino fluence from the representative GRB into the quasi-diffuse neutrino flux induced by all the sources at that redshift by rescaling the total fluence with the average rate of GRBs distributed over the full sky expected per year. This quantity is interesting since it allows us to compare the neutrino flux with the measurements reported by IceCube, to constrain the contribution of GRBs to the astrophysical neutrino flux. The results are displayed in Fig. 8.12. We immediately see the wide diversity in the predicted fluxes, both in terms of normalization and spectral shape, with the intensity and the position of the peak spanning three orders of magnitude. But, above all, it is clear that none of the explored GRB models are excluded by current searches.

7.1.3 Critical outlook

Here, we mention some caveats to our work. As previously stated, we utilized specific parameters to represent the entire GRB population and focused on the redshift at which their distribution peaks when calculating the quasi-diffuse flux. We made this choice because of our lack of knowledge regarding the proportion of observed LGRBs explained by various models and understanding of how these events are distributed throughout the history of the Universe. There may exist a predominant composition and dissipation scenario for the jets; in such a scenario, our assumption would be valid. In addition to this, we also expect a distribution in the characteristic jet parameters. In Fig. 8.13, we investigate the impact of the variation of two of the most uncertain ones, the variability timescale t_v and the Lorentz boost factor Γ . Only considering these two, we already see that the proton-synchrotron model can hit the expected sensitivity of IceCube-Gen2 and that it would be, in principle, possible to constrain extreme configurations responsible for the prompt neutrino emission. However, numerical calculations performed in Ref. [178] have found strong modifications of the broadband photon spectrum due to the emission of the secondary particles produced in $p\gamma$ interactions, hence strongly disfavoring marginally fast cooling protons as an explanation of the low-energy spectral break in the prompt GRB spectra.

So, by only considering the uncertainties of these two parameters, we cannot draw strong conclusions from the detection perspective of the diffuse neutrino flux. To provide quantitative estimates that encompass not only the diverse LGRB properties but also their redshift and luminosity distributions, it would be helpful to investigate, with a Monte Carlo method, the neutrino flux for each of the existing models, extending the study to the inner and opaque-to-radiation parts of the jet, as well as to the afterglow phase. Detailed observations and data analyses of the multi-wavelength prompt emission with future GRB observatories are necessary. With its unprecedented polarimetric capabilities, space missions like ASTENA (Advanced Surveyor of Transient Events and Nuclear Astrophysics) [222] will address the role of magnetic fields in the

jet and other unsolved issues in the GRB field. At the same time, since future detectors like IceCube Gen2 will have a significantly increased sensitivity, consistent neutrino predictions, which will complement the electromagnetic studies, are crucial.

On the other hand, our approach would be especially suitable to test models in case of point source discoveries. One example is provided by the GRB 221009A [105], also known as 'The BOAT' (Brightest Of All Time), which is the brightest LGRB ever detected in terms of peak flux and fluence, with unusual proximity to Earth. The non-observation of neutrinos has already allowed to put limits on the acceleration of protons near the photosphere [352], highlighting the potential of neutrinos in pinpointing the LGRB emission mechanism, as well the contribution of LGRBs to the UHECR flux [26], even if more careful investigation remains to be done.

7.2 Paper II

7.2.1 Context and motivation

In Sec. 6.2.1.2, we have introduced the reader to the main observable properties of the afterglow emission, which follows the prompt γ -ray burst. We have mentioned that, in several cases, late afterglow observations have revealed many unexpected features that are not easily accountable for within the classical framework of a decelerating blastwave in a circumburst medium (CBM).

The feature we wanted to explore in Paper II (Chapter 9) is represented by sudden rebrightenings in the optical lightcurve (see. Fig. 6.7), which we will simply call "optical jumps". As of today, these jumps still defy a satisfying explanation despite the various theoretical models proposed to explain them.

In our work, we consider the model that predicts a discrete episode of energy injection into the fireball by the late-time interaction of a fast shell launched by the central engine with the already decelerating slow shell that gave rise to the prompt emission. This second fast shell moves at a constant velocity in the empty medium swept up by the first shell's passage and eventually catches up with it. The collision between the two shells leads to the re-heating of the fireball material, resulting in an observed increase in flux. The origin of the late-time activity of the central engine is still uncertain but is appealing as it can successfully fit the lightcurves of some LGRBs with optical jumps. In this context, we expect an enhanced neutrino signal to be produced by the interaction of the accelerated protons with the intense burst of optical photons. The aim of Paper II is thus to investigate whether the detection of such neutrinos is possible using the IceCube Neutrino Observatory and future radio arrays. A successful observation would pinpoint the mechanism responsible for the optical jump and teach us about the properties of the colliding shells and the environment where the collision occurs.

7.2.2 Summary of the main results

In Chapter 9, we perform a simplified analytical modeling of the late merger of two relativistic shells and the resulting electromagnetic emission. We investigate the pre-collision standard afterglow emission of the first shell, the emission of the merged hot shell right at the collision, and the late afterglow emission of the merged shell. We consider a benchmark GRB with characteristic parameters dictated by the observations. Since there are no observational constraints on the properties of the merging shells, e.g., their relative Lorentz factor or the energetics of the fast shell, by keeping fixed the typical time at which the rebrightening is observed, we choose the setup for the collision, which produces the strongest rebrightening.

During all three stages, together with electrons, protons are also expected to be accelerated at the FS, and high-energy neutrinos will be produced via photo-hadronic interactions. We calculate the photon and neutrino flux in the case of a constant density profile resembling the interstellar medium (ISM) and a stellar wind profile. The resulting photon lightcurve at a specific optical frequency is shown in Fig. 9.2, while the corresponding neutrino cumulative number is displayed in Fig. 9.5. We note that in the ISM scenario, the number of neutrinos increases by a factor of 6 in the presence of an optical jump. In contrast, in the case of wind, the difference with respect to a standard afterglow without jumps is entirely negligible. This is because, for a decreasing density profile, the early-time emission strongly dominates the overall time-integrated neutrino flux so that a late collision does not affect the cumulative neutrino number.

Finally, we explore the detection prospects for the all-sky quasi-diffuse flux and point source searches. To get the quasi-diffuse flux, analogously to what we did in Paper I, we assume the predictions made for the benchmark GRB as representative of all the population of GRBs having optical jumps in their lightcurves. Even assuming that 10 – 30% of LGRB afterglows present such jumps and that the collision of relativistic shells can explain these jumps, the predicted flux falls well below the current IceCube sensitivity to the prompt phase. As for the point searches, Fig. 9.7 shows that, if our benchmark GRB occurred in an ISM, and within a distance ~ 40 Mpc, it could be in principle detectable by IceCube-Gen2. On the other hand, if taking the good studied GRB 100621A, with the realistic distance of these objects, as we can see from Fig. 9.8, the detection of neutrinos seems unlikely. We thus conclude that to have a successful point-like neutrino detection, very special conditions on the configuration of the merger, the energetics of the system, and the distance of the LGRBs displaying optical jumps during their afterglow should be fulfilled.

Paper I: Neutrino signal dependence on gamma-ray burst emission mechanism

This chapter is a reprint of:

Tetyana Pitik, Irene Tamborra, Maria Petropoulou

Neutrino signal dependence on gamma-ray burst emission mechanism

JCAP 05(2021) 034, [arXiv:2102.02223](https://arxiv.org/abs/2102.02223)

ABSTRACT

Long duration gamma-ray bursts (GRBs) are among the least understood astrophysical transients powering the high-energy universe. To date, various mechanisms have been proposed to explain the observed electromagnetic GRB emission. In this work, we show that, although different jet models may be equally successful in fitting the observed electromagnetic spectral energy distributions, the neutrino production strongly depends on the adopted emission and dissipation model. To this purpose, we compute the neutrino production for a benchmark high-luminosity GRB in the internal shock model, including a dissipative photosphere as well as three emission components, in the jet model invoking internal-collision-induced magnetic reconnection and turbulence (ICMART), in the case of a magnetic jet with gradual dissipation, and in a jet with dominant proton synchrotron radiation. We find that the expected neutrino fluence can vary up to three orders of magnitude in amplitude and peak at energies ranging from 10^4 to 10^8 GeV. For our benchmark input parameters, none of the explored GRB models is excluded by the targeted searches carried out by the IceCube and ANTARES Collaborations. However,

our work highlights the potential of high-energy neutrinos of pinpointing the underlying GRB emission mechanism and the importance of relying on different jet models for unbiased stacking searches.

8.1 Introduction

Gamma-ray bursts (GRBs) are irregular pulses of gamma-rays that have puzzled astronomers for a long time [269]. Exhibiting a non-thermal spectrum, typically peaking in $10\text{--}10^4$ keV energy band [218], bursts lasting for more than 2 s are named long-duration GRBs and are thought to be harbored within collapsing massive stars [508, 304, 509]. They are the brightest explosions in our universe and can release isotropic energies as high as 10^{54} erg in gamma-rays over few tens of seconds [64].

The central engine of a long-duration GRB jet can either be a hyper-accreting black hole or a rapidly spinning magnetar. Because the central engine cannot be directly observed, its nature can be inferred only indirectly through its impact on the electromagnetic properties of GRBs (see, e.g., Ref. [385] and references therein). A bipolar outflow is continuously powered for a certain time interval, during which gravitational energy [125, 288] (for accreting systems) or spin energy [93, 477] (for spinning-down systems) is released in the form of thermal energy or Poynting flux energy, respectively. Subsequently, the outflow propagates through the star and it is strongly collimated by the stellar envelope. Once it succeeds to break out of the stellar surface, it manifests itself as the jet responsible for the GRBs that we observe at Earth. The dynamical evolution of the jet strongly depends on the initial conditions of the central engine. If the magnetic field is negligible, the evolution of the outflow can be well described by the fireball model [373]. If instead the central engine harbours a strong magnetic field, the jet dynamics is significantly different [157].

Gamma-ray bursts are candidate sources of ultra-high energy cosmic rays and high energy neutrinos [317]. In the prompt phase, if the jet contains baryons, protons and nuclei are expected to be accelerated [237]. If a photon field is also present, photo-hadronic ($p\gamma$) interactions can lead to a significant flux of neutrinos [500, 221, 488]. Another copious source of neutrinos comes from hadronic collisions (pp or pn) which, however, are most efficient inside the progenitor star where the baryon density is large [409, 345, 325, 237]. Given the typical GRB parameters, neutrinos produced in the optically thin region are expected to be emitted in the TeV-PeV energy range [500, 321, 494, 337].

The IceCube Neutrino Observatory routinely detects neutrinos of astrophysical origin in the TeV-PeV energy range [46, 45, 23, 17]. However, despite the fact that several sources have been proposed as possible candidates to explain the neutrino flux that we observe [57, 321, 337, 494, 482], we are still lacking clear evidence on the sources producing the observed neutrinos. Among the candidate sources, high-luminosity GRBs

are deemed to be responsible for less than 10% of the observed diffuse emission in the TeV energy range [23, 49]. On the other hand, over the years, the IceCube and ANTARES Collaborations have searched for high-energy neutrinos emitted in coincidence with GRBs observed by the Fermi satellite [7, 16, 49], gradually placing more stringent upper limits on somewhat optimistic GRB emission models. Recent work suggests that current limits are still not stringent enough to rule out more realistic estimations proposed in the literature [291, 242, 237, 467, 468, 109, 235]. Intriguingly, besides the need for increased detection sensitivity, one of the reasons for the non-detection of GRB neutrinos could be connected to the theoretical modeling of the neutrino emission, which is strictly linked to the electromagnetic modeling of the jet. In fact, a comprehensive explanation of the GRB emission and dissipation mechanism is still lacking due to the failure of existing models in addressing all observations in the spectral and temporal domains. On the other hand, the scarce amount of data on high energy photons and the related statistical challenges allow for a certain flexibility in fitting the same set of data with different input models for GRBs—see, e.g., Refs. [370, 518, 38, 39, 104].

Different GRB models may lead to very different predictions for the neutrino emission. The latter depends on the target photon spectrum and the properties of the accelerated proton distribution (i.e., energy density, power-law slope, and maximum energy), both depending on the emission and dissipation mechanisms as well as the location of the proton acceleration region.

In this work, we compute the neutrino emission for a benchmark high luminosity GRB in various jet emission and dissipation scenarios. In particular, we consider an internal shock (IS) model [412], a dissipative photosphere model in the presence of ISs (PH-IS) [475], a three-component model (3-COMP) with emission arising from the photosphere, the IS, and external shock [224], and the internal-collision-induced magnetic reconnection and turbulence model (ICMART) [523]. We also compute, for the first time, the neutrino signal expected in two models where the jet is assumed to be magnetically dominated, namely a magnetized jet model with gradual dissipation (MAG-DISS) [87, 202], and a proton synchrotron emission model (p-SYNCH) [198]. Our goal is to make a fair comparison among the proposed models for dissipation and electromagnetic emission in GRBs for what concerns the expected neutrino signal.

This paper is organized as follows. In Sec. 8.2, we outline the basics of the dynamical evolution of the GRB jets considered in this paper. The main model ingredients as well as the proton energy distributions are reported in Sec. 8.3. The neutrino production mechanism is discussed in Sec. 8.4. The neutrino emission is presented in Sec. 8.5, first in various scenarios involving ISs, then in the case of magnetized jets, and lastly for the proton synchrotron mechanism. A discussion on our findings, also in the context of detection perspectives as well as uncertainties on the input GRB parameters, and conclusions are reported in Secs. 8.6 and 8.7, respectively. The fitting functions adopted for the photon spectral energy distributions are listed in Appendix A.1. A discussion

on the dependence of the neutrino emission on the input parameters for the magnetic model with gradual dissipation is reported in Appendix A.2. A comparison of the quasi-diffuse neutrino emission with standard input assumptions reported in the literature is provided in Appendix A.3.

8.2 Dynamical evolution of gamma-ray burst jets

In this section, we introduce the main physics describing the jet models considered in this work. We present the models in the context of kinetic dominated jets, then focus on two cases of Poynting flux dominated jets, and the proton synchrotron model. Note that, despite the fact that the proton synchrotron model has a Poynting luminosity larger than the kinetic one (see Ref. [178] for a dedicated discussion), we treat it separately from the Poynting flux dominated jets because it does not require knowledge of the jet dynamics.

The general GRB model envisages a relativistic jet propagating with Lorentz factor Γ , with respect to the central engine frame, and half opening angle θ_j . As long as $\Gamma^{-1} < \theta_j$, which is expected to hold during the prompt phase [100], the radiating region can be considered spherically symmetric. We therefore use isotropic equivalent quantities throughout the paper.

The reference frames used in our calculation are the observer frame (on Earth), the frame of the central engine (laboratory frame), and the jet comoving frame. A quantity characteristic of the jet is labeled as X , \tilde{X} , and X' , in each of these frames, respectively. For example, energy is transformed through the following relation: $\tilde{E} = (1+z)E = (1+z)\mathcal{D}E'$; time instead transforms as $t = (1+z)\tilde{t} = (1+z)\mathcal{D}^{-1}t'$, with $\mathcal{D} = [\Gamma(1 - \beta \cos \theta)]^{-1}$ being the Doppler factor, $\beta = v/c$, $\Gamma = 1/\sqrt{1 - \beta^2}$ the Lorentz boost factor and θ the angle of propagation of an ejecta element with respect to the line of sight. A characteristic quantity of the jet is the isotropic-equivalent energy, \tilde{E}_{iso} , which represents the energetic content of the outflow and it is related to the bolometric energy \tilde{E}_{bol} through the opening angle by the following relation: $\tilde{E}_{\text{bol}} = (1 - \cos \theta_j)\tilde{E}_{\text{iso}} \approx (\theta_j^2/2)\tilde{E}_{\text{iso}}$, where the approximation holds for small opening angles.

The dominant source of energy in a GRB jet is related to the initial conditions. The jet is powered by accretion onto a newly formed black hole [508] or a rapidly spinning massive neutron star [477]. Two mechanisms are invoked to extract energy from the central compact object and power the GRB jet: neutrino annihilation [164, 399, 125] or tapping of the spin energy of the central object by means of magnetic fields [93, 324].

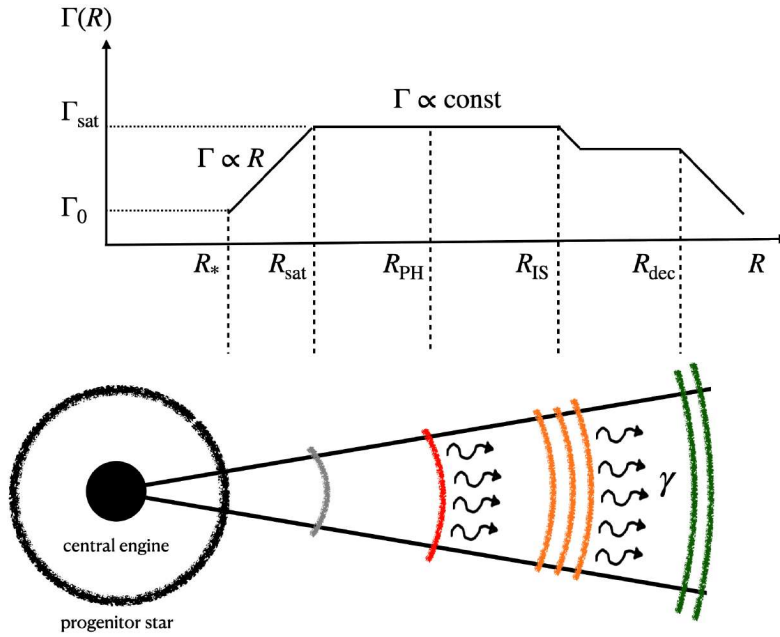


Figure 8.1: Schematic representation of a GRB jet (not in scale) where energy dissipation takes place through relativistic shocks. The Lorentz factor Γ is shown as a function of the fireball radius for the case in which the photosphere occurs in the coasting phase, so that the photospheric radius (R_{PH}) lies above the saturation radius (R_{sat}). The photosphere is assumed to produce thermal γ -rays, the ISs forming at R_{IS} are thought to produce non-thermal γ -rays, and the external shock, which starts to decelerate at R_{dec} , is responsible for the afterglow. When energy dissipation takes place below the photosphere, non-thermal radiation is also expected from R_{PH} .

8.2.1 Kinetic dominated jets

We start with the case of a generic fireball composed of photons, electron/positron pairs, and a small fraction of baryons (primarily protons and neutrons), with negligible magnetic fields [207, 395]. The dynamical evolution of the fireball is sketched in Fig. 8.1 and consists of three phases, namely acceleration, coasting, and deceleration:

1. *Fireball acceleration:* A hot relativistic fireball of isotropic energy $\tilde{E}_{\text{iso}} = \tilde{L}_{\text{iso}} \tilde{t}_{\text{dur}}$ is created and launched at the radius R_0 by the central engine emitting energy with luminosity \tilde{L}_{iso} for a time \tilde{t}_{dur} . Since after the propagation through the envelope of the progenitor star, the fireball can be re-born [283], we adopt as size of the jet base $R_0 = R_* \theta_j$, with $R_* \simeq 10^{11}$ cm being the progenitor star radius. The width of the emitted shell is $\tilde{\Delta} = c \tilde{t}_{\text{dur}}$. As the fireball shell undergoes adiabatic expansion, and while the pair plasma retains relativistic temperatures, baryons are accelerated by radiation pressure and the bulk Lorentz factor increases linearly

with radius ($\Gamma \propto R$), until it reaches its maximum value. We assume that the latter coincides with the dimensionless entropy per baryon $\eta = \tilde{E}_{\text{iso}}/Mc^2$, where M is the baryonic mass injected into the outflow. The maximum Lorentz factor is achieved at the saturation radius $R_{\text{sat}} = \eta R_0/\Gamma_0$, where $\Gamma_0 = \Gamma(R_*) \simeq 1-10$ [328] is the breakout Lorentz factor.

2. *Fireball coasting*: Beyond R_{sat} , the flow coasts with $\Gamma = \Gamma_{\text{sat}} \sim \eta = \text{const}$. As the fireball shell keeps on expanding, the baryon density, obtained by the mass continuity equation $\dot{M} = 4\pi R^2 \Gamma \rho' c = \text{const}$ [153] for a relativistic flow with spherical symmetry, drops as

$$n'_b = \frac{\rho'}{m_p} = \frac{\dot{M}}{4\pi m_p R^2 c \Gamma} \simeq \frac{\tilde{L}_{\text{iso}}}{4\pi R^2 m_p c^3 \eta \Gamma}, \quad (8.1)$$

where ρ' is the baryon density in the comoving frame, R is the distance from the central engine, and $\tilde{L}_{\text{iso}} = \eta \dot{M} c^2$. At a certain point, photons become optically thin to both pair production and Compton scattering off free leptons associated with baryons entrained in the fireball. Once the Thomson optical depth ($\tau_T = n'_l \sigma_T R/\Gamma$) drops below 1, the energy that has not been converted into kinetic energy is released at the photospheric radius R_{PH} . Let \mathcal{R} denote the number of leptons per baryon ($n'_l = \mathcal{R} n'_p$), we can define the critical dimensionless entropy [322]:

$$\eta_* = \left(\frac{\sigma_T \mathcal{R} \tilde{L}_{\text{iso}} \Gamma_0}{8\pi R_0 m_p c^3} \right)^{1/4}, \quad (8.2)$$

where $\sigma_T = 6.65 \times 10^{-25} \text{cm}^2$ is the Thomson cross section. η_* represents the limiting value of the Lorentz factor which separates two scenarios: $\eta > \eta_*$ (the photosphere occurs in the acceleration phase) and $\eta < \eta_*$ (the photosphere occurs in the coasting phase). For our choice of parameters, we will always be in the second case, thus we can introduce the photospheric radius as the distance such that $\tau_T = 1$ [319]:

$$R_{\text{PH}} = \frac{\sigma_T \tilde{L}_{\text{iso}} \mathcal{R}}{4\pi \eta^3 m_p c^3}. \quad (8.3)$$

The radiation coming from the photosphere is the first electromagnetic signal detectable from the fireball. It emerges peaking at [319]

$$k_B \tilde{T}_{\text{PH}} = k_B \left(\frac{\tilde{L}_{\text{iso}}}{4\pi R_0^2 \sigma_B} \right)^{1/4} \left(\frac{R_{\text{PH}}}{R_{\text{sat}}} \right)^{-2/3}, \quad (8.4)$$

where σ_B is the Stefan-Boltzmann constant and k_B the Boltzmann constant. The energy \tilde{E}_{PH} emerging from the photosphere is parametrized through $\epsilon_{\text{PH}} = \tilde{E}_{\text{PH}}/\tilde{E}_{\text{iso}}$.

Since the central engine responsible for the launch of the relativistic jet is expected to have an erratic activity, the produced outflow is unsteady and radially inhomogeneous. This causes internal collisions between shells of matter emitted with time lag t_v to occur at a distance [412]

$$R_{\text{IS}} \simeq \frac{2ct_v\Gamma^2}{1+z}; \quad (8.5)$$

this is the IS radius, where a fraction ε_{IS} of the total outflow energy (\tilde{E}_{iso}) is dissipated, and particles are accelerated.

3. *Fireball deceleration*: The fireball shell is eventually decelerated [395, 393, 163] by the circumburst medium that can either be the interstellar medium or the pre-ejected stellar wind from the progenitor before the collapse. Let us consider an external density profile [376]:

$$n_b(R) = AR^{-s}, \quad (8.6)$$

with $s = 0$ for a homogeneous medium and $s = 2$ for a wind ejected at constant speed. For a thin shell [432], the deceleration radius is defined as the distance where the swept mass from the circumburst medium is $m_{\text{CMB}} = M/\eta$ [or $\Gamma(R_{\text{dec}}) = \eta/2$] [94]:

$$R_{\text{dec}} = \left(\frac{3-s}{4\pi} \frac{\tilde{E}_{\text{K,iso}}}{m_p c^2 A \eta^2} \right)^{1/(3-s)}; \quad (8.7)$$

in alternative, R_{dec} can be obtained from the observed deceleration time t_{dec} [520]:

$$t_{\text{dec}} \simeq 1.3(1+z) \frac{R_{\text{dec}}}{\eta^2 c}, \quad (8.8)$$

where $\tilde{E}_{\text{K,iso}} = \tilde{E}_{\text{iso}} - \tilde{E}_{\gamma,\text{iso}}$ is the isotropic equivalent kinetic energy of the outflow after $\tilde{E}_{\gamma,\text{iso}}$ has been radiated during the prompt phase. At R_{dec} , an external shock forms and propagates into the medium, hence the deceleration radius is essentially the initial external shock radius.

8.2.1.1 Jet model with internal shocks

For long time, the IS model [412, 271, 144] has been considered as the standard model for the prompt emission in the literature. Among the merits of this model there is its ability to naturally explain the variability of the lightcurves, to provide natural sites for the dissipation of the kinetic energy of the baryonic fireball, as well as sites for particle acceleration and non-thermal radiation.

The erratic activity of the central engine is responsible for the creation of an outflow that can be visualized as being composed of several shells. Collisions of such shells with different masses and/or Lorentz factors cause the dissipation of the kinetic energy of the jet at R_{IS} ¹ (see Fig. 8.1).

Part of the dissipated energy, $\varepsilon_{\text{IS}}\tilde{E}_{\text{iso}}$, is used for particle acceleration. Non-thermal electrons (protons) receive a fraction ε_e (ε_p), while a fraction ε_B goes into the amplification of magnetic fields. In this scenario, electrons emit synchrotron radiation in the fast cooling regime. The radiated energy can thus be expressed as $E'_{\gamma,\text{iso}} = \varepsilon_e\varepsilon_{\text{IS}}E'_{\text{iso}}$ and the magnetic field as

$$B' = \sqrt{8\pi \frac{\varepsilon_B}{\varepsilon_e} \frac{E'_{\gamma,\text{iso}}}{V'_{\text{iso}}}}. \quad (8.9)$$

The protons co-accelerated with electrons interact with the prompt photons through photo-hadronic interactions and produce neutrinos, as discussed in Sec. 8.4. Here $V'_{\text{iso}} = 4\pi R_{\gamma}^2 \Gamma c \tilde{t}_{\text{dur}}$ represents the isotropic volume of the jet in the comoving frame.

Within a more realistic setup, various collisions between plasma shells occur along the jet. Scenarios involving collisions of multiple shells have been considered [220, 108, 424] and can lead to lower neutrino fluxes. Yet, in this work, since we aim to compare different jet models, we adopt one representative shell with average parameters and spectral properties for simplicity.

8.2.1.2 Jet model with a dissipative photosphere and internal shocks

In the class of photospheric models, it is assumed that the dominant radiation observed in the prompt phase is produced in the optically thick region below the photosphere [83]. Depending on the presence of dissipative processes acting in the optically thick parts of the outflow, photospheric models can be classified in non-dissipative or dissipative ones.

In the presence of a non-dissipative photosphere, according to the standard fireball model, the thermal radiation advected with the flow and unaffected by the propagation is released at R_{PH} , see Fig. 8.1. Depending on the dimensionless entropy of the outflow (see Eq. 8.2), this component can be very bright or highly inefficient and is characterized by the fraction $\varepsilon_{\text{PH}} = (\eta/\eta_*)^{8/3}$ [319].

For a dissipative photosphere, strong sub-photospheric dissipation is required in the optically thick inner parts of relativistic outflows in order to account for the detected non-thermal spectra [473, 200, 203, 413, 487, 486, 85]. In this scenario, the spectral peak and the low-energy spectrum below the peak are formed by quasi-thermal Comptonization of seed photons by mildly relativistic electrons when the Thomson optical depth of the flow is $1 \lesssim \tau_T \lesssim 100$ [201, 474]. In the literature, several sub-photospheric dissipative mechanisms have been proposed, including ISs at small-radii [413], collisional

¹If there is a large spread in the Γ values of the shells, then R_{IS} can also spread a lot [220, 108, 424].

nuclear processes [84], or dissipation of magnetic energy [201]. One of the most attractive features of these models is their ability to naturally explain the observed small dispersion of the sub-MeV peak and the high prompt emission efficiency [284, 283, 210], that the standard version of the IS model cannot easily explain.

The scenario explored in this work considers the main prompt emission as being released at R_{PH} with a non-thermal spectrum. These photons cross the IS region and interact with energetic protons accelerated at the IS to produce neutrinos. We do not consider neutrino production below and at the photosphere, as this would result in neutrino energies well below the PeV range that we are interested in (i.e., GeV neutrinos produced in proton-neutron collisions in the ejecta [70, 257] or TeV neutrinos produced via pp interactions of protons accelerated at sub-photospheric ISs [490, 341, 511, 345, 346]). Indeed, photo-hadronic interactions in the opaque region do not lead to efficient production of high-energy neutrinos because of inefficient Fermi acceleration that limits the maximum proton energy to low values [86]. We stress that the wording “dissipative photosphere” in this work is meant to highlight the non-thermal nature of the photospheric spectrum and it should not be associated with the neutrino production region below the photosphere, as usually done in the literature (see, e.g. [490]).

8.2.1.3 Jet model with three emission components

The three-component GRB model was introduced in Ref. [224], where the authors found that a thermal component described by a black body (BB) spectrum, a Band spectrum (sometimes statistically equivalent to a cut-off power-law, CPL) and a non-thermal power-law (PL) spectrum at high energies (with or without cut-off) represent a globally better description of the data than the Band spectral fit for a number of bursts. We refer the reader to Appendix A.1 for details on the spectral energy distributions of photons.

As argued in Ref. [224], the physical interpretation proposed for the three components is the following. The BB component, given its weakness, is interpreted as thermal photospheric emission of a magnetized jet not strongly affected by sub-photospheric dissipation. The non-thermal emission fitted by the Band (or CPL) component, given the observed variability, is assumed to be produced in the optically thin region of the jet from relativistic electrons. The third PL (or CPL) component, which extends over at least 5 decades in energy and sometimes emerges with a slight temporal delay with respect to the trigger of the burst, is the one with the least clear origin. Because of its initial temporal variability, it is assumed to be of internal origin; e.g., it might be due to inverse Compton processes, even if this scenario is not able to explain the extension of such a component to lower energies or the temporal delay. Finally, the fact that in some cases the PL component becomes dominant at the end of the bursts and lasts longer than the prompt emission led to identify it with the emergence of an early afterglow, which corresponds to the start of deceleration of the outflow.

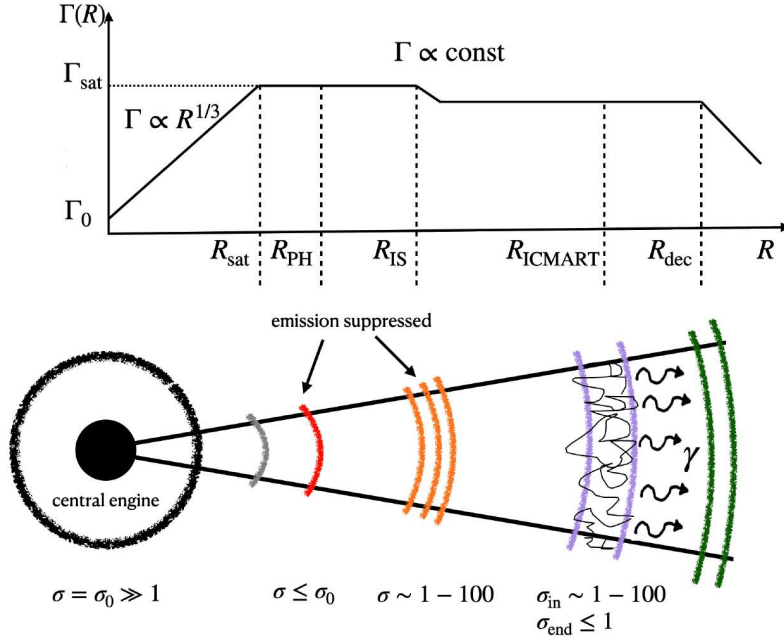


Figure 8.2: Schematic representation of a Poynting flux dominated jet (not in scale) in the ICMART model. The Lorentz factor Γ is shown as a function of jet radius. The radiation from the photosphere (R_{PH}) and ISs (R_{IS}) is strongly suppressed and can be at most $1/(\sigma + 1)$ of the total jet energy (see Eq. 8.10); typical values for the magnetization parameter σ are shown. The emitting region is located at R_{ICMART} , where magnetic reconnection causes a strong discharge of magnetic energy and the emission of gamma-rays. The magnetization at R_{ICMART} is σ_{in} and σ_{end} in the beginning and at the end of an ICMART event, respectively.

8.2.2 Poynting flux dominated jets

When the central compact object is a rapidly rotating black hole threaded by open magnetic field lines, it is possible to tap the black hole spin energy to produce Poynting-flux dominated jets [93]. The electromagnetic luminosity of this jet is much larger than the kinetic luminosity associated to matter.

A characteristic parameter is the magnetization σ , defined as the ratio of the Poynting luminosity and the kinetic luminosity:

$$\sigma(R) \equiv \frac{L_B}{L_K} = \frac{B^2(R)}{4\pi\Gamma\rho(R)c^2} = \frac{B'^2(R)}{4\pi\rho'(R)c^2}, \quad (8.10)$$

where $B'(R)$ and $\rho'(R)$ are the magnetic field strength and matter density in the comoving frame at a certain distance R from the central engine. Hence, the total jet luminosity at any radius is $L(R) = [1 + \sigma(R)]L_K(R)$. In this work we consider two models for magnetized jets: the ICMART model and the gradual magnetic dissipation model, which we briefly introduce below.

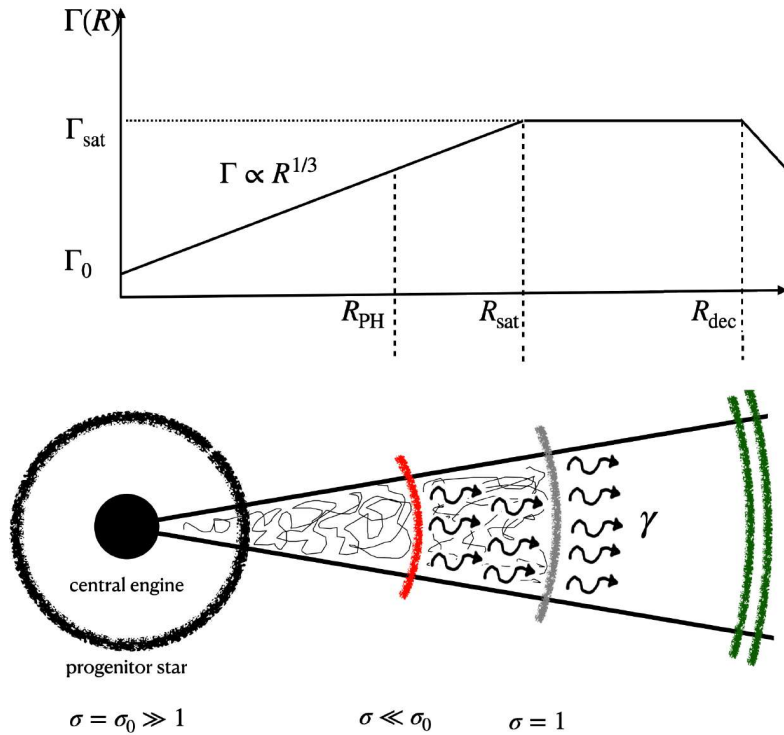


Figure 8.3: Schematic representation of a Poynting flux dominated jet (not in scale) in the gradual energy dissipation model. The Lorentz factor Γ is shown as a function of jet radius. The radiation from the photosphere (R_{PH}) can be very bright, depending on the initial magnetization σ_0 of the outflow. Typical values for the magnetization parameter σ are shown. The emitting region is located between R_{PH} and R_{sat} , where magnetic reconnection causes the dissipation of magnetic field energy, the emission of thermal gamma-rays at R_{PH} and synchrotron radiation from accelerated electrons in the optically thin region up to R_{sat} .

8.2.2.1 ICMART model

The ICMART model [523] considers Poynting flux dominated jets, whose energy is dissipated and radiated away at very large radii from the central engine, as shown in Fig. 8.2. The main motivation behind this model relies on the non-detection (or detection of a very weak) photospheric component in the spectra of some GRBs, hinting that the jet composition cannot be largely Poynting flux dominated at the photosphere.

The GRB central engine intermittently ejects an unsteady jet with variable Lorentz factor and with a nearly constant degree of magnetization $\sigma_0 \equiv \sigma(R_0)$. Such a jet is composed by many discrete magnetized shells which collide at R_{IS} (see Eq. 8.5 and Fig. 8.2). Yet, the kinetic energy dissipated at the ISs is smaller by a factor $[1 + \sigma(R_{\text{IS}})]$ with respect to the energy available in the traditional IS model. Hence, the total energy emitted in radiation could be completely negligible at this stage.

In the optically thin region, the early internal collisions have the role of altering, and eventually destroying, the ordered magnetic field configuration, triggering the first reconnection event. The ejection of plasma from the reconnection layer would disturb the nearby ambient plasma and produce turbulence, facilitating more reconnection events which would lead to a runaway catastrophic release of the stored magnetic field energy at the radius defined as R_{ICMART} . This would correspond to one ICMART event, which would compose one GRB pulse. Other collisions that trigger other reconnection-turbulence avalanches would give rise to other pulses.

This model successfully reproduces the observed GRB lightcurves with both fast and slow components [525]. The slow component, related to the central engine activity, would be caused by the superposition of emission from all the mini-jets due to multiple reconnection sites, while the erratic fast component would be related to the mini-jets pointing towards the observer.

8.2.2.2 Magnetized jet model with gradual dissipation

In this scenario, the energy dissipation through reconnection starts below the jet photosphere and occurs gradually over a wide range of radii [158, 157], as schematically shown in Fig. 8.3. Following Refs. [87, 202], we consider magnetized outflows with a striped-wind magnetic field structure, where energy is gradually dissipated through magnetic reconnection until the saturation radius. This model can naturally explain the double-hump electromagnetic spectra sometimes observed [202].

The jet is injected at $R_0 \sim 10^7$ cm with magnetization $\sigma_0 \gg 1$ and Lorentz factor $\Gamma_0 = \sqrt{\sigma_0 + 1} \approx \sigma_0$. As it propagates, the magnetic field lines of opposite polarity reconnect, causing the magnetic energy to be dissipated at a rate [158]:

$$\dot{E}_{\text{diss}} = -\frac{dL_B}{dR} = -\frac{d}{dR} \left(\frac{\sigma}{\sigma + 1} L \right) \propto R^{1/3}, \quad (8.11)$$

where $\sigma(R)$ is obtained from the conservation of the total specific energy $\Gamma(R)\sigma(R) = \Gamma_0\sigma_0$.

The Lorentz factor of the flow evolves as [158]

$$\Gamma(R) = \Gamma_{\text{sat}} \left(\frac{R}{R_{\text{sat}}} \right)^{1/3}, \quad (8.12)$$

until the saturation radius $R_{\text{sat}} = \lambda \Gamma_{\text{sat}}^2$ (see Fig. 8.3), where λ is connected to the characteristic length scale over which the magnetic field lines reverse polarity. This length scale can be related to the angular frequency of the central engine (e.g., of millisecond magnetars) or with the size of the magnetic loops threading the accretion disk [378].

Motivated by results of particle-in-cell (PIC) simulations of magnetic reconnection in magnetically dominated electron-proton plasmas [442, 226, 504], we assume that half of the dissipated energy in Eq. 8.11 is converted in kinetic energy of the jet, while

the other half goes into particle acceleration and is redistributed among electrons and protons². In particular, the fraction of energy which goes into electrons is [504]

$$\varepsilon_e \approx \frac{1}{4} \left(1 + \sqrt{\frac{\sigma}{10 + \sigma}} \right), \quad (8.13)$$

while the one that goes into protons has been extracted from Fig. 20 of Ref. [504] and is $\varepsilon_p \sim 1 - \varepsilon_e$. A fraction ξ of electrons injected into the dissipation region are accelerated into a power-law distribution $n'_e(\gamma'_e) \propto \gamma'^{-k_e}$ in the interval $[\gamma'_{e,\min}, \gamma'_{e,\max}]$ with the minimum electron Lorentz factor being

$$\gamma'_{e,\min}(R) = \frac{k_e - 2}{k_e - 1} \frac{\varepsilon_e}{2\xi} \sigma(R) \frac{m_p}{m_e}, \quad (8.14)$$

and $\gamma'_{e,\max}$ is the maximum electron energy obtained by equating the acceleration time and the total cooling time. The power-law slope of the accelerated particles in relativistic reconnection depends on the plasma magnetization in a way that harder spectra ($k_e < 2$) are obtained for $\sigma \gg 1$ [444, 228, 503]. Here, we adopt the following parameterization for the electron power-law slope [504]:

$$k_e(\sigma) \approx 1.9 + 0.7/\sqrt{\sigma}. \quad (8.15)$$

The proton spectrum will be discussed in detail in Sec. 8.5.2.2.

8.2.3 Proton synchrotron model

Recently, Refs. [369, 370, 406] have analyzed the spectra of a sample of GRBs for which data down to the soft X-ray band and, in some cases, in the optical are available. This extensive work has established the common presence of a spectral break in the low energy tail of the prompt spectra and led to realize that the spectra could be fitted by three power-laws. The spectral indices below and above the break are found to be $\alpha_1 \simeq -2/3$ and $\alpha_2 \simeq -3/2$ respectively, while the photon index of the third PL is $\beta < 2$. The values of all photon indexes are consistent with the predicted values for the synchrotron emission in a marginally fast cooling regime [143]. However, if electrons are responsible for the prompt emission, then the parameters of the jet have to change drastically with respect to the standard scenario, in which the emission takes place at relatively small radii and with strong magnetic fields in situ. One possible way out to this has been discussed in Ref. [198], where protons are considered to be the particles which radiate synchrotron emission in the marginally fast cooling regime; in this way, it is possible to recover the typical emitting region size at $R_\gamma \simeq 10^{13}$ cm.

²Rough energy equipartition between magnetic field, protons and electron-positron pairs is also found in kinetic simulations of reconnection in pair-proton plasmas [392].

8.3 Main model ingredients

In this section, we outline some of the quantities characterizing the energetics and geometry of the jet for all models. We also introduce the target particle distributions.

8.3.1 Reference model parameters

The gamma-ray emission is assumed to originate from an isotropic volume $V'_{\text{iso},s} = 4\pi R_\gamma^2 \Delta'_s$, where $\Delta'_s = R_\gamma/2\Gamma$ is the comoving thickness of the emitting shell and R_γ is the distance from the central engine where the electromagnetic radiation is produced. Dissipation—whether it occurs in the photosphere, in the optically thin region (e.g., ISs) or external shocks—causes the conversion of a fraction ε_d of the total jet energy \tilde{E}_{iso} into thermal energy, bulk kinetic energy, non-thermal particle energy, and magnetic energy. The energy stored in relativistic electrons, protons, and magnetic fields in the emitting region can be parameterized through the fractions ε_p , ε_e and ε_B , respectively.

These parameters ignore the detailed microphysics at the plasma level, but allow to establish a direct connection with the observables. The dissipation efficiency $\varepsilon_{\text{IS}} = 0.2$ has been chosen by following Refs. [271, 220]. In addition, for the IS models, we rely on PIC simulations of mildly relativistic shocks in electron-ion plasma. Recently, a relatively long 2D PIC simulation has been performed [140] and it has been shown that quasi-parallel shocks can be efficient particle accelerators. The energy fractions going into non-thermal protons, electrons and the turbulent magnetic field are found to be $\varepsilon_p \simeq 0.1$, $\varepsilon_e \simeq 5 \times 10^{-4}$ and $\varepsilon_B \gtrsim 0.1$, respectively. These results are valid for a shock with Lorentz factor $\Gamma_{\text{sh}} = 1.5$. We know, on the other hand, that efficient energy dissipation through ISs can take place only if a large spread in Lorentz gamma factors is present within a kinetic dominated jet [220], which would lead to $1 \lesssim \Gamma_{\text{sh}} \lesssim 5$. Unfortunately, as of today, the mildly relativistic regime is poorly explored, and a study of the transition regime from non relativistic to ultrarelativistic is still necessary. Nevertheless, the results from [140] can be considered as indicative for our case. Given that for the relativistic regime it has been found $\varepsilon_e \lesssim 0.1$ [443], we conservatively adopt $\varepsilon_e = 0.01$, while $\varepsilon_p = 0.1$ and $\varepsilon_B = 0.1$. For the magnetized jet models, instead, these parameters are found to depend on the magnetization of the jet, as we will see later. Finally, at the relativistic external shock, in the deceleration phase, we adopt $\varepsilon_e = 4 \times 10^{-2}$, $\varepsilon_B = 10^{-4}$ and $\varepsilon_p = 1 - \varepsilon_e - \varepsilon_B$, which turn out to be constrained by observations for a number of cases [279, 429, 88]. In addition, we use $k_e = k_p = 2.5$ for the power slope, motivated by PIC simulations for ultra-relativistic shocks [445].

For what concerns the energetics of our reference jet, motivated by recent observations of GRB afterglows [489], we choose $\tilde{E}_{\text{iso}} = 3.4 \times 10^{54}$ ergs, where a typical opening angle of $\theta_j = 3$ degrees is adopted. Our benchmark Lorentz factor is $\Gamma = \Gamma_{\text{sat}} = 300$ [404, 196]. The duration of the burst is taken to be $\tilde{t}_{\text{dur}} = 100 \text{ s}/(1+z)$, where

$z = 2$ is the redshift we adopt for our reference GRB. Finally we use $t_v = 0.5$ s as the variability timescale of the GRB lightcurve [49]. The parameters adopted for each model for our benchmark GRB are summarized in Table 8.1.

Table 8.1: Characteristic parameters assumed for our benchmark GRB jet for the scenarios considered in this paper: internal shock (IS) model, dissipative photosphere model with internal shocks (PH-IS), three components model (3-COMP), ICMART model, magnetized jet model with gradual dissipation (MAG-DISS), and proton synchrotron model (p-SYNCH). In the case of quantities varying along the jet, the variability range is reported. For the magnetic model with gradual dissipation, the electron fraction, the electron power-law index, and the proton power-law index are defined in Eqs. 8.13, and 8.15, respectively.

Parameter	Symbol	Model				
		IS	PH-IS	3-COMP	ICMART	MAG-DISS
Total jet energy	\tilde{E}_{iso}	3.4×10^{54} erg				n/a
Jet opening angle	θ_j	3°				
Lorentz boost factor	Γ	300				
Redshift	z	2				
Duration of the burst	t_{dur}	100 s				
Variability time scale	t_v	0.5 s				
Dissipation efficiency	ε_d	$\varepsilon_{\text{IS}} = 0.2$	n/a	$\varepsilon_d = 0.35$	0.24	n/a
Electron energy fraction	ε_e	0.01		0.5	0.35 – 0.36	n/a
Proton energy fraction	ε_p	0.1		0.5	0.64 – 0.65	n/a
Electron power-law index	k_e	2.2	n/a		2.4 – 2.6	n/a
Proton power-law index	k_p	2.2		2	2.4 – 2.6	2.6
Magnetization at R_γ	σ	n/a		45	1.35 – 1.81	n/a

A useful quantity that allows a comparison among different models is the radiative efficiency of the jet, defined as the fraction of the total jet energy which is radiated in photons [299]:

$$\eta_\gamma = \frac{\tilde{E}_{\gamma, \text{iso}}}{\tilde{E}_{\text{iso}}}. \quad (8.16)$$

For example $\eta_\gamma = \varepsilon_{\text{PH}}$ when the dominant radiation is of photospheric origin or $\eta_\gamma = \varepsilon_{\text{IS}}\varepsilon_e$ when the radiation is produced at the IS, assuming a fast cooling regime for electrons.

8.3.2 Spectral energy distribution of protons

For the purposes of this work, it is sufficient to assume that protons and electrons in the dissipation site are accelerated via Fermi-like mechanisms³. The accelerated particles acquire a non-thermal energy distribution that can be phenomenologically described as [296]:

$$n'_p(E'_p) = AE'_p{}^{-k} \exp \left[- \left(\frac{E'_p}{E'_{p,\max}} \right)^{\alpha_p} \right] \Theta(E'_p - E'_{p,\min}), \quad (8.17)$$

where $A = U'_p \left[\int_{E'_{p,\min}}^{E'_{p,\max}} n'_p(E'_p) E'_p dE'_p \right]^{-1}$ is the normalization of the spectrum (in units of $\text{GeV}^{-1} \text{cm}^{-3}$) and Θ is the Heaviside function, with $U'_p = \varepsilon_p \varepsilon_d E'_{\text{iso}}$ being the fraction of the dissipated jet energy that goes into acceleration of protons. The power-law index is found to be $k \approx 2.3$ in the ultra-relativistic shock limit in semi-analytical and Monte Carlo simulations, although it is predicted to be steeper from particle-in-cell simulations [445]. The power-law index is instead $k = 2$ for a non-relativistic shock [313], while it depends on the jet magnetization for magnetically dominated jets, as we will see later. The exponential cut-off with α_p is due to energy losses of protons and we adopt $\alpha_p = 2$ following Ref. [241], $E'_{p,\min}$ is the minimum energy of the protons that are injected within the acceleration region, and $E'_{p,\max}$ is the maximum proton energy. The latter is constrained by the Larmor radius being smaller than the size of the acceleration region, or imposing that the acceleration timescale,

$$t'_{p,\text{acc}}{}^{-1} = \frac{\zeta c e B'}{E'_p}, \quad (8.18)$$

is shorter than the total cooling timescale for protons. Here $\zeta = 1$ is the acceleration efficiency adopted throughout this work. The total cooling timescale is given by

$$t'_{p,\text{cool}}{}^{-1} = t'_{\text{sync}}{}^{-1} + t'_{p,\text{IC}}{}^{-1} + t'_{p,\text{BH}}{}^{-1} + t'_{p\gamma}{}^{-1} + t'_{p,\text{hc}}{}^{-1} + t'_{p,\text{ad}}{}^{-1}; \quad (8.19)$$

where t'_{sync} , $t'_{p,\text{IC}}$, $t'_{p,\text{BH}}$, $t'_{p\gamma}$, $t'_{p,\text{hc}}$, $t'_{p,\text{ad}}$ are the proton synchrotron (sync), inverse Compton (IC), Bethe-Heitler ($p\gamma \rightarrow pe^+e^-$, BH), hadronic (hc) and adiabatic (ad) cooling times, respectively. They are defined as follows [153, 410, 192]:

³In the reconnection region there are various particle acceleration sites, see e.g. Ref. [357]. It remains a matter of active research what is the dominant process responsible for the formation of the power-law, see e.g. Refs. [444, 228, 357, 390, 266]

$$t'_{p,\text{sync}}{}^{-1} = \frac{4\sigma_T m_e^2 E_p' B'^2}{3m_p^4 c^3 8\pi}, \quad (8.20)$$

$$t'_{p,\text{IC}}{}^{-1} = \frac{3(m_e c^2)^2 \sigma_T c}{16\gamma_p'^2 (\gamma_p' - 1) \beta_p'} \int_{E_{\gamma,\text{min}}'}^{E_{\gamma,\text{max}}'} \frac{dE_{\gamma}'}{E_{\gamma}'^2} F(E_{\gamma}', \gamma_p') n_{\gamma}'(E_{\gamma}'), \quad (8.21)$$

$$t'_{p,\text{BH}}{}^{-1} = \frac{7m_e \alpha \sigma_T c}{9\sqrt{2}\pi m_p \gamma_p'^2} \int_{\gamma_p'^{-1}}^{\frac{E_{\gamma,\text{max}}'}{m_e c^2}} d\epsilon' \frac{n_{\gamma}'(\epsilon')}{\epsilon'^2} \left\{ (2\gamma_p' \epsilon')^{3/2} \left[\ln(\gamma_p' \epsilon') - \frac{2}{3} \right] + \frac{2^{5/2}}{3} \right\} \quad (8.22)$$

$$t'_{p\gamma}{}^{-1} = \frac{c}{2\gamma_p'^2} \int_{\frac{E_{\text{th}}}{2\gamma_p'}}^{\infty} dE_{\gamma}' \frac{n_{\gamma}'(E_{\gamma}')}{E_{\gamma}'^2} \int_{E_{\text{th}}}^{2\gamma_p' E_{\gamma}'} dE_r E_r \sigma_{p\gamma}(E_r) K_{p\gamma}(E_r), \quad (8.23)$$

$$t'_{\text{hc}}{}^{-1} = c n_p' \sigma_{pp} K_{pp}, \quad (8.24)$$

$$t'_{p,\text{ad}}{}^{-1} = \frac{c\Gamma}{R}. \quad (8.25)$$

In the definitions above, $\epsilon' = E_{\gamma}'/m_e c^2$, $\gamma_p' = E_p'/m_p c^2$, and $\alpha = 1/137$ is the fine structure constant. The cross sections $\sigma_{p\gamma}$ and σ_{pp} , for $p\gamma$ and pp interactions respectively, are taken from Ref. [527]. The function $F(E_{\gamma}', \gamma_p')$ is provided in Ref. [252], while $K_{p\gamma}$ is the inelasticity of $p\gamma$ collisions [153]:

$$K_{p\gamma}(E_r) = \begin{cases} 0.2 & E_{\text{th}} < E_r < 1 \text{ GeV} \\ 0.6 & E_r > 1 \text{ GeV} \end{cases}, \quad (8.26)$$

where $E_r = \gamma_p' E_{\gamma}' (1 - \beta_p' \cos \theta')$ is the relative energy between a proton with gamma factor γ_p' and a photon of energy E_{γ}' , whose directions form an angle θ' in the comoving system, $E_{\text{th}} = 0.15 \text{ GeV}$ is the threshold for the photo-hadronic interaction, $n_{\gamma}'(E_{\gamma}')$ is the target photon density field (in units of $\text{GeV}^{-1} \text{cm}^{-3}$), $K_{pp} = 0.8$, and n_p' is the comoving proton density defined as $n_p' = n_b'/2$, where n_b' is the baryonic density defined in Eq. 8.1. As we will see in Sec. 8.5.3, the proton synchrotron scenario is such that the properties of the proton distribution (e.g., minimum energy, power-law slope), as well as the shape of energy distribution itself, can be directly inferred from the observed GRB prompt spectra.

8.4 Neutrino production in the gamma-ray burst jet

The simultaneous presence of a high density target photon field in the site of proton acceleration—that can be radiated by co-accelerated electrons, by protons themselves

or have an external origin—leads to an efficient production of high-energy neutrinos through photo-hadronic interactions. Since the number of target photons is always much larger than the number density of non-relativistic (cold) protons in all cases of study, we neglect the pp contribution.

Photo-hadronic interactions lead to charged pion and kaon (as well as neutron) production, which subsequently cool and decay in muons and neutrinos. According to the standard picture, pion production occurs through the $\Delta(1232)$ resonance channel:

$$p + \gamma \longrightarrow \Delta^+ \longrightarrow \begin{cases} n + \pi^+ & 1/3 \text{ of all cases} \\ p + \pi^0 & 2/3 \text{ of all cases} \end{cases} \quad (8.27)$$

followed by the decay chain

$$\pi^+ \rightarrow \mu^+ + \nu_\mu \quad (8.28)$$

$$\mu^+ \rightarrow \bar{\nu}_\mu + \nu_e + e^+ . \quad (8.29)$$

In order to accurately estimate the neutrino spectral energy distribution and the related neutrino flavor ratio, we rely on the photo-hadronic interaction model of Ref. [241] (model Sim-B and Sim-C) based on SOPHIA [336]. The latter includes higher resonances, direct and multi-pion production contributions. Note that, although we compute the neutrino and antineutrino spectral distributions separately, in the following we do not distinguish between them unless otherwise specified.

Given the photon and proton energy distributions in the comoving frame, $n'_\gamma(E'_\gamma)$ and $n'_p(E'_p)$, the production rate of secondary particles is given by [241] (in units of $\text{GeV}^{-1}\text{cm}^{-3}\text{s}^{-1}$)

$$Q'_l(E'_l) = \int_{E'_l}^{\infty} \frac{dE'_p}{E'_p} n'_p(E'_p) \int_{E_{\text{th}}/2\gamma'_p}^{\infty} dE'_\gamma n'_\gamma(E'_\gamma) cR_\alpha(x, y), \quad (8.30)$$

where $x = E'_l/E'_p$ is the fraction of proton energy going into daughter particles, $y = \gamma'_p E'_\gamma$, and l stands for π^+ , π^- , π^0 , and K^+ . Since kaons suffer less from radiative cooling than charged pions due to their larger mass and shorter lifetime, their contribution to the neutrino flux becomes important at high energies [62, 467, 388], whilst it is sub-leading at lower energies, given the low branching ratio for their production. The “response function” $R_l(x, y)$ contains all the information about the interaction type (cross section and multiplicity of the products); we refer the interested reader to Ref. [241] for more details.

Once produced, the charged mesons undergo different energy losses before decaying into neutrinos. Their energy distribution at decay is

$$Q'_l{}^{\text{dec}}(E'_l) = Q'_l(E'_l) \left[1 - \exp\left(-\frac{t'_{l,\text{cool}} m_l}{E'_l \tau'_l}\right) \right], \quad (8.31)$$

with $t'_{l,\text{cool}}$ being the cooling time scale and τ'_l the lifetime of the meson l . The neutrino energy distribution originating from the decay processes like the one in Eq. 8.28 is

$$Q'_{\nu_\alpha}(E'_{\nu_\alpha}) = \int_{E'_{\nu_\alpha}}^{\infty} Q_l^{\text{dec}}(E'_l) \frac{1}{E'_l} F_{l \rightarrow \nu_\alpha} \left(\frac{E'_{\nu_\alpha}}{E'_l} \right), \quad (8.32)$$

where $F_{l \rightarrow \nu_\alpha}$ is defined in Ref. [296] for ultra-relativistic parent particles. The same procedure is followed for antineutrinos.

The steps above also allow to compute the spectra of charged muons. Again, the cooled muon spectra are derived as in Eq. 8.31 and the neutrinos generated by the muon decay are computed following Ref. [296].

The total neutrino injection rate $Q'_{\nu_\alpha}(E'_{\nu_\alpha})$ at the source is obtained by summing over the contributions from all channels. Finally, the fluence for the flavor ν_α at Earth from a source at redshift z is (in units of $\text{GeV}^{-1} \text{cm}^{-2}$)

$$\Phi_{\nu_\alpha}(E_{\nu_\alpha}, z) = \hat{N} \frac{(1+z)^2}{4\pi d_L^2(z)} \sum_{\beta} P_{\nu_\beta \rightarrow \nu_\alpha}(E_{\nu_\alpha}) Q'_{\nu_\beta} \left[\frac{E_{\nu_\alpha}(1+z)}{\Gamma} \right], \quad (8.33)$$

where [57]

$$P_{\nu_e \rightarrow \nu_\mu} = P_{\nu_\mu \rightarrow \nu_e} = P_{\nu_e \rightarrow \nu_\tau} = \frac{1}{4} \sin^2 2\theta_{12}, \quad (8.34)$$

$$P_{\nu_\mu \rightarrow \nu_\mu} = P_{\nu_\mu \rightarrow \nu_\tau} = \frac{1}{8} (4 - \sin^2 2\theta_{12}), \quad (8.35)$$

$$P_{\nu_e \rightarrow \nu_e} = 1 - \frac{1}{2} \sin^2 2\theta_{12}, \quad (8.36)$$

with $\theta_{12} \simeq 33.5$ degrees [167], $P_{\nu_\beta \rightarrow \nu_\alpha} = P_{\nu_\beta \rightarrow \bar{\nu}_\alpha}$, and $\hat{N} = V'_{\text{iso},s} t_{\text{dur}}$ [69] being the normalization factor depending on the volume of the interaction region. The luminosity distance $d_L(z)$ is defined in a flat Λ CDM cosmology as

$$d_L(z) = (1+z) \frac{c}{H_0} \int_0^z \frac{dz'}{\sqrt{\Omega_\Lambda + \Omega_M(1+z')^3}} \quad (8.37)$$

with $\Omega_M = 0.315$, $\Omega_\Lambda = 0.685$ and the Hubble constant $H_0 = 67.4 \text{ km s}^{-1} \text{ Mpc}^{-1}$ [42].

8.5 Results: Gamma-ray burst neutrino emission

Each of the dissipation mechanisms introduced in Sec. 8.2, according to the radius at which it takes place, leads to different photon energy distributions. In Appendix A.1 we report the empirical functions usually adopted to fit the observed photon spectra. For

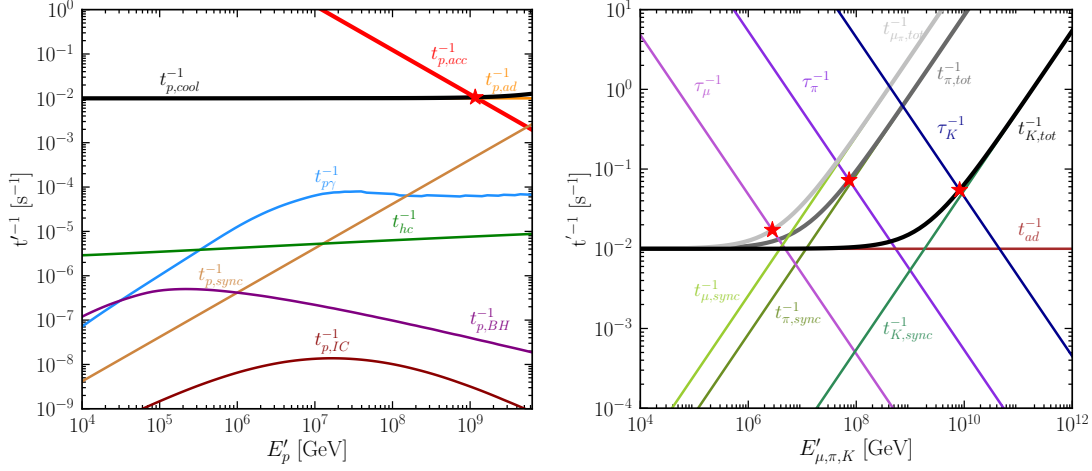


Figure 8.4: *Left:* Inverse cooling timescales for protons at the IS radius as functions of the proton energy in the comoving frame for our benchmark GRB, see Table 8.1. The thin solid lines mark the individual cooling processes introduced in Sec. 8.3.2; the thick black and red solid lines represent the total cooling timescale and the acceleration timescale, respectively. The red star marks the maximum comoving proton energy such that $t'_{p,cool}{}^{-1} = t'_{p,acc}{}^{-1}$. Protons are mainly cooled by adiabatic expansion and $p\gamma$ interactions. *Right:* Analogous to the left panel, but for the inverse cooling timescales for pions, muons, and kaons. The dominant energy losses in this case are adiabatic cooling at low energies and synchrotron cooling at higher energies.

each of the GRB models considered in this section, we assume that the spectral energy distribution of photons is either given by one of the fitting functions or a combination of them. In this section, we investigate the neutrino production in the prompt phase for each scenario.

8.5.1 Kinetic dominated jets

8.5.1.1 Jet model with internal shocks

We focus on the IS model introduced in Sec. 8.2.1.1 with the photon spectrum produced at the IS radius and described by the Band function in Eq. A.2. The radiative efficiency is $\eta_\gamma = \varepsilon_{IS}\varepsilon_e \simeq 0.002$ (see Table 8.1).

In order to establish the relative importance of the various energy loss processes in this scenario, we compute the proton and the secondary particle (K^\pm , π^\pm and μ^\pm) cooling times as illustrated in Sec. 8.3.2. The cooling times are shown in Fig. 8.4 as functions of the particle energy in the comoving frame. With the parameters adopted for our benchmark GRB, protons are mainly cooled by adiabatic expansion up to $E'_{p,max}$ (left panel of Fig. 8.4), with the second dominant energy loss mechanisms being photo-

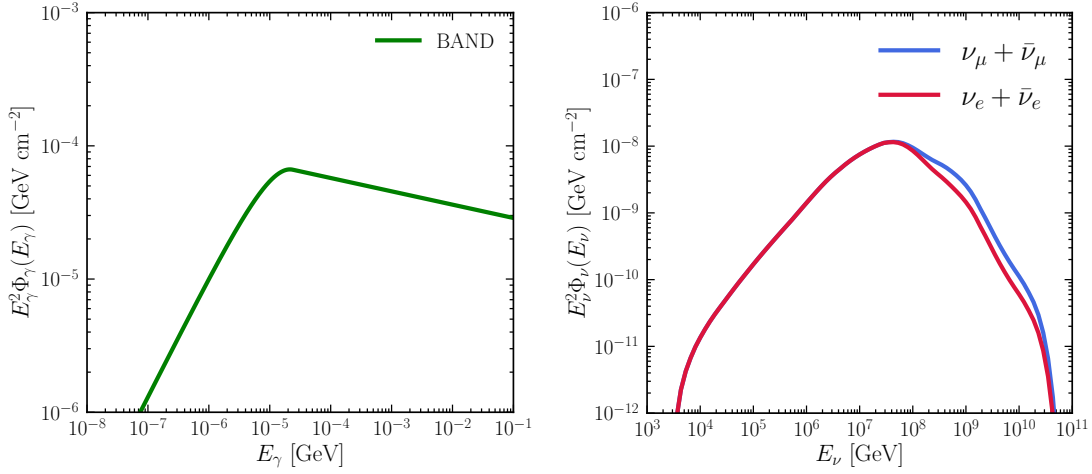


Figure 8.5: *Left:* Band photon fluence observed at Earth for our benchmark GRB in the IS model, see Table 8.1. *Right:* Correspondent $\nu_\alpha + \bar{\nu}_\alpha$ fluence in the observer frame (in red for the electron flavor and in blue for the muon flavor) in the presence of flavor conversions. The fluence for the muon flavor peaks at $E_\nu^{\text{peak}} = 4 \times 10^7$ GeV.

hadronic interaction at intermediate energies, and synchrotron loss at higher energies. For mesons and muons (right panel of Fig. 8.4) adiabatic and synchrotron cooling at low and high energies, respectively, are the two dominant cooling processes.

Following Sec. 8.4, we compute the neutrino production rate in the comoving frame at R_{IS} and the correspondent fluence at Earth including flavor conversions. The results are shown in the right panel of Fig. 8.5, while the photon spectrum described by the Band function is shown in the left panel.

Our results are in good agreement with analogous estimations reported in the literature for comparable input parameters, see e.g. Ref. [68]. In this scenario, the fluence for the muon flavor peaks at $E_\nu^{\text{peak}} = 4 \times 10^7$ GeV and rapidly declines at higher energies. The effects due to the cooling of kaons are not visible because, as shown in Fig. 8.4, the maximum proton energy is more than one order of magnitude lower than the one at which kaons cool by synchrotron radiation, and the pion cooling starts around $\lesssim E'_{p,\text{max}}/4$.

8.5.1.2 Jet model with a dissipative photosphere and internal shocks

We now explore the model introduced in Sec. 8.2.1.2 and consider a jet with an efficient photospheric emission, described by a Band spectrum peaking at the energy given by Eq. A.4, and undergoing further IS dissipation. At R_{IS} , protons and electrons are efficiently accelerated and turbulent magnetic fields may build up. In this scenario, electrons cool, other than by emitting synchrotron radiation, also by Compton

up-scattering of the non-thermal photospheric photons. As we are interested in investigating the case where the photospheric emission is dominant in the MeV energy range, we consider Case (I) of Table 1 of Ref. [475], corresponding to the luminosity hierarchy $L_{\text{PH}} \gg L_{\text{UP}} \gg L_{\text{SYNC}}$, where L_{PH} , L_{UP} , and L_{SYNC} stand for the photospheric luminosity, up-scattered photospheric luminosity of the accelerated electrons at R_{IS} , and synchrotron luminosity radiated by the electrons at R_{IS} , respectively.

Following Ref. [475], we define

$$x = \frac{\varepsilon_{\text{IS}} \varepsilon_{\text{B}}}{\varepsilon_{\text{PH}}} \quad \text{and} \quad Y = \frac{U'_{\text{SYNC}}}{U'_B} = \frac{4(k_e - 1)}{3(k_e - 2)} \tau_T \gamma'_{e,\text{min}} \gamma'_{e,\text{cool}} h, \quad (8.38)$$

where Y is the Compton parameter, k_e is the slope of the electron energy distribution, h is a function of $\gamma'_{e,\text{min}}$ and $\gamma'_{e,\text{cool}}$ and depends on the cooling regime, $\gamma'_{e,\text{min}}$ is the minimum Lorentz factor of the electrons injected in the acceleration region

$$\gamma'_{e,\text{min}} = \frac{m_p k_e - 2}{m_e k_e - 1} \mathcal{R}^{-1} \xi^{-1} \varepsilon_{\text{IS}} \varepsilon_e, \quad (8.39)$$

with ξ being the fraction of electrons accelerated at the shock and \mathcal{R} being the number of leptons per baryon. Finally, $\gamma'_{e,\text{cool}}$ is the electron cooling Lorentz factor obtained from $\gamma'_{e,\text{cool}} m_e c^2 = P(\gamma'_{e,\text{cool}}) t'_{\text{ad}}$ and given by

$$\gamma'_{e,\text{cool}}(R) \simeq \frac{3m_e \mathcal{R}}{4m_p \tau_T \varepsilon_{\text{PH}}} \frac{1}{x(1+Y) + 1}; \quad (8.40)$$

t'_{ad} being the adiabatic cooling timescale and $P(\gamma'_{e,\text{cool}}) = 4/3 \sigma_T c \gamma'^2_{e,\text{cool}} (U'_B + U'_{\text{SYNC}} + U'_{\text{PH}})$ the cooling rate for electrons. The conditions we need to fulfill in order to satisfy $L_{\text{PH}} \gg L_{\text{UP}} \gg L_{\text{SYNC}}$ are

$$\eta < \eta_*, \quad x \ll 1, \quad xY \ll 1, \quad Y = \frac{\varepsilon_{\text{IS}} \varepsilon_e h}{\varepsilon_{\text{PH}}} \ll 1. \quad (8.41)$$

In this way, it is possible to estimate $L_{\text{UP}} = Y L_{\text{PH}}$ and $L_{\text{SYNC}} = x Y L_{\text{PH}}$.

We adopt the electron slope $k_e = 2.2$ and fix ε_{IS} by relying on the observations in the optical band; by assuming that the synchrotron extended emission in this range should not be brighter than what is typically observed, the following constraint on the flux should hold: $F_{\nu}^{\text{sync}}(E_{\gamma,\text{opt}}) < 100$ mJy with $E_{\gamma,\text{opt}} = 2$ eV [428]. In our case, $\varepsilon_{\text{IS}} = 0.2$ satisfies such a condition. The radiative efficiency of this GRB is $\eta_{\gamma} = (\tilde{E}_{\text{PH}} + \tilde{E}_{\text{SYNC}} + \tilde{E}_{\text{UP}}) / \tilde{E}_{\text{iso}} = \tilde{E}_{\text{PH}}(1 + Y + xY) / \tilde{E}_{\text{iso}} \simeq 0.2$. Since the high-energy photospheric photons are absorbed by the e^{\pm} pair creation at R_{PH} , we use a cut-off for the Band spectrum at R_{PH} , defined in Eq. A.1.

We define the total photon energy distribution in the comoving frame at R_{IS} as

$$n'_{\gamma,\text{tot}}(E'_{\gamma}) = \left(\frac{R_{\text{PH}}}{R_{\text{IS}}} \right)^2 n'_{\gamma,\text{PH}}(E'_{\gamma}) + n'_{\gamma,\text{SYNC}}(E'_{\gamma}) + n'_{\gamma,\text{UP}}(E'_{\gamma}) \quad (8.42)$$

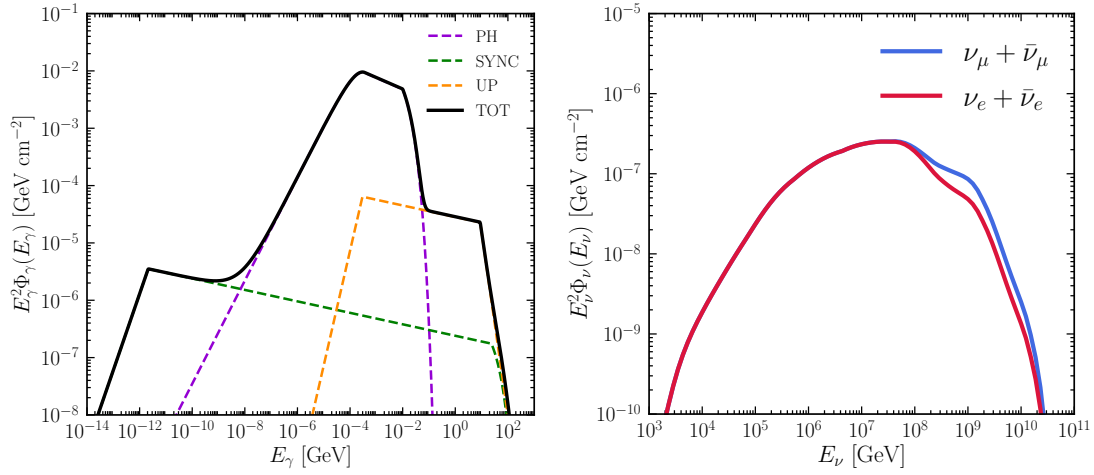


Figure 8.6: *Left:* Photon fluence observed at Earth for the IS model with dissipative photosphere. The photospheric emission (PH, violet line), the photospheric up-scattered emission (UP, orange line), and the synchrotron emission of electrons accelerated at R_{IS} (SYNC, green line) are plotted together with the total photon fluence (in black). *Right:* $\nu_\alpha + \bar{\nu}_\alpha$ fluence in the observer frame produced at R_{IS} with flavor oscillations included (in red for electron and blue for muon flavors). The astrophysical parameters for this GRB are reported in Table 8.1, and $\tilde{E}_{\text{PH}} = 6.8 \times 10^{53}$ erg, $\tilde{E}_{\text{SYNC}} \simeq 5.4 \times 10^{50}$ erg, $\tilde{E}_{\text{UP}} \simeq 6.8 \times 10^{51}$ erg, $\mathcal{R} = 1$, $\xi=1$. The fluence for the muon flavor peaks at $E_\nu^{\text{peak}} = 3.2 \times 10^7$ GeV and its normalization is larger than the one in Fig. 8.5, given a higher photon number density in the acceleration region.

and compute the cooling processes of protons at the IS. Because of the more intense photon field at R_{IS} with respect to the simple IS scenario, $t_{p\gamma}$ and t_{BH} are shorter, while the synchrotron losses are negligible.

Figure 8.6 shows the resultant photon (on the left panel) and neutrino (on the right panel) fluences for the IS shock scenario with a dissipative photosphere. The black curve in the left panel represents the overall photon fluence. The total spectrum is consistent with Fermi observations [48], being the high energy component subdominant with respect to the Band one. From the right panel of Fig. 8.6, one can see that the fluence peaks at $E_{\nu}^{\text{peak}} = 3.2 \times 10^7$ GeV and its normalization is only a factor $\mathcal{O}(10)$ larger than the one of the IS model (see Fig. 8.5), despite the larger available photon energy [a factor $\mathcal{O}(100)$]. The reason for this is the higher $E'_{\gamma,\text{peak}}$ in the IS scenario with dissipative photosphere, which affects the ratio of the photon number densities at $E'_{\gamma,\text{peak}}$. It should also be noted that here we do not take into account the anisotropy of the incoming photospheric photon field at R_{IS} , an effect that would cause a further reduction in the neutrino production efficiency, as pointed out also in Ref [521].

8.5.1.3 Jet model with three emission components

We are interested in a representative GRB of the class of bursts introduced in Sec. 8.2.1.3, hence we adopt average values for the spectral index and intensity of each component. To this purpose, we rely on Refs. [224, 225, 58].

Once the outflow becomes transparent to radiation, a BB component is emitted at R_{PH} , with spectral index $\alpha_{\text{BB}} = 0.4$ [38] and peaks at the temperature defined in Eq. 8.4. Subsequently, the kinetic energy of the outflow is dissipated at the ISs, and the main spectral component (CPL1) is produced. The latter is described by a CPL with spectral index $\alpha_{\text{CPL1}} = -1$. An additional cut-off power-law (CPL2) begins to appear after a slight delay with respect to CPL1, with the cut-off shifting to higher energies until its disappearance. At later times, this additional component is well described by a simple PL, and we associate it to the beginning of the afterglow. With this choice, we take into account both interpretations of the additional energetic component, namely the internal or external origin of CPL2.

At the deceleration radius R_{dec} (see Eq. 8.7), the external shock starts accelerating protons and electrons of the wind and the magnetic field builds up. Motivated by the afterglow modeling [89], we use the following values for the energy fractions: $\varepsilon_e = 4 \times 10^{-2}$, $\varepsilon_B = 10^{-4}$ and $\varepsilon_p = 1 - \varepsilon_e - \varepsilon_B$ [88], compatible with our choice for the prompt efficiency.

We consider a wind type circumburst medium with $A = 3 \times 10^{34} \text{ cm}^{-1}$ [407] and an adiabatic blastwave, with $\Gamma(t) = \Gamma(t_{\text{dec}}/4t)^{1/4}$ [407] and $R(t) = 2\Gamma^2(t)ct/(1+z)$ describing the temporal evolution of the Lorentz factor and the radius of the forward shock after t_{dec} , respectively. The energy of the accelerated particles in the blastwave,

at a time t after the deceleration, is $\tilde{U}_p = 4\pi\varepsilon_p AR(t)m_p c^2[\Gamma^2(t) - 1]$. By relying on the temporal evolution of the bright GRB investigated in Ref. [47], we consider a simple PL produced at the forward shock, with power slope $\alpha_{\text{PL}} = -1.8$ (Eq. A.6), and normalize it to $\tilde{E}_{\text{PL}} = \varepsilon_e/\varepsilon_p \tilde{U}_p$. The photon field target for $p\gamma$ interactions at the forward shock is the sum of the PL, BB and CPL1 components; the latter two being Lorentz transformed in the comoving frame of the blastwave.

Since we are interested in computing the neutrino fluence emitted at the forward shock during the prompt phase, we take a representative average radius R_* in logarithmic scale between R_{dec} and $R(t_{\text{dur}} - t_{\text{dec}})$. The photon energy distribution is

$$n'_{\text{tot}}(E'_\gamma, R_*) = n'_{\text{PL}}(E'_\gamma) + \left(\frac{R_{\text{PH}}}{R_*}\right)^2 n'_{\text{BB}}\left(\frac{E'_\gamma}{\Gamma_r}\right) + \left(\frac{R_{\text{IS}}}{R_*}\right)^2 n'_{\text{CPL1}}\left(\frac{E'_\gamma}{\Gamma_r}\right), \quad (8.43)$$

where Γ_r is the relative Lorentz factor between Γ and $\Gamma_* \equiv \Gamma(R_*)$.

The BB component is always subdominant, while CPL1 and CPL2 are expected to vary in absolute and relative intensity from burst to burst; this is true also in the same GRB, once the temporal evolution is considered. In order to investigate to what extent the neutrino spectrum may be affected by these factors, we considered two scenarios of study for the prompt phase: case (I) such that the energetics of the three components is $\tilde{E}_{\text{BB}} \simeq 0.1\tilde{E}_{\text{CPL1}}$ and $\tilde{E}_{\text{CPL1}} = 3\tilde{E}_{\text{CPL2}}$ (solid black line in the top left panel of Fig. 8.7) and case (II) with $\tilde{E}_{\text{CPL1}} = 1/3\tilde{E}_{\text{CPL2}}$ (dotted black line in the top left panel of Fig. 8.7). The three cut-off power-laws (BB, CPL1, and CPL2) follow Eq. A.5 with peak energies $E_{\text{BB,peak}} \simeq 2 \times 10^{-5}$ GeV, $E_{\text{CPL1,peak}} \simeq 7 \times 10^{-5}$ GeV, and $E_{\text{CPL2,peak}} \simeq 2 \times 10^{-2}$ GeV, respectively. These values are consistent with the ones in Refs. [224, 47]. With this set of parameters, the hierarchy and intensity of the various cooling processes is analogous to the IS case for the prompt phase (Fig. 8.4), while adiabatic cooling is the dominant cooling process by many orders of magnitude at R_* . For what concerns the forward shock, we assume a differential number density of protons $n'_p(E'_p) \propto E'_p{}^{-2.5}$ [445] injected between the minimum energy $E'_{p,\text{min}} = m_p c^2 \Gamma_*$ and the maximum $E'_{p,\text{max}}$, derived from the condition that the proton acceleration time t'_{acc} is limited by the adiabatic time t'_{ad} (see Sec. 8.3.2).

The neutrino fluence at the IS and forward shock is displayed in Fig. 8.7. In the top left panel, the solid line represents the neutrino fluence for case (I), while the dotted line stands for case (II). The enhancement of the energetic component CPL2 of almost one order of magnitude leads to a negligible impact on the neutrino energy distribution, producing only a slight increase of the fluence at low energies.

The bottom panels of Fig. 8.7 display the photon fluence and the correspondent neutrino fluence when the emission from the forward shock starts during the prompt phase. The dashed lines represent the neutrino fluence produced at the IS from the interaction of accelerated protons and the photon field (BB+CPL1), while the dash-dotted line represents the neutrino outcome from the forward shock at R_* , where we rely on

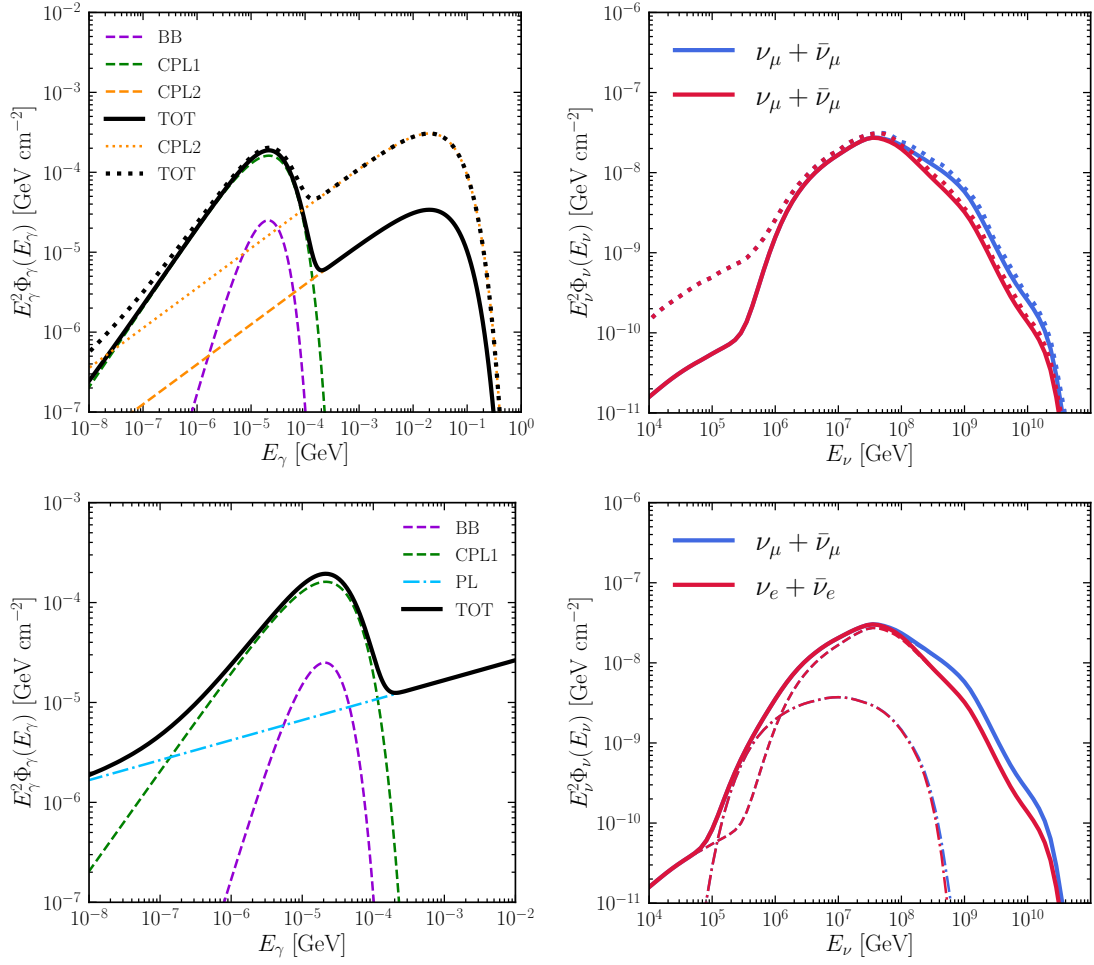


Figure 8.7: *Top left:* Photon fluence in the prompt phase for the model with three components. It is composed by a thermal BB component (violet dashed curve), a cut-off power law CPL1 (green dashed curve), and a second cut-off power law CPL2 (in orange dashed for case (I) such $\tilde{E}_{\text{CPL1}} = 3\tilde{E}_{\text{CPL2}}$; in orange dotted for case (II) with $\tilde{E}_{\text{CPL1}} = 1/3\tilde{E}_{\text{CPL2}}$). Furthermore $\tilde{E}_{\text{BB}} = 0.1\tilde{E}_{\text{CPL1}}$. The total fluence is plotted in black (solid and dotted lines). *Top right:* Correspondent $\nu_\alpha + \bar{\nu}_\alpha$ fluence in the observer frame with flavor oscillations included (in red for electron and blue for muon flavors). The solid line represents the total contribution during the prompt for case (I), while the dotted one is for case (II). The fluence for the muon flavor peaks at $E_\nu^{\text{peak}} = 4.2 \times 10^7$ GeV for the case (I). The low energy tail is affected by the interaction of protons with CPL2. *Bottom left:* Photon fluence for the scenario such that the emission from the forward shock (PL, blue dash-dotted line) starts during the prompt phase (dashed, BB+CPL1). *Bottom right:* Corresponding $\nu_\alpha + \bar{\nu}_\alpha$ fluence (dashed curve for the IS emission, dash-dotted for the forward shock, and solid line for the total).

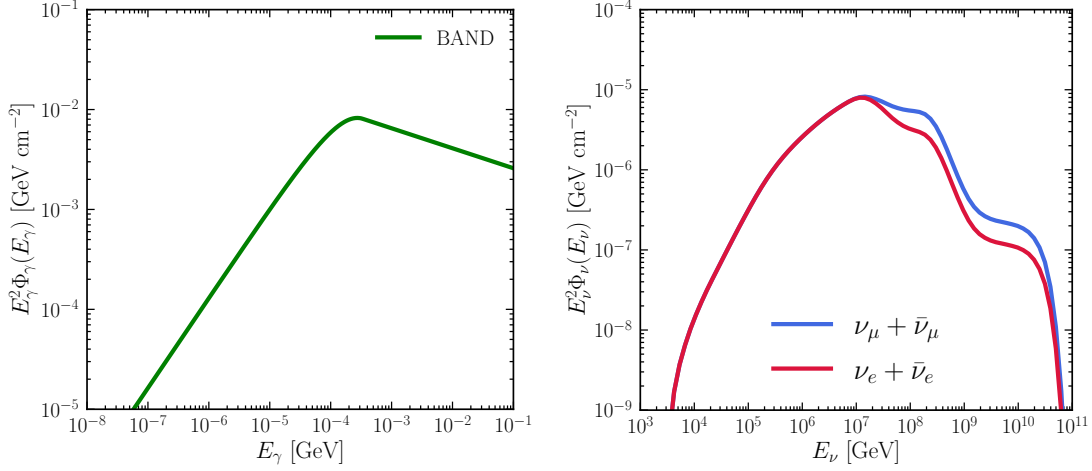


Figure 8.8: *Left:* Band photon fluence observed at Earth and emitted at $R_{\text{ICMART}} = 10^{15}$ cm for the ICMART model. The parameters of this GRB are reported in Table 8.1 and $\eta_\gamma = 0.17$. *Right:* Correspondent $\nu_\alpha + \bar{\nu}_\alpha$ fluence in the observer frame in the presence of flavor conversions for the ICMART model (in blue and red for the muon and the electron flavors, respectively). The muon neutrino fluence peaks at $E_\nu^{\text{peak}} = 1.3 \times 10^7$ GeV; the high energy tail of the neutrino distribution shows the double bump structure due to kaon decay.

Eq. 8.43 for the photon field. The solid line describes the total neutrino fluence expected during the prompt phase. The forward shock contribution is significantly higher than what expected for the afterglow phase [407]. This is mainly due to a much larger photon number density in the acceleration region. Furthermore, given the very low magnetic field and its inefficiency to accelerate particles to very high energies, the cutoff in the neutrino spectrum occurs at a lower energy compared to the prompt case (see dot-dashed line). The overall intensity at peak energy of the neutrino emission in this scenario is slightly larger than in the simple IS case.

8.5.2 Poynting flux dominated jets

8.5.2.1 ICMART model

For the model introduced in Sec. 8.2.2.1, the typical radius necessary to make sure that runaway reconnection has enough time to grow is $R_{\text{ICMART}} \simeq 10^{15}$ cm [523], while the typical width of the reconnection region is $\Delta = ct_v$, where we adopt $t_v \simeq 0.5$ s. The dissipation efficiency may be as high as 0.35 in this model [149] and this is the value we adopt for ε_d .

It has been shown that a Band-like spectrum may be reproduced in this scenario

by considering an appropriate time dependent injection rate of particles in the emitting region [297], and this is the spectrum we adopt for this model. If σ is the magnetization parameter at R_{ICMART} , the magnetic field in the bulk comoving frame can be expressed as [523]:

$$B' = \left(\frac{2\tilde{L}_{\text{iso}}}{\Gamma^2 c R_{\text{ICMART}}^2} \frac{\sigma}{\sigma + 1} \right)^{1/2}. \quad (8.44)$$

We use as initial jet magnetization $\sigma_0 = \sigma_{\text{in}} = 45$ (see Fig. 8.2); this choice, as shown in the following, allows for a consistent comparison with the results of Sec. 8.5.2.2. By relying on the results from particle-in-cell simulations, we assume $k_p(\sigma_0) \simeq 2$ (see Eq. 8.15). Furthermore, we set $\varepsilon_p = 0.5$ and $\varepsilon_e = 0.5$ (see Eq. 8.13). With this choice, the radiative efficiency of our benchmark GRB turns out to be $\eta_\gamma = \varepsilon_d \varepsilon_e \simeq 0.17$. The photon number density is normalized to $\eta_\gamma E'_{\text{iso}}$. Since $R_{\text{IS}} \simeq R_{\text{ICMART}}$, we obtain similar trends for the cooling times as in Fig. 8.4, except for the synchrotron loss that starts to dominate at $E'_p \sim 10^8$ GeV and a slightly increased rate of $p\gamma$ interactions due to a larger photon number density in the dissipation region.

The neutrino fluence is displayed in the right panel of Fig. 8.8. The fluence for the muon flavor peaks at $E'_\nu^{\text{peak}} = 1.3 \times 10^7$ GeV. Note that the double bump due to kaon decay is clearly visible in the high-energy tail of the energy distribution. This is due to $E'_{p,\text{max}} \sim E'_{K,\text{max}} \sim 2 \times 10^9$ GeV (while $E'_{\pi,\text{max}} \sim 1.2 \times 10^7$ GeV). This feature is determined by the stronger magnetic field in the acceleration region ($B' \simeq 9$ kG, while for example $B' \simeq 1$ kG in the IS model).

8.5.2.2 Magnetized jet model with gradual dissipation

For the model introduced in Sec. 8.2.2.2, we follow Ref. [87] and assume that the energy which is dissipated in the optically thick region is reprocessed into quasi-thermal emission, leading to a black-body-like emission from the photosphere. In the optically thin region, the synchrotron radiation from electrons is the dominant emission mechanism and it represents the non-thermal prompt emission. The energy emitted at the photosphere is obtained by integrating the energy dissipation rate (Eq. 8.11) up to R_{PH} and considering that only the fraction $(R/R_{\text{PH}})^{4/9}$ of the energy dissipated at R remains thermal at R_{PH} . In the optically thin region, electrons are always in the fast cooling regime and $E'_{\gamma,\text{ssa}} \gg E'_{\gamma,\text{cool}}$ for $R_{\text{ph}} < R < R_{\text{sat}}$ with our choice of parameters. Here $E'_{\gamma,\text{ssa}}$ is the synchrotron self-absorption energy [202]:

$$E'_{\gamma,\text{ssa}} \sim \left(\frac{h^3}{8\pi m_p} \frac{\xi \tilde{L}_{\text{iso}}}{4\pi \Gamma_{\text{sat}}} \frac{1}{R^2 \Gamma(R)} \right)^{1/3}. \quad (8.45)$$

The shape of the synchrotron spectrum follows Eq. A.10, but we replace E'_{cool} with $E'_{\gamma,\text{ssa}}$ and use $\alpha_\gamma = 1$ for $E'_\gamma < E'_{\gamma,\text{ssa}}$ [202]. Furthermore, only a fraction $\xi = 0.2$ [87] of electrons is accelerated.

For our reference GRB we adopt $\lambda = 4 \times 10^8$ cm [87]. The terminal Lorentz factor of the outflow is $\Gamma_{\text{sat}} \simeq \Gamma_0 \sigma_0$. We choose $\Gamma_{\text{sat}} = 300$ and the initial jet magnetization is $\sigma_0 = \Gamma_{\text{sat}}^{2/3} \sim 45$.

For what concerns protons, we assume that they are accelerated into a power-law distribution starting from a minimum Lorentz factor

$$\gamma'_{p,\min} = \max \left[1, \frac{k_p - 2 \epsilon_p}{k_p - 1} \frac{\sigma(R)}{2} \right] \quad (8.46)$$

and extending up to a maximum value determined by balancing the energy gain and loss rates, as described in Sec. 8.3.2. We also assume that the power of the proton distribution is the same as the one of electrons, namely $k_p = k_e$ (see Eq. 8.15). The latter assumption is motivated by particle-in-cell simulations of magnetic reconnection for $\sigma \gg 1$ [228], but it has to be yet demonstrated for $\sigma \sim 1$ [392].

We compute the neutrino production assuming that dissipation and particle acceleration start at $R_1 = a R_{\text{PH}}$ with $a = 3$. Being an arbitrary choice for the starting radius, we explore the effects of a on the neutrino fluence in Appendix A.2. For illustration purposes, we compute the neutrino production rate at three radii (R_1 , R_2 , and R_3) equally distanced in logarithmic scale. We make this choice in order to establish the qualitative trend of the neutrino production during the evolution of the outflow in the optically thin region. The photon and proton distributions are normalized at each radius R_i along the jet to the energy dissipated between R_{i-1} and R_i , where $R_0 = R_{\text{PH}}$ and $R_3 = R_{\text{sat}}$. At each R_i , the photon field coming from R_j is Lorentz transformed through the relative Lorentz factor

$$\Gamma_{\text{rel},ij} = \frac{1}{2} \left(\frac{\Gamma_i}{\Gamma_j} + \frac{\Gamma_j}{\Gamma_i} \right), \quad (8.47)$$

that holds as long as $\Gamma_i, \Gamma_j \gg 1$. The total photon number density used as input at each radius R_i for producing neutrinos is thus

$$n'_{\text{tot}}(E'_\gamma, R_i) = \sum_{j=0}^i \left(\frac{R_j}{R_i} \right)^2 n'_j \left(\frac{E'_\gamma}{\Gamma_{\text{rel},ij}} \right) \frac{1}{\Gamma_{\text{rel},ij}} \quad (8.48)$$

where $n'_j(E'_\gamma)$ is the photon energy distribution at R_j (in units of $\text{GeV}^{-1} \text{cm}^{-3}$).

Once the photon distributions are set, we evaluate the proton cooling times at each radius. In all the three cases, dominant losses are due to the adiabatic cooling up to $\simeq 10^5$ GeV, and $p\gamma$ interactions for $10^5 \text{ GeV} \lesssim E'_p \lesssim E'_{p,\max}$. Synchrotron losses become relevant around 10^7 GeV. Given the very strong magnetic field (see Table 8.2), the secondaries suffer strong synchrotron losses; this considerably affects the resulting neutrino spectrum, which is damped at energies much lower than in all the other models investigated so far in this work. A summary of the input parameters at the three R_i is reported in Table 8.2.

Table 8.2: Summary table for the input parameters adopted at the radii R_1 , R_2 and R_3 in the magnetic model with gradual dissipation: the radius (R), the comoving magnetic field (B'), the Lorentz factor (Γ), the maximum energy of protons ($E'_{p,\max}$), pions ($E'_{\pi,\max}$), muons ($E'_{\mu,\max}$), and kaons ($E'_{K,\max}$), as well as the power-law slope ($k_e = k_p$) of electrons and protons.

	R [cm]	B' [kG]	Γ	$E'_{p,\max}$ [GeV]	$E'_{\pi,\max}$ [GeV]	$E'_{\mu,\max}$ [GeV]	$E'_{K,\max}$ [GeV]	k_e
R_1	7.1×10^{12}	1.7×10^3	176	1.1×10^8	6.5×10^4	3.6×10^3	7.5×10^6	2.4
R_2	1.6×10^{13}	5.4×10^2	230	1.7×10^8	2×10^5	1.1×10^4	2.3×10^7	2.5
R_3	3.6×10^{13}	1.7×10^2	300	2.5×10^8	6.4×10^5	3.5×10^4	7.3×10^7	2.6

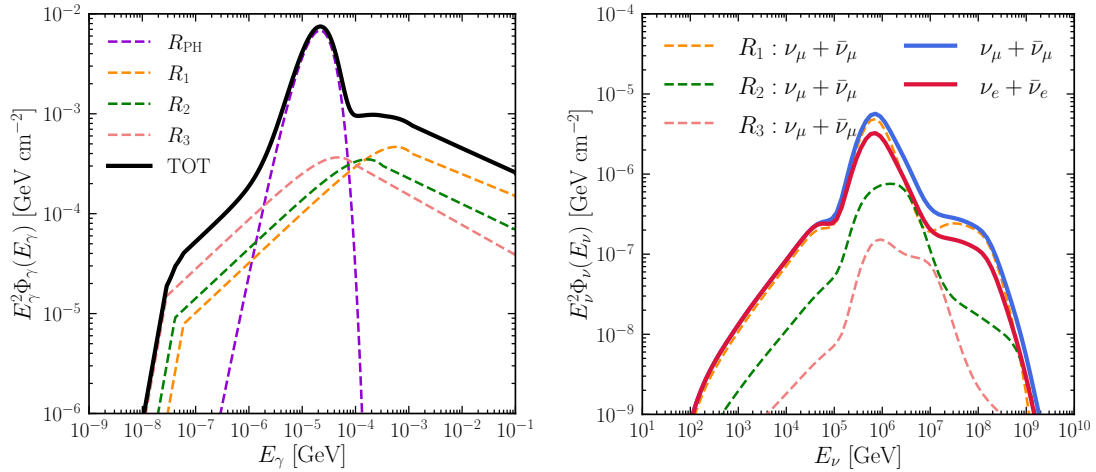


Figure 8.9: *Left:* Photon fluence in the observer frame for the GRB model invoking continuous magnetic dissipation for the parameters reported in Tables 8.1 and 8.2. The total photon energy distribution is shown in black, and its components at R_{PH} , R_1 , R_2 , and R_3 are plotted in violet, orange, green, and coral respectively. *Right:* Correspondent $\nu_\alpha + \bar{\nu}_\alpha$ fluence at Earth after flavor oscillations in the left panel (in blue for the muon flavor and in red for the electron one). The fluence for the muon flavor peaks at $E_\nu^{\text{peak}} = 7.2 \times 10^5$ GeV. An unusual spectral structure is clearly visible.

The (photon) neutrino fluence at Earth is shown in the (left) right panel of Fig. 8.9. The slope of the three non-thermal synchrotron components and their distribution peaks decrease as the distance from the source increases. The high energy cut-off of each spectral component is given by Eq. A.1. Notably, the dominant component comes from the smallest radius, while the contribution coming from larger radii gets lower and lower (67%, 26%, and 7% from R_1 , R_2 and R_3 , respectively). The significant drop in the neutrino flux between R_1 and R_3 is mainly due to the decrease of the proton power slope (see Table 8.2), which causes a more pronounced drop in proton number density in the energy range of interest. This is a peculiar feature of this model, which predicts parameters depending on the jet magnetization, and thus changing with the radius.

The neutrino fluence for the muon flavor peaks at $E_\nu^{\text{peak}} = 7.2 \times 10^5$ GeV, which is about $\mathcal{O}(10 - 100)$ GeV smaller than in the models presented in the previous sections, although roughly comparable in intensity at peak. This is due to the fact that, in this case, the main contribution to the neutrino flux comes from the interaction of protons with thermal photons, whose energy peaks at ~ 22 keV. The second bump visible in the spectrum is instead represented by the kaon contribution. Apart from the ICMART model, this is the only other case out of the ones studied in this work in which this feature is clearly identified at higher energies. The reason is the very strong magnetic field in these two magnetic models. Another peculiar feature of this model is the low-energy tail of the neutrino distribution, which is higher than in previous cases. This is due to a combination of the larger number density [$\mathcal{O}(10^3 - 10^4)$] of protons at low energies in the acceleration region and the extended photon field at higher energies.

8.5.3 Proton synchrotron model

In order to estimate the neutrino production in the proton synchrotron model (see Sec. 8.2.3), we need to evaluate the fraction of the proton energy which goes into $p\gamma$ interactions. We consider the photon spectral fit as in Eq. A.10 and follow Ref. [370], which provides the cooling energy $E_{\gamma,\text{cool}}$, the peak energy (or minimum injection energy) $E_{\gamma,\text{peak}} \equiv E_{\gamma,\text{min}}$, and the energy flux at the cooling energy ($F_{\gamma,\text{cool}}$).

Another inferred quantity is the cooling timescale of the radiating particles, $t_{\text{cool}} \sim 1$ s. The cooling time t_{cool} is related, after Lorentz transforming, to the comoving magnetic field B' and γ'_{cool} by means of Eq. A.7. The variability timescale is assumed to be $t_\nu = 0.5$ s; the duration of the burst, as well as the redshift information, is extracted from the GRB catalog [213]. These observables can be used to constrain the source

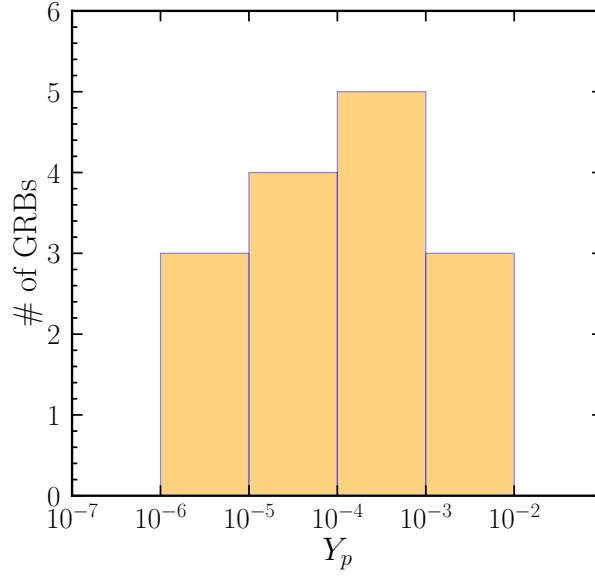


Figure 8.10: Histogram of Y_p (see Eq. 8.54) for a subset of GRBs analyzed in Ref. [370] for which redshift information is available; $\Gamma = 300$ and $t_v = 0.5$ s are adopted. The parameter Y_p quantifies the relative importance between the proton synchrotron emission and $p\gamma$ interactions. The very low values of Y_p for most of GRBs in the sample suggest a negligible neutrino production of this class of GRBs.

parameters, such as B' , γ'_{\min} , R_γ , Γ , and $E'_{\gamma,\text{bol,iso}}$ through the following relations [370]:

$$E_{\gamma,\text{peak}} = \frac{3 \hbar e B' \gamma_{\min}^2}{2 m_p c} \frac{\Gamma}{1+z}, \quad (8.49)$$

$$E_{\gamma,\text{cool}} = \left(\frac{m_p}{m_e}\right)^5 \frac{54 \pi^2 \hbar e m_e c}{\sigma_T^2 B'^3 t_{\text{cool}}^2} \frac{1+z}{\Gamma}, \quad (8.50)$$

$$F_\gamma = F_{\gamma,\text{cool}} \left(\frac{E_{\gamma,\text{cool}}}{h}\right) \left[\frac{3}{4} + 2 \sqrt{\frac{E_{\gamma,\text{peak}}}{E_{\gamma,\text{cool}}}} - 2 + \frac{2}{k_p - 2} \sqrt{\frac{E_{\gamma,\text{peak}}}{E_{\gamma,\text{cool}}}} \right], \quad (8.51)$$

$$E'_{\gamma,\text{bol,iso}} = \frac{4\pi d_L^2(z) F_\gamma t_{\text{dur}}}{\Gamma(1+z)}, \quad (8.52)$$

$$R_\gamma = \frac{2ct_v \Gamma^2}{(1+z)}. \quad (8.53)$$

where $F_\gamma = \tilde{L}_{\gamma,\text{bol,iso}}/4\pi d_L^2(z)$ is the bolometric isotropic radiative flux (in units of $\text{GeV cm}^{-2} \text{s}^{-1}$), $\tilde{L}_{\gamma,\text{bol,iso}}$ being the bolometric isotropic luminosity of the burst over the whole energy range. Using these relations we can infer B' , γ'_{\min} , R_γ and $E'_{\gamma,\text{bol,iso}}$ as functions of Γ .

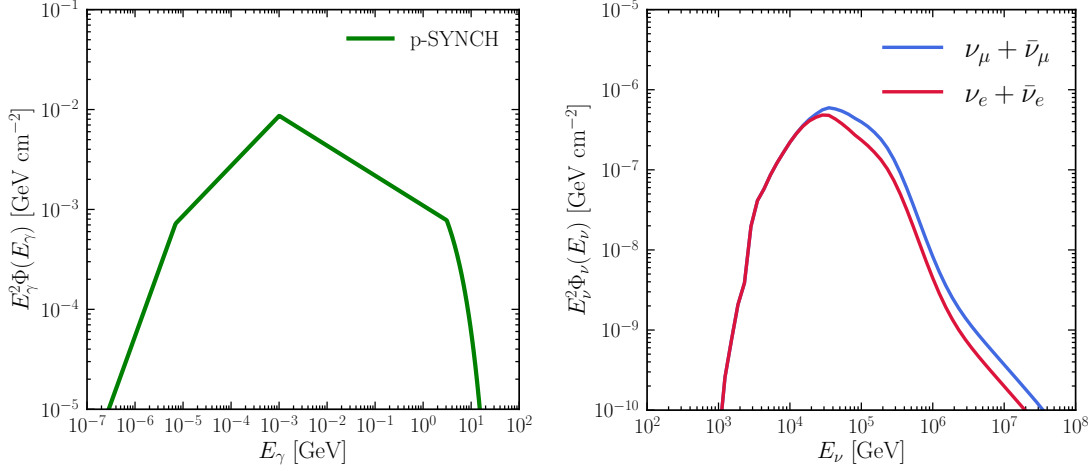


Figure 8.11: *Left:* Photon fluence in the observer frame for the proton synchrotron model; see Table 8.1 for the model parameters, in addition $\tilde{E}_{\text{bol,iso}} = 5 \times 10^{53}$ ergs, $t_{\text{cool}} = 0.5$ s, $\gamma_{\text{min}}/\gamma_{\text{cool}} = 12$, $E_{\gamma,\text{cool}} = 7$ keV. *Right:* Correspondent $\nu_{\alpha} + \bar{\nu}_{\alpha}$ fluence (in red and blue for the electron and muon flavors, respectively). The peak in the neutrino distribution ($E_{\nu}^{\text{peak}} = 3.5 \times 10^4$ GeV), due to the cooling energy break $E_{\gamma,\text{cool}}$, is shifted to lower energies with respect to the other analyzed models. The damping at high energies is due to the very strong magnetic field in the emitting region ($B' \simeq 8.5 \times 10^6$ G).

In order to figure out the relative importance between proton synchrotron and $p\gamma$ cooling for the sample of GRBs studied in Ref. [370], we introduce the following parameter [231]:

$$Y_p \equiv \frac{L'_{p,p\gamma}}{L'_{p,\text{syn}}} \approx \frac{\sigma_{p\gamma}}{\sigma_{p,T}} \frac{U'_{p,\text{syn}}}{U'_B} = \frac{\sigma_{p\gamma}}{\sigma_{p,T}} \frac{E'_{\gamma,\text{tot,iso}}}{V'_{\text{iso}}} \frac{8\pi}{B'^2} = \frac{\sigma_{p\gamma}}{\sigma_{p,T}} \frac{8\pi F_{\gamma} d_L^2(z)}{\Gamma^2 R_{\gamma}^2 c B'^2}, \quad (8.54)$$

where $L'_{p,p\gamma}$ and $L'_{p,\text{syn}}$ are the proton energy loss rates for $p\gamma$ interactions and synchrotron emission respectively, and $\sigma_{p,T} = \sigma_T (m_e/m_p)^2$. By relying on Eqs. 8.50 and 8.53, Y_p can be estimated as a function of the bulk Lorentz factor.

For our benchmark $\Gamma = 300$, we compute Y_p for the GRBs studied in Ref. [370] for which redshift information is available. The histogram of Y_p is shown in Fig. 8.10. We can see that Y_p spreads over almost three orders of magnitude, with very low typical values. Hence, assuming proton synchrotron radiation as the main emission mechanism, we expect this class of GRBs to be poor emitters of high energy neutrinos. To show this quantitatively, we compute the neutrino fluence for our representative GRB.

We adopt the following GRB parameters: $\gamma_{\text{min}}/\gamma_{\text{cool}} = 12$, $E_{\gamma,\text{cool}} = 7$ keV, $\Gamma = 300$, $z = 2$, $E_{\gamma,\text{peak}} = (\gamma_{\text{min}}/\gamma_{\text{cool}})^2 E_{\gamma,\text{cool}}$, which result in $\tilde{E}_{\gamma,\text{bol,iso}} \simeq 7 \times 10^{53}$ erg. These values are compatible with the average ones inferred from the sample considered in

Ref. [370], namely $\langle \tilde{E}_{\gamma, \text{bol}, \text{iso}} \rangle \simeq 7.4 \times 10^{53}$ erg, $\langle E_{\gamma, \text{cool}} \rangle \simeq 6.4$ keV, and $\langle \gamma_{\text{min}} / \gamma_{\text{cool}} \rangle \simeq 11.9$. Furthermore, we choose $k_p = 2.6$ for the slope of the injection proton spectrum $Q'(\gamma'_p)$, that reproduces the typical value of the high energy photon index $\beta \sim -2.3$; note that k_p is almost never constrained for the sample in Ref. [370].

As for the radiated energy, this fiducial GRB is comparable to the ones analyzed in the previous sections, except for the total energetics. In fact, given the very high magnetic field, $B' \simeq 8.5 \times 10^6$ G, the total isotropic energy is $\tilde{E}_{B, \text{iso}} \propto R_\gamma^2 \Gamma^2 B'^2 \sim \mathcal{O}(10^{60})$ erg, much larger than the typical energy that a GRB jets is able to release (spin down of magnetars or through the Blandford-Znajek mechanism [93]). Since the synchrotron radiation dominates by many orders of magnitude over all the other proton energy loss mechanisms, we assume $U'_{p, \text{iso}} \simeq E'_{\gamma, \text{bol}, \text{iso}}$, where U'_p is the total isotropic proton energy in the comoving frame. Such a jet turns out to be highly inefficient in radiating energy, given that $\tilde{E}_{\text{iso}} \sim \tilde{E}_{B, \text{iso}} \gg \tilde{E}_{\gamma, \text{bol}, \text{iso}}$.

By considering the proton energy distribution as in Eq. A.10 and normalizing it to U'_p , we compute the neutrino fluence and show it in the right panel of Fig. 8.11. The left of the same figure shows the total synchrotron photon fluence. Analogously to the model in Sec. 8.5.2.2, the peak in the neutrino distribution ($E_\nu^{\text{peak}} = 3.5 \times 10^4$ GeV) is due to the cooling energy break $E_{\gamma, \text{cool}}$ and it is shifted to lower energies. The neutrino spectrum is furthermore strongly damped at high energies due to the synchrotron cooling of mesons in the jet. Our estimation of the neutrino emission results to be in agreement with the one reported in the independent work of Ref. [178], for GRBs with similar parameters.

The proton synchrotron model, besides requiring unreasonable total jet energies, predicts the smallest neutrino fluence among all models considered in this work. We note that with the choice made of parameters, our representative GRB has $Y_p \sim \mathcal{O}(10^{-4})$; hence, our estimation may be considered an optimistic one, given the distribution of Y_p shown in Fig. 8.10. We refer the interested reader to Ref. [178] for additional details and discussion on this model.

8.6 Discussion

In this work, we have computed the neutrino fluence for a class of models adopted to describe the prompt phase of long GRBs, all having the same \tilde{E}_{iso} . Because of the diversity of electromagnetic GRB data and the uncertainties inherent to the models (e.g., jet composition, energy dissipation mechanism, particle acceleration, and radiation mechanisms), an exhaustive theoretical explanation of the mechanism powering GRBs is still lacking. To compare the neutrino production across models, we have selected fiducial input parameters for a benchmark GRB motivated by observations. In addition, the modeling of the dissipative and acceleration efficiencies, as well as the

Table 8.3: Summary of the derived quantities for the models considered in this work and our benchmark parameters value (see Table 8.1). The radiative efficiency of the jet (Eq. 8.16), the isotropic photon energy in the 1 keV–10 MeV energy range, the isotropic neutrino energy for neutrinos and antineutrinos of all flavors, the ratio between the isotropic total neutrino and photon energies, the neutrino energy at the fluence peak, and the maximum proton energy are listed. The model with the smallest radiative efficiency is the proton synchrotron model; this model has also the smallest $\tilde{E}_{\nu,\text{iso}}$. The most radiatively efficient model is the one with a dissipative photosphere.

<i>Model</i>	η_γ (%)	$\tilde{E}_{\gamma,\text{iso}}$ [erg]	$\tilde{E}_{\nu,\text{iso}}$ [erg]	$\tilde{E}_{\nu,\text{iso}}/\tilde{E}_{\gamma,\text{iso}}$	$E_{\nu_\mu}^{\text{peak}}$ [GeV]	$E_{p,\text{max}}$ [GeV]
IS	0.2	6.8×10^{51}	2.3×10^{48}	3.4×10^{-4}	4×10^7	1.2×10^{11}
PH-IS	20	6.9×10^{53}	7.2×10^{49}	1.1×10^{-4}	3.2×10^7	7.5×10^{10}
3-COMP	0.3	8.7×10^{51}	5.2×10^{48}	6×10^{-4}	4.2×10^7	1.2×10^{11}
ICMART	17.5	6×10^{53}	1.8×10^{51}	3×10^{-3}	1.3×10^7	1.7×10^{11}
MAG-DISS	8	2.7×10^{53}	5.2×10^{50}	2×10^{-3}	7.2×10^5	2.5×10^{10}
p-SYNCH	2×10^{-5}	4.8×10^{53}	7.2×10^{49}	1.4×10^{-4}	3.5×10^4	6.9×10^9

properties of the accelerated particle distributions have been guided by the most recent simulation findings. A summary of our input parameters is reported in Table 8.1. In this section, we compare the energetics of the GRB models explored in this work, discuss the the detection prospects of stacked neutrino fluxes as well as the variation of the quasi-diffuse neutrino flux due to the uncertainties in the jet parameters.

8.6.1 Energetics

A summary of our findings is reported in Table 8.3, where the radiative efficiency of the jet (Eq. 8.16) is listed for the six GRB models investigated in this paper together with the isotropic photon and neutrino (for six flavors) energies, as well as the ratio of the latter two. As already discussed in Sec. 8.5, the least efficient model in converting \tilde{E}_{iso} in $\tilde{E}_{\nu,\text{iso}}$ is the proton synchrotron model, whilst the most efficient one is the model which considers a dissipative photosphere as the main source of prompt emission. This is mainly due to the high dissipative efficiency suggested by recent three-dimensional simulations [210]. Note that the radiative efficiency is an input parameter of each model, since we do not compute the radiation spectra self-consistently.

Among the models considered in this work, all with identical \tilde{E}_{iso} , neutrinos carry the largest amount of energy in the ICMART model, followed by the model invoking magnetic dissipation; among the kinetic dominated jet scenarios, the case with a dissipative photosphere is the most efficient one in terms of neutrino production. It is worth

noting that, although in the model with three components $E_{\gamma,\text{iso}}$ is just 30% higher than in the IS one, $E_{\nu,\text{iso}}$ is a factor 2.3 larger. The reason for this lies in the fact that protons interact with a high-energy photon component comparable in intensity to the one in the γ -ray range (i.e., 1 keV–10 MeV) in the three component model, while the number density of photons above 10 MeV is negligible in the IS model. This also explains the trend for $\tilde{E}_{\nu,\text{iso}}/\tilde{E}_{\gamma,\text{iso}}$ reported in Table 8.3 (note that $\tilde{E}_{\gamma,\text{iso}}$ in Table 8.3 is estimated over the energy range 1 keV–10 MeV; hence, this ratio, when defined with the bolometric photon energy used for neutrino production, should be slightly smaller than the one reported for the IS model with a dissipative photosphere, the model with three components, the magnetic one with gradual dissipation, and the proton synchrotron model).

One last remark should be done on our results for the IS and ICMART models. In Ref. [521], the ICMART scenario predicts the least neutrino flux, given the larger emission radius than R_{IS} . This is not the case in our work for two reasons: first, the chosen representative variability timescale t_v provides emission radii comparable in the two scenarios; second, the microphysics parameter that we adopt for the IS case are less favorable in terms of radiative efficiency and neutrino production efficiency, if compared to the parameters adopted in Ref. [521], which result to be the same for all their cases of study.

8.6.2 Detection perspectives

In order to compare the neutrino detection perspectives for our six models, we compute the all-sky quasi-diffuse flux for neutrinos and antineutrinos. We assume that our benchmark GRB at $z = 2$ yields a neutrino emission that is representative of the entire GRB population. For $\dot{N} \simeq 667 \text{ yr}^{-1}$ long GRBs per year [7], the stacking flux for the muon flavor over the whole sky is defined as

$$E_{\nu_\mu}(E_\nu) = \frac{1}{4\pi} \dot{N} \Phi_{\nu_\mu}(E_\nu, z = 2). \quad (8.55)$$

Figure 8.12 shows the resultant all-sky quasi-diffuse fluxes for the muon flavor for the six GRB models as functions of the neutrino energy (colored curves). For comparison, we also show the GRB staking limits of IceCube [7] and the projected ones for IceCube-Gen2 [10] (black curves). In agreement with the non-detection of high-energy neutrinos from targeted GRB searches [7], our forecast for the neutrino fluxes lies below the experimental limits and is in agreement with the upper limits reported by the ANTARES Collaboration [49] and with the ones expected for KM3NeT [40]. The ICMART and the magnetic model with gradual dissipation predict comparable neutrino flux at peak energy. The models invoking ISs (IS, PH-IS, 3-COMP) are the ones with the lowest photon and neutrino yield. This is due to the microphysics parameters adopted

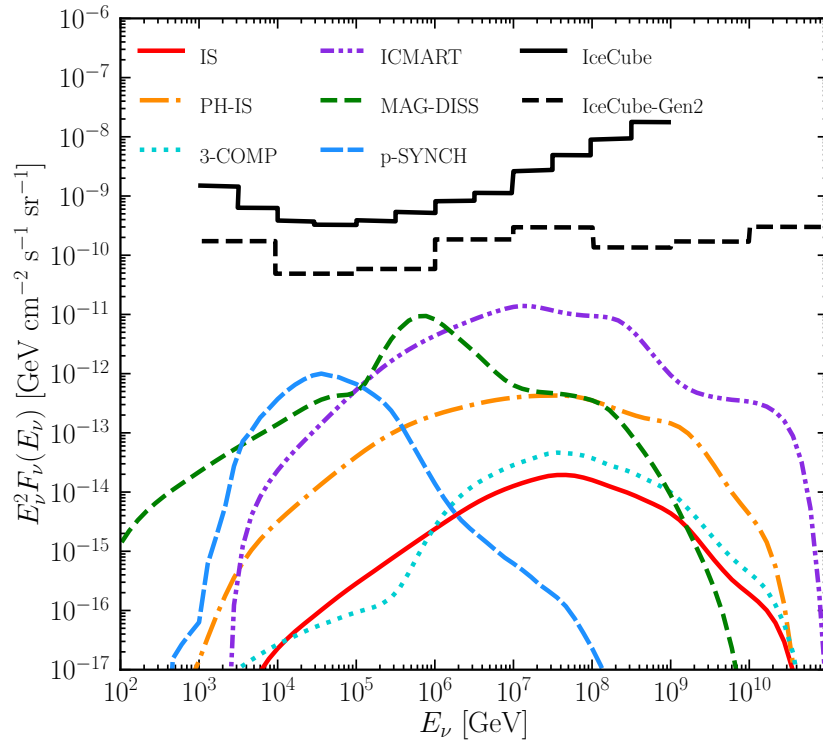


Figure 8.12: Model comparison of the expected all-sky quasi-diffuse fluxes for the six GRB models considered in this work for the benchmark jet parameters listed in Table 8.1. The quasi-diffuse flux has been computed by relying on Eq. 8.55 for $\nu_\mu + \bar{\nu}_\mu$; all models have identical \tilde{E}_{iso} . For comparison, the IceCube staking limits (combined analysis for 1172 GRBs) [7] and the expected sensitivity for IceCube-Gen2 (based on a sample of 1000 GRBs) [10] are reported (solid and dashed black lines). By relying on the most up-to-date best-fit GRB parameters, all models predict a quasi-diffuse flux that lies below the sensitivity curves; however, a large spread in energy and shape of the expected neutrino fluxes is expected for different jet models.

in this work; we refer the reader to Appendix A.3 for details on the differences with respect to standard assumptions commonly used in the literature.

An important aspect to consider in targeted GRB searches is the large spread in energy and shape of the expected neutrino fluxes for different jet models. It is evident from Fig. 8.12 that the neutrino flux peak energy ranges from $\mathcal{O}(10^4)$ GeV for the proton synchrotron model to $\mathcal{O}(10^8 - 10^9)$ GeV for the IS model with a dissipative photosphere. As such, targeted searches assuming one specific GRB model, such as the IS one, as benchmark case for the GRB neutrino emission may lead to biased results.

Another caveat of our modeling is that the spectral energy distributions of photons and the ones of the secondary particles produced through $p\gamma$ interactions are not computed self-consistently; this may affect the overall expected emission, see e.g. Refs. [387, 391, 354, 61, 310] for dedicated discussions. In addition, since none of the considered jet models can account for all observational constraints, a population study [39] may further affect the expected quasi-diffuse emission.

8.6.3 Uncertainties in the jet parameters

In this work, we have chosen one benchmark GRB as representative of the whole population and have relied on the best fit values of the input parameters. However, there are intrinsic uncertainties of the characteristic jet parameters, which can lead to variations of the expected neutrino flux, see e.g. Refs. [467, 424]. Hence, we now investigate the impact of the variation of two of the most uncertain parameters, the variability timescale t_v and the Lorentz boost factor Γ , on the quasi-diffuse neutrino flux.

Consistently with dedicated analysis [404, 196], we adopt $\Gamma_{\min} = 100$ and $\Gamma_{\max} = 1000$ as the minimum and maximum values of the Lorentz factor, respectively. The resulting neutrino fluxes are displayed in the top panel of Fig. 8.13. A variation up to five orders of magnitude for the proton synchrotron case is observable. We note that a band for the model with magnetic dissipation case is missing. This is due to the fact that the outflow saturates below the photosphere for $\Gamma_{\text{sat}} = 100$ ($R_{\text{sat}} > R_{\text{PH}}$ for $\Gamma_{\text{sat}} \gtrsim 121$; since we focus on the production of neutrinos in the optically thin region above the photosphere, we do not provide information about the $\Gamma_{\text{sat}} = 100$ case); we instead show the case with $\Gamma = 1000$ (see Appendix A.2 for a discussion on the dependence of the neutrino emission on the input parameters in the magnetized model with gradual dissipation). The neutrino flux for the ICMART case is shifted to higher energies for larger boost factors; this is determined by a compensation effect due to the fact that the distance of the emitting region from the central engine is assumed to be constant and around $\sim 10^{15}$ cm in this model, thus being completely independent on the bulk Lorentz factor.

In the bottom panel of Fig. 8.13, the variation of the quasi-diffuse neutrino flux is shown as a function of the variability timescale. According to the analysis performed

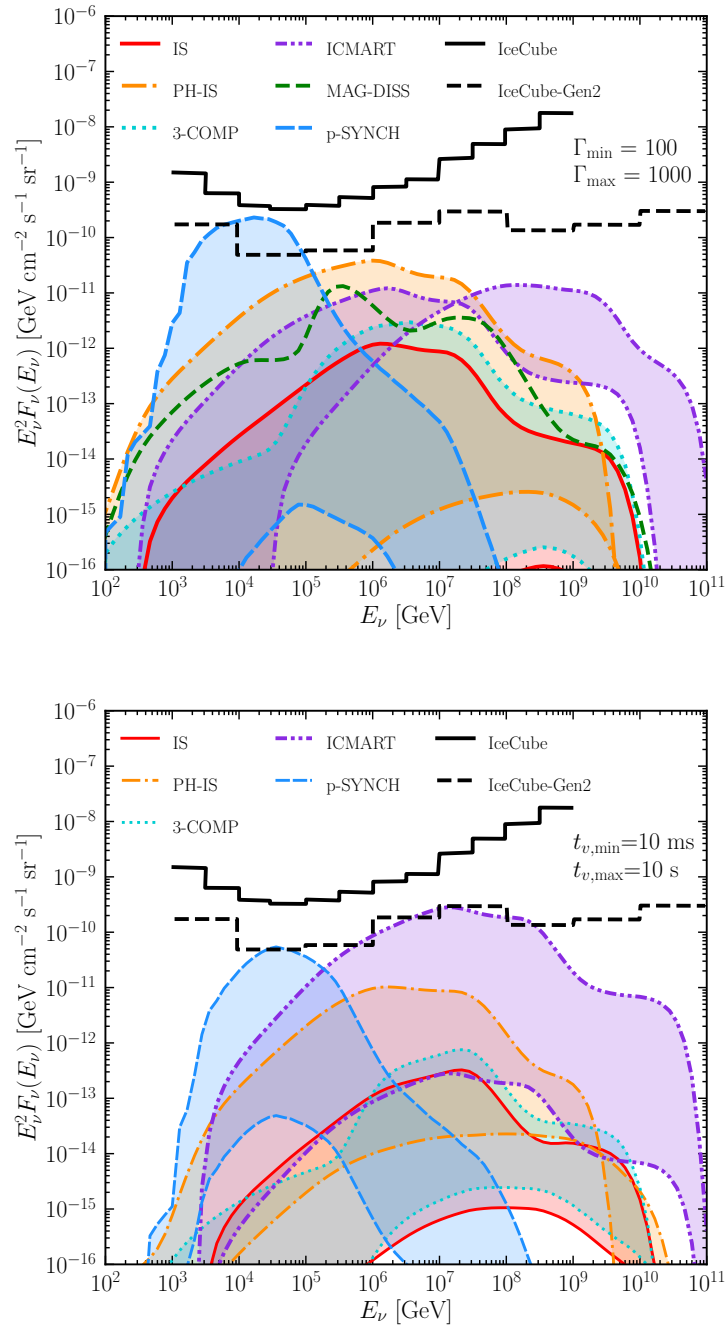


Figure 8.13: Same as Fig. 8.12, but for extreme values of boost factor Γ and the variability timescale t_ν . *Top:* The bands for the quasi-diffuse neutrino flux are displayed for $\Gamma_{\min} = 100$ and $\Gamma_{\max} = 1000$. *Bottom:* The bands for the quasi-diffuse neutrino flux are displayed for $t_\nu = 10 \text{ ms}$ and $t_\nu = 10 \text{ s}$.

on a wide sample of GRB lightcurves [49], we choose $t_{v,\min} = 10$ ms and $t_{v,\max} = 10$ s as representative extreme values for the variability time. For the simple IS model, the model with three components, the proton-synchrotron model, and the ICMART model, t_v is directly connected to the size of the emitting region. For the IS model with dissipative photosphere and the magnetic model with gradual dissipation instead, t_v is not related to any observable erratic behavior in the electromagnetic signal; this explains why no band is considered for the magnetic model with gradual dissipation, while the band in the case of the IS model with dissipative photosphere comes from simply varying R_{IS} .

It is worth noting that while the quasi-diffuse fluxes shown in Fig. 8.12 sit below the IceCube stacking limits and expected sensitivity of IceCube-Gen2, once taking into account the variability ranges of t_v and Γ , the quasi-diffuse fluxes for the different models can hit the expected sensitivity of IceCube-Gen2; this hints that it may be possible to constrain extreme configurations responsible for the prompt neutrino emission.

8.7 Conclusions

Long duration gamma-ray bursts (GRBs) are subject of investigation since long time, being among the most mysterious transients occurring in our universe. In the attempt of explaining the observed electromagnetic GRB emission, various models have been proposed. The main goal of this work is to show that the neutrino emission strongly depends on the chosen jet model, despite the fact that different jet models may be equally successful in fitting the observed electromagnetic spectral energy distributions.

To this purpose, we choose a benchmark GRB and compute the neutrino emission for kinetic dominated jets, i.e. in the internal shock model, also including a dissipative photosphere as well as three spectral components. We also consider Poynting flux dominated jets: a jet model invoking internal-collision-induced magnetic reconnection and turbulence (ICMART) and a magnetic jet model with gradual dissipation. A jet model with dominant proton synchrotron radiation in the keV-MeV energy range is also taken into consideration. In particular, the neutrino production for the latter two models has been investigated for the first time in this work.

Defining the radiative efficiency as the ratio of isotropic gamma-ray energy to the total isotropic energy of the jet, we find that the least radiatively efficient model is the proton synchrotron one, while the most efficient one is the model with a dissipative photosphere. However, the model predicting the largest amount of isotropic-equivalent energy going into neutrinos is the ICMART one.

In the context of targeted searches, it should be noted that the expected quasi-diffuse neutrino flux can vary up to 3 orders of magnitude in amplitude and peak at energies ranging from 10^4 to 10^8 GeV. The predicted spectral shape of the neutrino distribution is also strongly dependent on the adopted jet model. A summary of our findings is

reported in Table 8.3 and Fig. 8.12.

This work highlights the great potential of neutrinos in pinpointing the GRB emission mechanism in the case of successful neutrino detection. In particular, it suggests the need to rely on a wide range of jet models in targeted stacking searches.

Paper II: High-energy neutrinos from afterglow optical-bumps

This chapter is a reprint of:

Ersilia Guarini, Irene Tamborra, Damien Bogue, **Tetyana Pitik**, Jochen Greiner
Multi-messenger detection prospects of gamma-ray burst afterglows with optical jumps
JCAP 06 (2022) 06, 034, [arXiv:2112.07690](https://arxiv.org/abs/2112.07690)

ABSTRACT

Some afterglow light curves of gamma-ray bursts (GRBs) exhibit very complex temporal and spectral features, such as a sudden intensity jump about one hour after the prompt emission in the optical band. We assume that this feature is due to the late collision of two relativistic shells and investigate the corresponding high-energy neutrino emission within a multi-messenger framework, while contrasting our findings with the ones from the classic afterglow model. For a constant density circumburst medium, the total number of emitted neutrinos can increase by about an order of magnitude when an optical jump occurs with respect to the self-similar afterglow scenario. By exploring the detection prospects with the IceCube Neutrino Observatory and future radio arrays such as IceCube-Gen2 radio, RNO-G and GRAND200k, as well as the POEMMA spacecraft, we conclude that the detection of neutrinos with IceCube-Gen2 radio could enable us to constrain the fraction of GRB afterglows with a jump as well as the properties of the circumburst medium. We also investigate the neutrino signal expected for the afterglows of GRB 100621A and a GRB 130427A-like burst with an optical jump. The detection of neutrinos from GRB afterglows could be crucial to explore the yet-to-be unveiled mechanism powering the optical jumps.

9.1 Introduction

Gamma-ray bursts (GRBs) are among the brightest and most poorly understood transients occurring in our Universe [269, 394, 281]. There are two classes of GRBs; the short ones, lasting less than 2 s, and the long ones [276, 194]. The latter are the focus of this work. They are thought to be harbored within collapsing massive stars [508, 304, 509]. The isotropic equivalent energy release in gamma-rays spans 10^{49} – 10^{55} erg and it occurs within a few tens of seconds [281, 64]. The observed spectrum is non-thermal, typically peaking in the 10 – 10^4 keV energy band [73, 218, 265].

The delayed emission following the prompt phase of GRBs—observed in the X-ray, optical/infrared, radio and as of recently TeV bands [323, 34, 32, 33]—is the so-called afterglow. It is observed for several weeks after the trigger of the burst and, in some cases, up to months or even years, making GRBs electromagnetically detectable across all wavebands. The afterglow emission results from the interaction between the ejecta and the circumburst medium (CBM). The physical mechanism responsible for the multi-wavelength observation is broadly believed to be synchrotron radiation from the relativistic electrons accelerated at the external shock, developing when the relativistic outflow expands in the CBM [323, 497, 496, 259].

Observations in the X-ray and optical bands show a rich set of additional features, not described by the simplest afterglow model. At X-rays, data from the Gehrels Swift Observatory display a rapid decline during the first few hundred seconds [74, 295, 366], strong X-ray flaring during the first few thousand seconds [309, 134], and a shallow decay up to ten-thousand seconds. A canonical view of GRB afterglow is presented in e.g. [363, 524]. In the optical band, the forward [e.g., 315] and reverse shocks [e.g., 430, 251] dominate during the first thousand seconds, together with plateaus in the majority of afterglows, and with X-ray flares, occasionally accompanied by optical flares [278, 290]. At later times [i.e., at about 7 – $10(1+z)$ days, with z being the redshift], the supernova signal emerges [98, 286]¹. In this context, one of the biggest surprises was the observation of sudden rebrightenings in the afterglow light curve occurring at one to few hours after the prompt emission, primarily visible in the optical band (hereafter called optical jump) [405, 485, 359, 215, 358]. These optical jumps are very rare, as opposed to e.g. X-ray flares occurring in about 50% of all GRB afterglows. The optical jump can be very large in amplitude (>1 mag) and is typically brighter than the one observed in X-rays. So far, about 10 out of 146 GRBs with well sampled optical light curves collected between February 1997 and November 2011 have displayed an optical jump [294]; for half of these, the brightness at the jump peak is comparable to the peak of the afterglow associated to the forward shock.

Several theoretical models attempt to explain such optical jumps. For instance, they might be due to CBM inhomogeneities generated by anisotropic wind ejection of the

¹It is worth highlighting that we are only listing typical values for all the aforementioned timescales.

GRB progenitor or interstellar turbulence [285, 492]; however, numerical simulations of spherical explosions exhibit rather regular features and, in addition, density fluctuations of the CBM cannot give rise to significant time variability in the afterglow light curve [356, 161, 162]. Alternatively, the late variability of the afterglow light curve could be explained by invoking a late energy injection in the first blast wave emitted by the central engine. In this picture, the central engine undergoes intermittent late explosions, producing multiple shells of matter that propagate and collide with the slower ones previously emitted, as proposed in Ref. [483]. The origin of the late time activity of the central engine is unclear [247]. For example, it might be related to the disk fragmentation due to gravitational instabilities in the outer regions of the disk, with the resulting fragments being accreted into the central compact object over different timescales, and causing the observed time variability in the afterglow light curve [384]. Despite the uncertain origin of the central engine late time activity, this model predicts that the second blast wave emitted by the central engine injects new energy in the initially ejected one, causing the observed rebrightening in the light curve [280, 212]. Even though there is to date no smoking-gun signature favoring a specific mechanism to explain the appearance of optical jumps, the late collision of two relativistic shells [483] is appealing in light of its ability to successfully fit the light curves of some GRBs with optical jumps [215, 282].

These peculiar features of the light curve of GRB afterglows raise questions on the possibly related neutrino emission. In fact, GRBs have been proposed as sources of ultra-high energy cosmic rays and high-energy neutrinos [500, 221, 317]. In the prompt phase, a copious amount of neutrinos could be produced by photo-hadronic ($p\gamma$) [500, 221, 488] or hadronic interactions (pp or pn), the latter being more efficient in the innermost regions where the baryon density is large [409, 345, 325, 237]. The neutrinos produced during the prompt GRB phase in the optically thin region have TeV–PeV energies, and their spectral distribution strongly depends on the emission mechanism [500, 321, 494, 337, 396, 475, 523].

High energy neutrinos could also be produced during the afterglow phase through $p\gamma$ interactions in the PeV–EeV energy range. Protons can be accelerated in the blast-wave through Fermi acceleration [495, 480] and interact with the synchrotron photons produced by accelerated electrons. Within the framework of the classic afterglow model, the neutrino emission from GRB afterglows has been computed by considering the interaction of the GRB blastwave with the external medium in two possible scenarios: the forward shock one, according to which particles are accelerated at the shock between the blastwave and the CBM [501, 151, 292, 407] and the reverse shock model, that assumes acceleration of particles at the reverse shock propagating back towards the ejecta [338].

Since the neutrino production during the GRB afterglow phase strictly depends on the photon distribution, an increase of the photon flux as observed for late time jumps

in the light curve should result in an increased neutrino flux, potentially detectable by current and future high energy neutrinos facilities. In fact, optical photons are ideal targets for the production of PeV neutrinos. The detection prospects with the IceCube Neutrino Observatory, which routinely observes neutrinos with energies up to a few PeV [46, 45, 23, 17], of GRB afterglows displaying an optical jump have not been investigated up to now. In addition, the possibly higher neutrino flux could be detectable by upcoming detectors, such as IceCube-Gen2 and its radio extension [10], the Radio Neutrino Observatory in Greenland (RNO-G) [43] and the full planned configuration of the Giant Radio Array for Neutrino Detection (GRAND200k) [54]. The orbiting Probe of Extreme Multi-Messenger Astrophysics (POEMMA) spacecraft may also have promising perspectives for the detection of neutrinos from GRB afterglows [479].

If a jump is observed in the optical light curve of a GRB, what is its signature in neutrinos? Can we use neutrinos to learn more about this enigmatic feature of some GRBs? In this paper, we address these questions and explore the corresponding neutrino detection prospects. Our reference model is the late collision of two relativistic shells [483, 215, 282]. Nevertheless, we stress that our goal is not to prove that the shell collision is the main mechanism explaining the GRBs light curves displaying jumps; rather, this scenario provides us with the framework within which we aim explore the associated neutrino signal.

This paper is organized as follows. In Sec. 9.2, we present the theoretical model for the late collision of two relativistic shells that we consider to be the mechanism responsible for the sudden jump in the afterglow light curve. Section 9.3 focuses on the modeling of the electromagnetic signal from GRB afterglows in the presence of optical jumps, while Sec. 9.4 is centered on the proton distribution in the blastwave and the resulting neutrino signals. Section 9.5 presents our findings on the neutrino and photon signals expected during the GRB afterglow phase, in the absence as well as in the presence of optical jumps; while Sec. 9.6 investigates the neutrino detection prospects in the context of quasi-diffuse and point source searches. In particular, we discuss the neutrino detection prospects for the well studied GRB 100621A [215] and a burst with model parameters inspired by GRB 130427A [377, 382, 147] having a hypothetical optical jump. Finally, our findings are summarized in Sec. 9.7. The analytical model on the late collision and merger of two relativistic shells is detailed in Appendix B.1, a discussion on the degeneracies among the parameters of our model is reported in Appendix B.2, while Appendix B.3 focuses on the cooling times of protons and mesons of our GRB afterglow model.

9.2 Modelling of the merger of two relativistic shells

In this section, we outline the blastwave physics, introducing the scaling relations describing the temporal evolution of the radius and Lorentz factor of the blastwave. By relying on the late activity scenario for the central engine [247, 168, 421, 524], our model on the late collision of two relativistic shells is then presented.

9.2.1 Physics of the blastwave

According to the standard picture, the relativistic GRB jet propagates with half opening angle θ_j and Lorentz factor $\Gamma \gg 100$ [194] in the reference frame of the central engine. As long as $\Gamma^{-1} < \theta_j$, the emitting region can approximately be considered spherical. In order to investigate the afterglow physics, it is useful to introduce the isotropic equivalent energy of the blastwave, \tilde{E}_{iso} ². We denote with $\tilde{E}_{k,\text{iso}}$ the isotropic equivalent kinetic energy of the blastwave, defined as $\tilde{E}_{k,\text{iso}} = \tilde{E}_{\text{iso}} - \tilde{E}_{\gamma,\text{iso}}$ and representing the energy content of the outflow after $\tilde{E}_{\gamma,\text{iso}}$ has been released in γ -rays during the prompt phase.

Two shocks develop at the interaction front between the burst and the CBM: a reverse shock, that propagates towards the core of the jet, and a forward shock propagating in the CBM. After the reverse shock crosses the relativistic ejecta, the blastwave enters the so-called Blandford and McKee self-similar regime [94] (dubbed BM hereafter). In the following, we focus on the BM phase, during which the emission is associated with the forward shock only. The particle density profile of the CBM is assumed to scale as a function of the distance from the central engine as $n \propto R^{-k}$. In this work, we consider two CBM scenarios: a constant density profile resembling the one of the interstellar medium ($k = 0$, ISM) and a stellar wind one ($k = 2$, wind).

We assume that the ejecta initially have isotropic kinetic energy $\tilde{E}_{k,\text{iso}}$ and Lorentz factor Γ_0 . Two extreme scenarios for the hydrodynamical evolution of the blastwave can be described analytically: fully adiabatic and fully radiative [94, 431]. In the former case, the blastwave does not radiate a significant amount of energy while propagating. On the contrary, it quickly cools in the latter scenario, radiating all the internal energy released in the shock while being decelerated by the CBM. Observational evidence suggests that GRB afterglow blastwaves are in the adiabatic regime rather than in

²We adopt three reference frames: the blastwave comoving frame, the center of explosion (i.e. the central compact object) frame, and the observer frame (the Earth). Quantities in these frame are denoted as X' , \tilde{X} and X , respectively. Energy, for example, transforms as $\tilde{E} = (1 + z)E = \mathcal{D}E'$. Here z is the redshift and $\mathcal{D} = [\Gamma(1 - \beta \cos \theta)]^{-1}$ is the Doppler factor, where $\beta = \sqrt{1 - 1/\Gamma^2}$ and θ is the angle of propagation of an element of the ejecta relative to the line of sight.

the radiative one [520]. Therefore, in this paper we focus on the adiabatic scenario.

Within the assumption of a thin shell (for which the reverse shock is mildly relativistic at most), if propagation occurs through a CBM with constant density $n = n_0$, the blastwave starts to be decelerated at [94, 520]:

$$T_{\text{dec,ISM}} = \left[\frac{3\tilde{E}_{k,\text{iso}}(1+z)^3}{64\pi n_0 m_p c^5 \Gamma_0^8} \right]^{1/3}; \quad (9.1)$$

while if it occurs in a wind profile, $n = AR^{-2}$, the deceleration occurs at [133]:

$$T_{\text{dec,wind}} = \frac{\tilde{E}_{k,\text{iso}}(1+z)}{16\pi A m_p c^3 \Gamma_0^4}, \quad (9.2)$$

where $A = \dot{M}_w/(4\pi v_w m_p) = 3.02 \times 10^{35} A_\star \text{ cm}^{-1}$, with $A_\star = \dot{M}_{-5}/v_8$ corresponding to the typical mass loss rate $\dot{M}_{-5} = \dot{M}/(10^{-5} M_\odot) \text{ yr}^{-1}$ and wind velocity $v_8 = v_w/(10^8 \text{ cm s}^{-1})$ [129, 407]³. Here $c = 3 \times 10^{10} \text{ cm s}^{-1}$ is the speed of light and $m_p = 0.938 \text{ GeV } c^{-2}$ is the proton mass.

After the deceleration begins, the Lorentz factor of the shell decreases with time as [94, 431, 133, 197]:

$$\Gamma_{\text{ISM}} = \Gamma_0 \left(\frac{T_{\text{dec,ISM}}}{4t} \right)^{3/8}; \quad (9.3)$$

$$\Gamma_{\text{wind}} = \Gamma_0 \left(\frac{T_{\text{dec,wind}}}{4t} \right)^{1/4}; \quad (9.4)$$

The radius of the blastwave evolves with time according to [407]:

$$R = \frac{\zeta \Gamma^2 t c}{(1+z)}, \quad (9.5)$$

where the correction factor ζ depends on the hydrodynamical evolution of the shock; we assume $\zeta = 8$ [431, 407, 150].

In this work we are mainly interested in estimating the neutrino signal, whose accuracy is mainly dominated by other local uncertainties (e.g. the proton acceleration efficiency and the fraction of the blastwave internal energy that goes into accelerated protons, that we introduce in Sec. 9.4.1). Hereafter, we adopt the uniform shell approximation of the BM solution, as presented in this section. This assumption suits our purposes, since the particle density of a BM shell quickly drops outside the region of width $\propto R/\Gamma^2$ behind the forward shock and thus the corresponding neutrino emission is negligible.

³Care should be taken when comparing our definition of the density profile for a wind CBM (which follows the convention adopted in e.g. Ref. [281]) with the one often adopted in the literature, i.e. $\rho = AR^{-2}$, where $A = 5 \times 10^{-11} \text{ g cm}^{-1} A_\star$ and $A_\star = \dot{M}_{-5}/v_8$. The difference between the two definitions is the normalization in units of proton mass.

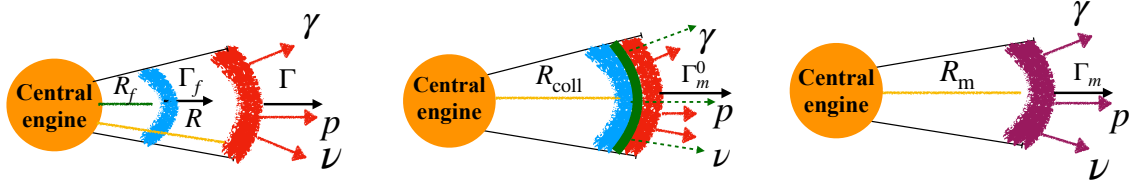


Figure 9.1: Sketch of the collision and merger of two relativistic shells (not in scale). *Left panel:* The slow shell (marked in red) is launched by the central engine and decelerated by the interaction with the external medium. A shock develops at the contact surface, leading to the classic afterglow emission. The fast shell (marked in blue) is launched by the central engine with a temporal delay Δ_T and propagates freely. *Middle panel:* The fast shell reaches the slow BM blastwave. Two shocks develop at the collision (marked in green); the internal energy released in this process is emitted through radiation of secondary particles. *Right panel:* The merged shell (plotted in purple) propagates through the external medium, emitting afterglow radiation.

9.2.2 Merger of two relativistic shells

The late merger of two relativistic shells has been investigated through hydrodynamical simulations [483] and applied to fit the light curve of GRB 100621A [215]. However, a simplified analytical modeling aiming to estimate the corresponding neutrino signal is presented in this paper for the first time. We assume that the first shell is launched by the central engine. At the onset of its deceleration, it is heated up, as its kinetic energy $\tilde{E}_{k,\text{iso}}$ is converted in internal energy \tilde{W} . From now on, we refer to this shell as the “slow shell.” Its dynamics is described by the simplified BM solution in the uniform blastwave approximation introduced in Sec. 9.2.1, its Lorentz factor Γ and radius R evolve by following Eq. 9.3 and Eq. 9.5, respectively.

Assuming that the central engine undergoes late activity, a second shell with energy \tilde{E}_f is emitted with a time delay Δ_T with respect to the slow one, see the left panel of Fig. 9.1. We refer to this second shell as the “fast shell.” This shell propagates in an almost empty environment since most of the matter has been swept up by the slow shell [483]. Thus, the fast shell moves with a constant Lorentz factor Γ_f , eventually reaches the slow shell, and merges with it, as sketched in the middle and right panels of Fig. 9.1. Details on the analytical model describing the shell merger and the related conserved quantities are reported in Appendix B.1.

In order for the collision to happen at a given time T_{coll} , the slow and fast shells must be at the same position at $t = T_{\text{coll}}$: $R(T_{\text{coll}}) = R_f(T_{\text{coll}})$. As extensively discussed in Appendix B.2, this condition gives rise to a degeneracy between Γ_f and Δ_T (see also Appendix C of [282] for a similar discussion). Indeed, a shell launched with a large delay and large speed could reach the slow shell at the same time of a slower shell launched with a smaller time delay. Understanding this degeneracy among the characteristic shell parameters is important, since Γ_f directly affects the dynamics of the collision

between the two shells.

As the slow and fast shells collide, two shocks develop: a reverse shock, propagating back towards the fast shell, and a forward shock, propagating through the slow shell. A detailed modeling of the collision between the fast and the slow shell is not necessary to estimate the production of neutrinos. Therefore, we assume that both the forward and reverse shocks created in the shell collision instantly cross the slow (forward shock) and the fast (reverse shock) shell, which thus merge in a single shell at T_{coll} . In other words, when the collision occurs, a hot “merged” shell instantaneously forms as described in Appendix B.1; see the right panel of Fig. 9.1. Despite the simplifying assumption of instantaneous merger between the two shells, our overarching goal of computing the time-integrated neutrino event rate is not affected since the neutrino emission during the merger interval is overall negligible, see discussion in Sec. 9.5.

In order to characterize the properties of the merged shell, we apply the energy-momentum conservation equations, expanding on the model describing the collision of two relativistic shells for the internal shock scenario employed to model the prompt phase [271, 144]. The main difference with respect to the internal shock scenario [271, 144] is that our slow shell is hot and is sweeping up material from the external medium. Thus, we need to include the internal energy of the slow shell and the swept up mass in our calculation. As discussed in Appendix B.1, the following equations are obtained within the assumption of instantaneous merger. Therefore, we evaluate the quantities describing the slow and the fast shells at time $t = T_{\text{coll}}$. The initial Lorentz factor of the merged shell is

$$\Gamma_m^0 \simeq \sqrt{\frac{m_f \Gamma_f + m_{\text{eff}} \Gamma}{m_f / \Gamma_f + m_{\text{eff}} / \Gamma}}, \quad (9.6)$$

where $m_f = \tilde{E}_f / (\Gamma_f c^2)$ is the mass of the fast shell and $m_{\text{eff}} = m + \hat{\gamma} W' / (c^2)$ is the effective mass of the slow shell. Here $\hat{\gamma} = 4/3$ is the adiabatic index in the relativistic limit (which holds since the slow shell is hot) and m is the mass of the slow shell, i.e. the sum between the initial mass of the ejecta $m_0 = \tilde{E}_{\text{iso}} / (\Gamma_0 c^2)$ and the swept up mass from the CBM up to the radius R ,

$$m = m_0 + 4\pi \int_0^R dR' R'^2 n(R') m_p. \quad (9.7)$$

Furthermore, at the collision, the internal energy \tilde{W}_m^0 is generated:

$$\tilde{W}_m^0 \equiv \Gamma_m^0 W_m'^0 = \frac{1}{\hat{\gamma}} [(m_f \Gamma_f + m \Gamma) c^2 - (m + m_f) \Gamma_m^0 c^2] + \Gamma W'. \quad (9.8)$$

In the last stage of evolution, the merged shell moves in the CBM and interacts with it, giving rise to the standard afterglow radiation. Note that another degeneracy occurs. In fact, the same value of Γ_m^0 can be obtained for different pairs of $(\tilde{E}_{k,\text{iso}}, n_0)$ or

$(\tilde{E}_{k,\text{iso}}, A_\star)$. Thus, different initial conditions can lead to the same initial setup of the merged shell, nevertheless as discussed in Appendix B.2 and in Sec. 9.3, this degeneracy is not reflected in the observed photon flux.

The dynamics of the slow shell depends on the comoving dynamical time [407],

$$t'_{\text{dyn}} \simeq \frac{R}{8\Gamma c}, \quad (9.9)$$

and the related comoving width is [94]

$$l' \simeq ct'_{\text{dyn}} = \frac{R}{8\Gamma}, \quad (9.10)$$

where the radius R is defined in Eq. 9.5.

The fast shell propagates with constant Lorentz factor $\Gamma_f \gg 1$, thus its radius evolves as [281]:

$$R_f = \frac{2\Gamma_f^2(t - \Delta_T)c}{(1+z)}. \quad (9.11)$$

The comoving dynamical time of the fast shell is given by

$$t'_{\text{dyn},f} \simeq \frac{R_f}{2\Gamma_f c}, \quad (9.12)$$

and its comoving width is

$$l'_f \simeq ct'_{\text{dyn},f} = \frac{R_f}{2\Gamma_f}. \quad (9.13)$$

The initial width of the merged shell is approximated as

$$l'_m \simeq \Gamma_m^0 \left(\frac{l'_f}{\Gamma_f} + \frac{l'}{\Gamma} \right); \quad (9.14)$$

while the dynamical time characterizing the merged shell at the collision is

$$t'^0_{\text{dyn},m} \simeq \frac{l'_m}{c}, \quad (9.15)$$

where we have considered the Lorentz transformation for the length between the comoving and laboratory frames.

After a transient phase during which the merged shell relaxes, it is decelerated by the CBM and enters the BM regime. Since we neglect the time needed by the merged shell to relax soon after the merger, a sharp jump results in the light curve; this treatment is not adequate for realistic fits of the electromagnetic signal, see Sec. 9.3.2 for a discussion, but such task is beyond the scope of this paper. The semi-analytical treatment of the hydrodynamics of the collision, also taking into account the reverse shock

crossing the fast shell was obtained in Ref. [280]; considering such a treatment would not substantially affect the neutrino signal, since current and future neutrino telescopes may only be sensitive to the time-integrated spectral distribution in the most optimistic scenarios (see Sec. 9.6).

Once the merged shell enters the BM regime, its Lorentz factor Γ_m evolves as described by Eqs. 9.3, by replacing $\Gamma_0 \rightarrow \Gamma_m^0$ and using the appropriate deceleration time. Indeed, even though the dynamics of the merged shell resembles the BM solution, there are some important and non trivial precautions to take into account for the definition of its deceleration radius and time, see Appendix B.1. This is due to the fact that the merged shell is already hot and contains swept-up material. Once the deceleration time of the merged shell is properly defined, its radius R_m follows Eq. 9.5 by replacing $\Gamma \rightarrow \Gamma_m$. Finally, the width and dynamical time of the merged shell after its deceleration are given by Eqs. 9.9 and 9.10, with $\Gamma \rightarrow \Gamma_m$ and $R \rightarrow R_m$.

9.3 Photon energy distribution and light curve

In this section, we introduce the main ingredients for the modeling of the emission of electromagnetic radiation during the classic afterglow and at the shell merger which produces the optical jump. In the following, we consider a generic shell with Lorentz factor Γ for the sake of simplicity, however our treatment holds for the afterglow generated both by the slow and the merged shell. The proper Lorentz factor has to be taken into account for each case, i.e. Eqs. 9.3 and 9.4 for the slow and the merged shell during the afterglow with the appropriate initial Lorentz factor and deceleration time, as discussed in Sec. 9.2.2. As for the collision, the relevant Lorentz factor is given by Eq. 9.6.

9.3.1 Photon energy distribution during the afterglow

It is assumed that particles undergo Fermi acceleration [495, 480, 498] at the forward shock. The synchrotron radiation coming from shock accelerated electrons is broadly considered to be the origin of the observed afterglow light curve [431]. For the modeling of the synchrotron photon spectrum, we follow Refs. [431, 129, 376]. The internal energy density of the blastwave is given by the shock jump conditions (Eqs. B.3 and B.4). Therefore, the internal energy density generated by the forward shock is [94]:

$$w' = 4m_p c^2 \Gamma(\Gamma - 1)n, \quad (9.16)$$

where $n = n_0$ and $n = AR^{-2}$ for the ISM and wind scenarios, respectively. A fraction ϵ_e of this energy goes into accelerated electrons, a fraction ϵ_B into magnetic field, while

protons receive the fraction $\epsilon_p \lesssim 1 - \epsilon_e - \epsilon_B$. Thus, the magnetic field generated by the shock at the BM blastwave front is

$$B' = \sqrt{32\pi m_p c^2 n \Gamma (\Gamma - 1) \epsilon_B}. \quad (9.17)$$

Electrons are expected to be accelerated to a power-law distribution $N_e(\gamma_e) \propto \gamma_e^{-k_e}$, where k_e is the electron spectral index. The resulting electron distribution has three characteristic Lorentz factors: minimum ($\gamma'_{e,\min}$), cooling ($\gamma'_{e,\text{cool}}$), and maximum ($\gamma'_{e,\max}$) ones. The minimum Lorentz factor corresponds to the minimum injection energy of electrons in the blastwave; the cooling Lorentz factor characterizes the energy of electrons that have time to radiate a substantial fraction of their energy in one dynamical time; the maximum Lorentz factor corresponds to the maximum energy that electrons can achieve in the acceleration region [431, 520]. These characteristic Lorentz factors are given by [431]:

$$\gamma'_{e,\min} = \epsilon_e \frac{m_p (k_e - 2)}{m_e (k_e - 1)} (\Gamma - 1), \quad (9.18)$$

$$\gamma'_{e,\text{cool}} = \frac{6\pi m_e c (1+z)}{\sigma_T B'^2 t \Gamma}, \quad (9.19)$$

$$\gamma'_{e,\max} = \left(\frac{6\pi e}{\sigma_T B' \xi} \right)^{1/2}, \quad (9.20)$$

where $\sigma_T = 6.65 \times 10^{-25} \text{ cm}^{-2}$ is the Thompson cross section, ξ represents the number of gyroradii needed for accelerating particles, $m_e = 5 \times 10^{-4} \text{ GeV } c^{-2}$ is the electron mass and $e = \sqrt{\alpha \hbar c}$ is the electron charge, where $\alpha \sim 1/137$ is the fine-structure constant and $\hbar \simeq 6.58 \times 10^{-25} \text{ GeV s}$ is the reduced Planck constant. We take $\xi \equiv 10$ [192]. The three characteristic Lorentz factors result into three observed characteristics break energies $E_{\gamma,\min}$, $E_{\gamma,\text{cool}}$ and $E_{\gamma,\max}$, in the synchrotron photon spectrum at Earth:

$$E_\gamma \equiv h\nu_\gamma = \frac{3}{2} \frac{B'}{B_Q} m_e c^2 \gamma_e'^2 \frac{\Gamma}{(1+z)}, \quad (9.21)$$

where $B_Q = 4.41 \times 10^{13} \text{ G}$. The electrons are in the “fast cooling regime” when $\nu_{\gamma,\min} > \nu_{\gamma,\text{cool}}$, while the “slow cooling regime” occurs when $\nu_{\gamma,\min} < \nu_{\gamma,\text{cool}}$.

For the picture to be complete, the synchrotron self-absorption (SSA) frequency should be considered as well. However, properly accounting for the SSA requires detailed information about the shell structure and the eventual thermal electron distribution [493]. Since this frequency is expected to be in the radio band [520], and since its inclusion does not change the results presented herein, we neglect SSA in the rest of this paper.

We are interested in the comoving photon density in the blastwave [in units of $\text{GeV}^{-1} \text{cm}^{-3}$]. In the fast cooling regime, it is given by [431, 472]:

$$n'_\gamma(E'_\gamma) = A'_\gamma \begin{cases} \left(\frac{E'_\gamma}{E'_{\gamma,\text{cool}}}\right)^{-\frac{2}{3}} & E'_\gamma < E'_{\gamma,\text{cool}} \\ \left(\frac{E'_\gamma}{E'_{\gamma,\text{cool}}}\right)^{-\frac{3}{2}} & E'_{\gamma,\text{cool}} \leq E'_\gamma \leq E'_{\gamma,\text{min}} \\ \left(\frac{E'_{\gamma,\text{min}}}{E'_{\gamma,\text{cool}}}\right)^{-\frac{3}{2}} \left(\frac{E'_\gamma}{E'_{\gamma,\text{min}}}\right)^{-\frac{(k_e+2)}{2}} e^{-\frac{E'_\gamma}{E'_{\gamma,\text{max}}}} & E'_{\gamma,\text{min}} < E'_\gamma \leq E'_{\gamma,\text{max}} \end{cases} \quad (9.22)$$

while, in the slow cooling regime, it is

$$n'_\gamma(E'_\gamma) = A'_\gamma \begin{cases} \left(\frac{E'_\gamma}{E'_{\gamma,\text{min}}}\right)^{-\frac{2}{3}} & E'_\gamma < E'_{\gamma,\text{min}} \\ \left(\frac{E'_\gamma}{E'_{\gamma,\text{min}}}\right)^{-\frac{(k_e+1)}{2}} & E'_{\gamma,\text{min}} \leq E'_\gamma \leq E'_{\gamma,\text{cool}} \\ \left(\frac{E'_{\gamma,\text{cool}}}{E'_{\gamma,\text{min}}}\right)^{-\frac{(k_e+1)}{2}} \left(\frac{E'_\gamma}{E'_{\gamma,\text{cool}}}\right)^{-\frac{(k_e+2)}{2}} e^{-\frac{E'_\gamma}{E'_{\gamma,\text{max}}}} & E'_{\gamma,\text{cool}} < E'_\gamma \leq E'_{\gamma,\text{max}} \end{cases} \quad (9.23)$$

Here $E'_\gamma \equiv h\nu'_\gamma$ is the comoving photon energy. The normalization constant is

$$A'_\gamma = \frac{1}{2} \frac{L'_{\gamma,\text{max}}}{4\pi R^2 c \min(E'_{\gamma,\text{min}}, E'_{\gamma,\text{cool}})}, \quad (9.24)$$

where $L'_{\gamma,\text{max}} = N_e P'_{\text{max}}(\gamma'_{e,\text{min}}) \phi_e / (E'_{\gamma,\text{min}})$ is the comoving specific luminosity [in units of s^{-1}], and $1/2$ is the geometrical correction coming from the assumption of isotropic synchrotron emission in the comoving frame [151]. The number of electrons in the blastwave is $N_e = 4/3\pi n_0 R^3$ in the ISM scenario and $N_e = 4\pi AR$ in the wind scenario, while $P'_{\text{max}}(\gamma'_{e,\text{min}})$ is the maximum synchrotron power emitted by electrons with Lorentz factor $\gamma'_{e,\text{min}}$ and defined as $P'_{\text{max}}(\gamma'_{e,\text{min}}) = c\sigma_T B'^2 \gamma'_{e,\text{min}}{}^2 / (6\pi)$. Finally, $\phi_e \simeq 0.6$ is a constant depending on the spectral index k_e [506]; we adopt $k_e = 2.5$, as suggested from simulations of relativistic collisionless shocks [268, 445]. This value is also consistent with that obtained from the study of X-ray afterglows, see e.g. [141]. Note that for the classic afterglow, we consider the transition from fast to slow cooling through the time evolution of the blastwave. Indeed, at late times the blastwave is in the slow cooling regime, in agreement with observations (see e.g. [216, 367]).

9.3.2 Photon energy distribution during the shell merger

When the two shells collide, the internal energy \tilde{W}_m^0 is released, see Eq. 9.8⁴. Assuming that $\epsilon_{B,m}^0$ is the fraction of the internal comoving energy density released during the collision and going in magnetic energy density, the comoving magnetic field is

$$B_m^0 = \sqrt{8\pi\epsilon_{B,m}^0 w_m^0}, \quad (9.25)$$

where the comoving internal energy density is defined as

$$w_m^0 = \frac{\tilde{W}_m^0}{\Gamma_m^0 V_m^0} = \frac{\tilde{W}_m^0}{\Gamma_m^0 4\pi R(T_{\text{coll}})^2 l_m^0}, \quad (9.26)$$

where l_m^0 is given by Eq. 9.14 and $V_m^0 = 4\pi R(T_{\text{coll}})^2 l_m^0$ is the volume of the merged shell right after its creation.

We assume that, at the collision, electrons are accelerated with the same index as the one of the particles accelerated at the shock between the slow blastwave and the CBM ($k_e = 2.5$). The fraction $\epsilon_{e,m}^0$ of internal energy density released at the collision goes into accelerated electrons, which cool through synchrotron radiation. The characteristic energies of the resulting photon spectrum are $E_{\gamma,\text{min}}^{m,0}$, $E_{\gamma,\text{cool}}^{m,0}$ and $E_{\gamma,\text{max}}^{m,0}$ and are defined as in Eq. 9.21 by replacing $\Gamma \rightarrow \Gamma_m^0$, and where the magnetic field is given by Eq. 9.25.

The shell collision and the afterglow are two distinct processes. The former involves a hot and a cold shell, the latter is related to the interaction between the slow, hot shell and the cold CBM. Therefore, the microphysical parameters $\epsilon_{e,m}^0$ and $\epsilon_{B,m}^0$ do not need to be the same as ϵ_e and ϵ_B . Moreover, while observations suggest a slow cooling regime for the classic afterglow at late times, electrons accelerated at the collision might be either in the fast or in the slow cooling regime, depending on the relevant parameters.

If for fixed initial conditions of the colliding shells and collision time the condition $\gamma_{e,\text{min}}^{m,0} > \gamma_{e,\text{cool}}^{m,0}$ is verified, then the spectral energy distribution at the collision is

$$n_{\gamma}^{\prime m,0}(E_{\gamma}') = A_{\gamma}^{\prime m,0} \begin{cases} \left(\frac{E_{\gamma}'}{E_{\gamma,\text{cool}}^{\prime m,0}}\right)^{-\frac{2}{3}} & E_{\gamma}' < E_{\gamma,\text{cool}}^{\prime m,0} \\ \left(\frac{E_{\gamma}'}{E_{\gamma,\text{cool}}^{\prime m,0}}\right)^{-\frac{3}{2}} & E_{\gamma,\text{cool}}^{\prime m,0} \leq E_{\gamma}' \leq E_{\gamma,\text{min}}^{\prime m,0} \\ \left(\frac{E_{\gamma,\text{min}}^{\prime m,0}}{E_{\gamma,\text{cool}}^{\prime m,0}}\right)^{-\frac{3}{2}} \left(\frac{E_{\gamma}'}{E_{\gamma,\text{min}}^{\prime m,0}}\right)^{-\frac{(k_e+2)}{2}} e^{-\frac{E_{\gamma}'}{E_{\gamma,\text{max}}^{\prime m,0}}} & E_{\gamma,\text{min}}^{\prime m,0} < E_{\gamma}' \leq E_{\gamma,\text{max}}^{\prime m,0} \end{cases} \quad (9.27)$$

⁴For the sake of clarity, we denote the physical quantities characteristic of shell collision with the apex “0”, to distinguish them from the parameters describing the deceleration phase of the merged shell (marked with the subscript “m”).

where

$$A_{\gamma}^{\prime m,0} = \frac{\epsilon_{e,m}^0 \omega_m^{\prime 0}}{\int_{\gamma_{\min}^{\prime m,0}}^{\gamma_{\text{sat}}^{\prime m,0}} dE'_{\gamma} n_{\gamma}^{\prime m,0}(E'_{\gamma}) E'_{\gamma}}. \quad (9.28)$$

If instead $\gamma_{e,\min}^{\prime m,0} < \gamma_{e,\text{cool}}^{\prime m,0}$, then the photon density is properly described by a slow cooling spectrum

$$n_{\gamma}^{\prime m,0}(E'_{\gamma}) = A_{\gamma}^{\prime m,0} \begin{cases} \left(\frac{E'_{\gamma}}{E_{\gamma,\min}^{\prime m,0}}\right)^{-\frac{2}{3}} & E'_{\gamma} < E_{\gamma,\min}^{\prime m,0} \\ \left(\frac{E'_{\gamma}}{E_{\gamma,\min}^{\prime m,0}}\right)^{-\frac{(k_e+1)}{2}} & E_{\gamma,\min}^{\prime m,0} \leq E'_{\gamma} \leq E_{\gamma,\text{cool}}^{\prime m,0} \\ \left(\frac{E_{\gamma,\text{cool}}^{\prime m,0}}{E_{\gamma,\min}^{\prime m,0}}\right)^{-\frac{(k_e+1)}{2}} \left(\frac{E'_{\gamma}}{E_{\gamma,\text{cool}}^{\prime m,0}}\right)^{-\frac{(k_e+2)}{2}} e^{-\frac{E'_{\gamma}}{E_{\gamma,\text{max}}^{\prime m,0}}} & E_{\gamma,\text{cool}}^{\prime m,0} < E'_{\gamma} \leq E_{\gamma,\text{max}}^{\prime m,0} \end{cases} \quad (9.29)$$

where

$$A_{\gamma}^{\prime m,0} = \frac{\epsilon_{e,m}^0 \omega_m^{\prime 0}}{\int_{\gamma_{\min}^{\prime m,0}}^{\gamma_{\text{sat}}^{\prime m,0}} dE'_{\gamma} n_{\gamma}^{\prime m,0}(E'_{\gamma}) E'_{\gamma}} \left(\frac{\gamma_{e,\text{cool}}^{\prime m,0}}{\gamma_{e,\min}^{\prime m,0}}\right)^{-(k_e+2)}. \quad (9.30)$$

In the last expression we have taken into account the fact that only a fraction of electrons radiates.

9.3.3 Light curve

We now have all the ingredients for investigating the expected light curve if the merger of two relativistic shells occurs. We can distinguish between three time windows in the photon light curve: an “afterglow phase” ($T_{\text{dec}} \leq t < T_{\text{coll}}$), the “merging phase” responsible for the jump origin ($t = T_{\text{coll}}$), and a “late afterglow phase” ($t > T_{\text{dec},m}$, with $T_{\text{dec},m}$ given by Eq. B.28).

In our simplified model, the photon lightcurve is a stepwise function obtained as follows. For $T_{\text{dec}} \leq t < T_{\text{coll}}$, the flux results from the interaction between the slow shell and the external medium. Therefore, it is described by the synchrotron spectrum introduced in Sec. 9.3.1. At $t = T_{\text{coll}}$, the flux undergoes a sharp increase: this is obtained as the sum between the afterglow radiation generated by the slow shell at $t = T_{\text{coll}}$ and the synchrotron radiation instantaneously emitted at the collision, see Sec. 9.3.2 for its description. Finally, for $t > T_{\text{dec},m}$, the radiation comes from the deceleration of the merged shell. Thus, the light curve follows again the predicted broken power-law for the classic afterglow. The relations derived in Sec. 9.3.1 hold by applying the temporal evolution of the Lorentz factor and the radius of the merged shell as prescribed in Appendix B.1.

Let $F_\gamma^s(E_\gamma)$ and $F_\gamma^m(E_\gamma)$ be the photon fluxes at Earth obtained from the photon distributions of the slow and merged shell, respectively, i.e. Eqs. 9.22–9.23, taken with the proper Lorentz factor and radius; $F_\gamma^{m,0}(E_\gamma)$ is instead the photon flux from electrons accelerated at the collision, corresponding to the photon distributions Eqs. 9.27–9.29. Therefore, the resulting flux at Earth $F_\gamma(E_\gamma)$ reads as

$$F_\gamma(E_\gamma) = \begin{cases} F_\gamma^s(E_\gamma) & T_{\text{dec}} \leq t < T_{\text{coll}} \\ F_\gamma^s(E_\gamma, t = T_{\text{coll}}) + F_\gamma^{m,0}(E_\gamma) & t = T_{\text{coll}} \\ F_\gamma^m(E_\gamma) & t \geq T_{\text{dec,m}} \end{cases} \quad (9.31)$$

This prescription does not aim to fit the afterglow light curves in the presence of a jump. Rather, it is a qualitative parametrization useful for contrasting the neutrino signal in the presence of a jump with the classic afterglow case.

We conclude by observing that we cannot model the transition phase $T_{\text{coll}} < t < T_{\text{dec,m}}$ analytically. Indeed, we should take into account the time needed by the merged shell to relax before starting its deceleration; on the contrary, we are assuming an instantaneous merger. This approximation may lead to overestimate or underestimate the photon flux in the aforementioned time window. Even though this is may be problematic for the electromagnetic signal, it does not affect the neutrino forecast substantially, as discussed in Sec. 9.5.

9.4 Energy distributions of protons and neutrinos

In this section, the energy distribution of protons is introduced together with the most relevant cooling timescales. The steps followed to compute the neutrino flux expected at Earth are also outlined.

9.4.1 Proton energy distribution

We assume that protons are Fermi accelerated at the shock front, although the process responsible for particle acceleration is still subject to debate, see e.g. Refs. [445, 228, 357, 390, 266]. Accelerated protons have a non-thermal power-law plus exponential cutoff distribution defined in the frame comoving with the blastwave as

$$n'_p(E'_p) = A'_p E_p'^{-k_p} \exp\left[-\left(\frac{E'_p}{E'_{p,\text{max}}}\right)^{\alpha_p}\right] \Theta(E'_p - E'_{p,\text{min}}), \quad (9.32)$$

where Θ is the Heaviside function, $\alpha_p = 2$ [241] and k_p is the proton spectral index. The proton spectral index resulting from non-relativistic shock diffusive acceleration

theory is expected to be $k_p \simeq 2$ [313], while it is estimated to be $k_p \simeq 2.2$ from Monte Carlo simulations of ultra-relativistic shocks [445], assuming isotropic diffusion in the downstream. In this work, we assume $k_p = 2$. The normalization constant is $A'_p = \epsilon_p w' [\int_{E'_{p,\min}}^{E'_{p,\max}} dE'_p E'_p n'_p(E'_p)]^{-1}$, where $\epsilon_p + \epsilon_e + \epsilon_B \lesssim 1$ and w' is the comoving energy density of the blastwave. For the slow and merged shells, w' is given by Eq. 9.16, by considering the Lorentz factor and radius of the respective shell, while the energy density during the merger is given by Eq. 9.26. The minimum energy of accelerated protons is $E'_{p,\min} = \Gamma m_p c^2$ [151, 338, 407]. Finally, $E'_{p,\max}$ is the maximum energy up to which protons can be accelerated in the blastwave and is obtained by the constraint of the Larmor radius being smaller than the size of the acceleration region or imposing that the acceleration timescale,

$$t'_{p,\text{acc}} = \frac{ceB'}{\xi E'_p}, \quad (9.33)$$

is smaller than the total cooling timescale for protons. Similarly to the electrons, we assume that $\xi = 10$ for protons [192].

The total cooling timescale for protons, at a fixed time of the evolution of the blastwave, is

$$t'_{p,\text{cool}} = t'_{\text{ad}} + t'_{p,\text{sync}} + t'_{p\gamma} + t'_{pp} + t'_{p,\text{BH}} + t'_{p,\text{IC}}, \quad (9.34)$$

where t'_{ad} , $t'_{p,\text{sync}}$, $t'_{p\gamma}$, t'_{pp} , $t'_{p,\text{BH}}$, $t'_{p,\text{IC}}$ are the adiabatic, synchrotron, photo-hadronic ($p\gamma$), hadronic (pp), Bethe-Heitler (BH, $p\gamma \rightarrow pe^+e^-$) and inverse Compton (IC) cooling timescales, respectively; these are defined as follows [153, 192, 410]:

$$t'_{\text{ad}} = \frac{8c\Gamma}{R}, \quad (9.35)$$

$$t'_{p,\text{sync}} = \frac{4\sigma_T m_e^2 E'_p B'^2}{3m_p^4 c^3 8\pi}, \quad (9.36)$$

$$t'_{p\gamma} = \frac{c}{2\gamma_p'^2} \int_{E_{\text{th}}}^{\infty} dE'_\gamma \frac{n'_\gamma(E'_\gamma)}{E_\gamma'^2} \int_{E_{\text{th}}}^{2\gamma_p' E'_\gamma} dE_r E_r \sigma_{p\gamma}(E_r) K_{p\gamma}(E_r), \quad (9.37)$$

$$t'_{pp} = cn'_p \sigma_{pp} K_{pp}, \quad (9.38)$$

$$t'_{p,\text{BH}} = \frac{7m_e \alpha \sigma_T c}{9\sqrt{2}\pi m_p \gamma_p'^2} \int_{\gamma_p'^{-1}}^{\frac{E'_{\gamma,\max}}{m_e c^2}} d\epsilon' \frac{n'_\gamma(\epsilon')}{\epsilon'^2} \left\{ (2\gamma_p' \epsilon')^{3/2} \left[\ln(\gamma_p' \epsilon') - \frac{2}{3} \right] + \frac{2^{5/2}}{3} \right\}, \quad (9.39)$$

$$t'_{p,\text{IC}} = \frac{3(m_e c^2)^2 \sigma_T c}{16\gamma_p'^2 (\gamma_p' - 1) \beta_p'} \int_{E'_{\gamma,\min}}^{E'_{\gamma,\max}} \frac{dE'_\gamma}{E_\gamma'^2} F(E'_\gamma, \gamma_p') n'_\gamma(E'_\gamma), \quad (9.40)$$

where $\gamma_p = E'_p/m_p c^2$, $\epsilon' = E'_\gamma/m_e c^2$, $E_{\text{th}} = 0.150$ GeV is the threshold for photo-pion production, and $\beta_p' \approx 1$ for relativistic particles. The function $F(E'_\gamma, \gamma_p')$ is given in

Ref. [252], with the replacement $m_e \rightarrow m_p$. The cross sections for $p\gamma$ and pp interactions, $\sigma_{p\gamma}$ and σ_{pp} , are defined following Ref. [527]. The function $K_{p\gamma}(E_r)$ is the $p\gamma$ inelasticity, given by Eq. 9.9 in [153]:

$$K_{p\gamma}(E_r) = 0.2 \quad E_{\text{th}} < E_r < 1 \text{ GeV} \quad E_r > 1 \text{ GeV} \quad (9.41)$$

where $E_r = \gamma'_p E'_\gamma (1 - \beta'_p \cos \theta')$ is the relative energy between a proton with Lorentz factor γ'_p and a photon with energy E'_γ , moving such that they form an angle θ' in the comoving frame of the blastwave. The comoving proton density in the blastwave, n'_p , is obtained from the jump conditions (see Appendix B.1) and is such that $n'_p = 4n\Gamma$. The inelasticity of pp interactions is $K_{pp} \simeq 0.8$ [396] and $n'_\gamma(E'_\gamma)$ is the photon target for accelerated protons.

9.4.2 Neutrino energy distribution and flux expected at Earth

The blastwave is rich of photons radiated by shock accelerated electrons, which are ideal targets for protons co-accelerated at the shock. This results in efficient neutrino production through $p\gamma$ interactions, mostly dominated by the Δ^+ resonance:

$$p + \gamma \longrightarrow \Delta^+ \longrightarrow \begin{cases} n + \pi^+ & 1/3 \text{ of all cases} \\ p + \pi^0 & 2/3 \text{ of all cases} . \end{cases} \quad (9.42)$$

Neutral pions decay in two photons: $\pi^0 \longrightarrow 2\gamma$; while charged pions can produce neutrinos through the decay chain $\pi^+ \longrightarrow \mu^+ + \nu_\mu$, followed by the muon decay $\mu^+ \longrightarrow \bar{\nu}_\mu + \nu_e + e^+$. Note that, since the number of photons in the blastwave is much larger than the number of protons swept up from the CBM by the blastwave, we can safely neglect the contribution to the neutrino emission due to pp interactions. Indeed, the cooling timescales satisfy $t_{pp}^{-1} \ll t_{p\gamma}^{-1}$ for typical GRB afterglow parameters, as shown in Appendix B.3.

In order to compute the neutrino spectral energy distribution resulting from $p\gamma$ interactions, we rely on the semi-analytic photo-hadronic model described in Ref. [241]. This model is based on SOPHIA [336], which takes into account the Δ^+ channel in Eq. 9.42, as well as the N resonances, the multi-pion and direct-pion production channels.

The procedure adopted to compute the neutrino energy distribution is the same for all three time windows of our GRB afterglow model, after taking into account the corresponding distributions of photons and protons. Given the comoving photon energy distribution, $n'_\gamma(E'_\gamma)$, and the comoving proton energy distribution $n'_p(E'_p)$ [both in units of $\text{GeV}^{-1} \text{ cm}^{-3}$], the rate of production of secondary particles $l = \pi^\pm, \pi^0, K^+$ in the comoving frame [in units of $\text{GeV}^{-1} \text{ cm}^{-3} \text{ s}^{-1}$] is given by [241]:

$$Q'_l(E'_l) = c \int_{E'_l}^{\infty} \frac{dE'_p}{E'_p} n'_p(E'_p) \int_{E_{\text{th}}/2\gamma'_p}^{\infty} dE'_\gamma n'_\gamma(E'_\gamma) R(x, y), \quad (9.43)$$

where $x = E'_l/E'_p$ is the fraction of proton energy that goes into the secondary particles, $y = \gamma'_p E'_l$ and $R(x, y)$ is the response function, which contains information on the interaction, i.e. cross section and multiplicity.

Before decaying, charged mesons undergo energy losses. Their energy distribution at decay is approximated by:

$$Q'_l{}^{\text{dec}}(E'_l) = Q'_l(E'_l) \left[1 - \exp\left(-\frac{t'_{l,\text{cool}} m_l}{E'_l \tau'_l}\right) \right], \quad (9.44)$$

where $t'_{l,\text{cool}}$ is the cooling time scale of the l meson, m_l its mass and τ'_l its lifetime. Finally, mesons decay and the resulting neutrino comoving spectrum [in units of $\text{GeV cm}^{-3} \text{s}^{-1}$] is

$$Q'_{\nu_\alpha}(E'_\nu) = \int_{E'_\nu}^{\infty} \frac{dE'_l}{E'_l} Q'_l{}^{\text{dec}}(E'_l) F_{l \rightarrow \nu_\alpha}\left(\frac{E'_\nu}{E'_l}\right), \quad (9.45)$$

where $\alpha = e, \mu$ is the neutrino flavor at production and $F_{l \rightarrow \nu_\alpha}$ is a function defined as in Ref. [296]. Kaons suffer less from radiative cooling compared to charged pions, due to their larger mass and shorter lifetime. Thus, their contribution to the resulting neutrino spectrum is always sub-leading at lower energies, but may become dominant at higher energies [235, 62, 388, 467].

For a source at redshift z , the flux of neutrinos of flavor α expected at Earth [in units of $\text{GeV}^{-1} \text{cm}^{-2} \text{s}^{-1}$] is:

$$\Phi_{\nu_\alpha}(E_\nu, z) = \frac{(1+z)^2}{4\pi d_L^2(z)} V'_{\text{shell}} \sum_{\beta} P_{\nu_\beta \rightarrow \nu_\alpha}(E_\nu) Q'_{\nu_\beta}\left[\frac{E_\nu(1+z)}{\Gamma}\right], \quad (9.46)$$

where $V'_{\text{shell}} = 4\pi R^2 l'$ is the volume of the emitting shell [69] and l' its width. The neutrino oscillation probability $P_{\nu_\beta \rightarrow \nu_\alpha}(E_\nu)$ is such that $P_{\nu_\beta \rightarrow \nu_\alpha} = P_{\bar{\nu}_\beta \rightarrow \bar{\nu}_\alpha}$ and is given by [57]:

$$P_{\nu_e \rightarrow \nu_\mu} = P_{\nu_\mu \rightarrow \nu_e} = P_{\nu_e \rightarrow \nu_\tau} = \frac{1}{4} \sin^2 2\theta_{12}, \quad (9.47)$$

$$P_{\nu_\mu \rightarrow \nu_\mu} = P_{\nu_\mu \rightarrow \nu_\tau} = \frac{1}{8}(4 - \sin^2 \theta_{12}), \quad (9.48)$$

$$P_{\nu_e \rightarrow \nu_e} = 1 - \frac{1}{2} \sin^2 2\theta_{12}, \quad (9.49)$$

with $\theta_{12} \simeq 33.5^\circ$ [167]. The luminosity distance in a standard flat Λ CDM cosmology is

$$d_L(z) = (1+z) \frac{c}{H_0} \int_0^z \frac{dz'}{\sqrt{\Omega_\Lambda + \Omega_M(1+z')^3}}, \quad (9.50)$$

where we adopt $H_0 = 67.4 \text{ km s}^{-1} \text{ Mpc}^{-1}$, $\Omega_M = 0.315$, and $\Omega_\Lambda = 0.685$ [110].

9.5 Afterglow signals

In this section, we present our findings on the particle distributions expected at Earth from the GRB afterglow. We explore the photon light curve as well as the temporal evolution of the neutrino spectral energy distribution in three time windows: the afterglow generated by the first shell launched by the central engine, the time at which the fast shell collides and merges with the slow one, and the afterglow generated by the merged shell.

9.5.1 Particle emission in the absence of a late shell collision

We consider a benchmark GRB with characteristic parameters as in Table 9.1 and located at $z = 1$. The chosen value for the isotropic kinetic energy is motivated by post-Swift observations reporting an average isotropic energy emitted in photons $\tilde{E}_{\gamma,\text{iso}} = \mathcal{O}(10^{52})$ erg [117] and assuming a conversion efficiency of $\sim 10\% \tilde{E}_{\text{iso}}$ into gamma-rays, therefore leading to the isotropic kinetic energy $\tilde{E}_{k,\text{iso}} \sim 10^{53}$ erg. Moreover, we rely on the standard microphysical parameters reported in Ref. [431]. Since there is no evidence for the values of typical microphysical parameters characteristic of the collision, we fix $\epsilon_{e,m}^0 = \epsilon_e$ and $\epsilon_{B,m}^0 = \epsilon_B$. Finally, as for the CBM densities, we follow Refs. [431, 129].

Concerning the fast shell, we fix Γ_f by taking $\Delta_T \ll T_{\text{coll}}$, so that $\Gamma_f \simeq 2\Gamma(T_{\text{coll}})$ (see Appendix B.2). Since there are no theoretical constraints on the energy \tilde{E}_f , we fix the latter by following Ref. [483]. We choose $\tilde{E}_f = 2\tilde{E}_{\text{iso}}$ relying on the results of “case 4” of Ref. [483], for which the strongest rebrightening is obtained. Moreover, we fix $T_{\text{coll}} = 5 \times 10^3$ s both for the ISM and the wind scenarios. At this time the light curve is decreasing in both scenarios, and it has been chosen consistently with the observation of jumps between a few hundred seconds and ~ 1 day after the onset of the burst [358, 215, 290, 294].

In the classic afterglow scenario, the time evolution of the photon light curve at Earth, computed as described in Sec. 9.3.1, for our benchmark GRB is shown in Fig. 9.2

Table 9.1: Characteristic parameters assumed for our benchmark GRB afterglow in the ISM and wind CBM scenarios.

	$\tilde{E}_{k,\text{iso}}$ (erg)	Γ_0	n_0 (cm $^{-3}$) or A_\star	ϵ_e	ϵ_B	$\epsilon_{e,m}^0$	$\epsilon_{B,m}^0$	T_{coll} (s)	\tilde{E}_f (erg)	k_e	k_p
ISM	10^{53}	300	1.0	0.1	0.1	0.1	0.1	5×10^3	2×10^{53}	2.5	2
Wind	10^{53}	100	0.1	0.1	0.1	0.1	0.1	5×10^3	2×10^{53}	2.5	2

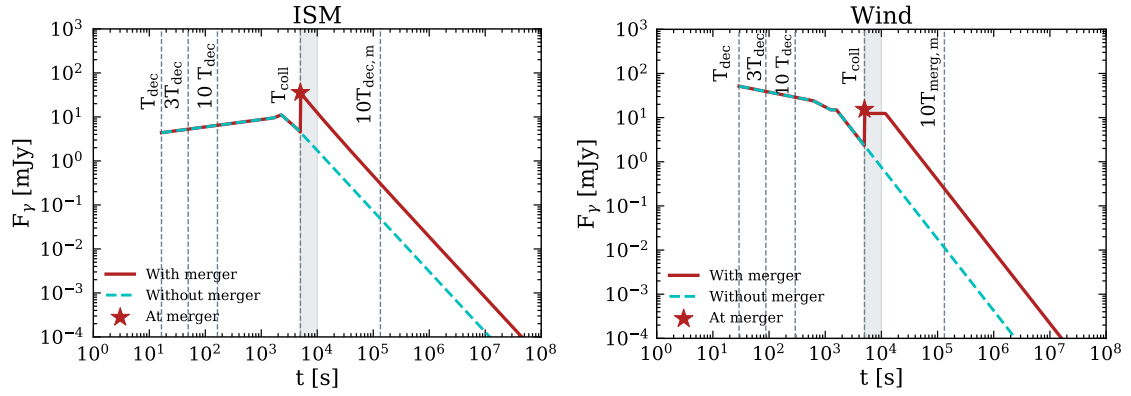


Figure 9.2: Light curves expected at Earth for our benchmark GRB at $z = 1$ for the classic afterglow scenario (cyan dashed line) and in the presence of an optical jump (brown solid line) for an observed photon frequency $\nu_\gamma = 6 \times 10^{14}$ Hz. The brown star marks the flux generated at T_{coll} . At the merger and after it, the observed flux is larger than the one expected from the classic afterglow. The gray shadowed region ($T_{\text{coll}} < t < T_{\text{dec,m}}$) is excluded from the computation of the neutrino signal since we cannot treat this transition phase analytically (see the main text for details). We assume a photon spectral index $k_e = 2.5$. In order to guide the eye, the vertical grey dashed lines mark the times at which we show snapshots of the spectral energy distribution of photons and neutrinos (see Figs. 9.3 and 9.4). These light curves should be considered for illustrative purposes only, since we assume the instantaneous shell collision for simplicity.

(cyan dashed line). The light curve is computed for an observed photon frequency $\nu_\gamma = 6 \times 10^{14}$ Hz, i.e. in the optical band. For both the ISM and wind scenarios, the breaks in the light curve are determined by the times at which the break frequencies $\nu_{\gamma,\text{min}}$ and $\nu_{\gamma,\text{cool}}$ cross the observed one ν_γ , and $\nu_{\gamma,\text{min}} = \nu_{\gamma,\text{cool}}$.

The photon and neutrino fluxes expected at Earth (see Sec. 9.4.2) are shown in Fig. 9.3 for $t = T_{\text{dec}}$, $3T_{\text{dec}}$, and $10T_{\text{dec}}$ (marked with vertical lines in Fig. 9.2) for the ISM and wind scenarios. We refer the interested reader to Appendix B.3 for a discussion on the characteristic cooling times of protons and mesons affecting the neutrino distributions. For both CBM cases, the flux at Earth decreases with time, as expected [431]. Moreover, the peak of the photon energy distribution and its energy breaks shift to lower energies as time increases. This is due to the fact that the minimum and cooling energies scale with time as $E_{\gamma,\text{min}} \propto t^{-3/2}$ $E_{\gamma,\text{cool}} \propto t^{-1/2}$, respectively [431].

In the right panels of Fig. 9.3, we show our results concerning the neutrino flux. In the wind scenario, the neutrino flux peaks at $E_\nu^{\text{peak}} \simeq 8.1 \times 10^7$ GeV for $t = T_{\text{dec}}$ and then decreases up to $E_\nu^{\text{peak}} \simeq 6.3 \times 10^7$ GeV for $t = 10T_{\text{dec}}$. For the ISM scenario, the neutrino flux peaks at $E_\nu^{\text{peak}} \simeq 7.7 \times 10^7$ GeV and at $E_\nu^{\text{peak}} \simeq 7.3 \times 10^7$ GeV for $t = 10T_{\text{dec}}$. The effect of kaon cooling is not visible, since as shown in Appendix B.3

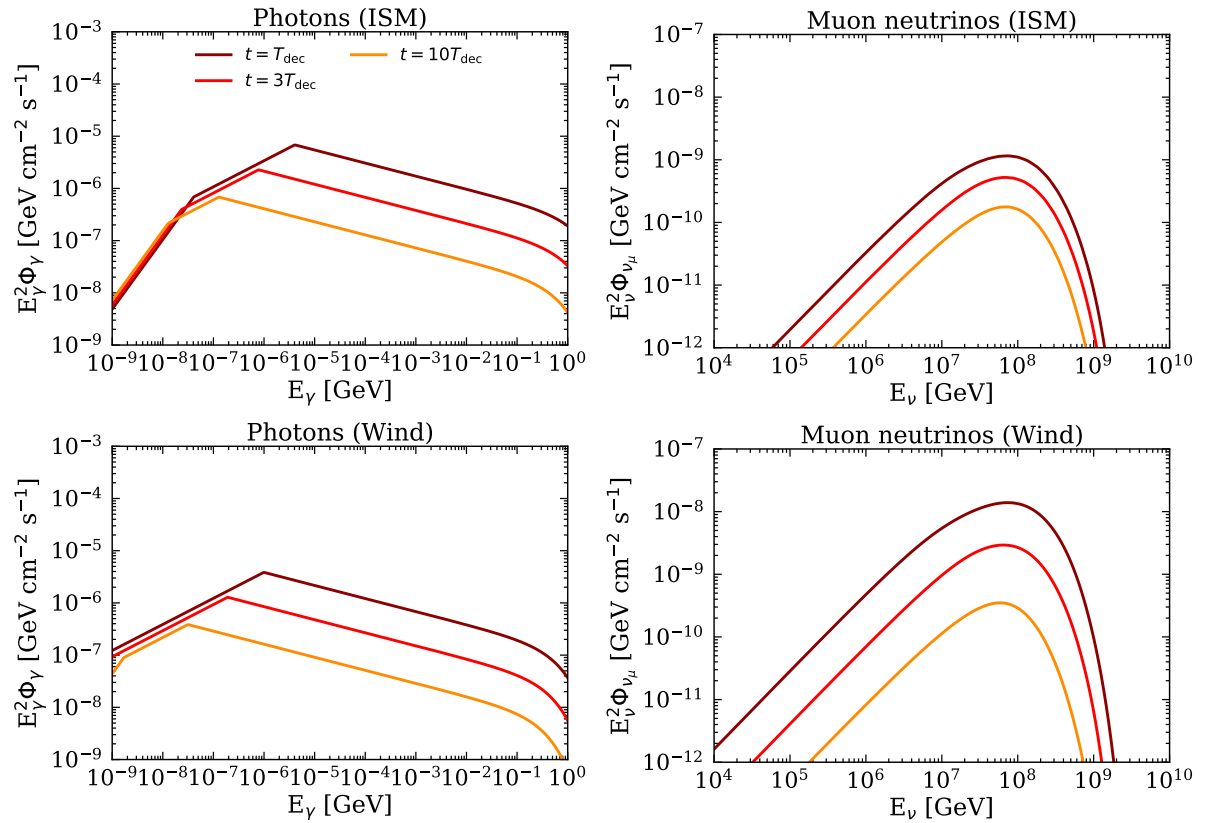


Figure 9.3: *Left:* Synchrotron photon flux expected at Earth for the classic afterglow scenario for $t = T_{\text{dec}}$, $3T_{\text{dec}}$, and $10T_{\text{dec}}$ (see the gray vertical lines in Fig. 9.2) for our benchmark GRB in Table 9.1 at $z = 1$. *Right:* Corresponding neutrino flux expected at Earth. Both fluxes for the wind scenario decrease faster than for the ISM scenario.

(see Fig. B.5) kaons cool at energies larger than the maximum energy of protons in the blastwave. Note that both the photon and the neutrino fluxes are larger in the wind scenario than in the ISM one, but they decrease faster in the wind case [407]. This is due to the fact that higher densities of the external medium can be initially reached within the wind profile. At such densities, the blastwave decelerates faster, leading to a rapidly decreasing flux [407]. The higher densities in the wind scenario also allow for higher magnetic fields, which cause the shift of the cooling frequency in the photon spectrum at energies lower than the ISM case. Of course, this is a direct consequence of the value adopted for ϵ_B .

The standard afterglow scenario has been already investigated in the literature for what concerns neutrino emission. Nevertheless, there are some relevant differences with respect to the results presented in this section. Our classic afterglow model resembles the one investigated in Refs. [407, 472]. However, by using the benchmark input parameters of Refs. [407, 472], we find a neutrino flux that is almost 5 orders of magnitude larger, but with an identical shape. This discrepancy might be caused by several reasons. First, there is a missing factor $(E'_{\gamma,\min}/E'_{\gamma,\text{cool}})^{-1/2}$ in the photon distribution in Eq. 11 of Ref. [407]; second, in the definition of the proton flux of Ref. [407] there is a factor $1/[4\pi(1+z)^2]$ in excess, which contributes to further lower the corresponding neutrino flux. On the other hand, our results on the photon and neutrino fluxes are in agreement with the ones in Refs. [431, 151], respectively.

The afterglow flux produced by the reverse shock has been investigated in Ref. [338], while we focus on the contribution from the forward shock. The neutrino flux obtained in Ref. [338] strictly depends on the assumptions on the thickness of the shell. For example, in the case of a thin shell with $\tilde{E}_{\text{iso}} = 4 \times 10^{52}$ erg and propagating in an ISM with $n_0 = 0.5 \text{ cm}^{-3}$, the estimated flux peaks at $E_\nu^{\text{peak}} \simeq 10^{10}$ GeV, where it should reach about $10^{-10} \text{ GeV cm}^{-2} \text{ s}^{-1}$ for a GRB at $z = 1$. This result is comparable with our maximum flux $\simeq 2 \times 10^{-9} \text{ GeV cm}^{-2} \text{ s}^{-1}$, considering that the isotropic energy adopted in Ref. [338] is one order of magnitude smaller than the one we adopt in this work. Nevertheless, the neutrino flux peaks at energies higher than ours in Ref. [338]. Indeed, our fluxes peak at $E_\nu \simeq 10^8$ GeV, in contrast with the peak at $\simeq 10^{10}$ GeV in [338], probably because of the different initial Γ_0 and because protons are expected to be accelerated at higher energies at the reverse shock. The most optimistic case considered in Ref. [338] is a thick shell propagating in a wind environment. In the latter scenario, the afterglow flux reaches an amplitude about ~ 2 orders of magnitude larger than ours at the peak energy $E_\nu \sim 10^9$ GeV, which is shifted by ~ 1 order of magnitude with respect to ours. Also for the wind scenario, the differences are mainly due to the energy of the ejecta, assumed to be ~ 4 times larger than ours, and the density of the environment up to 10 times larger than our benchmark value. Moreover, we rely on the thin shell assumption rather than the thick one, hence the results are not directly comparable. Finally, note that the emission from the reverse shock lasts

longer than the emission from the forward shock.

9.5.2 Particle emission in the presence of a late shell collision

In the presence of an optical jump, we model the afterglow light curve through the late collision of two relativistic shells. At $t = T_{\text{coll}}$, we compute the neutrino flux as described in Sec. 9.4.2 and by using the photon distribution introduced in Sec. 9.3.2. After the merger, the resulting merged shell starts to be decelerated by the external medium, emitting radiation with the standard features expected during the afterglow, as discussed in Sec. 9.5.1, but with the parameters characteristic of the merged shell. Since energy has been injected in the slow shell during the merger, the merged shell is more energetic than the slow one. Thus, we obtain a higher photon flux as shown in Fig. 9.2 (brown continuous line). The star denotes the flux at $t = T_{\text{coll}}$, given by the sum of the afterglow radiation (see Sec. 9.5.1) generated by the slow shell and the radiation from the shocks developing at the collision. For our choice of parameters, electrons accelerated at the collision are in the slow cooling regime both in the ISM and wind scenario (see Appendix B.1 and figures therein). Therefore, the appropriate photon distribution is given by Eq. 9.29.

Since it is assumed that the merger occurs instantaneously at the collision time, we are not taking into account the time needed by the merged shell to relax before being decelerated to the BM solution. Because of this approximation, we neglect the neutrinos produced for $T_{\text{coll}} < t < T_{\text{dec,m}}$, since an analytic treatment in this transition phase is not feasible, as already mentioned in Sec. 9.3.3. The time window excluded from our calculations of the neutrino signal corresponds to the gray shadowed area in Fig. 9.2. Note that, for most of the initial configurations of the slow shell, we find $T_{\text{dec,m}} \simeq 2 T_{\text{coll}}$. The exclusion of such a time window in our calculation negligibly affects the overall time-integrated neutrino signal, which is the main goal of this work (see Sec. 9.6).

Figure 9.4 shows the photon and muon neutrino fluxes at $t = T_{\text{coll}}$ and after the merger at $t = 10T_{\text{dec,m}}$ for the ISM and wind scenarios. These times are marked in Fig. 9.2 by vertical lines. For comparison, we also show the photon and neutrino fluxes that would be generated at $t = 10T_{\text{dec,m}}$ if no merger occurred. In both CBM scenarios, the neutrino flux increases in the presence of a jump, as expected, due to the denser photon field leading to more efficient $p\gamma$ interactions (see also the cumulative number of muon neutrinos plotted as a function of time in Fig. 9.5).

The peak of the neutrino distribution at late times in Fig. 9.4 is shifted at higher energies compared to the case without merger. This is explained because the energy density content of the merged shell is larger than the one of the slow shell, thus the corresponding magnetic field is larger as well. This results into a greater maximum

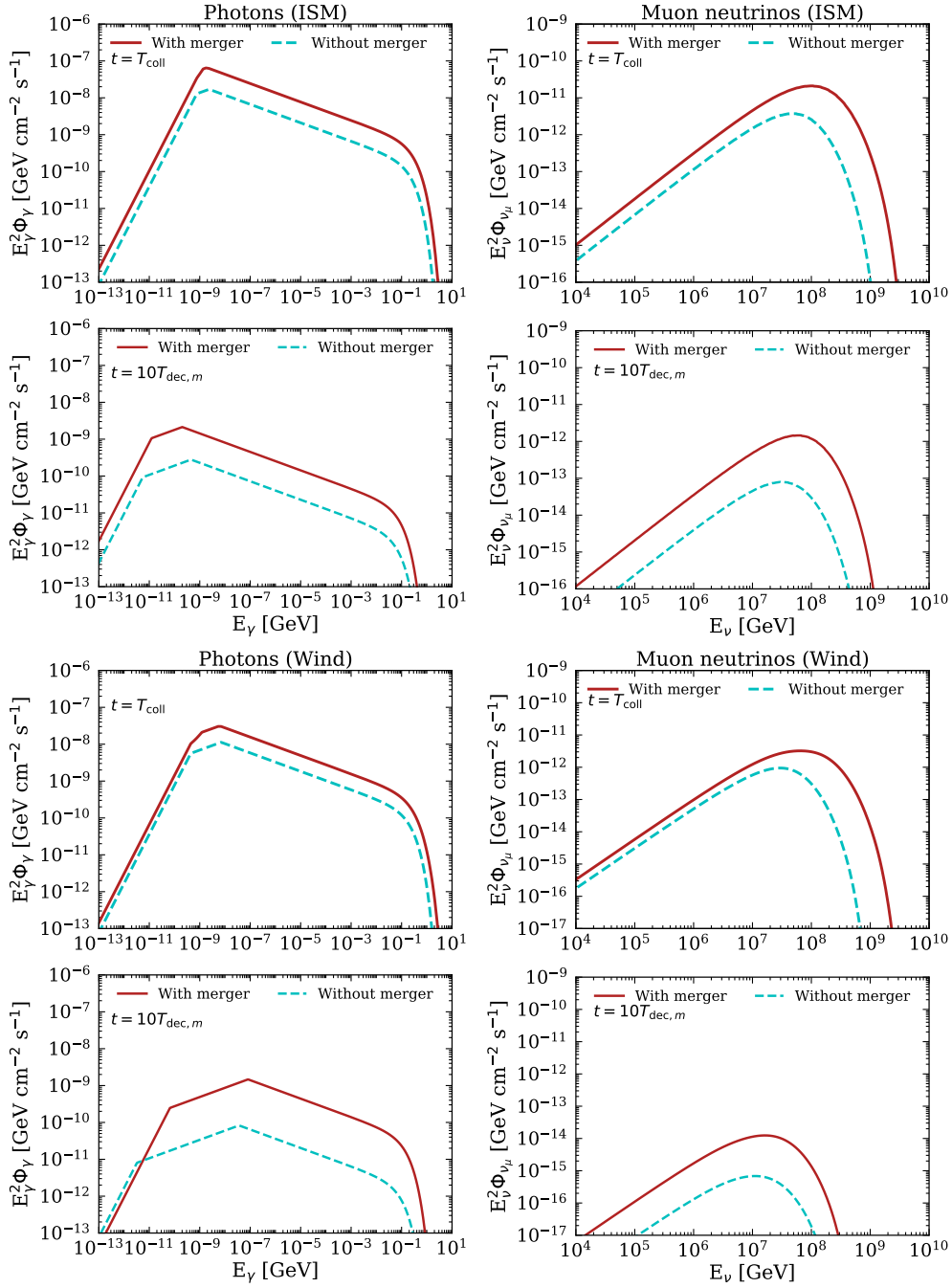


Figure 9.4: Photon (on the left) and neutrino (on the right) fluxes expected at Earth as functions of the particle energy from the afterglow when the merger of two relativistic shells occurs for the ISM (top two panels) and wind (bottom two panels) scenarios for our benchmark GRB in Table 9.1 at $z = 1$. For each CBM scenario, the fluxes are shown at $t = T_{\text{coll}}$ and $10 T_{\text{dec},m}$ (see vertical lines in Fig. 9.2). The brown lines display the total expected flux in the presence of a merger, while the cyan lines represent the flux that would be observed in the absence of a jump. The late shell merger enhances the photon and neutrino fluxes compared to the standard afterglow scenario and shifts the peak of the energy distributions at larger energies.

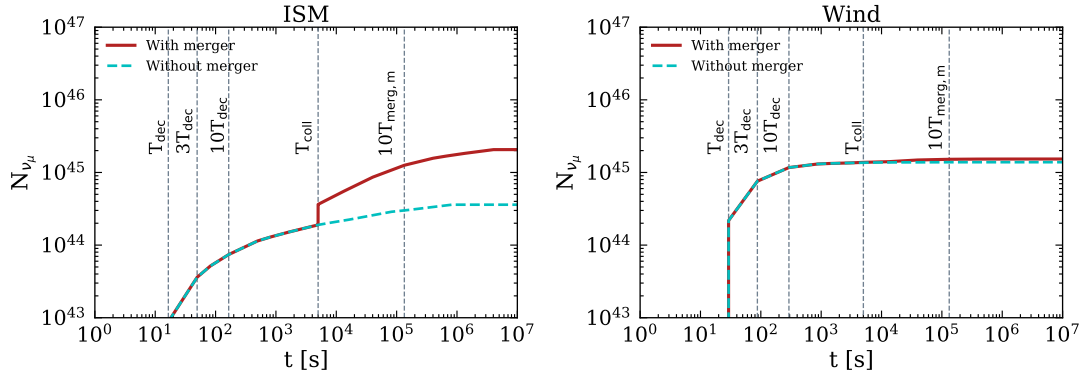


Figure 9.5: Cumulative number of muon neutrinos expected at Earth for the ISM (left panel) and wind (right panel) scenarios as a function of time for our benchmark GRB (Table 9.1) at $z = 1$. The brown solid line represents the number of muon neutrinos produced when the shell merger occurs, while the cyan dashed line corresponds to the case of the classic afterglow. In order to guide the eye, the gray vertical lines mark the times at which we show the neutrino flux at Earth for the classic afterglow scenario (Fig. 9.3) and when a jump occurs (Fig. 9.4). In the ISM environment, the jump significantly increases the cumulative number of neutrinos, while the difference between the two scenarios is negligible in the wind case.

energy of protons in the merged blastwave since $E'_{p,\max}$ depends linearly on the magnetic field; indeed, the acceleration time (see Eq. (9.33)) limits the maximum energy of protons. Finally, the quantities entering the Lorentz transformation of the flux at Earth (e.g. the Lorentz factor) are larger for the merged shell than for the slow one.

From Fig. 9.5, we can see that the number of neutrinos at T_{coll} is given by the sum of the neutrinos produced at the shock front between the slow shell and the CBM and the neutrinos produced at the collision between the slow and fast shells. After the merger, the only contribution comes from the afterglow of the merged shell. By comparing the left and right panels of Fig. 9.5, we note that a larger efficiency in the neutrino production is achieved in the ISM scenario in the presence of shell merger. In particular, for the ISM scenario the number of neutrinos increases by a factor of 6. This result is justified in light of the fact that the neutrino flux rapidly decreases for a wind-like CBM. Thus, the early time emission dominates the time-integrated neutrino flux. Motivated by these results, in the next section we discuss the detection prospects for neutrinos produced during the GRB afterglow when a jump occurs in the light curve.

9.6 Neutrino detection perspectives

In this section, we explore whether the increase in the number of neutrinos expected in the presence of an optical jump could reflect improved detection perspectives at

ongoing and future generation neutrino telescopes. We explore the detection prospects for the all-sky quasi-diffuse flux as well as point source searches. Finally, we forecast the expected neutrino fluence from GRB 100621A and for a second hypothetical GRB with parameters inspired by the bright GRB 130427A.

9.6.1 All-sky quasi-diffuse flux

The average isotropic kinetic energy from the catalogue of the Gehrels Swift Observatory is $\bar{E}_{k,\text{iso}} \simeq 10^{53}$ erg [293] and the redshift distribution peaks at $z \simeq 2$ [248]. Hence, we compute the all-sky quasi-diffuse flux by placing our benchmark GRB at $z = 2$ and assuming that its flux is representative of the GRB population. For a GRB rate of $\dot{N} \sim 700 \text{ yr}^{-1}$ [27, 7, 372] and an isotropic distribution of all the sources in the sky, the all-sky quasi-diffuse flux is:

$$F_{\nu_\mu}(E_\nu) = \frac{\dot{N}}{4\pi} \int dt \Phi_{\nu_\mu}(E_\nu, z = 2), \quad (9.51)$$

being Φ_{ν_μ} defined as in Eq. 9.46. In the case of the afterglow generated by the slow and the merged shells, we perform the time integration for $t \in [T_{\text{dec}}, T_{\text{Sedov}}]$, where T_{Sedov} marks the Sedov time when the blastwave becomes non-relativistic and enters the Newtonian regime. At T_{coll} the integration over time is replaced by the product with $t_{\text{dyn},m}^0 = t'_{\text{dyn},m}(1+z)/\Gamma_m^0$, where $t'_{\text{dyn},m}$ is given by Eq. (9.15), since the collision is considered to be an instantaneous process.

The top panels of Fig. 9.6 show the all-sky quasi-diffuse neutrino flux in the absence of shell merger, i.e. if the light curve resembles the standard afterglow scenario, for the ISM and wind scenarios. For the ISM scenario, the band corresponds to $1 \lesssim n_0 \lesssim 10 \text{ cm}^{-3}$; while for the wind scenario, the band includes $0.01 \lesssim A_\star \lesssim 0.1$.

So far, the IceCube Neutrino Observatory has detected neutrinos with energies up to a few PeV [46, 45, 23, 17]. Even though several sources have been proposed to explain the origin of high-energy neutrinos [321, 494, 337, 57, 482], only a handful of possible associations have been presented between neutrinos and active galactic nuclei, tidal disruption events (TDEs), and superluminous supernovae [11, 205, 180, 193, 277, 254, 455, 416, 397]. In particular, limits on the quasi-diffuse neutrino flux from GRBs have been placed by the IceCube Collaboration by taking into account the prompt emission [7], while a similar analysis on the afterglow phase is missing. A statistical analysis aiming to look for temporal and spatial coincidences between GRB afterglows and neutrinos detected by the IceCube Neutrino Observatory has been carried out in Ref. [27]. In agreement with the findings of Ref. [27], our quasi-diffuse flux does not overshoot existing upper limits on the prompt emission reported by IceCube [7] and by the ANTARES collaboration [49], as well as the ones expected for KM3NeT [40]. Despite differences

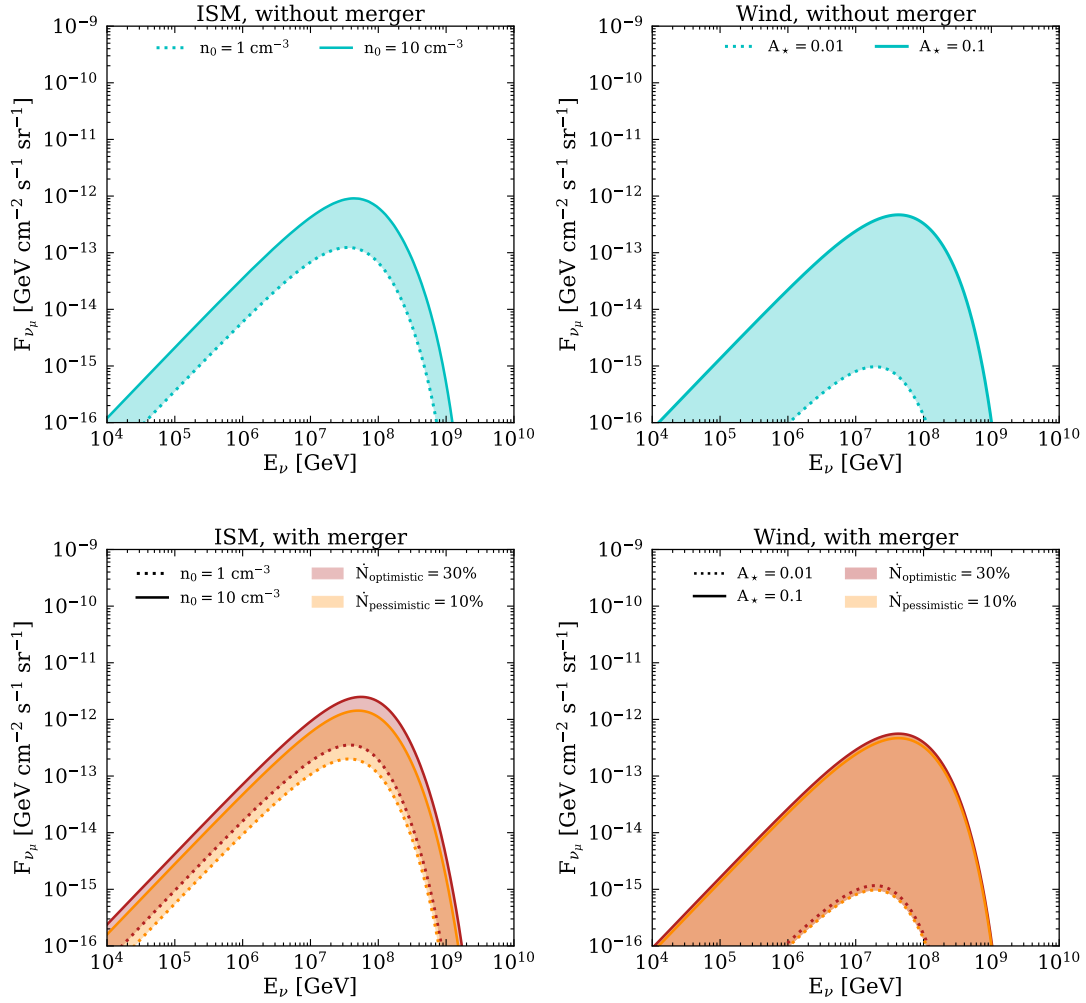


Figure 9.6: All-sky quasi-diffuse muon neutrino flux from GRB afterglows for the constant density (left panels) and wind (right panels) CBM scenarios, for the standard GRB afterglow (top panels) and the case with optical jumps (bottom panels). For the ISM scenario, the band is defined by $1 \lesssim n_0 \lesssim 10 \text{ cm}^{-3}$ (dotted and solid lines, respectively). For the wind scenario, the band is defined by $0.01 \lesssim A_\star \lesssim 0.1$. For the bottom panels, the quasi-diffuse neutrino flux is computed for the optimistic scenario with $\dot{N}_{\text{optimistic}} = 30\% \dot{N}$ (brown shadowed region) and $\dot{N}_{\text{pessimistic}} = 10\% \dot{N}$ (orange shadowed region). In the presence of optical jumps, the all-sky quasi-diffuse flux slightly increases for the ISM scenario, while negligible changes occur for the wind case. For the wind environment, there is no difference between the optimistic and pessimistic cases since the classic afterglow always dominates the neutrino fluence. In the cases with and without shell merger, the all-sky quasi-diffuse neutrino flux is in agreement with the results on GRB afterglow neutrino searches reported in Ref. [27] and it does not overshoot the IceCube limits on the GRB prompt emission [7], as well as the limits placed by the ANTARES collaboration [49] and the expected ones for KM3NeT [40].

in the theoretical modeling of the expected signal, our conclusions are also consistent with the detection prospects for the GRB afterglow neutrinos outlined in Ref. [411].

Assuming that jumps occur in the afterglow light curve, the corresponding all-sky quasi-diffuse muon neutrino flux is shown in the bottom panels of Fig. 9.6 for the two CBM scenarios. Since the fraction of GRB afterglows having optical jumps is largely uncertain [290, 294], we consider an optimistic (pessimistic) case such that the rate of GRBs per year with jumps is 30% (10%) of \dot{N} (see Eq. 9.51). The “pessimistic” fraction of GRBs with optical jumps is extrapolated by the analysis carried out in Ref. [294], where they estimate that 10 out of 146 GRBs with well resolved optical light curves displayed a jump. The “optimistic” fraction of GRBs with optical jumps is obtained by considering that the actual fraction of GRBs with optical jumps is not known and existing constraints may be plagued by observational biases, most notably the missing complete coverage over the first few hours. Therefore, we assume an upper limit of $\sim 30\%$ of the GRB population displaying a jump in the light curve.

The all-sky quasi-diffuse neutrino flux for the ISM scenario is enhanced by a factor ~ 3 by assuming that 30% of the GRB afterglows shows jumps. On the contrary, for the wind scenario, the variation is basically null since the neutrino fluence is dominated by the early-time flux, i.e. the neutrino emission expected from the standard afterglow. This is due to the fact that, as mentioned in Sec. 9.4.2, the flux quickly decreases for the wind profile. Thus, at the time of the shell collision, the flux is already small and does not contribute to the quasi-diffuse emission substantially. Even though the presence of optical jumps slightly enhances the all-sky quasi-diffuse flux, the latter is still below the limit for the prompt phase of IceCube and is consistent with the results of Ref. [27].

The neutrino diffuse emission associated with late optical jumps has been investigated in [229] for optical flares occurring after 1 day from the onset of the prompt emission, thus at times larger than the ones considered in this work. Moreover, Ref. [229] carries out an approximated theoretical modeling of the jump and uses fixed values for the radius of the outflow and its Lorentz factor, while we embed the temporal evolution of the blastwave and consistently model the shell merger. In Ref. [229], a distance of $R \simeq 10^{13}$ cm with Lorentz factor $\Gamma \simeq 10$ at $t = 1$ day is assumed. Through our approach and for the same luminosity, we obtain for the ejecta (that we assumed to be the slow shell) $R \simeq 10^{17}$ cm for $\Gamma \simeq 4$. In the light of these differences, we conclude that our results are not directly comparable to the ones in Ref. [229]. Furthermore, the estimation reported in Ref. [229] is based on Ref. [348], where the expected neutrino signal from the X-ray flares is computed by assuming the late internal shock scenario of Ref. [169]. This model assumes that shock heated electrons in the BM shell are cooled through external inverse Compton scattering. On the other hand, in this work, we only consider synchrotron emission. Despite the major differences in the modeling with respect to this work, Ref. [229] also concludes that the optical jump leads to an increase in the expected number of neutrinos.

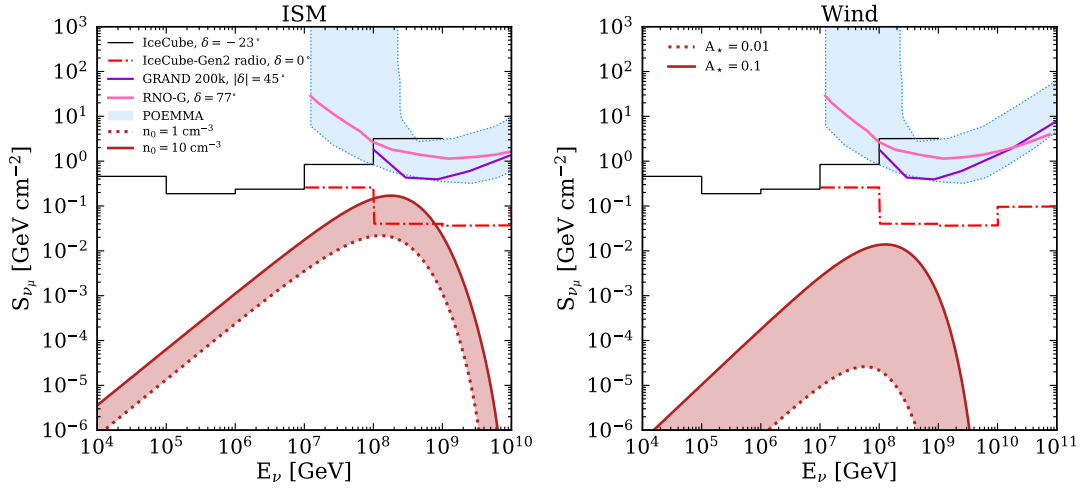


Figure 9.7: Muon neutrino fluence for our benchmark GRB afterglow with an optical jump at $d_L = 40$ Mpc (brown shadowed region) for the ISM (left panel) and wind (right panel) scenarios. The fluence bands correspond to $1 \lesssim n_0 \lesssim 10 \text{ cm}^{-3}$ and $0.1 \lesssim A_* \lesssim 0.01$ (dotted and solid lines for the lower and upper bounds, respectively). The expected fluence is compared with the estimated sensitivities of IceCube-Gen2 radio for a source at $\delta = 0^\circ$ [28], IceCube for a source located at $\delta = -23^\circ$ [28, 9], RNO-G for a source at $\delta = 77^\circ$ [43], GRAND200k for a source at $|\delta| = 45^\circ$ [54], and the full range time-averaged sensitivity of POEMMA [479]. For the ISM scenario, IceCube-Gen2 radio shows promising detection prospects.

9.6.2 Point source searches

Figure 9.7 shows the fluence S_{ν_μ} for our benchmark GRB (Table 9.1) with an optical jump assuming a distance of 40 Mpc (brown-shadowed region) for the ISM (on the left) and wind (on the right) scenarios. We also assume a band for $1 \lesssim n_0 \lesssim 10 \text{ cm}^{-3}$ (ISM density) and $0.1 \lesssim A_* \lesssim 0.01$ (wind). We compare the expected muon neutrino fluence with the most optimistic sensitivity of IceCube-Gen2 radio expected for the declination angle of the source in the sky ($\delta = 0^\circ$) [28], the sensitivity of IceCube for a source located at $\delta = -23^\circ$ [28, 9], the sensitivity of RNO-G for a source at $\delta = 77^\circ$ [43], the sensitivity of GRAND200k for $|\delta| = 45^\circ$ [54], and the full range time-averaged sensitivity of POEMMA [479]⁵.

Other radio neutrinos detectors have already been operating in the past years, such as the Askaryan Radio Array (ARA) [52, 51], the Antarctic Ross Ice-Shelf ANTenna

⁵The declination angles for the detectors are not the same for all instruments since they have been chosen to guarantee the most optimistic conditions for detection. In addition, GRAND200k and POEMMA are designed to be sensitive to showers initiated by tau neutrinos. Nevertheless, the following flavor composition ($\nu_e : \nu_\mu : \nu_\tau$) $\simeq (1 : 1 : 1)$ [174] is expected at detection. Thus, the fluence of tau neutrinos expected at Earth is comparable to the one of muon neutrinos.

Neutrino Array (ARIANNA) [76, 77] and the Antarctic Impulsive Transient Antenna (ANITA) [209, 208]. Nevertheless, in the energy region where the afterglow fluence peaks these detectors have worse sensitivity compared to the ones displayed in Fig. 9.7 and thus we did not consider them in our analysis. Note also that, at these energies, the neutrino background could also be populated by cosmogenic neutrinos [275, 330, 484], neutrinos from TDE [219], newborn pulsars and millisecond magnetars [170, 173], in addition to GRB afterglow neutrinos [407, 338].

For a source at $d_L = 40$ Mpc, no detection of neutrinos is expected neither at IceCube—consistently with current non-observations—nor at GRAND 200k and RNO-G for both CBM scenarios. On the contrary, a successful detection could be possible with the radio extension of IceCube-Gen2 for the ISM scenario. In principle, in this case through the detection of neutrinos with IceCube-Gen2 radio, we could be able to constrain the CBM through neutrinos as well as probe the mechanism powering the optical jump. Indeed, the results presented in this paper are based on the assumption of a late collision between two shells, but other mechanisms may lead to different signatures in the neutrino signal. Furthermore, if no neutrino event is detected in temporal and spatial coincidence with the GRB event, constraints could be set on the parameters describing the jump in the afterglow light curve.

9.6.3 Detection prospects for GRB 100621A and a GRB 130427A-like burst

We now explore the neutrino detection prospects for GRB 100621A, whose optical jump [215] has been detected in seven channels simultaneously with GROND [214]. We also investigate the detection prospects for a second GRB whose parameters are inspired by the bright and nearby GRB 130427A [377, 382, 147]. An optical jump has not been observed for GRB 130427A, however we assume that it has one (hereafter GRB 130427A-like). The model parameters inferred for these two GRB afterglows and related uncertainties are summarized in Table 9.2. We fix $T_{\text{coll}} = 5 \times 10^3$ s for GRB 100621A, according to observations. As for GRB 130427A-like, we choose $T_{\text{coll}} = 1 \times 10^4$ s for the ISM and wind scenarios, in order to have the light curves decreasing at T_{coll} in both scenarios.

For GRB 100621A, we fix $\epsilon_{e,m}^0$ and $\epsilon_{B,m}^0$ by matching the amplitude of the jump in the light curve. For GRB 130427A-like, we fix $\epsilon_{e,m}^0 = \epsilon_e$ and we choose $\epsilon_{B,m}^0$ in order to get the same rebrightening both for the ISM and wind scenarios. We note that there is a substantial freedom in the choice of $\epsilon_{e,m}^0$ and $\epsilon_{B,m}^0$.

The wind scenario has been excluded for GRB 100621A, thus we perform the calculations only for the ISM case. For our GRB 130427A-like, instead, we explore the detection perspectives both for the ISM [377] and wind [377, 382] scenarios.

The expected neutrino fluences are shown in Fig. 9.8. For both GRBs, the detection

Table 9.2: Parameters characteristic of GRB 100621A [215] (second column) and GRB 130427A-like (inspired by GRB 130427A [377, 382, 147], third and fourth columns). For GRB 100621A, only the wind scenario is considered, while both CBM scenarios are investigated for GRB 130427A-like, see main text for more details.

	GRB 100621A (ISM)	GRB 130427A-like (ISM)	GRB 130427A-like (wind)
$\tilde{E}_{k,\text{iso}}$ (erg)	2.8×10^{53}	3.8×10^{54}	4.2×10^{53}
z	0.54	0.34	0.34
$n_0(\text{cm}^{-3})$ or A_\star	1–100	$(2-7) \times 10^{-3}$	$(1-5) \times 10^{-3}$
Γ_0	60–104	850	430
ϵ_e	$(2-6) \times 10^{-2}$	0.3	0.3
ϵ_B	$6 \times 10^{-6} - 6 \times 10^{-4}$	10^{-4}	3×10^{-2}
$\epsilon_{e,m}^0$	0.1	0.3	0.3
$\epsilon_{B,m}^0$	$10^{-4} - 10^{-3}$	10^{-4}	0.1

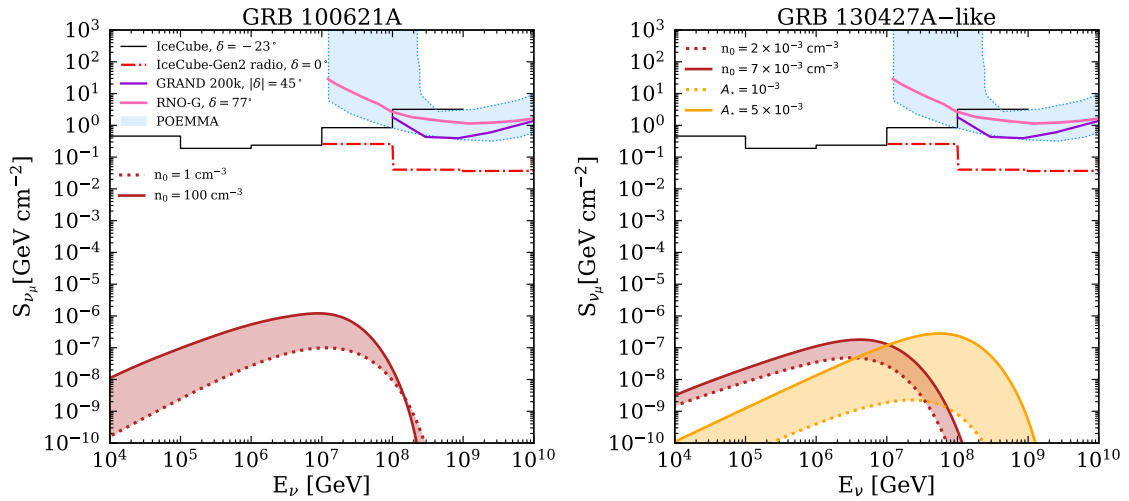


Figure 9.8: Neutrino fluence for GRB 100621A (left panel) and GRB 130427A-like (right panel) for the parameters in Table 9.2. The brown (orange) bands represent the ISM (wind) scenario. For GRB 100621A, the dotted (solid) line corresponds to $n_0 = 1 \text{ cm}^{-3}$ ($n_0 = 100 \text{ cm}^{-3}$). For GRB 130427A-like, the dotted lines correspond to $n_0 = 2 \times 10^{-3} \text{ cm}^{-3}$ (ISM) and $A_\star = 10^{-3}$ (wind), while the solid lines refer to $n_0 = 7 \times 10^{-3} \text{ cm}^{-3}$ (ISM) and $A_\star = 5 \times 10^{-3}$ (wind). The expected fluence is compared with the estimated sensitivities of IceCube-Gen2 radio for a source at $\delta = 0^\circ$ [28], IceCube for a source at $\delta = -23^\circ$ [28, 9], RNO-G for a source at $\delta = 77^\circ$ [43], GRAND200k for a source located at $|\delta| = 45^\circ$ [54], and the full range time-averaged sensitivity of POEMMA [479]. For both GRBs, the neutrino fluence lies below the point source sensitivities for all detectors.

of neutrinos seems unlikely. Thus, if GRBs with properties similar to GRB 100621A or GRB 130427A-like should be observed, no associated neutrino signal should be expected, unless the burst propagates in an ISM with n_0 larger than the one inferred for GRB 130427A [377] or the bursts occur at smaller distances.

9.7 Conclusions

The light curve of some gamma-ray burst afterglows exhibits a sudden intensity jump in the optical band between about one hour and one day after the prompt emission. The origin of this peculiar emission is not known yet, nor the fraction of GRBs displaying this feature. In this paper, we assume that the optical jump results from the late collision of two relativistic shells, as proposed in Ref. [483].

After modeling the shell merger analytically, we compute the neutrino emission from the GRB afterglow within a multi-messenger framework by considering two scenarios for the circumburst medium: a constant density case (ISM) and a stellar wind profile. We find that the presence of an optical jump can increase the number of produced neutrinos by about an order of magnitude.

The expected quasi-diffuse flux of afterglow neutrinos falls below the upper limits placed by the non-detection of neutrinos during the GRB prompt phase. IceCube-Gen2 radio shows the most promising detection prospects for point source searches, potentially being able to constrain the mechanism powering the optical jump as well as the properties of the circumburst medium through neutrinos; for a source at $d_L = 40$ Mpc, a successful detection could be possible with IceCube-Gen2 radio for the ISM scenario.

We also explore the neutrino emission from GRB 100621A and a burst similar to GRB 130427A but with an optical jump, assuming both these GRBs as benchmark cases given their respective luminosity and redshift. However, because of their distance, the neutrino detection prospects from the afterglow of GRBs similar to these ones could not be probed with next generation neutrino telescopes.

This work shows that the (non)-detection of neutrinos from GRB afterglows could offer an independent way to explore the mechanism powering the jump as well as the properties of the circumburst medium, if a GRB occurs relatively nearby or is especially bright.

Paper III and IV: description and summary of the main results

In this Chapter, we summarize the projects carried out in Paper III and Paper IV, whose reprints are reproduced in Chapters 11 and 12, respectively. Both articles are related to interaction-powered SNe that we introduced in Sec. 6.1. Here, we provide the motivation underlying the projects, summarize and discuss the main results.

10.1 Paper III

10.1.1 Context and motivation

The advent of modern optical time-domain surveys, particularly the Zwicky Transient Facility (ZTF) [82], has significantly boosted the discovery rate of rare optical transients. Tidal disruption events (TDEs) have recently gained particular interest among these. A follow-up campaign of alerts released by the IceCube Neutrino Observatory allows one to directly search for electromagnetic counterparts to individual high-energy neutrinos that have a high probability of being of astrophysical origin. Based on spatial and temporal coincidence, this approach has allowed us to identify three candidates of electromagnetic counterparts to date, even though at $\sim 3\sigma$ level. We already mentioned the first one, the flaring blazar TXS 0506+056. The other two are the transients AT2019dsg and AT2019fdr.

AT2019dsg is a bonafide TDE, detailedly analyzed by works on ZTF TDE sample (see, e.g., [478]) that reached the peak ~ 180 days before the detection of the neutrino. In contrast, the classification of AT2019fdr was somewhat uncertain, as the flare happened in a known AGN, and an extreme AGN flare could not be ruled out. AT2019fdr was first discovered by ZTF one year prior to the neutrino detection, and reached an extremely

bright peak luminosity of $L_{\text{peak}} \sim 3 \times 10^{44} \text{ erg s}^{-1}$ in the optical, about 300 days before the neutrino event IC200530A. Photometric and spectroscopic properties initially favored a SLSN interpretation¹. Later, it was suggested to be a TDE [416]. Some of the arguments disfavoring the SLSN scenario are the flare’s longevity, its proximity to the nucleus of the galaxy, late-time X-ray detection, and the detection of a strong infrared echo.

In Section 6.1, we have seen that interaction-powered events can exhibit high luminosity due to their interaction with a dense CSM. The class of SLSNe is widely believed to possess massive and extended CSM, which would naturally produce long and slowly declining light curves [190, 331]. The presence of soft, late-time X-ray emission or its absence aligns well with the expected behavior of these objects, where a severe inhibition of X-rays by photoelectric absorption and Compton down-scattering in the unshocked upstream CSM is predicted (see Sec. 6.1.2). The infrared echo requires a bright optical transient surrounded by a substantial amount of dust capable of reprocessing intercepted radiation and emitting it at longer wavelengths. The requirement remains the same whether the radiation source is a TDE or an SLSNe. Typically, TDEs exhibit broad spectral lines due to the high velocities ($\sim 10^4 \text{ km/s}$) of the outflows launched after accretion into the SMBH. In the case of AT2019fdr, velocities of $\sim 10^3 \text{ km/s}$ were observed, which are more typical of interacting SNe. Additionally, the photometry reveals irregular features, commonly observed in other interaction-powered transients, attributed to the CSM’s inhomogeneities, not simply accountable for in the TDE scenario.

Within the TDE interpretation, to explain the neutrino observation, three different scenarios have been put forward: a disk-corona model, a sub-relativistic wind model, and a jet model [416]. There is no straightforward way to observationally confirm or rule out the formation of a corona in a TDE transient accretion, so this model remains a speculation. Regarding the jet model, high-energy γ -ray, hard X-ray, and radio emissions should have been observed. However, none of them were. The same holds for the sub-relativistic wind, which should have revealed itself in radio observations. The only radio emission observed was associated with the AGN host due to the lack of a temporal evolution during the epochs of observations of AT2019fdr. Ref. [416] confirms that it is not related to the transient.

Given these premises and the fact that it would not be the first time that the origin of a transient of this type is controversial² (see, e.g., [92, 334]), in Paper III we decided to investigate the SLSN interpretation of AT2019fdr. We aimed to determine if the observed neutrino could be naturally explained within the framework of SLSN scenarios without relying on models unsupported by observational evidence.

¹<https://www.wis-tns.org/object/2019fdr>

²The transient CSS100217:102913+404220 is one example. With a similar peak luminosity and bolometric energy to the ones of AT2019fdr, it also occurred in the nucleus of a Narrow-line Seyfert1 galaxy. In this case a SLSN interpretation was favored over the TDE and AGN flare ones (see [156]).

10.1.2 Summary of the main results

In Chapter 11, we adopt the SLSN interpretation of the transient AT2019fdr, and investigate the possibility that the neutrino observed by IceCube has been produced in the interaction region between the SN ejecta and a dense CSM. In particular, we focus only on the FS, which is expected to be significantly brighter than the RS for the typical parameters characterizing these events (see Sec. 6.1.2). Moreover, unlike the case of GRBs, in such dense media, the rate of pp collisions is much higher than that of $p\gamma$. Hence, we estimate the production of neutrinos considering the evolution of the relativistic protons in the shocked shell and their interaction with the cold protons swept up from the CSM.

In general, the output lightcurve for SNe powered by SN ejecta–CSM interaction depends on the properties of the progenitor star (E_k , M_{ej} , δ , and n) and the properties of the CSM (s , R_{CSM} , κ , and M_{CSM}), that we have introduced in Sec. 6.1.1. The fact that so many unknown parameters are involved in this problem makes it no surprise that the observed lightcurves are so diverse.

In our work, we investigated the case of a wind-like CSM with solar composition and considered as free parameters the ones with the biggest impact on the produced emission, namely E_k , M_{ej} , M_{CSM} , and R_{CSM} . We performed a scan over the parameters compatible with the observed radiated energy, the lightcurve’s rise time, and the neutrino’s detection day. The latter is considered by requiring that the shock is still inside the CSM at the moment of the neutrino observation. The results are shown in Figs. 11.7 and 11.8. We can see that the configurations leading to the highest event rate in IceCube are described by relatively low ejecta mass and large kinetic energies, which maximize the shock velocity, and intermediate masses of the CSM, which control the target density in pp interactions. Large M_{CSM} are needed to explain the very long rise time to the peak in the lightcurve, but too large values cause the ejecta to transition into the blast-wave regime relatively soon, while still deep inside the wind. This strongly affects the neutrino outcome, which is rather sensitive to the shock velocity, but also the duration of interaction in the optically thin region, where the shock is collisionless.

The highest number of neutrino events compatible with the electromagnetic observations is $\sim 5 \times 10^{-2}$. With a single neutrino observed, it has been shown that the inference of the neutrino flux is subject to a large Eddington bias [459]. Once considering the rate of the SLSN population in the Universe, such a number can become compatible with the production of at least one or two neutrino events within the temporal window of investigation³. This result would demonstrate that an SLSN interpretation of AT2019fdr is plausible and confirm the ejecta-CSM interaction as the powering mechanism of these phenomena. Finally, in the SLSN scenario, the delay of the neutrino de-

³We note that the predicted numbers for the TDE corona and sub-relativistic models in Ref. [416] are a factor ~ 10 smaller than ours.

tection compared to the bolometric peak can be naturally explained. As we also show in Paper IV, there are configurations of the SN-CSM parameters that allow a significant increase with time of the maximum proton energy and can account for a delayed peak in the high-energy neutrino lightcurve.

10.1.3 Critical outlook

The first caveat to our work is related to interpreting the nature of AT2019fdr. If new upcoming multiwavelength data should strongly favor another scenario, possibly even AGN flare case, then our study would remain, as already stated, an attempt to investigate the plausibility of the SLSN interpretation.

After we published our paper, new data have shown rebrightenings in the optical transient lightcurve⁴. Such behavior could be explained within the framework of ejecta-CSM interaction, once considering a progenitor that has undergone multiple violent mass-loss processes before the SN explosion. In general, the CSM structure may be very complex. It can consist of smooth parts produced through the classical stellar wind or eruptive mass losses in different stages of evolution. However, such peculiar structures typically reveal themselves in similarly peculiar behavior of the transient's lightcurve and spectra. These substantial deviations have not been seen in the initial two years of AT2019fdr observations, and our wind assumption can be reasonable. Moreover, in Paper IV, we investigate the case of constant-density shells surrounding the star, and we find that the bulk of the high-energy neutrinos should be produced before the bolometric peak for most parameters. So, assuming that the association of the neutrino event with AT2019fdr is confirmed, we could use this information to constrain and discard hard slopes of the CSM density distribution.

We need to mention that during our investigation, no data from other wavebands were available. X-ray and infrared observations were presented in Ref. [416] after our submission. Including X-ray data would have better constrained the parameter space we explored. However, we anticipate that our results remain largely unaffected since very late X-ray emission necessitates a dense and opaque CSM with high opacity for photoelectric absorption. This implies a substantial CSM mass relative to the luminosity, which aligns with our findings from the current study.

Finally, we note that a more detailed investigation of this event could be possible by modeling the complete evolution of the lightcurve. One potential approach would involve utilizing the Modular Open Source Fitter for Transients (MOSFiT; [223]). However, caution should be exercised when interpreting the results of MOSFiT, as it is based on a single-zone model for the expanding ejecta with the heating source deeply embedded. Significant discrepancies have been observed between MOSFiT predictions and those derived from radiation-hydrodynamic simulations (e.g., Ref. [362, 464]). The

⁴<https://alerce.online/object/ZTF19aatubsj>

latter simulations spatially resolve the interaction layer between the ejecta and the CSM, which moves outward with time, and employ a more sophisticated approach to solve the radiation transport in the CSM. For instance, in the case of the extremely luminous event SN 2016aps, MOSFiT predicted CSM and ejecta masses $\gtrsim 100 M_{\odot}$ [362], while detailed radiation-hydrodynamic simulations came out with $M_{\text{CSM}} \sim 8 M_{\odot}$ and $M_{\text{ej}} \sim 30 M_{\odot}$ [464]. Conducting such simulations would be definitely fruitful, but was beyond the scope of our work.

10.2 Paper IV

10.2.1 Context and motivation

Our findings in Paper III, combined with the ever-growing detection rate of SNe IIn and SLSN II by ZTF, highlight the timeliness of searching for high-energy neutrinos from interaction-powered SNe. Like with other promising sources of high-energy neutrinos, the IceCube Collaboration intends to conduct a stacked search for neutrinos from SLSNe II. In the stacked search, data from multiple sources or events are combined and analyzed collectively to enhance the statistical significance of potential neutrino signals. By stacking the data, we can increase sensitivity to detect neutrino signals that may be individually weak but collectively significant. However, this approach requires weighting the sources relative to each other. Previous searches assumed that all sources are neutrino standard candles, i.e., the neutrino flux at Earth would scale with the inverse of the square of the luminosity distance or used the optical peak flux as a weight. However, the first assumption is overly simplified, as we do not expect standard behavior from these transients. As for the second, it can be tested, and this is one of the findings of the Paper IV.

In Paper IV, we aimed to investigate more carefully whether we can establish a connection between the efficiency of high-energy neutrino production and "first-order" properties of the optical lightcurves of interaction-powered SNe. Specifically, we focused on the optical luminosity peak, L_{peak} , and the rise to the peak of the lightcurve, t_{rise} (see Fig. 6.3). Discovering a correlation between these properties would help identify a suitable weighting scheme for the stacked search, thus significantly improving the analysis sensitivity, and also help optimize future multimessenger searches of neutrinos from these objects.

10.2.2 Summary of the main results

In Paper IV, we conducted a comprehensive analysis by scanning a wide range of values for E_k , M_{ej} , M_{CSM} , and R_{CSM} , while considering two radial distributions for the CSM:

a wind-like density profile and a constant density shell. We first focused on understanding the behaviors and relationships among the peak luminosity, L_{peak} , the total dissipated energy within the optically thick part of the wind, and the rise time, t_{rise} . To define these parameters, we utilized analytical relations supported by studies that successfully reproduced similar trends using more sophisticated radiation-hydrodynamic simulations across a wide range of CSM and ejecta properties [462].

Insured that our results were compatible with the Ref. [462], for each ejecta-CSM configuration, we computed L_{peak} , t_{rise} , and the total energy emitted in neutrinos, $\mathcal{E}_{\bar{\nu}+\nu}$ with $E_{\nu} > 1$ teV between the breakout time and the time when the forward shock reaches the edge of the CSM. The results are shown in Fig. 12.5. We observe an interesting pattern: when fixing two parameters and varying the remaining two, there is always an optimal combination that maximizes neutrino production. The neutrino yield is $\propto \rho_{\text{CSM}} R_{\text{sh}}^2 v_{\text{sh}}^3$, while the maximum achievable proton energy, $E_{p,\text{max}}^*$, and thus the maximum obtainable neutrino energy, is determined by v_{sh} which sets the acceleration rate, and the primary energy loss channel for protons. The latter depends on the interaction parameters and the stage of shock evolution. The transition observed in each plot for increasing CSM masses indicates that at a certain value, the CSM becomes dense enough to significantly decelerate the ejecta, leading to more efficient pp interactions and a reduction in the maximum proton energy.

By considering the dependence of t_{rise} , L_{peak} , $E_{p,\text{max}}$ and $\mathcal{E}_{\bar{\nu}+\nu}$ on the model parameters, we find that the configurations resulting in the highest $\mathcal{E}_{\bar{\nu}+\nu}$, are characterized by a bolometric luminosity peak $L_{\text{peak}} \sim 10^{43}\text{--}10^{44}$ erg and rise time $10 \text{ days} \lesssim t_{\text{rise}} \lesssim 40 \text{ days}$. Excessively long rising times are obtained with relatively large M_{CSM} . Slow-rising lightcurves, in general, indicate inefficient neutrino production unless E_k and R_{CSM} are increased to unreasonable values. On the other hand, comparable L_{peak} and t_{rise} can be achieved with parameters that are not optimal for neutrino emission. Therefore, the main conclusion is that there is a significant degeneracy, which complicates establishing a straightforward connection between neutrinos and the photometric features of the lightcurve. As an illustrative example, we considered two of the brightest SLSN sources detected by ZTF so far and demonstrated that, within the uncertainties of the measured lightcurve properties and radiative efficiencies, the predicted neutrino numbers can be smaller by up to two orders of magnitude compared to their best prediction (see Fig. 12.8).

Unfortunately, the most promising SNe that could be significant neutrino sources are located at relatively large redshifts. This observational fact places the most luminous events far from us. In Fig. 12.10, we demonstrate that in order to be detected as a point source with high significance, the SLSN with the “right” parameters should be at least at a distance of ~ 13 Mpc from us.

One important finding from Paper IV is the timing of the high-energy neutrino lightcurve peak. When considering typical and reasonable parameters for these events, the

maximum proton energy peaks at $\sim \mathcal{O}(100 \text{ days})$ after the bolometric peak, as shown in Fig. D.2. Fig. 12.9 provides an example of this. This finding aligns with the detection of a neutrino approximately 300 days after the optical peaks in the transient AT2019fdr, as discussed in Paper III.

Additionally, we explore the case of a constant density shell. The results are presented in Fig. D.3. The main difference compared to a wind-density profile is the breakout radius. At a fixed M_{CSM} , the wind is many orders of magnitude denser at smaller radii compared to a constant-density shell. Hence, in large regions of the parameter space, the breakout happens at the stellar radius rather than inside the CSM, which limits the peak luminosity. For neutrinos, their peak time occurs at earlier times, typically before the bolometric lightcurve peak. A successful observation of this kind would clearly help constrain also the geometrical density distributions of interaction-powered events.

10.2.3 Critical outlook

In Paper IV, we aimed to develop an efficient strategy for detecting neutrinos from interaction-powered supernovae (SNe). Our findings indicate that neither of the weighting schemes assuming these transients as standard candles or assuming the neutrino flux is proportional to the optical peak is physically motivated. The presence of parameter degeneracy prevents us from establishing a simple correlation. Additionally, restricting the search window around the optical peak is not optimal, as it excludes a significant portion of the neutrino signal with late peaks.

To address and mitigate this degeneracy, it is crucial to complement optical data with multiwavelength observations in X-ray and radio bands. Neutrinos can help reduce the degeneracy, but only if a successful detection occurs, which is contingent upon favorable ejecta-CSM configurations. Non-detection can also provide valuable constraints, but its effectiveness is limited for sources at typical distances of the most luminous events. Measurements of optical spectra, which reveal the interaction duration, can further aid in constraining the parameter space. Unfortunately, only a few spectra per event are available in the best-case scenarios. Therefore, we strongly encourage spectroscopic follow-up observations to enable a comprehensive characterization of the CSM properties.

Paper III: IceCube event from a hydrogen-rich superluminous supernova?

This chapter is a reprint of:

Tetyana Pitik, Irene Tamborra, Charlotte R. Angus, Katie Auchettl

Is the high-energy neutrino event IceCube-200530A associated with a hydrogen-rich superluminous supernova?

ApJ 929 (2022) 2, 163, [arXiv:2110.06944](https://arxiv.org/abs/2110.06944)

ABSTRACT

The Zwicky Transient Facility (ZTF) follow-up campaign of alerts released by the IceCube Neutrino Observatory has led to the likely identification of the transient AT2019fdr as the source of the neutrino event IC200530A. AT2019fdr was initially suggested to be a tidal disruption event in a Narrow-Line Seyfert 1 galaxy. However, the combination of its spectral properties, color evolution, and feature-rich light curve suggests that AT2019fdr may be a Type II_n superluminous supernova. In the latter scenario, IC200530A may have been produced via inelastic proton-proton collisions between the relativistic protons accelerated at the forward shock and the cold protons of the circumstellar medium. Here, we investigate this possibility and find that at most 4.6×10^{-2} muon neutrino and antineutrino events are expected to be detected by the IceCube Neutrino Observatory within 394 days of discovery in the case of excellent discrimination of the atmospheric background. After correcting for the Eddington bias, which occurs when a single cosmic neutrino event is adopted to infer the neutrino emission at the source, we conclude that IC200530A may originate from the hydrogen rich superluminous supernova AT2019fdr.

11.1 Introduction

In 2013, the IceCube Collaboration reported the detection of a flux of high-energy neutrinos of astrophysical origin, marking the beginning of the high-energy neutrino astronomy era. Despite the growing number of high-energy neutrino events detected by the IceCube Neutrino Observatory, the sources of the cosmic neutrino flux remain to be unveiled [5, 20, 23, 3].

High energy neutrino events have been reported to be in likely coincidence with blazars [11, 205, 180, 193, 277, 254]. However, association studies of blazars hint towards no excess from the broader population [12]. Various other source classes have been proposed as factories of the observed cosmic neutrino flux [317, 46, 482], such as gamma-ray bursts, cluster of galaxies, star-forming galaxies, and tidal disruption events [321, 396, 337, 494, 469, 516, 491, 142, 439, 303]. Nevertheless, the neutrino emission from each of these source classes cannot fully account for the observed neutrino flux.

The growing number of cosmic neutrino alerts has triggered follow-up searches for coincident detection of electromagnetic radiation, see e.g. [19, 193, 35]. On October 1st 2019, the IceCube Collaboration reported the detection of a muon track neutrino of likely astrophysical origin, IC191001A. This event has been suggested to be the neutrino counterpart of the tidal disruption event (TDE) candidate AT2019dsg which was discovered by the Zwicky Transient Facility (ZTF) – see e.g. [455, 82]. Various theoretical models have been discussed to interpret this likely association [507, 298, 351], however the jetted version of these models is being challenged by the most recent work on the radio properties of AT2019dsg [115, 329, 311, 312].

More recently, the follow-up campaign of IceCube neutrino alerts carried out by the ZTF Collaboration has led to another transient association. On May 31st 2020, [246, 419] detected another muon track candidate (IC200530A), which was suggested to be associated with the optical transient AT2019fdr/ZTF19aatubsj¹ located at redshift $z = 0.2666$. The IC200530A event was detected ~ 394 days after the discovery of the transient (hereafter identified with the onset of the shock breakout) and about 300 days after the peak of the electromagnetic emission. This neutrino event has a reconstructed neutrino energy of $E_\nu \simeq 80$ TeV and a signalness larger than 50% [246, 419, 456].

The intriguing coincidence of two IceCube neutrino events with two ZTF transient sources has triggered searches by the ANTARES Collaboration [50] and led to stringent upper limits on the neutrino emission from both sources. In addition, the Baikal-GVD Collaboration is currently investigating clusters of neutrino events detected along the same angular directions of both ZTF sources [461].

AT2019fdr is located close to the nucleus of its host galaxy and shows strong narrow hydrogen emission lines within its spectra. This led to the initial classification of

¹<https://www.wis-tns.org/object/2019fdr>

AT2019fdr as either a flaring active galactic nucleus (AGN) in a Narrow-Line Seyfert 1 galaxy [182], or a tidal disruption event [135]. This has resulted in interpretations of IC200530A being associated with an accreting black hole transient event [456]. However, [512] proposed that AT2019fdr is a hydrogen-rich superluminous supernova (otherwise named superluminous supernova of Type IIn, SLSN IIn). Hydrogen rich SLSNe exhibit strong narrow Balmer emission lines within their spectra, but are more luminous than standard type IIn supernovae (SNe IIn), achieving luminosities typically with $M \lesssim -20$ at peak brightness [187, 449, 190]. The narrow emission lines within SNe IIn are indicative of interaction between the SN ejecta with a dense shell of surrounding circumstellar material (CSM) in which kinetic energy is efficiently converted into thermal energy. The high luminosity of SLSNe IIn is thought to be the result of either an highly energetic explosion [with typical energies $E_{ej} \simeq \mathcal{O}(10^{51}-10^{52})$ ergs], interaction with an unusually massive CSM [331], or some combination of the two scenarios.

Proton acceleration, even beyond PeV energies, could take place in the proximity of the SLSN shock expanding in the dense CSM. The interaction of these protons with those of the shocked CSM may lead to copious neutrino emission [353, 258, 349, 114, 526, 389, 386, 340]. In this work, we investigate the possibility that IC200530A originates from AT2019fdr, under the framework that this transient is a SLSN IIn.

This paper is organized as follows. After introducing the main features characterizing AT2019fdr in Sec. 11.2, we outline the setup adopted to predict the neutrino signal in Sec. 11.3. Our findings are presented in Sec. 11.4 together with a discussion on the dependence of the neutrino signal on the uncertain parameters characteristic of AT2019fdr. A discussion on our findings and caveats is reported in Sec. 11.5, followed by our conclusions in Sec. 11.6. In addition, Appendix C.1 discusses how the AT2019fdr parameter space is constrained by the observational constraints on AT2019fdr that we apply from neutrino and electromagnetic data. We investigate the temporal evolution of the maximum proton energy as a function of the model parameters considered for AT2019fdr in Appendix C.2.

11.2 AT2019fdr: A type IIn superluminous supernova

AT2019fdr exhibits many properties compatible with those of other documented SLSNe IIn from the literature. Spectroscopically, the event shows intermediate-width (~ 1000 km s⁻¹) Balmer emission lines combined with narrow galaxy emission lines from the host, superimposed upon a blue continuum². The intermediate width Balmer emission features are characteristic of interacting core-collapse SNe (SNe IIn and SLSNe IIn), see

²The classification spectra are publicly available on <https://www.wiserep.org/object/12537>

e.g. [188, 331]. Although these lines are also observed within nuclear transients (AGN flares and TDEs), the lack of intermediate components to the other host galaxy emission features (e.g. O III) disfavors the interpretation of this transient as an AGN flare. It is unlikely that these features mark AT2019fdr as a TDE, as these events generally exhibit much broader emission profiles than seen in AT2019fdr (typically line widths $\sim 10^4$ km s⁻¹, [243, 121]).

The photometric behavior of AT2019fdr shows several features within the multi-band light curve, as displayed in Fig. 11.1, consistent with interaction-powered SNe. Although the slow rise time (~ 80 days in the rest frame) and lengthy decline of the transient can be interpreted under each of the three potential paradigms suggested for its origin, the photometric evolution of AT2019fdr is not smooth. The light curve has a clear bump close to the peak (around 60 days from first light in the rest frame) alongside the beginning of an apparent re-brightening feature around 70 days after the optical peak. Episodes of re-brightening have been observed within some SNe IIn [e.g. 458, 364] and are attributed to changes in the CSM density and variable progenitor mass-loss rates.

The late-time evolution of the transient (> 160 days from peak brightness) exhibits a slower decline than either Co⁵⁶-decay (from a standard Ni⁵⁶ powered light curve) or the $\alpha = -5/3$ power-law decline predicted by models of fallback accretion in TDEs [e.g. 414], but consistent with the range of typically slow declines in interacting SNe [365]. AT2019fdr also exhibits a gradual reddening in color from peak to late times (transitioning from $g - r \sim -0.12$ – -0.2 mag), a property not predicted in nuclear transients, which shows an almost constant optical color in the majority of their light curves, but accordant with observations of normal SN IIn [466]. Finally, pre-explosion variability is also not observed within the ZTF and ATLAS imaging [512], which disfavors an AGN origin.

Given the redshift of AT2019fdr, it is not possible to recover its complete rise in the ZTF photometry. However, non-detections in the ZTF g-band prior to first light place the breakout epoch 6 days (5 rest frame days) before the first ZTF detection (see Fig. 11.1). Fitting a low order polynomial to the rise of the ZTF curve suggests that the start of the optical light curve coincides with these non-detections. Based on this, we assume the onset of the shock breakout at the first detection of MJD = 58606 \pm 6 days.

We also note that AT2019fdr was not the only source suggested to be associated with the neutrino event IC200530A. AT2020lam³ and AT2020lls⁴ were also suggested to be possibly associated, as they were found within a 90.0% localization of the neutrino event [419]. AT2020lam was classified using the Nordic Optical Telescope as a Type II SN located at $z = 0.033$ [417]. However, the spectrum and light curve showed no evidence of CSM interaction, necessary for neutrino producing, leading [417] to suggest

³<https://wis-tns.weizmann.ac.il/object/2020lam>

⁴<https://wis-tns.weizmann.ac.il/object/2020lls>

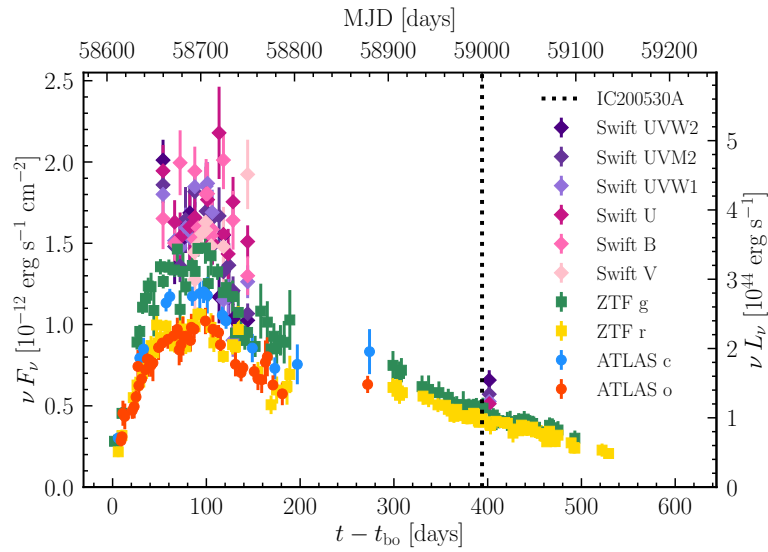


Figure 11.1: Ultraviolet-optical light curve of AT2019fdr. Public data taken from ZTF [380], ATLAS [476, 447] and *Swift* [195]. The detection epoch of IC200530A is marked as the black dashed vertical line and was observed ~ 394 days after the first optical detection of the SN in the observer frame. We display the time from estimated shock breakout (t_{bo}), along the x -axis.

that it was not associated with the neutrino event IC200530A. AT2020lls was also classified using the Nordic Optical Telescope, but as a Type Ic SN located at $z = 0.04106$ that occurred ~ 8 days prior to the detection of IC200530A [418]. As this source did not show broad absorption features consistent with a subclass of Type Ic SN called Type Ic-BL, which are commonly associated with off-axis gamma-ray bursts or choked jets, [418] suggested this was not associated with the neutrino event IC200530A.

11.3 Model setup

In this section, we introduce the method adopted to compute the neutrino spectral energy distribution from AT2019fdr and its temporal evolution, as well as the properties of AT2019fdr useful to this purpose. Details on the estimation of the neutrino flux and event rate expected at Earth follow.

11.3.1 Spectral energy distributions of protons and neutrinos

We assume a spherical, steady and wind-like circumstellar medium (CSM) with solar composition ejected from the massive progenitor in the final stages of its evolution, as sketched in Fig. 11.2. We define its number density profile as

$$n_{\text{CSM}}(R) = \frac{\rho_{\text{CSM}}(R)}{m} = \frac{\dot{M}}{4\pi v_w m R^2}, \quad (11.1)$$

where \dot{M} is the stellar mass loss rate, v_w the wind velocity, $m = \mu m_{\text{H}}$, with $\mu = 1.3$ being the mean molecular weight for a neutral gas of solar abundance, and R the distance to the stellar core.

The interaction of the stellar ejecta with the CSM leads to the formation of a forward shock (propagating in the CSM) and a reverse shock (propagating back into the stellar ejecta). Both the forward and reverse shocks could, in principle, contribute to the neutrino emission. Working under the assumption that the ejecta density profile decreases steeply [128], we neglect the contribution of the reverse shock since the forward shock is expected to predominantly contribute to the total energy dissipation rate and dominate the particle acceleration observed in SN remnants, e.g. [166, 379, 438, 446, 435, 462]. Hence, we focus on the neutrino emission from the forward shock for the sake of simplicity.

Following [126, 332], we assume that spherically symmetric SN ejecta of mass M_{ej} and kinetic energy E_k expand in the surrounding CSM homologously. The CSM extends up to an external radius R_{CSM} (see Fig. 11.5). The outer ejecta density profile, which is relevant for the interactions leading to neutrino production, scales as $n_{\text{ej}} \propto R^{-s}$, where we assume $s = 10$. The shocked SN ejecta and CSM form a thin dense shell because of efficient radiative cooling. Being the thickness of the thin shocked shell much smaller than its radius, one can describe its evolution through the radius $R_{\text{sh}}(t)$. In the ejecta dominated phase, namely in the phase in which most part of the ejecta is still freely expanding (i.e., when the mass of the ejecta is larger than the swept-up CSM mass), the shock radius is given by [332, 131]:

$$R_{\text{sh}}(t) = \left[\frac{2}{s(s-4)(s-3)} \frac{[10(s-5)E_k]^{(s-3)/2} v_w}{[3(s-3)M_{\text{ej}}]^{(s-5)/2} \dot{M}} \right]^{1/(s-2)} t^{(s-3)/(s-2)}, \quad (11.2)$$

with the corresponding shock velocity $v_{\text{sh}} = dR_{\text{sh}}/dt$.

Because of the high CSM density, the forward shock is initially expanding in a radiation dominated region, and particle acceleration is not efficient [502, 289, 258, 353]. Efficient particle acceleration takes place at radii larger than that of the shock breakout

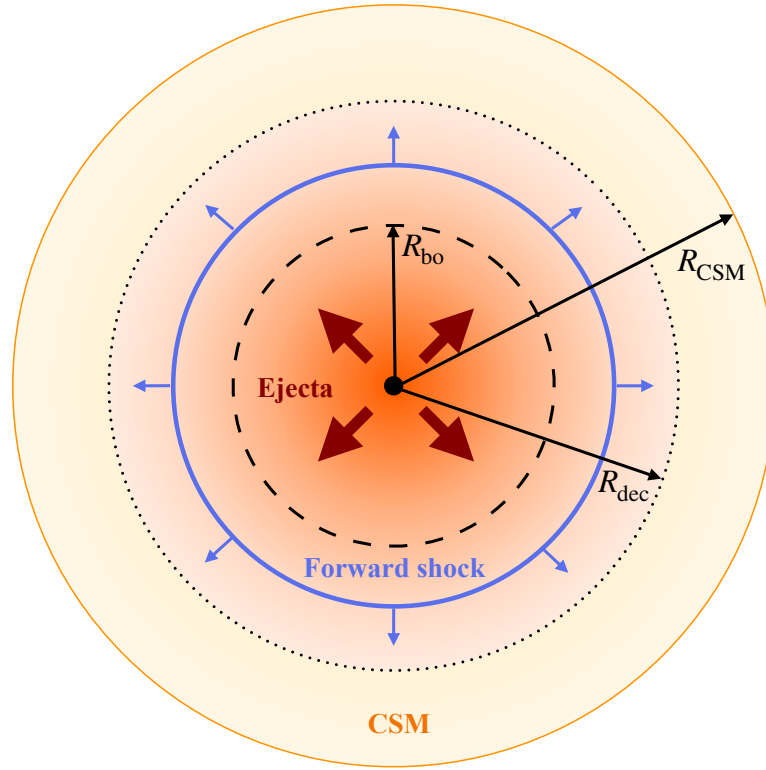


Figure 11.2: Schematic representation of AT2019fdr after the explosion, assuming spherical symmetry. The central compact object (in black) is surrounded by the SN ejecta (orange region, with the bordeaux arrows indicating the propagation of the ejected material) and a dense CSM envelope (yellow region) which extends up to its outer edge marked by R_{CSM} . The color gradient describes the density gradient (from darker to lighter hues as the density decreases). The dashed black line marks the position of the breakout radius (R_{bo}). The indigo line represents the forward shock that propagates radially outwards. The black dotted line marks the location of the deceleration radius of the ejecta (R_{dec}). The latter is located at radii smaller than R_{CSM} (as in this sketch) for a relatively large CSM mass compared to the ejecta mass or larger than R_{CSM} for very massive ejecta and rarefied CSM; see Eq. 11.4. For extremely large $M_{\text{CSM}}/M_{\text{ej}}$, it is possible that $R_{\text{dec}} < R_{\text{bo}}$.

(R_{bo}), where initially trapped photons are free to diffuse out to the photosphere; the shock breakout radius is computed by solving the following equation:

$$\tau_T(R_{\text{bo}}) = \int_{R_{\text{bo}}}^{R_{\text{CSM}}} \rho_{\text{CSM}}(R) \kappa_{\text{es}} dR = \frac{c}{v_{\text{sh}}}, \quad (11.3)$$

where $\kappa_{\text{es}} \sim 0.34 \text{ cm}^2 \text{ g}^{-1}$ [375] is the electron scattering opacity at solar abundances, and c is the speed of light. When the SN ejecta mass M_{ej} becomes comparable to the swept-up mass from the CSM, the ejecta enters the CSM-dominated phase. This transition happens at the deceleration radius

$$R_{\text{dec}} = \frac{M_{\text{ej}} v_w}{\dot{M}}. \quad (11.4)$$

Note that R_{dec} may be located at radii smaller than R_{CSM} as shown in Fig. 11.2, or larger than R_{CSM} according to the relative ratio between M_{ej} and M_{CSM} (i.e., if $M_{\text{CSM}} > M_{\text{ej}}$, then $R_{\text{dec}} < R_{\text{CSM}}$ and viceversa). Furthermore, for M_{CSM} extremely large with respect to M_{ej} , R_{dec} can even be smaller than R_{bo} . For $R > R_{\text{dec}}$, the forward shock radius evolves as [462]

$$R_{\text{sh}}(t) = R_{\text{dec}} \left(\frac{t}{t_{\text{dec}}} \right)^{2/3}. \quad (11.5)$$

where we have assumed adiabatic dynamical evolution for the sake of simplicity. At radii larger than R_{bo} , diffusive shock acceleration of the incoming CSM protons takes place. Following [177, 389], the proton injection rate for a wind density profile is

$$Q_p(\gamma_p, R) \equiv \frac{d^2 N_p}{d\gamma_p dR} = \frac{9\pi\epsilon_p R_{\text{bo}}^2 n_{\text{bo}}}{8\ln(\gamma_{p,\text{max}}/\gamma_{p,\text{min}})} \left[\frac{v_{\text{sh}}(R_{\text{bo}})}{c} \right]^2 \times \left(\frac{R}{R_{\text{bo}}} \right)^{2\alpha} \gamma_p^{-k} H(\gamma_p - \gamma_{p,\text{min}}) H(\gamma_{p,\text{max}} - \gamma_p), \quad (11.6)$$

where the parameter α dictates the radial dependence of the shock velocity ($v_{\text{sh}} \propto R^\alpha$), it is $\alpha = -1/7$ in the free expansion phase ($R < R_{\text{dec}}$) and $\alpha = -1/2$ in the decelerating phase ($R > R_{\text{dec}}$). The fraction of the shocked thermal energy stored in relativistic protons is ϵ_p , while $H(x) = 1$ for $x > 0$ and zero otherwise. We set the proton spectral index $k = 2$ and the minimum Lorentz factor of the accelerated protons $\gamma_{p,\text{min}} = 1$. The maximum Lorentz factor of protons ($\gamma_{p,\text{max}}$) is obtained by requiring that the acceleration timescale in the Bohm limit, $t_{\text{acc}} \sim 20\gamma_p m_p c^3 / 3eBv_{\text{sh}}^2$ [401], is shorter than the total cooling timescale for protons: $t_{\text{acc}} \leq t_{\text{p,cool}}$. $B = \sqrt{32\pi\epsilon_B m_p v_{\text{sh}}^2 n_{\text{CSM}}}$ is the magnetic field in the post-shock region, whose energy density is a fraction ϵ_B of the post-shock thermal energy density $U_{\text{th}} = (9/8)m_p v_{\text{sh}}^2 n_{\text{CSM}}$. The latter is obtained by considering

the Rankine-Hugoniot jump conditions across a strong non-relativistic shock with compression ratio approximately equal to 4.

The most relevant energy loss mechanisms for protons are inelastic pp collisions and the cooling due to adiabatic expansion of the shocked shell, hence $t_{p,\text{cool}}^{-1} = t_{pp}^{-1} + t_{\text{ad}}^{-1}$, with $t_{pp} = (4k_{pp}\sigma_{pp}n_{\text{CSM}}c)^{-1}$, where we assume constant inelasticity $k_{pp} = 0.5$ and energy-dependent cross-section $\sigma_{pp}(E_p)$ [527]. Following [172], the adiabatic cooling is $t_{\text{ad}} = \min[t_{\text{dyn}}, t_{\text{cool}}]$, where t_{cool} is the typical cooling time of the thermal gas behind the shock and t_{dyn} is the dynamical time of the shock. When the shock is radiative, the particle acceleration region is shrank to a characteristic length $\sim v_{\text{sh}}t_{\text{cool}}$, limiting the maximum achievable particle energy. The cooling time is $t_{\text{cool}} = 3k_B T / 2n_{\text{sh}}\Lambda(T)$ [181] where k_B is the Boltzmann constant, $n_{\text{sh}} = 4n_{\text{CSM}}$ is the density of the shocked region, and $\Lambda(T)$ is the cooling function capturing the physics of radiative cooling. Here T is the gas temperature immediately behind the forward shock front obtained by the Rankine-Hugoniot conditions, given by:

$$T = 2 \frac{(\gamma - 1)}{(\gamma + 1)^2} \frac{\mu m_{\text{H}} u_{\text{sh}}^2}{k_B}, \quad (11.7)$$

where $\gamma = 5/3$ is the adiabatic index of the gas. Finally, the cooling function [in units of $\text{erg cm}^3 \text{s}^{-1}$] is given by the following approximation [130]:

$$\Lambda(T) = \begin{cases} 6.2 \times 10^{-19} T^{-0.6} & 10^5 < T \lesssim 4.7 \times 10^7 \text{ K} \\ 2.5 \times 10^{-27} T^{0.2} & T > 4.7 \times 10^7 \text{ K}. \end{cases} \quad (11.8)$$

where line emission dominates at low T and free-free emission at high T .

Relativistic protons in the shocked region may also interact with the ambient photons via $p\gamma$ interactions. However, in this work we ignore this energy loss channel, consistent with the work of [353, 172], which show that $p\gamma$ interactions can be safely neglected for a wide range of parameters.

Since we aim to compute the neutrino emission, we track the temporal evolution of the proton distribution in the shocked region between the shock breakout radius R_{bo} and the outer radius R_{CSM} .

The evolution of the proton distribution is given by [460, 177, 389]:

$$\frac{\partial N_p(\gamma_p, R)}{\partial R} - \frac{\partial}{\partial \gamma_p} \left[\frac{\gamma_p}{R} N_p(\gamma_p, R) \right] + \frac{N_p(\gamma_p, R)}{v_{\text{sh}}(R)t_{pp}(R)} = Q_p(\gamma_p, R), \quad (11.9)$$

where $N_p(\gamma_p, R)$ represents the total number of protons in the shell at a given radius R with Lorentz factor between γ_p and $\gamma_p + d\gamma_p$. The radius R is related to the time t measured by an observer at Earth: $t = \tilde{t}(R)(1 + z)$, where we denote with a tilde all parameters in the reference frame of the central compact object hereafter. The second term on the left hand side of Eq. 11.9 takes into account energy losses due to the adiabatic expansion of the SN shell, while pp collisions are treated as an escape term [460].

Other energy loss channels for protons are negligible [353]. Furthermore, in Eq. 11.9 the diffusion term has been neglected since the shell is assumed to be homogeneous.

The neutrino production rates, $Q_{\nu_i+\bar{\nu}_i}$ [$\text{GeV}^{-1}\text{cm}^{-1}$], for muon and electron flavor (anti)neutrinos are given by [262]:

$$Q_{\nu_\mu+\bar{\nu}_\mu}(E_\nu, R) = \frac{4n_{\text{CSM}}(R)m_p c^3}{v_{\text{sh}}} \int_0^1 dx \frac{\sigma_{\text{pp}}(E_\nu/x)}{x} \quad (11.10)$$

$$N_p\left(\frac{E_\nu}{xm_p c^2}, R\right) \left(F_{\nu_\mu}^{(1)}(E_\nu, x) + F_{\nu_\mu}^{(2)}(E_\nu, x)\right),$$

$$Q_{\nu_e+\bar{\nu}_e}(E_\nu, R) = \frac{4n_{\text{CSM}}(R)m_p c^3}{v_{\text{sh}}} \int_0^1 dx \frac{\sigma_{\text{pp}}(E_\nu/x)}{x} \quad (11.11)$$

$$N_p\left(\frac{E_\nu}{xm_p c^2}, R\right) F_{\nu_e}(E_\nu, x),$$

where $x = E_\nu/E_p$. The functions $F_{\nu_\mu}^{(1)}$, $F_{\nu_\mu}^{(2)}$ and F_{ν_e} follow the definitions in [262]. Equations 11.10 and 11.11 are valid for $E_p > 0.1$ TeV, corresponding to the energy range under investigation.

11.3.2 Parameters characteristic of AT 2019fdr

Numerical simulations aiming to model SLSNe II in light curves are undergoing, see e.g. [154, 122, 464, 463]; however, the exact underlying physics which powers these sources is still uncertain. In the following, we outline the properties of AT2019fdr useful to model its neutrino emission.

By relying on existing data on AT2019fdr from ZTF [380], ATLAS [476, 447] and *Swift* [195], we integrate the observed pseudo-bolometric light curve and estimate that the total radiated energy from AT2019fdr is $\tilde{E}_{\text{rad}} = 1.66 \pm 0.01 \times 10^{52}$ erg. To take into account the uncertainties on the radiative efficiency, namely the fraction of the total energy that is radiated, we consider two characteristic values of the kinetic energy \tilde{E}_k of the ejecta: 5×10^{52} erg and 10^{53} erg, which correspond to a radiative efficiency of $\sim 35\%$ and 18% , respectively (see [132], where the total radiated energy is estimated to be $E_{\text{rad}} = 0.32E_k$).

We assume the proton fraction equal to $\varepsilon_p = 0.1$ [353]. This value is consistent with simulations of particle acceleration and magnetic field amplification at non-relativistic quasi-parallel shocks [113]. A discussion on the impact of different values of ε_p on the expected neutrino event rate is reported in Sec. 11.5. The fraction of the post-shock internal energy that goes into amplification of the magnetic field is instead assumed to be $\varepsilon_B = 3 \times 10^{-4}$ [386].

The wind velocity is considered to be $v_w = 100 \text{ km s}^{-1}$ [333]. The average mass loss rate is given by [464]:

$$\dot{M} = 0.3 M_\odot \text{ yr}^{-1} \left(\frac{M_{\text{CSM}}}{10 M_\odot} \right) \left(\frac{R_{\text{CSM}}}{10^{16} \text{ cm}} \right)^{-1} \left(\frac{v_w}{100 \text{ km s}^{-1}} \right), \quad (11.12)$$

where M_{CSM} is the CSM mass contained within a shell of radius R_{CSM} .

By fitting a basic polynomial to the bolometric light curve and available non-detections of AT2019fdr to extrapolate beyond the detection limits of ZTF, we estimate that its rise time (i.e., the time during which the luminosity reaches peak value, see Fig. 11.1) is $t_{\text{rise}} \sim 98$ days. In addition, in order to link t_{rise} to the other model parameters characteristic of AT2019fdr, we rely on the following relation [462]:

$$t_{\text{rise}} \simeq t_{\text{diff}}(t) = \frac{(R_{\text{ph}} - R)\tau_T(R)}{c}, \quad (11.13)$$

where the diffusion time is the time required for the radiation to travel from R to R_{ph} ⁵, and $\tau_T(R)$ is the optical depth of the CSM at radius R . The rise time is expected to increase as a function of M_{CSM} , since a massive and dense CSM prolong the photon diffusion timescale. Yet, in order to predict the correct behavior of t_{rise} , one should take into account the effect of the variation of all the parameters: E_k , M_{ej} , M_{CSM} , and R_{CSM} .

The exact values of M_{ej} , M_{CSM} , and R_{CSM} are highly uncertain for AT2019fdr and degeneracies may be at play when interpreting the AT2019fdr light curve. The reprocessing of information from the explosion by interaction with the CSM masks the properties of the SLSN explosion underneath it. Although the CSM density can be estimated in several ways, e.g. from the strength of the $H\text{-}\alpha$ line [466] or through X-ray and radio observations [120], AT2019fdr lacks the necessary time series multi-wavelength and spectroscopic data required to constrain it. Hence, we consider ranges of variability for the most uncertain parameters: $M_{\text{ej}} \in [5, 150] M_\odot$, $M_{\text{CSM}} \in [5, 150] M_\odot$, and $R_{\text{CSM}} \in [2, 4] \times 10^{16} \text{ cm}$. Out of these, we only take into account the ones in agreement with the measured t_{rise} (allowing for an uncertainty of 50%) and requiring that the production of the neutrinos observed by the IceCube Observatory at ~ 394 days after the breakout takes place inside the CSM, namely $t(R_{\text{CSM}}) - t(R_{\text{bo}}) \gtrsim 394$ days. See Appendix C.1 for more details. A summary of the default values for the parameters considered for AT2019fdr is reported in Table 11.1.

⁵The photospheric radius is obtained by considering $\tau_T(R_{\text{ph}}) = 1$.

Table 11.1: Benchmark values for the parameters characteristic of AT2019fdr. For the most uncertain ones, we consider a range of variability.

<i>Parameter</i>	<i>Symbol</i>	<i>Default value</i>
Radiated energy	\tilde{E}_{rad}	1.66×10^{52} erg
Radiative efficiency	η	18–35%
Rise time	t_{rise}	98 days
Redshift	z	0.2666
Declination	δ	26.85 deg
Right ascension	α	257.28 deg
Accelerated proton energy fraction	ε_p	0.1
Magnetic energy density fraction	ε_B	3×10^{-4}
Proton spectral index	k	2
Wind velocity	v_w	100 km s^{-1}
Ejecta density slope	s	10
Ejecta mass	M_{ej}	5–150 M_{\odot}
CSM mass	M_{CSM}	5–150 M_{\odot}
CSM radius	R_{CSM}	$(2-4) \times 10^{16}$ cm

11.3.3 Neutrino flux and event rate at Earth

The neutrino and antineutrino flux ($F_{\nu_{\alpha}+\bar{\nu}_{\alpha}}$ with $\alpha = e, \mu, \tau$) at Earth from a SN at redshift z and as a function of time in the observer frame is [$\text{GeV}^{-1}\text{s}^{-1}\text{cm}^{-2}$]:

$$F_{\nu_{\alpha}+\bar{\nu}_{\alpha}}(E_{\nu}, t) = \frac{(1+z)^2}{4\pi d_L^2(z)} v_{\text{sh}}(t) \sum_{\beta} P_{\nu_{\beta} \rightarrow \nu_{\alpha}} Q_{\nu_{\beta}+\bar{\nu}_{\beta}}(E_{\nu_{\alpha}}(1+z), R(t)), \quad (11.14)$$

where $Q_{\nu_{\beta}+\bar{\nu}_{\beta}}$ is defined as in Eqs. 11.10 and 11.11. Neutrinos change their flavor while propagating, hence the flavor transition probabilities are given by [57]:

$$P_{\nu_e \rightarrow \nu_{\mu}} = P_{\nu_{\mu} \rightarrow \nu_e} = P_{\nu_e \rightarrow \nu_{\tau}} = \frac{1}{4} \sin^2 2\theta_{12}, \quad (11.15)$$

$$P_{\nu_{\mu} \rightarrow \nu_{\mu}} = P_{\nu_{\mu} \rightarrow \nu_{\tau}} = \frac{1}{8}(4 - \sin^2 2\theta_{12}), \quad (11.16)$$

$$P_{\nu_e \rightarrow \nu_e} = 1 - \frac{1}{2} \sin^2 2\theta_{12}, \quad (11.17)$$

with $\theta_{12} \simeq 33.5$ deg [167], and $P_{\nu_\beta \rightarrow \nu_\alpha} = P_{\bar{\nu}_\beta \rightarrow \bar{\nu}_\alpha}$. The luminosity distance $d_L(z)$ is defined in a flat Λ CDM cosmology as

$$d_L(z) = (1+z) \frac{c}{H_0} \int_0^z \frac{dz'}{\sqrt{\Omega_\Lambda + \Omega_M(1+z')^3}}, \quad (11.18)$$

where $\Omega_M = 0.315$, $\Omega_\Lambda = 0.685$ and the Hubble constant is $H_0 = 67.4 \text{ km s}^{-1} \text{ Mpc}^{-1}$ [42].

The neutrino fluence [$\text{GeV}^{-1} \text{ cm}^{-2}$] is calculated using

$$\Phi_{\nu_\alpha + \bar{\nu}_\alpha}(E_\nu) = \int_{t_{\text{bo}}}^{t_{\text{bo}}+394} F_{\nu_\alpha + \bar{\nu}_\alpha}(E_\nu, t) dt, \quad (11.19)$$

with $t_{\text{bo}} = t(R_{\text{bo}})$ and the time integral being restricted to 394 days.

Finally, the event rate of muon neutrinos and antineutrinos expected at the IceCube Neutrino Observatory is

$$\dot{N}_{\nu_\mu + \bar{\nu}_\mu}(t) = \int_{E_{\nu, \text{min}}}^{E_{\nu, \text{max}}} dE_\nu A_{\text{eff}}(E_\nu, \delta) F_{\nu_\mu + \bar{\nu}_\mu}(E_\nu, t) \quad (11.20)$$

where $A_{\text{eff}}(E_\nu, \delta)$ is the detector effective area [20]. The minimum neutrino energy is $E_{\nu, \text{min}} = 100$ GeV for the declination of interest [20], and $F_{\nu_\mu + \bar{\nu}_\mu}(E_\nu, t)$ has been introduced in Eq. 11.14. In the following, we work under the assumption of perfect discrimination between astrophysical and atmospheric neutrinos; see Sec. 11.5 for a discussion on the expected event rate if the event sample should be contaminated by atmospheric neutrinos in the energy region below 100 TeV. The maximum neutrino energy $E_{\nu, \text{max}}$ is related to the maximum proton energy: $E_{\nu, \text{max}} = xE_{p, \text{max}}$.

The total number of muon neutrinos and antineutrinos is computed over the temporal interval of 394 days:

$$N_{\nu_\mu + \bar{\nu}_\mu} = \int_{t_{\text{bo}}}^{t_{\text{bo}}+394} dt \dot{N}_{\nu_\mu + \bar{\nu}_\mu}(t). \quad (11.21)$$

11.4 Forecast of the neutrino signal

In this section, we present the results on the neutrino signal expected from AT2019fdr. First, we discuss the neutrino spectral energy distribution and the event rate expected in the IceCube Neutrino Observatory. We then investigate the dependence of the expected signal on the uncertainties of the SLSN II model.

11.4.1 Energy fluence and temporal evolution of the neutrino event rate

Before focusing on the energy fluence and event rate of the detectable neutrino signal, we explore the characteristic cooling times of protons and the acceleration timescale characteristic of AT2019fdr, introduced in Sec. 11.3.1. In order to give an idea of the variation of the cooling and acceleration timescales across the SLSN shell, Fig. 11.3 shows the proton cooling times as a function of the proton energy in the reference frame of the central compact object and at the representative radii R_{bo} and R_{CSM} for the SLSN configuration with $(\tilde{E}_k, R_{\text{CSM}}, M_{\text{ej}}, M_{\text{CSM}}) = (10^{53} \text{ erg}, 4 \times 10^{16} \text{ cm}, 6 M_{\odot}, 49 M_{\odot})$. As discussed in the following, this SLSN configuration leads to the most optimistic scenario for neutrino production.

Proton-proton collisions are responsible for the dominant energy loss channel. Even though Fig. 11.3 represents the characteristic cooling times for one specific SLSN configuration, the hierarchy between pp and adiabatic losses is representative of all SLSN configurations considered in this work (lower \tilde{E}_k and R_{CSM} larger than the ones adopted here would lead to scenarios with adiabatic energy losses being dominant over pp ones).

The evolution of $E_{p,\text{max}}$ depends on the specific choice of parameters \tilde{E}_k , R_{CSM} , M_{ej} , and R_{CSM} , determining whether $R_{\text{bo}} \lesssim R_{\text{dec}}$. For the typical values of \tilde{E}_k and R_{CSM} considered in this work, the condition $t_{pp} < t_{\text{ad}}$ is always fulfilled, and $E_{p,\text{max}}$ increases as a function of R up to R_{dec} , and decreases otherwise. In fact, by using Eqs. 11.1, 11.2 and 11.5, we find:

$$E_{p,\text{max}} = \frac{eBu_{\text{sh}}^2}{24c^2k_{pp}\sigma_{pp}n_{\text{CSM}}} \propto \begin{cases} M_{\text{ej}}^{-15/14} M_{\text{CSM}}^{-13/14} R^{4/7} & R < R_{\text{dec}} \\ M_{\text{CSM}}^{-2} R^{-1/2} & R \geq R_{\text{dec}} \end{cases} \quad (11.22)$$

Appendix C.2 provides more details on the scaling of $E_{p,\text{max}}$ as a function of the SLSN model parameters.

The muon neutrino and antineutrino fluence, defined as in Eq. 11.19, is shown in Fig. 11.4 as a function of the neutrino energy. The band takes into account the uncertainties on the parameters characterizing AT2019fdr (see Sec. 11.3.2) and is defined by the parameter configurations leading to the highest and lowest neutrino fluence. Note that, for the SLSN parameters adopted in this work, the synchrotron cooling of charged pions and muons produced via pp interactions is negligible. In fact, the typical energies for which this energy loss becomes relevant are at least three orders of magnitude larger than the maximum achievable proton energies. Therefore, the neutrino spectra are not affected by the cooling of mesons.

Given our selection criterion (i.e., the observation of IC200530 about 394 days after the shock breakout and the constraints on the rising time of the light curve of AT2019fdr), the scenarios with the lowest fluence are the ones corresponding to configurations with

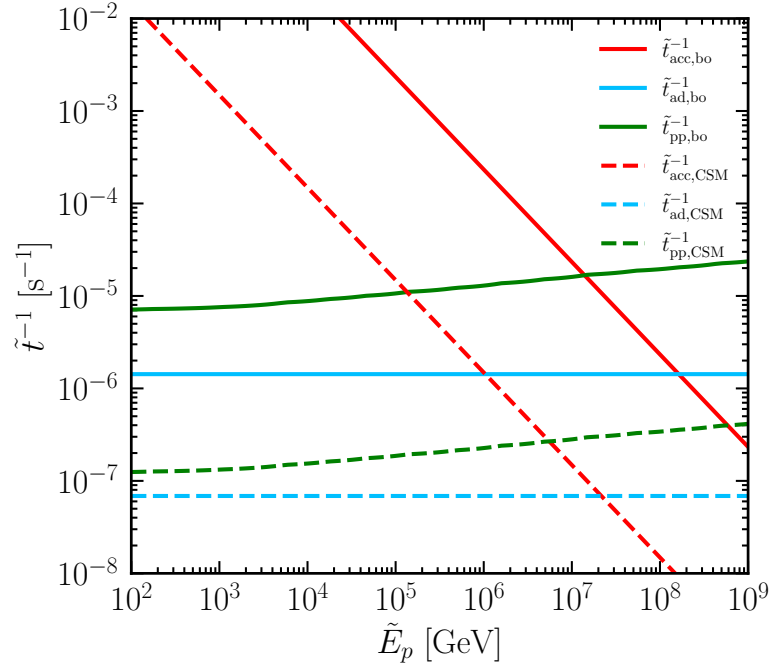


Figure 11.3: Inverse cooling and acceleration timescales for protons at the breakout radius (R_{bo} , solid lines) and at the outer edge R_{CSM} (dashed lines) as functions of the proton energy in rest frame for the SLSN configuration with $(\tilde{E}_k, R_{CSM}, M_{ej}, M_{CSM}) = (10^{53} \text{ erg}, 4 \times 10^{16} \text{ cm}, 6 M_{\odot}, 49 M_{\odot})$. The acceleration timescale, pp and adiabatic cooling timescales are represented in red, green and light blue, respectively. Protons are strongly cooled by pp energy losses for all the SLSN parameter configurations considered in this work.

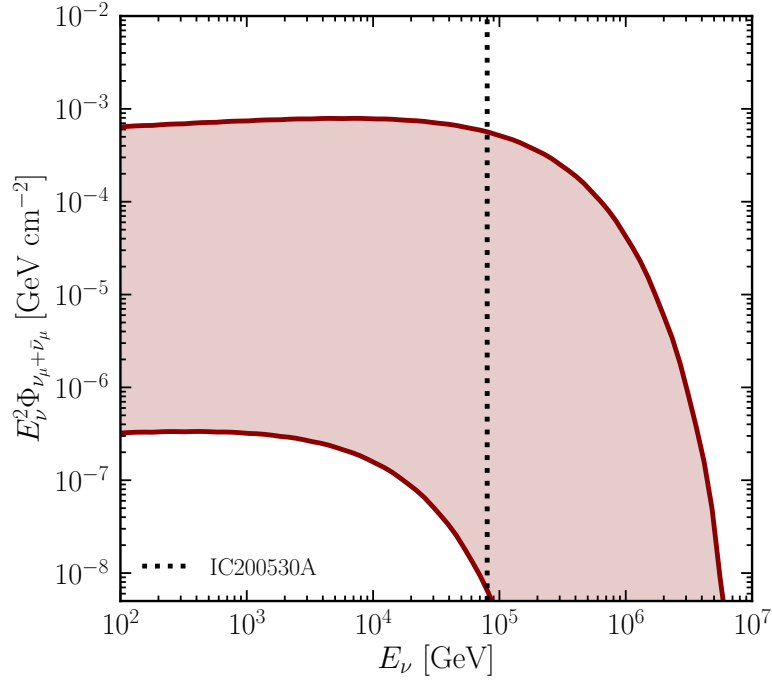


Figure 11.4: Muon neutrino and antineutrino fluence from AT2019fdr as a function of the neutrino energy. The reconstructed neutrino energy ($E_\nu \sim 80$ TeV) for IC200530 is marked by a black dotted vertical line. The band encloses the uncertainties on the parameters characterizing AT2019fdr, see Table 11.1. In the proximity of the energy of interest for the interpretation of IC200530, the fluence can vary up to a factor $\mathcal{O}(10^5)$ in magnitude. Within the allowed parameter space, the lowest fluence is foreseen for configurations with large R_{CSM} , low M_{CSM} and high M_{ej} . The largest neutrino fluence is instead obtained for intermediate values of M_{CSM} and low M_{ej} , which moreover allow a higher proton energy cutoff.

large R_{CSM} , low M_{CSM} and high M_{ej} . On the other hand, given the reduced parameter space allowed for low R_{CSM} (see Appendix C.1), the most optimistic scenario corresponds to the highest R_{CSM} , the lowest accessible M_{ej} , and intermediate values of M_{CSM} ($M_{\text{CSM}} \simeq 30\text{--}50M_\odot$). We refer the reader to Sec. 11.4.2 for a discussion on the dependence of the neutrino fluence from the SLSN characteristic parameters.

The reconstructed neutrino energy for the IC200530 neutrino event is marked with a dotted vertical line and it falls in the same energy range as the predicted fluence. One can see that, around the reconstructed energy of IC200530, the fluence can vary up to $\mathcal{O}(10^5)$ in magnitude. However, it is worth noting that the reconstructed energy carries an intrinsic uncertainty and may differ from the real energy of the detected neutrino, nevertheless we show it in order to guide the eye.

The muon neutrino and antineutrino event rate expected in IceCube (Eq. 11.20) is shown in Fig. 11.5 as a function of time. The band in Fig. 11.5 takes into account the

uncertainties on the characteristic quantities of AT2019fdr summarized in Table 11.1. For all SLSN cases within the envelope in Fig. 11.5, the event rate increases rapidly at early times. After the peak, depending on whether $R_{\text{dec}} > R_{\text{bo}}$ or $R_{\text{dec}} < R_{\text{bo}}$, the neutrino event rate has a steeper or shallower decay. These two different trends are related to the evolution of the shock velocity and the maximum proton energy $E_{\text{p,max}}$. Indeed, $E_{\text{p,max}}$ increases up to R_{dec} as t increases and declines later. Since the detector effective area A_{eff} increases as a function of E_{ν} [20] and the decline of v_{sh} for $R_{\text{bo}} < R < R_{\text{dec}}$ is shallow, a compensation effect can arise among the two quantities; hence, the drop of the $\dot{N}_{\nu_{\mu}+\bar{\nu}_{\mu}}$ curve can be slow. Viceversa, when both $E_{\text{p,max}}$ and v_{sh} decrease, the event rate drops faster. Around the day of detection of IC200530 (marked by a vertical dotted line), the neutrino event rate is expected to vary between $[1.3 \times 10^{-8}, 3.3 \times 10^{-5}]$ days $^{-1}$.

It is important to note that only a sub-sample of the SLSN parameter set reported in Table 11.1 allows us to obtain a neutrino signal compatible with our observational constraints. For example, none of the SLSN scenarios with $\tilde{E}_{\text{k}} = 10^{53}$ erg and $R_{\text{CSM}} = 2 \times 10^{16}$ cm passes our selection criteria, since the shock crosses the CSM envelope in a time shorter than 394 days.

11.4.2 Dependence of the neutrino signal on the parameters of AT2019fdr

In order to better explore the dependence of the neutrino signal expected in IceCube on M_{ej} and M_{CSM} , for $\tilde{E}_{\text{k}} = 10^{53}$ erg, first we investigate the neutrino fluence as a function of M_{CSM} for fixed R_{CSM} and M_{ej} and then we fix M_{CSM} and vary M_{ej} . The choice of M_{CSM} and M_{ej} is guided by the SLSN configurations that better highlight the changes in the neutrino fluence for $R_{\text{bo}} \lesssim R_{\text{dec}}$. From the panel on the left in Fig. 11.6, we see that the fluence increases as M_{CSM} increases up to $M_{\text{CSM}} = 85 M_{\odot}$. For larger M_{CSM} , $R_{\text{bo}} > R_{\text{dec}}$, and therefore a turnover with a slow drop can be observed. Furthermore, a slight shift of the neutrino cutoff energy towards lower energies is visible as M_{CSM} increases. The latter is due to the enhanced pp energy loss determined by the larger density as well as the smaller v_{sh} , which prevent particles from being accelerated to higher energies (see Eq. 11.22).

In the right panel of Fig. 11.6, we observe an enhancement of the fluence as M_{ej} decreases. Nevertheless, this trend is inverted for $M_{\text{ej}} \lesssim 13 M_{\odot}$, representative of the regime with $R_{\text{bo}} > R_{\text{dec}}$, where the lower v_{sh} is responsible for a slight decrease in the neutrino production, together with a shift of the neutrino energy cutoff to lower energies.

Figure 11.7 shows the temporal evolution of the muon neutrino and antineutrino flux for the scenarios with the highest (left panel) and the lowest (right panel) expected number of neutrinos. In all cases, the flux decreases as time increases and shifts to

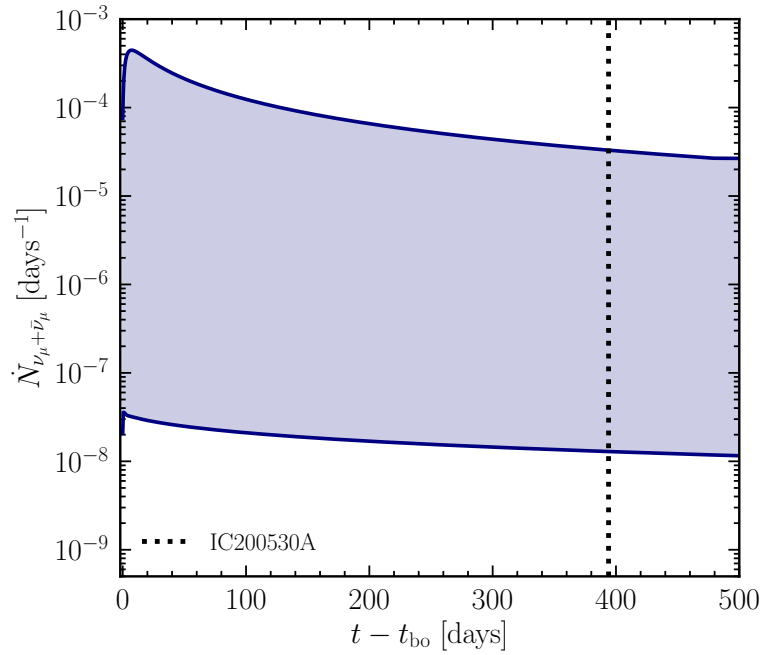


Figure 11.5: Muon neutrino and antineutrino event rate expected at the IceCube Neutrino Observatory from AT2019fdr as a function of the time after the shock breakout. The band marks the uncertainty on the neutrino event rate due to the SLSN model parameters, see Table 11.1. The event rate increases rapidly at early times. After peak, the event rates for the SLSN scenarios representing the edges of the envelope decline because of the dominant decreasing trend of v_{sh} as a function of time. In some intermediate scenarios, the increasing trend of $E_{\text{p,max}}$ and shallow decrease of v_{sh} can be compensated, providing an increasing event rate at the moment of the detection. The neutrino event IC200530 has been observed ~ 394 days after t_{bo} as indicated by the dotted vertical line. In the proximity of the detection day, the event rate can vary up to a factor $\mathcal{O}(10^3)$ in magnitude.

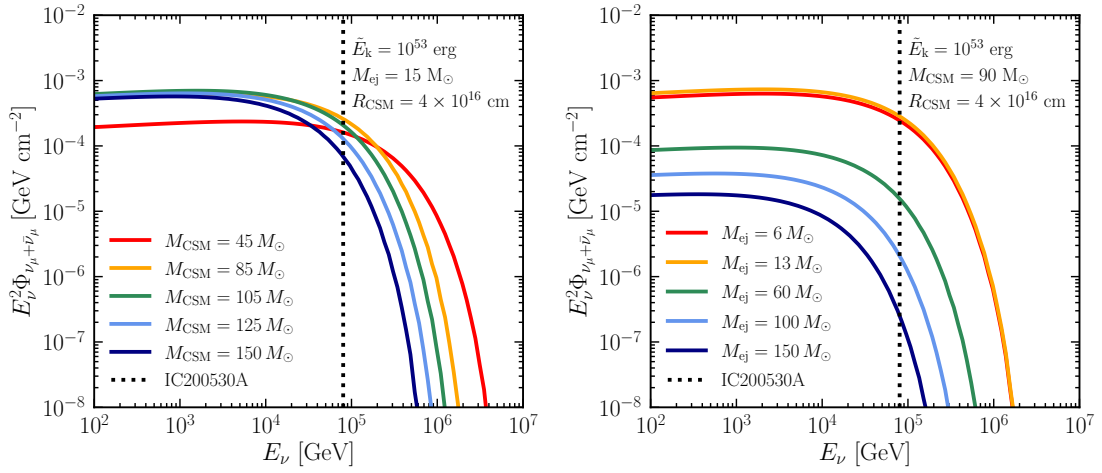


Figure 11.6: *Left panel:* Muon neutrino and antineutrino fluence for AT2019fdr as a function of the neutrino energy for fixed R_{CSM} , M_{ej} , $\tilde{E}_k = 10^{53}$ erg and variable M_{CSM} . The fluence increases as M_{CSM} increases up to $M_{\text{CSM}} = 85 M_\odot$, where one transitions into the regime with $R_{\text{bo}} > R_{\text{dec}}$. Then a slow decrease in amplitude is observed. Furthermore, a slight shift of the neutrino cutoff energy towards lower energies occurs as M_{CSM} increases because of the enhanced pp energy loss which prevents particles from being accelerated to higher energies. *Right panel:* Same as in the left panel, but for fixed M_{CSM} and variable M_{ej} . The fluence increases as M_{ej} decreases. This trend is inverted for $M_{\text{ej}} \lesssim 13 M_\odot$, since $R_{\text{bo}} > R_{\text{dec}}$, and thus the overall shock velocity becomes lower.

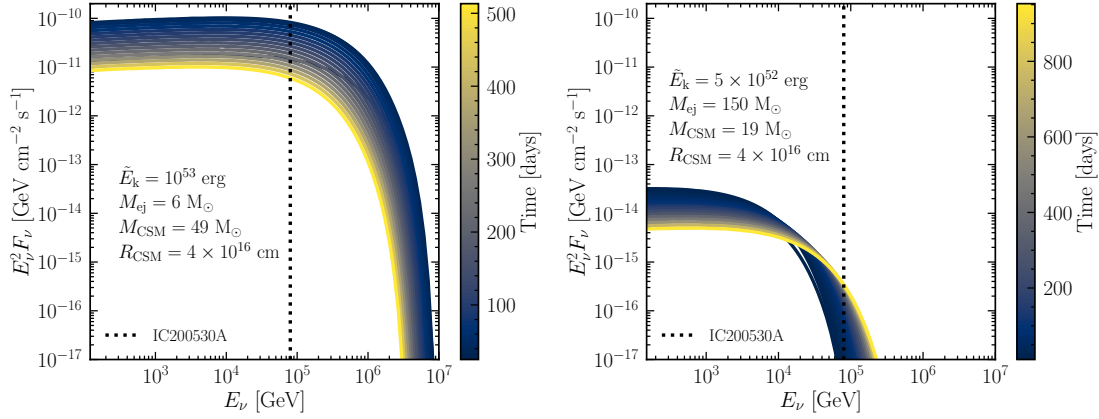


Figure 11.7: Temporal evolution of muon neutrino and antineutrino flux from AT2019fdr as a function of the neutrino energy for the most optimistic, $(\tilde{E}_k, R_{\text{CSM}}, M_{\text{ej}}, M_{\text{CSM}}) = (10^{53} \text{ erg}, 4 \times 10^{16} \text{ cm}, 6 M_{\odot}, 49 M_{\odot})$ and pessimistic scenario $(5 \times 10^{52} \text{ erg}, 4 \times 10^{16} \text{ cm}, 150 M_{\odot}, 19 M_{\odot})$. The reconstructed energy for the IC200530 neutrino event is marked with a dotted vertical. In all cases, the flux decreases with time with a reduction (growth) of the maximum neutrino energy in the optimistic (pessimistic) scenario.

lower or higher energies, for the most optimistic and pessimistic scenarios, respectively. Around the day of detection, the flux in the best scenario is a factor $\mathcal{O}(10^5)$ larger than the most pessimistic scenario.

In order to investigate the origin of IC200530, we integrate the event rate over 394 days of the neutrino signal for all selected SLSN configurations and obtain the total number of muon neutrino and antineutrino events, $N_{\nu_{\mu} + \bar{\nu}_{\mu}}$ (Eq. 11.21). A contour plot of $N_{\nu_{\mu} + \bar{\nu}_{\mu}}$ in the plane spanned by M_{ej} and M_{CSM} is shown in Fig. 11.8 for $R_{\text{CSM}} = 4 \times 10^{16} \text{ cm}$ and $\tilde{E}_k = 10^{53} \text{ erg}$ as a representative example. The allowed region of the parameter space is delimited by the solid black line and plotted in orange (with the color gradient representing a low number of events in lighter hues), while the excluded parameter space is displayed in light yellow. The dotted contour lines show how the neutrino number is affected as the line $R_{\text{bo}} = R_{\text{dec}}$ (along which the cusps of the dotted lines lie) is crossed. In the region $R_{\text{dec}} > R_{\text{bo}}$, for fixed M_{ej} , the number of neutrino events increases as M_{CSM} increases, whilst for fixed M_{CSM} and increasing M_{ej} we find the opposite trend. The opposite behaviour occurs for $R_{\text{dec}} < R_{\text{bo}}$.

For the SLSN parameter configurations under consideration, the most optimistic scenarios for the neutrino emission lead to $N_{\nu_{\mu} + \bar{\nu}_{\mu}} \simeq 4.6 \times 10^{-2}$; the latter is achieved for relatively low values of $M_{\text{ej}} = 6\text{--}9 M_{\odot}$ and intermediate $M_{\text{CSM}} = 49\text{--}68 M_{\odot}$, with the best scenario corresponding to $(\tilde{E}_k, R_{\text{CSM}}, M_{\text{ej}}, M_{\text{CSM}}) \simeq (10^{53} \text{ erg}, 4 \times 10^{16} \text{ cm}, 6 M_{\odot}, 49 M_{\odot})$.

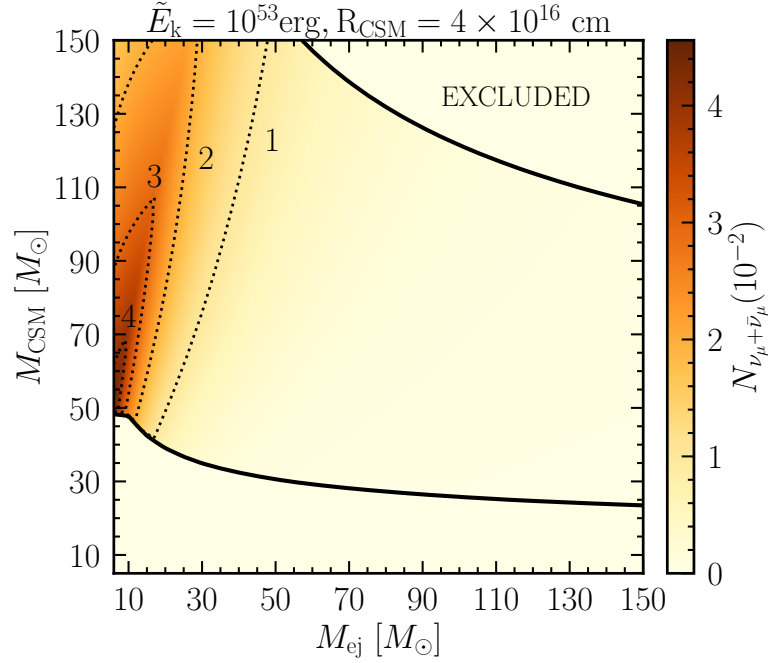


Figure 11.8: Contour plot of the total number of muon neutrino and antineutrino events expected at the IceCube Neutrino Observatory from AT2019fdr in 394 days and in the plane spanned by M_{ej} and M_{CSM} for $\tilde{E}_k = 10^{53}$ erg and $R_{CSM} = 4 \times 10^{16}$ cm. The black solid lines marks the allowed region of the parameter space, defined by requiring that the location of the shock at the day of neutrino production is still in the CSM envelope and that the SLSN model parameters are compatible with the the light curve rise time. For fixed M_{CSM} , the total neutrino number decreases as M_{ej} increases, given the decline of the shock velocity v_{sh} . Viceversa, for fixed M_{ej} , the number increases as M_{CSM} increases, given the larger number of proton targets for pp interactions. In the region $R_{bo} > R_{dec}$, one can see an inverted trend. The dotted lines correspond to the contour lines which track the scenarios providing the number of neutrino events displayed, and show how the neutrino number is affected in the transtition from $R_{bo} > R_{dec}$ to $R_{bo} < R_{dec}$ regions. See the main text for more details.

Table 11.2: Number of muon neutrino and antineutrino events expected in 394 days from the shock breakout from AT2019fdr for the most optimistic and pessimistic scenarios, with the low energy cutoff fixed at 100 GeV (i.e., excellent discrimination between the astrophysical and atmospheric signals) and 100 TeV (i.e., under the conservative assumption that the atmospheric background could not be eliminated). The most optimistic and pessimistic scenarios correspond to the following SLSN model parameters: $(\tilde{E}_k, R_{\text{CSM}}, M_{\text{ej}}, M_{\text{CSM}}) = (10^{53} \text{ erg}, 4 \times 10^{16} \text{ cm}, 6 M_{\odot}, 49 M_{\odot})$ and $(5 \times 10^{52} \text{ erg}, 4 \times 10^{16} \text{ cm}, 150 M_{\odot}, 19 M_{\odot})$, respectively. In the last column we estimate the signalness $[N_{\nu_{\mu} + \bar{\nu}_{\mu}, \text{astro}} / (N_{\nu_{\mu} + \bar{\nu}_{\mu}, \text{astro}} + N_{\nu_{\mu} + \bar{\nu}_{\mu}, \text{atm}})]$, by computing the number of atmospheric neutrino events over a period of 394 days, for 0.75° around the direction of the source.

Energy cut	$N_{\nu_{\mu} + \bar{\nu}_{\mu}, \text{pessimistic}}$	$N_{\nu_{\mu} + \bar{\nu}_{\mu}, \text{optimistic}}$	Signalness
$E_{\nu, \text{min}} = 100 \text{ GeV}$	8×10^{-6}	4.6×10^{-2}	$10^{-4} - 1\%$
$E_{\nu, \text{min}} = 100 \text{ TeV}$	9.5×10^{-9}	4.6×10^{-3}	$10^{-4} - 40\%$

11.5 Discussion

Table 11.2 summarizes the total number of muon neutrino and antineutrino events expected within 394 days from the shock breakout from AT2019fdr for the most optimistic and pessimistic SLSN configurations in terms of neutrino emission. The largest [smallest] number of events is obtained for the SLSN configuration with $(\tilde{E}_k, R_{\text{CSM}}, M_{\text{ej}}, M_{\text{CSM}}) = (10^{53} \text{ erg}, 4 \times 10^{16} \text{ cm}, 6 M_{\odot}, 49 M_{\odot})$ [$(5 \times 10^{52} \text{ erg}, 4 \times 10^{16} \text{ cm}, 150 M_{\odot}, 19 M_{\odot})$], and correspond to the edges of the band in Fig. 11.5.

An important aspect to consider in the interpretation of the neutrino event IC200530 concerns the discrimination of the atmospheric neutrino background, which dominates over the astrophysical neutrino flux below $\simeq 100 \text{ TeV}$. As such, in Table 11.2 we distinguish between one case with the lower energy cutoff fixed at 100 GeV, mimicking excellent discrimination of the atmospheric neutrino background (see Sec. 11.3.3), and one more conservative case with the lower energy cutoff at 100 TeV. The latter case reproduces a situation where the atmospheric neutrino events could not be distinguished from the astrophysical ones in the lower energy range. Although a dedicated likelihood analysis is beyond the scope of this work, the last column of Table 11.2 reports $N_{\nu_{\mu} + \bar{\nu}_{\mu}, \text{astro}} / (N_{\nu_{\mu} + \bar{\nu}_{\mu}, \text{astro}} + N_{\nu_{\mu} + \bar{\nu}_{\mu}, \text{atm}})$, which should give an idea of the expected signalness and gives an indication of the probability that a detected neutrino event could be of astrophysical origin. It is evident that only an optimal discrimination of the atmospheric neutrino background allows to obtain a signalness of 40%, roughly comparable with the one of the neutrino event IC200530. The evolution of the neutrino curve shown in Fig. 11.5 should be considered carefully. In fact, some intermediate SLSN scenarios

enclosed in the envelope in Fig. 11.5, and compatible with the reconstructed energy of the neutrino event IC200530A, have an event rate still increasing at the day of detection, therefore increasing the neutrino detection chances at later times, as it is the case for the neutrino event IC200530.

In order to assess whether the number of expected events in Table 11.2 is compatible with the detection of one neutrino event (IC200530) after 394 days from the shock breakout, we take into account the Eddington bias on neutrino observations. The Eddington bias must be taken into account when dealing with very small number of neutrino events, such as in this case; we refer the interested reader to [459] for a dedicated discussion. By relying on the local rate of SLSN IIn provided in [403] and integrating over the cosmic history by assuming that the redshift evolution of SLSN IIn follows the star formation rate [515], we obtain an average effective density of SLSN IIn equal to $\mathcal{O}(3 \times 10^3) \text{ Mpc}^{-3}$. Although Fig. 2 of Strotjohann:2018ufz was derived within a simplified framework and for constant redshift evolution, by extrapolating to larger effective source densities we conclude that the number of expected events in Table 11.2 may be compatible with the detection of at least one or two neutrino events from AT2019fdr. By taking into account the fact that the neutrino energy distribution of AT2019fdr falls in a region where the discrimination of the atmospheric neutrino background may be challenging, our findings hint towards a possible association of the neutrino event IC200530 to AT2019fdr. In addition, our results are compatible with the upper limits on the neutrino emission from the AT2019fdr source placed by the ANTARES Collaboration [50].

We should stress that the forecasted number of expected neutrino events includes some caveats related to our modeling. For example, one of the sources of uncertainty in the computation of the neutrino flux is the proton acceleration efficiency ε_p . In this paper, we have adopted an optimistic $\varepsilon_p = 0.1$, assuming that the shocks accelerating protons are parallel or quasi-parallel and therefore efficient diffusive shock acceleration occurs [113]. However, lower values of ε_p would be possible for oblique shocks, with poorer particle acceleration efficiency. Values as low as $\varepsilon_p \simeq 0.003\text{--}0.01$ have been inferred in [67] for a nova, assuming shocks as the powering source of the simultaneously observed optical and γ -rays. However, observational constraints from other optical transients, including SLSNe, are still lacking; in addition, AT2019fdr is much more luminous than classical novae, possibly hinting to different conditions present in the acceleration region.

We stress that the neutrino flux scales linearly with ε_p , allowing the reader to easily scale our results. All cases summarized in Table 11.2 would be compatible with the detection of one neutrino event, after taking into account the Eddington bias. Indeed, the detection of a single neutrino event may actually hint towards intermediate SLSN configurations, as well as values of ε_p lower than our benchmark one.

Similarly, in this work we have assumed that protons are accelerated at the shock to a power law with slope $k = 2$, which is predicted by the test particle theory of diffusive

shock acceleration. Nonetheless, non-linear effects involving the amplified magnetic field can kick in, modifying the shock structure and making the cosmic ray spectra mildly steeper than $k = 2$ [112]. Larger k would result in steeper neutrino spectra, since the latter inherit the shape of the parent proton spectrum; as a consequence, lower fluxes should be expected in the energy of interest.

Another caveat to take into account concerns the use of the AT2019fdr discovery date in the observer frame as the breakout time of the shock. In fact, based on the non-detections in the ZTF data, we have assumed an explosion epoch at the first detection at $\text{MJD} = 58606 \pm 6$ days on the basis of a fit on the existing data. Nevertheless, even allowing for an onset of the shock breakout to be as much as ~ 20 days earlier than the first observed light, our predictions in Table 11.2 would not be affected by a factor larger than 10%.

Since initial submission of this manuscript, other publications have analysed IC200530 under the paradigm of a TDE origin [416]. The additional data presented within these works suggest that an apparent increase in the late time near infrared (NIR) emission may be attributed to a dust from the TDE emission. However, increasing late time NIR emission has been seen in other interacting SNe. For instance, the bright SN II In SN2010jl exhibits such a NIR increase at late times; high-resolution spectroscopic observations show that this increasing emission was the result of rapid dust formation within the SN ejecta [191].

In addition, the vast majority of TDEs show bright X-ray emission over the full optical/UV evolution of an event [e.g., 65, 102, 238, 505]. Of those whose emission is dominated by optical/UV but has been detected in X-rays, the X-ray luminosities are an order of magnitude or more fainter than the eROSITA detection [e.g., 253, 240, 245, 244]. In addition, AT2019fdr is found close to the nucleus in a Narrow-Line Seyfert 1 active galaxy [182]. Seyfert AGN galaxies are known to exhibit bright X-rays, with a mean X-ray luminosity of $\sim 10^{43}$ erg s $^{-1}$ [e.g., 420] similar to that detected by eROSITA. Furthermore, [420] and references therewithin showed that a significant fraction of unobscured AGN, and particularly those selected in optical, tend to exhibit excess soft X-ray emission that can be best described by an absorbed blackbody. They found that this excess can be well fit with a rest-frame blackbody temperature ranging between ~ 0.5 – 0.25 keV, with a mean temperature of ~ 0.1 keV, which is consistent with the blackbody temperature derived by [416]. Due to the angular resolution of eROSITA, further high resolution X-ray observations would be necessary to confirm whether the detected X-ray emission arises from its host galaxy's AGN or is consistent with the location of AT2019fdr.

If the latter was the case, a detection of X-rays from a SLSN at late times would not be surprising. The total luminosity of the shock and the pre-shock column density of the CSM medium determine the observation features of high-energy radiation. Unless we are in the presence of extremely high shock temperatures or a high ratio of the

shock luminosity to the column density, which would guarantee the CSM ionization to a large extent, the photoelectric absorption is an important energy loss channel for high energy photons. The latter could explain the non observation of X-rays at earlier times [375]. Unfortunately, as already discussed, there could be degeneracies among the parameters, leading to similar properties of the SLSN light curve. Nevertheless, the slow rise of the optical light curve, the very high luminosity peak, and the non observation of X-rays for a considerable amount of time after the first detection would point towards scenarios with highly energetic and relatively low mass ejecta moving through extended high CSM mass stellar winds or shells.

11.6 Conclusions

The IceCube neutrino event IC200530 has been proposed to be in likely coincidence with the source AT2019fdr located at $z = 0.2666$, observed in the ultraviolet and optical bands, and interpreted as a tidal disruption event candidate in a Narrow-Line Seyfert 1 galaxy. In this paper, we show that the spectra, light curve and color evolution of AT2019fdr may be compatible with the ones of a hydrogen rich superluminous supernova instead.

Under this assumption, the neutrino event IC200530, detected ~ 300 days after the peak of the electromagnetic emission and with a reconstructed energy of 80 TeV, may have originated as a result of inelastic proton-proton collisions due to the interaction of the supernova ejecta with the circumstellar medium. We find that approximately 10^{-8} – 5×10^{-2} muon neutrino and antineutrino events could have been produced by AT2019fdr within the timeframe of interest (see Table 11.2), by taking into account the uncertainties on the total ejecta energetics, ejecta mass and on the properties of the the circumstellar medium, as well as the uncertainties in the discrimination of the atmospheric and astrophysical neutrino fluxes. By considering the Eddington bias on neutrino observations, our findings may be compatible with the detection of one neutrino event from AT2019fdr.

In conclusion, the neutrino event IC200530 may be associated with the hydrogen rich superluminous supernova AT2019fdr. As a deeper understanding of the electromagnetic data will become available, neutrinos could be powerful messengers to help to disentangle the nature of AT2019fdr and discover its physics.

Paper IV: High-energy neutrinos from interaction-powered supernovae

This chapter is a reprint of:

Tetyana Pitik, Irene Tamborra, Massimiliano Lincetto, Anna Franckowiak
Optically Informed Searches of High-Energy Neutrinos from Interaction-Powered Supernovae, *MNRAS*, [arXiv:2306.01833](https://arxiv.org/abs/2306.01833)

ABSTRACT

The interaction between the ejecta of supernovae (SNe) of Type II_n and a dense circumstellar medium (CSM) can efficiently generate thermal UV/optical radiation and lead to the emission of neutrinos in the 1-10³ TeV range. We investigate the connection between the neutrino signal detectable at the IceCube Neutrino Observatory and the electromagnetic signal observable by optical wide-field, high-cadence surveys to outline the best strategy for upcoming follow-up searches. We outline a semi-analytical model that connects the optical lightcurve properties to the SN parameters and find that a large peak luminosity ($L_{\text{peak}} \gtrsim 10^{43} - 10^{44} \text{ erg s}^{-1}$) and an average rise time ($t_{\text{rise}} \gtrsim 10 - 40$ days) are necessary for copious neutrino emission. Nevertheless, the most promising L_{peak} and t_{rise} can be obtained for SN configurations that are not optimal for neutrino emission. Such ambiguous correspondence between the optical lightcurve properties and the number of IceCube neutrino events implies that relying on optical observations only, a range of expected neutrino events should be considered (e.g. the expected number of neutrino events can vary up to two orders of magnitude for some among the brightest SNe II_n observed by the Zwicky Transient Facility up to now, SN 2020usa and SN 2020in). In addition, the peak in the high-energy neutrino curve should be expected a few t_{rise} after the peak in the optical lightcurve. Our findings highlight

that it is crucial to infer the SN properties from multi-wavelength observations rather than focusing on the optical band only to enhance upcoming neutrino searches.

12.1 Introduction

Astrophysical neutrinos with TeV–PeV energy are routinely observed by the IceCube Neutrino Observatory [232, 46, 23]. While the sources of the observed neutrino flux are not yet known [317, 482], a number of follow-up programs aims to link the observed neutrinos to their electromagnetic counterparts. In this context, the All-Sky Automated Survey for SuperNovae (ASAS-SN) [440, 273], the Zwicky Transient Facility (ZTF) [82, 148] and the Panoramic Survey Telescope and Rapid Response System 1 (Pan-STARRS1) [118] perform dedicated target-of-opportunity searches for optical counterparts of neutrino events [457, 255, 361], and vice versa the IceCube Neutrino Observatory looks for neutrinos in the direction of the sources discovered by optical surveys, see e.g. [24, 19]. The importance of such multi-messenger searches will be strengthened as large-scale transient facilities come online, such as the Rubin Observatory [233].

The putative coincidence of the high-energy neutrino event IC200530A with the candidate superluminous supernova (SLSN) AT2019fdr [397]¹ makes searches of high-energy neutrinos from SNe timely. SLSNe are $\mathcal{O}(10\text{--}100)$ times brighter than standard core-collapse SNe [190, 331], with kinetic energy sometimes larger than 10^{51} erg [415, 362]. SLSNe are broadly divided into two different spectral types: the ones with hydrogen emission lines (SLSNe II) and those without (SLSNe I), see e.g. [187]. The majority of SLSNe II displays strong and narrow hydrogen emission lines similar to those of the less luminous SNe IIn [368, 415, 452] and often dubbed SLSNe IIn. Type IIn SNe are a sub-class of core-collapse SNe [451, 189] characterized by bright and narrow Balmer lines of hydrogen in their spectra which persist for weeks to years after the explosion [437, 176, 188]. Type IIn SNe are expected to have a dense circumstellar material (CSM) surrounding the exploding star. The large luminosity of SNe IIn and the evidence of slowly moving material ahead of the ejecta indicate an efficient interaction of the ejecta with the CSM, which has long been considered a major energy source of the observed optical radiation [448, 97]. Given the similarities of the spectral characteristics, SLSNe IIn are deemed to be extreme cases of SNe IIn, albeit it is unclear whether SLSNe IIn are just the most luminous SNe IIn or they represent a separate population.

The collision between the expanding SN ejecta and the dense CSM gives rise to the forward shock, propagating in the dense SN environment, and the reverse shock moving backward in the SN ejecta. The plasma heated by the forward shock radiates

¹Note that the identification of the nature AT2019fdr is still under debate; it has been suggested that its properties might be compatible with the ones of a tidal disruption event [416].

its energy thermally in the UV/X-ray band. Depending on the column density of the CSM, energetic photons can be reprocessed through photoelectric absorption and/or Compton scattering downwards into the visible waveband, producing the observed optical lightcurve. Alongside the thermal population, a non-thermal distribution of protons and electrons can be created via diffusive shock acceleration.

Once accelerated, the relativistic protons undergo inelastic hadronic collisions with the non-relativistic protons of the shocked CSM, possibly leading to copious production of high-energy neutrinos and gamma-rays [353, 526, 386, 434]. While gamma-rays are absorbed and reprocessed to a large extent in the dense medium (see, e.g., [434]), neutrinos stream freely and reach Earth without absorption [353, 258, 526, 114, 264, 434, 433, 101]. If detected, neutrinos with energies $\gtrsim 100$ TeV from an interacting SN would represent a smoking gun of acceleration of cosmic rays up to PeV energies [78, 95, 139, 138].

In this paper, we consider SNe IIn and SLSNe IIn as belonging to the same population, distinguished primarily by the ejecta energetics and CSM density. We investigate how neutrino production depends on the characteristic quantities describing interaction-powered SNe and connect the main features of the optical lightcurve to the observable neutrino signal in order to optimize joint multi-messenger search strategies.

This work is organized as follows. Section 12.2 outlines the SN model. As for the CSM structure, we mostly focus on the scenario involving SN ejecta propagating in an extended envelope surrounding the progenitor with a wind-like density profile; we then extend our findings to the case involving SN ejecta propagating into a shell of CSM material with uniform density, which might result from a violent eruption shortly before the death of the star. In Sec. 12.3, we introduce the scaling relations for the SN lightcurve properties. Section 12.4 focuses on investigating the dependence of the maximum proton energy on the SN model parameters. In Sec. 12.5, after introducing the method adopted to compute the neutrino spectral energy distribution, the dependence of the total energy emitted in neutrinos is investigated as a function of the SN model parameters. Section 12.6 outlines the detection prospects of neutrinos by relying on two benchmark SLSNe IIn observed by ZTF and discusses the most promising strategies to detect neutrinos by relying on optical observations as well multi-messenger follow-up programs. Finally, our findings are summarized in Sec. 12.7. In addition, the dependence of the SN lightcurve properties and maximum proton energy on the SN model parameters are discussed in Appendix D.1 and D.2, respectively. Moreover, details on the constant density scenario are provided in Appendix D.3.

12.2 Model for interaction-powered supernovae

In this section, we present the theoretical framework of our work. First, we describe the CSM configurations. Then, we focus on the modeling of the interaction between

the SN ejecta and the CSM, leading to the observed electromagnetic radiation. We also outline the SN model parameters and the related uncertainty ranges adopted in this work.

12.2.1 Modeling of the circumstellar medium

Observational data and existing theoretical models indicate that the matter envelope surrounding massive stars could be spherical in shape or exhibit bipolar shells, disks or clumps, with non-trivial density profiles. This is the result of steady or eruptive mass loss episodes, as well as binary interactions of the progenitor prior to the explosion [448]. To this purpose, we consider two CSM configurations: a uniform shell extended up to a radius $R_{\text{CSM},s}$ from the center of the explosion and a spherically symmetric shell with a wind radial profile extending smoothly from the progenitor surface up to an external radius ($R_{\text{CSM},w}$), as sketched in Fig. 12.1. Henceforth we name the former “shell scenario” (s) and the latter “wind scenario” (w).

We assume that the CSM has a mass M_{CSM} , radial extent R_{CSM} , and it is spherically distributed around the SN with a density profile described by a power-law function of the radius:

$$n_{\text{CSM}}(R) = \frac{\rho_{\text{CSM}}(R)}{m} = \frac{(3-s)M_{\text{CSM}}}{4\pi R_{\text{CSM}}^3} \left(\frac{R}{R_{\text{CSM}}} \right)^{-s} \equiv \frac{B}{m} R^{-s}, \quad (12.1)$$

where $m = \mu m_{\text{H}}$, with $\mu = 1.3$ [300] being the mean molecular weight for a neutral gas of solar abundance. We neglect the density dependence on the inner radius of the CSM and consider it to be the same as the progenitor radius $R_{\star} = 10^{13} \text{ cm} \ll R_{\text{CSM}}$. The case $s = 2$ represents the stellar wind scenario, whereas $s = 0$ denotes a shell of uniform density. We assume that the density external to the CSM shell ($R > R_{\text{CSM}}$) is much smaller than the one at $R < R_{\text{CSM}}$.

12.2.2 Shock dynamics

After the SN explodes, and the shock wave passes through the stellar layers, the ejecta gas evolves to free homologous expansion. Relying on numerical simulations, e.g. [314], we assume that during this phase the outer part of the SN ejecta has a power-law density profile [130, 332]:

$$\rho_{\text{ej}}(R, t) = g_n t^{n-3} R^{-n}, \quad (12.2)$$

with

$$g_n = \frac{1}{4\pi(n-\delta)} \frac{[2(5-\delta)(n-5)E_{\text{k}}]^{(n-3)/2}}{[(3-\delta)(n-3)M_{\text{ej}}]^{(n-5)/2}}, \quad (12.3)$$

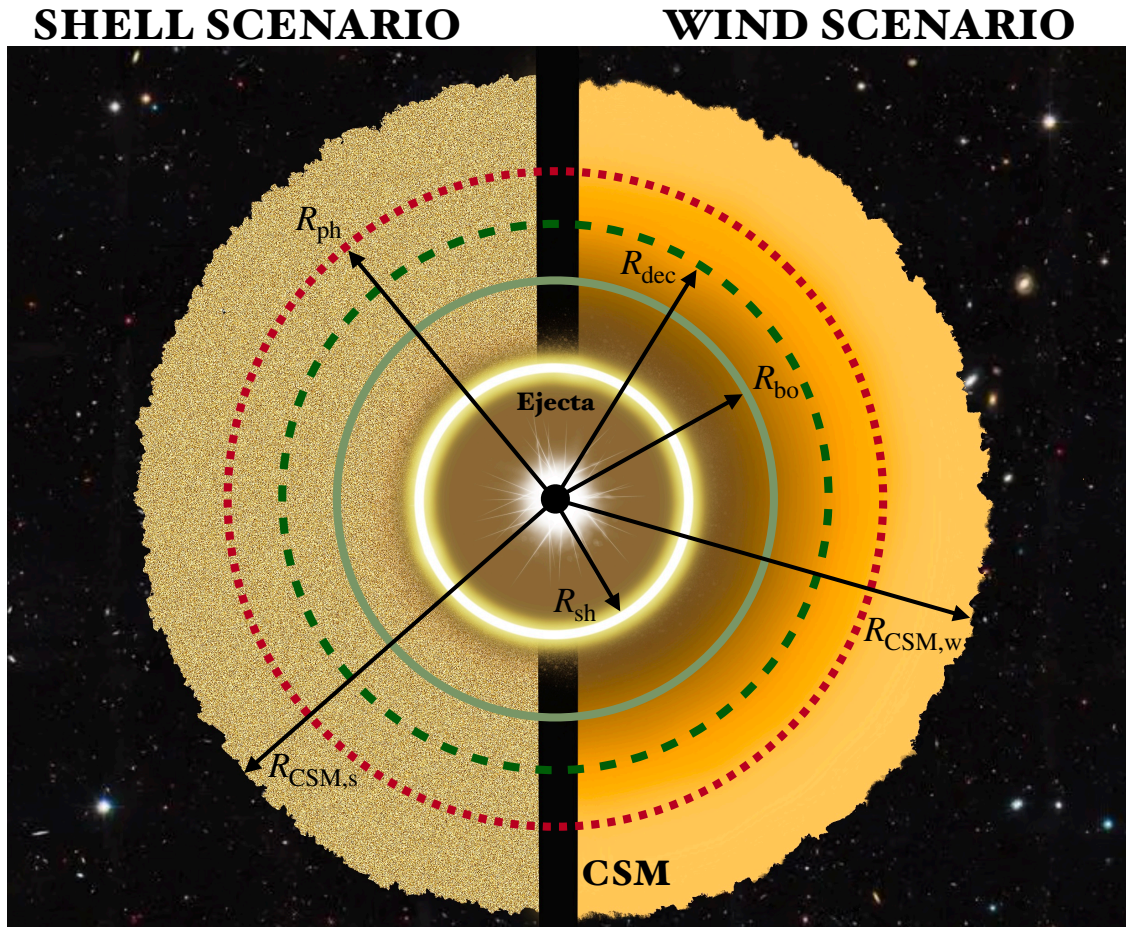


Figure 12.1: Schematic representation of an interaction-powered SN, under the assumption of spherical symmetry. The central compact object (in black) is surrounded by the SN ejecta (brown) and a compact shell extended up to $R_{\text{CSM},s}$ ($R_{\text{CSM},w}$) from the center of explosion for the shell scenario on the left (and the wind scenario, on the right). For the wind density profile, the color gradient tracks the density gradient (from darker to lighter hues as the density decreases). The region of interaction marked through the yellow-white circle represents the forward shock R_{sh} that propagates radially outwards. The solid olive line marks the position of the breakout radius (R_{bo}), where the first light leaks out, and the shock becomes collisionless. The dashed dark green line marks the location of the deceleration radius of the ejecta (R_{dec}). The latter is located at radii smaller than R_{CSM} (as in this sketch) for a relatively large CSM mass compared to the ejecta mass or radii larger than R_{CSM} for massive ejecta and rarefied CSM; note that we could have $R_{\text{dec}} < R_{\text{bo}}$ for extremely large $M_{\text{CSM}}/M_{\text{ej}}$. The dashed bordeaux line represents the photospheric radius R_{ph} , where the radiation decouples from the CSM matter and stream in the outer space freely.

where E_k is the total SN kinetic energy, M_{ej} is the total mass of the SN ejecta, n is the density slope of the outer part of the ejecta, and δ the slope of the inner one. The parameter n depends on the progenitor properties and the nature (convective or radiative) of the envelope; $n \simeq 12$ is typical of red supergiant stars [314], while lower values are expected for more compact progenitors. In this work, we adopt $n = 10$ and $\delta = 1$, following [462].

The interaction between the SN ejecta and the CSM results in a forward shock moving in the CSM and a reverse shock propagating back in the stellar envelope. For our purposes, only the forward shock is relevant. It is indeed estimated that the contribution of the reverse shock to the electromagnetic emission, as well as its efficiency in accelerating particles during the timescales of interest, is significantly lower than the one of the forward shock [166, 379, 438, 446, 435, 462, 526].

Following [127, 332], we assume that the thickness of the shocked region is much smaller than its radius, R_{sh} . As long as the mass of the SN ejecta is larger than the swept-up CSM mass, which we define as the ejecta dominated phase (or free expansion phase), the expansion of the forward shock radius is described by [332]:

$$R_{sh}(t) = R_{\star} + \left[\frac{(3-s)(4-s)}{(n-4)(n-3)} \frac{g_n}{B} \right]^{\frac{1}{n-s}} t^{\frac{n-3}{n-s}}, \quad (12.4)$$

with B defined as in Eq. 12.1, and hereafter we assume that the interaction starts at $t = 0$.

When the swept-up CSM mass becomes comparable to the SN ejecta mass, the ejecta start to slow down, entering the CSM dominated phase. This happens at the deceleration radius, defined as the radius R_{dec} at which $\int_{R_{\star}}^{R_{dec}} 4\pi R^2 \rho_{CSM} dR = M_{ej}$, namely

$$R_{dec} = \left[\frac{3-s}{4\pi B} M_{ej} + R_{\star}^{3-s} \right]^{\frac{1}{3-s}}. \quad (12.5)$$

According to the relative ratio between M_{ej} and M_{CSM} , the deceleration can occur inside or outside the CSM shell (where a dilute stellar wind surrounds the collapsing star). After this transition, the forward shock evolves as [462]:

$$R_{sh}(t) = R_{dec} \left(\frac{t}{t_{dec}} \right)^{\frac{2}{5-s}}. \quad (12.6)$$

Differentiating Eqs. 12.4 and 12.6, we obtain the forward shock velocity as a function of time:

$$v_{sh}(t) = \frac{dR_{sh}(t)}{dt} = \begin{cases} \frac{n-3}{n-s} \left[\frac{(3-s)(4-s)}{(n-4)(n-3)} \frac{g_n}{B} \right]^{\frac{1}{n-s}} t^{\frac{s-3}{n-s}} & R < R_{dec} \\ \frac{2}{5-s} R_{dec} \left(\frac{t}{t_{dec}} \right)^{\frac{s-3}{5-s}} & R \geq R_{dec} \end{cases}. \quad (12.7)$$

We consider the dynamical evolution under the assumption that the shock is adiabatic for two reasons. First, we want to compare our results with the literature on the properties of the SN lightcurves extrapolated by relying on semi-analytic models for the adiabatic expansion, see e.g. [462]. Second, it has been shown that, in the radiative regime, R_{sh} has the same temporal dependence as the self-similar solution $\propto t^{(n-3)/(n-s)}$ in the free expansion phase with radiative losses having a strong impact on the evolution of the shock [332].

While the shock propagates in the CSM, the ejecta kinetic energy is dissipated in the interaction and converted into thermal energy. The shock-heated gas behind the forward shock front cools by emitting thermal energy in the form of free-free radiation (thermal bremsstrahlung). However, if the CSM ahead of the shock is optically thick, such radiation is trapped and remains confined until the shock breakout, which occurs at the breakout radius (R_{bo}). The latter is computed by solving the following equation for the Thomson optical depth (due to photon scattering on electrons)²:

$$\tau_T = \int_{R_{\text{bo}}}^{R_{\text{CSM}}} \rho_{\text{CSM}}(R) \kappa_{\text{es}} dR = \frac{c}{v_{\text{sh}}}, \quad (12.8)$$

where κ_{es} is the electron scattering opacity, c the speed of light, and v_{sh} is defined in Eq. 12.7. If $R_{\text{bo}} \leq R_{\star}$, $R_{\text{bo}} = R_{\star}$.

We make use of the assumption of constant opacity, valid for electron Compton scattering. The value of κ_{es} , which depends on the composition, typically ranges from $\kappa_{\text{es}} \sim 0.2 \text{ cm}^2 \text{ g}^{-1}$ for hydrogen-free matter to $\kappa_{\text{es}} \sim 0.4 \text{ cm}^2 \text{ g}^{-1}$ for pure hydrogen. We consider solar composition of the CSM, namely $\kappa_{\text{es}} = 0.2(1 + X_{\text{H}}) \simeq 0.34 \text{ cm}^2 \text{ g}^{-1}$ [425], where $X_{\text{H}} = 0.73$ is the hydrogen mass fraction [300].

As long as $\tau_T \gg c/v_{\text{sh}}$, the shock is radiation-mediated (energy density of the radiation is larger than the energy density of the gas) and radiation pressure rather than plasma instabilities mediate the shock. In this regime, non-thermal particle acceleration is inefficient, since a shock width much larger than the particle gyro-radius hinders standard Fermi acceleration [502, 289, 258, 353]. Furthermore, diffusion can be neglected. When $\tau_T < c/v_{\text{sh}}$, the shock becomes collisionless, and efficient particle acceleration begins.

12.2.3 Interaction-powered supernova emission

When the forward shock propagates in the region with $\tau_T < c/v_{\text{sh}}$, the gas immediately behind the shock is heated to a temperature T_{sh} . Assuming electron-ion equilibrium,

²Note that we do not adopt the common approximation $R_{\text{bo}} \equiv (\kappa_{\text{es}} K v_{\text{sh}})/c$, valid only when $R_{\text{bo}} \ll R_{\text{CSM}}$ and v_{sh} independent on R [132].

such a temperature can be obtained by the Rankine–Hugoniot conditions:

$$k_B T_{\text{sh}} = 2 \frac{(\gamma - 1)}{(\gamma + 1)^2} \tilde{\mu} m_{\text{H}} v_{\text{sh}}^2 \approx 118 \text{ keV} \left(\frac{v_{\text{sh}}}{10^9 \text{ cm s}^{-1}} \right)^2, \quad (12.9)$$

where $\gamma = 5/3$ is the adiabatic index of the gas. We adopt mean molecular weight $\tilde{\mu} = 0.6$; such a choice is appropriate for fully ionized CSM with solar composition as it is the case for the matter right behind the shock (this is different from Eq. 12.1 where the CSM is assumed to be neutral). The thermal emission properties of the shock-heated material can be fully characterized by the shock velocity v_{sh} and the other parameters characterizing the CSM [308].

The observational signatures of the SN lightcurve and spectra depend on the radiative processes, which shape the thermal emission. The main photon production mechanism is free-free emission of the shocked electrons, whose typical timescale is [155]:

$$t_{\text{cool}} = \frac{3k_B T_{\text{sh}}}{2n_{\text{sh}} \Lambda(T)}, \quad (12.10)$$

where k_B is the Boltzmann constant, $n_{\text{sh}} = 4n_{\text{CSM}}$ is the density of the shocked region. The factor 4 comes from the Rankine–Hugoniot jump conditions across a strong non-relativistic shock. $\Lambda(T)$ is the cooling function (in units of $\text{erg cm}^3 \text{ s}^{-1}$) that captures the physics of radiative cooling [130]:

$$\Lambda(T) = \begin{cases} 6.2 \times 10^{-19} T^{-0.6} & 10^5 < T \lesssim T_* \\ 2.5 \times 10^{-27} T^{0.5} & T > T_* \end{cases}. \quad (12.11)$$

The temperature $T_* = 4.7 \times 10^7 \text{ K}$ represents the transition from the regime where free-free emission is dominant ($T \gtrsim T_*$) to the one where line-emission becomes relevant ($T \lesssim T_*$). If the free-free cooling timescale is shorter than the dynamical time, the shock becomes radiative. In this regime, particles behind the shock cool within a layer of width $(t_{\text{cool}}/t_{\text{dyn}})R_{\text{sh}}$.

Although the radiation created during the interaction could diffuse from the CSM, the presence of dense pre-shock material causes the emitted photons to experience multiple scattering episodes before they reach the photosphere (defined as the surface where $\tau_T = 1$):

$$R_{\text{ph}} = \left[\frac{s-1}{\kappa_{\text{es}} B} + R_{\text{CSM}}^{1-s} \right]^{\frac{1}{1-s}}. \quad (12.12)$$

The dominant mechanisms responsible for the photon field degradation in the medium are photoelectric absorption and Compton scattering, that generate inelastic energy transfer from photons to electrons during propagation. The result of such energy losses is that the bulk of thermal X-ray photons (see Eq. 12.9) is absorbed and reprocessed via

Table 12.1: Supernova model parameters for the SN wind and shell scenarios. The reference values adopted for our benchmark SN model are provided together with the uncertainty range for the most uncertain parameters.

Parameter	Symbol	Benchmark value	Parameter range
Accelerated proton energy fraction	ε_p	0.1	—
Magnetic energy density fraction	ε_B	3×10^{-4}	—
Proton spectral index	k	2	—
External ejecta density slope	n	10	—
Internal ejecta density slope	δ	1	—
Kinetic energy	E_k	10^{51} erg	10^{50} – 10^{53} erg
Ejecta mass	M_{ej}	$10 M_\odot$	1– $70 M_\odot$
CSM mass	M_{CSM}	$10 M_\odot$	1– $70 M_\odot$
CSM radius	R_{CSM}	10^{16} cm	5×10^{15} – 10^{17} cm

continuum and line emission in the optical. This phenomenon is strongly dependent on the CSM mass and extent, as well as on the stage of the shock evolution.

Alongside bremsstrahlung photons, a collisionless shock may produce non-thermal radiation from a relativistic population of electrons accelerated through diffusive shock acceleration. Synchrotron emission of these electrons is mainly expected in the radio band; it has been shown that the CSM mass and radius play an important role in defining the radio peak time and luminosity, see, e.g. [389].

12.2.4 Supernova model parameters

The parameters characterizing SNe/SLSNe of Type II_n carry large uncertainties. For our benchmark SN model, we take into account uncertainty ranges for the SN energetics, CSM and ejecta masses, as well as the CSM radial extent as summarized in Table 12.1. A number of other uncertainties can significantly impact the observational features, e.g. the composition and geometry of the stellar environment or the stellar structure.

The electromagnetic emission of SLSNe II_n can be explained invoking a massive CSM shell with enough inertia to decelerate and dissipate most of the kinetic energy of the ejecta: $M_{CSM} \gtrsim 40 M_\odot$, $M_{ej} \gtrsim 50 M_\odot$, and $E_k \gtrsim 10^{52}$ erg have been invoked for SLSNe in the tail of the distribution (see e.g., [362, 156]), consistent with pair-instability SN models. On the other hand, SNe II_n may result from the interaction with a less dense surrounding medium, or simply fall in the class of less powerful explosions, with $M_{CSM} \lesssim 5 M_\odot$, $E_k \sim$ a few 10^{51} erg, and $M_{ej} \lesssim 50 M_\odot$ (see, e.g., [123]).

To encompass the wide range of SN properties and the related uncertainties, we

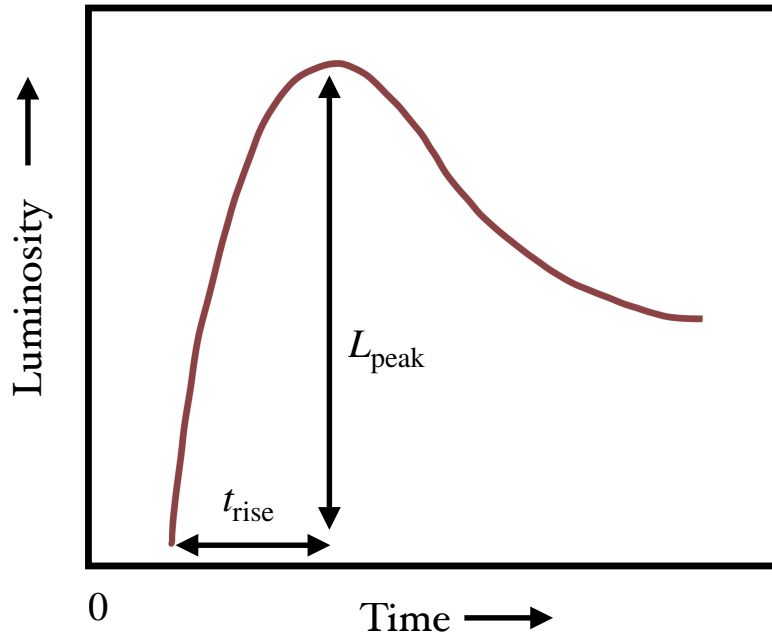


Figure 12.2: Sketch of the SN luminosity evolution (in arbitrary units) resulting from the interaction of the SN shock with the dense CSM. The origin ($t = 0$) coincides with the SN explosion time. Note that t_{rise} is defined from the time of the shock breakout.

consider the space of parameters summarized in Table 12.1. In the following, we systematically investigate the dependence of the lightcurve features, such as the rise time and the peak luminosity on the SN parameters. For the sake of completeness, we choose generous uncertainty ranges, albeit most of the observed SN events do not require kinetic energies larger than 10^{52} erg or CSM masses larger than $50 M_{\odot}$ for example.

12.3 Scaling relations for the photometric supernova properties

In this section, we introduce the scaling relations for the peak luminosity and the rise time of a SN lightcurve powered by shock interaction. Such relations connect these two observable quantities to the SN model parameters.

We are interested in the shock evolution after shock breakout, when $\tau_T < c/v_{\text{sh}}$. During this regime, the lightcurve is powered by continuous conversion of the ejecta kinetic energy—see e.g. [124, 204, 332]. Such a phase, however, reproduces the decreasing-flat part of the SN lightcurve at later times (see Fig. 12.2), while the initial rising part of the optical signal can be explained considering photon diffusion in the optically thick

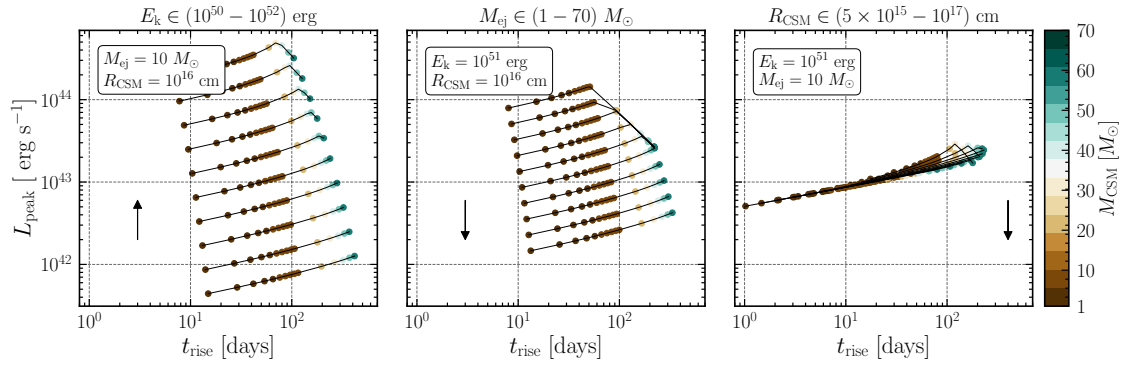


Figure 12.3: Bolometric peak luminosity as a function of the rise time, for fixed M_{ej} and R_{CSM} (left panel, and varying E_k), fixed E_k and R_{CSM} (middle panel, and varying M_{ej}), and fixed E_k and M_{ej} (right panel, and varying R_{CSM}). In each panel, the arrow points in the direction of increasing values of the parameter indicated on top of the plot (e.g. in the left panel, the highest curve is obtained with the the largest kinetic energy, 10^{52} erg). For each curve, the color hues mark the variation of M_{CSM} . The longest rise times and brightest lightcurves are obtained for large kinetic energies (left panel), the low ejecta mass (middle panel), large CSM mass and small CSM extension (right panel). Models with intermediate t_{rise} can reach the largest peak luminosities. The largest dispersion of long-lasting interaction-powered SNe can be achieved by increasing the kinetic energy. By keeping E_k fixed, an upper limit on L_{peak} is expected for different M_{ej} and R_{CSM} .

region—see e.g. [132, 124].

Since we are interested in exploring a broad space of SN model parameters, we rely on semi-analytical expressions for the characteristic quantities that describe the optical lightcurve, namely the bolometric luminosity peak L_{peak} and the rise time to the peak t_{rise} (see Fig. 12.2). By performing 1D radiation-hydrodynamic simulations for a large region of the space of parameters, [462] fitted the output of their numerical simulations with semi-analytical scaling relations, investigating the relation between L_{peak} and t_{rise} . In this way, it is possible to analyze the dependence of the lightcurve properties on the parameters characterizing the SN interaction, i.e. the kinetic energy of the ejecta (E_k), the mass of the ejecta (M_{ej}), the mass of the CSM (M_{CSM}), and the extent of the CSM (R_{CSM}). [462] found that the semi-analytical scaling relations describe relatively well the numerical results, once accounting for some calibration factors. In this section, we review the scaling relations we adopt throughout our work.

As the forward shock propagates in the CSM, the post-shock thermal energy per unit radius coming from the dissipation of the kinetic energy is given by

$$\mathcal{E}_k(R) = \frac{dE_k}{dR} = \frac{9}{8}\pi R^2 v_{\text{sh}}^2(R) \rho_{\text{CSM}}(R). \quad (12.13)$$

where we have used the Rankine–Hugoniot jump conditions across a strong non-relativistic shock that provide a compression ratio $\simeq 4$.

We define the bolometric peak luminosity as the kinetic power of the shock at breakout:

$$L_{\text{peak}} = \left. \frac{dE_k}{dt} \right|_{R_{\text{bo}}} = \frac{9}{8}\pi R_{\text{bo}}^2 v_{\text{sh}}^3(R_{\text{bo}}) \rho_{\text{CSM}}(R_{\text{bo}}). \quad (12.14)$$

When the shock is still crossing the CSM envelope, the radiated photons undergo multiple scatterings before reaching the photosphere. The diffusion coefficient is $D(R) \sim c\lambda(R)$, with $\lambda(R) = 1/\kappa_{\text{es}}\rho_{\text{CSM}}(R)$ being the photon mean free path. The time required to diffuse from R_{bo} to the photosphere R_{ph} represents the rise time of the bolometric lightcurve [204]³:

$$t_{\text{rise}} \approx \int_{R_{\text{bo}}}^{R_{\text{ph}}} \frac{d(R - R_{\text{bo}})^2}{D(R)} \sim \int_{R_{\text{bo}}}^{R_{\text{ph}}} \frac{2(R - R_{\text{bo}})\kappa_{\text{es}}\rho_{\text{CSM}}(R)dR}{c}. \quad (12.15)$$

Furthermore, after the forward shock breaks out from the optically thick part of the CSM at R_{ph} , its luminosity is expected to be primarily emitted in the UV/X-ray region of the spectrum, and not in the optical [204]. Hence, we consider the photospheric radius as the radius beyond which the optical emission is negligible. Distinguishing

³This definition of the rise time is valid as long as the CSM is dense enough to cause shock breakout in the CSM wind. If this is not the case, the breakout occurs at the surface of the collapsing star; the CSM masses responsible for this scenario are not considered in our investigation.

the free-expansion regime (FE, $M_{\text{ej}} \gg M_{\text{CSM}}$) and the blast-wave regime (BW, $M_{\text{ej}} \ll M_{\text{CSM}}$) [462]⁴, the kinetic energy dissipated during the shock evolution in the optically thick region is:

$$E_{\text{diss,thick}} = \begin{cases} \int_{R_{\star}}^{R_{\text{ph}}} \mathcal{E}_k(R) dR & \text{for FE} \\ \frac{(3-s)(\gamma+1)}{3+9\gamma-2s-2\gamma s} E_k & \text{for BW .} \end{cases} \quad (12.16)$$

Part of this energy is converted into thermal energy and radiated. The fraction radiated in the band of interest depends on multiple factors, including the cooling regime of the shock during the evolution, as well as the ionization state and CSM properties. We parametrize these unknowns by introducing the fraction ϵ_{rad} of the total dissipated energy $E_{\text{diss,thick}}$ that is emitted in the optical band. We note that we adopt a definition of the rise time which differs from the Arnett's rule employed in [462], leading to comparable results, except for extremely low values of R_{CSM} ($\sim 10^{15}$ cm), which we do not consider in this work. In Appendix D.1 we provide illustrative examples of the dependence of L_{peak} , t_{rise} , and $E_{\text{diss,thick}}$ on the parameters characterizing the SN lightcurve for the wind CSM configuration ($s = 2$).

Figure 12.3 shows L_{peak} as a function of t_{rise} , obtained by adopting the semi-analytic modeling in the FE and BW regimes. We note that the largest dispersion in the peak luminosity for long-lasting SNe/SLSNe II is obtained by varying the ejecta kinetic energy (left panel). For fixed kinetic energy, we see that the SN models corresponding to different ejecta mass (middle panel) all converge to approximately similar peak luminosity for longer t_{rise} , which corresponds to the region where the shock evolution is in the BW regime. This means that there is an upper limit on L_{peak} for a certain t_{rise} , and the only way to overcome this limit is by increasing the ejecta energy. Changes in R_{CSM} (right panel) lead to the smallest dispersion in L_{peak} among all the considered parameters. It is the variation of the kinetic energy that causes the largest spread in L_{peak} . Our findings are in agreement with the ones of [462].

12.4 Maximum proton energy

In order to estimate the number of neutrinos and their typical energy during the shock evolution in the CSM, we first need to examine the energy gain and loss mechanisms that determine the maximum energy up to which protons can be accelerated. We assume first-order Fermi acceleration, which takes place at the shock front with the accelerating particles gaining energy as they cross the shock front back and forth.

⁴Note that this distinction should not be confused with the ejecta/CSM-dominated phases introduced in Sec. 12.2.2.

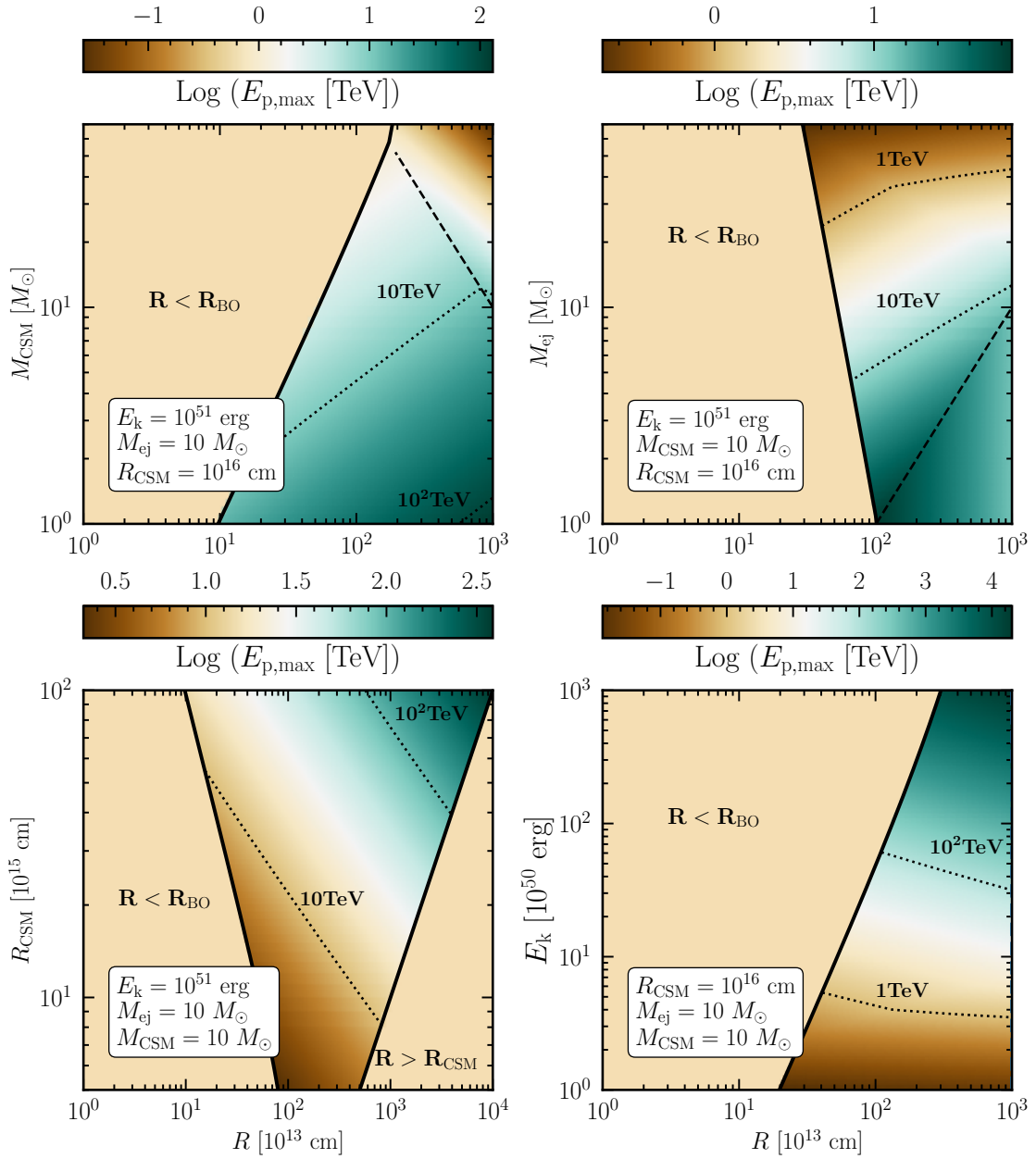


Figure 12.4: Contour plots of the maximum proton energy for the wind scenario in the plane spanned by the distance from the central engine and M_{CSM} (top left panel), M_{ej} (top right panel), R_{CSM} (bottom left panel), and E_k (bottom right panel), while the remaining three SN model parameters are fixed to their benchmark values. In each panel, the dashed line marks the deceleration radius, after which $E_{p,\max}$ decreases. The maximum proton energy increases with the radius (and therefore with time). Indeed, the largest $E_{p,\max}$ is obtained in the late stages of the shock evolution. Large R_{CSM} and M_{ej} , and small M_{CSM} and E_k lead to the longest interaction times. This statement is not true when $M_{\text{ej}} \ll M_{\text{CSM}}$ (see left upper and bottom right panels). The black solid lines define the edges of the interaction region, $R_{\text{bo}} \leq R \leq R_{\text{CSM}}$.

In the Bohm limit, where the proton mean free path is equal to its gyroradius $r_g = \gamma_p m_p c^2 / eB$, the proton acceleration timescale is $t_{\text{acc}} \sim 6\gamma_p m_p c^3 / eBv_{\text{sh}}^2$ (see, e.g., [401, 470, 113]), where $B = \sqrt{9\pi\epsilon_B v_{\text{sh}}^2 \rho_{\text{CSM}}}$ is the turbulent magnetic field in the post-shock region, whose energy density is assumed to be a fraction ϵ_B of the post-shock thermal energy $U_{\text{th}} = (9/8)v_{\text{sh}}^2 \rho_{\text{CSM}}$.

The maximum energy up to which protons can be accelerated is determined by the competition between particle acceleration and energy loss mechanisms, such that $t_{\text{acc}} \leq t_{\text{p,cool}}$, with $t_{\text{p,cool}}$ being the total proton cooling time. The relevant cooling times are the advection time ($t_{\text{adv}} \sim \Delta R_{\text{acc}} / v_{\text{sh}}$, with ΔR_{acc} being the width of the acceleration region) and the proton-proton interaction time ($t_{\text{pp}} = (4k_{\text{pp}} \sigma_{\text{pp}} n_{\text{CSM}} c)^{-1}$, where we assume constant inelasticity $k_{\text{pp}} = 0.5$ and energy-dependent cross-section $\sigma_{\text{pp}}(E_p)$ [527]).

As pointed out in [172], taking $\Delta R_{\text{acc}} \sim R_{\text{sh}}$ may be appropriate for adiabatic shocks only. If the shock is radiative, particles in the post-shock region cool via free-free emission within a layer of width $\sim (t_{\text{cool}} / t_{\text{dyn}}) R_{\text{sh}}$ (see Sec. 12.2.3), making the gas far from the shock quasi-neutral, and thus hindering the magnetic field amplification crucial in the acceleration mechanism [80]. Hence, we adopt $\Delta R_{\text{acc}} = (t_{\text{cool}} / t_{\text{dyn}}) R_{\text{sh}}$ for $t_{\text{cool}} < t_{\text{dyn}}$, and $\Delta R_{\text{acc}} = R_{\text{sh}}$ otherwise.

The total proton cooling time can thus be written as $t_{\text{p,cool}}^{-1} = t_{\text{pp}}^{-1} + \max[t_{\text{dyn}}^{-1}, t_{\text{cool}}^{-1}]$. It is important to note that relativistic protons in the shocked region may also interact with the ambient photons via $p\gamma$ interactions. However, we ignore such an energy loss channel, by relying on the findings of [353, 172] that showed that $p\gamma$ interactions can be neglected for a wide range of SN parameters.

Figure 12.4 shows contours of $E_{\text{p,max}}$ for the wind scenario. The black solid lines mark the edges of the interaction region, hence Fig. 12.4 also provides an idea of the typical interaction duration. Fixing three of the SN model parameters to their benchmark values (see Table 12.1), the shortest period of interaction is obtained for small R_{CSM} and large M_{CSM} , or small M_{ej} and large E_k . In fact in both cases the shock breakout is delayed. The maximum proton energy increases with the radius, and the largest $E_{\text{p,max}}$ can be obtained in the late stages of the shock evolution, hinting that high-energy neutrino production should be favored at later times after the bolometric peak.

The breaks observed in the contour lines in the upper and lower right panels of Fig. 12.4 represent the transition between the regimes where free-free and line-emission dominate. From the two upper panels, we see that $E_{\text{p,max}}$ reaches its maximum value at R_{dec} , and declines later. But this is not always the case; as shown in Appendix D.2, when the proton energy loss times are longer than the dynamical time, the maximum proton energy decreases throughout the evolution.

12.5 Expected neutrino emission from interaction-powered supernovae

In this section, the spectral energy distribution of neutrinos is introduced. We then present our findings on the dependence of the expected number of neutrinos on the SN model parameters and link the neutrino signal to the properties of the SN lightcurves.

12.5.1 Spectral energy distribution of neutrinos

A fraction ε_p of the dissipated kinetic energy of the shock (Eq. 12.13) is used to accelerate protons swept-up from the CSM; we adopt $\varepsilon_p = 0.1$, assuming that the shocks accelerating protons are parallel or quasi-parallel and therefore efficient diffusive shock acceleration occurs [113]. However, lower values of ε_p would be possible for oblique shocks, with poorer particle acceleration efficiency. Given the linear dependence of proton and neutrino spectra on this parameter, it is straightforward to rescale our results.

Assuming a power-law energy distribution with spectral index $k = 2$, the number of protons injected per unit radius and unit Lorentz factor is

$$Q_p(\gamma_p, R) = A(R)\gamma_p^{-2} \log^{-1} \left(\frac{\gamma_{p,\max}}{\gamma_{p,\min}} \right), \quad (12.17)$$

for $\gamma_{p,\min} < \gamma < \gamma_{p,\max}$, and zero otherwise. We set the minimum Lorentz factor of accelerated protons $\gamma_{p,\min} = 1$, while $\gamma_{p,\max}$ is obtained by comparing the acceleration and the energy-loss time scales at each radius during the shock evolution, as discussed in Sec. 12.4. The normalization factor $A(R)$ is

$$A(R) = \frac{9}{8}\pi\varepsilon_p R^2 v_{\text{sh}}^2(R) \rho_{\text{CSM}}(R) \propto \begin{cases} R^{\frac{2n-sn+5s-12}{n-3}} & \text{for } R \leq R_{\text{dec}} \\ R^{-1} & \text{for } R > R_{\text{dec}}. \end{cases} \quad (12.18)$$

The injection rate of protons in the deceleration phase does not depend on the SN density structure nor the CSM density profile. Since we aim to compute the neutrino emission, we track the temporal evolution of the proton distribution in the shocked region between the shock breakout radius R_{bo} and the outer radius R_{CSM} .

The evolution of the proton distribution is given by [460, 177, 389]:

$$\frac{\partial N_p(\gamma_p, R)}{\partial R} - \frac{\partial}{\partial \gamma_p} \left[\frac{\gamma_p}{R} N_p(\gamma_p, R) \right] + \frac{N_p(\gamma_p, R)}{v_{\text{sh}}(R)t_{\text{pp}}(R)} = Q_p(\gamma_p, R), \quad (12.19)$$

where $N_p(\gamma_p, R)$ represents the total number of protons in the shell at a given radius R with Lorentz factor between γ_p and $\gamma_p + d\gamma_p$. The second term on the left hand side of

Eq. 12.19 takes into account energy losses due to the adiabatic expansion of the SN shell, while pp collisions are treated as an escape term [460]. Other energy loss channels for protons are negligible [353]. Furthermore, in Eq. 12.19, the diffusion term has been neglected since the shell is assumed to be homogeneous.

The neutrino production rates, $Q_{\nu_i+\bar{\nu}_i}$ [$\text{GeV}^{-1}\text{s}^{-1}$], for muon and electron flavor (anti)neutrinos are given by [262]:

$$Q_{\nu_\mu+\bar{\nu}_\mu}(E_\nu, R) = 4n_{\text{CSM}}(R)m_p c^3 \int_0^1 dx \frac{\sigma_{pp}(E_\nu/x)}{x} \times \quad (12.20)$$

$$N_p\left(\frac{E_\nu}{xm_p c^2}, R\right) \left(F_{\nu_\mu}^{(1)}(E_\nu, x) + F_{\nu_\mu}^{(2)}(E_\nu, x)\right),$$

$$Q_{\nu_e+\bar{\nu}_e}(E_\nu, R) = 4n_{\text{CSM}}(R)m_p c^3 \int_0^1 dx \frac{\sigma_{pp}(E_\nu/x)}{x} \times \quad (12.21)$$

$$N_p\left(\frac{E_\nu}{xm_p c^2}, R\right) F_{\nu_e}(E_\nu, x),$$

where $x = E_\nu/E_p$. The functions $F_{\nu_\mu}^{(1)}$, $F_{\nu_\mu}^{(2)}$ and F_{ν_e} follow the definitions in [262]. Equations 12.20 and 12.21 are valid for $E_p > 0.1$ TeV, corresponding to the energy range under investigation. Note that, for the parameters we use in this work, the synchrotron cooling of charged pions and muons produced via pp interactions is negligible. Therefore, the neutrino spectra are not affected by the cooling of mesons.

12.5.2 Energy emitted in neutrinos

The total energy that goes in neutrinos in the energy range $[E_{\nu,1}, E_{\nu,2}]$ during the entire interaction period is given by

$$\mathcal{E}_{\nu+\bar{\nu}} = \int_{t_{\text{BO}}}^{t_{\text{CSM}}} dt \int_{E_{\nu,1}}^{E_{\nu,2}} dE_\nu E_\nu [Q_{\nu_\mu+\bar{\nu}_\mu}(E_\nu, R) + Q_{\nu_e+\bar{\nu}_e}(E_\nu, R)], \quad (12.22)$$

where t_{BO} and t_{CSM} are expressed in the progenitor reference frame.

In order to connect the observed properties of the SN lightcurve to the neutrino ones (e.g., the total energy that goes in neutrinos or their typical spectral energy), for each configuration of SN model parameters we integrate the neutrino production rate between t_{BO} and t_{CSM} , for $E_\nu \geq 1$ TeV, as in Eq. 12.22. The results are shown in Fig. 12.5, where we fix two of the SN parameters at their benchmark values (see Table 12.1) and investigate $\mathcal{E}_{\nu+\bar{\nu}}$ in the plane spanned by the remaining two. Note that we do not consider the regions of the SN parameter space with the maximum achievable proton energy ($E_{p,\text{max}}^*$, see Appendix D.2 for more details) smaller than 10 TeV since they would

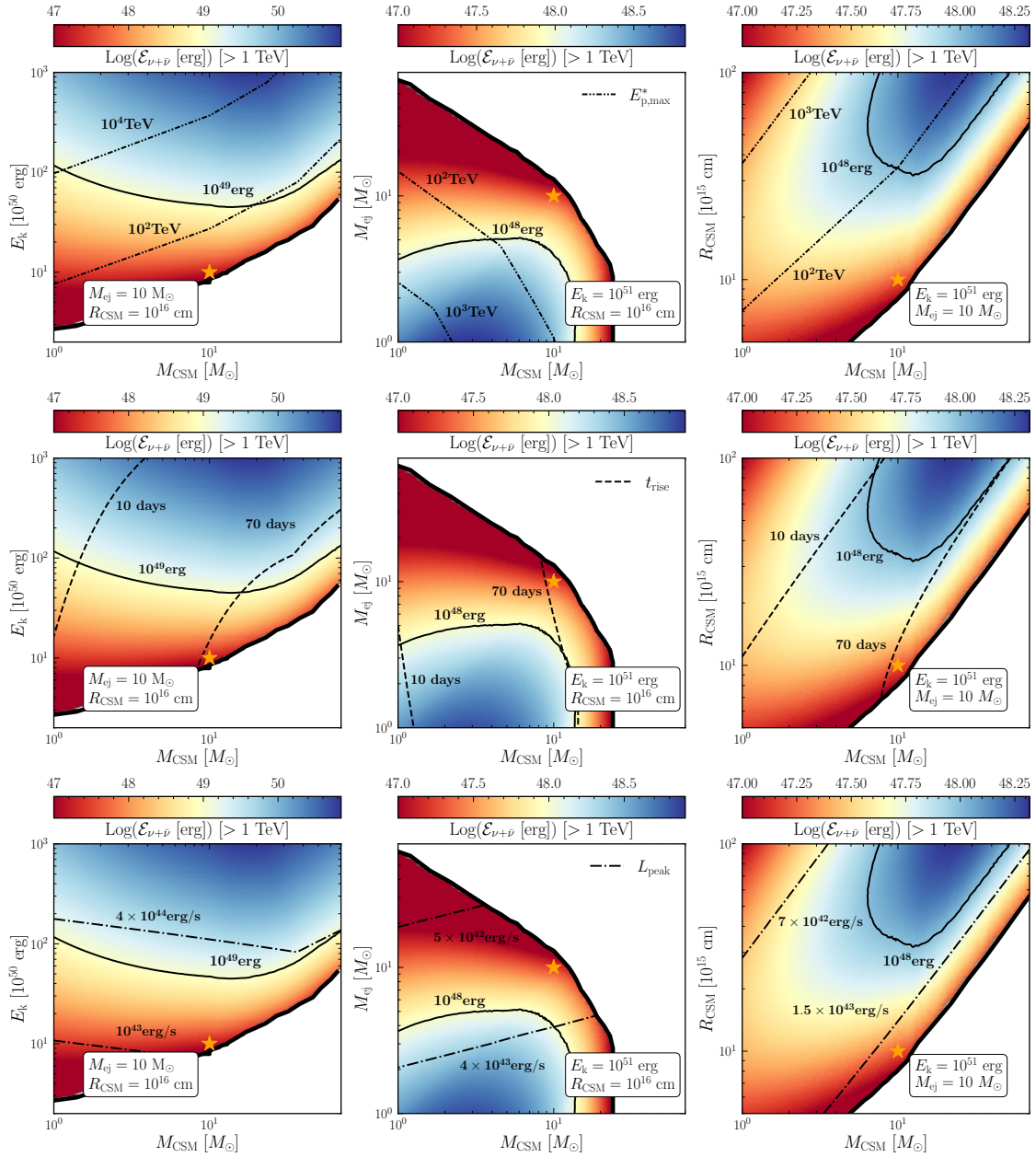


Figure 12.5: Contour plots of the total neutrino energy $\mathcal{E}_{\nu+\bar{\nu}}$ integrated for $E_{\nu} \geq 1$ TeV through the evolution of the shock in the CSM, as a function of M_{CSM} and E_k (left panels), M_{ej} (middle panels), and R_{CSM} (right panels) for the wind scenario. In order to highlight the dependence on the SN properties, isocontours of the maximum proton energy $E_{\text{p,max}}^*$ (double-dot dashed contours, top row), t_{rise} (dashed contours, middle row), and L_{peak} (dot dashed contours, bottom row) are displayed. All quantities are expressed in the SN reference frame. The white regions represent parts of the parameter space with $E_{\text{p,max}}^* \lesssim 10$ TeV excluded from our investigation. Our benchmark SN model is marked with an orange star. The SN configurations leading to the largest $\mathcal{E}_{\nu+\bar{\nu}}$ are given by large SN kinetic energies ($E_k \gtrsim 10^{51}$ erg), small ejecta masses ($M_{\text{ej}} \lesssim 10 M_{\odot}$), intermediate CSM masses with respect to M_{ej} (i.e., $1 M_{\odot} \lesssim M_{\text{CSM}} \lesssim 30 M_{\odot}$), and relatively large CSM extent ($R_{\text{CSM}} \gtrsim 10^{16}$ cm).

lead to neutrinos in the energy range dominated by atmospheric events in IceCube (see Sec. 12.6). If we were to integrate the neutrino rate for $E_{\nu,1} > 1$ TeV (Eq. 12.22), the contour lines for $\mathcal{E}_{\nu+\bar{\nu}}$ would be shifted to the left. Isocontours of the maximum achievable proton energy $E_{p,\max}^*$ (first row), the rise time t_{rise} (second row), and the bolometric peak L_{peak} (third row) are also displayed on top of the $\mathcal{E}_{\nu+\bar{\nu}}$ colormap in Fig. 12.5.

In all panels of Fig. 12.5, $\mathcal{E}_{\nu+\bar{\nu}}$ increases with M_{CSM} , due to the larger target proton number. Nevertheless, such a trend saturates once the critical n_{CSM} (corresponding to a critical M_{CSM}) is reached, where either pp interactions or the cooling of thermal plasma significantly limit the maximum proton energy, thus decreasing the number of neutrinos produced with high energy. For masses larger than the critical CSM mass, neutrinos could be abundantly produced either appreciably increasing the kinetic energy (left panel), or decreasing the ejecta mass (middle panel), or increasing the CSM radius (right panel). From the contour lines in each panel, we see that the optimal configuration for what concerns neutrino production results from large E_k and small M_{ej} , which lead to large shock velocities v_{sh} , large R_{CSM} , and not extremely large M_{CSM} , compared to a fixed M_{ej} . Nevertheless, the panels in the upper row of Fig. 12.5 indicate that the configurations with the largest proton energies (and thus spectral neutrino energies) always prefer a balance between E_k , M_{ej} , and R_{CSM} with M_{CSM} .

It is important to observe the peculiar behavior resulting from the variation of R_{CSM} (right panels of Fig. 12.5). For fixed M_{CSM} , $\mathcal{E}_{\nu+\bar{\nu}}$ increases, then saturates at a certain R_{CSM} , and decreases thereafter. For very small R_{CSM} , the CSM density is relatively large, and the shock becomes collisionless close to R_{CSM} , probing a low fraction of the total CSM mass and thus producing a small number of neutrinos. This suppression is alleviated by increasing R_{CSM} . Nevertheless, a large R_{CSM} for fixed M_{CSM} leads to a low CSM density, and thus the total neutrino energy drops. For increasing M_{CSM} , such inversion in $\mathcal{E}_{\nu+\bar{\nu}}$ happens at larger R_{CSM} . We also see that the largest $\mathcal{E}_{\nu+\bar{\nu}}$ is obtained in the right upper corner of the right panels. This is mainly related to the duration of the shock interaction. The longer the interaction time, the larger the CSM mass swept-up by the collisionless shock.

The panels in the middle row of Fig. 12.5 show how the neutrino energy varies as a function of t_{rise} . Large neutrino energy is obtained for slow rising lightcurves. In particular, given our choice of the parameters for these contour plots, the most optimistic scenarios for neutrinos lie in the region with 10 days $\lesssim t_{\text{rise}} \lesssim 50$ days. Such findings hold for a wide range of parameters for interacting SNe. Extremely large t_{rise} , on the other hand, are expected to be determined by very large M_{CSM} , which can substantially limit the production of particles in the high energy regime.

The bottom panels of Fig. 12.5 illustrate how $\mathcal{E}_{\nu+\bar{\nu}}$ is linked to L_{peak} . In particular, L_{peak} closely tracks $\mathcal{E}_{\nu+\bar{\nu}}$. However, L_{peak} can increase with M_{CSM} to larger values than what neutrinos do, given its linear dependence on the CSM density (see Eq. 12.14).

Overall, the regions where the largest $\mathcal{E}_{\nu+\bar{\nu}}$ (and hence number of neutrinos) is obtained are also the regions where L_{peak} is the largest. It is not always true the opposite. Hence, large L_{peak} is a necessary, but not sufficient condition to have large $\mathcal{E}_{\nu+\bar{\nu}}$.

To summarize, a large $\mathcal{E}_{\nu+\bar{\nu}}$ is expected for large SN kinetic energy ($E_k \gtrsim 10^{51}$ erg), small ejecta mass ($M_{\text{ej}} \lesssim 10 M_{\odot}$), intermediate CSM mass with respect to M_{ej} ($1 M_{\odot} \lesssim M_{\text{CSM}} \lesssim 30 M_{\odot}$), and relatively extended CSM ($R_{\text{CSM}} \gtrsim 10^{16}$ cm). These features imply large bolometric luminosity peak ($L_{\text{peak}} \gtrsim 10^{43}\text{--}10^{44}$ erg) and average rise time ($t_{\text{rise}} \gtrsim 10\text{--}20$ days). On the other hand, it is important to note that degeneracies are present in the SN parameter space (see also [397]) and comparable L_{peak} and t_{rise} can be obtained for SN model parameters (E_k , M_{ej} , R_{CSM} , and M_{ej}) that are not optimal for neutrino emission.

It is important to stress that in this section we have considered $\mathcal{E}_{\nu+\bar{\nu}}$ as a proxy of the expected number of neutrino events that is investigated in Sec. 12.6. Moreover, we have compared $\mathcal{E}_{\nu+\bar{\nu}}$ to the bolometric luminosity expected at the peak and not to the luminosity effectively radiated, $L_{\text{peak,obs}}$.

12.6 Neutrino detection prospects

In this section, we investigate the neutrino detection prospects. In order to do so, we select two especially bright SNe observed by ZTF, SN 2020usa and SN 2020in. On the basis of our findings, we also discuss the most promising strategies for neutrino searches and multi-messenger follow-up programs.

12.6.1 Expected number of neutrino events at Earth

The neutrino and antineutrino flux ($F_{\nu_{\alpha}+\bar{\nu}_{\alpha}}$ with $\alpha = e, \mu, \tau$) at Earth from a SN at redshift z and as a function of time in the observer frame is [$\text{GeV}^{-1}\text{s}^{-1}\text{cm}^{-2}$]:

$$F_{\nu_{\alpha}+\bar{\nu}_{\alpha}}(E_{\nu}, t) = \frac{(1+z)^2}{4\pi d_L^2(z)} v_{\text{sh}} \sum_{\beta} P_{\nu_{\beta} \rightarrow \nu_{\alpha}} Q_{\nu_{\beta}+\bar{\nu}_{\beta}} \left(E_{\nu_{\alpha}}(1+z), \frac{v_{\text{sh}} t}{1+z} \right), \quad (12.23)$$

where $Q_{\nu_{\beta}+\bar{\nu}_{\beta}}$ is defined as in Eqs. 12.20 and 12.21. Neutrinos change their flavor while propagating, hence the flavor transition probabilities are given by [57]:

$$P_{\nu_e \rightarrow \nu_{\mu}} = P_{\nu_{\mu} \rightarrow \nu_e} = P_{\nu_e \rightarrow \nu_{\tau}} = \frac{1}{4} \sin^2 2\theta_{12}, \quad (12.24)$$

$$P_{\nu_{\mu} \rightarrow \nu_{\mu}} = P_{\nu_{\mu} \rightarrow \nu_{\tau}} = \frac{1}{8} (4 - \sin^2 2\theta_{12}), \quad (12.25)$$

$$P_{\nu_e \rightarrow \nu_e} = 1 - \frac{1}{2} \sin^2 2\theta_{12}, \quad (12.26)$$

Table 12.2: Characteristic properties of our representative SLSNe, SN 2020usa and SN 2020in.

	Redshift	$t_{\text{rise,obs}}$ [days]	$L_{\text{peak,obs}}$ [erg s ⁻¹]	$E_{\text{rad,obs}}$ [erg]	$t_{\text{dur,obs}}$ [days]	Declination [deg]
SN 2020usa	0.26	65	8×10^{43}	1.3×10^{51}	350	-2.3
SN 2020in	0.11	42	3×10^{43}	3.3×10^{50}	413	20.2

with $\theta_{12} \simeq 33.5$ deg [167], and $P_{\nu_\beta \rightarrow \nu_\alpha} = P_{\bar{\nu}_\beta \rightarrow \bar{\nu}_\alpha}$. The luminosity distance $d_L(z)$ is defined in a flat Λ CDM cosmology:

$$d_L(z) = (1+z) \frac{c}{H_0} \int_0^z \frac{dz'}{\sqrt{\Omega_\Lambda + \Omega_M(1+z')^3}}, \quad (12.27)$$

where $\Omega_M = 0.315$, $\Omega_\Lambda = 0.685$ and the Hubble constant is $H_0 = 67.4$ km s⁻¹ Mpc⁻¹ [42].

Due to the better angular resolution of muon-induced track events compared to cascades, we focus on muon neutrinos and antineutrinos. Therefore, the event rate expected at the IceCube Neutrino Observatory, after taking into account neutrino flavor conversion, is

$$\dot{N}_{\nu_\mu + \bar{\nu}_\mu} = \int_{E_{\nu,1}}^{E_{\nu,2}} dE_\nu A_{\text{eff}}(E_\nu, \alpha) F_{\nu_\mu + \bar{\nu}_\mu}(E_\nu, t), \quad (12.28)$$

where $A_{\text{eff}}(E_\nu, \alpha)$ is the detector effective area [20] for a SN at declination α .

12.6.2 Expected number of neutrino events for SN 2020usa and SN 2020in

To investigate the expected number of neutrino events, we select two among the brightest sources from the Bright Transient Survey of the Zwicky Transient Facility [183, 383]. Their observable properties are summarized in Table 12.2: SN2020usa⁵ and SN2020in⁶. We retrieve the photometry data of the sources in the ZTF-g and ZTF-r bands, and correct the measured fluxes for Galactic extinction [436]. Using linear interpolation of the individual ZTF-r and ZTF-g light curves, we perform a trapezoid integration between the respective center wavelengths to estimate the radiated energy at each time of measurement. The resulting lightcurve is interpolated with Gaussian process regression [56] and taken as a lower limit to the bolometric SN emission. From such pseudo-bolometric lightcurve, the rise time and peak luminosity are determined. The rise time is defined as the difference between the peak time and the estimated SN breakout time. The

⁵<https://lasair-ztf.lsst.ac.uk/objects/ZTF20acbcfaa/>

⁶<https://lasair-ztf.lsst.ac.uk/objects/ZTF20aaaweke/>

latter is determined by taking the average between the time of the first detection in ZTF-g or ZTF-r bands and the last non-detection in either band. In what follows, we consider the radiative efficiency $\varepsilon_{\text{rad}} = L_{\text{peak,obs}}/L_{\text{peak}}$ as a free parameter in the range $\varepsilon_{\text{rad}} \in [0.2, 0.7]$ [481]. Furthermore, we assume that $\varepsilon_{\text{rad}} = E_{\text{rad,obs}}/E_{\text{diss,thick}}$ also holds.

For both SNe, we perform a scan over the SN model parameters (E_{k} , M_{ej} , M_{CSM} , and R_{CSM}) which fulfill the following conditions:

- $t_{\text{rise}} \in [1, 1.5] \times t_{\text{rise,obs}}$, namely we allow an error up to 50% on the estimation of t_{rise} ;
- $L_{\text{peak}} \geq L_{\text{peak,obs}}$;
- $E_{\text{k}} > E_{\text{rad,obs}}$. We narrow the investigation range to $E_{\text{k}} \in [10^{51}, 2 \times 10^{52}]$ erg for SN2020usa and $E_{\text{k}} \in [4 \times 10^{50}, 5 \times 10^{51}]$ erg for SN2020in, assuming that at least $\sim 10\%$ and at most 80% of the total energy E_{k} is radiated.
- $t_{\text{dur,th}} \geq t_{\text{dur,obs}}$. Here $t_{\text{dur,obs}}$ is the observational temporal window available for each SN event, while $t_{\text{dur,th}} = t(R_{\text{ph}}) - t(R_{\text{bo}})$ is the time that the shock takes to cross the optically thick part of the CSM envelope after breakout (as mentioned in Sec. 12.2.3, the shock is expected to peak in the X-ray band once out of the optically thick part).

Figure 12.6 shows the total number of muon neutrino and antineutrino events, integrated over the duration of the interaction in the CSM for $E_{\nu} \geq 1$ TeV, expected at IceCube in the the wind scenario, for E_{k} selected to maximize the space of parameters compatible with the conditions mentioned above. Similarly to Fig. 12.5, the regions with the largest number of neutrino events are those with lower M_{ej} and larger R_{CSM} , for fixed M_{CSM} . It is important to note that, for given observed SN properties ($L_{\text{peak,obs}}$ and $t_{\text{rise,obs}}$), the expected number of neutrino events is not unique; in fact, as shown in Sec. 12.5, there is degeneracy in the SN model parameters that leads to the same $L_{\text{peak,obs}}$ and $t_{\text{rise,obs}}$.

Figure 12.7 represents the muon neutrino and antineutrino event rate expected at IceCube for SN2020usa and SN2020in, each as a function of time for two energy ranges, and for the most optimistic scenario. Figure 12.8 displays the corresponding cumulative neutrino number of events for both most optimistic and pessimistic scenarios. The two cases are selected after scanning over ε_{rad} . The smaller is ε_{rad} , the higher E_{k} is needed to explain the observations, and since we adopt a fixed fraction of the shock energy ε_{p} that goes into acceleration of relativistic protons, the best case for neutrino production is the one with the lowest ε_{rad} . Choosing $\varepsilon_{\text{rad,min}} = 0.2$, we only select the SN parameters that satisfy the following conditions: $t_{\text{rise}} \in [1, 1.5] \times t_{\text{rise,obs}}$, $L_{\text{peak}} \in [1, 1.5] \times L_{\text{peak,obs}}/\varepsilon_{\text{rad,min}}$, and $E_{\text{rad}} \in [1, 1.5] \times E_{\text{rad,obs}}/\varepsilon_{\text{rad,min}}$, hence considering an error on $L_{\text{peak,obs}}$ and $E_{\text{rad,obs}}$ of at most 50%. After an initial rise, the neutrino event rate for

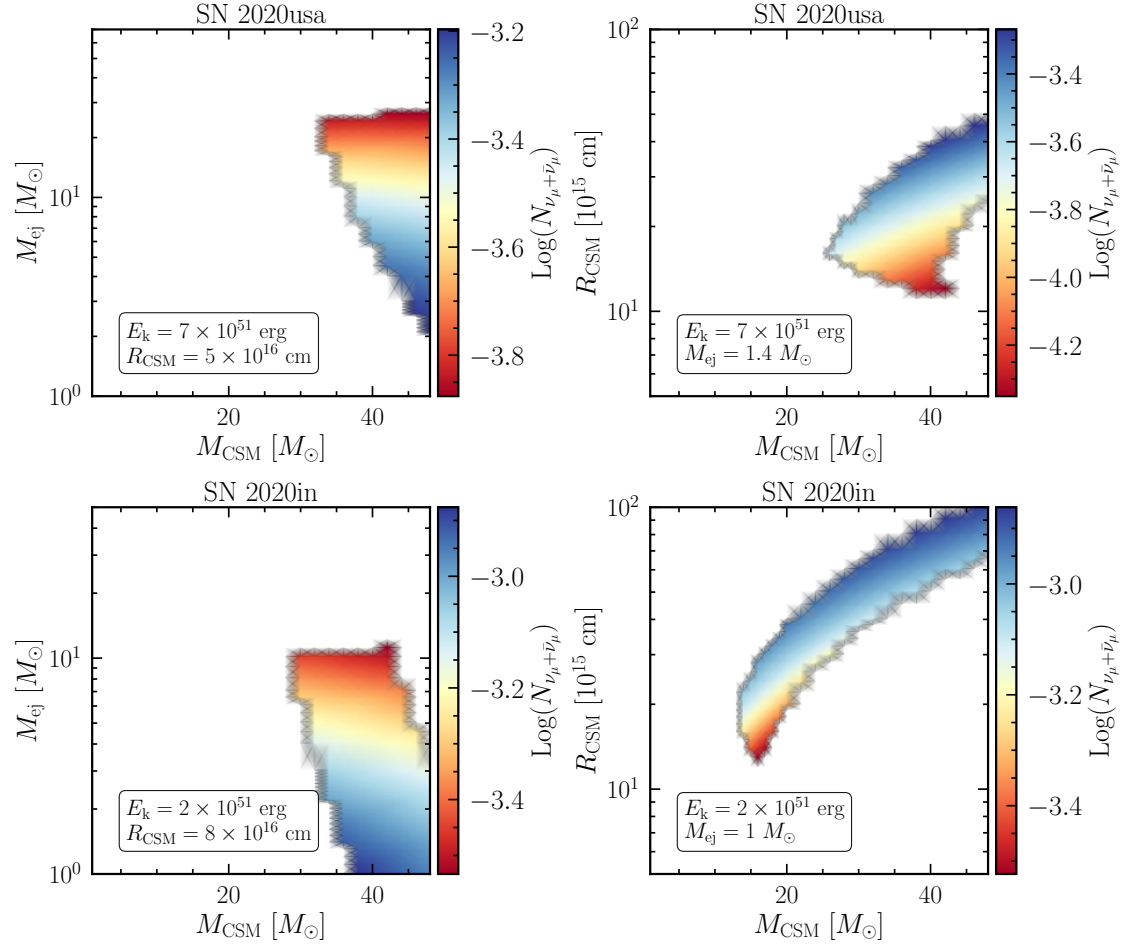


Figure 12.6: Contour plot of the number of muon neutrino and antineutrino events expected at the IceCube Neutrino Observatory (for the wind scenario and integrated over the duration of CSM interaction) in the SN model parameter space compatible with the observation of SN2020usa (top panels) and SN2020in (bottom panels). Only a fraction of the SN parameter space is compatible with the optical data. Importantly, for fixed $L_{\text{peak,obs}}$ and $t_{\text{rise,obs}}$, a different number of neutrino events could be obtained according to the specific combination of M_{ej} , M_{CSM} , R_{CSM} , E_k compatible with the observed optical properties.

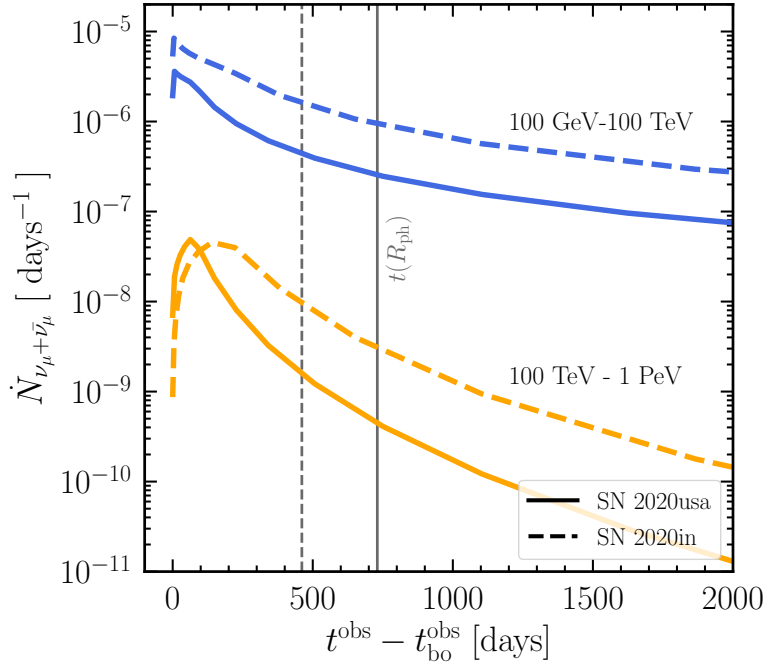


Figure 12.7: Muon neutrino and antineutrino event rates predicted for SN 2020usa and SN 2020in at the IceCube Neutrino Observatory as functions of time in the observer frame, after the shock breakout, assuming $\varepsilon_{\text{rad}} = 0.2$. The SN model parameters have been chosen to optimize neutrino production [$M_{\text{ej}} = 5.5 M_{\odot}$, $M_{\text{CSM}} = 48 M_{\odot}$, $R_{\text{CSM}} = 5.5 \times 10^{16}$ cm, $E_{\text{k}} = 10^{52}$ erg for SN2020usa; $M_{\text{ej}} = 5 M_{\odot}$, $M_{\text{CSM}} = 46 M_{\odot}$, $R_{\text{CSM}} = 10^{17}$ cm, $E_{\text{k}} = 5 \times 10^{51}$ erg for SN2020in]. The event rate increases slightly more slowly in the high energy band (100 TeV–1 PeV) with respect to the low energy one at early times, and it declines after peak because of the decreasing trend of v_{sh} as a function of time. The gray vertical lines indicate the time at which the shock reaches the photospheric radius R_{ph} (solid and dashed for SN 2020 usa and SN 2020in, respectively).

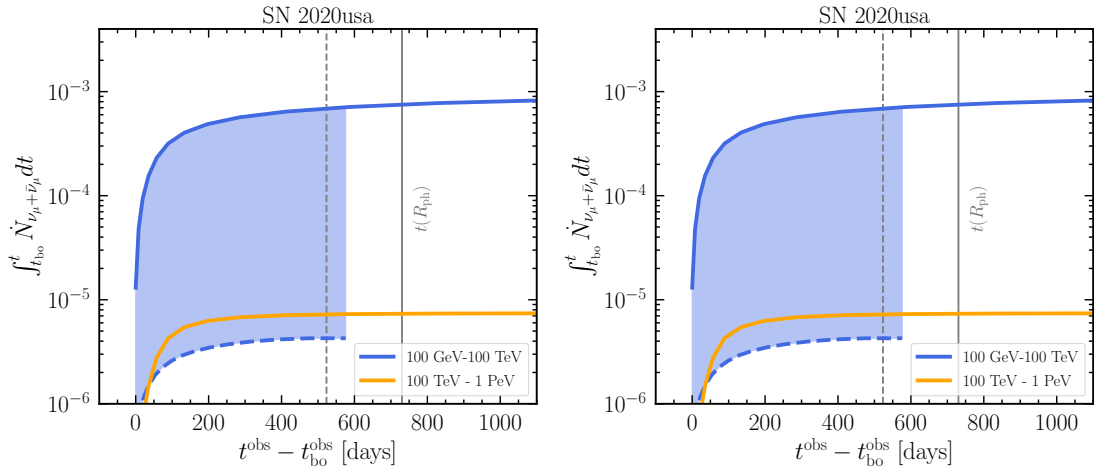


Figure 12.8: Cumulative number of muon neutrino and antineutrino events for SN 2020usa and SN2020in, as functions of time in the observer frame. The solid and dashed lines correspond to the the most optimistic and pessimistic cumulative number of events in the indicated energy range, respectively. The SN model parameters for the most optimistic scenario are the same as the ones in Fig. 12.7, while the parameters leading to the most pessimistic conditions for neutrino production are $M_{\text{ej}} = 1 M_{\odot}$, $M_{\text{CSM}} = 25 M_{\odot}$, $R_{\text{CSM}} = 9 \times 10^{15}$ cm, $E_{\text{k}} = 2 \times 10^{51}$ erg for SN 2020usa, and $M_{\text{ej}} = 1.6 M_{\odot}$, $M_{\text{CSM}} = 10 M_{\odot}$, $R_{\text{CSM}} = 9 \times 10^{15}$ cm, $E_{\text{k}} = 7 \times 10^{50}$ erg, for SN2020in. In both cases $\varepsilon_{\text{rad}} = 0.7$. Neutrinos in the the energy range [100 TeV, 1 PeV] are not produced in the pessimistic scenarios. The gray vertical lines indicate the time at which the shock reaches the photospheric radius R_{ph} .

both considered energy ranges (100 GeV–100 TeV and 100 TeV–1 PeV) decreases with time, with a steeper rate for the high-energy range, where the slow increase of $E_{p,\max}$ does not compensate the drop in the CSM density. Note that the cumulative number of neutrino events is relatively small because, although the SN 2020usa and SN 2020in have large $L_{\text{peak,obs}}$, they occurred at relatively large distance from Earth (\sim Gpc), as evident from Table 12.2. If other SNe exhibiting similar photometric properties should be observed at smaller z , then the expected neutrino flux should be rescaled with respect to the results shown here by the SN distance squared (see Sec. 12.6.4 and Fig. 12.10).

Figure 12.9 shows, for the most optimistic SN model parameter configuration, a comparison between $L_{\gamma_\mu+\bar{\nu}_\mu}$ (obtained taking into account flavor oscillation) and the optical luminosity for SN 2020usa and SN 2020in. Besides the difference in the intrinsic optical brightness, the two SNe display comparable evolution in the neutrino luminosity, with the neutrino luminosity peak being ~ 3 times brighter for SN 2020usa than SN 2020in. This is due to the fact that t_{rise} and L_{peak} for both SNe are such to lead to similar SN model parameters for what concerns the most optimistic prospects for neutrino emission. Note that an investigation that also takes into account the late evolution of the optical lightcurve might have an impact on this result, but it is out of the scope of this work.

12.6.3 Characteristics of the detectable neutrino signal

The neutrino luminosity curve does not peak at the same time as the optical lightcurve, as visible from Fig. 12.9. In fact the position of the optical peak is intrinsically related to propagation effects of photons in the CSM, and thus to the CSM properties, as discussed in Sec. 12.3 and Appendix D.1. The peak in the neutrino curve, instead, solely depends on the CSM radial density distribution and the evolution of the maximum spectral energy. Because of this, the neutrino event rate as well as the neutrino luminosity in the high-energy range (100 TeV–1 PeV) peak at $t|_{E_{p,\max}^*}$, namely the time at which the maximum proton energy is reached (see Appendix D.2 for $E_{p,\max}$ and Fig. 12.11 for the trend of the neutrino flux at Earth).

The most favorable time window for detecting energetic neutrinos ($\gtrsim 100$ TeV) would be a few times t_{rise} around the electromagnetic bolometric peak, which corresponds to $\mathcal{O}(100 \text{ days})$ days for $E_k \lesssim 10^{52}$ erg, $M_{\text{ej}} \lesssim 10M_\odot$, $M_{\text{CSM}} \lesssim 20M_\odot$, and $R_{\text{CSM}} \lesssim \text{few} \times 10^{16}$ cm (see Fig. D.2). Interestingly, the IceCube neutrino event IC200530A associated with the candidate SLSN event AT2019fdr was detected about 300 days after the optical peak [397], in agreement with our findings ⁷.

⁷AT2019fdr occurred at $z \simeq 0.27$, and the optical lightcurve displayed $t_{\text{rise}} = 98$ days and $L_{\text{peak}} = 2.1 \times 10^{44}$ erg/s, considering a radiative efficiency of 18–35%, [397] estimated that about 4.6×10^{-2} muon neutrino and antineutrino events were expected assuming excellent discrimination of the atmospheric background.

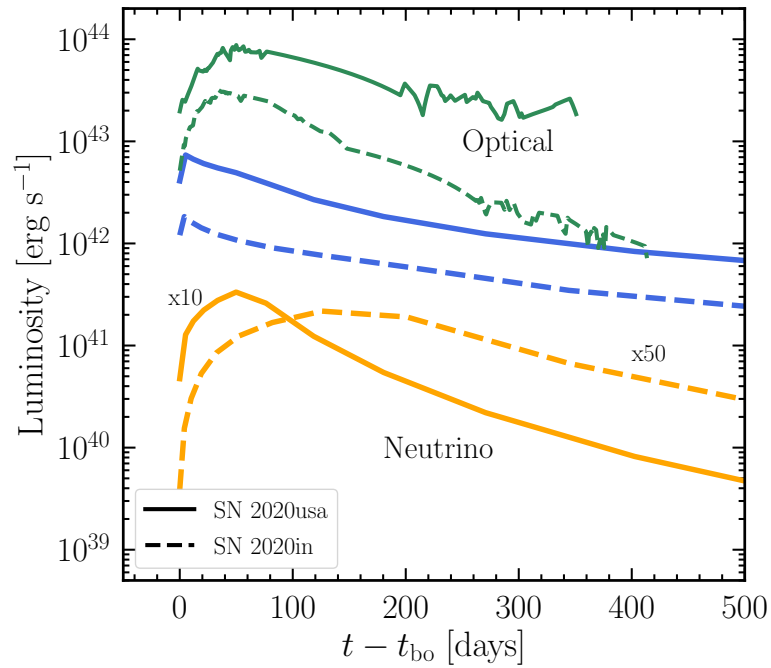


Figure 12.9: Muon neutrino and antineutrino (taking into account flavor oscillation, in blue and orange) and optical luminosities (after interpolation, in green) for SN 2020usa (solid lines) and SN 2020in (dashed lines) as functions of time in the source frame. The two selected SNe exhibit a comparable evolution of the total neutrino luminosity (blue lines) because t_{rise} and L_{peak} for both SNe are such to lead to similar parameters for what concerns the most optimistic prospects for neutrino emission. The blue curves have been obtained by considering the 100 GeV–1 PeV energy range. The orange lines represent the neutrino luminosity in the high energy range 100 TeV–1 PeV and show how the peak of the high energy neutrinos is shifted [up to $\mathcal{O}(100 \text{ days})$] with respect to the optical peak.

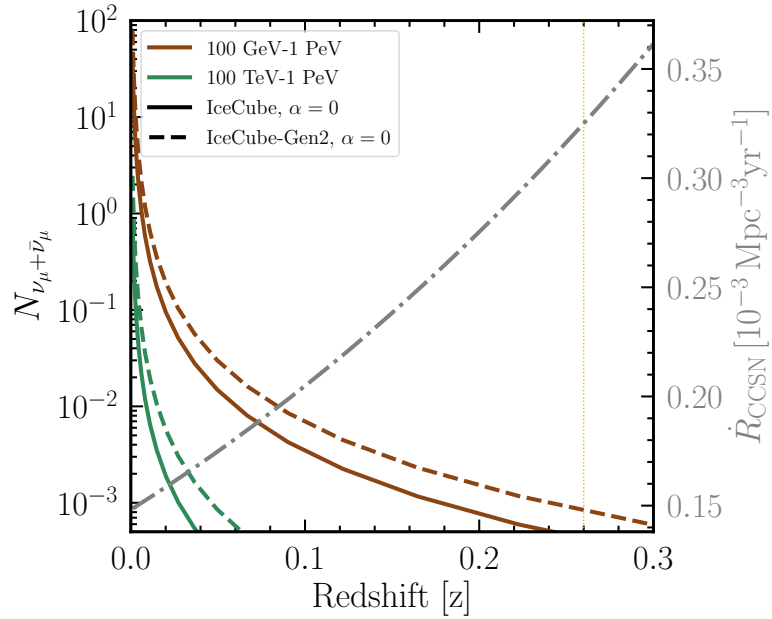


Figure 12.10: Number of muon neutrino and antineutrino events expected at the IceCube Neutrino Observatory (solid lines) and IceCube Gen2 (dashed lines) as functions of the redshift for a benchmark SN with the same properties of SN 2020usa but located at declination $\alpha = 0$ and variable z . The number of neutrino events is obtained integrating up to 200 days to optimize the signal discrimination with respect to the background. The redshift of SN 2020usa is marked with a dashed orange line to guide the eye. The core-collapse SN rate is plotted as a dot-dashed line (see y-axis scale on the right), in order to compare the expected number of neutrino events with the probability of finding SNe at a given z ; the core-collapse SNe rate should be considered as an upper limit of the rate of interaction-powered SNe and SLSNe (see main text for details). We expect $N_{\nu_{\mu} + \bar{\nu}_{\mu}} = 10$ at $z \simeq 0.002$ ($d_L \simeq 9$ Mpc) for IceCube and $z \simeq 0.003$ ($d_L \simeq 13$ Mpc) for IceCube-Gen2.

Figure 12.10 shows the dependence of the number of neutrino events expected in IceCube and IceCube-Gen2 in a temporal window of 200 days and as functions of the redshift for a benchmark SN with the same properties of SN 2020usa, but placed at declination $\alpha = 0$ deg and redshift z . We consider the number of neutrino events expected in a time window of 200 days in order to optimize the signal over background classification (see Sec. 12.6.5). One can see that IceCube expects to detect $N_{\nu_{\mu}+\bar{\nu}_{\mu}} \gtrsim 10$ for SNe at distance $\lesssim 9$ Mpc ($z \lesssim 0.002$); while $N_{\nu_{\mu}+\bar{\nu}_{\mu}} \gtrsim 10$ should be detected for SNe at a distance $\lesssim 13$ Mpc ($z \lesssim 0.003$) for IceCube-Gen2 [10].

In order to compare the expected number of neutrino events with the likelihood of finding SNe at redshift z , Fig. 12.10 also shows the core-collapse SN rate [515, 482] for reference. Note that the rate of interaction-powered SNe is very uncertain and it is not clear whether their redshift evolution follows the star-formation rate [451]; hence the core-collapse SN rate should be considered as an upper limit of the rate of interaction-powered SNe and SLSNe, under the assumption that the latter follow the same redshift evolution.

The evolution of the energy flux of neutrinos is displayed in Fig. 12.11. One can see that for $E_{\nu} \gtrsim 100$ TeV, the energy flux increases up to around 100 days, and then decreases. This trend can be explained considering the evolution of $E_{p,\max}$ (see also Fig. 12.9).

12.6.4 Follow-up strategy for neutrino searches

Our findings in Sec. 12.5.1 suggest that a large L_{peak} and average t_{rise} are necessary, but not sufficient, to guarantee large neutrino emission. This is due to the large degeneracy existing in the SN model parameter space that could lead to SN lightcurves with comparable properties in the optical, but largely different neutrino emission.

Despite the degeneracy in the SN properties leading to comparable optical signals, the semi-analytical procedure outlined in this work allows to restrict the range of E_k , M_{ej} , M_{CSM} , and R_{CSM} that matches the measured t_{rise} and L_{peak} . This procedure then forecasts an expectation range for the number of neutrino events detectable by IceCube to guide upcoming follow-up searches (see Sec. 12.6.2 for an application to two SNe detected by ZTF), also taking into account the unknown radiative efficiency ϵ_{rad} .

For measured t_{rise} and L_{peak} , through the method outlined in this paper, it is possible to predict the largest expected number of neutrino events. On the other hand, if an interaction-powered SN should be detected in the optical, and no neutrino should be observed, this would imply that the SN model parameters compatible with the measured t_{rise} and L_{peak} are not optimal for neutrino production.

Our findings highlight the need to carry out multi-wavelength SN observations to better infer the SN properties and then optimize neutrino searches through the procedure presented in this work. In fact, relying on radio and X-ray all-sky surveys, one could

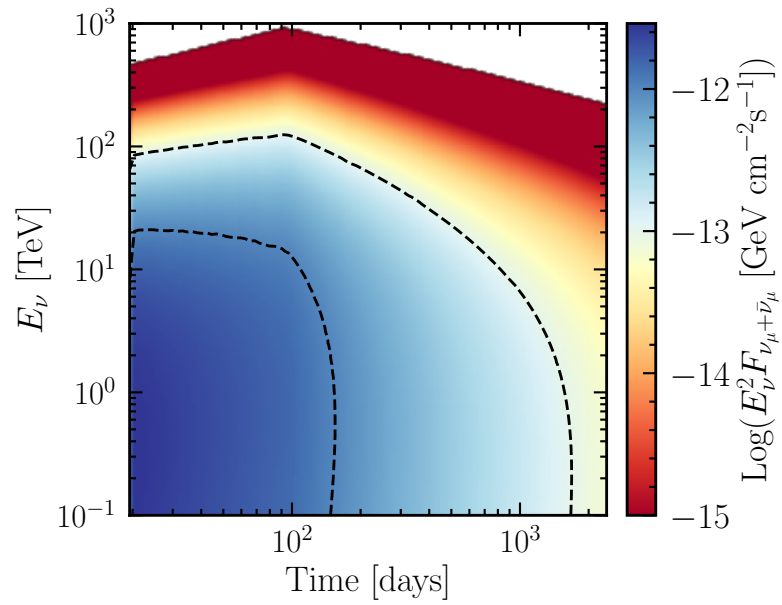


Figure 12.11: Contour plot of the muon neutrino and antineutrino energy flux expected at Earth for SN2020usa in the best case scenario and in the plane spanned by the arrival time of neutrinos and the neutrino energy. At low energies the neutrino flux decreases with time after the breakout. At high energies ($E_\nu \gtrsim 100$ TeV), instead, it increases with time, peaks at around 100 days, and then decreases. This is related to the time of maximum $E_{p,\text{max}}$ (see also Fig. 12.9). The white color marks the regions where the flux is zero.

narrow down the values of M_{ej} , M_{CSM} , and R_{CSM} compatible with the data [308, 131]. Because CSM interaction signatures appear clearly in the UV, early SN observations by future ultraviolet satellites, such as ULTRASAT [441], will be critical to provide insights into the CSM properties. Further information on the CSM can be obtained in the X-ray regime [308], e.g. through surveys such as the extended ROentgen Survey with an Imaging Telescope Array (eROSITA,[400]). In addition, the Vera Rubin Observatory [302] will detect numerous SNe providing a large sample for a neutrino stacking analysis.

12.6.5 Multi-messenger follow-up programs

There are two ways to search for neutrinos from SNe.

- One can compile a catalog of SNe detected by electromagnetic surveys and use archival all-sky neutrino data to search for an excess of neutrinos from the catalogued sources. Such a search is most sensitive when a stacking of all sources is applied (see e.g.,[24]). The stacking requires a weighting of the sources relative to each other. Previous searches assumed that all sources are neutrino standard candles, i.e. the neutrino flux at Earth would scale with the inverse of the square of the luminosity distance, or used the optical peak flux as a weight. This work indicates that neither of those assumptions is justified. Modeling of the multi-wavelength emission can yield a source-by-source prediction of the neutrino emission, which can be used as a weight.

Another important analysis choice is the time window to consider for the neutrino search. A too long time window increases the background of atmospheric neutrinos, while a too short time window cuts parts of the signal. The prediction of the temporal evolution of the neutrino signal by our modeling allows to optimize the neutrino search time window. Finally, also the spectral energy distribution of neutrinos from SNe can be used to optimize the analysis in terms of background rejection.

- One can utilize electromagnetic follow-up observations of neutrino alerts released by neutrino telescopes (see e.g., [15]). Also here, defining a time window in order to assess the coincidence between an electromagnetic counterpart and the neutrino alert will be crucial. Once a potential counterpart is identified further follow-up observations (e.g. spectroscopy and multiple wavelength) can be scheduled to ensure classification of the source as SN and allow for a characterization of the CSM properties.

In order to forecast the expected neutrino signal reliably and better guide neutrino searches, in addition to optical data, input from X-ray and radio surveys would allow to characterize the CSM properties (see Sec. 12.6.4). In addition, it

would be helpful to guide neutrino searches relying on the optical spectra at different times to characterize the duration of the interaction.

In summary, the modeling of particle emission from SNe presented in this paper will be crucial to guide targeted multi-messenger searches.

12.7 Conclusions

Supernovae and SLSNe of Type IIn show in their spectra strong signs of circumstellar interaction with a hydrogen-rich medium. The interaction between the SN ejecta and the CSM powers thermal UV/optical emission as well as high-energy neutrino emission. This work aims to explore the connection between the energy emitted in neutrinos detectable at the IceCube Neutrino Observatory (and its successor IceCube-Gen2) and the photometric properties of the optical signals observable by wide-field, high-cadence surveys. Our main goal is to outline the best follow-up strategy for upcoming multi-messenger searches.

We rely on a semi-analytical model that connects the optical lightcurve observables to the SN properties and the correspondent neutrino emission, we find that the largest energy emitted in neutrinos and antineutrino is expected for large SN kinetic energy ($E_k \gtrsim 10^{51}$ erg), small ejecta mass ($M_{ej} \lesssim 10 M_\odot$), intermediate CSM mass ($1 M_\odot \lesssim M_{CSM} \lesssim 30 M_\odot$), and extended CSM ($R_{CSM} \gtrsim 10^{16}$ cm). Such parameters lead to large bolometric peak luminosity ($L_{peak} \gtrsim 10^{43} - 10^{44}$ erg) and average rise time ($t_{rise} \gtrsim 10 - 40$ days). However, these lightcurve features are necessary but not sufficient to guarantee ideal conditions for neutrino detection. In fact, different configurations of the SN model parameters could lead to comparable optical lightcurves, but vastly different neutrino emission.

The degeneracy between the optical lightcurve properties and the SN model parameters challenges the possibility of outlining a simple procedure to determine the expected number of IceCube neutrino events by solely relying on SN observations in the optical. While our method allows to foresee the largest possible number of neutrino events for given L_{peak} and t_{rise} , the eventual lack of neutrino detection for upcoming nearby SNe could hint towards SN properties that are different with respect to the ones maximizing the neutrino signal, therefore constraining the SN model parameter space compatible with neutrino and optical observations.

We also find that the peak of the neutrino curve does not coincide with the one of the optical lightcurve. Hence, one should consider a time window of a few t_{rise} around L_{peak} when looking for neutrinos. The time window should indeed be optimized to guarantee a fair signal discrimination with respect to the background.

Our findings suggest that previous neutrino stacking searches that assumed all SNe as neutrino standard candles, or used weights based on optical peak flux, might have not

been optimal, as they do not take into account the diversity in the SN properties leading to a large variation in the number of neutrinos expected at Earth. Importantly, multi-wavelength observations are necessary to break the degeneracy between the optical lightcurve and the SN properties and will be essential to forecast the expected neutrino signal and optimize multi-messenger searches.

Summary and conclusions

In this thesis, we investigate the potential of high-energy neutrinos to provide insights into the mechanisms underlying two extremely bright astrophysical transient phenomena: long gamma-ray bursts (LGRBs) and superluminous supernovae (SLSNe).

In Sec. 6.2 and Chapter 7, we highlight that there are still open questions in the LGRB field concerning jet composition, energy dissipation, emission, and particle acceleration mechanisms, that to date have not found a satisfying answer due to the limits presented by exploiting the observation of the electromagnetic emission alone. Hence, the necessity to use other available cosmic messengers like neutrinos. In particular, in Paper I (Chapter 8), we focus on the brightest emission phase of an LGRB, given by the prompt radiation. We examine different jet compositions and prompt emission models, including internal shock, dissipative photosphere, magnetized jet, and proton synchrotron emission models. The models are compared based on their ability to produce high-energy neutrinos. We show a wide diversity in the predicted neutrino fluxes in intensity and spectral shape. However, none of the explored GRB models are excluded by current neutrino flux measurements reported by IceCube. We conclude that point source detections are more suitable for putting strong jet mechanism constraints. On the other hand, an analysis that considers burst properties, understanding the fractions of matter-dominated and magnetized jets, redshift and luminosity distributions of the GRB population, will be crucial when predicting diffuse flux.

In Paper II (Chapter 9), we explore the late merger of two relativistic shells as a possible explanation of optical jumps observed in the afterglow phase of some LGRBs. By calculating the photon and neutrino fluxes for both constant density (ISM) and stellar wind profiles, we show that in the ISM scenario, the number of neutrinos significantly increases in the presence of an optical jump. In contrast, the impact on neutrino flux is negligible in the wind scenario. We then explore the detection prospects for quasi-diffuse flux and point source searches. The predicted flux falls below the current IceCube sensitivity for the quasi-diffuse flux, and point source detection depends on specific conditions like merger configuration, system energetics, and GRB distance. We conclude that a successful point-like neutrino detection requires rare and specific

conditions in the merger configuration and the properties of LGRBs displaying optical jumps during their afterglow, limiting neutrinos' ability to pinpoint the optical jumps' origin.

In Paper III (Chapter 11), we investigate the possibility that the neutrino event IC200530A detected by IceCube originated from the interaction between the supernova ejecta and a dense circumstellar medium (CSM) in the transient event AT2019fdr. By analyzing configurations compatible with observed radiated energy, lightcurve rise time, and the neutrino's detection day, we find that the ejecta-CSM interaction can explain the observed neutrino event. Our study indicates that the SLSN interpretation of AT2019fdr is plausible, especially considering the population rate of SLSNs in the Universe, and that, if confirmed, the neutrino association would be a direct proof of the idea that the powering mechanism of SLSNe is the conversion of ejecta kinetic energy into radiation.

In Paper IV (Chapter 12), our goal is to devise an effective strategy to optimize future multimessenger searches for neutrinos from interaction-powered SNe. To this aim, we study the connection between the production efficiency of high-energy neutrinos and key properties of optical lightcurves of these events, such as optical luminosity peak and rise time to the peak. Our results reveal a significant degeneracy of the parameters characterizing the interaction, making it challenging to establish a straightforward connection between neutrinos and the photometric features of the lightcurve. Indeed, similar luminosity peaks and rise times can be associated with a neutrino flux varying significantly in intensity. Another important finding is the timing of the high-energy neutrino light curve peak, which typically occurs around $\mathcal{O}(100 \text{ days})$ days after the bolometric peak. We conclude that traditional weighting schemes, assuming these events as standard candles or correlating neutrino flux with the optical peak, lack a physical basis due to inherent parameter degeneracy. We emphasize the importance of complementing optical data with multiwavelength observations in X-ray and radio bands to overcome this degeneracy. Furthermore, restricting the search window around the optical peak also proves suboptimal, as it can exclude significant late-peaking neutrino signals.

The findings in this thesis confirm that high-energy neutrinos stand as invaluable cosmic messengers, holding the promise to unravel numerous longstanding open questions in the high-energy Universe, but their potential will be fully realized only with upcoming advanced detectors. It will be essential to combine neutrino observations with multiwavelength electromagnetic data in a practical and complementary manner. This balanced approach is key to a comprehensive understanding of cosmic phenomena.

A

Appendix Paper I

A.1 Spectral energy distributions of photons: fitting functions

In order to describe the electromagnetic emission, in this appendix we introduce the main spectral functions used to fit the electromagnetic data: the Band function, the cut-off power-law, a simple power-law, and a double broken power-law usually representing the synchrotron emission from a marginally fast cooling particle population. The various spectral functions introduced here are then employed to model the GRB emission in Sec. 8.5.

When the energy distribution does not present an intrinsic cut-off at high energies (e.g., Band function and synchrotron spectrum), we define $E'_{\gamma,\text{cutoff}}$ as the energy at which the opacity to photon-photon pair production becomes unity

$$\tau_{\gamma\gamma}(E'_{\gamma,\text{cutoff}}) \simeq 0.1\sigma_T E'_* n'_\gamma(E'_*) \frac{R_\gamma}{2\Gamma} = 1 \quad (\text{A.1})$$

where $E'_* = m_e^2 c^4 / E'_{\gamma,\text{cutoff}}$ and $\tau_{\gamma\gamma}(E'_{\gamma,\text{cutoff}})$ is the opacity for the photons with energy $E'_{\gamma,\text{cutoff}}$ and number density distribution $n'_\gamma(E'_\gamma)$.

A.1.1 Band function

The Band function [73] is the most used empirical function to fit the time-integrated electromagnetic spectra. Despite fitting well the data, it is still lacking a clear physical

meaning. It consists of a smoothly joint broken power-law:

$$n_{\gamma}^{\text{Band}}(E_{\gamma}) = C \begin{cases} \left(\frac{E_{\gamma}}{100 \text{ keV}}\right)^{\alpha_{\gamma}} \exp\left[-\frac{(\alpha_{\gamma}+2)E_{\gamma}}{E_{\gamma,\text{peak}}}\right] & E_{\gamma} < E_{\gamma,c} \\ \left(\frac{E_{\gamma}}{100 \text{ keV}}\right)^{\beta_{\gamma}} \exp(\beta_{\gamma} - \alpha_{\gamma}) \left(\frac{E_{\gamma,c}}{100 \text{ KeV}}\right)^{\alpha_{\gamma}-\beta_{\gamma}} & E_{\gamma} \geq E_{\gamma,c} \end{cases} \quad (\text{A.2})$$

where

$$E_{\gamma,c} = \left(\frac{\alpha_{\gamma} - \beta_{\gamma}}{\alpha_{\gamma} + 2}\right) E_{\gamma,\text{peak}}, \quad (\text{A.3})$$

C is a normalization constant (in units of $\text{GeV}^{-1} \text{cm}^{-3}$), α_{γ} and β_{γ} are the low-energy and high-energy power-law photon indices, $E_{\gamma,c}$ represents the energy where the low-energy power-law with an exponential cutoff ends and the pure high energy power-law begins. The peak energy $E_{\gamma,\text{peak}}$ is chosen to satisfy the Amati relation [55]:

$$\tilde{E}_{\gamma,\text{peak}} = 80 \left(\frac{\tilde{E}_{\gamma,\text{iso}}}{10^{52} \text{ erg}}\right)^{0.57} \text{ keV}. \quad (\text{A.4})$$

The typical spectral parameters inferred from observations are: $\alpha_{\gamma} \simeq -1.1$, $\beta_{\gamma} \simeq -2.2$, and $E_{\gamma,\text{peak}} \simeq 300 \text{ keV}$ [218].

A.1.2 Cut-off power-law

Although the Band spectrum is the best fitting function for most GRBs, it has been shown that in some cases a cut-off power-law (CPL) can represent the preferred model [513, 514, 63]. The CPL is a power-law model with a high energy exponential cut-off :

$$n_{\gamma}^{\text{CPL}}(E_{\gamma}) = C \left(\frac{E_{\gamma}}{100 \text{ keV}}\right)^{\alpha_{\gamma}} \exp\left[-\frac{(\alpha_{\gamma} + 2)E_{\gamma}}{E_{\gamma,\text{peak}}}\right], \quad (\text{A.5})$$

where α_{γ} is the photon index and $E_{\gamma,\text{peak}}$ the peak energy, whose value will be specified later. In an optically thick thermal scenario, $\alpha_{\gamma} = 1$ in the Rayleigh-Jeans limit, $\alpha_{\gamma} = 2$ in the Wien limit, $\alpha_{\gamma} = 0.4$ for a non-dissipative photosphere in the coasting phase and $\alpha_{\gamma} < 0$ for all non-thermal emissions [38].

A.1.3 Power law

In the cases of faint bursts or narrow detector bandpass, the whole GRB spectrum, or one of its components, can be fitted with a simple power-law [427] defined as

$$n_{\gamma}^{\text{PL}}(E_{\gamma}) = C \left(\frac{E_{\gamma}}{100 \text{ keV}}\right)^{\alpha_{\gamma}}, \quad (\text{A.6})$$

where C is the normalization and α_{γ} is the power-law photon index.

A.1.4 Double broken power law

This is a spectral model that is commonly adopted to describe the synchrotron emission of a fast cooling population of particles that are being injected into the emitting region with a power-law distribution at a rate $Q(\gamma) \propto \gamma^{-k}$ with $\gamma_{\min} < \gamma < \gamma_{\max}$. During an emission period t , the charged particles of mass m lose most of their energy above the characteristic value γ_{cool} :

$$\gamma_{\text{cool}}(t) = \frac{6\pi mc}{\sigma_T \beta^2 B^2 t} \left(\frac{m}{m_e} \right)^2, \quad (\text{A.7})$$

where m_e is the electron mass. Considering a constant injection rate of particles in the emitting region which radiate in the fast cooling regime ($\gamma_{\min} > \gamma_{\text{cool}}$) at a rate $\propto \gamma^2$, after a time t the emitting particle distribution has the following shape [520]:

$$n(\gamma, t) \propto \begin{cases} 0 & \gamma < \gamma_{\text{cool}} \text{ and } \gamma > \gamma_{\max} \\ \gamma^{-2} & \gamma_{\text{cool}} < \gamma < \gamma_{\min} \\ \gamma^{-(k+1)} & \gamma_{\min} < \gamma < \gamma_{\max} \end{cases} \quad (\text{A.8})$$

Given that each particle radiates photons with a characteristic synchrotron energy

$$E_\gamma(\gamma) = \frac{3}{2} \frac{\hbar e}{mc} \gamma^2 B, \quad (\text{A.9})$$

the particle distribution in Eq. A.8 emits the following synchrotron spectrum:

$$n_\gamma^{\text{sync}}(E_\gamma) = C \begin{cases} \left(\frac{E_\gamma}{E_{\gamma,\text{cool}}} \right)^{-\frac{2}{3}} & E_\gamma < E_{\gamma,\text{cool}} \\ \left(\frac{E_\gamma}{E_{\gamma,\text{cool}}} \right)^{-\frac{3}{2}} & E_{\gamma,\text{cool}} < E_\gamma < E_{\gamma,\text{min}} \\ \left(\frac{E_{\gamma,\text{min}}}{E_{\gamma,\text{cool}}} \right)^{-\frac{3}{2}} \left(\frac{E_\gamma}{E_{\gamma,\text{min}}} \right)^{-\frac{k+2}{2}} & E_{\gamma,\text{min}} < E_\gamma < E_{\gamma,\text{max}} \end{cases} \quad (\text{A.10})$$

where $E_{\gamma,\text{cool}}$, $E_{\gamma,\text{min}}$, and $E_{\gamma,\text{max}}$ correspond to the characteristic photon energies mainly emitted by particles with gamma factors γ_{cool} , γ_{\min} , and γ_{\max} , respectively.

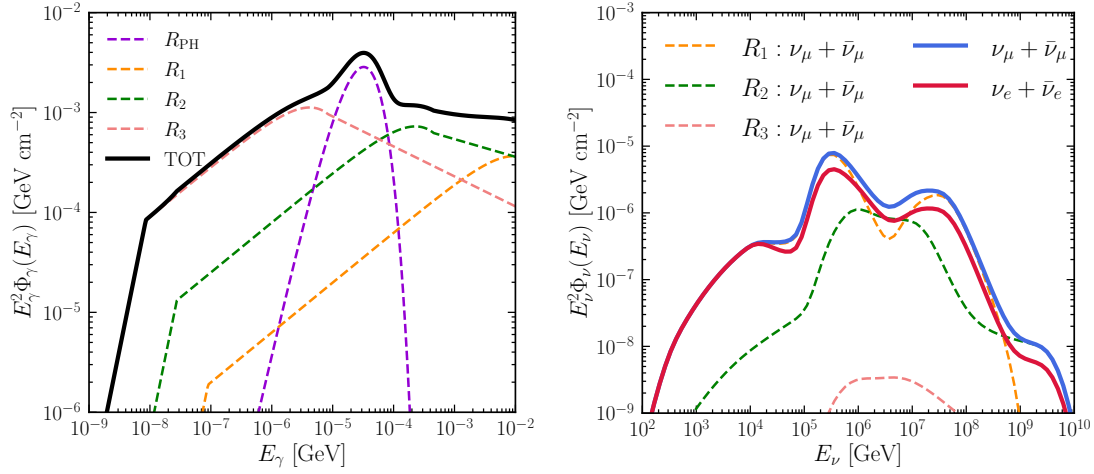


Figure A.1: Similar to Fig. 8.9, but for $\sigma_0 = 100$. The fluence for the muon flavor peaks at $E_\nu^{\text{peak}} = 3.3 \times 10^5$ GeV. In addition, $E_{\nu,\text{iso}} = 8.6 \times 10^{50}$ erg, $E_{\gamma,\text{iso}} = 2.3 \times 10^{53}$ erg, $\Gamma_{\text{sat}} = 1000$, $\sigma_0 = 100$, $R_{\text{PH}} = 7.1 \times 10^{11}$ cm, $R_1 = 2.1 \times 10^{12}$ cm, $R_2 = 3 \times 10^{13}$ cm, $R_3 = 4 \times 10^{14}$ cm, $\Gamma_1 = 180$, $\Gamma_2 = 422$, $\Gamma_3 = 1000$, $\tilde{E}_{\nu,\text{iso}}/\tilde{E}_{\gamma,\text{iso}} = 3.7 \times 10^{-3}$, $\eta_\gamma = 7\%$.

A.2 Magnetized jet model with gradual dissipation: dependence of the neutrino emission on the input parameters

One of the main, but less certain, parameters of the jet model with gradual magnetic dissipation is the initial magnetization σ_0 . This, in turn, determines the photospheric radius, the saturation Lorentz factor, the energy dissipation rate, and other parameters. For this reason, we investigate the impact of σ_0 on the photon and neutrino fluences by considering a case with $\sigma_0 = 100$. All the other parameters, like \tilde{E}_{iso} , are identical to the ones adopted in Sec. 8.5.2.2. We follow the same procedure to calculate the neutrino flux as outlined in Sec. 8.5.2.2.

In Fig. A.1, we show snapshots of the photon fluence (left panel) and neutrino fluence (right panel) for $\sigma_0 = 100$ at three indicative radii. A comparison between the $\sigma_0 = 45$ and $\sigma_0 = 100$ cases is shown in Fig. A.2.

A noticeable difference is appreciable between the photon spectral energy distributions. As the initial magnetization increases, the saturation Lorentz factor increases, namely $\Gamma_{\text{sat}} = \sigma_0^{3/2} = 1000$ for $\sigma_0 = 100$. The energy is dissipated at a rate $\dot{E} \propto R^{1/3}$, while the photosphere occurs at a smaller distance from the source ($R_{\text{PH}} \propto 1/\Gamma_{\text{sat}}$). As a result, less energy is dissipated during the optically thick regime (most of the energy is dissipated at $R > R_{\text{PH}}$) and the photospheric emission becomes dimmer (compare

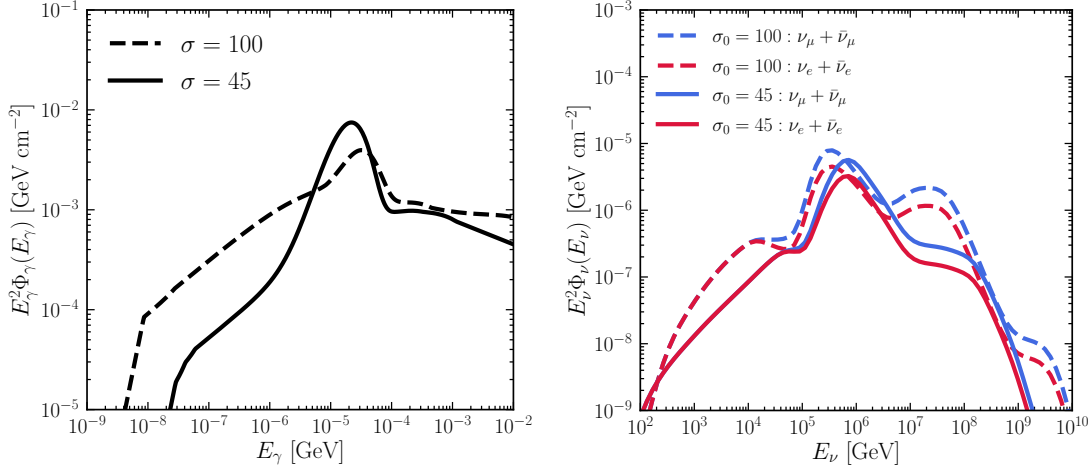


Figure A.2: *Left:* Total photon fluence in the observer reference frame, obtained as the sum of the components produced at R_{PH} , R_1 , R_2 and R_3 for the $\sigma_0 = 45$ (solid line) and $\sigma_0 = 100$ (dashed line) cases, respectively. *Right:* Correspondent $\nu_\alpha + \bar{\nu}_\alpha$ fluence (in red and in blue for the electron and muon flavors, respectively). For parameters used, see captions of Figs. 8.9 and A.1.

dashed and solid lines at $E_\gamma \sim 10^{-5} - 10^{-4}$ GeV in Fig. A.2). The characteristic synchrotron energy $E_{\gamma, \text{min}} \propto \Gamma \gamma_{\text{min}}'^2 B'$ (Eq. A.9) decreases with the radius (see, e.g., dashed colored curves in the left panel of Fig. A.1), while the normalization of the synchrotron photon spectra increases with respect to the case of $\sigma_0 = 45$ (see dashed curve in the left panel of Fig. A.2) because of the higher dissipation rate (Eq. 8.11). For a higher σ_0 , particle acceleration begins at smaller radii and so does the production of neutrinos. Moreover, the power slopes of the electron and proton distributions (accelerated via reconnection) are harder [444, 227] because of the higher magnetization in the acceleration region. Because of the larger saturation radius ($R_{\text{sat}} \propto \Gamma_{\text{sat}}^2$) found for higher σ_0 , the dissipated energy up to $R_1 = aR_{\text{ph}} \propto \Gamma_{\text{sat}}^{-1}$ that is available for relativistic particles is less than in the case of lower initial magnetizations.

The combination of a smaller amount of dissipated energy up to a given radius, smaller volume and harder proton power slope leads to a neutrino flux at peak (whose main contribution comes from R_1) comparable to the one with $\sigma_0 = 45$ (see right panel of Fig. A.2).

For the case of $\sigma_0 = 100$, the second bump in the neutrino spectrum has a fluence that is comparable to the one of the first bump at $\sim 10^6$ GeV. On the contrary, the second bump is barely visible in the neutrino energy distribution with $\sigma_0 = 45$ (compare solid and dashed lines in the right panel of Fig. A.2). This is because in the $\sigma_0 = 100$ case, pions suffer stronger synchrotron losses, hence the neutrino intensity resulting from the decay of pions decreases to the level of the one produced by kaons. This is also the reason for a slight shift in the neutrino flux peak to lower energies. Another noticeable

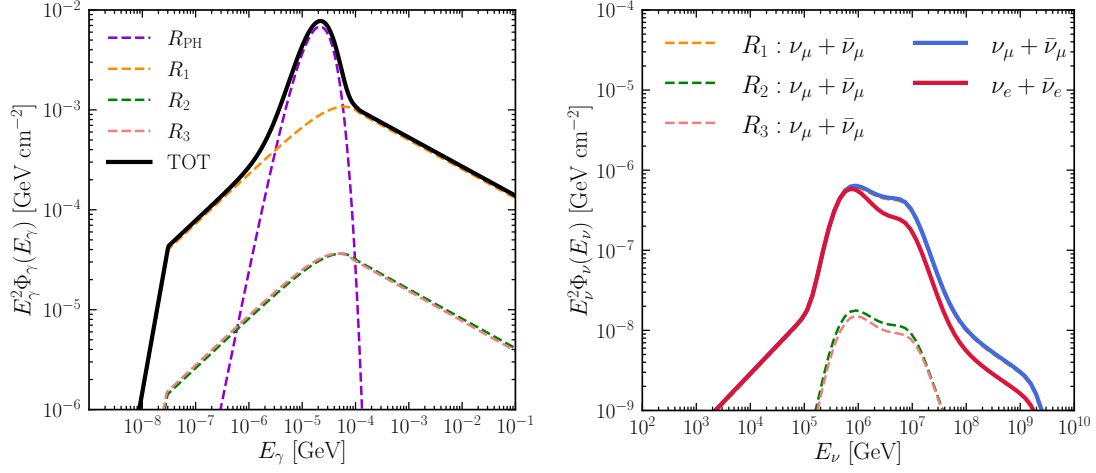


Figure A.3: *Left:* Total photon fluence in the observer reference frame, obtained as the sum of the components produced at R_{PH} , R_1 , R_2 and R_3 for the $\sigma_0 = 45$ and $a = 13$ case. *Right:* Correspondent $\nu_\alpha + \bar{\nu}_\alpha$ fluence (in red and in blue for the electron and muon flavors, respectively).

feature is the low energy tail. The latter turns out to be higher in the $\sigma_0 = 100$ case, given the higher number density of photons at higher energies.

Finally, in order to explore the effects of the arbitrary choice of the parameter a , we considered the case with $\sigma_0 = 45$ and $a = 13$, where $R_1 \sim R_{\text{sat}}$, see Fig. A.3. Since most of the energy is dissipated within R_1 , the neutrino contribution from R_1 is dominant, although lower by a factor $\mathcal{O}(10)$ if compared to the case with $a = 3$. However, since the case $a = 13$ represents an extreme case, such that all the energy is locally dissipated near the saturation radius, the fluence of $\mathcal{O}(10^{-6}) \text{ GeV cm}^{-2}$ should be considered as the lower limit for the neutrino production from a GRB described by the magnetic model with gradual dissipation for the specific set of parameters adopted in this work.

A.3 Quasi-diffuse neutrino flux for standard internal shock parameters

In this work, we have adopted input parameters inspired by the results of recent PIC simulations of mildly relativistic shocks for the IS models (see Sec. 8.3.1). However, in the literature, under the assumption that GRBs are the main sources of ultra-high-energy cosmic rays, the following parameters are often adopted: $\varepsilon_p = 10/12$, $\varepsilon_e = \varepsilon_B = 1/12$, and $k_p = 2$, see e.g. [525]. Fig. A.4 shows the quasi-diffuse neutrino emission for these input parameters, in order to facilitate a comparison with the existing literature. One can see that the flux normalization of the simple IS model, the IS model with dissip-

ative photosphere and the IS model with three components is indeed larger than what is shown in Fig. 8.12, and roughly at the same level of the ICMART model, the proton synchrotron model and magnetized jet model with gradual dissipation.

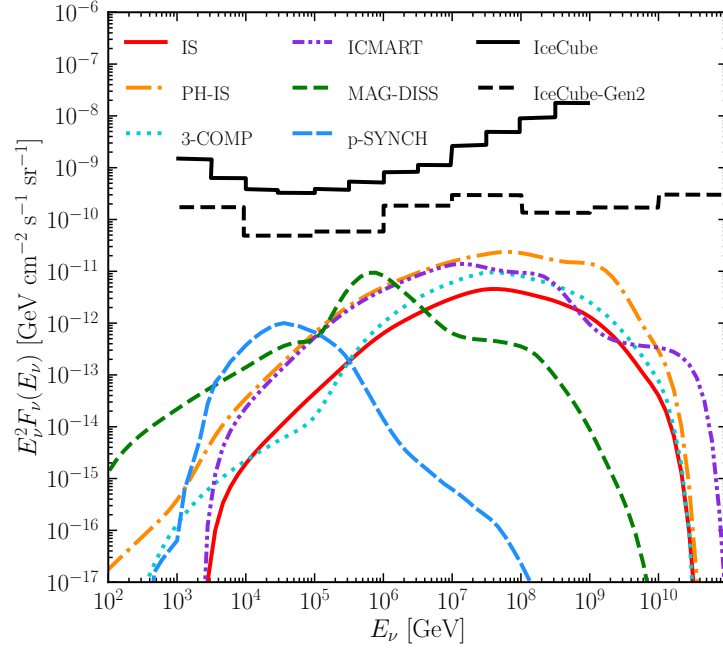


Figure A.4: Quasi-diffuse neutrino flux for the six models considered in this work and computed as in Fig. 8.12, but with the classically adopted microphysics parameters for the Internal shocks: $\varepsilon_p = 10/12$, $\varepsilon_e = \varepsilon_B = 1/12$, and $k_p = 2$.

B

Appendix Paper II

B.1 A model for the late collision and merger of two relativistic shells

In this appendix, we revisit the relativistic shock jump conditions. We then model the dynamical merger of two relativistic shells. In the following, we rely on the assumption of thin shells, for which the reverse shock is at most mildly relativistic. We further assume that the reverse shock has already crossed the ejecta, hence we focus on the forward shock only.

The first ultrarelativistic, isotropic shell launched by the central engine starts to be decelerated by the ambient medium when it acquires a mass comparable to m_0/Γ_0 , with m_0 being the initial mass of the jet and Γ_0 its initial Lorentz factor [520]. The number of particles, momentum and energy are conserved across the forward shock; this leads to the Rankine-Hugoniot jump conditions at the shock front, see e.g. [471, 94], which in the fluid rest frame read as:

$$w' = (\Gamma_u - 1)n' \frac{h_u}{n_u}, \quad (\text{B.1})$$

$$n' = \frac{2\Gamma_{\text{sh},u}^2}{\Gamma_u} n_u, \quad (\text{B.2})$$

$$\Gamma_u^2 = \frac{1}{2}\Gamma_{\text{sh},u}^2; \quad (\text{B.3})$$

where u refers to the upstream quantities, while the primed quantities are measured in the downstream region. Here h_u is the enthalpy density of the upstream medium, which corresponds to the cold CBM, therefore $h_u \equiv \rho_u = n_u m_p c^2$. The quantities w' , ρ' , and n' denote the comoving pressure, internal energy density, density and number

of particles, respectively. $\Gamma_{\text{sh},u}$ is the Lorentz factor of the shock in the frame of the unshocked external medium and Γ_u is the Lorentz factor of the shocked region measured in the same frame. Since the upstream medium is the unshocked CBM, assumed to be at rest in the stellar reference frame, the Lorentz factors in these frames satisfy the equivalence $\tilde{\Gamma} \equiv \Gamma_u$. Therefore, as for the Lorentz factors, hereafter we do not distinguish between the stellar and the unshocked CBM frames and simply denote them as Γ . The shock heats the matter, so that the region behind the shock is a hot plasma for which the equation of state $p' = (\hat{\gamma} - 1)w'$ holds, being $\hat{\gamma}$ the adiabatic index of the fluid and p' its comoving pressure. For a hot fluid $\hat{\gamma} = 4/3$, therefore the equation of state reads $p' = w'/3$. Using the shock jump conditions, we can rewrite the first equation in Eq. B.3:

$$w' = 4\Gamma(\Gamma - 1)\rho_u = 4\Gamma(\Gamma - 1)n_u m_p c^2, \quad (\text{B.4})$$

which corresponds to Eq. 9.16. Note that from Eq. B.3 one obtains that the plasma behind the shock moves with a velocity $\Gamma = \Gamma_{\text{sh}}/\sqrt{2}$. This region of hot plasma corresponds to a blastwave decelerated to the BM solution [94], i.e. our slow shell.

The details of the collision between the slow and the fast shells depend on the hydrodynamical modeling (see, e.g., [483]) and are beyond the scope of this paper. We refer the interested reader to Ref. [280] for a semi-analytic treatment of the shell collision including the reverse shock. Here, we rely on a simplified collision model, expanding on the one adopted to model the internal shock [271, 108]. The main difference with respect to the internal shock prescription is that our slow shell is hot and continuously sweeps up material from the CBM. As a result, we need to include its internal energy at the collision time [360] as well as the mass swept up by the slow shell from the CBM until the time of the collision.

In the following, we focus on a merger whose duration is smaller than the dynamical time, considering that the jet has an opening angle θ_j small enough such that the merger process can be approximated as planar. Hence, the comoving volume of the shells can be expressed as $V' \simeq \pi\theta_j^2 R^2 l'$, where l' is the width of the shell. This assumption is valid as long as the Lorentz factor $\Gamma \gg 1$.

In order to obtain the total energy and momentum of the slow shell at a fixed time t , we introduce the energy-momentum tensor of a relativistic fluid in the laboratory frame [360, 520]:

$$\tilde{T}^{\mu\nu} = (\rho' c^2 + w' + p')\tilde{u}^\mu \tilde{u}^\nu + p' \eta^{\mu\nu}, \quad (\text{B.5})$$

where $\tilde{u}^\mu = \Gamma(1, \vec{v}/c)$ is the adimensional 4-velocity of the fluid in the laboratory frame, $\eta^{\mu\nu} = \text{diag}(-1, 1, 1, 1)$ the Minkowski flat space-time and $p' = w'/3$, since we only consider the relativistic shock case. From the component with $\mu = \nu = 0$ in Eq. B.5, we obtain the energy density in the blastwave at the fixed time t :

$$\tilde{T}^{00} = \Gamma^2(\rho' c^2 + w' + p') - p' = \Gamma^2 \rho' c^2 + (\hat{\gamma}\Gamma^2 - \hat{\gamma} + 1)w'. \quad (\text{B.6})$$

The total energy of the slow shell in the laboratory frame is computed by integrating Eq. B.6 over $\tilde{V} = V'/\Gamma$, where V' is defined as described previously. By denoting the total internal energy of the slow shell in the comoving frame as $W' = w'V'$, its total energy is [360]:

$$\tilde{E} = \Gamma c^2 m + \frac{\hat{\gamma}\Gamma^2 - \hat{\gamma} + 1}{\Gamma} W' = \Gamma c^2 m + \Gamma_{\text{eff}} W', \quad (\text{B.7})$$

where m is the mass of the slow shell given by Eq. 9.7. Furthermore, the effective Lorentz factor of the slow shell Γ_{eff} in Eq. B.7 is

$$\Gamma_{\text{eff}} = \frac{\hat{\gamma}\Gamma^2 - \hat{\gamma} + 1}{\Gamma} \simeq \hat{\gamma}\Gamma = \frac{4}{3}\Gamma, \quad (\text{B.8})$$

where we have done the approximation $\Gamma \gg 1$ (valid in the time window we are looking at) and the relativistic $\hat{\gamma} = 4/3$ has been adopted.

Similarly, taking the ($\mu = 1, \nu = 0$) component in Eq. B.5, the 4-momentum density of the slow shell at a fixed time t is

$$\tilde{T}^{10} = \Gamma^2 \frac{\tilde{v}^1}{c} (\rho' c^2 + w' + p'), \quad (\text{B.9})$$

where $\eta^{10} = 0$. The 1-st component of the total momentum of the slow shell is $\tilde{P}^1 = 1/c \int_{\tilde{V}} \tilde{T}^{10} d\tilde{V}$, from which:

$$\tilde{P} = c\Gamma\beta \left(m + \hat{\gamma} \frac{W'}{c^2} \right) = c\sqrt{\Gamma^2 - 1} \left(m + \frac{\hat{\gamma}W'}{c^2} \right). \quad (\text{B.10})$$

Equations B.7 and B.10 represent the energy and momentum of the slow shell.

If the second shell is emitted with energy \tilde{E}_f and Lorentz factor $\Gamma_f = \text{const.}$, its mass is $m_f = \tilde{E}_f/(\Gamma_f c^2)$. The fast shell is cold, since it propagates freely, thus its energy and momentum are

$$\tilde{E}_f = \Gamma_f m_f c^2 \quad \text{and} \quad \tilde{P}_f = c m_f \sqrt{\Gamma_f^2 - 1}. \quad (\text{B.11})$$

In order to obtain the Lorentz factor and energy of the resulting merged shell right after the collision, we impose energy and momentum conservation:

$$\tilde{T}_f^{00} \tilde{V}_f + \tilde{T}^{00} \tilde{V} = \tilde{T}_m^{00} \tilde{V}_m^0; \quad (\text{B.12})$$

$$\tilde{T}_f^{i0} \tilde{V}_f + \tilde{T}^{i0} \tilde{V} = \tilde{T}_m^{i0} \tilde{V}_m^0, \quad (\text{B.13})$$

being $\tilde{T}_m^{\mu\nu}$ the energy-momentum tensor of the merged shell and \tilde{V}_m^0 its volume, both evaluated at the collision time. Hereafter, we denote all relevant quantities of the merged shell computed at the collision time with the apex “0,” in order to distinguish

them from the ones describing its deceleration phase. Plugging Eqs. B.7-B.11 in Eq. B.12, we obtain:

$$\Gamma_f m_f + \Gamma m + \frac{\Gamma_{\text{eff}} W'}{c^2} = \Gamma_m^0 m_m^0 + \frac{\Gamma_{m,\text{eff}}^0 W_m'^0}{c^2}, \quad (\text{B.14})$$

$$\sqrt{\Gamma_f^2 - 1} m_f + \sqrt{\Gamma^2 - 1} \left(m + \frac{\hat{\gamma} W'}{c^2} \right) = \sqrt{\Gamma_m^0{}^2 - 1} \left(m_m^0 + \frac{\hat{\gamma} W_m'^0}{c^2} \right), \quad (\text{B.15})$$

where Γ_m^0 , $m_m^0 \equiv m + m_f$, $W_m'^0$ are the initial Lorentz factor, the initial mass and the comoving internal energy of the merged shell, respectively. $\Gamma_{m,\text{eff}}^0$ is the effective Lorentz factor of the merged shell and is defined as in Eq. B.8 by replacing $\Gamma \rightarrow \Gamma_m^0$. Note that all the physical quantities of the merged shell are evaluated at the collision time, thus they describe its initial setup. Equations B.14 and B.15 have a simple solution in the relativistic case, i.e. for $\Gamma_f \gg 1$ and $\Gamma \gg 1$, which also implies $\Gamma_m^0 \gg 1$. Indeed, in this case $\Gamma_{\text{eff}} \approx \hat{\gamma}\Gamma$ and $\Gamma_{m,\text{eff}}^0 \approx \hat{\gamma}\Gamma_m^0$ so that we can rewrite Eqs. B.14 and B.15 as follows:

$$m_f \Gamma_f + \Gamma m_{\text{eff}} = \Gamma_m^0 m_{m,\text{eff}}^0; \quad (\text{B.16})$$

$$m_f \sqrt{\Gamma_f^2 - 1} + m_{\text{eff}} \sqrt{\Gamma^2 - 1} = m_{m,\text{eff}}^0 \sqrt{\Gamma_m^0{}^2 - 1}, \quad (\text{B.17})$$

where we have introduced the effective masses of the slow and merged shells: $m_{\text{eff}} = m + \hat{\gamma} W'/c^2$ and $m_{m,\text{eff}}^0 = m_m^0 + \hat{\gamma} W_m'^0/c^2$. After performing a Taylor expansion around $1/\Gamma_f$, $1/\Gamma$ and $1/\Gamma_m^0$ in Eq. B.16, we obtain the initial Lorentz factor of the merged shell:

$$\Gamma_m^0 \approx \sqrt{\frac{m_f \Gamma_f + m_{\text{eff}} \Gamma}{m_f / \Gamma_f + m_{\text{eff}} / \Gamma}}. \quad (\text{B.18})$$

From energy conservation (Eq. B.16), we obtain the internal energy \tilde{W}_m^0 of the merged shell in the laboratory frame:

$$\tilde{W}_m^0 \equiv \Gamma_m^0 W_m'^0 = \frac{1}{\hat{\gamma}} [(m_f \Gamma_f + m \Gamma) c^2 - (m + m_f) \Gamma c^2] + \Gamma W'. \quad (\text{B.19})$$

Equations B.18 and B.19 describe the initial conditions of the merged shell.

We assume that the shocks immediately cross the plasma. During the crossing, the resulting shell will be compressed, so that the correct expression of the initial width of the resulting merged shell is the one in Eq. 7 of Ref. [271]. In this paper, we make the simple assumption that its width is given by the sum of the widths of the slow shell \tilde{l} and the fast shell \tilde{l}_f :

$$\tilde{l}_m^0 \simeq \tilde{l} + \tilde{l}_f. \quad (\text{B.20})$$

This result differs from the one in Ref. [271] for a small numerical correction factor.

After the merged shell forms, it interacts with the CBM. Even though in our model the merged shell is expected to produce a standard afterglow flux through its interaction with the CBM, its dynamics is slightly different from the one of the slow shell. This is because the merged shell is already hot and thus already has internal energy. Moreover, it also contains the matter material previously swept up by the slower shell. The total initial energy of the merged shell is:

$$\tilde{E}_{\text{tot},m}^0 \simeq \frac{4}{3} \tilde{W}_m^0 + \Gamma_m^0 m_m^0 c^2. \quad (\text{B.21})$$

At the collision, a fraction $\epsilon_{e,m}^0$ of the internal energy \tilde{W}_m^0 goes into electrons and a fraction $\epsilon_{B,m}^0$ to the magnetic field. For our choice of parameters, electrons accelerated at the collision are in the slow cooling regime both in the ISM and wind scenarios, as shown in Fig. B.1. Hence only a small fraction of electrons efficiently radiates, and all the internal energy \tilde{W}_m^0 stays in the merged shell. Nevertheless, it is worth stressing that even if the fast cooling condition should be satisfied and all the electrons should cool through synchrotron radiation, the fraction of energy carried away by photons is rather small ($\simeq 10\text{--}30\%$ of the internal energy, depending on the assumptions on the microphysical parameter ϵ_e). Therefore, also in the fast cooling regime, most of the internal energy released at the collision stays in the merged shell as it is carried by protons which predominantly lose their energy via adiabatic cooling. Thus, the isotropic kinetic energy of the merged shell at the beginning of its deceleration is $\tilde{E}_{k,m} = \tilde{E}_{\text{tot},m}^0$.

When the mass $m_{m,\text{swept}}$ is swept up from the CBM by the expanding blastwave, conservation of energy reads as:

$$\Gamma_m^0 \left(\frac{\tilde{E}_{k,m}}{\Gamma_m^0 c^2} \right) + m_{m,\text{swept}} = \Gamma_m \left[\left(\frac{\tilde{E}_{k,m}}{\Gamma_m c^2} \right) + \hat{\gamma} \Gamma_m m_{m,\text{swept}} \right], \quad (\text{B.22})$$

where Γ_m is the Lorentz factor of the merged shell after the interaction with the medium and $m_{m,\text{swept}}$ is the swept up mass dependent on the density profile of the external medium. The shell starts to be decelerated when the two terms on the right side of Eq. B.22 become comparable [520]:

$$m_{m,\text{swept}} \simeq \frac{1}{\hat{\gamma} \Gamma_m} \left(\frac{\tilde{E}_{k,m}}{\Gamma_m^0 c^2} \right) \simeq \frac{1}{\Gamma_m^0} \left(\frac{\tilde{E}_{k,m}}{\Gamma_m^0 c^2} \right), \quad (\text{B.23})$$

where we have considered that the Lorentz factor of the merged shell at the deceleration onset has been reduced to half of its initial value ($\Gamma_m \simeq \Gamma_m^0/2$) and we have neglected the numerical correction factor 2/3.

By integrating the density profile between $R_{\text{coll}} \equiv R(T_{\text{coll}})$ and $R_{\text{dec},m}$ and equating

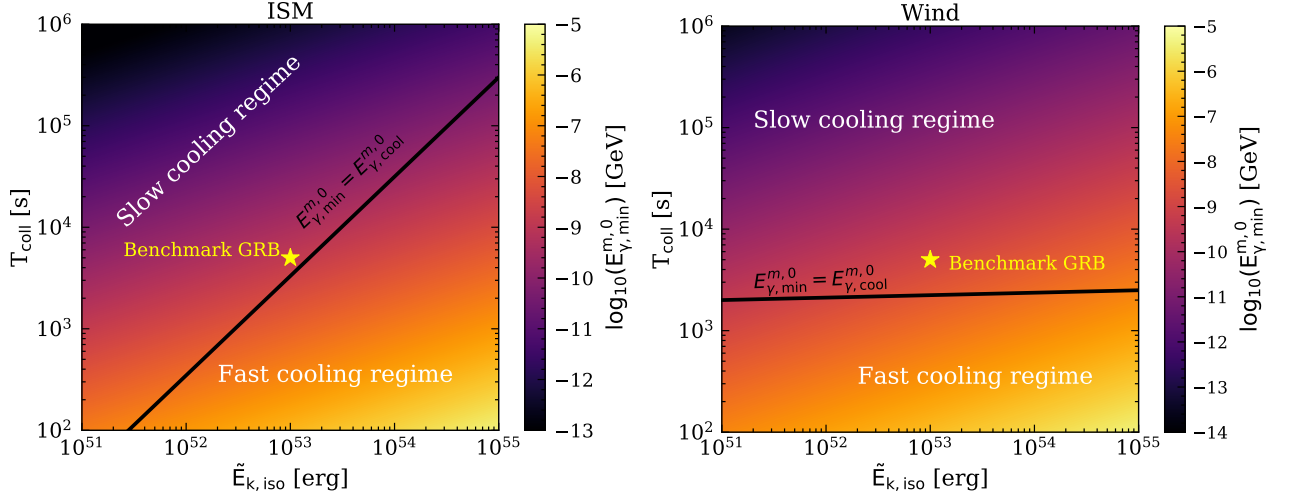


Figure B.1: Contour plot of the minimum energy of the synchrotron photons emitted at the collision ($E_{\gamma,\min}^{m,0}$) in the plane spanned by $(\tilde{E}_{k,\text{iso}}, T_{\text{coll}})$, where $\tilde{E}_{k,\text{iso}}$ is the isotropic kinetic energy of the slow shell and T_{coll} the collision time. The ISM (wind) scenario is shown on the left (right). The black solid line marks $E_{\gamma,\min}^{m,0} = E_{\gamma,\text{cool}}^{m,0}$. For our set of parameters, electrons accelerated at the collision are in the slow cooling regime for the ISM and wind CBM scenarios.

with Eq. B.23, we finally obtain:

$$\frac{4}{3}\pi n_0 m_p c^2 (R_{\text{dec},m}^{\text{ISM}})^3 - R_{\text{coll}}^3 \simeq \frac{\tilde{E}_{k,m}}{\Gamma_m^0{}^2}, \quad (\text{B.24})$$

$$4\pi A (R_{\text{dec},m}^{\text{wind}} - R_{\text{coll}}) m_p c^2 \simeq \frac{\tilde{E}_{k,m}}{\Gamma_m^0{}^2}, \quad (\text{B.25})$$

for the ISM and wind scenarios, respectively. Thus the deceleration radius for the merged shell is

$$R_{\text{dec},m}^{\text{ISM}} \simeq \left(\frac{3\tilde{E}_{k,m}}{8\pi n_0 m_p c^2 \Gamma_m^0{}^2} + R_{\text{coll}}^3 \right)^{1/3}, \quad (\text{B.26})$$

$$R_{\text{dec},m}^{\text{wind}} \simeq \frac{\tilde{E}_{k,m}}{4\pi A m_p c^2 \Gamma_m^0{}^2} + R_{\text{coll}}. \quad (\text{B.27})$$

Finally, the deceleration time of the merged shell is

$$T_{\text{dec},m}^{\text{ISM,wind}} \simeq \frac{R_{\text{dec},m}^{\text{ISM,wind}} (1+z)}{2\Gamma_m^0{}^2 c}. \quad (\text{B.28})$$

From $T_{\text{dec},m}^{\text{ISM,wind}}$ on, the merged shell follows the standard BM solution. In particular, the temporal evolution of its Lorentz factor Γ_m is described by Eq. 9.3, by considering Eq. B.28 for the deceleration time and replacing $\Gamma_0 \rightarrow \Gamma_m^0$.

B.2 Degeneracies among the parameters characteristic of the merging shells

The two shells in our model collide when their position relative to the central engine coincides, i.e. when $R(T_{\text{coll}}) = R_f(T_{\text{coll}})$ (see Eqs. 9.5 and 9.11) [282]:

$$\frac{8\Gamma^2 T_{\text{coll}} c}{(1+z)} = \frac{2\Gamma_f^2 (T_{\text{coll}} - \Delta_T) c}{(1+z)}. \quad (\text{B.29})$$

The collision of the two shells entails degeneracies among the parameters characteristic of the merging shells. One of these degeneracies occurs between the Lorentz factor of the fast shell Γ_f and the time delay Δ_T relative to the emission time of the first shell. Indeed, from Eq. B.29:

$$\Gamma_f = 2\Gamma(T_{\text{coll}}) \left(1 - \frac{\Delta_T}{T_{\text{coll}}}\right)^{-1/2}, \quad (\text{B.30})$$

i.e. a shell launched with a large Δ_T can reach the first slow shell at the same collision time T_{coll} of a shell launched with a smaller delay and smaller Γ_f . This degeneracy can be better understood by looking at the left panel of Fig. B.2 for our benchmark GRB (see Table 9.1). A shortcoming of our model is that it is not possible to distinguish between Γ_f and Δ_T , if no other information is available except for the amplitude of the optical jump. Perhaps, an analysis of the reverse shock may break this degeneracy, but it is out of the scope of this paper. Hence, in this work, we take $\Delta_T/T_{\text{coll}} \ll 1$, meaning that the emission of the second shell would occur shortly after the explosion.

Another degeneracy in our model is in the definition of Γ (see Eqs. 9.3). The same value of Γ can be obtained for different $(\tilde{E}_{k,\text{iso}}, n_0)$ pairs for the ISM scenario or (\tilde{E}_k, A_\star) for the wind scenario. Once the collision time has been fixed, this results in the same value of Γ_m^0 , as displayed in the right panel of Fig. B.2 for the ISM case. Similar results are obtained in the case of a wind environment, by replacing $n_0 \rightarrow A_\star$ (results not shown here). We do not exclude any region of the parameter space in Fig. B.2, since there are not observational constraints for the jump component. In principle, $\tilde{E}_{k,\text{iso}}$ can be estimated from modeling the afterglow or by assuming that it is in the same order as $\tilde{E}_{\gamma,\text{iso}}$, see e.g. [116].

Even though the same Γ and Γ_m^0 can be obtained at a fixed time for different values of the energy and density of the external environment, the degeneracy is not observable in

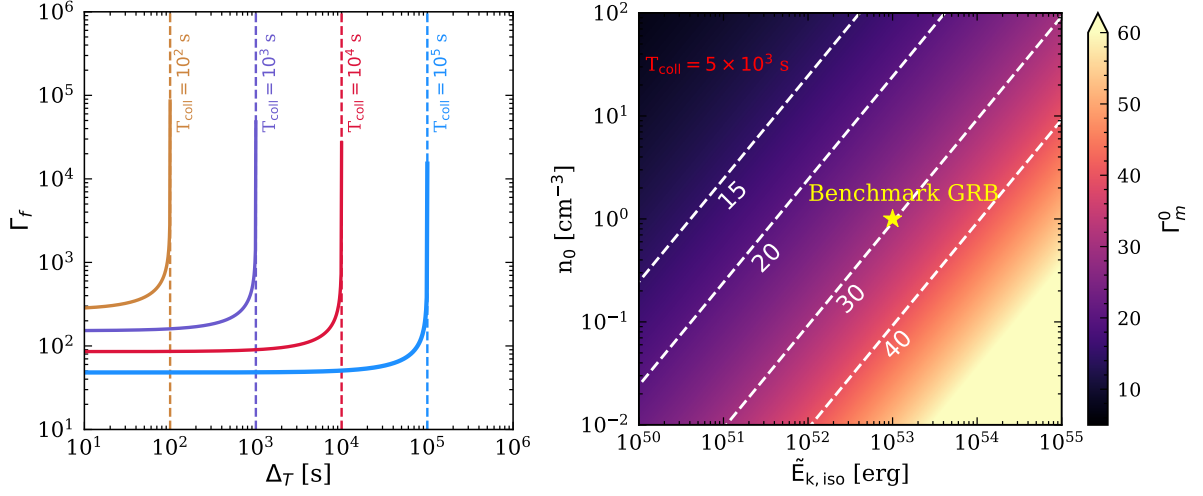


Figure B.2: *Left:* Isocontours of T_{coll} in the plane spanned by Δ_T and Γ_f in the ISM scenario. The function Γ_f diverges when $\Delta_T \rightarrow T_{\text{coll}}$. *Right:* Contour plot of Γ_m^0 in the plane spanned by $\tilde{E}_{k,\text{iso}}$ and n_0 (ISM scenario) for $T_{\text{coll}} = 5 \times 10^4$ s. The red dashed lines denote $\Gamma_m^0 = 15, 20, 30,$ and 40 . The yellow stars mark our benchmark GRB (Table 9.1). Similar results also hold for the wind case, both for the degeneracy between Γ_f and Δ_T and for Γ_m^0 , by replacing $n_0 \rightarrow A_\star$.

the resulting spectrum. Indeed, there are other parameters (e.g. the break frequencies and magnetic field) that strictly depend on the density of the environment and thus allow to break this degeneracy—see Fig. B.3 for the ISM scenario (similar conclusions hold for the wind scenario, results not shown here).

B.3 Cooling timescales of protons and mesons

In order to compute the neutrino energy distributions, we need to take into account the main cooling processes for accelerated protons, π^\pm , μ^\pm , and K^\pm . The proton inverse cooling timescales for our benchmark GRB (see Table 9.1) are shown in Fig. B.4 at $t = T_{\text{dec}}$ for the ISM and wind scenarios. Both in the ISM scenario (left panel) and in the wind scenario (right panel), the main cooling process for protons is the adiabatic one, that defines $E'_{p,\text{max}}$. The adiabatic timescale decreases with time, as a consequence of the fact that Γ of the shell decreases, while its radius increases.

Concerning the π^\pm, μ^\pm, K^\pm , the cooling time scales for the slow shell at $t = T_{\text{dec}}$ are shown in Fig. B.5. For the ISM scenario, adiabatic cooling can be important, yet not relevant, for muons at the onset of the deceleration. Pions and kaons, instead, are expected to cool at energies larger than the maximum proton energy. Thus, their cooling does not affect the resulting neutrino energy distribution. For the wind case, the cooling timescales of mesons at $t = T_{\text{dec}}$ are shown in Fig. B.5. In this scenario, muons

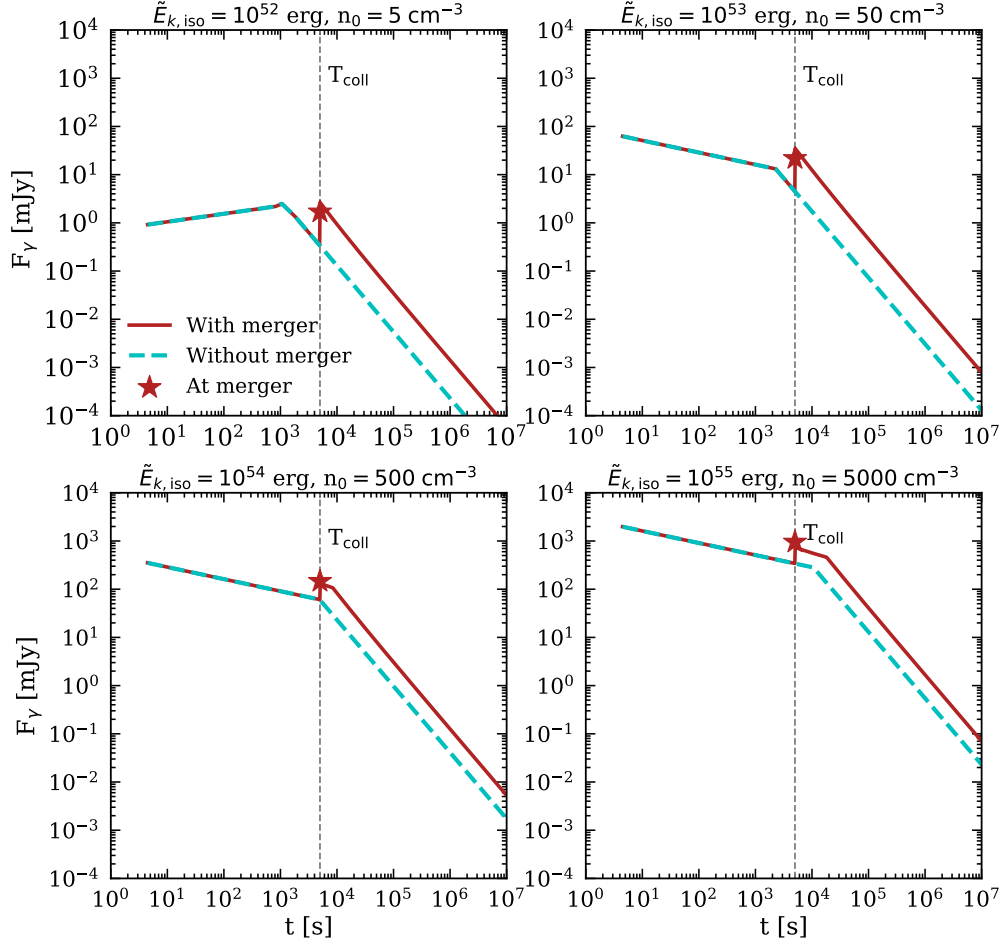


Figure B.3: Light curves, generated from different $(\tilde{E}_{k,\text{iso}}, n_0)$ pairs in the ISM scenario, with the same Γ_m^0 ($z = 1$ for all the panels). Each pair leads to a different light curve, both in the absence (cyan dashed line) and in the presence (brown solid line) of the shell merger. The flux at the optical jump (marked by a brown star) is different for each $(\tilde{E}_{k,\text{iso}}, n_0)$ pair. Similar conclusions hold for the wind scenario.

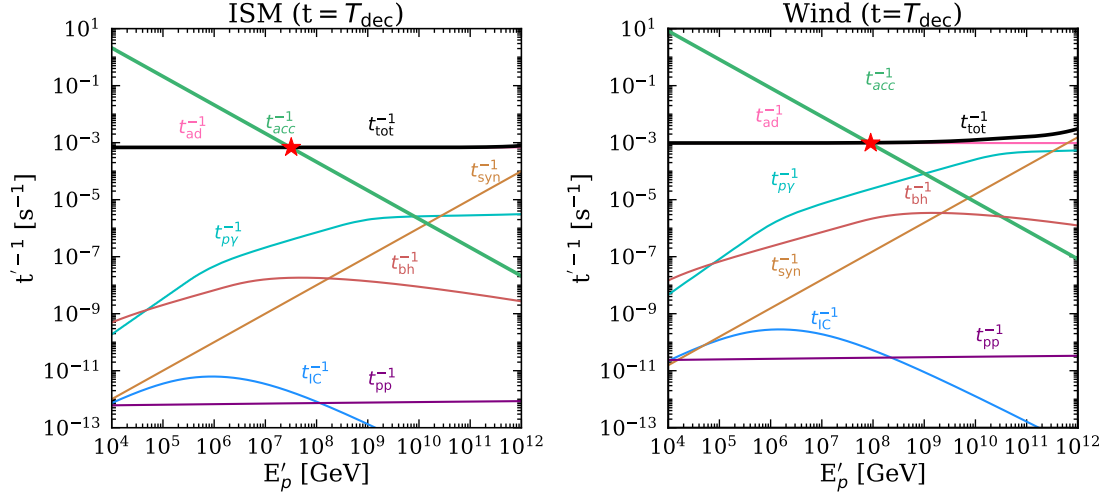


Figure B.4: Inverse cooling timescales of protons as functions of the comoving proton energy at the deceleration time T_{dec} for our benchmark GRB (Table 9.1) placed at $z = 1$ in the ISM (left panel) and wind (right panel) scenarios. The red star marks the maximum energy up to which protons can be accelerated. The main cooling process for the ISM scenario is the adiabatic one; for the wind scenario, adiabatic cooling dominates at lower energies, while synchrotron and the $p\gamma$ interactions become important at higher energies.

cool at energies lower than the maximum energy of protons, affecting the neutrino energy distribution. For our benchmark GRB, kaons always cool at energies that are higher than the maximum proton energy. Thus, their contribution is negligible. In both scenarios, the cooling of secondary particles becomes less relevant at larger times and it does not affect the shape of the resulting neutrino distribution.

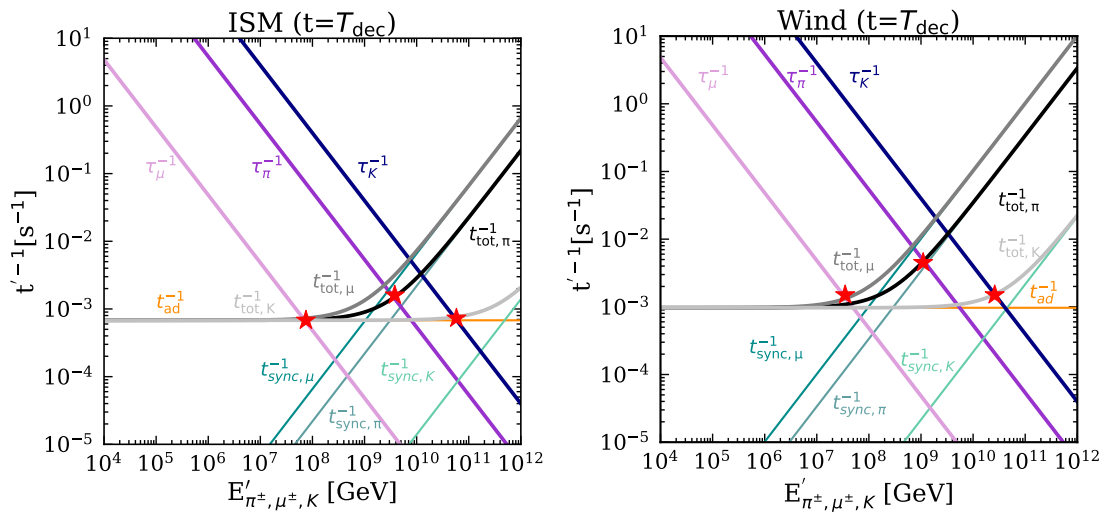


Figure B.5: Same as Fig. B.4 but for π^\pm , μ^\pm , and K^\pm . For the ISM scenario, adiabatic cooling is the most important process for kaons and muons, while synchrotron losses are important for pions. For the wind scenario, both synchrotron and adiabatic cooling are relevant for pions and muons. In both scenarios, the cooling of kaons occurs at energies larger than the maximum proton energy $E'_{p, \text{max}}$; thus, their cooling is negligible.



Appendix Paper III

C.1 Parameter space adopted in the modeling of AT2019fdr

In this Appendix we investigate how the space of the AT2019fdr parameters reported in Table 11.1 is constrained by our two selection criteria: 1) the time necessary for the forward shock to cross the CSM envelope between R_{bo} and R_{CSM} is at least 394 days, and 2) the rising time to the peak of the bolometric lightcurve (see Fig. 11.1) is 98 days in the observer frame.

Because of the approximations involved in the definition of t_{diff} in Eq. 11.13, we take into account an uncertainty of 50% on the diffusion time. Figure C.1 shows a contour plot of the time that the shock takes to travel from R_{bo} to R_{CSM} for $\tilde{E}_k = 10^{53}$ erg. We can see that the smaller the CSM width, the shorter the time it takes for the shock to reach R_{CSM} . Indeed, in the left panel of Fig. C.1, as opposed to the right one, almost half of the SLSN configurations with $M_{\text{ej}} \lesssim 70 M_{\odot}$ and $M_{\text{CSM}} \lesssim 70 M_{\odot}$ are excluded. This is mainly due to the fact that $R_{\text{bo}} \ll R_{\text{dec}}$ for $M_{\text{ej}}/M_{\text{CSM}}$ that is not large, implying that most of the evolution of the shock in the CSM is in the free expansion phase (see Eq. 11.2), thus with larger velocities. Furthermore, this criterion completely excludes all the configurations with $R_{\text{CSM}} = 2 \times 10^{16}$ cm and $\tilde{E}_k = 10^{53}$ erg. As R_{CSM} increases (see the right panel of Fig. C.1), the most stringent constraint comes from the compatibility of t_{diff} with the observed light curve.

The same trend holds for the case with $\tilde{E}_k = 5 \times 10^{52}$ erg (not shown here), with the difference that there are compatible scenarios with our requirements already for $R_{\text{CSM}} = 2 \times 10^{16}$ cm. For this latter case, for fixed $M_{\text{ej}}, M_{\text{CSM}}$ and R_{CSM} , the shock velocity v_{sh} is lower, allowing for longer times required to cross the CSM.

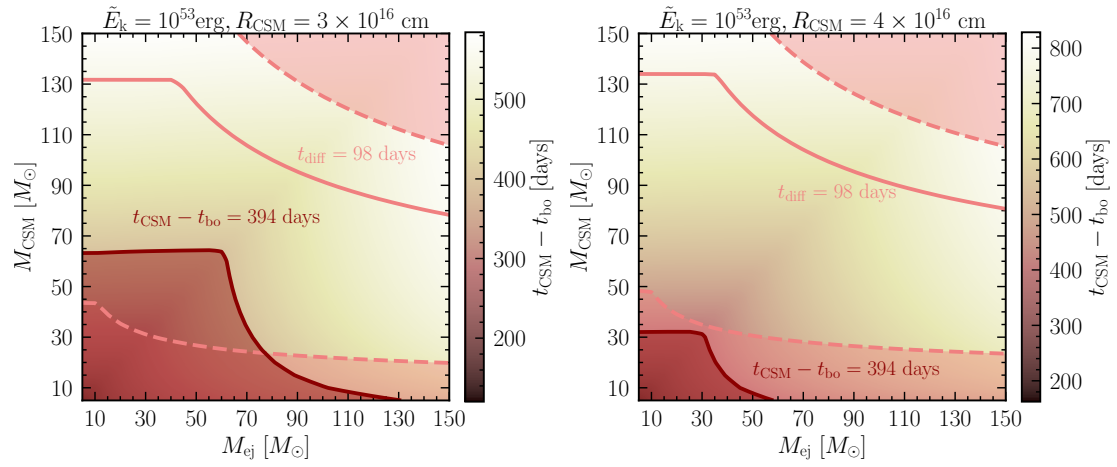


Figure C.1: *Left panel:* Contour plot of the time the shock takes to travel from R_{bo} to R_{CSM} in the plane spanned by M_{ej} and M_{CSM} . The solid bordeaux line constrains the allowed parameter space by requiring that $t_{\text{CSM}} - t_{\text{bo}} \geq 394$ days (solid bordeaux line). The dashed pink lines constrain the allowed parameter space by requiring that the rising time of the AT2019fdr light-curve is compatible within a 50% uncertainty with the analytic estimate of the diffusion time provided in Eq. 11.13; the latter is represented by the solid pink line. *Right panel:* The same as in the left panel, but for $R_{\text{CSM}} = 4 \times 10^{16}$ cm. For larger R_{CSM} , the crossing time constraint becomes looser, whilst the one related to t_{diff} slowly becomes more stringent.

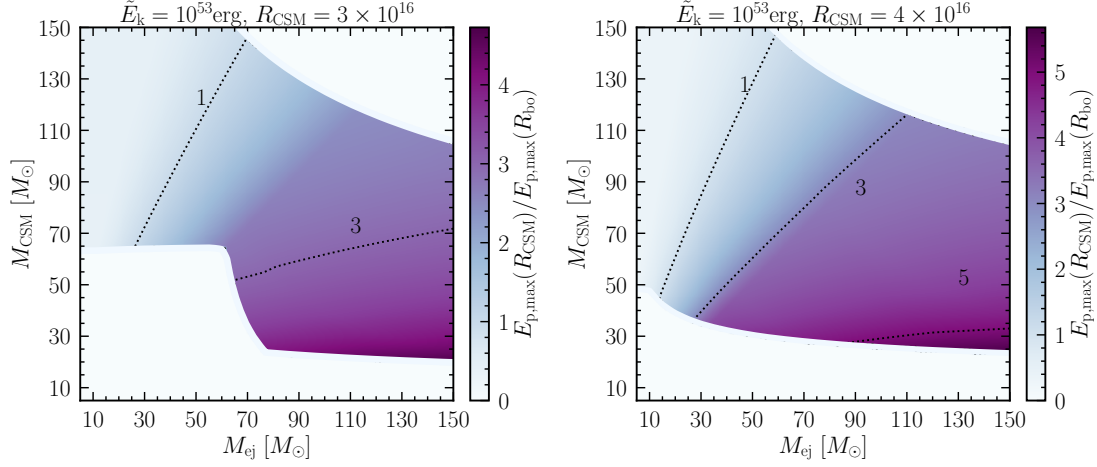


Figure C.2: *Left panel:* Contour plot of the ratio between the maximum proton energy $E_{p,\max}$ at $R_{\text{CSM}} = 3 \times 10^{16}$ cm and at the breakout radius R_{bo} in the plane spanned by M_{ej} and M_{CSM} . For relatively low values of M_{ej} with respect to M_{CSM} , this ratio tends to decrease. This is due to the fact that for very low $M_{\text{ej}}/M_{\text{CSM}}$, $R_{\text{dec}} < R_{\text{bo}}$, causing a fast drop of $E_{p,\max}$. Viceversa, for very large $M_{\text{ej}}/M_{\text{CSM}}$, the deceleration always occurs at $R > R_{\text{CSM}}$, allowing for a continual increase of $E_{p,\max}$ as the time goes by. Intermediate values of $M_{\text{ej}}/M_{\text{CSM}}$ lead to intermediate trends, with the free expansion and decelerating phase both being present between R_{bo} and R_{CSM} . The dotted black lines indicate the regions the ratio is larger than 1 and 3. *Right panel:* The same as in the left panel, but for a larger R_{CSM} . The effect of increasing R_{CSM} , while keeping fixed all the other parameters, is to decrease the CSM density and thus to allow for larger $E_{p,\max}$, since the pp interactions become less efficient.

C.2 Maximum proton energy

In this appendix, we explore the temporal evolution of $E_{p,\max}$ for the set of parameters \tilde{E}_k , R_{CSM} , M_{ej} and M_{CSM} considered in this work (see Table 11.1). We provide an idea of the behaviour of $E_{p,\max}$ by displaying in Fig. C.2 the ratio between its value at the CSM radius R_{CSM} and the breakout radius R_{bo} , for $\tilde{E}_k = 10^{53}$ erg with $R_{\text{CSM}} = 3 \times 10^{16}$ cm (left panel) and $R_{\text{CSM}} = 4 \times 10^{16}$ cm (right panel). In both cases, the region where $E_{p,\max}(R_{\text{CSM}})/E_{p,\max}(R_{\text{bo}}) < 1$ is the one with relatively low values of $M_{\text{ej}}/M_{\text{CSM}}$. Here, either $R_{\text{bo}} > R_{\text{dec}}$ or $R_{\text{bo}} \lesssim R_{\text{dec}}$, meaning that most of the shock evolution occurs in the decelerating phase (see Eq. 11.5). When this is the case, the acceleration efficiency drops at a faster rate, leading to decreasing $E_{p,\max}$ (see Eq. 11.22).

On the other hand, for large $M_{\text{ej}}/M_{\text{CSM}}$, $R_{\text{dec}} > R_{\text{CSM}}$ is satisfied, implying an increase of $E_{p,\max}$. The intermediate regimes [$M_{\text{ej}}/M_{\text{CSM}} \sim \mathcal{O}(1)$] are those in which both free expansion and deceleration occur between R_{bo} and R_{CSM} , being the latter shorter

compared to the former, and thus leaving the tendency of $E_{p,\max}(R_{\text{CSM}})/E_{p,\max}(R_{\text{bo}})$ to increase unaffected. By keeping $\tilde{E}_k, M_{\text{ej}}$ and M_{CSM} fixed, a larger R_{CSM} leads to a lower CSM density, with longer t_{pp} ; thus, a larger $E_{p,\max}(R_{\text{CSM}})$ is achievable. This effect is more significant than the slight increase of $E_{p,\max}(R_{\text{bo}})$ for larger R_{CSM} .

Finally, lower values of \tilde{E}_k do not compromise the overall trend outlined above. The only effect of decreasing the energy, whilst keeping all other parameters fixed, is to reduce v_{sh} (see Eq. 11.2) and in turn the acceleration rate, which result in overall smaller values of $E_{p,\max}$.

D

Appendix Paper IV

D.1 Dependence of the supernova lightcurve properties on the model parameters

In this appendix, we investigate the dependence of the parameters characteristic of the lightcurve on the SN model properties. Figure D.1 displays how the rise time t_{rise} (defined in Sec. 12.3) of the bolometric luminosity depends on the SN parameters of interest. For any fixed combination of E_k , M_{ej} and R_{CSM} , the rise time increases with M_{CSM} , since a denser CSM extends the photon diffusion time. In the left panel, we see that the larger the kinetic energy, the shorter t_{rise} . This is explained by the fact that large shock velocities cause the breakout to happen later and shorten the time that photons take to reach the photosphere. The same trend is expected for decreasing M_{ej} , as shown in the middle panel, where a mild trend in this direction is noticeable. Furthermore in the BW regime (which corresponds to the breaks in the curves) we see that t_{rise} is independent of M_{ej} (the curves for low M_{ej} saturate at the same value), a trend confirmed by the numerical simulations presented in Suzuki:2020qui. In the right panel of Fig. D.1, one can observe that for large CSM masses, there is a transition region shifting towards larger R_{CSM} where the trend of t_{rise} is reversed. The reason of this inversion is to be found in the dependence of the photospheric radius on R_{CSM} (see Eq. 12.12), which for fixed M_{CSM} increases and saturates at a certain R_{CSM} , to turn and decrease for larger CSM radii.

The middle panels of Fig. D.1 show that an increase in M_{CSM} makes L_{peak} larger in all cases, since a larger M_{CSM} causes more kinetic energy to be dissipated and radiated. This is true as long as the shock is in the FE regime. In the BW regime, L_{peak} declines with M_{CSM} . The left and middle panels show that the peak luminosity increases with larger ejecta energy and smaller ejecta masses, since both make the shock velocity larger

and thus more energetic. In the BW regime, the peak luminosity becomes independent of the ejecta mass, as confirmed by the saturation to the same branch for low M_{ej} . The right panel shows that the brightest lightcurves are obtained when the CSM is more compact, i.e. for the smallest R_{CSM} (apart from the transition region visible for large M_{CSM} , due to the transition into the BW regime).

The bottom panels show the trend of $E_{\text{diss,thick}}$. The dissipated energy in the optically thick part of the CSM increases with M_{CSM} , is very large for small M_{ej} and R_{CSM} , since the first allows for high shock velocity, and the second for very compact region, and thus high densities.

D.2 Dependence of the maximum proton energy on the supernova model parameters

In this appendix, we analyze the dependence of the maximum $E_{\text{p,max}}$ on the SN model parameters. To do so, we first highlight the dependence on the SN parameters of the main timescales entering the problem. From Eqs. 12.10 and 12.11, we see that the plasma cooling timescale scales as:

$$t_{\text{cool}} \propto \frac{1}{n_{\text{sh}}} \times \begin{cases} v_{\text{sh}}^{16/5} & \text{if } 10^5 < T \lesssim 4.7 \times 10^7 \text{ K} \\ v_{\text{sh}} & \text{if } T > 4.7 \times 10^7 \text{ K} . \end{cases} \quad (\text{D.1})$$

For the wind scenario, it becomes

- for $R < R_{\text{dec}}$:

$$t_{\text{cool}} \propto \left(\frac{R_{\text{CSM,w}}}{M_{\text{CSM,w}}} \right) \times \begin{cases} R^{54/35} & \text{if } 10^5 < T \lesssim 4.7 \times 10^7 \text{ K} \\ R^{13/7} & \text{if } T > 4.7 \times 10^7 \text{ K} . \end{cases} \quad (\text{D.2})$$

- for $R > R_{\text{dec}}$:

$$t_{\text{cool}} \propto \left(\frac{R_{\text{CSM,w}}}{M_{\text{CSM,w}}} \right) \times \begin{cases} R^{2/5} & \text{if } 10^5 < T \lesssim 4.7 \times 10^7 \text{ K} \\ R^{3/2} & \text{if } T > 4.7 \times 10^7 \text{ K} . \end{cases} \quad (\text{D.3})$$

For the shell scenario, it is

- for $R < R_{\text{dec}}$:

$$t_{\text{cool}} \propto \left(\frac{R_{\text{CSM,s}}^3}{M_{\text{CSM,s}}} \right) \times \begin{cases} R^{-48/35} & \text{if } 10^5 < T \lesssim 4.7 \times 10^7 \text{ K} \\ R^{-3/7} & \text{if } T > 4.7 \times 10^7 \text{ K} . \end{cases} \quad (\text{D.4})$$

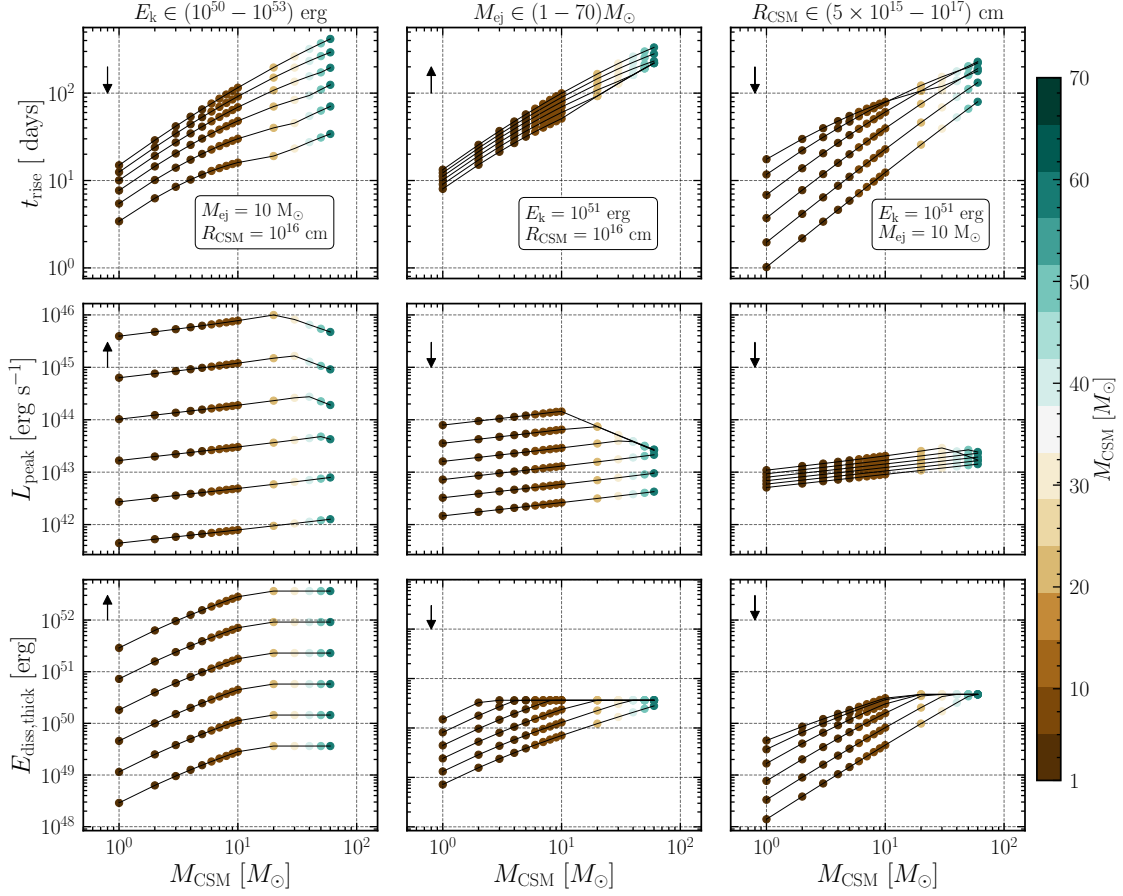


Figure D.1: Rise time of the bolometric lightcurve (top panels), bolometric peak luminosity (middle panels), dissipated energy in the optically thick part of the CSM envelope (bottom panels) as functions of the CSM mass and E_k (left panels, for fixed M_{ej} and R_{CSM}), the ejecta mass (middle panels, for fixed E_k and R_{CSM}), and R_{CSM} (right panels, for fixed E_k and M_{ej}), respectively. In each panel, the arrow indicates the direction of increase of the parameter under investigation, e.g. in the left panel of the first row, t_{rise} decreases for increasing E_k , for fixed M_{CSM} ; t_{rise} increases with M_{CSM} since a denser CSM envelope increases the optical depth and delays the photon escape. From the top left and middle panels, we see that for increasing E_k or decreasing M_{ej} , the diffusion time becomes shorter. Indeed both the increase of E_k and the decrease of M_{ej} are responsible for an increase of the shock velocity, which in turn causes the radius where the photon diffusion velocity exceeds the shock velocity to shift outwards. In the top right panel, we observe that for small R_{CSM} an initial increase of t_{rise} , which declines again for larger CSM radii. This transition region is related to the photosphere dependence on M_{CSM} and R_{CSM} . For what concerns L_{peak} , in all three middle panels we see that L_{peak} initially increases with M_{CSM} in the FE regime. When transitioning to the BW regime (indicated by the breaks in the curves), a saturation of the radiated energy occurs and this, together with the increase of t_{rise} , causes L_{peak} to drop as M_{CSM} increases. Larger E_k and smaller M_{ej} are responsible for a larger shock velocity, and thus an increase of L_{peak} , as it can be seen in the left and middle panels. In the right middle panel, we observe that small R_{CSM} , for fixed M_{CSM} , make the medium denser and therefore it is easier to dissipate the ejecta energy, leading to an increase of L_{peak} . Similarly, $E_{diss,thick}$ increases with M_{CSM} , and saturates to a constant fraction of E_k in the BW regime. The dots are colored according to the M_{CSM} value, as shown in the color bar.

- for $R > R_{\text{dec}}$:

$$t_{\text{cool}} \propto \left(\frac{R_{\text{CSM},s}^3}{M_{\text{CSM},s}} \right) \times \begin{cases} R^{-24/5} & \text{if } 10^5 < T \lesssim 4.7 \times 10^7 \text{ K} \\ R^{-3/2} & \text{if } T > 4.7 \times 10^7 \text{ K} . \end{cases} \quad (\text{D.5})$$

The acceleration time scales as $t_{\text{acc}} \propto E_p v_{\text{sh}}^{-3} n_{\text{sh}}^{-1/2}$, given $B \propto v_{\text{sh}} n_{\text{sh}}^{1/2}$. For the wind scenario it is

$$t_{\text{acc}} \propto \left(\frac{R_{\text{CSM},w}}{M_{\text{CSM},w}} \right)^{1/2} E_p \times \begin{cases} R^{10/7} & \text{if } R < R_{\text{dec}} \\ R^{5/2} & \text{if } R > R_{\text{dec}} ; \end{cases} \quad (\text{D.6})$$

while for the shell scenario, it is

$$t_{\text{acc}} \propto \left(\frac{R_{\text{CSM},s}^3}{M_{\text{CSM},s}} \right)^{1/2} E_p \times \begin{cases} R^{9/7} & \text{if } R < R_{\text{dec}} \\ R^{9/2} & \text{if } R > R_{\text{dec}} . \end{cases} \quad (\text{D.7})$$

The proton-proton interaction time $t_{\text{pp}} = (cn_{\text{sh}}\sigma_{\text{pp}})^{-1}$ is

$$t_{\text{pp}} \propto \begin{cases} \frac{R_{\text{CSM},w}}{M_{\text{CSM},w}} \times R^2 & \text{for the wind} \\ \frac{R_{\text{CSM},s}^3}{M_{\text{CSM},s}} & \text{for the shell} . \end{cases} \quad (\text{D.8})$$

Using the relations above, we can investigate how $E_{p,\text{max}}$ depends on the SN model parameters and how it evolves with the shock radius. If t_{cool} is the $\min[t_{\text{cool}}, t_{\text{dyn}}, t_{\text{pp}}]$, the maximum proton energy is determined by $t_{\text{acc}} = t_{\text{cool}}$. For the wind scenario,

- for $R < R_{\text{dec}}$:

$$E_{p,\text{max}} \propto \left(\frac{R_{\text{CSM},w}}{M_{\text{CSM},w}} \right)^{1/2} \times \begin{cases} R^{4/35} & \text{if } 10^5 < T \lesssim 4.7 \times 10^7 \text{ K} \\ R^{3/7} & \text{if } T > 4.7 \times 10^7 \text{ K} ; \end{cases} \quad (\text{D.9})$$

- for $R > R_{\text{dec}}$:

$$E_{p,\text{max}} \propto \left(\frac{R_{\text{CSM},w}}{M_{\text{CSM},w}} \right)^{1/2} \times \begin{cases} R^{-21/10} & \text{if } 10^5 < T \lesssim 4.7 \times 10^7 \text{ K} \\ R^{-1} & \text{if } T > 4.7 \times 10^7 \text{ K} . \end{cases} \quad (\text{D.10})$$

For the shell scenario, instead, it is

- for $R < R_{\text{dec}}$:

$$E_{p,\text{max}} \propto \left(\frac{R_{\text{CSM},s}^3}{M_{\text{CSM},s}} \right)^{1/2} \times \begin{cases} R^{-93/35} & \text{if } 10^5 < T \lesssim 4.7 \times 10^7 \text{ K} \\ R^{-12/7} & \text{if } T > 4.7 \times 10^7 \text{ K} ; \end{cases} \quad (\text{D.11})$$

- for $R > R_{\text{dec}}$:

$$E_{p,\text{max}} \propto \left(\frac{R_{\text{CSM},s}^3}{M_{\text{CSM}}} \right)^{1/2} \times \begin{cases} R^{-93/10} & \text{if } 10^5 < T \lesssim 4.7 \times 10^7 \text{ K} \\ R^{-6} & \text{if } T > 4.7 \times 10^7 \text{ K}. \end{cases} \quad (\text{D.12})$$

If t_{pp} corresponds to the $\min[t_{\text{cool}}, t_{\text{dyn}}, t_{\text{pp}}]$, then the maximum proton energy is determined by $t_{\text{acc}} = t_{\text{pp}}$ and can be written for the wind scenario as

$$E_{p,\text{max}} \propto \left(\frac{R_{\text{CSM},w}}{M_{\text{CSM},w}} \right)^{1/2} \times \begin{cases} R^{4/7} & \text{for } R < R_{\text{dec}} \\ R^{-1/2} & \text{for } R > R_{\text{dec}}, \end{cases} \quad (\text{D.13})$$

and for the shell scenario as

$$E_{p,\text{max}} \propto \left(\frac{R_{\text{CSM},s}^3}{M_{\text{CSM},s}} \right)^{1/2} \times \begin{cases} R^{-9/7} & \text{for } R < R_{\text{dec}} \\ R^{-9/2} & \text{for } R > R_{\text{dec}}. \end{cases} \quad (\text{D.14})$$

Finally, if t_{dyn} corresponds to $\min[t_{\text{cool}}, t_{\text{dyn}}, t_{\text{pp}}]$, the maximum proton energy is determined by $t_{\text{acc}} = t_{\text{dyn}}$ and for the wind scenario it is

$$E_{p,\text{max}} \propto \left(\frac{M_{\text{CSM},w}}{R_{\text{CSM},w}} \right)^{1/2} \times \begin{cases} R^{-2/7} & \text{for } R < R_{\text{dec}} \\ R^{-1} & \text{for } R > R_{\text{dec}}, \end{cases} \quad (\text{D.15})$$

while, for the shell scenario, it is

$$E_{p,\text{max}} \propto \left(\frac{M_{\text{CSM},s}}{R_{\text{CSM},s}^3} \right)^{1/2} \times \begin{cases} R^{1/7} & \text{for } R < R_{\text{dec}} \\ R^{-2} & \text{for } R > R_{\text{dec}}. \end{cases} \quad (\text{D.16})$$

Note that we assume constant $\sigma_{\text{pp}} \sim 3 \times 10^{-26} \text{ cm}^2$ for the sake of simplicity in this appendix in order to obtain the above analytical relations.

We immediately see from the relations above that for the wind scenario, independently on the cooling mechanism, the maximum proton energy has a decreasing trend with R in the deceleration phase ($R > R_{\text{dec}}$). However, in the ejecta-dominated phase ($R < R_{\text{dec}}$), the maximum proton energy always increases, except for the case in which the adiabatic cooling is dominant (Eq. D.15). Finally, in the shell scenario, $E_{p,\text{max}}$ always decreases, apart from the case where t_{cool} and t_{pp} are too long compared to the dynamical time, and it slowly increases in the free-expansion phase.

We define R_{cool} as the radius where $t_{\text{dyn}} = t_{\text{cool}}$, and R_{pp} the radius where $t_{\text{dyn}} = t_{\text{pp}}$. The maximum value of $E_{p,\text{max}}$, denoted as $E_{p,\text{max}}^*$, can be achieved at any of the following radii: R_{bo} , R_{cool} , R_{pp} , R_{dec} , or R_{CSM} . There are various configurations of such radii. If for example $R_{\text{bo}} < R_{\text{cool}} < R_{\text{pp}} < R_{\text{CSM}} < R_{\text{dec}}$, and both $t_{\text{dyn}} < t_{\text{cool}}$ for $R > R_{\text{cool}}$ and $t_{\text{dyn}} < t_{\text{pp}}$ for $R > R_{\text{pp}}$, then the maximum $E_{p,\text{max}}$ is obtained at R_{pp} .

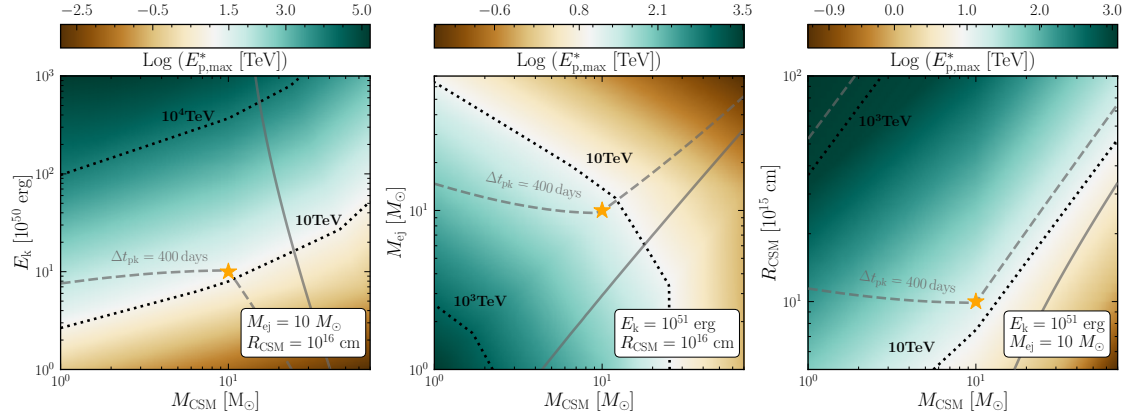


Figure D.2: Contour plots of the maximum proton energy $E_{p,\max}^*$ reached throughout the evolution of the shock in the wind scenario, in the plane spanned by M_{CSM} and E_k (left panel), M_{ej} (middle panel), and R_{CSM} (right panel). The dotted contours mark isocontours of $E_{p,\max}^*$ to guide the eye. The largest proton energies can be achieved with large E_k and small M_{ej} , both maximizing v_{sh} , and thus the acceleration rate; low M_{CSM} and/or large R_{CSM} , both making the CSM less dense, and thus the proton energy losses less severe. For each panel, the gray line represents $\Delta t_{\text{pk}} = t|_{E_{p,\max}^*} - t_{\text{peak}}$, i.e. the time at which the maximum proton energy is reached with respect to the bolometric peak of the lightcurve. The solid gray lines correspond to $\Delta t_{\text{pk}} = 0$. From the dashed gray line, we can see that the largest time interval is expected for low E_k , and large M_{ej} and R_{CSM} . The parameter space between the solid and the dashed gray lines leads to $0 < \Delta t_{\text{pk}} < 400$ days, which is the follow-up time window adopted for SNe. The orange star marks our benchmark scenario (see Table 12.1).

Note that this procedure serves to inspect the dependence of the maximum proton energy analytically. However, the total cooling time is the sum of t_{dyn} and t_{pp} or t_{cool} and t_{pp} ; since the energy dependence of t_{pp} increases slightly at higher energies, the value of $E_{p,\max}^*$ that we find is underestimated by a few percent in the transition region $t_{\text{dyn}} \sim t_{\text{cool}}$ and at very large energies. Figure D.2 displays how $E_{p,\max}^*$ depends on the SN parameters. The most promising configurations that allow to reach large $E_{p,\max}^*$ are the ones with large E_k and low M_{CSM} (left panel), or low M_{ej} and low M_{CSM} (middle panel), or high R_{CSM} and low M_{CSM} (right panel), which maximize the acceleration rate and minimize the energy loss rate.

For the fiducial parameters adopted in each panel of Fig. D.2, total energies $\gtrsim 10^{51}$ erg, relatively low ejecta ($\lesssim 20M_{\odot}$), CSM masses ($\lesssim 10M_{\odot}$), and extended CSM envelopes ($\gtrsim 10^{16}$ cm) are required to obtain protons with \sim PeV energy. Furthermore, as shown through the gray contour lines, which display $t|_{E_{p,\max}^*} - t_{\text{peak}}$ (where $t|_{E_{p,\max}^*}$ is the time at which the maximum proton energy is reached), the maximum $E_{p,\max}^*$ is achieved at relatively late times [$\mathcal{O}(100)$ days] with respect to the peak time $t_{\text{peak}} = t_{\text{bo}} + t_{\text{rise}}$. Such longer timescales are expected for low kinetic energies of the ejecta, and large M_{ej}

and R_{CSM} . Only the configurations with large CSM mass, due to the onset of the decelerating phase, are expected to invert the increasing trend of $E_{\text{p,max}}^*$ before the lightcurve reaches its peak.

D.3 Constant density scenario

In this appendix, we explore the dependence of neutrino production in the scenario of a radially independent CSM mass distribution. We follow a similar approach to the wind-profile case discussed in Sec. 12.5.2. Specifically, we investigate the connection between the total energy in neutrinos ($\mathcal{E}_{\nu+\bar{\nu}}$, see Eq. 12.22) with $E_{\nu} \geq 1$ TeV. The results are shown in Fig. D.3.

We exclude from our investigation the region of the SN parameter space where the maximum achievable proton energy is $E_{\text{p,max}}^* \leq 10$ TeV. Additionally, we disregard parameters that lead to a shock breakout at the surface of the progenitor star ($R_{\text{bo}} \equiv R_{\star}$), as indicated by the beige region in the contour plots. In this work, our focus is on the parameter space that results in the shock breakout occurring inside the CSM envelope. This is the first difference with the wind case, where the much higher density at smaller radii cause the shock to occur inside the wind for all the considered parameters. Isocontours of $E_{\text{p,max}}^*$ (first row), the rise time t_{rise} (second row), and the bolometric peak L_{peak} (third row) are also displayed on top of the $\mathcal{E}_{\nu+\bar{\nu}}$ colormap in Fig. D.3.

The dependence of $\mathcal{E}_{\nu+\bar{\nu}}$ on the SN model parameters is analogous to the wind scenario. Indeed we see that in all panels of Fig. D.3, $\mathcal{E}_{\nu+\bar{\nu}}$ increases with M_{CSM} , namely with larger target proton numbers, and then saturates once the critical ρ_{CSM} is reached. Beyond such critical density, pp interactions or the cooling of thermal plasma becomes too strong, limiting the maximum achievable proton energy, and thus the neutrino outcome. From the contour lines in each panel, analogously to the wind case, we see that the optimal configuration for what concerns neutrino production, results from large E_{k} , $M_{\text{CSM}} \gtrsim M_{\text{ej}}$, and R_{CSM} larger as M_{CSM} increases.

We see from Fig. D.3 that we do not have the same regions of the parameter space excluded as in the wind case (see Fig. 12.5) that lead to $E_{\text{p,max}}^* \leq 10$ TeV. Indeed in a constant density shell the proton maximum energy has a rather different dependence especially on the radius as discussed in Appendix D.2. This leads to overall higher values of $E_{\text{p,max}}^*$ in the parameter space, as well as the times at which they are achieved during the shock evolution. Most of the parameter space in all panels leads to $\Delta t_{\text{pk}} = t|_{E_{\text{p,max}}^*} - t_{\text{peak}} < 0$ (see Fig. D.2 for the wind case). This means that in the constant density scenario most of the energetic neutrinos are produced earlier than the bolometric peak.

With respect to the wind scenario, another difference lies in the relation between t_{rise} and L_{peak} , as can be seen from the second and third row of Fig. D.3. In the case of a constant density shell, the CSM density is considerably lower. Consequently, the shock

breakout tends to occur earlier than in the wind scenario, resulting in significantly smaller peak luminosities across a significant portion of the parameter space. Nonetheless, the lower CSM density leads to larger deceleration radii compared to the wind case. As a result, a larger M_{CSM} is required to enter the decelerating regime, delaying the transition to the decreasing trend of L_{peak} with M_{CSM} in the blast-wave regime (as observed in the wind case in Fig. D.1). As for t_{rise} , lower CSM densities result in longer photon mean free paths, enabling faster diffusion through the CSM envelope. Furthermore, as shown in the second row of Fig. D.3, t_{rise} increases with M_{CSM} , but remains independent on M_{ej} and E_{k} for most of the parameter space. This is explained because R_{bo} is significantly smaller than R_{ph} , making the diffusion time unaffected by the shock velocity.

In summary, similar to the wind scenario, large $\mathcal{E}_{\nu+\bar{\nu}}$ is expected for large SN kinetic energy ($E_{\text{k}} \gtrsim 10^{51}$ erg), small ejecta mass ($M_{\text{ej}} \lesssim 10 M_{\odot}$), and large CSM radii, $R_{\text{CSM}} \gtrsim 10^{16}$ cm. Unlike in the wind case, a larger range of M_{CSM} leads to comparable predictions, even if scenarios with $M_{\text{CSM}} \gg M_{\text{ej}}$ would limit neutrino production. Such parameters imply large bolometric luminosity peak ($L_{\text{peak}} \gtrsim 10^{43} - 10^{44}$ erg) and relatively long rise times ($t_{\text{rise}} \gtrsim 10 - 90$ days). In the shell case, large t_{rise} do not necessarily correspond to low $\mathcal{E}_{\nu+\bar{\nu}}$, as it is the case for the wind scenario. Furthermore, energetic neutrinos are produced at early times. Hence, if neutrinos should be observed from long-rising optical lightcurves relatively soon with respect to the optical peak, this might hint towards a constant density of the CSM envelope.

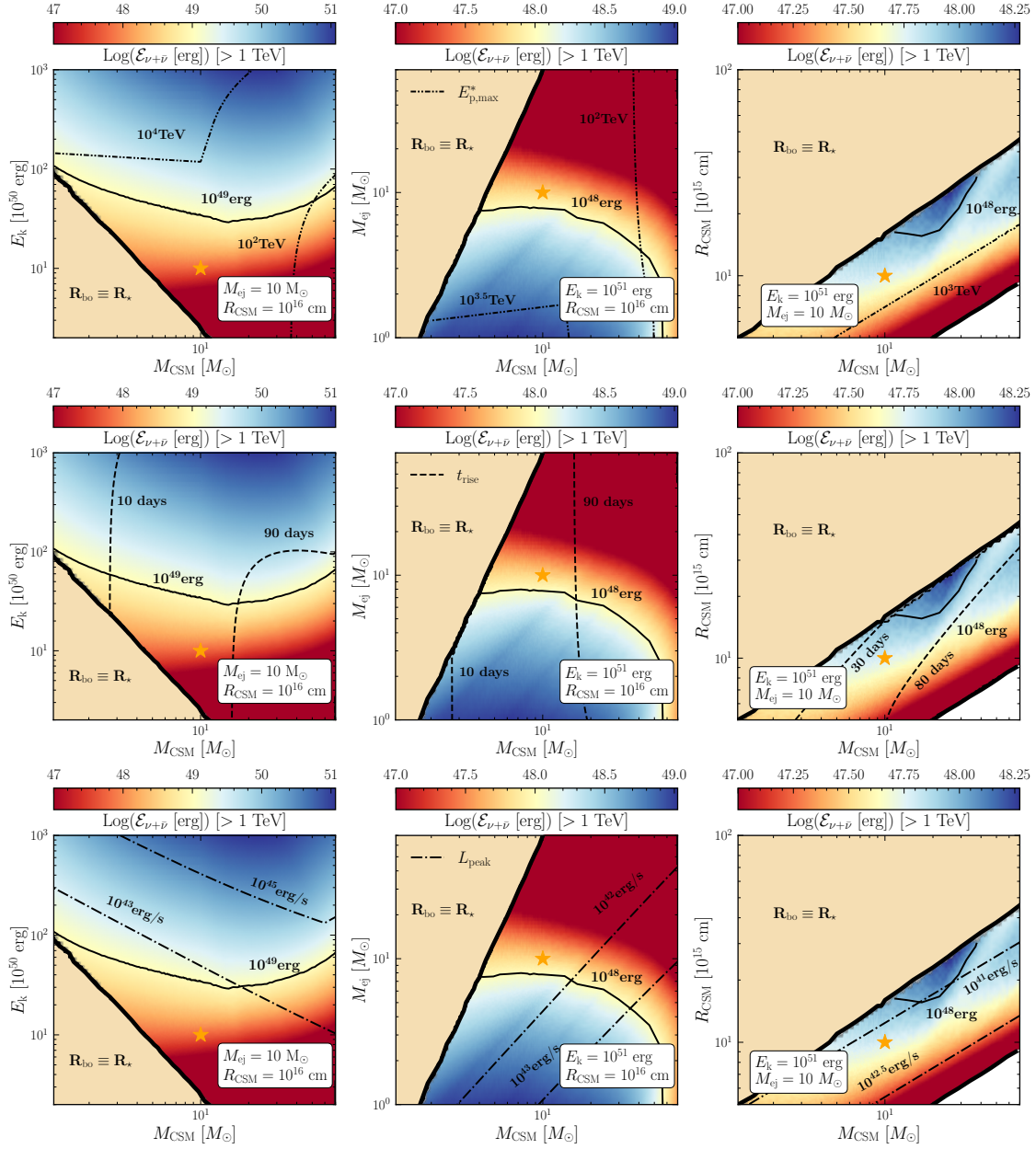


Figure D.3: The same as in Fig. 12.5, but for the constant density shell scenario. The beige region has been excluded from our investigation since here the breakout of the shock does not occur in the CSM shell, but at the radius of the progenitor star. The white region, visible only in the lower right corner of the third column, has instead been excluded because leading to $E_{p,\max}^* < 10\text{TeV}$. The SN configurations leading to the largest outcomes in neutrinos are similar to the ones in the wind case, and are given by large SN kinetic energies ($E_k \gtrsim 10^{51}$ erg), small ejecta masses ($M_{ej} \lesssim 10 M_\odot$), intermediate CSM masses with respect to M_{ej} ($1M_\odot \lesssim M_{\text{CSM}} \lesssim 30M_\odot$), and relatively large CSM extent ($R_{\text{CSM}} \gtrsim 10^{16}$ cm).

References

- [1] ALEXANDER AAB ET AL.:
'Combined fit of spectrum and composition data as measured by the Pierre Auger Observatory',
in: *JCAP* 04 (2017). [Erratum: *JCAP* 03, E02 (2018)], p. 038. DOI: [10.1088/1475-7516/2017/04/038](https://doi.org/10.1088/1475-7516/2017/04/038). arXiv: [1612.07155](https://arxiv.org/abs/1612.07155) [[astro-ph.HE](#)].
- [2] M. G. AARTSEN ET AL.:
'Astrophysical neutrinos and cosmic rays observed by IceCube',
in: *Adv. Space Res.* 62 (2018), pp. 2902–2930. DOI: [10.1016/j.asr.2017.05.030](https://doi.org/10.1016/j.asr.2017.05.030). arXiv: [1701.03731](https://arxiv.org/abs/1701.03731) [[astro-ph.HE](#)].
- [3] M. G. AARTSEN ET AL.:
'Characteristics of the diffuse astrophysical electron and tau neutrino flux with six years of IceCube high energy cascade data',
in: *Phys. Rev. Lett.* 125.12 (2020), p. 121104. DOI: [10.1103/PhysRevLett.125.121104](https://doi.org/10.1103/PhysRevLett.125.121104). arXiv: [2001.09520](https://arxiv.org/abs/2001.09520) [[astro-ph.HE](#)].
- [4] M. G. AARTSEN ET AL.:
'Detection of a particle shower at the Glashow resonance with IceCube',
in: *Nature* 591.7849 (2021). [Erratum: *Nature* 592, E11 (2021)], pp. 220–224. DOI: [10.1038/s41586-021-03256-1](https://doi.org/10.1038/s41586-021-03256-1). arXiv: [2110.15051](https://arxiv.org/abs/2110.15051) [[hep-ex](#)].
- [5] M. G. AARTSEN ET AL.:
'Differential limit on the extremely-high-energy cosmic neutrino flux in the presence of astrophysical background from nine years of IceCube data',
in: *Phys. Rev. D* 98.6 (2018), p. 062003. DOI: [10.1103/PhysRevD.98.062003](https://doi.org/10.1103/PhysRevD.98.062003). arXiv: [1807.01820](https://arxiv.org/abs/1807.01820) [[astro-ph.HE](#)].
- [6] M. G. AARTSEN ET AL.:
'Evidence for High-Energy Extraterrestrial Neutrinos at the IceCube Detector',
in: *Science* 342 (2013), p. 1242856. DOI: [10.1126/science.1242856](https://doi.org/10.1126/science.1242856). arXiv: [1311.5238](https://arxiv.org/abs/1311.5238) [[astro-ph.HE](#)].
- [7] M. G. AARTSEN ET AL.:
'Extending the search for muon neutrinos coincident with gamma-ray bursts in IceCube data',
in: *Astrophys. J.* 843.2 (2017), p. 112. DOI: [10.3847/1538-4357/aa7569](https://doi.org/10.3847/1538-4357/aa7569). arXiv: [1702.06868](https://arxiv.org/abs/1702.06868) [[astro-ph.HE](#)].
- [8] M. G. AARTSEN ET AL.:
'First observation of PeV-energy neutrinos with IceCube',
in: *Phys. Rev. Lett.* 111 (2013), p. 021103. DOI: [10.1103/PhysRevLett.111.021103](https://doi.org/10.1103/PhysRevLett.111.021103). arXiv: [1304.5356](https://arxiv.org/abs/1304.5356) [[astro-ph.HE](#)].

- [9] M. G. AARTSEN ET AL.:
'IceCube Search for Neutrinos Coincident with Compact Binary Mergers from LIGO-Virgo's First Gravitational-wave Transient Catalog',
in: *Astrophys. J. Lett.* 898.1 (2020), p. L10. DOI: [10.3847/2041-8213/ab9d24](https://doi.org/10.3847/2041-8213/ab9d24). arXiv: 2004.02910 [astro-ph.HE].
- [10] M. G. AARTSEN ET AL.:
'IceCube-Gen2: the window to the extreme Universe',
in: *J. Phys. G* 48.6 (2021), p. 060501. DOI: [10.1088/1361-6471/abbd48](https://doi.org/10.1088/1361-6471/abbd48). arXiv: 2008.04323 [astro-ph.HE].
- [11] M. G. AARTSEN ET AL.:
'Multimessenger observations of a flaring blazar coincident with high-energy neutrino IceCube-170922A',
in: *Science* 361.6398 (2018), eaat1378. DOI: [10.1126/science.aat1378](https://doi.org/10.1126/science.aat1378). arXiv: 1807.08816 [astro-ph.HE].
- [12] M. G. AARTSEN ET AL.:
'The contribution of Fermi-2LAC blazars to the diffuse TeV-PeV neutrino flux',
in: *Astrophys. J.* 835.1 (2017), p. 45. DOI: [10.3847/1538-4357/835/1/45](https://doi.org/10.3847/1538-4357/835/1/45). arXiv: 1611.03874 [astro-ph.HE].
- [13] M. G. AARTSEN ET AL.:
'The IceCube Neutrino Observatory - Contributions to ICRC 2017 Part II: Properties of the Atmospheric and Astrophysical Neutrino Flux',
in: (Oct. 2017). arXiv: 1710.01191 [astro-ph.HE].
- [14] M. G. AARTSEN ET AL.:
'The IceCube Neutrino Observatory: Instrumentation and Online Systems',
in: *JINST* 12.03 (2017), P03012. DOI: [10.1088/1748-0221/12/03/P03012](https://doi.org/10.1088/1748-0221/12/03/P03012). arXiv: 1612.05093 [astro-ph.IM].
- [15] M. G. AARTSEN ET AL.:
'The IceCube Realtime Alert System',
in: *Astropart. Phys.* 92 (2017), pp. 30–41. DOI: [10.1016/j.astropartphys.2017.05.002](https://doi.org/10.1016/j.astropartphys.2017.05.002). arXiv: 1612.06028 [astro-ph.HE].
- [16] M.G. AARTSEN ET AL.:
'An All-Sky Search for Three Flavors of Neutrinos from Gamma-Ray Bursts with the IceCube Neutrino Observatory',
in: *Astrophys. J.* 824.2 (2016), p. 115. DOI: [10.3847/0004-637X/824/2/115](https://doi.org/10.3847/0004-637X/824/2/115). arXiv: 1601.06484 [astro-ph.HE].
- [17] R. ABBASI ET AL.:
'Detection of astrophysical tau neutrino candidates in IceCube',
in: *Eur. Phys. J. C* 82.11 (2022), p. 1031. DOI: [10.1140/epjc/s10052-022-10795-y](https://doi.org/10.1140/epjc/s10052-022-10795-y). arXiv: 2011.03561 [hep-ex].
- [18] R. ABBASI ET AL.:
'Evidence for neutrino emission from the nearby active galaxy NGC 1068',
in: *Science* 378.6619 (2022), pp. 538–543. DOI: [10.1126/science.abg3395](https://doi.org/10.1126/science.abg3395). arXiv: 2211.09972 [astro-ph.HE].

- [19] R. ABBASI ET AL.:
'Follow-up of Astrophysical Transients in Real Time with the IceCube Neutrino Observatory',
in: *Astrophys. J.* 910.1 (2021), p. 4. DOI: [10.3847/1538-4357/abe123](https://doi.org/10.3847/1538-4357/abe123). arXiv: [2012.04577](https://arxiv.org/abs/2012.04577) [[astro-ph.HE](#)].
- [20] R. ABBASI ET AL.:
'IceCube Data for Neutrino Point-Source Searches Years 2008-2018',
in: (Jan. 2021). DOI: [10.21234/CPKQ-K003](https://doi.org/10.21234/CPKQ-K003). arXiv: [2101.09836](https://arxiv.org/abs/2101.09836) [[astro-ph.HE](#)].
- [21] R. ABBASI ET AL.:
'Improved Characterization of the Astrophysical Muon-neutrino Flux with 9.5 Years of IceCube Data',
in: *Astrophys. J.* 928.1 (2022), p. 50. DOI: [10.3847/1538-4357/ac4d29](https://doi.org/10.3847/1538-4357/ac4d29). arXiv: [2111.10299](https://arxiv.org/abs/2111.10299) [[astro-ph.HE](#)].
- [22] R. ABBASI ET AL.:
'Observation of high-energy neutrinos from the Galactic plane',
in: *Science* 380.6652 (2023), adc9818. DOI: [10.1126/science.adc9818](https://doi.org/10.1126/science.adc9818). arXiv: [2307.04427](https://arxiv.org/abs/2307.04427) [[astro-ph.HE](#)].
- [23] R. ABBASI ET AL.:
'The IceCube high-energy starting event sample: Description and flux characterization with 7.5 years of data',
in: *Phys. Rev. D* 104 (2021), p. 022002. DOI: [10.1103/PhysRevD.104.022002](https://doi.org/10.1103/PhysRevD.104.022002). arXiv: [2011.03545](https://arxiv.org/abs/2011.03545) [[astro-ph.HE](#)].
- [24] R. ABBASI ET AL.:
'Constraining High-energy Neutrino Emission from Supernovae with IceCube',
in: *Astrophys. J. Lett.* 949.1, L12 (May 2023), p. L12. DOI: [10.3847/2041-8213/acd2c9](https://doi.org/10.3847/2041-8213/acd2c9). arXiv: [2303.03316](https://arxiv.org/abs/2303.03316) [[astro-ph.HE](#)].
- [25] R. ABBASI ET AL.:
'Measurement of the high-energy all-flavor neutrino-nucleon cross section with IceCube',
in: *Phys. Rev. D* 104 (2 July 2021), p. 022001. DOI: [10.1103/PhysRevD.104.022001](https://doi.org/10.1103/PhysRevD.104.022001). URL: <https://link.aps.org/doi/10.1103/PhysRevD.104.022001>.
- [26] RASHA ABBASI ET AL.:
'IceCube search for neutrinos from GRB 221009A',
in: *PoS ICRC2023* (2023), p. 1511. DOI: [10.22323/1.444.1511](https://doi.org/10.22323/1.444.1511). arXiv: [2307.16354](https://arxiv.org/abs/2307.16354) [[astro-ph.HE](#)].
- [27] RASHA ABBASI ET AL.:
'Searches for Neutrinos from Precursors and Afterglows of Gamma-Ray Bursts using the IceCube Neutrino Observatory',
in: *PoS ICRC2021* (2021), p. 1118. DOI: [10.22323/1.395.1118](https://doi.org/10.22323/1.395.1118). arXiv: [2107.08870](https://arxiv.org/abs/2107.08870) [[astro-ph.HE](#)].
- [28] RASHA ABBASI ET AL.:
'Sensitivity studies for the IceCube-Gen2 radio array',
in: *PoS ICRC2021* (2021), p. 1183. DOI: [10.22323/1.395.1183](https://doi.org/10.22323/1.395.1183). arXiv: [2107.08910](https://arxiv.org/abs/2107.08910) [[astro-ph.HE](#)].

- [29] B. P. ABBOTT ET AL.:
‘GW170817: Observation of Gravitational Waves from a Binary Neutron Star Inspiral’,
in: *Phys. Rev. Lett.* 119.16 (2017), p. 161101. DOI: [10.1103/PhysRevLett.119.161101](https://doi.org/10.1103/PhysRevLett.119.161101). arXiv: [1710.05832](https://arxiv.org/abs/1710.05832) [gr-qc].
- [30] B. P. ABBOTT ET AL.:
‘Multi-messenger Observations of a Binary Neutron Star Merger’,
in: *Astrophys. J. Lett.* 848.2 (2017), p. L12. DOI: [10.3847/2041-8213/aa91c9](https://doi.org/10.3847/2041-8213/aa91c9). arXiv: [1710.05833](https://arxiv.org/abs/1710.05833) [astro-ph.HE].
- [31] B. P. ABBOTT ET AL.:
‘Observation of Gravitational Waves from a Binary Black Hole Merger’,
in: *Phys. Rev. Lett.* 116.6 (2016), p. 061102. DOI: [10.1103/PhysRevLett.116.061102](https://doi.org/10.1103/PhysRevLett.116.061102). arXiv: [1602.03837](https://arxiv.org/abs/1602.03837) [gr-qc].
- [32] H. ABDALLA ET AL.:
‘A very-high-energy component deep in the γ -ray burst afterglow’,
in: *Nature* 575.7783 (2019), pp. 464–467. DOI: [10.1038/s41586-019-1743-9](https://doi.org/10.1038/s41586-019-1743-9). arXiv: [1911.08961](https://arxiv.org/abs/1911.08961) [astro-ph.HE].
- [33] H. ABDALLA ET AL.:
‘Revealing x-ray and gamma ray temporal and spectral similarities in the GRB 190829A afterglow’,
in: *Science* 372.6546 (2021), pp. 1081–1085. DOI: [10.1126/science.abe8560](https://doi.org/10.1126/science.abe8560). arXiv: [2106.02510](https://arxiv.org/abs/2106.02510) [astro-ph.HE].
- [34] V. A. ACCIARI ET AL.:
‘Observation of inverse Compton emission from a long γ -ray burst’,
in: *Nature* 575.7783 (2019), pp. 459–463. DOI: [10.1038/s41586-019-1754-6](https://doi.org/10.1038/s41586-019-1754-6). arXiv: [2006.07251](https://arxiv.org/abs/2006.07251) [astro-ph.HE].
- [35] VICTOR A. ACCIARI ET AL.:
‘Searching for VHE gamma-ray emission associated with IceCube neutrino alerts using FACT, H.E.S.S., MAGIC, and VERITAS’,
in: *Proceedings of 37th International Cosmic Ray Conference — PoS(ICRC2021)*. Vol. 395. 2021, p. 960.
DOI: [10.22323/1.395.0960](https://doi.org/10.22323/1.395.0960).
- [36] ABRAHAM ACHTERBERG ET AL.:
‘Particle acceleration by ultrarelativistic shocks: Theory and simulations’,
in: *Mon. Not. Roy. Astron. Soc.* 328 (2001), p. 393. DOI: [10.1046/j.1365-8711.2001.04851.x](https://doi.org/10.1046/j.1365-8711.2001.04851.x).
arXiv: [astro-ph/0107530](https://arxiv.org/abs/astro-ph/0107530).
- [37] M. ACKERMANN ET AL.:
‘The spectrum of isotropic diffuse gamma-ray emission between 100 MeV and 820 GeV’,
in: *Astrophys. J.* 799 (2015), p. 86. DOI: [10.1088/0004-637X/799/1/86](https://doi.org/10.1088/0004-637X/799/1/86). arXiv: [1410.3696](https://arxiv.org/abs/1410.3696) [astro-ph.HE].
- [38] ZEYNEP ACUNER, FELIX RYDE and HOI-FUNG YU:
‘Non-dissipative photospheres in GRBs: Spectral appearance in the Fermi/GBM catalogue’,
in: *Mon. Not. Roy. Astron. Soc.* 487.4 (2019), pp. 5508–5519. DOI: [10.1093/mnras/stz1356](https://doi.org/10.1093/mnras/stz1356).
arXiv: [1906.01318](https://arxiv.org/abs/1906.01318) [astro-ph.HE].

- [39] ZEYNEP ACUNER ET AL.:
'The Fraction of Gamma-Ray Bursts with an Observed Photospheric Emission Episode',
in: *Astrophys. J.* 893.2, 128 (2020), p. 128. DOI: [10.3847/1538-4357/ab80c7](https://doi.org/10.3847/1538-4357/ab80c7). arXiv: 2003.06223 [astro-ph.HE].
- [40] S. ADRIAN-MARTINEZ ET AL.:
'Letter of intent for KM3NeT 2.0',
in: *J. Phys. G* 43.8 (2016), p. 084001. DOI: [10.1088/0954-3899/43/8/084001](https://doi.org/10.1088/0954-3899/43/8/084001). arXiv: 1601.07459 [astro-ph.IM].
- [41] M. AGERON ET AL.:
'ANTARES: the first undersea neutrino telescope',
in: *Nucl. Instrum. Meth. A* 656 (2011), pp. 11–38. DOI: [10.1016/j.nima.2011.06.103](https://doi.org/10.1016/j.nima.2011.06.103). arXiv: 1104.1607 [astro-ph.IM].
- [42] N. AGHANIM ET AL.:
'Planck 2018 results. VI. Cosmological parameters',
in: *Astron. Astrophys.* 641 (2020), A6. DOI: [10.1051/0004-6361/201833910](https://doi.org/10.1051/0004-6361/201833910). arXiv: 1807.06209 [astro-ph.CO].
- [43] J. A. AGUILAR ET AL.:
'Design and Sensitivity of the Radio Neutrino Observatory in Greenland (RNO-G)',
in: *JINST* 16.03 (2021), P03025. DOI: [10.1088/1748-0221/16/03/P03025](https://doi.org/10.1088/1748-0221/16/03/P03025). arXiv: 2010.12279 [astro-ph.IM].
- [44] B. AHARMIM ET AL.:
'Combined Analysis of all Three Phases of Solar Neutrino Data from the Sudbury Neutrino Observatory',
in: *Phys. Rev. C* 88 (2013), p. 025501. DOI: [10.1103/PhysRevC.88.025501](https://doi.org/10.1103/PhysRevC.88.025501). arXiv: 1109.0763 [nucl-ex].
- [45] MARKUS AHLERS and FRANCIS HALZEN:
'High-energy cosmic neutrino puzzle: a review',
in: *Rept. Prog. Phys.* 78.12 (2015), p. 126901. DOI: [10.1088/0034-4885/78/12/126901](https://doi.org/10.1088/0034-4885/78/12/126901).
- [46] MARKUS AHLERS and FRANCIS HALZEN:
'Opening a New Window onto the Universe with IceCube',
in: *Prog. Part. Nucl. Phys.* 102 (2018), pp. 73–88. DOI: [10.1016/j.pnpnp.2018.05.001](https://doi.org/10.1016/j.pnpnp.2018.05.001). arXiv: 1805.11112 [astro-ph.HE].
- [47] M. AJELLO ET AL.:
'Fermi and Swift Observations of GRB 190114C: Tracing the Evolution of High-Energy Emission from Prompt to Afterglow',
in: *Astrophys. J.* 890.1 (2020), p. 9. DOI: [10.3847/1538-4357/ab5b05](https://doi.org/10.3847/1538-4357/ab5b05). arXiv: 1909.10605 [astro-ph.HE].
- [48] M. AJELLO ET AL.:
'Investigating the Nature of Late-time High-energy GRB Emission through Joint Fermi/Swift Observations',
in: *Astrophys. J.* 863.2 (2018), p. 138. DOI: [10.3847/1538-4357/aad000](https://doi.org/10.3847/1538-4357/aad000). arXiv: 1808.01683 [astro-ph.HE].

- [49] A. ALBERT ET AL.:
'Constraining the contribution of Gamma-Ray Bursts to the high-energy diffuse neutrino flux with 10 yr of ANTARES data',
in: *Mon. Not. R. Astron. Soc.* 500.4 (2020), pp. 5614–5628. DOI: [10.1093/mnras/staa3503](https://doi.org/10.1093/mnras/staa3503).
arXiv: [2008.02127](https://arxiv.org/abs/2008.02127) [astro-ph.HE].
- [50] A. ALBERT ET AL.:
'Search for neutrinos from the tidal disruption events AT2019dsg and AT2019fdp with the ANTARES telescope',
in: (Mar. 2021). arXiv: [2103.15526](https://arxiv.org/abs/2103.15526) [astro-ph.HE].
- [51] P. ALLISON ET AL.:
'Design and Initial Performance of the Askaryan Radio Array Prototype EeV Neutrino Detector at the South Pole',
in: *Astropart. Phys.* 35 (2012), pp. 457–477. DOI: [10.1016/j.astropartphys.2011.11.010](https://doi.org/10.1016/j.astropartphys.2011.11.010).
arXiv: [1105.2854](https://arxiv.org/abs/1105.2854) [astro-ph.IM].
- [52] P. ALLISON ET AL.:
'Performance of two Askaryan Radio Array stations and first results in the search for ultrahigh energy neutrinos',
in: *Phys. Rev. D* 93.8 (2016), p. 082003. DOI: [10.1103/PhysRevD.93.082003](https://doi.org/10.1103/PhysRevD.93.082003). arXiv: [1507.08991](https://arxiv.org/abs/1507.08991) [astro-ph.HE].
- [53] ATHEM W. ALSABTI and PAUL MURDIN:
Handbook of Supernovae,
2017. DOI: [10.1007/978-3-319-21846-5](https://doi.org/10.1007/978-3-319-21846-5).
- [54] JAIME ÁLVAREZ-MUÑIZ ET AL.:
'The Giant Radio Array for Neutrino Detection (GRAND): Science and Design',
in: *Sci. China Phys. Mech. Astron.* 63.1 (2020), p. 219501. DOI: [10.1007/s11433-018-9385-7](https://doi.org/10.1007/s11433-018-9385-7).
arXiv: [1810.09994](https://arxiv.org/abs/1810.09994) [astro-ph.HE].
- [55] LORENZO AMATI:
'The E(p,i) - E(iso) correlation in grbs: updated observational status, re-analysis and main implications',
in: *Mon. Not. Roy. Astron. Soc.* 372 (2006), pp. 233–245. DOI: [10.1111/j.1365-2966.2006.10840.x](https://doi.org/10.1111/j.1365-2966.2006.10840.x). arXiv: [astro-ph/0601553](https://arxiv.org/abs/astro-ph/0601553).
- [56] SIVARAM AMBIKASARAN ET AL.:
'Fast Direct Methods for Gaussian Processes',
in: *IEEE Transactions on Pattern Analysis and Machine Intelligence* 38 (June 2015), p. 252. DOI: [10.1109/TPAMI.2015.2448083](https://doi.org/10.1109/TPAMI.2015.2448083). arXiv: [1403.6015](https://arxiv.org/abs/1403.6015) [math.NA].
- [57] LUIS A. ANCHORDOQUI ET AL.:
'Cosmic Neutrino Pevatrons: A Brand New Pathway to Astronomy, Astrophysics, and Particle Physics',
in: *JHEAp* 1-2 (2014), pp. 1–30. DOI: [10.1016/j.jheap.2014.01.001](https://doi.org/10.1016/j.jheap.2014.01.001). arXiv: [1312.6587](https://arxiv.org/abs/1312.6587) [astro-ph.HE].
- [58] MAKOTO ARIMOTO ET AL.:
'High-energy Non-thermal and Thermal Emission From GRB 141207a Detected by Fermi',
in: *Astrophys. J.* 833.2 (2016), p. 139. DOI: [10.3847/1538-4357/833/2/139](https://doi.org/10.3847/1538-4357/833/2/139). arXiv: [1610.04867](https://arxiv.org/abs/1610.04867) [astro-ph.HE].

- [59] DAVID ARNETT:
Supernovae and Nucleosynthesis: An Investigation of the History of Matter from the Big Bang to the Present,
1996.
- [60] W. D. ARNETT:
‘Type I supernovae. I - Analytic solutions for the early part of the light curve’,
in: 253 (Feb. 1982), pp. 785–797. DOI: [10.1086/159681](https://doi.org/10.1086/159681).
- [61] K. ASANO and P. MÉSZÁROS:
‘Photon and Neutrino Spectra of Time-Dependent Photospheric Models of Gamma-Ray Bursts’,
in: *JCAP* 09 (2013), p. 008. DOI: [10.1088/1475-7516/2013/09/008](https://doi.org/10.1088/1475-7516/2013/09/008). arXiv: [1308.3563](https://arxiv.org/abs/1308.3563) [[astro-ph.HE](https://arxiv.org/archive/hep)].
- [62] KATSUAKI ASANO and S. NAGATAKI:
‘Very high energy neutrinos originating from kaons in gamma-ray bursts’,
in: *Astrophys. J. Lett.* 640 (2006), pp. L9–L12. DOI: [10.1086/503291](https://doi.org/10.1086/503291). arXiv: [astro-ph/0603107](https://arxiv.org/abs/astro-ph/0603107).
- [63] KATSUAKI ASANO and TOSHIO TERASAWA:
‘Stochastic Acceleration Model of Gamma-Ray Burst with Decaying Turbulence’,
in: *Mon. Not. Roy. Astron. Soc.* 454.2 (2015), pp. 2242–2248. DOI: [10.1093/mnras/stv2152](https://doi.org/10.1093/mnras/stv2152).
arXiv: [1509.04477](https://arxiv.org/abs/1509.04477) [[astro-ph.HE](https://arxiv.org/archive/hep)].
- [64] J.L. ATTEIA ET AL.:
‘The maximum isotropic energy of gamma-ray bursts’,
in: *Astrophys. J.* 837.2 (2017), p. 119. DOI: [10.3847/1538-4357/aa5ffa](https://doi.org/10.3847/1538-4357/aa5ffa). arXiv: [1702.02961](https://arxiv.org/abs/1702.02961) [[astro-ph.HE](https://arxiv.org/archive/hep)].
- [65] KATIE AUCHETTL, JAMES GUILLOCHON and ENRICO RAMIREZ-RUIZ:
‘New Physical Insights about Tidal Disruption Events from a Comprehensive Observational Inventory at X-Ray Wavelengths’,
in: 838.2, 149 (Apr. 2017), p. 149. DOI: [10.3847/1538-4357/aa633b](https://doi.org/10.3847/1538-4357/aa633b). arXiv: [1611.02291](https://arxiv.org/abs/1611.02291) [[astro-ph.HE](https://arxiv.org/archive/hep)].
- [66] A. D. AVRORIN ET AL.:
‘Status of the Baikal-GVD Neutrino Telescope’,
in: *EPJ Web Conf.* 207 (2019). Ed. by C. Spiering, p. 01003. DOI: [10.1051/epjconf/201920701003](https://doi.org/10.1051/epjconf/201920701003).
- [67] ELIAS AYDI ET AL.:
‘Direct evidence for shock-powered optical emission in a nova’,
in: *Nature Astron.* 4.8 (2020), pp. 776–780. DOI: [10.1038/s41550-020-1070-y](https://doi.org/10.1038/s41550-020-1070-y). arXiv: [2004.05562](https://arxiv.org/abs/2004.05562) [[astro-ph.HE](https://arxiv.org/archive/hep)].
- [68] PHILIPP BAERWALD, MAURICIO BUSTAMANTE and WALTER WINTER:
‘UHECR escape mechanisms for protons and neutrons from GRBs, and the cosmic ray-neutrino connection’,
in: *Astrophys. J.* 768 (2013), p. 186. DOI: [10.1088/0004-637X/768/2/186](https://doi.org/10.1088/0004-637X/768/2/186). arXiv: [1301.6163](https://arxiv.org/abs/1301.6163) [[astro-ph.HE](https://arxiv.org/archive/hep)].
- [69] PHILIPP BAERWALD, SVENJA HÜMMER and WALTER WINTER:
‘Systematics in the Interpretation of Aggregated Neutrino Flux Limits and Flavor Ratios from Gamma-Ray Bursts’,
in: *Astropart. Phys.* 35 (2012), pp. 508–529. DOI: [10.1016/j.astropartphys.2011.11.005](https://doi.org/10.1016/j.astropartphys.2011.11.005).
arXiv: [1107.5583](https://arxiv.org/abs/1107.5583) [[astro-ph.HE](https://arxiv.org/archive/hep)].

- [70] JOHN N. BAHCALL and PETER MÉSZÁROS:
'5-GeV to 10-GeV neutrinos from gamma-ray burst fireballs',
in: *Phys. Rev. Lett.* 85 (2000), pp. 1362–1365. DOI: [10.1103/PhysRevLett.85.1362](https://doi.org/10.1103/PhysRevLett.85.1362). arXiv: [hep-ph/0004019](https://arxiv.org/abs/hep-ph/0004019).
- [71] JOHN N. BAHCALL, M. H. PINSONNEAULT and SARBANI BASU:
'Solar models: Current epoch and time dependences, neutrinos, and helioseismological properties',
in: *Astrophys. J.* 555 (2001), pp. 990–1012. DOI: [10.1086/321493](https://doi.org/10.1086/321493). arXiv: [astro-ph/0010346](https://arxiv.org/abs/astro-ph/0010346).
- [72] SHMUEL BALBERG and ABRAHAM LOEB:
'Supernova Shock Breakout Through a Wind',
in: *Mon. Not. Roy. Astron. Soc.* 414 (2011), p. 1715. DOI: [10.1111/j.1365-2966.2011.18505.x](https://doi.org/10.1111/j.1365-2966.2011.18505.x). arXiv: [1101.1489](https://arxiv.org/abs/1101.1489) [[astro-ph.HE](https://arxiv.org/abs/1101.1489)].
- [73] D. BAND ET AL.:
'BATSE observations of gamma-ray burst spectra. 1. Spectral diversity',
in: *Astrophys. J.* 413 (1993), pp. 281–292. DOI: [10.1086/172995](https://doi.org/10.1086/172995).
- [74] S. D. BARTHELMI ET AL.:
'Discovery of an afterglow extension of the prompt phase of two gamma ray bursts observed by swift',
in: *Astrophys. J. Lett.* 635 (2005), pp. L133–L136. DOI: [10.1086/499432](https://doi.org/10.1086/499432). arXiv: [astro-ph/0511576](https://arxiv.org/abs/astro-ph/0511576).
- [75] IMRE BARTOS and MAREK KOWALSKI:
Multimessenger Astronomy,
2399-2891. IOP Publishing, 2017. ISBN: 978-0-7503-1369-8. DOI: [10.1088/978-0-7503-1369-8](https://doi.org/10.1088/978-0-7503-1369-8). URL: <https://dx.doi.org/10.1088/978-0-7503-1369-8>.
- [76] S. W. BARWICK ET AL.:
'A First Search for Cosmogenic Neutrinos with the ARIANNA Hexagonal Radio Array',
in: *Astropart. Phys.* 70 (2015), pp. 12–26. DOI: [10.1016/j.astropartphys.2015.04.002](https://doi.org/10.1016/j.astropartphys.2015.04.002). arXiv: [1410.7352](https://arxiv.org/abs/1410.7352) [[astro-ph.HE](https://arxiv.org/abs/1410.7352)].
- [77] S. W. BARWICK ET AL.:
'Design and Performance of the ARIANNA HRA-3 Neutrino Detector Systems',
in: *IEEE Trans. Nucl. Sci.* 62.5 (2015), pp. 2202–2215. DOI: [10.1109/TNS.2015.2468182](https://doi.org/10.1109/TNS.2015.2468182). arXiv: [1410.7369](https://arxiv.org/abs/1410.7369) [[astro-ph.IM](https://arxiv.org/abs/1410.7369)].
- [78] A. R. BELL:
'Cosmic ray acceleration',
in: *Astropart. Phys.* 43 (2013), pp. 56–70. DOI: [10.1016/j.astropartphys.2012.05.022](https://doi.org/10.1016/j.astropartphys.2012.05.022).
- [79] A. R. BELL:
'The acceleration of cosmic rays in shock fronts - I',
in: 182 (Jan. 1978), pp. 147–156. DOI: [10.1093/mnras/182.2.147](https://doi.org/10.1093/mnras/182.2.147).
- [80] A. R. BELL:
'Turbulent amplification of magnetic field and diffusive shock acceleration of cosmic rays',
in: *Mon. Not. Roy. Astron. Soc.* 353.2 (Sept. 2004), pp. 550–558. DOI: [10.1111/j.1365-2966.2004.08097.x](https://doi.org/10.1111/j.1365-2966.2004.08097.x).

- [81] AR BELL ET AL.:
'Cosmic ray acceleration and escape from supernova remnants',
in: *Mon. Not. Roy. Astron. Soc.* 431 (2013), p. 415. DOI: [10.1093/mnras/stt179](https://doi.org/10.1093/mnras/stt179). arXiv: [1301.7264](https://arxiv.org/abs/1301.7264) [astro-ph.HE].
- [82] ERIC C. BELLM ET AL.:
'The Zwicky Transient Facility: System Overview, Performance, and First Results',
in: 131.995 (Jan. 2019), p. 018002. DOI: [10.1088/1538-3873/aaecbe](https://doi.org/10.1088/1538-3873/aaecbe). arXiv: [1902.01932](https://arxiv.org/abs/1902.01932) [astro-ph.IM].
- [83] A.M. BELOBORODOV and P. MÉSZÁROS:
'Photospheric Emission of Gamma-Ray Bursts',
in: *Space Sci. Rev.* 207.1-4 (2017), pp. 87–110. DOI: [10.1007/s11214-017-0348-6](https://doi.org/10.1007/s11214-017-0348-6). arXiv: [1701.04523](https://arxiv.org/abs/1701.04523) [astro-ph.HE].
- [84] ANDREI M. BELOBORODOV:
'Collisional mechanism for GRB emission',
in: *Mon. Not. Roy. Astron. Soc.* 407 (2010), p. 1033. DOI: [10.1111/j.1365-2966.2010.16770.x](https://doi.org/10.1111/j.1365-2966.2010.16770.x). arXiv: [0907.0732](https://arxiv.org/abs/0907.0732) [astro-ph.HE].
- [85] ANDREI M. BELOBORODOV:
'Regulation of the spectral peak in gamma-ray bursts',
in: *Astrophys. J.* 764 (2013), p. 157. DOI: [10.1088/0004-637X/764/2/157](https://doi.org/10.1088/0004-637X/764/2/157). arXiv: [1207.2707](https://arxiv.org/abs/1207.2707) [astro-ph.HE].
- [86] ANDREI M. BELOBORODOV:
'Sub-photospheric shocks in relativistic explosions',
in: *Astrophys. J.* 838.2 (2017), p. 125. DOI: [10.3847/1538-4357/aa5c8c](https://doi.org/10.3847/1538-4357/aa5c8c). arXiv: [1604.02794](https://arxiv.org/abs/1604.02794) [astro-ph.HE].
- [87] PAZ BENIAMINI and DIMITRIOS GIANNIOS:
'Prompt Gamma Ray Burst emission from gradual magnetic dissipation',
in: *Mon. Not. Roy. Astron. Soc.* 468.3 (2017), pp. 3202–3211. DOI: [10.1093/mnras/stx717](https://doi.org/10.1093/mnras/stx717). arXiv: [1703.07380](https://arxiv.org/abs/1703.07380) [astro-ph.HE].
- [88] PAZ BENIAMINI, LARA NAVA and TSVI PIRAN:
'A revised analysis of gamma-ray bursts' prompt efficiencies',
in: *Mon. Not. Roy. Astron. Soc.* 461.1 (2016), pp. 51–59. DOI: [10.1093/mnras/stw1331](https://doi.org/10.1093/mnras/stw1331). arXiv: [1606.00311](https://arxiv.org/abs/1606.00311) [astro-ph.HE].
- [89] PAZ BENIAMINI ET AL.:
'Energies of GRB blast waves and prompt efficiencies as implied by modelling of X-ray and GeV afterglows',
in: *Mon. Not. Roy. Astron. Soc.* 454.1 (2015), pp. 1073–1085. DOI: [10.1093/mnras/stv2033](https://doi.org/10.1093/mnras/stv2033). arXiv: [1504.04833](https://arxiv.org/abs/1504.04833) [astro-ph.HE].
- [90] H. BETHE and R. PEIERLS:
'The 'neutrino'',
in: *Nature* 133 (1934), p. 532. DOI: [10.1038/133532a0](https://doi.org/10.1038/133532a0).
- [91] H. A. BETHE and J. R. WILSON:
'Revival of a stalled supernova shock by neutrino heating',
in: 295 (Aug. 1985), pp. 14–23. DOI: [10.1086/163343](https://doi.org/10.1086/163343).

- [92] P. K. BLANCHARD ET AL.:
'PS16dtm: A Tidal Disruption Event in a Narrow-line Seyfert 1 Galaxy',
in: *Astrophys. J.* 843.2 (2017), p. 106. DOI: [10.3847/1538-4357/aa77f7](https://doi.org/10.3847/1538-4357/aa77f7). arXiv: [1703.07816](https://arxiv.org/abs/1703.07816) [astro-ph.HE].
- [93] R. D. BLANDFORD and R. L. ZNAJEK:
'Electromagnetic extractions of energy from Kerr black holes',
in: *Mon. Not. Roy. Astron. Soc.* 179 (1977), pp. 433–456. DOI: [10.1093/mnras/179.3.433](https://doi.org/10.1093/mnras/179.3.433).
- [94] R.D. BLANDFORD and C.F. MCKEE:
'Fluid dynamics of relativistic blast waves',
in: *Phys. Fluids* 19 (1976), pp. 1130–1138. DOI: [10.1063/1.861619](https://doi.org/10.1063/1.861619).
- [95] PASQUALE BLASI:
'The Origin of Galactic Cosmic Rays',
in: *Astron. Astrophys. Rev.* 21 (2013), p. 70. DOI: [10.1007/s00159-013-0070-7](https://doi.org/10.1007/s00159-013-0070-7). arXiv: [1311.7346](https://arxiv.org/abs/1311.7346) [astro-ph.HE].
- [96] PASQUALE BLASI and MARIO VIETRI:
'On particle acceleration around shocks. 2. A Fully general method for arbitrary shock velocities and scattering media',
in: *Astrophys. J.* 626 (2005), pp. 877–886. DOI: [10.1086/430164](https://doi.org/10.1086/430164). arXiv: [astro-ph/0503220](https://arxiv.org/abs/astro-ph/0503220).
- [97] SERGEI BLINNIKOV:
'Interacting Supernovae: Spectra and Light Curves',
in: *Handbook of Supernovae*. Ed. by Athem W. Alsabti and Paul Murdin. 2017, p. 843. DOI: [10.1007/978-3-319-21846-5_31](https://doi.org/10.1007/978-3-319-21846-5_31).
- [98] J. S. BLOOM ET AL.:
'The Unusual afterglow of GRB 980326: Evidence for the gamma-ray burst - supernova connection',
in: *Nature* 401 (1999), p. 453. DOI: [10.1038/46744](https://doi.org/10.1038/46744). arXiv: [astro-ph/9905301](https://arxiv.org/abs/astro-ph/9905301).
- [99] DAVID BRANCH and J. CRAIG WHEELER:
Supernova Explosions,
2017. DOI: [10.1007/978-3-662-55054-0](https://doi.org/10.1007/978-3-662-55054-0).
- [100] OMER BROMBERG ET AL.:
'The propagation of relativistic jets in external media',
in: *Astrophys. J.* 740 (2011), p. 100. DOI: [10.1088/0004-637X/740/2/100](https://doi.org/10.1088/0004-637X/740/2/100). arXiv: [1107.1326](https://arxiv.org/abs/1107.1326) [astro-ph.HE].
- [101] R. BROSE, I. SUSHCH and J. MACKAY:
'Core-collapse supernovae in dense environments - particle acceleration and non-thermal emission',
in: *Mon. Not. Roy. Astron. Soc.* 516.1 (Oct. 2022), pp. 492–505. DOI: [10.1093/mnras/stac2234](https://doi.org/10.1093/mnras/stac2234). arXiv: [2208.04185](https://arxiv.org/abs/2208.04185) [astro-ph.HE].
- [102] J. S. BROWN ET AL.:
'The Long Term Evolution of ASASSN-14li',
in: 466.4 (Apr. 2017), pp. 4904–4916. DOI: [10.1093/mnras/stx033](https://doi.org/10.1093/mnras/stx033). arXiv: [1609.04403](https://arxiv.org/abs/1609.04403) [astro-ph.HE].

- [103] N. BUCCIANINI ET AL.:
'Magnetar Driven Bubbles and the Origin of Collimated Outflows in Gamma-ray Bursts',
in: *Mon. Not. Roy. Astron. Soc.* 380 (2007), p. 1541. DOI: [10.1111/j.1365-2966.2007.12164.x](https://doi.org/10.1111/j.1365-2966.2007.12164.x). arXiv: [0705.1742](https://arxiv.org/abs/0705.1742) [astro-ph].
- [104] J. MICHAEL BURGESS ET AL.:
'Gamma-ray bursts as cool synchrotron sources',
in: *Nature Astron.* 4.2 (2019), pp. 174–179. DOI: [10.1038/s41550-019-0911-z](https://doi.org/10.1038/s41550-019-0911-z). arXiv: [1810.06965](https://arxiv.org/abs/1810.06965) [astro-ph.HE].
- [105] ERIC BURNS ET AL.:
'GRB 221009A: The BOAT',
in: *Astrophys. J. Lett.* 946.1 (2023), p. L31. DOI: [10.3847/2041-8213/acc39c](https://doi.org/10.3847/2041-8213/acc39c). arXiv: [2302.14037](https://arxiv.org/abs/2302.14037) [astro-ph.HE].
- [106] ADAM BURROWS:
'Colloquium: Perspectives on core-collapse supernova theory',
in: *Rev. Mod. Phys.* 85 (2013), p. 245. DOI: [10.1103/RevModPhys.85.245](https://doi.org/10.1103/RevModPhys.85.245). arXiv: [1210.4921](https://arxiv.org/abs/1210.4921) [astro-ph.SR].
- [107] ADAM BURROWS ET AL.:
'A new mechanism for core-collapse supernova explosions',
in: *Astrophys. J.* 640 (2006), pp. 878–890. DOI: [10.1086/500174](https://doi.org/10.1086/500174). arXiv: [astro-ph/0510687](https://arxiv.org/abs/astro-ph/0510687).
- [108] MAURICIO BUSTAMANTE ET AL.:
'Multi-messenger light curves from gamma-ray bursts in the internal shock model',
in: *Astrophys. J.* 837.1 (2017), p. 33. DOI: [10.3847/1538-4357/837/1/33](https://doi.org/10.3847/1538-4357/837/1/33). arXiv: [1606.02325](https://arxiv.org/abs/1606.02325) [astro-ph.HE].
- [109] MAURICIO BUSTAMANTE ET AL.:
'Neutrino and cosmic-ray emission from multiple internal shocks in gamma-ray bursts',
in: *Nature Commun.* 6 (2015), p. 6783. DOI: [10.1038/ncomms7783](https://doi.org/10.1038/ncomms7783). arXiv: [1409.2874](https://arxiv.org/abs/1409.2874) [astro-ph.HE].
- [110] KEVIN CAHILL:
'Flat Space, Dark Energy, and the Cosmic Microwave Background',
in: *Eur. J. Phys.* 41.3 (2020), p. 035603. DOI: [10.1088/1361-6404/ab738d](https://doi.org/10.1088/1361-6404/ab738d). arXiv: [2002.11464](https://arxiv.org/abs/2002.11464) [physics.gen-ph].
- [111] DAMIANO CAPRIOLI:
'Particle Acceleration at Shocks: An Introduction',
in: *International School "Enrico Fermi" 2022: Foundations of Cosmic Ray Astrophysics*. July 2023.
arXiv: [2307.00284](https://arxiv.org/abs/2307.00284) [astro-ph.HE].
- [112] DAMIANO CAPRIOLI, COLBY HAGGERTY and PASQUALE BLASI:
'The Theory of Efficient Particle Acceleration at Shocks',
in: *PoS ICRC2021* (2021), p. 482. DOI: [10.22323/1.395.0482](https://doi.org/10.22323/1.395.0482). arXiv: [2111.10629](https://arxiv.org/abs/2111.10629) [astro-ph.HE].
- [113] DAMIANO CAPRIOLI and ANATOLY SPITKOVSKY:
'Simulations of Ion Acceleration at Non-relativistic Shocks. I. Acceleration Efficiency',
in: *Astrophys. J.* 783 (2014), p. 91. DOI: [10.1088/0004-637X/783/2/91](https://doi.org/10.1088/0004-637X/783/2/91). arXiv: [1310.2943](https://arxiv.org/abs/1310.2943) [astro-ph.HE].

- [114] MARTINA CARDILLO, ELENA AMATO and PASQUALE BLASI:
'On the cosmic ray spectrum from type II Supernovae expanding in their red giant presupernova wind',
in: *Astropart. Phys.* 69 (2015), pp. 1–10. DOI: [10.1016/j.astropartphys.2015.03.002](https://doi.org/10.1016/j.astropartphys.2015.03.002). arXiv: [1503.03001](https://arxiv.org/abs/1503.03001) [astro-ph.HE].
- [115] Y. CENDES ET AL.:
'Radio Observations of an Ordinary Outflow from the Tidal Disruption Event AT2019dsg',
in: *Astrophys. J.* 919.2 (2021), p. 127. DOI: [10.3847/1538-4357/ac110a](https://doi.org/10.3847/1538-4357/ac110a). arXiv: [2103.06299](https://arxiv.org/abs/2103.06299) [astro-ph.HE].
- [116] S. B. CENKO ET AL.:
'Afterglow Observations of Fermi Large Area Telescope Gamma-ray Bursts and the Emerging Class of Hyper-energetic Events',
in: *Astrophys. J.* 732.1, 29 (May 2011), p. 29. DOI: [10.1088/0004-637X/732/1/29](https://doi.org/10.1088/0004-637X/732/1/29). arXiv: [1004.2900](https://arxiv.org/abs/1004.2900) [astro-ph.HE].
- [117] S. B. CENKO ET AL.:
'The Collimation and Energetics of the Brightest Swift Gamma-ray Bursts',
in: *Astrophys. J.* 711.2 (2010), pp. 641–654. DOI: [10.1088/0004-637X/711/2/641](https://doi.org/10.1088/0004-637X/711/2/641). arXiv: [0905.0690](https://arxiv.org/abs/0905.0690) [astro-ph.HE].
- [118] K. C. CHAMBERS ET AL.:
'The Pan-STARRS1 Surveys',
in: *arXiv e-prints*, arXiv:1612.05560 (Dec. 2016), arXiv:1612.05560. DOI: [10.48550/arXiv.1612.05560](https://doi.org/10.48550/arXiv.1612.05560). arXiv: [1612.05560](https://arxiv.org/abs/1612.05560) [astro-ph.IM].
- [119] POONAM CHANDRA:
'Circumstellar interaction in supernovae in dense environments - an observational perspective',
in: *Space Sci. Rev.* 214.1 (2018), p. 27. DOI: [10.1007/s11214-017-0461-6](https://doi.org/10.1007/s11214-017-0461-6). arXiv: [1712.07405](https://arxiv.org/abs/1712.07405) [astro-ph.HE].
- [120] POONAM CHANDRA:
'Circumstellar Interaction in Supernovae in Dense Environments—An Observational Perspective',
in: *Sp. Sci. Rev.* 214.1, 27 (Feb. 2018), p. 27. DOI: [10.1007/s11214-017-0461-6](https://doi.org/10.1007/s11214-017-0461-6). arXiv: [1712.07405](https://arxiv.org/abs/1712.07405) [astro-ph.HE].
- [121] P. CHARALAMPOPOULOS ET AL.:
'A detailed spectroscopic study of Tidal Disruption Events',
in: *arXiv e-prints*, arXiv:2109.00016 (Aug. 2021), arXiv:2109.00016. arXiv: [2109.00016](https://arxiv.org/abs/2109.00016) [astro-ph.HE].
- [122] E. CHATZOPOULOS and RICHARD TUMINELLO:
'A Systematic Study of Superluminous Supernova Light-curve Models Using Clustering',
in: *Astrophys. J.* 874.1, 68 (Mar. 2019), p. 68. DOI: [10.3847/1538-4357/ab0ae6](https://doi.org/10.3847/1538-4357/ab0ae6). arXiv: [1902.09484](https://arxiv.org/abs/1902.09484) [astro-ph.HE].
- [123] E. CHATZOPOULOS ET AL.:
'Analytical Light Curve Models of Superluminous Supernovae: χ^2 -minimization of Parameter Fits',
in: *Astrophys. J.* 773 (2013), p. 76. DOI: [10.1088/0004-637X/773/1/76](https://doi.org/10.1088/0004-637X/773/1/76). arXiv: [1306.3447](https://arxiv.org/abs/1306.3447) [astro-ph.HE].

- [124] EMMANOUIL CHATZOPOULOS, J. CRAIG WHEELER and JOZSEF VINKO:
'Generalized Semi-Analytical Models of Supernova Light Curves',
in: *Astrophys. J.* 746 (2012), p. 121. DOI: [10.1088/0004-637X/746/2/121](https://doi.org/10.1088/0004-637X/746/2/121). arXiv: [1111.5237](https://arxiv.org/abs/1111.5237) [astro-ph.HE].
- [125] WEN-XIN CHEN and ANDREI M. BELOBORODOV:
'Neutrino-Cooled Accretion Disks around Spinning Black Hole',
in: *Astrophys. J.* 657 (2007), pp. 383–399. DOI: [10.1086/508923](https://doi.org/10.1086/508923). arXiv: [astro-ph/0607145](https://arxiv.org/abs/astro-ph/0607145).
- [126] R. A. CHEVALIER:
'Self-similar solutions for the interaction of stellar ejecta with an external medium',
in: 258 (July 1982), pp. 790–797. DOI: [10.1086/160126](https://doi.org/10.1086/160126).
- [127] R. A. CHEVALIER:
'The radio and X-ray emission from type II supernovae',
in: 259 (Aug. 1982), pp. 302–310. DOI: [10.1086/160167](https://doi.org/10.1086/160167).
- [128] R. A. CHEVALIER and C. FRANSSON:
'Supernova Interaction with a Circumstellar Medium',
in: *Supernovae and Gamma-Ray Bursters*. Ed. by K. Weiler. Vol. 598. 2003, pp. 171–194. DOI: [10.1007/3-540-45863-8_10](https://doi.org/10.1007/3-540-45863-8_10).
- [129] R.A. CHEVALIER and Z.Y. LI:
'Gamma-ray burst environments and progenitors',
in: *Astrophys. J. Lett.* 520 (1999), pp. L29–L32. DOI: [10.1086/312147](https://doi.org/10.1086/312147). arXiv: [astro-ph/9904417](https://arxiv.org/abs/astro-ph/9904417).
- [130] ROGER A. CHEVALIER and CLAES FRANSSON:
'Emission from Circumstellar Interaction in Normal Type II Supernovae',
in: *Astrophys. J.* 420 (Jan. 1994), p. 268. DOI: [10.1086/173557](https://doi.org/10.1086/173557).
- [131] ROGER A. CHEVALIER and CLAES FRANSSON:
'Thermal and non-thermal emission from circumstellar interaction',
in: Dec. 2016. DOI: [10.1007/978-3-319-21846-5_34](https://doi.org/10.1007/978-3-319-21846-5_34). arXiv: [1612.07459](https://arxiv.org/abs/1612.07459) [astro-ph.HE].
- [132] ROGER A. CHEVALIER and CHRISTOPHER M. IRWIN:
'Shock Breakout in Dense Mass Loss: Luminous Supernovae',
in: *Astrophys. J. Lett.* 729 (2011), p. L6. DOI: [10.1088/2041-8205/729/1/L6](https://doi.org/10.1088/2041-8205/729/1/L6). arXiv: [1101.1111](https://arxiv.org/abs/1101.1111) [astro-ph.HE].
- [133] ROGER A. CHEVALIER and ZHI-YUN LI:
'Wind interaction models for gamma-ray burst afterglows: The Case for two types of progenitors',
in: *Astrophys. J.* 536 (2000), pp. 195–212. DOI: [10.1086/308914](https://doi.org/10.1086/308914). arXiv: [astro-ph/9908272](https://arxiv.org/abs/astro-ph/9908272).
- [134] G. CHINCARINI ET AL.:
'Unveiling the origin of X-ray flares in gamma-ray bursts',
in: *MNRAS* 406.4 (Aug. 2010), pp. 2113–2148. DOI: [10.1111/j.1365-2966.2010.17037.x](https://doi.org/10.1111/j.1365-2966.2010.17037.x).
arXiv: [1004.0901](https://arxiv.org/abs/1004.0901) [astro-ph.HE].
- [135] R. CHORNOCK ET AL.:
'Transient Classification Report for 2019-06-15',
in: *Transient Name Server Classification Report 2019-1016* (June 2019), p. 1.
- [136] STIRLING A. COLGATE and RICHARD H. WHITE:
'The Hydrodynamic Behavior of Supernovae Explosions',
in: 143 (Mar. 1966), p. 626. DOI: [10.1086/148549](https://doi.org/10.1086/148549).

- [137] JR. COWAN C. L. ET AL.:
'Detection of the Free Neutrino: A Confirmation',
in: *Science* 124.3212 (July 1956), pp. 103–104. DOI: [10.1126/science.124.3212.103](https://doi.org/10.1126/science.124.3212.103).
- [138] PIERRE CRISTOFARI:
'The Hunt for Pevatrons: The Case of Supernova Remnants',
in: *Universe* 7.9 (2021), p. 324. DOI: [10.3390/universe7090324](https://doi.org/10.3390/universe7090324). arXiv: [2110.07956](https://arxiv.org/abs/2110.07956) [astro-ph.HE].
- [139] PIERRE CRISTOFARI, PASQUALE BLASI and ELENA AMATO:
'The low rate of Galactic pevatrons',
in: *Astropart. Phys.* 123 (2020), p. 102492. DOI: [10.1016/j.astropartphys.2020.102492](https://doi.org/10.1016/j.astropartphys.2020.102492).
arXiv: [2007.04294](https://arxiv.org/abs/2007.04294) [astro-ph.HE].
- [140] PATRICK CRUMLEY ET AL.:
'Kinetic simulations of mildly relativistic shocks – I. Particle acceleration in high Mach number shocks',
in: *Mon. Not. Roy. Astron. Soc.* 485.4 (2019), pp. 5105–5119. DOI: [10.1093/mnras/stz232](https://doi.org/10.1093/mnras/stz232). arXiv: [1809.10809](https://arxiv.org/abs/1809.10809) [astro-ph.HE].
- [141] P. A. CURRAN ET AL.:
'On the Electron Energy Distribution Index of Swift Gamma-ray Burst Afterglows',
in: *Astrophys. J. Letter* 716.2 (June 2010), pp. L135–L139. DOI: [10.1088/2041-8205/716/2/L135](https://doi.org/10.1088/2041-8205/716/2/L135). arXiv: [0908.0891](https://arxiv.org/abs/0908.0891) [astro-ph.HE].
- [142] LIXIN DAI and KE FANG:
'Can tidal disruption events produce the IceCube neutrinos?',
in: *Mon. Not. Roy. Astron. Soc.* 469.2 (2017), pp. 1354–1359. DOI: [10.1093/mnras/stx863](https://doi.org/10.1093/mnras/stx863). arXiv: [1612.00011](https://arxiv.org/abs/1612.00011) [astro-ph.HE].
- [143] F. DAIGNE, Z. BOSNJAK and GUILLAUME DUBUS:
'Reconciling observed GRB prompt spectra with synchrotron radiation?',
in: *Astron. Astrophys.* 526 (2011), A110. DOI: [10.1051/0004-6361/201015457](https://doi.org/10.1051/0004-6361/201015457). arXiv: [1009.2636](https://arxiv.org/abs/1009.2636) [astro-ph.HE].
- [144] F. DAIGNE and R. MOCHKOVITCH:
'Gamma-ray bursts from internal shocks in a relativistic wind: temporal and spectral properties',
in: *Mon. Not. Roy. Astron. Soc.* 296 (1998), p. 275. DOI: [10.1046/j.1365-8711.1998.01305.x](https://doi.org/10.1046/j.1365-8711.1998.01305.x).
arXiv: [astro-ph/9801245](https://arxiv.org/abs/astro-ph/9801245).
- [145] G. DANBY ET AL.:
'Observation of High-Energy Neutrino Reactions and the Existence of Two Kinds of Neutrinos',
in: *Phys. Rev. Lett.* 9 (1962), pp. 36–44. DOI: [10.1103/PhysRevLett.9.36](https://doi.org/10.1103/PhysRevLett.9.36).
- [146] RAYMOND DAVIS:
'A review of the homestake solar neutrino experiment',
in: *Progress in Particle and Nuclear Physics* 32 (Jan. 1994), pp. 13–32. DOI: [10.1016/0146-6410\(94\)90004-3](https://doi.org/10.1016/0146-6410(94)90004-3).
- [147] M. DE PASQUALE ET AL.:
'The 80 Ms follow-up of the X-ray afterglow of GRB 130427A challenges the standard forward shock model',
in: *Mon. Not. Roy. Astron. Soc.* 462.1 (2016), pp. 1111–1122. DOI: [10.1093/mnras/stw1704](https://doi.org/10.1093/mnras/stw1704).
arXiv: [1602.04158](https://arxiv.org/abs/1602.04158) [astro-ph.HE].

- [148] RICHARD DEKANY ET AL.:
'The Zwicky Transient Facility: Observing System',
in: 132.1009, 038001 (Mar. 2020), p. 038001. DOI: [10.1088/1538-3873/ab4ca2](https://doi.org/10.1088/1538-3873/ab4ca2). arXiv: 2008.04923 [astro-ph.IM].
- [149] WEI DENG ET AL.:
'Relativistic MHD simulations of collision-induced magnetic dissipation in Poynting-flux-dominated jets/outflows',
in: *Astrophys. J.* 805 (2015), p. 163. DOI: [10.1088/0004-637X/805/2/163](https://doi.org/10.1088/0004-637X/805/2/163). arXiv: 1501.07595 [astro-ph.HE].
- [150] EVGENY DERISHEV and TSVI PIRAN:
'GRB Afterglow Parameters in the Era of TeV Observations: The Case of GRB 190114C',
in: *Astrophys. J.* 923.2 (2021), p. 135. DOI: [10.3847/1538-4357/ac2dec](https://doi.org/10.3847/1538-4357/ac2dec). arXiv: 2106.12035 [astro-ph.HE].
- [151] CHARLES D. DERMER:
'Neutrino, neutron, and cosmic ray production in the external shock model of gamma-ray bursts',
in: *Astrophys. J.* 574 (2002), pp. 65–87. DOI: [10.1086/340893](https://doi.org/10.1086/340893). arXiv: astro-ph/0005440.
- [152] CHARLES D. DERMER and ARMEN ATOYAN:
'High energy neutrinos from gamma-ray bursts',
in: *Phys. Rev. Lett.* 91 (2003), p. 071102. DOI: [10.1103/PhysRevLett.91.071102](https://doi.org/10.1103/PhysRevLett.91.071102). arXiv: astro-ph/0301030.
- [153] CHARLES D. DERMER and GOVIND MENON:
High Energy Radiation from Black Holes: Gamma Rays, Cosmic Rays, and Neutrinos,
2009.
- [154] LUC DESSART, EDOUARD AUDIT and D. JOHN HILLIER:
'Numerical simulations of superluminous supernovae of type II_n',
in: *Mon. Not. Roy. Astron. Soc.* 449.4 (2015), pp. 4304–4325. DOI: [10.1093/mnras/stv609](https://doi.org/10.1093/mnras/stv609). arXiv: 1503.05463 [astro-ph.SR].
- [155] BRUCE T. DRAINE:
Physics of the Interstellar and Intergalactic Medium,
2011.
- [156] A. J. DRAKE ET AL.:
'The Discovery and Nature of Optical Transient CSS100217:102913+404220',
in: *Astrophys. J.* 735 (2011), p. 106. DOI: [10.1088/0004-637X/735/2/106](https://doi.org/10.1088/0004-637X/735/2/106). arXiv: 1103.5514 [astro-ph.CO].
- [157] G. DRENKHahn and H.C. SPRUIT:
'Efficient acceleration and radiation in Poynting flux powered GRB outflows',
in: *Astron. Astrophys.* 391 (2002), p. 1141. DOI: [10.1051/0004-6361:20020839](https://doi.org/10.1051/0004-6361:20020839). arXiv: astro-ph/0202387.
- [158] GEORG DRENKHahn:
'Acceleration of GRB outflows by Poynting flux dissipation',
in: *Astron. Astrophys.* 387 (2002), p. 714. DOI: [10.1051/0004-6361:20020390](https://doi.org/10.1051/0004-6361:20020390). arXiv: astro-ph/0112509.

- [159] L. O’C. DRURY:
‘First order Fermi acceleration driven by magnetic reconnection’,
in: *Mon. Not. Roy. Astron. Soc.* 422 (2012), pp. 2474–2476. DOI: [10.1111/j.1365-2966.2012.20804.x](https://doi.org/10.1111/j.1365-2966.2012.20804.x). arXiv: [1201.6612](https://arxiv.org/abs/1201.6612) [astro-ph.HE].
- [160] VIKRAM V DWARKADAS:
‘On Luminous Blue Variables as the Progenitors of Core-Collapse Supernovae, especially Type II_n Supernovae’,
in: *Mon. Not. Roy. Astron. Soc.* 412 (2011), p. 1639. DOI: [10.1111/j.1365-2966.2010.18001.x](https://doi.org/10.1111/j.1365-2966.2010.18001.x). arXiv: [1011.3484](https://arxiv.org/abs/1011.3484) [astro-ph.SR].
- [161] H. J. VAN EERTEN and R. A. M. J. WIJERS:
‘Gamma-Ray Burst afterglow scaling coefficients for general density profile via post-processing of blastwave solutions’,
in: *Mon. Not. R. Astron. Soc.* 394 (2009), p. 2164. DOI: [10.1111/j.1365-2966.2009.14482.x](https://doi.org/10.1111/j.1365-2966.2009.14482.x). arXiv: [0810.2250](https://arxiv.org/abs/0810.2250) [astro-ph].
- [162] H. J. VAN EERTEN ET AL.:
‘No visible optical variability from a relativistic blast wave encountering a wind-termination shock’,
in: *Mon. Not. R. Astron. Soc.* 398 (2009), p. 63. DOI: [10.1111/j.1745-3933.2009.00711.x](https://doi.org/10.1111/j.1745-3933.2009.00711.x). arXiv: [0906.3629](https://arxiv.org/abs/0906.3629) [astro-ph.HE].
- [163] HENDRIK VAN EERTEN:
‘Gamma-ray burst afterglow blast waves’,
in: *Int. J. Mod. Phys. D* 27.13 (2018), p. 1842002. DOI: [10.1142/S0218271818420026](https://doi.org/10.1142/S0218271818420026). arXiv: [1801.01848](https://arxiv.org/abs/1801.01848) [astro-ph.HE].
- [164] DAVID EICHLER ET AL.:
‘Nucleosynthesis, neutrino bursts and γ -rays from coalescing neutron stars’,
in: *Nature* 340.6229 (July 1989), pp. 126–128. DOI: [10.1038/340126a0](https://doi.org/10.1038/340126a0).
- [165] DONALD C. ELLISON and GLEN P. DOUBLE:
‘Nonlinear particle acceleration in relativistic shocks’,
in: *Astropart. Phys.* 18 (2002), pp. 213–228. DOI: [10.1016/S0927-6505\(02\)00142-1](https://doi.org/10.1016/S0927-6505(02)00142-1). arXiv: [astro-ph/0202106](https://arxiv.org/abs/astro-ph/0202106).
- [166] DONALD C. ELLISON ET AL.:
‘Particle Acceleration in Supernova Remnants and the Production of Thermal and Nonthermal Radiation’,
in: 661.2 (June 2007), pp. 879–891. DOI: [10.1086/517518](https://doi.org/10.1086/517518). arXiv: [astro-ph/0702674](https://arxiv.org/abs/astro-ph/0702674) [astro-ph].
- [167] IVAN ESTEBAN ET AL.:
‘The fate of hints: updated global analysis of three-flavor neutrino oscillations’,
in: *JHEP* 09 (2020), p. 178. DOI: [10.1007/JHEP09\(2020\)178](https://doi.org/10.1007/JHEP09(2020)178). arXiv: [2007.14792](https://arxiv.org/abs/2007.14792) [hep-ph].
- [168] ABRAHAM D. FALCONE ET AL.:
‘The giant x-ray flare of grb 050502b: evidence for late-time internal engine activity’,
in: *Astrophys. J.* 641 (2006), pp. 1010–1017. DOI: [10.1086/500655](https://doi.org/10.1086/500655). arXiv: [astro-ph/0512615](https://arxiv.org/abs/astro-ph/0512615).
- [169] YIZHONG FAN and TSVI PIRAN:
‘Sub-gev flashes in gamma-ray burst afterglows as probes of underlying bright uv flares’,
in: *Mon. Not. R. Astron. Soc.* 370 (2006), pp. L24–L28. DOI: [10.1111/j.1745-3933.2006.00181.x](https://doi.org/10.1111/j.1745-3933.2006.00181.x). arXiv: [astro-ph/0601619](https://arxiv.org/abs/astro-ph/0601619).

- [170] KE FANG and BRIAN D. METZGER:
'High-Energy Neutrinos from Millisecond Magnetars formed from the Merger of Binary Neutron Stars',
in: *Astrophys. J.* 849.2 (2017), p. 153. DOI: [10.3847/1538-4357/aa8b6a](https://doi.org/10.3847/1538-4357/aa8b6a). arXiv: [1707.04263](https://arxiv.org/abs/1707.04263) [[astro-ph.HE](#)].
- [171] KE FANG and KOHTA MURASE:
'Linking High-Energy Cosmic Particles by Black Hole Jets Embedded in Large-Scale Structures',
in: *Nature Phys.* 14.4 (2018), pp. 396–398. DOI: [10.1038/s41567-017-0025-4](https://doi.org/10.1038/s41567-017-0025-4). arXiv: [1704.00015](https://arxiv.org/abs/1704.00015) [[astro-ph.HE](#)].
- [172] KE FANG ET AL.:
'High-energy Neutrinos and Gamma Rays from Nonrelativistic Shock-powered Transients',
in: *Astrophys. J.* 904.1 (2020), p. 4. DOI: [10.3847/1538-4357/abbc6e](https://doi.org/10.3847/1538-4357/abbc6e). arXiv: [2007.15742](https://arxiv.org/abs/2007.15742) [[astro-ph.HE](#)].
- [173] KE FANG ET AL.:
'Testing the Newborn Pulsar Origin of Ultrahigh Energy Cosmic Rays with EeV Neutrinos',
in: *Phys. Rev. D* 90.10 (2014). [Erratum: *Phys.Rev.D* 92, 129901 (2015)], p. 103005. DOI: [10.1103/PhysRevD.90.103005](https://doi.org/10.1103/PhysRevD.90.103005). arXiv: [1311.2044](https://arxiv.org/abs/1311.2044) [[astro-ph.HE](#)].
- [174] YASAMAN FARZAN and ALEXEI YU. SMIRNOV:
'Coherence and oscillations of cosmic neutrinos',
in: *Nucl. Phys. B* 805 (2008), pp. 356–376. DOI: [10.1016/j.nuclphysb.2008.07.028](https://doi.org/10.1016/j.nuclphysb.2008.07.028). arXiv: [0803.0495](https://arxiv.org/abs/0803.0495) [[hep-ph](#)].
- [175] ENRICO FERMI:
'On the Origin of the Cosmic Radiation',
in: *Phys. Rev.* 75 (8 Apr. 1949), pp. 1169–1174. DOI: [10.1103/PhysRev.75.1169](https://doi.org/10.1103/PhysRev.75.1169). URL: <https://link.aps.org/doi/10.1103/PhysRev.75.1169>.
- [176] ALEXEI V. FILIPPENKO:
'Optical spectra of supernovae',
in: *Ann. Rev. Astron. Astrophys.* 35 (1997), pp. 309–355. DOI: [10.1146/annurev.astro.35.1.309](https://doi.org/10.1146/annurev.astro.35.1.309).
- [177] JUSTIN D. FINKE and CHARLES D. DERMER:
'Cosmic-Ray Electron Evolution in the Supernova Remnant RX J1713.7-3946',
in: *Astrophys. J.* 751.1, 65 (May 2012), p. 65. DOI: [10.1088/0004-637X/751/1/65](https://doi.org/10.1088/0004-637X/751/1/65). arXiv: [1203.4242](https://arxiv.org/abs/1203.4242) [[astro-ph.HE](#)].
- [178] IOULIA FLOROU, MARIA PETROPOULOU and APOSTOLOS MASTICHIADIS:
'A marginally fast-cooling proton-synchrotron model for prompt GRBs',
in: (Feb. 2021). arXiv: [2102.02501](https://arxiv.org/abs/2102.02501) [[astro-ph.HE](#)].
- [179] J. A. FORMAGGIO and G. P. ZELLER:
'From eV to EeV: Neutrino Cross Sections Across Energy Scales',
in: *Rev. Mod. Phys.* 84 (2012), pp. 1307–1341. DOI: [10.1103/RevModPhys.84.1307](https://doi.org/10.1103/RevModPhys.84.1307). arXiv: [1305.7513](https://arxiv.org/abs/1305.7513) [[hep-ex](#)].
- [180] A. FRANCKOWIAK ET AL.:
'Patterns in the Multiwavelength Behavior of Candidate Neutrino Blazars',
in: *Astrophys. J.* 893.2 (2020), p. 162. DOI: [10.3847/1538-4357/ab8307](https://doi.org/10.3847/1538-4357/ab8307). arXiv: [2001.10232](https://arxiv.org/abs/2001.10232) [[astro-ph.HE](#)].

- [181] JOSE FRANCO, FEDERICO FERRINI and GUILLERMO TENORIO-TAGLE:
'Star formation galaxies and interstellar medium',
in: *Proceedings of the 4th EIPC Astrophysical Workshop*. 1992.
- [182] SARA FREDERICK ET AL.:
'A Family Tree of Optical Transients from Narrow-line Seyfert 1 Galaxies',
in: 920.1, 56 (Oct. 2021), p. 56. DOI: [10 . 3847 / 1538 - 4357 / ac110f](https://doi.org/10.3847/1538-4357/ac110f). arXiv: [2010 . 08554](https://arxiv.org/abs/2010.08554)
[\[astro-ph.HE\]](https://arxiv.org/abs/2010.08554).
- [183] U. C. FREMLING ET AL.:
'The Zwicky Transient Facility Bright Transient Survey. I. Spectroscopic Classification and the Redshift Completeness of Local Galaxy Catalogs',
in: *Astrophys. J.* 895.1 (2020), p. 32. DOI: [10 . 3847 / 1538 - 4357 / ab8943](https://doi.org/10.3847/1538-4357/ab8943). arXiv: [1910 . 12973](https://arxiv.org/abs/1910.12973)
[\[astro-ph.HE\]](https://arxiv.org/abs/1910.12973).
- [184] Y. FUKUDA ET AL.:
'Evidence for oscillation of atmospheric neutrinos',
in: *Phys. Rev. Lett.* 81 (1998), pp. 1562–1567. DOI: [10 . 1103 / PhysRevLett . 81 . 1562](https://doi.org/10.1103/PhysRevLett.81.1562). arXiv:
[hep - ex / 9807003](https://arxiv.org/abs/hep-ex/9807003).
- [185] Y. FUKUDA ET AL.:
'Measurement of the solar neutrino energy spectrum using neutrino electron scattering',
in: *Phys. Rev. Lett.* 82 (1999), pp. 2430–2434. DOI: [10 . 1103 / PhysRevLett . 82 . 2430](https://doi.org/10.1103/PhysRevLett.82.2430). arXiv:
[hep - ex / 9812011](https://arxiv.org/abs/hep-ex/9812011).
- [186] GEORGE M. FULLER, ALEXANDER KUSENKO and KALLIOPI PETRAKI:
'Heavy sterile neutrinos and supernova explosions',
in: *Phys. Lett. B* 670 (2009), pp. 281–284. DOI: [10 . 1016 / j . physletb . 2008 . 11 . 016](https://doi.org/10.1016/j.physletb.2008.11.016). arXiv:
[0806 . 4273](https://arxiv.org/abs/0806.4273) [\[astro-ph\]](https://arxiv.org/abs/0806.4273).
- [187] AVISHAY GAL-YAM:
'Luminous Supernovae',
in: *Science* 337 (2012), p. 927. DOI: [10 . 1126 / science . 1203601](https://doi.org/10.1126/science.1203601). arXiv: [1208 . 3217](https://arxiv.org/abs/1208.3217) [\[astro-ph.CO\]](https://arxiv.org/abs/1208.3217).
- [188] AVISHAY GAL-YAM:
'Observational and Physical Classification of Supernovae',
in: *Handbook of Supernovae*. Ed. by Athem W. Alsabti and Paul Murdin. 2017, p. 195. DOI: [10 . 1007 / 978 - 3 - 319 - 21846 - 5 _ 35](https://doi.org/10.1007/978-3-319-21846-5_35).
- [189] AVISHAY GAL-YAM ET AL.:
'On the progenitor of SN 2005gl and the nature of Type II_n supernovae',
in: *Astrophys. J.* 656 (2007), pp. 372–381. DOI: [10 . 1086 / 510523](https://doi.org/10.1086/510523). arXiv: [astro - ph / 0608029](https://arxiv.org/abs/astro-ph/0608029).
- [190] AVISHAY GAL-YAM:
'The Most Luminous Supernovae',
in: *Ann. Rev. Astron. Astrophys.* 57 (2019), pp. 305–333. DOI: [10 . 1146 / annurev - astro - 081817 - 051819](https://doi.org/10.1146/annurev-astro-081817-051819). arXiv: [1812 . 01428](https://arxiv.org/abs/1812.01428) [\[astro-ph.HE\]](https://arxiv.org/abs/1812.01428).
- [191] CHRISTA GALL ET AL.:
'Rapid formation of large dust grains in the luminous supernova 2010jl',
in: 511.7509 (July 2014), pp. 326–329. DOI: [10 . 1038 / nature13558](https://doi.org/10.1038/nature13558). arXiv: [1407 . 4447](https://arxiv.org/abs/1407.4447) [\[astro-ph.SR\]](https://arxiv.org/abs/1407.4447).

- [192] SHAN GAO, KATSUAKI ASANO and PETER MÉSZÁROS:
'High Energy Neutrinos from Dissipative Photospheric Models of Gamma Ray Bursts',
in: *JCAP* 11 (2012), p. 058. DOI: [10.1088/1475-7516/2012/11/058](https://doi.org/10.1088/1475-7516/2012/11/058). arXiv: [1210.1186](https://arxiv.org/abs/1210.1186) [[astro-ph.HE](#)].
- [193] S. GARRAPPA ET AL.:
'Investigation of two Fermi-LAT gamma-ray blazars coincident with high-energy neutrinos detected by IceCube',
in: *Astrophys. J.* 880.2 (2019), p. 103. DOI: [10.3847/1538-4357/ab2ada](https://doi.org/10.3847/1538-4357/ab2ada). arXiv: [1901.10806](https://arxiv.org/abs/1901.10806) [[astro-ph.HE](#)].
- [194] N. GEHRELS, E. RAMIREZ-RUIZ and DEREK B. FOX:
'Gamma-Ray Bursts in the Swift Era',
in: *Ann. Rev. Astron. Astrophys.* 47 (2009), pp. 567–617. DOI: [10.1146/annurev.astro.46.060407.145147](https://doi.org/10.1146/annurev.astro.46.060407.145147). arXiv: [0909.1531](https://arxiv.org/abs/0909.1531) [[astro-ph.HE](#)].
- [195] N. GEHRELS ET AL.:
'The Swift Gamma-Ray Burst Mission',
in: 611 (Aug. 2004), pp. 1005–1020. DOI: [10.1086/422091](https://doi.org/10.1086/422091).
- [196] G. GHIRLANDA ET AL.:
'Bulk Lorentz factors of Gamma-Ray Bursts',
in: *Astron. Astrophys.* 609 (2018), A112. DOI: [10.1051/0004-6361/201731598](https://doi.org/10.1051/0004-6361/201731598). arXiv: [1711.06257](https://arxiv.org/abs/1711.06257) [[astro-ph.HE](#)].
- [197] G. GHISELLINI, G. GHIRLANDA and L. NAVA:
'GeV emission from Gamma Ray Bursts: a radiative fireball?',
in: *Mon. Not. R. Astron. Soc.* 403 (2010), p. 926. DOI: [10.1111/j.1365-2966.2009.16171.x](https://doi.org/10.1111/j.1365-2966.2009.16171.x). arXiv: [0910.2459](https://arxiv.org/abs/0910.2459) [[astro-ph.HE](#)].
- [198] G. GHISELLINI ET AL.:
'Proton-synchrotron as the radiation mechanism of the prompt emission of gamma-ray bursts?',
in: *Astron. Astrophys.* 636 (2020), A82. DOI: [10.1051/0004-6361/201937244](https://doi.org/10.1051/0004-6361/201937244). arXiv: [1912.02185](https://arxiv.org/abs/1912.02185) [[astro-ph.HE](#)].
- [199] GABRIELE GHISELLINI:
Radiative Processes in High Energy Astrophysics,
vol. 873. 2013. DOI: [10.1007/978-3-319-00612-3](https://doi.org/10.1007/978-3-319-00612-3).
- [200] DIMITRIOS GIANNIOS:
'Prompt emission spectra from the photosphere of a GRB',
in: *Astron. Astrophys.* 457 (2006), pp. 763–770. DOI: [10.1051/0004-6361:20065000](https://doi.org/10.1051/0004-6361:20065000). arXiv: [astro-ph/0602397](https://arxiv.org/abs/astro-ph/0602397).
- [201] DIMITRIOS GIANNIOS and HENK C. SPRUIT:
'Spectral and timing properties of a dissipative GRB photosphere',
in: *Astron. Astrophys.* 469 (2007), pp. 1–9. DOI: [10.1051/0004-6361:20066739](https://doi.org/10.1051/0004-6361:20066739). arXiv: [astro-ph/0611385](https://arxiv.org/abs/astro-ph/0611385).
- [202] RAMANDEEP GILL, JONATHAN GRANOT and PAZ BENIAMINI:
'GRB Spectrum from Gradual Dissipation in a Magnetized Outflow',
in: *Mon. Not. Roy. Astron. Soc.* 499.1 (2020), pp. 1356–1372. DOI: [10.1093/mnras/staa2870](https://doi.org/10.1093/mnras/staa2870). arXiv: [2008.10729](https://arxiv.org/abs/2008.10729) [[astro-ph.HE](#)].

- [203] RAMANDEEP GILL and CHRISTOPHER THOMPSON:
‘Non-thermal Gamma-ray Emission from Delayed Pair Breakdown in a Magnetized and Photon-rich Outflow’,
in: *Astrophys. J.* 796.2 (2014), p. 81. DOI: [10.1088/0004-637X/796/2/81](https://doi.org/10.1088/0004-637X/796/2/81). arXiv: [1406.4774](https://arxiv.org/abs/1406.4774) [[astro-ph.HE](#)].
- [204] SIVAN GINZBURG and SHMUEL BALBERG:
‘Superluminous Light Curves from Supernovae Exploding in a Dense Wind’,
in: *Astrophys. J.* 757 (2012), p. 178. DOI: [10.1088/0004-637X/757/2/178](https://doi.org/10.1088/0004-637X/757/2/178). arXiv: [1205.3455](https://arxiv.org/abs/1205.3455) [[astro-ph.SR](#)].
- [205] P. GIOMMI ET AL.:
‘3HSP J095507.9+355101: a flaring extreme blazar coincident in space and time with IceCube-200107A’,
in: *Astron. Astrophys.* 640 (2020), p. L4. DOI: [10.1051/0004-6361/202038423](https://doi.org/10.1051/0004-6361/202038423). arXiv: [2003.06405](https://arxiv.org/abs/2003.06405) [[astro-ph.HE](#)].
- [206] SHELDON L. GLASHOW:
‘Resonant Scattering of Antineutrinos’,
in: *Phys. Rev.* 118 (1960), pp. 316–317. DOI: [10.1103/PhysRev.118.316](https://doi.org/10.1103/PhysRev.118.316).
- [207] J. GOODMAN:
‘Are gamma-ray bursts optically thick?’,
in: *Astrophys. J. Lett.* 308 (1986), pp. L47–L50. DOI: [10.1086/184741](https://doi.org/10.1086/184741).
- [208] P. W. GORHAM ET AL.:
‘Observational Constraints on the Ultra-high Energy Cosmic Neutrino Flux from the Second Flight of the ANITA Experiment’,
in: *Phys. Rev. D* 82 (2010). [Erratum: *Phys.Rev.D* 85, 049901 (2012)], p. 022004. DOI: [10.1103/PhysRevD.82.022004](https://doi.org/10.1103/PhysRevD.82.022004). arXiv: [1003.2961](https://arxiv.org/abs/1003.2961) [[astro-ph.HE](#)].
- [209] P. W. GORHAM ET AL.:
‘The Antarctic Impulsive Transient Antenna Ultra-high Energy Neutrino Detector Design, Performance, and Sensitivity for 2006-2007 Balloon Flight’,
in: *Astropart. Phys.* 32 (2009), pp. 10–41. DOI: [10.1016/j.astropartphys.2009.05.003](https://doi.org/10.1016/j.astropartphys.2009.05.003). arXiv: [0812.1920](https://arxiv.org/abs/0812.1920) [[astro-ph](#)].
- [210] ORE GOTTLIEB, AMIR LEVINSON and EHUD NAKAR:
‘High efficiency photospheric emission entailed by formation of a collimation shock in gamma-ray bursts’,
in: *Mon. Not. Roy. Astron. Soc.* 488.1 (2019), pp. 1416–1426. DOI: [10.1093/mnras/stz1828](https://doi.org/10.1093/mnras/stz1828). arXiv: [1904.07244](https://arxiv.org/abs/1904.07244) [[astro-ph.HE](#)].
- [211] JONATHAN GRANOT:
‘Interaction of a highly magnetized impulsive relativistic flow with an external medium’,
in: *Mon. Not. Roy. Astron. Soc.* 421 (2012), pp. 2442–2466. DOI: [10.1111/j.1365-2966.2012.20473.x](https://doi.org/10.1111/j.1365-2966.2012.20473.x). arXiv: [1109.5314](https://arxiv.org/abs/1109.5314) [[astro-ph.HE](#)].
- [212] JONATHAN GRANOT, EHUD NAKAR and TSVI PIRAN:
‘The variable light curve of GRB 030329: The case for refreshed shocks’,
in: *Nature* 426 (2003), pp. 138–139. DOI: [10.1038/426138a](https://doi.org/10.1038/426138a). arXiv: [astro-ph/0304563](https://arxiv.org/abs/astro-ph/0304563).
- [213] GRB WEB CATALOG,
https://icecube.wisc.edu/~grbweb_public/.

- [214] J. GREINER ET AL.:
'GROND - a 7-channel imager',
in: *Publ. Astron. Soc. Pac.* 120 (2008), p. 405. DOI: [10.1086/587032](https://doi.org/10.1086/587032). arXiv: [0801.4801](https://arxiv.org/abs/0801.4801) [astro-ph].
- [215] J. GREINER ET AL.:
'The unusual afterglow of the Gamma-Ray Burst 100621A',
in: *Astron. Astrophys.* 560 (2013), A70. DOI: [10.1051/0004-6361/201321284](https://doi.org/10.1051/0004-6361/201321284). arXiv: [1304.5852](https://arxiv.org/abs/1304.5852) [astro-ph.HE].
- [216] J. GREINER ET AL.:
'The nature of "dark" gamma-ray bursts',
in: *Astronomy and Astrophysics* 526, A30 (Feb. 2011), A30. DOI: [10.1051/0004-6361/201015458](https://doi.org/10.1051/0004-6361/201015458). arXiv: [1011.0618](https://arxiv.org/abs/1011.0618) [astro-ph.HE].
- [217] V. N. GRIBOV and B. PONTECORVO:
'Neutrino astronomy and lepton charge',
in: *Phys. Lett. B* 28 (1969), p. 493. DOI: [10.1016/0370-2693\(69\)90525-5](https://doi.org/10.1016/0370-2693(69)90525-5).
- [218] DAVID GRUBER ET AL.:
'The Fermi GBM Gamma-Ray Burst Spectral Catalog: Four Years Of Data',
in: *Astrophys. J. Suppl.* 211 (2014), p. 12. DOI: [10.1088/0067-0049/211/1/12](https://doi.org/10.1088/0067-0049/211/1/12). arXiv: [1401.5069](https://arxiv.org/abs/1401.5069) [astro-ph.HE].
- [219] CLAIRE GUÉPIN ET AL.:
'Ultra-High Energy Cosmic Rays and Neutrinos from Tidal Disruptions by Massive Black Holes',
in: *Astron. Astrophys.* 616 (2018). [Erratum: *Astron. Astrophys.* 636, C3 (2020)], A179. DOI: [10.1051/0004-6361/201732392](https://doi.org/10.1051/0004-6361/201732392). arXiv: [1711.11274](https://arxiv.org/abs/1711.11274) [astro-ph.HE].
- [220] D. GUETTA, M. SPADA and E. WAXMAN:
'Efficiency and spectrum of internal gamma-ray burst shocks',
in: *Astrophys. J.* 557 (2001), p. 399. DOI: [10.1086/321543](https://doi.org/10.1086/321543). arXiv: [astro-ph/0011170](https://arxiv.org/abs/astro-ph/0011170).
- [221] DAFNE GUETTA ET AL.:
'Neutrinos from individual gamma-ray bursts in the BATSE catalog',
in: *Astropart. Phys.* 20 (2004), pp. 429–455. DOI: [10.1016/S0927-6505\(03\)00211-1](https://doi.org/10.1016/S0927-6505(03)00211-1). arXiv: [astro-ph/0302524](https://arxiv.org/abs/astro-ph/0302524).
- [222] C. GUIDORZI ET AL.:
'A deep study of the high-energy transient sky',
in: *Exper. Astron.* 51.3 (2021), pp. 1203–1223. DOI: [10.1007/s10686-021-09725-9](https://doi.org/10.1007/s10686-021-09725-9).
- [223] JAMES GUILLOCHON ET AL.:
'MOSFIT: Modular Open-Source Fitter for Transients',
in: *Astrophys. J. Suppl.* 236.1 (2018), p. 6. DOI: [10.3847/1538-4365/aab761](https://doi.org/10.3847/1538-4365/aab761). arXiv: [1710.02145](https://arxiv.org/abs/1710.02145) [astro-ph.IM].
- [224] S. GUIRIEC ET AL.:
'Towards a Better Understanding of the GRB Phenomenon: a New Model for GRB Prompt Emission and its effects on the New $L_i^{NT}-E_{peak,i}^{rest,NT}$ relation',
in: *Astrophys. J.* 807.2 (2015), p. 148. DOI: [10.1088/0004-637X/807/2/148](https://doi.org/10.1088/0004-637X/807/2/148). arXiv: [1501.07028](https://arxiv.org/abs/1501.07028) [astro-ph.HE].

- [225] S. GUIRIEC ET AL.:
'A Unified Model for GRB Prompt Emission from Optical to γ -Rays; Exploring GRBs as Standard Candle',
in: *Astrophys. J. Lett.* 831.1 (2016), p. L8. DOI: [10 . 3847 / 2041 - 8205 / 831 / 1 / L8](https://doi.org/10.3847/2041-8205/831/1/L8). arXiv: [1606.07193](https://arxiv.org/abs/1606.07193) [astro-ph.HE].
- [226] FAN GUO ET AL.:
'Efficient Production of High-energy Nonthermal Particles During Magnetic Reconnection in a Magnetically Dominated Ion–electron Plasma',
in: *Astrophys. J. Lett.* 818.1 (2016), p. L9. DOI: [10 . 3847 / 2041 - 8205 / 818 / 1 / L9](https://doi.org/10.3847/2041-8205/818/1/L9). arXiv: [1511.01434](https://arxiv.org/abs/1511.01434) [astro-ph.HE].
- [227] FAN GUO ET AL.:
'Formation of Hard Power Laws in the Energetic Particle Spectra Resulting from Relativistic Magnetic Reconnection',
in: *Phys. Rev. Lett.* 113 (15 Oct. 2014), p. 155005. DOI: [10 . 1103 / PhysRevLett . 113 . 155005](https://doi.org/10.1103/PhysRevLett.113.155005). URL: <https://link.aps.org/doi/10.1103/PhysRevLett.113.155005>.
- [228] FAN GUO ET AL.:
'Formation of Hard Power-laws in the Energetic Particle Spectra Resulting from Relativistic Magnetic Reconnection',
in: *Phys. Rev. Lett.* 113 (2014), p. 155005. DOI: [10 . 1103 / PhysRevLett . 113 . 155005](https://doi.org/10.1103/PhysRevLett.113.155005). arXiv: [1405.4040](https://arxiv.org/abs/1405.4040) [astro-ph.HE].
- [229] GANG GUO, YONG-ZHONG QIAN and MENG-RU WU:
'Neutrino Production Associated with Late Bumps in Gamma-Ray Bursts and Potential Contribution to Diffuse Flux at IceCube',
in: *Astrophys. J.* 890 (2020), p. 83. DOI: [10 . 3847 / 1538 - 4357 / ab6bcf](https://doi.org/10.3847/1538-4357/ab6bcf). arXiv: [1911.07568](https://arxiv.org/abs/1911.07568) [astro-ph.HE].
- [230] NAYANTARA GUPTA and BING ZHANG:
'Neutrino Spectra from Low and High Luminosity Populations of Gamma Ray Bursts',
in: *Astropart. Phys.* 27 (2007), pp. 386–391. DOI: [10 . 1016 / j . astropartphys . 2007 . 01 . 004](https://doi.org/10.1016/j.astropartphys.2007.01.004). arXiv: [astro-ph/0606744](https://arxiv.org/abs/astro-ph/0606744).
- [231] NAYANTARA GUPTA and BING ZHANG:
'Prompt Emission of High Energy Photons from Gamma Ray Bursts',
in: *Mon. Not. Roy. Astron. Soc.* 380 (2007), p. 78. DOI: [10 . 1111 / j . 1365 - 2966 . 2007 . 12051 . x](https://doi.org/10.1111/j.1365-2966.2007.12051.x). arXiv: [0704.1329](https://arxiv.org/abs/0704.1329) [astro-ph].
- [232] FRANCIS HALZEN and ALI KHEIRANDISH:
'IceCube and High-Energy Cosmic Neutrinos',
in: *arXiv e-prints*, arXiv:2202.00694 (Feb. 2022), arXiv:2202.00694. arXiv: [2202 . 00694](https://arxiv.org/abs/2202.00694) [astro-ph.HE].
- [233] KELLY M. HAMBLETON ET AL.:
'Rubin Observatory LSST Transients and Variable Stars Roadmap',
in: *arXiv e-prints*, arXiv:2208.04499 (Aug. 2022), arXiv:2208.04499. arXiv: [2208 . 04499](https://arxiv.org/abs/2208.04499) [astro-ph.IM].
- [234] KIMITAKE HAYASAKI:
'Neutrinos from tidal disruption events',
in: (Feb. 2021). DOI: [10 . 1038 / s41550 - 021 - 01309 - z](https://doi.org/10.1038/s41550-021-01309-z). arXiv: [2102.11879](https://arxiv.org/abs/2102.11879) [astro-ph.HE].

- [235] HAO-NING HE ET AL.:
‘Icecube non-detection of GRBs: Constraints on the fireball properties’,
in: *Astrophys. J.* 752 (2012), p. 29. DOI: [10.1088/0004-637X/752/1/29](https://doi.org/10.1088/0004-637X/752/1/29). arXiv: [1204.0857](https://arxiv.org/abs/1204.0857) [[astro-ph.HE](#)].
- [236] A. HEGER ET AL.:
‘How Massive Single Stars End Their Life’,
in: 591.1 (July 2003), pp. 288–300. DOI: [10.1086/375341](https://doi.org/10.1086/375341). arXiv: [astro-ph/0212469](https://arxiv.org/abs/astro-ph/0212469) [[astro-ph](#)].
- [237] JONAS HEINZE ET AL.:
‘Systematic parameter space study for the UHECR origin from GRBs in models with multiple internal shocks’,
in: *Mon. Not. Roy. Astron. Soc.* 498.4 (2020), pp. 5990–6004. DOI: [10.1093/mnras/staa2751](https://doi.org/10.1093/mnras/staa2751). arXiv: [2006.14301](https://arxiv.org/abs/2006.14301) [[astro-ph.HE](#)].
- [238] JASON T. HINKLE ET AL.:
‘Discovery and follow-up of ASASSN-19dj: an X-ray and UV luminous TDE in an extreme post-starburst galaxy’,
in: 500.2 (Jan. 2021), pp. 1673–1696. DOI: [10.1093/mnras/staa3170](https://doi.org/10.1093/mnras/staa3170). arXiv: [2006.06690](https://arxiv.org/abs/2006.06690) [[astro-ph.HE](#)].
- [239] K. HIRATA ET AL.:
‘Observation of a neutrino burst from the supernova SN1987A’,
in: 58.14 (Apr. 1987), pp. 1490–1493. DOI: [10.1103/PhysRevLett.58.1490](https://doi.org/10.1103/PhysRevLett.58.1490).
- [240] THOMAS W. -S. HOLOIEN ET AL.:
‘Discovery and Early Evolution of ASASSN-19bt, the First TDE Detected by TESS’,
in: 883.2, 111 (Oct. 2019), p. 111. DOI: [10.3847/1538-4357/ab3c66](https://doi.org/10.3847/1538-4357/ab3c66). arXiv: [1904.09293](https://arxiv.org/abs/1904.09293) [[astro-ph.HE](#)].
- [241] S. HÜMMER ET AL.:
‘Simplified models for photohadronic interactions in cosmic accelerators’,
in: *Astrophys. J.* 721 (2010), pp. 630–652. DOI: [10.1088/0004-637X/721/1/630](https://doi.org/10.1088/0004-637X/721/1/630). arXiv: [1002.1310](https://arxiv.org/abs/1002.1310) [[astro-ph.HE](#)].
- [242] SVENJA HÜMMER, PHILIPP BAERWALD and WALTER WINTER:
‘Neutrino Emission from Gamma-Ray Burst Fireballs, Revised’,
in: *Phys. Rev. Lett.* 108 (2012), p. 231101. DOI: [10.1103/PhysRevLett.108.231101](https://doi.org/10.1103/PhysRevLett.108.231101). arXiv: [1112.1076](https://arxiv.org/abs/1112.1076) [[astro-ph.HE](#)].
- [243] T. HUNG ET AL.:
‘Revisiting Optical Tidal Disruption Events with iPTF16axa’,
in: 842.1, 29 (June 2017), p. 29. DOI: [10.3847/1538-4357/aa7337](https://doi.org/10.3847/1538-4357/aa7337). arXiv: [1703.01299](https://arxiv.org/abs/1703.01299) [[astro-ph.HE](#)].
- [244] TIARA HUNG ET AL.:
‘Discovery of a Fast Iron Low-ionization Outflow in the Early Evolution of the Nearby Tidal Disruption Event AT 2019qiz’,
in: 917.1, 9 (Aug. 2021), p. 9. DOI: [10.3847/1538-4357/abf4c3](https://doi.org/10.3847/1538-4357/abf4c3). arXiv: [2011.01593](https://arxiv.org/abs/2011.01593) [[astro-ph.HE](#)].

- [245] TIARA HUNG ET AL.:
'Double-peaked Balmer Emission Indicating Prompt Accretion Disk Formation in an X-Ray Faint Tidal Disruption Event',
in: 903.1, 31 (Nov. 2020), p. 31. DOI: [10 . 3847 / 1538 - 4357 / abb606](https://doi.org/10.3847/1538-4357/abb606). arXiv: [2003 . 09427](https://arxiv.org/abs/2003.09427) [[astro-ph.HE](#)].
- [246] ICECUBE COLLABORATION:
'IceCube-200530A - IceCube observation of a high-energy neutrino candidate event',
in: *GRB Coordinates Network* 27865 (May 2020), p. 1.
- [247] KUNIHITO IOKA, SHIHO KOBAYASHI and BING ZHANG:
'Long-acting engine or strong temporal anisotropy inferred from variabilities of gamma-ray burst afterglows',
in: *Astrophys. J.* 631 (2005), p. 429. DOI: [10 . 1086 / 432567](https://doi.org/10.1086/432567). arXiv: [astro-ph/0409376](https://arxiv.org/abs/astro-ph/0409376).
- [248] P. JAKOBSSON ET AL.:
'The Optically Unbiased GRB Host (TOUGH) Survey. III. Redshift Distribution',
in: *Astrophys. J.* 752.1, 62 (2012), p. 62. DOI: [10 . 1088 / 0004 - 637X / 752 / 1 / 62](https://doi.org/10.1088/0004-637X/752/1/62). arXiv: [1205 . 3490](https://arxiv.org/abs/1205.3490) [[astro-ph.CO](#)].
- [249] H. -TH. JANKA:
'Neutrino Emission from Supernovae',
in: (Feb. 2017). DOI: [10 . 1007 / 978 - 3 - 319 - 21846 - 5 _4](https://doi.org/10.1007/978-3-319-21846-5_4). arXiv: [1702 . 08713](https://arxiv.org/abs/1702.08713) [[astro-ph.HE](#)].
- [250] HANS-THOMAS JANKA:
'Explosion Mechanisms of Core-Collapse Supernovae',
in: *Ann. Rev. Nucl. Part. Sci.* 62 (2012), pp. 407–451. DOI: [10 . 1146 / annurev - nucl - 102711 - 094901](https://doi.org/10.1146/annurev-nucl-102711-094901). arXiv: [1206 . 2503](https://arxiv.org/abs/1206.2503) [[astro-ph.SR](#)].
- [251] J. JAPELJ ET AL.:
'Phenomenology of Reverse-shock Emission in the Optical Afterglows of Gamma-Ray Bursts',
in: *Astrophys. J.* 785.2, 84 (2014), p. 84. DOI: [10 . 1088 / 0004 - 637X / 785 / 2 / 84](https://doi.org/10.1088/0004-637X/785/2/84). arXiv: [1402 . 3701](https://arxiv.org/abs/1402.3701) [[astro-ph.HE](#)].
- [252] FRANK C. JONES:
'Inverse Compton Scattering of Cosmic-Ray Electrons',
in: *Phys. Rev.* 137 (5B Mar. 1965), B1306–B1311. DOI: [10 . 1103 / PhysRev . 137 . B1306](https://doi.org/10.1103/PhysRev.137.B1306). URL: <https://link.aps.org/doi/10.1103/PhysRev.137.B1306>.
- [253] P. G. JONKER ET AL.:
'Implications from Late-time X-Ray Detections of Optically Selected Tidal Disruption Events: State Changes, Unification, and Detection Rates',
in: 889.2, 166 (Feb. 2020), p. 166. DOI: [10 . 3847 / 1538 - 4357 / ab659c](https://doi.org/10.3847/1538-4357/ab659c). arXiv: [1906 . 12236](https://arxiv.org/abs/1906.12236) [[astro-ph.HE](#)].
- [254] M. KADLER ET AL.:
'Coincidence of a high-fluence blazar outburst with a PeV-energy neutrino event',
in: *Nature Phys.* 12.8 (2016), pp. 807–814. DOI: [10 . 1038 / NPHYS3715](https://doi.org/10.1038/NPHYS3715). arXiv: [1602 . 02012](https://arxiv.org/abs/1602.02012) [[astro-ph.HE](#)].
- [255] E. KANKARE ET AL.:
'Search for transient optical counterparts to high-energy IceCube neutrinos with Pan-STARRS1',
in: *Astron. Astrophys.* 626 (2019), A117. DOI: [10 . 1051 / 0004 - 6361 / 201935171](https://doi.org/10.1051/0004-6361/201935171). arXiv: [1901 . 11080](https://arxiv.org/abs/1901.11080) [[astro-ph.HE](#)].

- [256] DANIEL KASEN and S. E. WOOSLEY:
'Type II Supernovae: Model Light Curves and Standard Candle Relationships',
in: *Astrophys. J.* 703 (2009), p. 2205. DOI: [10.1088/0004-637X/703/2/2205](https://doi.org/10.1088/0004-637X/703/2/2205). arXiv: [0910.1590](https://arxiv.org/abs/0910.1590) [astro-ph.CO].
- [257] KAZUMI KASHIYAMA, KOHTA MURASE and PETER MÉSZÁROS:
'Neutron-Proton-Converter Acceleration Mechanism at Subphotospheres of Relativistic Outflows',
in: *Phys. Rev. Lett.* 111 (2013), p. 131103. DOI: [10.1103/PhysRevLett.111.131103](https://doi.org/10.1103/PhysRevLett.111.131103). arXiv: [1304.1945](https://arxiv.org/abs/1304.1945) [astro-ph.HE].
- [258] BOAZ KATZ, NIR SAPIR and ELI WAXMAN:
'X-rays, gamma-rays and neutrinos from collisionless shocks in supernova wind breakouts',
in: *arXiv e-prints*, arXiv:1106.1898 (June 2011), arXiv:1106.1898. arXiv: [1106.1898](https://arxiv.org/abs/1106.1898) [astro-ph.HE].
- [259] J. I. KATZ and T. PIRAN:
'Persistent Counterparts to Gamma-Ray Bursts',
in: *Astrophys. J.* 490.2 (1997), pp. 772–778. DOI: [10.1086/304913](https://doi.org/10.1086/304913).
- [260] BORIS KAYSER:
'On the quantum mechanics of neutrino oscillation',
in: *Phys. Rev. D* 24 (1 July 1981), pp. 110–116. DOI: [10.1103/PhysRevD.24.110](https://doi.org/10.1103/PhysRevD.24.110). URL: <https://link.aps.org/doi/10.1103/PhysRevD.24.110>.
- [261] S. R. KELNER and F. A. AHARONIAN:
'Energy spectra of gamma-rays, electrons and neutrinos produced at interactions of relativistic protons with low energy radiation',
in: *Phys. Rev. D* 78 (2008). [Erratum: *Phys.Rev.D* 82, 099901 (2010)], p. 034013. DOI: [10.1103/PhysRevD.82.099901](https://doi.org/10.1103/PhysRevD.82.099901). arXiv: [0803.0688](https://arxiv.org/abs/0803.0688) [astro-ph].
- [262] S. R. KELNER, FELEX A. AHARONIAN and V. V. BUGAYOV:
'Energy spectra of gamma-rays, electrons and neutrinos produced at proton-proton interactions in the very high energy regime',
in: *Phys. Rev. D* 74 (2006). [Erratum: *Phys.Rev.D* 79, 039901 (2009)], p. 034018. DOI: [10.1103/PhysRevD.74.034018](https://doi.org/10.1103/PhysRevD.74.034018). arXiv: [astro-ph/0606058](https://arxiv.org/abs/astro-ph/0606058).
- [263] URI KESHET and ELI WAXMAN:
'The Spectrum of particles accelerated in relativistic, collisionless shocks',
in: *Phys. Rev. Lett.* 94 (2005), p. 111102. DOI: [10.1103/PhysRevLett.94.111102](https://doi.org/10.1103/PhysRevLett.94.111102). arXiv: [astro-ph/0408489](https://arxiv.org/abs/astro-ph/0408489).
- [264] ALI KHEIRANDISH and KOHTA MURASE:
'Detecting High-Energy Neutrino Minibursts from Local Supernovae with Multiple Neutrino Observatories',
in: *arXiv e-prints*, arXiv:2204.08518 (Apr. 2022), arXiv:2204.08518. arXiv: [2204.08518](https://arxiv.org/abs/2204.08518) [astro-ph.HE].
- [265] A. VON KIENLIN ET AL.:
'The Fourth Fermi-GBM Gamma-Ray Burst Catalog: A Decade of Data',
in: *Astrophys. J.* 893 (2020), p. 46. DOI: [10.3847/1538-4357/ab7a18](https://doi.org/10.3847/1538-4357/ab7a18). arXiv: [2002.11460](https://arxiv.org/abs/2002.11460) [astro-ph.HE].

- [266] PATRICK KILIAN ET AL.:
'Exploring the acceleration mechanisms for particle injection and power-law formation during trans-relativistic magnetic reconnection',
in: *Astrophys. J.* 899.2 (2020), p. 151. DOI: [10.3847/1538-4357/aba1e9](https://doi.org/10.3847/1538-4357/aba1e9). arXiv: [2001.02732](https://arxiv.org/abs/2001.02732) [astro-ph.HE].
- [267] J. G. KIRK, P. DUFFY and Y. A. GALLANT:
'Stochastic particle acceleration at shocks in the presence of braided magnetic fields',
in: 314 (Oct. 1996), pp. 1010–1016. DOI: [10.48550/arXiv.astro-ph/9604056](https://doi.org/10.48550/arXiv.astro-ph/9604056). arXiv: [astro-ph/9604056](https://arxiv.org/abs/astro-ph/9604056) [astro-ph].
- [268] J. G. KIRK ET AL.:
'Particle acceleration at ultrarelativistic shocks: an eigenfunction method',
in: *Astrophys. J.* 542 (2000), p. 235. DOI: [10.1086/309533](https://doi.org/10.1086/309533). arXiv: [astro-ph/0005222](https://arxiv.org/abs/astro-ph/0005222).
- [269] RAY W. KLEBSADEL, IAN B. STRONG and ROY A. OLSON:
'Observations of Gamma-Ray Bursts of Cosmic Origin',
in: *Astrophys. J. Lett.* 182 (1973), pp. L85–L88. DOI: [10.1086/181225](https://doi.org/10.1086/181225).
- [270] SHIHO KOBAYASHI and PETER MESZAROS:
'Gravitational radiation from gamma-ray burst progenitors',
in: *Astrophys. J.* 589 (2003), pp. 861–870. DOI: [10.1086/374733](https://doi.org/10.1086/374733). arXiv: [astro-ph/0210211](https://arxiv.org/abs/astro-ph/0210211).
- [271] SHIHO KOBAYASHI, TSVI PIRAN and RE'EM SARI:
'Can internal shocks produce the variability in GRBs?',
in: *Astrophys. J.* 490 (1997), pp. 92–98. DOI: [10.1086/512791](https://doi.org/10.1086/512791). arXiv: [astro-ph/9705013](https://arxiv.org/abs/astro-ph/9705013).
- [272] SHIHO KOBAYASHI, TSVI PIRAN and RE'EM SARI:
'Hydrodynamics of a relativistic fireball: the complete evolution',
in: *Astrophys. J.* 513 (1999), p. 669. DOI: [10.1086/306868](https://doi.org/10.1086/306868). arXiv: [astro-ph/9803217](https://arxiv.org/abs/astro-ph/9803217).
- [273] C. S. KOCHANEK ET AL.:
'The All-Sky Automated Survey for Supernovae (ASAS-SN) Light Curve Server v1.0',
in: 129.980 (Oct. 2017), p. 104502. DOI: [10.1088/1538-3873/aa80d9](https://doi.org/10.1088/1538-3873/aa80d9). arXiv: [1706.07060](https://arxiv.org/abs/1706.07060) [astro-ph.SR].
- [274] K. KODAMA ET AL.:
'Observation of tau neutrino interactions',
in: *Phys. Lett. B* 504 (2001), pp. 218–224. DOI: [10.1016/S0370-2693\(01\)00307-0](https://doi.org/10.1016/S0370-2693(01)00307-0). arXiv: [hep-ex/0012035](https://arxiv.org/abs/hep-ex/0012035).
- [275] K. KOTERA, D. ALLARD and A. V. OLINTO:
'Cosmogenic Neutrinos: parameter space and detectability from PeV to ZeV',
in: *JCAP* 10 (2010), p. 013. DOI: [10.1088/1475-7516/2010/10/013](https://doi.org/10.1088/1475-7516/2010/10/013). arXiv: [1009.1382](https://arxiv.org/abs/1009.1382) [astro-ph.HE].
- [276] CHRYSsa KOUVELIOTOU ET AL.:
'Identification of two classes of gamma-ray bursts',
in: *Astrophys. J. Lett.* 413 (1993), pp. L101–104. DOI: [10.1086/186969](https://doi.org/10.1086/186969).
- [277] F. KRAUß ET AL.:
'Fermi/LAT counterparts of IceCube neutrinos above 100 TeV',
in: *Astron. Astrophys.* 620 (2018), A174. DOI: [10.1051/0004-6361/201834183](https://doi.org/10.1051/0004-6361/201834183). arXiv: [1810.08482](https://arxiv.org/abs/1810.08482) [astro-ph.HE].

- [278] T. KRÜHLER ET AL.:
‘Correlated Optical and X-Ray Flares in the Afterglow of XRF 071031’,
in: *Astrophys. J.* 697.1 (2009), pp. 758–768. DOI: [10.1088/0004-637X/697/1/758](https://doi.org/10.1088/0004-637X/697/1/758). arXiv: [0903.1184](https://arxiv.org/abs/0903.1184) [astro-ph.HE].
- [279] PAWAN KUMAR and RODOLFO BARNIOL DURAN:
‘On the generation of high energy photons detected by the Fermi Satellite from gamma-ray bursts’,
in: *Mon. Not. Roy. Astron. Soc.* 400 (2009), p. 75. DOI: [10.1111/j.1745-3933.2009.00766.x](https://doi.org/10.1111/j.1745-3933.2009.00766.x). arXiv: [0905.2417](https://arxiv.org/abs/0905.2417) [astro-ph.HE].
- [280] PAWAN KUMAR and TSVI PIRAN:
‘Some observational consequences of grb shock models’,
in: *Astrophys. J.* 523 (1999), p. 286. DOI: [10.1086/308537](https://doi.org/10.1086/308537). arXiv: [astro-ph/9906002](https://arxiv.org/abs/astro-ph/9906002).
- [281] PAWAN KUMAR and BING ZHANG:
‘The physics of gamma-ray bursts & relativistic jets’,
in: *Phys. Rept.* 561 (2014), pp. 1–109. DOI: [10.1016/j.physrep.2014.09.008](https://doi.org/10.1016/j.physrep.2014.09.008). arXiv: [1410.0679](https://arxiv.org/abs/1410.0679) [astro-ph.HE].
- [282] TANMOY LASKAR ET AL.:
‘A VLA Study of High-redshift GRBs. I. Multiwavelength Observations and Modeling of GRB 140311A’,
in: *Astrophys. J.* 858.1 (2018), p. 65. DOI: [10.3847/1538-4357/aab8f5](https://doi.org/10.3847/1538-4357/aab8f5). arXiv: [1707.05358](https://arxiv.org/abs/1707.05358) [astro-ph.HE].
- [283] D. LAZZATI ET AL.:
‘Photospheric emission as the dominant radiation mechanism in long-duration gamma-ray bursts’,
in: *Astrophys. J.* 765 (2013), p. 103. DOI: [10.1088/0004-637X/765/2/103](https://doi.org/10.1088/0004-637X/765/2/103). arXiv: [1301.3920](https://arxiv.org/abs/1301.3920) [astro-ph.HE].
- [284] DAVIDE LAZZATI, BRIAN J. MORSONY and MITCH BEGELMAN:
‘Very high efficiency photospheric emission in long duration gamma-ray bursts’,
in: *Astrophys. J. Lett.* 700 (2009), pp. L47–L50. DOI: [10.1088/0004-637X/700/1/L47](https://doi.org/10.1088/0004-637X/700/1/L47). arXiv: [0904.2779](https://arxiv.org/abs/0904.2779) [astro-ph.HE].
- [285] DAVIDE LAZZATI ET AL.:
‘The Afterglow of GRB 021004: Surfing on density waves’,
in: *Astron. Astrophys.* 396 (2002), pp. L5–L10. DOI: [10.1051/0004-6361:20021618](https://doi.org/10.1051/0004-6361:20021618). arXiv: [astro-ph/0210333](https://arxiv.org/abs/astro-ph/0210333).
- [286] LAZZATI, D. ET AL.:
‘The optical afterglow of GRB 000911: Evidence for an associated supernova?’,
in: *Astron. Astrophys.* 378.3 (2001), pp. 996–1002. DOI: [10.1051/0004-6361:20011282](https://doi.org/10.1051/0004-6361:20011282). URL: <https://doi.org/10.1051/0004-6361:20011282>.
- [287] J. M. LEBLANC and J. R. WILSON:
‘A Numerical Example of the Collapse of a Rotating Magnetized Star’,
in: *Astrophys. J.* 161 (1970), p. 541. DOI: [10.1086/150558](https://doi.org/10.1086/150558).
- [288] WEI-HUA LEI ET AL.:
‘Hyperaccreting Black Hole as Gamma-Ray Burst Central Engine. II. Temporal Evolution of the Central Engine Parameters during the Prompt and Afterglow Phases’,
in: *Astrophys. J.* 849.1 (2017), p. 47. DOI: [10.3847/1538-4357/aa9074](https://doi.org/10.3847/1538-4357/aa9074). arXiv: [1708.05043](https://arxiv.org/abs/1708.05043) [astro-ph.HE].

- [289] AMIR LEVINSON and OMER BROMBERG:
'Relativistic Photon Mediated Shocks',
in: *Phys. Rev. Lett.* 100 (2008), p. 131101. DOI: [10.1103/PhysRevLett.100.131101](https://doi.org/10.1103/PhysRevLett.100.131101). arXiv: [0711.3281](https://arxiv.org/abs/0711.3281) [astro-ph].
- [290] LIANG LI ET AL.:
'A Comprehensive Study of Gamma-Ray Burst Optical Emission. I. Flares and Early Shallow-decay Component',
in: *Astrophysical Journal* 758.1, 27 (2012), p. 27. DOI: [10.1088/0004-637X/758/1/27](https://doi.org/10.1088/0004-637X/758/1/27). arXiv: [1203.2332](https://arxiv.org/abs/1203.2332) [astro-ph.HE].
- [291] ZHUO LI:
'Fermi Limit on the Neutrino Flux from Gamma-Ray Bursts',
in: *Astrophys. J. Lett.* 770 (2013), p. L40. DOI: [10.1088/2041-8205/770/2/L40](https://doi.org/10.1088/2041-8205/770/2/L40). arXiv: [1210.6594](https://arxiv.org/abs/1210.6594) [astro-ph.HE].
- [292] ZHUO LI, Z. G. DAI and T. LU:
'Long term neutrino afterglows from gamma-ray bursts',
in: *Astron. Astrophys.* 396 (2002), pp. 303–308. DOI: [10.1051/0004-6361:20021397](https://doi.org/10.1051/0004-6361:20021397). arXiv: [astro-ph/0208435](https://arxiv.org/abs/astro-ph/0208435).
- [293] EN-WEI LIANG ET AL.:
'A Comprehensive Analysis of the Swift/XRT Data. 3. Jet Break Candidates in the X-ray and Optical Afterglow Lightcurves',
in: *Astrophys. J.* 675 (2008), p. 528. DOI: [10.1086/524701](https://doi.org/10.1086/524701). arXiv: [0708.2942](https://arxiv.org/abs/0708.2942) [astro-ph].
- [294] EN-WEI LIANG ET AL.:
'A Comprehensive Study of Gamma-Ray Burst Optical Emission. II. Afterglow Onset and Late Re-brightening Components',
in: *Astrophysical Journal* 774.1, 13 (2013), p. 13. DOI: [10.1088/0004-637X/774/1/13](https://doi.org/10.1088/0004-637X/774/1/13). arXiv: [1210.5142](https://arxiv.org/abs/1210.5142) [astro-ph.HE].
- [295] DA-BIN LIN ET AL.:
'Steep Decay Phase Shaped by the Curvature Effect. I. Flux Evolution',
in: *Astrophys. J.* 840.2 (2017), p. 95. DOI: [10.3847/1538-4357/aa6d61](https://doi.org/10.3847/1538-4357/aa6d61). arXiv: [1704.04233](https://arxiv.org/abs/1704.04233) [astro-ph.HE].
- [296] PAOLO LIPARI, MAURIZIO LUSIGNOLI and DAVIDE MELONI:
'Flavor Composition and Energy Spectrum of Astrophysical Neutrinos',
in: *Phys. Rev. D* 75 (2007), p. 123005. DOI: [10.1103/PhysRevD.75.123005](https://doi.org/10.1103/PhysRevD.75.123005). arXiv: [0704.0718](https://arxiv.org/abs/0704.0718) [astro-ph].
- [297] KUAN LIU ET AL.:
'Gamma-ray Burst Spectrum with a Time-dependent Injection Rate of High-energy Electrons',
in: *Astrophys. J. Lett.* 893.1 (2020), p. L14. DOI: [10.3847/2041-8213/ab838e](https://doi.org/10.3847/2041-8213/ab838e). arXiv: [2003.12231](https://arxiv.org/abs/2003.12231) [astro-ph.HE].
- [298] RUO-YU LIU, SHAO-QIANG XI and XIANG-YU WANG:
'Neutrino emission from an off-axis jet driven by the tidal disruption event AT2019dsg',
in: *Phys. Rev. D* 102.8 (2020), p. 083028. DOI: [10.1103/PhysRevD.102.083028](https://doi.org/10.1103/PhysRevD.102.083028). arXiv: [2011.03773](https://arxiv.org/abs/2011.03773) [astro-ph.HE].
- [299] NICOLE M. LLOYD-RONNING and BING ZHANG:
'On the kinetic energy and radiative efficiency of gamma-ray bursts',
in: *Astrophys. J.* 613 (2004), pp. 477–483. DOI: [10.1086/423026](https://doi.org/10.1086/423026). arXiv: [astro-ph/0404107](https://arxiv.org/abs/astro-ph/0404107).

- [300] KATHARINA LODDERS:
'Solar Elemental Abundances',
in: *arXiv e-prints*, arXiv:1912.00844 (Dec. 2019), arXiv:1912.00844. arXiv: [1912.00844 \[astro-ph.SR\]](#).
- [301] MALCOLM S. LONGAIR:
High Energy Astrophysics,
2011.
- [302] LSST SCIENCE COLLABORATION ET AL.:
'LSST Science Book, Version 2.0',
in: *arXiv e-prints*, arXiv:0912.0201 (Dec. 2009), arXiv:0912.0201. DOI: [10.48550/arXiv.0912.0201](#). arXiv: [0912.0201 \[astro-ph.IM\]](#).
- [303] CECILIA LUNARDINI and WALTER WINTER:
'High Energy Neutrinos from the Tidal Disruption of Stars',
in: *Phys. Rev. D* 95.12 (2017), p. 123001. DOI: [10.1103/PhysRevD.95.123001](#). arXiv: [1612.03160 \[astro-ph.HE\]](#).
- [304] A. MACFADYEN and S.E. WOOSLEY:
'Collapsars: Gamma-ray bursts and explosions in 'failed supernovae'',
in: *Astrophys. J.* 524 (1999), p. 262. DOI: [10.1086/307790](#). arXiv: [astro-ph/9810274](#).
- [305] DAN MAOZ:
Astrophysics in a Nutshell-Second Edition,
Princeton University Press, 2016. URL: <https://press.princeton.edu/books/hardcover/9780691164793/astrophysics-in-a-nutshell>.
- [306] A. MARCOWITH ET AL.:
'The microphysics of collisionless shock waves',
in: *Rept. Prog. Phys.* 79 (2016), p. 046901. DOI: [10.1088/0034-4885/79/4/046901](#). arXiv: [1604.00318 \[astro-ph.HE\]](#).
- [307] A. MARCOWITH ET AL.:
'Multi-scale simulations of particle acceleration in astrophysical systems',
in: *Liv. Rev. Comput. Astrophys.* 6 (2020), p. 1. DOI: [10.1007/s41115-020-0007-6](#). arXiv: [2002.09411 \[astro-ph.HE\]](#).
- [308] BEN MARGALIT, ELIOT QUATAERT and ANNA Y. Q. HO:
'Optical to X-Ray Signatures of Dense Circumstellar Interaction in Core-collapse Supernovae',
in: *Astrophys. J.* 928.2 (2022), p. 122. DOI: [10.3847/1538-4357/ac53b0](#). arXiv: [2109.09746 \[astro-ph.HE\]](#).
- [309] R. MARGUTTI ET AL.:
'On the average gamma-ray burst X-ray flaring activity',
in: *MNRAS* 410.2 (Jan. 2011), pp. 1064–1075. DOI: [10.1111/j.1365-2966.2010.17504.x](#). arXiv: [1009.0172 \[astro-ph.HE\]](#).
- [310] APOSTOLOS MASTICHIADIS ET AL.:
'A roadmap to hadronic supercriticalities: a comprehensive study of the parameter space for high-energy astrophysical sources',
in: *Mon. Not. Roy. Astron. Soc.* 495.2 (2020), pp. 2458–2474. DOI: [10.1093/mnras/staa1308](#). arXiv: [2003.06956 \[astro-ph.HE\]](#).

- [311] TATSUYA MATSUMOTO and TSVI PIRAN:
'Radio constraint on outflows from tidal disruption events',
in: *Mon. Not. Roy. Astron. Soc.* 507.3 (Nov. 2021), pp. 4196–4210. DOI: [10.1093/mnras/stab2418](https://doi.org/10.1093/mnras/stab2418).
arXiv: [2107.06289](https://arxiv.org/abs/2107.06289) [astro-ph.HE].
- [312] TATSUYA MATSUMOTO, TSVI PIRAN and JULIAN H. KROLIK:
'What powers the radio emission in TDE AT2019dsg: a long-lived jet or the disruption itself?',
in: *arXiv e-prints*, arXiv:2109.02648 (Sept. 2021), arXiv:2109.02648. arXiv: [2109.02648](https://arxiv.org/abs/2109.02648) [astro-ph.HE].
- [313] JAMES MATTHEWS, ANTHONY BELL and KATHERINE BLUNDELL:
'Particle acceleration in astrophysical jets',
in: *New Astron. Rev.* 89 (2020), p. 101543. DOI: [10.1016/j.newar.2020.101543](https://doi.org/10.1016/j.newar.2020.101543). arXiv: [2003.06587](https://arxiv.org/abs/2003.06587) [astro-ph.HE].
- [314] CHRISTOPHER D. MATZNER and CHRISTOPHER F. MCKEE:
'The expulsion of stellar envelopes in core-collapse supernovae',
in: *Astrophys. J.* 510 (1999), p. 379. DOI: [10.1086/306571](https://doi.org/10.1086/306571). arXiv: [astro-ph/9807046](https://arxiv.org/abs/astro-ph/9807046).
- [315] A. MELANDRI ET AL.:
'The Early-Time Optical Properties of Gamma-Ray Burst Afterglows',
in: *Astrophys. J.* 686.2 (2008), pp. 1209–1230. DOI: [10.1086/591243](https://doi.org/10.1086/591243). arXiv: [0804.0811](https://arxiv.org/abs/0804.0811) [astro-ph].
- [316] MICKAËL MELZANI:
'Collisionless magnetic reconnection in relativistic plasmas with particle-in-cell simulations',
Theses. Ecole normale supérieure de lyon - ENS LYON, Nov. 2014. URL: <https://theses.hal.science/tel-01126912>.
- [317] P. MESZAROS:
'Astrophysical Sources of High Energy Neutrinos in the IceCube Era',
in: *Ann. Rev. Nucl. Part. Sci.* 67 (2017), pp. 45–67. DOI: [10.1146/annurev-nucl-101916-123304](https://doi.org/10.1146/annurev-nucl-101916-123304). arXiv: [1708.03577](https://arxiv.org/abs/1708.03577) [astro-ph.HE].
- [318] P. MESZAROS and M. J. REES:
'Relativistic Fireballs and Their Impact on External Matter: Models for Cosmological Gamma-Ray Bursts',
in: 405 (Mar. 1993), p. 278. DOI: [10.1086/172360](https://doi.org/10.1086/172360).
- [319] P. MESZAROS and M. J. REES:
'Steep slopes and preferred breaks in GRB spectra: The Role of photospheres and comptonization',
in: *Astrophys. J.* 530 (2000), pp. 292–298. DOI: [10.1086/308371](https://doi.org/10.1086/308371). arXiv: [astro-ph/9908126](https://arxiv.org/abs/astro-ph/9908126).
- [320] PETER MESZAROS:
'Gamma-Ray Bursts',
in: *Rept. Prog. Phys.* 69 (2006), pp. 2259–2322. DOI: [10.1088/0034-4885/69/8/R01](https://doi.org/10.1088/0034-4885/69/8/R01). arXiv: [astro-ph/0605208](https://arxiv.org/abs/astro-ph/0605208).
- [321] P. MÉSZÁROS:
'Gamma Ray Bursts as Neutrino Sources',
in: (2017), pp. 1–14. DOI: [10.1142/9789814759410_0001](https://doi.org/10.1142/9789814759410_0001). arXiv: [1511.01396](https://arxiv.org/abs/1511.01396) [astro-ph.HE].

- [322] P. MÉSZÁROS, P. LAGUNA and M.J. REES:
‘Gas dynamics of relativistically expanding gamma-ray burst sources: Kinematics, energetics, magnetic fields and efficiency’,
in: *Astrophys. J.* 415 (1993), pp. 181–190. DOI: [10.1086/173154](https://doi.org/10.1086/173154). arXiv: [astro-ph/9301007](https://arxiv.org/abs/astro-ph/9301007).
- [323] P. MÉSZÁROS and M. J. REES:
‘Optical and long wavelength afterglow from gamma-ray bursts’,
in: *Astrophys. J.* 476 (1997), pp. 232–237. DOI: [10.1086/303625](https://doi.org/10.1086/303625). arXiv: [astro-ph/9606043](https://arxiv.org/abs/astro-ph/9606043).
- [324] P. MÉSZÁROS and M. J. REES:
‘Poynting Jets from Black Holes and Cosmological Gamma-Ray Bursts’,
in: *Astrophys. J. Lett.* 482.1 (June 1997), pp. L29–L32. DOI: [10.1086/310692](https://doi.org/10.1086/310692). arXiv: [astro-ph/9609065](https://arxiv.org/abs/astro-ph/9609065) [[astro-ph](https://arxiv.org/abs/astro-ph)].
- [325] BRIAN D. METZGER, DIMITRIOS GIANNIOS and SHUNSAKU HORIUCHI:
‘Heavy Nuclei Synthesized in Gamma-Ray Burst Outflows as the Source of UHECRs’,
in: *Mon. Not. Roy. Astron. Soc.* 415 (2011), p. 2495. DOI: [10.1111/j.1365-2966.2011.18873.x](https://doi.org/10.1111/j.1365-2966.2011.18873.x). arXiv: [1101.4019](https://arxiv.org/abs/1101.4019) [[astro-ph](https://arxiv.org/abs/astro-ph).HE].
- [326] ANTHONY MEZZACAPPA:
‘ASCERTAINING THE CORE COLLAPSE SUPERNOVA MECHANISM: The State of the Art and the Road Ahead’,
in: *Annual Review of Nuclear and Particle Science* 55.1 (Dec. 2005), pp. 467–515. DOI: [10.1146/annurev.nucl.55.090704.151608](https://doi.org/10.1146/annurev.nucl.55.090704.151608).
- [327] MORDEHAI MILGROM and VLADIMIR USOV:
‘Possible association of ultrahigh-energy cosmic ray events with strong gamma-ray bursts’,
in: *Astrophys. J. Lett.* 449 (1995), p. L37. DOI: [10.1086/309633](https://doi.org/10.1086/309633). arXiv: [astro-ph/9505009](https://arxiv.org/abs/astro-ph/9505009).
- [328] AKIRA MIZUTA and KUNIHITO IOKA:
‘Opening Angles of Collapsar Jets’,
in: *Astrophys. J.* 777 (2013), p. 162. DOI: [10.1088/0004-637X/777/2/162](https://doi.org/10.1088/0004-637X/777/2/162). arXiv: [1304.0163](https://arxiv.org/abs/1304.0163) [[astro-ph](https://arxiv.org/abs/astro-ph).HE].
- [329] PRASHANTH MOHAN ET AL.:
‘Decelerated non-relativistic expansion in a tidal disruption event with a potential neutrino association’,
in: *arXiv e-prints*, arXiv:2106.15799 (June 2021), arXiv:2106.15799. arXiv: [2106.15799](https://arxiv.org/abs/2106.15799) [[astro-ph](https://arxiv.org/abs/astro-ph).HE].
- [330] KLAES MØLLER, PETER B. DENTON and IRENE TAMBORRA:
‘Cosmogenic Neutrinos Through the GRAND Lens Unveil the Nature of Cosmic Accelerators’,
in: *JCAP* 05 (2019), p. 047. DOI: [10.1088/1475-7516/2019/05/047](https://doi.org/10.1088/1475-7516/2019/05/047). arXiv: [1809.04866](https://arxiv.org/abs/1809.04866) [[astro-ph](https://arxiv.org/abs/astro-ph).HE].
- [331] TAKASHI J. MORIYA, ELENA I. SOROKINA and ROGER A. CHEVALIER:
‘Superluminous supernovae’,
in: *Space Sci. Rev.* 214.2 (2018), p. 59. DOI: [10.1007/s11214-018-0493-6](https://doi.org/10.1007/s11214-018-0493-6). arXiv: [1803.01875](https://arxiv.org/abs/1803.01875) [[astro-ph](https://arxiv.org/abs/astro-ph).HE].
- [332] TAKASHI J. MORIYA ET AL.:
‘An Analytic Bolometric Light Curve Model of Interaction-Powered Supernovae and its Application to Type II_n Supernovae’,
in: *Mon. Not. Roy. Astron. Soc.* 435 (2013), p. 1520. DOI: [10.1093/mnras/stt1392](https://doi.org/10.1093/mnras/stt1392). arXiv: [1307.2644](https://arxiv.org/abs/1307.2644) [[astro-ph](https://arxiv.org/abs/astro-ph).HE].

- [333] TAKASHI J. MORIYA ET AL.:
'Mass-loss histories of Type II_n supernova progenitors within decades before their explosion',
in: *Mon. Not. Roy. Astron. Soc.* 439.3 (2014), pp. 2917–2926. DOI: [10.1093/mnras/stu163](https://doi.org/10.1093/mnras/stu163). arXiv: [1401.4893](https://arxiv.org/abs/1401.4893) [astro-ph.SR].
- [334] TAKASHI J. MORIYA ET AL.:
'Superluminous transients at AGN centers from interaction between black-hole disk winds and broad-line region clouds',
in: *Astrophys. J. Lett.* 843.2 (2017), p. L19. DOI: [10.3847/2041-8213/aa7af3](https://doi.org/10.3847/2041-8213/aa7af3). arXiv: [1706.06855](https://arxiv.org/abs/1706.06855) [astro-ph.HE].
- [335] G. MORLINO, P. BLASI and M. VIETRI:
'Particle acceleration at shock waves moving at arbitrary speed: the case of large scale magnetic field and anisotropic scattering',
in: *Astrophys. J.* 658 (2007), p. 1069. DOI: [10.1086/512026](https://doi.org/10.1086/512026). arXiv: [astro-ph/0701173](https://arxiv.org/abs/astro-ph/0701173).
- [336] A. MÜCKE ET AL.:
'SOPHIA: Monte Carlo simulations of photohadronic processes in astrophysics',
in: *Comput. Phys. Commun.* 124 (2000), pp. 290–314. DOI: [10.1016/S0010-4655\(99\)00446-4](https://doi.org/10.1016/S0010-4655(99)00446-4).
arXiv: [astro-ph/9903478](https://arxiv.org/abs/astro-ph/9903478).
- [337] KOHTA MURASE:
'Active Galactic Nuclei as High-Energy Neutrino Sources',
in: (2017). Ed. by Thomas Gaisser and Albrecht Karle, pp. 15–31. DOI: [10.1142/9789814759410_0002](https://doi.org/10.1142/9789814759410_0002). arXiv: [1511.01590](https://arxiv.org/abs/1511.01590) [astro-ph.HE].
- [338] KOHTA MURASE:
'High energy neutrino early afterglows gamma-ray bursts revisited',
in: *Phys. Rev. D* 76 (2007), p. 123001. DOI: [10.1103/PhysRevD.76.123001](https://doi.org/10.1103/PhysRevD.76.123001). arXiv: [0707.1140](https://arxiv.org/abs/0707.1140) [astro-ph].
- [339] KOHTA MURASE:
'Multi-Messenger Connections among High-Energy Cosmic Particles',
in: *PoS ICRC2019* (2020), p. 965. DOI: [10.22323/1.358.0965](https://doi.org/10.22323/1.358.0965). arXiv: [1912.05764](https://arxiv.org/abs/1912.05764) [astro-ph.HE].
- [340] KOHTA MURASE:
'New Prospects for Detecting High-Energy Neutrinos from Nearby Supernovae',
in: *Phys. Rev. D* 97.8 (2018), p. 081301. DOI: [10.1103/PhysRevD.97.081301](https://doi.org/10.1103/PhysRevD.97.081301). arXiv: [1705.04750](https://arxiv.org/abs/1705.04750) [astro-ph.HE].
- [341] KOHTA MURASE:
'Prompt High-Energy Neutrinos from Gamma-Ray Bursts in the Photospheric and Synchrotron Self-Compton Scenarios',
in: *Phys. Rev. D* 78 (2008), p. 101302. DOI: [10.1103/PhysRevD.78.101302](https://doi.org/10.1103/PhysRevD.78.101302). arXiv: [0807.0919](https://arxiv.org/abs/0807.0919) [astro-ph].
- [342] KOHTA MURASE, MARKUS AHLERS and BRIAN C. LACKI:
'Testing the Hadronuclear Origin of PeV Neutrinos Observed with IceCube',
in: *Phys. Rev. D* 88.12 (2013), p. 121301. DOI: [10.1103/PhysRevD.88.121301](https://doi.org/10.1103/PhysRevD.88.121301). arXiv: [1306.3417](https://arxiv.org/abs/1306.3417) [astro-ph.HE].

- [343] KOHTA MURASE and IMRE BARTOS:
'High-Energy Multimessenger Transient Astrophysics',
in: *Ann. Rev. Nucl. Part. Sci.* 69 (2019), pp. 477–506. DOI: [10.1146/annurev-nucl-101918-023510](https://doi.org/10.1146/annurev-nucl-101918-023510). arXiv: [1907.12506](https://arxiv.org/abs/1907.12506) [astro-ph.HE].
- [344] KOHTA MURASE, DAFNE GUETTA and MARKUS AHLERS:
'Hidden Cosmic-Ray Accelerators as an Origin of TeV-PeV Cosmic Neutrinos',
in: *Phys. Rev. Lett.* 116.7 (2016), p. 071101. DOI: [10.1103/PhysRevLett.116.071101](https://doi.org/10.1103/PhysRevLett.116.071101). arXiv: [1509.00805](https://arxiv.org/abs/1509.00805) [astro-ph.HE].
- [345] KOHTA MURASE and KUNIHITO IOKA:
'TeV–PeV Neutrinos from Low-Power Gamma-Ray Burst Jets inside Stars',
in: *Phys. Rev. Lett.* 111.12 (2013), p. 121102. DOI: [10.1103/PhysRevLett.111.121102](https://doi.org/10.1103/PhysRevLett.111.121102). arXiv: [1306.2274](https://arxiv.org/abs/1306.2274) [astro-ph.HE].
- [346] KOHTA MURASE, KAZUMI KASHIYAMA and PETER MÉSZÁROS:
'Subphotospheric Neutrinos from Gamma-Ray Bursts: The Role of Neutrons',
in: *Phys. Rev. Lett.* 111 (2013), p. 131102. DOI: [10.1103/PhysRevLett.111.131102](https://doi.org/10.1103/PhysRevLett.111.131102). arXiv: [1301.4236](https://arxiv.org/abs/1301.4236) [astro-ph.HE].
- [347] KOHTA MURASE and SHIGEHIRO NAGATAKI:
'High energy neutrino emission and neutrino background from gamma-ray bursts in the internal shock model',
in: *Phys. Rev. D* 73 (2006), p. 063002. DOI: [10.1103/PhysRevD.73.063002](https://doi.org/10.1103/PhysRevD.73.063002). arXiv: [astro-ph/0512275](https://arxiv.org/abs/astro-ph/0512275).
- [348] KOHTA MURASE and SHIGEHIRO NAGATAKI:
'High Energy Neutrino Flash from Far-UV/X-ray Flares of Gamma-Ray Bursts',
in: *Phys. Rev. Lett.* 97 (2006), p. 051101. DOI: [10.1103/PhysRevLett.97.051101](https://doi.org/10.1103/PhysRevLett.97.051101). arXiv: [astro-ph/0604437](https://arxiv.org/abs/astro-ph/0604437).
- [349] KOHTA MURASE, TODD A. THOMPSON and ERAN O. OFEK:
'Probing cosmic ray ion acceleration with radio-submm and gamma-ray emission from interaction-powered supernovae',
in: *Mon. Not. Roy. Astron. Soc.* 440.3 (May 2014), pp. 2528–2543. DOI: [10.1093/mnras/stu384](https://doi.org/10.1093/mnras/stu384). arXiv: [1311.6778](https://arxiv.org/abs/1311.6778) [astro-ph.HE].
- [350] KOHTA MURASE and ELI WAXMAN:
'Constraining High-Energy Cosmic Neutrino Sources: Implications and Prospects',
in: *Phys. Rev. D* 94.10 (2016), p. 103006. DOI: [10.1103/PhysRevD.94.103006](https://doi.org/10.1103/PhysRevD.94.103006). arXiv: [1607.01601](https://arxiv.org/abs/1607.01601) [astro-ph.HE].
- [351] KOHTA MURASE ET AL.:
'High-Energy Neutrino and Gamma-Ray Emission from Tidal Disruption Events',
in: *Astrophys. J.* 902.2 (2020), p. 108. DOI: [10.3847/1538-4357/abb3c0](https://doi.org/10.3847/1538-4357/abb3c0). arXiv: [2005.08937](https://arxiv.org/abs/2005.08937) [astro-ph.HE].
- [352] KOHTA MURASE ET AL.:
'Neutrinos from the Brightest Gamma-Ray Burst?',
in: *Astrophys. J. Lett.* 941.1 (2022), p. L10. DOI: [10.3847/2041-8213/aca3ae](https://doi.org/10.3847/2041-8213/aca3ae). arXiv: [2210.15625](https://arxiv.org/abs/2210.15625) [astro-ph.HE].

- [353] KOHTA MURASE ET AL.:
‘New Class of High-Energy Transients from Crashes of Supernova Ejecta with Massive Circumstellar Material Shells’,
in: *Phys. Rev. D* 84 (2011), p. 043003. DOI: [10.1103/PhysRevD.84.043003](https://doi.org/10.1103/PhysRevD.84.043003). arXiv: [1012.2834](https://arxiv.org/abs/1012.2834) [[astro-ph.HE](#)].
- [354] KOHTA MURASE ET AL.:
‘The Role of Stochastic Acceleration in the Prompt Emission of Gamma-Ray Bursts: Application to Hadronic Injection’,
in: *Astrophys. J.* 746 (2012), p. 164. DOI: [10.1088/0004-637X/746/2/164](https://doi.org/10.1088/0004-637X/746/2/164). arXiv: [1107.5575](https://arxiv.org/abs/1107.5575) [[astro-ph.HE](#)].
- [355] SHIGEHIRO NAGATAKI:
‘Theories of central engine for long gamma-ray bursts’,
in: *Rept. Prog. Phys.* 81.2 (2018), p. 026901. DOI: [10.1088/1361-6633/aa97a8](https://doi.org/10.1088/1361-6633/aa97a8).
- [356] EHUD NAKAR and JONATHAN GRANOT:
‘Smooth Light Curves from a Bumpy Ride: Relativistic Blast Wave Encounters a Density Jump’,
in: *Mon. Not. R. Astron. Soc.* 380 (2007), pp. 1744–1760. DOI: [10.1111/j.1365-2966.2007.12245.x](https://doi.org/10.1111/j.1365-2966.2007.12245.x). arXiv: [astro-ph/0606011](https://arxiv.org/abs/astro-ph/0606011).
- [357] KRZYSZTOF NALEWAJKO ET AL.:
‘On the distribution of particle acceleration sites in plasmoid-dominated relativistic magnetic reconnection’,
in: *Astrophys. J.* 815.2 (2015), p. 101. DOI: [10.1088/0004-637X/815/2/101](https://doi.org/10.1088/0004-637X/815/2/101). arXiv: [1508.02392](https://arxiv.org/abs/1508.02392) [[astro-ph.HE](#)].
- [358] M. NARDINI ET AL.:
‘Afterglow rebrightenings as a signature of a long-lasting central engine activity? The emblematic case of GRB 100814A’,
in: *Astron. Astrophys.* 562 (2014), A29. DOI: [10.1051/0004-6361/201321525](https://doi.org/10.1051/0004-6361/201321525). arXiv: [1312.1335](https://arxiv.org/abs/1312.1335) [[astro-ph.HE](#)].
- [359] M. NARDINI ET AL.:
‘On the nature of the extremely fast optical rebrightening of the afterglow of GRB 081029’,
in: *Astron. Astrophys.* 531 (2011), A39. DOI: [10.1051/0004-6361/201116814](https://doi.org/10.1051/0004-6361/201116814). arXiv: [1105.0917](https://arxiv.org/abs/1105.0917) [[astro-ph.HE](#)].
- [360] L. NAVA ET AL.:
‘Afterglow emission in gamma-ray bursts - I. Pair-enriched ambient medium and radiative blast waves’,
in: *Mon. Not. R. Astron. Soc.* 433.3 (2013), pp. 2107–2121. DOI: [10.1093/mnras/stt872](https://doi.org/10.1093/mnras/stt872). arXiv: [1211.2806](https://arxiv.org/abs/1211.2806) [[astro-ph.HE](#)].
- [361] JANNIS NECKER ET AL.:
‘ASAS-SN follow-up of IceCube high-energy neutrino alerts’,
in: *Mon. Not. Roy. Astron.* 516.2 (Oct. 2022), pp. 2455–2469. DOI: [10.1093/mnras/stac2261](https://doi.org/10.1093/mnras/stac2261). arXiv: [2204.00500](https://arxiv.org/abs/2204.00500) [[astro-ph.HE](#)].
- [362] MATT NICHOLL ET AL.:
‘An extremely energetic supernova from a very massive star in a dense medium’,
in: *Nature Astron.* 4 (Apr. 2020), pp. 893–899. DOI: [10.1038/s41550-020-1066-7](https://doi.org/10.1038/s41550-020-1066-7). arXiv: [2004.05840](https://arxiv.org/abs/2004.05840) [[astro-ph.HE](#)].

- [363] J. A. NOUSEK ET AL.:
'Evidence for a Canonical Gamma-Ray Burst Afterglow Light Curve in the Swift XRT Data',
in: *Astrophys. J.* 642.1 (2006), pp. 389–400. DOI: [10.1086/500724](https://doi.org/10.1086/500724). arXiv: [astro-ph/0508332](https://arxiv.org/abs/astro-ph/0508332) [[astro-ph](#)].
- [364] A. NYHOLM ET AL.:
'The bumpy light curve of Type II_n supernova iPTF13z over 3 years',
in: *Astron. Astrophys.* 605, A6 (Aug. 2017), A6. DOI: [10.1051/0004-6361/201629906](https://doi.org/10.1051/0004-6361/201629906). arXiv: [1703.09679](https://arxiv.org/abs/1703.09679) [[astro-ph.SR](#)].
- [365] A. NYHOLM ET AL.:
'Type II_n supernova light-curve properties measured from an untargeted survey sample',
in: *Astron. Astrophys.* 637, A73 (May 2020), A73. DOI: [10.1051/0004-6361/201936097](https://doi.org/10.1051/0004-6361/201936097). arXiv: [1906.05812](https://arxiv.org/abs/1906.05812) [[astro-ph.SR](#)].
- [366] PAUL T. O'BRIEN ET AL.:
'The early x-ray emission from grbs',
in: *Astrophys. J.* 647 (2006), pp. 1213–1237. DOI: [10.1086/505457](https://doi.org/10.1086/505457). arXiv: [astro-ph/0601125](https://arxiv.org/abs/astro-ph/0601125).
- [367] S. R. OATES ET AL.:
'A statistical comparison of the optical/UV and X-ray afterglows of gamma-ray bursts using the Swift Ultraviolet Optical and X-ray Telescopes',
in: *MNRAS* 412.1 (Mar. 2011), pp. 561–579. DOI: [10.1111/j.1365-2966.2010.17928.x](https://doi.org/10.1111/j.1365-2966.2010.17928.x). arXiv: [1010.6212](https://arxiv.org/abs/1010.6212) [[astro-ph.HE](#)].
- [368] ERAN O. OFEK ET AL.:
'SN 2006gy: An extremely luminous supernova in the early-type galaxy NGC 1260',
in: *Astrophys. J. Lett.* 659 (2007), pp. L13–L16. DOI: [10.1086/516749](https://doi.org/10.1086/516749). arXiv: [astro-ph/0612408](https://arxiv.org/abs/astro-ph/0612408).
- [369] GOR OGANESYAN ET AL.:
'Detection of Low-energy Breaks in Gamma-Ray Burst Prompt Emission Spectra',
in: *Astrophys. J.* 846 (2017), p. 137. DOI: [10.3847/1538-4357/aa831e](https://doi.org/10.3847/1538-4357/aa831e). arXiv: [1709.04689](https://arxiv.org/abs/1709.04689) [[astro-ph.HE](#)].
- [370] GOR OGANESYAN ET AL.:
'Prompt optical emission as a signature of synchrotron radiation in gamma-ray bursts',
in: *Astron. Astrophys.* 628 (2019), A59. DOI: [10.1051/0004-6361/201935766](https://doi.org/10.1051/0004-6361/201935766). arXiv: [1904.11086](https://arxiv.org/abs/1904.11086) [[astro-ph.HE](#)].
- [371] A. V. OLINTO ET AL.:
'The POEMMA (Probe of Extreme Multi-Messenger Astrophysics) observatory',
in: *JCAP* 06 (2021), p. 007. DOI: [10.1088/1475-7516/2021/06/007](https://doi.org/10.1088/1475-7516/2021/06/007). arXiv: [2012.07945](https://arxiv.org/abs/2012.07945) [[astro-ph.IM](#)].
- [372] W. S. PACIESAS ET AL.:
'The Fourth batse gamma-ray burst catalog (revised)',
in: *Astrophys. J. Suppl.* 122 (1999), pp. 465–495. DOI: [10.1086/313224](https://doi.org/10.1086/313224). arXiv: [astro-ph/9903205](https://arxiv.org/abs/astro-ph/9903205).
- [373] BOHDAN PACZYNSKI:
'Gamma-ray bursters at cosmological distances',
in: *Astrophys. J. Lett.* 308 (1986), pp. L43–L46. DOI: [10.1086/184740](https://doi.org/10.1086/184740).

- [374] P. PADMANABHAN:
Theoretical astrophysics. Vol.1: Astrophysical processes,
2000.
- [375] TONY PAN, DANIEL J. PATNAUDE and ABRAHAM LOEB:
‘Super-luminous X-ray Emission from the Interaction of Supernova Ejecta with Dense Circumstellar Shells’,
in: *Mon. Not. Roy. Astron. Soc.* 433 (2013), p. 838. DOI: [10.1093/mnras/stt780](https://doi.org/10.1093/mnras/stt780). arXiv: [1303.6958](https://arxiv.org/abs/1303.6958) [astro-ph.HE].
- [376] A. PANAITESCU and P. KUMAR:
‘Analytic light-curves of gamma-ray burst afterglows: homogeneous versus wind external media’,
in: *Astrophys. J.* 543 (2000), p. 66. DOI: [10.1086/317090](https://doi.org/10.1086/317090). arXiv: [astro-ph/0003246](https://arxiv.org/abs/astro-ph/0003246).
- [377] A. PANAITESCU, W. T. VESTRAND and P. WOZNAK:
‘An external-shock model for GRB afterglow 130427A’,
in: *Mon. Not. R. Astron. Soc.* 436 (2013), p. 3106. DOI: [10.1093/mnras/stt1792](https://doi.org/10.1093/mnras/stt1792). arXiv: [1311.5867](https://arxiv.org/abs/1311.5867) [astro-ph.HE].
- [378] KYLE PARFREY, DIMITRIOS GIANNIOS and ANDREI M. BELOBORODOV:
‘Black-hole jets without large-scale net magnetic flux’,
in: *Mon. Not. Roy. Astron. Soc.* 446.1 (2015), pp. L61–L65. DOI: [10.1093/mnrasl/slu162](https://doi.org/10.1093/mnrasl/slu162). arXiv: [1410.0374](https://arxiv.org/abs/1410.0374) [astro-ph.HE].
- [379] DANIEL J. PATNAUDE and ROBERT A. FESEN:
‘Proper Motions and Brightness Variations of Nonthermal X-ray Filaments in the Cassiopeia A Supernova Remnant’,
in: *Astrophys. J.* 697 (2009), pp. 535–543. DOI: [10.1088/0004-637X/697/1/535](https://doi.org/10.1088/0004-637X/697/1/535). arXiv: [0808.0692](https://arxiv.org/abs/0808.0692) [astro-ph].
- [380] MARIA T. PATTERSON ET AL.:
‘The Zwicky Transient Facility Alert Distribution System’,
in: *Publ. Astron. Soc. Pac.* 131.995 (Jan. 2019), p. 018001. DOI: [10.1088/1538-3873/aae904](https://doi.org/10.1088/1538-3873/aae904). arXiv: [1902.02227](https://arxiv.org/abs/1902.02227) [astro-ph.IM].
- [381] WOLFGAN PAULI:
‘Neutrino invention’,
in: (1930). URL: <https://www.symmetrymagazine.org/article/march-2007/neutrino-invention>.
- [382] D. A. PERLEY ET AL.:
‘The Afterglow of GRB 130427A from 1 to 10^{16} GHz’,
in: *Astrophys. J.* 781 (2014), p. 37. DOI: [10.1088/0004-637X/781/1/37](https://doi.org/10.1088/0004-637X/781/1/37). arXiv: [1307.4401](https://arxiv.org/abs/1307.4401) [astro-ph.HE].
- [383] DANIEL A. PERLEY ET AL.:
‘The Zwicky Transient Facility Bright Transient Survey. II. A Public Statistical Sample for Exploring Supernova Demographics’,
in: *Astrophys. J.* 904.1 (2020), p. 35. DOI: [10.3847/1538-4357/abbd98](https://doi.org/10.3847/1538-4357/abbd98). arXiv: [2009.01242](https://arxiv.org/abs/2009.01242) [astro-ph.HE].

- [384] ROSALBA PERNA, PHILIP J. ARMITAGE and BING ZHANG:
'Flares in long and short gamma-ray bursts: a common origin in a hyperaccreting accretion disk',
in: *Astrophys. J. Lett.* 636 (2005), pp. L29–L32. DOI: [10 . 1086 / 499775](https://doi.org/10.1086/499775). arXiv: [astro - ph / 0511506](https://arxiv.org/abs/astro-ph/0511506).
- [385] M. PETROPOULOU ET AL.:
'Deciphering the properties of the central engine in GRB collapsars',
in: *Mon. Not. Roy. Astron. Soc.* 496.3 (Aug. 2020), pp. 2910–2921. DOI: [10 . 1093 / mnras / staa1695](https://doi.org/10.1093/mnras/staa1695).
arXiv: [2006 . 07482](https://arxiv.org/abs/2006.07482) [[astro-ph.HE](https://arxiv.org/abs/2006.07482)].
- [386] M. PETROPOULOU ET AL.:
'Point-source and diffuse high-energy neutrino emission from Type II_n supernovae',
in: *Mon. Not. Roy. Astron. Soc.* 470.2 (2017), pp. 1881–1893. DOI: [10 . 1093 / mnras / stx1251](https://doi.org/10.1093/mnras/stx1251).
arXiv: [1705 . 06752](https://arxiv.org/abs/1705.06752) [[astro-ph.HE](https://arxiv.org/abs/1705.06752)].
- [387] MARIA PETROPOULOU:
'The role of hadronic cascades in GRB models of efficient neutrino production',
in: *Mon. Not. Roy. Astron. Soc.* 442.4 (2014), pp. 3026–3036. DOI: [10 . 1093 / mnras / stu1079](https://doi.org/10.1093/mnras/stu1079).
arXiv: [1405 . 7669](https://arxiv.org/abs/1405.7669) [[astro-ph.HE](https://arxiv.org/abs/1405.7669)].
- [388] MARIA PETROPOULOU, DIMITRIOS GIANNIOS and STAVROS DIMITRAKOUDIS:
'Implications of a PeV neutrino spectral cutoff in GRB models',
in: *Mon. Not. Roy. Astron. Soc.* 445.1 (2014), pp. 570–580. DOI: [10 . 1093 / mnras / stu1757](https://doi.org/10.1093/mnras/stu1757). arXiv:
[1405 . 2091](https://arxiv.org/abs/1405.2091) [[astro-ph.HE](https://arxiv.org/abs/1405.2091)].
- [389] MARIA PETROPOULOU, ATISH KAMBLE and LORENZO SIRONI:
'Radio synchrotron emission from secondary electrons in interaction-powered supernovae',
in: *Mon. Not. Roy. Astron. Soc.* 460.1 (2016), pp. 44–66. DOI: [10 . 1093 / mnras / stw920](https://doi.org/10.1093/mnras/stw920). arXiv:
[1603 . 00891](https://arxiv.org/abs/1603.00891) [[astro-ph.HE](https://arxiv.org/abs/1603.00891)].
- [390] MARIA PETROPOULOU and LORENZO SIRONI:
'The steady growth of the high-energy spectral cut-off in relativistic magnetic reconnection',
in: *Mon. Not. R. Astron. Soc.* 481.4 (2018), pp. 5687–5701. DOI: [10 . 1093 / mnras / sty2702](https://doi.org/10.1093/mnras/sty2702). arXiv:
[1808 . 00966](https://arxiv.org/abs/1808.00966) [[astro-ph.HE](https://arxiv.org/abs/1808.00966)].
- [391] MARIA PETROPOULOU ET AL.:
'Hadronic supercriticality as a trigger for γ -ray burst emission',
in: *Mon. Not. Roy. Astron. Soc.* 444.3 (2014), pp. 2186–2199. DOI: [10 . 1093 / mnras / stu1362](https://doi.org/10.1093/mnras/stu1362).
arXiv: [1407 . 2915](https://arxiv.org/abs/1407.2915) [[astro-ph.HE](https://arxiv.org/abs/1407.2915)].
- [392] MARIA PETROPOULOU ET AL.:
'Relativistic Magnetic Reconnection in Electron-Positron-Proton Plasmas: Implications for Jets
of Active Galactic Nuclei',
in: *Astrophys. J.* 880.1, 37 (July 2019), p. 37. DOI: [10 . 3847 / 1538 - 4357 / ab287a](https://doi.org/10.3847/1538-4357/ab287a). arXiv: [1906 . 03297](https://arxiv.org/abs/1906.03297) [[astro-ph.HE](https://arxiv.org/abs/1906.03297)].
- [393] T. PIRAN:
'Gamma-ray bursts and the fireball model',
in: *Phys. Rept.* 314 (1999), pp. 575–667. DOI: [10 . 1016 / S0370 - 1573 \(98\) 00127 - 6](https://doi.org/10.1016/S0370-1573(98)00127-6). arXiv:
[astro - ph / 9810256](https://arxiv.org/abs/astro-ph/9810256).
- [394] TSVI PIRAN:
'The physics of gamma-ray bursts',
in: *Rev. Mod. Phys.* 76 (2004), pp. 1143–1210. DOI: [10 . 1103 / RevModPhys . 76 . 1143](https://doi.org/10.1103/RevModPhys.76.1143). arXiv:
[astro - ph / 0405503](https://arxiv.org/abs/astro-ph/0405503).

- [395] TSVI PIRAN, AMOTZ SHEMI and RAMESH NARAYAN:
'Hydrodynamics of relativistic fireballs',
in: *Mon. Not. Roy. Astron. Soc.* 263 (1993), p. 861. DOI: [10.1093/mnras/263.4.861](https://doi.org/10.1093/mnras/263.4.861). arXiv: [astro-ph/9301004](https://arxiv.org/abs/astro-ph/9301004).
- [396] TETYANA PITIK, IRENE TAMBORRA and MARIA PETROPOULOU:
'Neutrino signal dependence on gamma-ray burst emission mechanism',
in: *JCAP* 05 (2021), p. 034. DOI: [10.1088/1475-7516/2021/05/034](https://doi.org/10.1088/1475-7516/2021/05/034). arXiv: [2102.02223](https://arxiv.org/abs/2102.02223) [[astro-ph.HE](https://arxiv.org/abs/2102.02223)].
- [397] TETYANA PITIK ET AL.:
'Is the High-energy Neutrino Event IceCube-200530A Associated with a Hydrogen-rich Superluminous Supernova?',
in: *Astrophys. J.* 929.2 (2022), p. 163. DOI: [10.3847/1538-4357/ac5ab1](https://doi.org/10.3847/1538-4357/ac5ab1). arXiv: [2110.06944](https://arxiv.org/abs/2110.06944) [[astro-ph.HE](https://arxiv.org/abs/2110.06944)].
- [398] B. PONTECORVO:
'Inverse beta processes and nonconservation of lepton charge',
in: *Zh. Eksp. Teor. Fiz.* 34 (1957), p. 247.
- [399] ROBERT POPHAM, S. E. WOOSLEY and CHRIS FRYER:
'Hyperaccreting Black Holes and Gamma-Ray Bursts',
in: *Astrophys. J.* 518.1 (June 1999), pp. 356–374. DOI: [10.1086/307259](https://doi.org/10.1086/307259). arXiv: [astro-ph/9807028](https://arxiv.org/abs/astro-ph/9807028) [[astro-ph](https://arxiv.org/abs/astro-ph/9807028)].
- [400] PETER PREDEHL ET AL.:
'eROSITA on SRG',
in: *Space Telescopes and Instrumentation 2010: Ultraviolet to Gamma Ray*. Ed. by Monique Arnaud, Stephen S. Murray and Tadayuki Takahashi. Vol. 7732. International Society for Optics and Photonics. SPIE, 2010, 77320U. DOI: [10.1117/12.856577](https://doi.org/10.1117/12.856577). URL: <https://doi.org/10.1117/12.856577>.
- [401] RAY J. PROTHEROE and R. W. CLAY:
'Ultrahigh energy cosmic rays',
in: *Publ. Astron. Soc. Pac.* 21.1 (2004), pp. 1–22. DOI: [10.1071/AS03047](https://doi.org/10.1071/AS03047). arXiv: [astro-ph/0311466](https://arxiv.org/abs/astro-ph/0311466).
- [402] YONG-ZHONG QIAN ET AL.:
'A Connection between flavor mixing of cosmologically significant neutrinos and heavy element nucleosynthesis in supernovae',
in: *Phys. Rev. Lett.* 71 (1993), pp. 1965–1968. DOI: [10.1103/PhysRevLett.71.1965](https://doi.org/10.1103/PhysRevLett.71.1965).
- [403] ROBERT M. QUIMBY ET AL.:
'Rates of Superluminous Supernovae at $z \sim 0.2$ ',
in: *Mon. Not. Roy. Astron. Soc.* 431 (2013), p. 912. DOI: [10.1093/mnras/stt213](https://doi.org/10.1093/mnras/stt213). arXiv: [1302.0911](https://arxiv.org/abs/1302.0911) [[astro-ph.CO](https://arxiv.org/abs/1302.0911)].
- [404] J. L. RACUSIN ET AL.:
'Fermi and Swift Gamma-Ray Burst Afterglow Population Studies',
in: *Astrophys. J.* 738 (2011), p. 138. DOI: [10.1088/0004-637X/738/2/138](https://doi.org/10.1088/0004-637X/738/2/138). arXiv: [1106.2469](https://arxiv.org/abs/1106.2469) [[astro-ph.HE](https://arxiv.org/abs/1106.2469)].

- [405] VIKRAM RANA ET AL.:
'Multi-wavelength Study of GRB 060906',
in: *American Astronomical Society Meeting Abstracts #213*. Vol. 213. American Astronomical Society Meeting Abstracts. 2009, p. 610.03.
- [406] M.E. RAVASIO ET AL.:
'Evidence of two spectral breaks in the prompt emission of gamma ray bursts',
in: *Astron. Astrophys.* 625 (2019), A60. DOI: [10.1051/0004-6361/201834987](https://doi.org/10.1051/0004-6361/201834987). arXiv: [1903.02555](https://arxiv.org/abs/1903.02555) [[astro-ph.HE](https://arxiv.org/abs/1903.02555)].
- [407] SOEBUR RAZZAQUE:
'Long-lived PeV–EeV neutrinos from gamma-ray burst blastwave',
in: *Phys. Rev. D* 88.10 (2013), p. 103003. DOI: [10.1103/PhysRevD.88.103003](https://doi.org/10.1103/PhysRevD.88.103003). arXiv: [1307.7596](https://arxiv.org/abs/1307.7596) [[astro-ph.HE](https://arxiv.org/abs/1307.7596)].
- [408] SOEBUR RAZZAQUE, PETER MESZAROS and ELI WAXMAN:
'High energy neutrinos from gamma-ray bursts with precursor supernovae',
in: *Phys. Rev. Lett.* 90 (2003), p. 241103. DOI: [10.1103/PhysRevLett.90.241103](https://doi.org/10.1103/PhysRevLett.90.241103). arXiv: [astro-ph/0212536](https://arxiv.org/abs/astro-ph/0212536).
- [409] SOEBUR RAZZAQUE, PETER MESZAROS and ELI WAXMAN:
'Neutrino tomography of gamma-ray bursts and massive stellar collapses',
in: *Phys. Rev. D* 68 (2003), p. 083001. DOI: [10.1103/PhysRevD.68.083001](https://doi.org/10.1103/PhysRevD.68.083001). arXiv: [astro-ph/0303505](https://arxiv.org/abs/astro-ph/0303505).
- [410] SOEBUR RAZZAQUE, PETER MÉSZÁROS and ELI WAXMAN:
'High energy neutrinos from a slow jet model of core collapse supernovae',
in: *Mod. Phys. Lett. A* 20 (2005), pp. 2351–2368. DOI: [10.1142/S0217732305018414](https://doi.org/10.1142/S0217732305018414). arXiv: [astro-ph/0509729](https://arxiv.org/abs/astro-ph/0509729).
- [411] SOEBUR RAZZAQUE and LILI YANG:
'PeV–EeV neutrinos from GRB blast waves in IceCube and future neutrino telescopes',
in: *Phys. Rev. D* 91 (2015), p. 043003. DOI: [10.1103/PhysRevD.91.043003](https://doi.org/10.1103/PhysRevD.91.043003). arXiv: [1411.7491](https://arxiv.org/abs/1411.7491) [[astro-ph.HE](https://arxiv.org/abs/1411.7491)].
- [412] M.J. REES and P. MÉSZÁROS:
'Unsteady outflow models for cosmological gamma-ray bursts',
in: *Astrophys. J. Lett.* 430 (1994), pp. L93–L96. DOI: [10.1086/187446](https://doi.org/10.1086/187446). arXiv: [astro-ph/9404038](https://arxiv.org/abs/astro-ph/9404038).
- [413] M.J. REES and PETER MÉSZÁROS:
'Dissipative photosphere models of gamma-ray bursts and x-ray flashes',
in: *Astrophys. J.* 628 (2005), pp. 847–852. DOI: [10.1086/430818](https://doi.org/10.1086/430818). arXiv: [astro-ph/0412702](https://arxiv.org/abs/astro-ph/0412702).
- [414] MARTIN J. REES:
'Tidal disruption of stars by black holes of 10^6 – 10^8 solar masses in nearby galaxies',
in: *Nature* 333.6173 (June 1988), pp. 523–528. DOI: [10.1038/333523a0](https://doi.org/10.1038/333523a0).
- [415] A. REST ET AL.:
'Pushing the Boundaries of Conventional Core-Collapse Supernovae: The Extremely Energetic Supernova SN 2003ma',
in: *Astrophys. J.* 729 (2011), p. 88. DOI: [10.1088/0004-637X/729/2/88](https://doi.org/10.1088/0004-637X/729/2/88). arXiv: [0911.2002](https://arxiv.org/abs/0911.2002) [[astro-ph.CO](https://arxiv.org/abs/0911.2002)].

- [416] SIMEON REUSCH ET AL.:
'The candidate tidal disruption event AT2019fdr coincident with a high-energy neutrino',
in: (2021). arXiv: [2111.09390](https://arxiv.org/abs/2111.09390) [[astro-ph.HE](#)].
- [417] SIMEON REUSCH ET AL.:
'IceCube-200530A - SN2020lam classified as SN II without evidence of CSM interaction',
in: *GRB Coordinates Network* 27910 (June 2020), p. 1.
- [418] SIMEON REUSCH ET AL.:
'IceCube-200530A - SN2020lls likely unrelated',
in: *GRB Coordinates Network* 27980 (June 2020), p. 1.
- [419] SIMEON REUSCH ET AL.:
'IceCube-200530A: Candidate Counterparts from the Zwicky Transient Facility',
in: *GRB Coordinates Network* 27872 (May 2020), p. 1.
- [420] C. RICCI ET AL.:
'BAT AGN Spectroscopic Survey. V. X-Ray Properties of the Swift/BAT 70-month AGN Catalog',
in: 233.2, 17 (Dec. 2017), p. 17. DOI: [10.3847/1538-4365/aa96ad](https://doi.org/10.3847/1538-4365/aa96ad). arXiv: [1709.03989](https://arxiv.org/abs/1709.03989) [[astro-ph.HE](#)].
- [421] PATRIZIA ROMANO ET AL.:
'X-ray flare in xrf 050406: evidence for prolonged engine activity',
in: *Astron. Astrophys.* 450 (2006), pp. 59–68. DOI: [10.1051/0004-6361:20054172](https://doi.org/10.1051/0004-6361:20054172). arXiv: [astro-ph/0601173](https://arxiv.org/abs/astro-ph/0601173).
- [422] ESTEBAN ROULET and FRANCESCO VISSANI:
Neutrinos in Physics and Astrophysics,
WORLD SCIENTIFIC, 2022. DOI: [10.1142/12982](https://doi.org/10.1142/12982). eprint: <https://www.worldscientific.com/doi/pdf/10.1142/12982>. URL: <https://www.worldscientific.com/doi/abs/10.1142/12982>.
- [423] ESTEBAN ROULET and FRANCESCO VISSANI:
'On the energy of the protons producing the very high-energy astrophysical neutrinos',
in: *JCAP* 03 (2021), p. 050. DOI: [10.1088/1475-7516/2021/03/050](https://doi.org/10.1088/1475-7516/2021/03/050). arXiv: [2011.12769](https://arxiv.org/abs/2011.12769) [[astro-ph.HE](#)].
- [424] ANNIKA RUDOLPH ET AL.:
'Impact of the Collision Model on the Multi-messenger Emission from Gamma-Ray Burst Internal Shocks',
in: *Astrophys. J.* 893 (2020), p. 72. DOI: [10.3847/1538-4357/ab7ea7](https://doi.org/10.3847/1538-4357/ab7ea7). arXiv: [1907.10633](https://arxiv.org/abs/1907.10633) [[astro-ph.HE](#)].
- [425] GEORGE B. RYBICKI and ALAN P. LIGHTMAN:
Radiative Processes in Astrophysics,
1986.
- [426] I. SAGERT ET AL.:
'Signals of the QCD phase transition in core-collapse supernovae',
in: *Phys. Rev. Lett.* 102 (2009), p. 081101. DOI: [10.1103/PhysRevLett.102.081101](https://doi.org/10.1103/PhysRevLett.102.081101). arXiv: [0809.4225](https://arxiv.org/abs/0809.4225) [[astro-ph](#)].
- [427] T. SAKAMOTO ET AL.:
'The First Swift BAT Gamma-Ray Burst Catalog',
in: *Astrophys. J. Suppl.* 175 (2008), pp. 179–190. DOI: [10.1086/523646](https://doi.org/10.1086/523646). arXiv: [0707.4626](https://arxiv.org/abs/0707.4626) [[astro-ph](#)].

- [428] FILIP SAMUELSSON ET AL.:
'The Limited Contribution of Low- and High-Luminosity Gamma-Ray Bursts to Ultra-High Energy Cosmic Rays',
in: *Astrophys. J.* 876.2 (2019), p. 93. DOI: [10.3847/1538-4357/ab153c](https://doi.org/10.3847/1538-4357/ab153c). arXiv: [1810.06579](https://arxiv.org/abs/1810.06579) [[astro-ph.HE](#)].
- [429] RODOLFO SANTANA, RODOLFO BARNIOL DURAN and PAWAN KUMAR:
'Magnetic Fields In Relativistic Collisionless Shocks',
in: *Astrophys. J.* 785 (2014), p. 29. DOI: [10.1088/0004-637X/785/1/29](https://doi.org/10.1088/0004-637X/785/1/29). arXiv: [1309.3277](https://arxiv.org/abs/1309.3277) [[astro-ph.HE](#)].
- [430] RE'EM SARI and TSVI PIRAN:
'GRB 990123: The Optical Flash and the Fireball Model',
in: *Astrophys. J. Lett.* 517.2 (1999), pp. L109–L112. DOI: [10.1086/312039](https://doi.org/10.1086/312039). arXiv: [astro-ph/9902009](https://arxiv.org/abs/astro-ph/9902009) [[astro-ph](#)].
- [431] RE'EM SARI, TSVI PIRAN and RAMESH NARAYAN:
'Spectra and light curves of gamma-ray burst afterglows',
in: *Astrophys. J. Lett.* 497 (1998), p. L17. DOI: [10.1086/311269](https://doi.org/10.1086/311269). arXiv: [astro-ph/9712005](https://arxiv.org/abs/astro-ph/9712005).
- [432] REEM SARI and TSVI PIRAN:
'Hydrodynamic time scales and temporal structure in GRBs',
in: *AIP Conf. Proc.* 384.1 (1996). Ed. by C. Kouveliotou, G.J. Fishman and M.F. Briggs, pp. 782–786. DOI: [10.1063/1.51659](https://doi.org/10.1063/1.51659). arXiv: [astro-ph/9512125](https://arxiv.org/abs/astro-ph/9512125).
- [433] PRANTIK SARMAH ET AL.:
'Gamma-rays and neutrinos from supernovae of Type Ib/c with late time emission',
in: *arXiv e-prints*, arXiv:2303.13576 (Mar. 2023), arXiv:2303.13576. DOI: [10.48550/arXiv.2303.13576](https://doi.org/10.48550/arXiv.2303.13576). arXiv: [2303.13576](https://arxiv.org/abs/2303.13576) [[astro-ph.HE](#)].
- [434] PRANTIK SARMAH ET AL.:
'High energy particles from young supernovae: gamma-ray and neutrino connections',
in: 2022.8, 011 (Aug. 2022), p. 011. DOI: [10.1088/1475-7516/2022/08/011](https://doi.org/10.1088/1475-7516/2022/08/011). arXiv: [2204.03663](https://arxiv.org/abs/2204.03663) [[astro-ph.HE](#)].
- [435] TOSHIKI SATO ET AL.:
'X-Ray Measurements of the Particle Acceleration Properties at Inward Shocks in Cassiopeia A',
in: 853.1, 46 (Jan. 2018), p. 46. DOI: [10.3847/1538-4357/aaa021](https://doi.org/10.3847/1538-4357/aaa021). arXiv: [1710.06992](https://arxiv.org/abs/1710.06992) [[astro-ph.HE](#)].
- [436] EDWARD F. SCHLAFLY and DOUGLAS P. FINKBEINER:
'Measuring Reddening with Sloan Digital Sky Survey Stellar Spectra and Recalibrating SFD',
in: 737.2, 103 (Aug. 2011), p. 103. DOI: [10.1088/0004-637X/737/2/103](https://doi.org/10.1088/0004-637X/737/2/103). arXiv: [1012.4804](https://arxiv.org/abs/1012.4804) [[astro-ph.GA](#)].
- [437] ERIC M. SCHLEGEL:
'A new subclass of type II supernovae?',
in: *Mon. Not. Roy. Astron. Soc.* 244 (May 1990), pp. 269–271.
- [438] K. M. SCHURE ET AL.:
'Time-dependent particle acceleration in supernova remnants in different environments',
in: 406.4 (Aug. 2010), pp. 2633–2649. DOI: [10.1111/j.1365-2966.2010.16857.x](https://doi.org/10.1111/j.1365-2966.2010.16857.x). arXiv: [1004.2766](https://arxiv.org/abs/1004.2766) [[astro-ph.HE](#)].

- [439] NICHOLAS SENNO, KOHTA MURASE and PETER MÉSZÁROS:
‘High-energy Neutrino Flares from X-Ray Bright and Dark Tidal Disruption Events’,
in: *Astrophys. J.* 838.1 (2017), p. 3. DOI: [10 . 3847 / 1538 - 4357 / aa6344](https://doi.org/10.3847/1538-4357/aa6344). arXiv: [1612 . 00918](https://arxiv.org/abs/1612.00918)
[\[astro-ph.HE\]](#).
- [440] B. J. SHAPPEE ET AL.:
‘The Man behind the Curtain: X-Rays Drive the UV through NIR Variability in the 2013 Active Galactic Nucleus Outburst in NGC 2617’,
in: 788.1, 48 (June 2014), p. 48. DOI: [10 . 1088 / 0004 - 637X / 788 / 1 / 48](https://doi.org/10.1088/0004-637X/788/1/48). arXiv: [1310 . 2241](https://arxiv.org/abs/1310.2241)
[\[astro-ph.HE\]](#).
- [441] Y. SHVARTZVALD ET AL.:
‘ULTRASAT: A wide-field time-domain UV space telescope’,
in: *arXiv e-prints*, arXiv:2304.14482 (Apr. 2023), arXiv:2304.14482. DOI: [10 . 48550 / arXiv . 2304 . 14482](https://doi.org/10.48550/arXiv.2304.14482). arXiv: [2304 . 14482](https://arxiv.org/abs/2304.14482) [\[astro-ph.IM\]](#).
- [442] LORENZO SIRONI, MARIA PETROPOULOU and DIMITRIOS GIANNIOS:
‘Relativistic jets shine through shocks or magnetic reconnection?’,
in: *Mon. Not. Roy. Astron. Soc.* 450.1 (2015), pp. 183–191. DOI: [10 . 1093 / mnras / stv641](https://doi.org/10.1093/mnras/stv641). arXiv: [1502 . 01021](https://arxiv.org/abs/1502.01021) [\[astro-ph.HE\]](#).
- [443] LORENZO SIRONI and ANATOLY SPITKOVSKY:
‘Particle Acceleration in Relativistic Magnetized Collisionless Electron-Ion Shocks’,
in: *Astrophys. J.* 726 (2011), p. 75. DOI: [10 . 1088 / 0004 - 637X / 726 / 2 / 75](https://doi.org/10.1088/0004-637X/726/2/75). arXiv: [1009 . 0024](https://arxiv.org/abs/1009.0024)
[\[astro-ph.HE\]](#).
- [444] LORENZO SIRONI and ANATOLY SPITKOVSKY:
‘Relativistic Reconnection: an Efficient Source of Non-Thermal Particles’,
in: *Astrophys. J. Lett.* 783 (2014), p. L21. DOI: [10 . 1088 / 2041 - 8205 / 783 / 1 / L21](https://doi.org/10.1088/2041-8205/783/1/L21). arXiv: [1401 . 5471](https://arxiv.org/abs/1401.5471) [\[astro-ph.HE\]](#).
- [445] LORENZO SIRONI, ANATOLY SPITKOVSKY and JONATHAN ARONS:
‘The Maximum Energy of Accelerated Particles in Relativistic Collisionless Shocks’,
in: *Astrophys. J.* 771 (2013), p. 54. DOI: [10 . 1088 / 0004 - 637X / 771 / 1 / 54](https://doi.org/10.1088/0004-637X/771/1/54). arXiv: [1301 . 5333](https://arxiv.org/abs/1301.5333)
[\[astro-ph.HE\]](#).
- [446] P. SLANE ET AL.:
‘Erratum: “A CR-hydro-NEI Model of the Structure and Broadband Emission from Tycho’s Supernova Remnant”’ (2014, ApJ, 783, 33)’,
in: 799.2, 238 (Feb. 2015), p. 238. DOI: [10 . 1088 / 0004 - 637X / 799 / 2 / 238](https://doi.org/10.1088/0004-637X/799/2/238). arXiv: [1401 . 2556](https://arxiv.org/abs/1401.2556)
[\[astro-ph.HE\]](#).
- [447] K. W. SMITH ET AL.:
‘Design and Operation of the ATLAS Transient Science Server’,
in: *Publ. Astron. Soc. Pac.* 132.1014, 085002 (Aug. 2020), p. 085002. DOI: [10 . 1088 / 1538 - 3873 / ab936e](https://doi.org/10.1088/1538-3873/ab936e). arXiv: [2003 . 09052](https://arxiv.org/abs/2003.09052) [\[astro-ph.IM\]](#).
- [448] NATHAN SMITH:
‘Interacting Supernovae: Types II_n and Ib_n’,
in: *Handbook of Supernovae*. Ed. by Athem W. Alsabti and Paul Murdin. 2017, p. 403. DOI: [10 . 1007 / 978 - 3 - 319 - 21846 - 5 _ 38](https://doi.org/10.1007/978-3-319-21846-5_38).

- [449] NATHAN SMITH:
'Mass Loss: Its Effect on the Evolution and Fate of High-Mass Stars',
in: *Ann. Rev. Astron. Astrophys.* 52 (2014), pp. 487–528. DOI: [10.1146/annurev-astro-081913-040025](https://doi.org/10.1146/annurev-astro-081913-040025). arXiv: [1402.1237](https://arxiv.org/abs/1402.1237) [astro-ph.SR].
- [450] NATHAN SMITH ET AL.:
'Mass and Kinetic Energy of the Homunculus Nebula around η Carinae',
in: 125.3 (Mar. 2003), pp. 1458–1466. DOI: [10.1086/346278](https://doi.org/10.1086/346278).
- [451] NATHAN SMITH ET AL.:
'Observed Fractions of Core-Collapse Supernova Types and Initial Masses of their Single and Binary Progenitor Stars',
in: *Mon. Not. Roy. Astron. Soc.* 412 (2011), p. 1522. DOI: [10.1111/j.1365-2966.2011.17229.x](https://doi.org/10.1111/j.1365-2966.2011.17229.x). arXiv: [1006.3899](https://arxiv.org/abs/1006.3899) [astro-ph.HE].
- [452] NATHAN SMITH ET AL.:
'SN 2006tf: Precursor Eruptions and the Optically Thick Regime of Extremely Luminous Type II_n Supernovae',
in: *Astrophys. J.* 686 (2008), p. 467. DOI: [10.1086/591021](https://doi.org/10.1086/591021). arXiv: [0804.0042](https://arxiv.org/abs/0804.0042) [astro-ph].
- [453] NATHAN SMITH ET AL.:
'The brightest supernova ever recorded, powered by the death of an extremely massive star',
in: *Astrophys. J.* 666 (2007), pp. 1116–1128. DOI: [10.1086/519949](https://doi.org/10.1086/519949). arXiv: [astro-ph/0612617](https://arxiv.org/abs/astro-ph/0612617).
- [454] H.C. SPRUIT, F. DAIGNE and G. DRENKHAHN:
'Large scale magnetic fields and their dissipation in grb fireballs',
in: *Astron. Astrophys.* 369 (2001), p. 694. DOI: [10.1051/0004-6361:20010131](https://doi.org/10.1051/0004-6361:20010131). arXiv: [astro-ph/0004274](https://arxiv.org/abs/astro-ph/0004274).
- [455] ROBERT STEIN ET AL.:
'A tidal disruption event coincident with a high-energy neutrino',
in: *Nature Astron.* 5.5 (2021), pp. 510–518. DOI: [10.1038/s41550-020-01295-8](https://doi.org/10.1038/s41550-020-01295-8). arXiv: [2005.05340](https://arxiv.org/abs/2005.05340) [astro-ph.HE].
- [456] ROBERT STEIN:
'Tidal Disruption Events and High-energy Neutrinos',
in: *Proceedings of 37th International Cosmic Ray Conference — PoS(ICRC2021)*. Vol. 395. 2021, p. 009.
DOI: [10.22323/1.395.0009](https://doi.org/10.22323/1.395.0009).
- [457] ROBERT STEIN ET AL.:
'Neutrino follow-up with the Zwicky transient facility: results from the first 24 campaigns',
in: *Mon. Not. Roy. Astron. Soc.* 521.4 (June 2023), pp. 5046–5063. DOI: [10.1093/mnras/stad767](https://doi.org/10.1093/mnras/stad767).
arXiv: [2203.17135](https://arxiv.org/abs/2203.17135) [astro-ph.HE].
- [458] MAXIMILIAN STRITZINGER ET AL.:
'Multi-wavelength Observations of the Enduring Type II_n Supernovae 2005ip and 2006jd',
in: *Astrophys. J.* 756.2, 173 (Sept. 2012), p. 173. DOI: [10.1088/0004-637X/756/2/173](https://doi.org/10.1088/0004-637X/756/2/173). arXiv: [1206.5575](https://arxiv.org/abs/1206.5575) [astro-ph.CO].
- [459] NORA L. STROTJOHANN, MAREK KOWALSKI and ANNA FRANCKOWIAK:
'Eddington bias for cosmic neutrino sources',
in: *Astron. Astrophys.* 622 (2019), p. L9. DOI: [10.1051/0004-6361/201834750](https://doi.org/10.1051/0004-6361/201834750). arXiv: [1809.06865](https://arxiv.org/abs/1809.06865) [astro-ph.HE].

- [460] STEVEN J. STURNER ET AL.:
‘Temporal Evolution of Nonthermal Spectra from Supernova Remnants’,
in: *Astrophys. J.* 490.2 (Dec. 1997), pp. 619–632. DOI: [10.1086/304894](https://doi.org/10.1086/304894).
- [461] OLGA SUVOROVA ET AL.:
‘Multi-messenger and real-time astrophysics with the Baikal-GVD telescope’,
in: *Proceedings of 37th International Cosmic Ray Conference – PoS(ICRC2021)*. Vol. 395. 2021, p. 946.
DOI: [10.22323/1.395.0946](https://doi.org/10.22323/1.395.0946).
- [462] AKIHIRO SUZUKI, TAKASHI J. MORIYA and TOMOYA TAKIWAKI:
‘A Systematic Study on the Rise Time–Peak Luminosity Relation for Bright Optical Transients
Powered by Wind Shock Breakout’,
in: *Astrophys. J.* 899.1 (2020), p. 56. DOI: [10.3847/1538-4357/aba0ba](https://doi.org/10.3847/1538-4357/aba0ba). arXiv: [2006.16494](https://arxiv.org/abs/2006.16494)
[astro-ph.HE].
- [463] AKIHIRO SUZUKI, TAKASHI J. MORIYA and TOMOYA TAKIWAKI:
‘Supernova Ejecta Interacting with a Circumstellar Disk. I. Two-dimensional Radiation-hydrodynamic
Simulations’,
in: *Astrophys. J.* 887.2, 249 (Dec. 2019), p. 249. DOI: [10.3847/1538-4357/ab5a83](https://doi.org/10.3847/1538-4357/ab5a83). arXiv:
[1911.09261](https://arxiv.org/abs/1911.09261) [astro-ph.HE].
- [464] AKIHIRO SUZUKI ET AL.:
‘Extremely energetic supernova explosions embedded in a massive circumstellar medium: the
case of SN 2016aps’,
in: *Astrophys. J.* 908.1 (2021), p. 99. DOI: [10.3847/1538-4357/abd6ce](https://doi.org/10.3847/1538-4357/abd6ce). arXiv: [2012.13283](https://arxiv.org/abs/2012.13283)
[astro-ph.HE].
- [465] GILAD SVIRSKI, EHUD NAKAR and RE’EM SARI:
‘Optical to X-rays supernovae light curves following shock breakout through a thick wind’,
in: *Astrophys. J.* 759 (2012), p. 108. DOI: [10.1088/0004-637X/759/2/108](https://doi.org/10.1088/0004-637X/759/2/108). arXiv: [1202.3437](https://arxiv.org/abs/1202.3437)
[astro-ph.HE].
- [466] F. TADDIA ET AL.:
‘Carnegie Supernova Project: Observations of Type II_n supernovae’,
in: *Astron. Astrophys.* 555, A10 (July 2013), A10. DOI: [10.1051/0004-6361/201321180](https://doi.org/10.1051/0004-6361/201321180). arXiv:
[1304.3038](https://arxiv.org/abs/1304.3038) [astro-ph.CO].
- [467] IRENE TAMBORRA and SHIN’ICHIRO ANDO:
‘Diffuse emission of high-energy neutrinos from gamma-ray burst fireballs’,
in: *JCAP* 09 (2015), p. 036. DOI: [10.1088/1475-7516/2015/9/036](https://doi.org/10.1088/1475-7516/2015/9/036). arXiv: [1504.00107](https://arxiv.org/abs/1504.00107)
[astro-ph.HE].
- [468] IRENE TAMBORRA and SHIN’ICHIRO ANDO:
‘Inspecting the supernova–gamma-ray-burst connection with high-energy neutrinos’,
in: *Phys. Rev. D* 93.5 (2016), p. 053010. DOI: [10.1103/PhysRevD.93.053010](https://doi.org/10.1103/PhysRevD.93.053010). arXiv: [1512.01559](https://arxiv.org/abs/1512.01559)
[astro-ph.HE].
- [469] IRENE TAMBORRA, SHIN’ICHIRO ANDO and KOHTA MURASE:
‘Star-forming galaxies as the origin of diffuse high-energy backgrounds: Gamma-ray and neut-
rino connections, and implications for starburst history’,
in: *JCAP* 09 (2014), p. 043. DOI: [10.1088/1475-7516/2014/09/043](https://doi.org/10.1088/1475-7516/2014/09/043). arXiv: [1404.1189](https://arxiv.org/abs/1404.1189)
[astro-ph.HE].

- [470] JONI TAMMI and PETER DUFFY:
'Particle-acceleration timescales in TeV blazar flares',
in: *AIP Conf. Proc.* 1085.1 (2009). Ed. by Felix A. Aharonian, Werner Hofmann and Frank Rieger,
pp. 475–478. DOI: [10.1063/1.3076711](https://doi.org/10.1063/1.3076711). arXiv: [0811.3573](https://arxiv.org/abs/0811.3573) [astro-ph].
- [471] A. H. TAUB:
'Relativistic Rankine-Hugoniot Equations',
in: *Phys. Rev.* 74 (1948), pp. 328–334. DOI: [10.1103/PhysRev.74.328](https://doi.org/10.1103/PhysRev.74.328).
- [472] JESSYMOL K. THOMAS, REETANJALI MOHARANA and SOEBUR RAZZAQUE:
'Ultrahigh energy neutrino afterglows of nearby long duration gamma-ray bursts',
in: *Phys. Rev. D* 96.10 (2017), p. 103004. DOI: [10.1103/PhysRevD.96.103004](https://doi.org/10.1103/PhysRevD.96.103004). arXiv: [1710.04024](https://arxiv.org/abs/1710.04024) [astro-ph.HE].
- [473] C. THOMPSON:
'A Model of gamma-ray bursts',
in: *Mon. Not. Roy. Astron. Soc.* 270 (1994), p. 480.
- [474] CHRISTOPHER THOMPSON and RAMANDEEP GILL:
'Hot Electromagnetic Outflows. III. Displaced Fireball in a Strong Magnetic Field',
in: *Astrophys. J.* 791 (2014), p. 46. DOI: [10.1088/0004-637X/791/1/46](https://doi.org/10.1088/0004-637X/791/1/46). arXiv: [1310.2480](https://arxiv.org/abs/1310.2480) [astro-ph.HE].
- [475] KENJI TOMA, XUE-FENG WU and PETER MÉSZÁROS:
'A Photosphere-Internal Shock Model of Gamma-Ray Bursts: Case Studies of Fermi/LAT Bursts',
in: *Mon. Not. Roy. Astron. Soc.* 415 (2011), pp. 1663–1680. DOI: [10.1111/j.1365-2966.2011.18807.x](https://doi.org/10.1111/j.1365-2966.2011.18807.x). arXiv: [1002.2634](https://arxiv.org/abs/1002.2634) [astro-ph.HE].
- [476] J. L. TONRY ET AL.:
'ATLAS: A High-cadence All-sky Survey System',
in: *Publ. Astron. Soc. Pac.* 130.988 (June 2018), p. 064505. DOI: [10.1088/1538-3873/aabadf](https://doi.org/10.1088/1538-3873/aabadf).
arXiv: [1802.00879](https://arxiv.org/abs/1802.00879) [astro-ph.IM].
- [477] VLADIMIR V. USOV:
'On the nature of nonthermal radiation from cosmological gamma-ray bursters',
in: *Mon. Not. Roy. Astron. Soc.* 267 (1994), p. 1035. DOI: [10.1093/mnras/267.4.1035](https://doi.org/10.1093/mnras/267.4.1035). arXiv: [astro-ph/9312024](https://arxiv.org/abs/astro-ph/9312024).
- [478] SJOERT VAN VELZEN ET AL.:
'Seventeen Tidal Disruption Events from the First Half of ZTF Survey Observations: Entering a New Era of Population Studies',
in: *Astrophys. J.* 908.1 (2021), p. 4. DOI: [10.3847/1538-4357/abc258](https://doi.org/10.3847/1538-4357/abc258). arXiv: [2001.01409](https://arxiv.org/abs/2001.01409) [astro-ph.HE].
- [479] TONIA M. VENTERS ET AL.:
'POEMMA's Target of Opportunity Sensitivity to Cosmic Neutrino Transient Sources',
in: *Phys. Rev. D* 102 (2020), p. 123013. DOI: [10.1103/PhysRevD.102.123013](https://doi.org/10.1103/PhysRevD.102.123013). arXiv: [1906.07209](https://arxiv.org/abs/1906.07209) [astro-ph.HE].
- [480] MARIO VIETRI:
'On the acceleration of ultrahigh-energy cosmic rays in gamma-ray bursts',
in: *Astrophys. J.* 453 (1995), pp. 883–889. DOI: [10.1086/176448](https://doi.org/10.1086/176448). arXiv: [astro-ph/9506081](https://arxiv.org/abs/astro-ph/9506081).

- [481] V. ASHLEY VILLAR ET AL.:
‘Theoretical Models of Optical Transients. I. A Broad Exploration of the Duration-Luminosity Phase Space’,
in: *Astrophys. J.* 849 (2017), p. 70. DOI: [10.3847/1538-4357/aa8fcb](https://doi.org/10.3847/1538-4357/aa8fcb). arXiv: [1707.08132](https://arxiv.org/abs/1707.08132) [[astro-ph.HE](#)].
- [482] EDOARDO VITAGLIANO, IRENE TAMBORRA and GEORG RAFFELT:
‘Grand Unified Neutrino Spectrum at Earth: Sources and Spectral Components’,
in: *Rev. Mod. Phys.* 92 (2020), p. 45006. DOI: [10.1103/RevModPhys.92.045006](https://doi.org/10.1103/RevModPhys.92.045006). arXiv: [1910.11878](https://arxiv.org/abs/1910.11878) [[astro-ph.HE](#)].
- [483] A. VLASIS ET AL.:
‘Two-shell collisions in the gamma-ray burst afterglow phase’,
in: *Mon. Not. R. Astron. Soc.* 415.1 (2011), pp. 279–291. DOI: [10.1111/j.1365-2966.2011.18696.x](https://doi.org/10.1111/j.1365-2966.2011.18696.x).
- [484] ARJEN VAN VLIET, RAFAEL ALVES BATISTA and JÖRG R. HÖRANDEL:
‘Determining the fraction of cosmic-ray protons at ultrahigh energies with cosmogenic neutrinos’,
in: *Phys. Rev. D* 100.2 (2019), p. 021302. DOI: [10.1103/PhysRevD.100.021302](https://doi.org/10.1103/PhysRevD.100.021302). arXiv: [1901.01899](https://arxiv.org/abs/1901.01899) [[astro-ph.HE](#)].
- [485] A. VOLNOVA ET AL.:
‘GRB 100901A: optical observations in Mondy and r-light curve.’,
in: *GRB Coordinates Network* 11270 (2010), p. 1.
- [486] INDREK VURM and ANDREI M. BELOBORODOV:
‘Radiative Transfer Models for Gamma-Ray Bursts’,
in: *Astrophys. J.* 831.2 (2016), p. 175. DOI: [10.3847/0004-637X/831/2/175](https://doi.org/10.3847/0004-637X/831/2/175). arXiv: [1506.01107](https://arxiv.org/abs/1506.01107) [[astro-ph.HE](#)].
- [487] INDREK VURM, YURI LYUBARSKY and TSVI PIRAN:
‘On thermalization in gamma-ray burst jets and the peak energies of photospheric spectra’,
in: *Astrophys. J.* 764 (2013), p. 143. DOI: [10.1088/0004-637X/764/2/143](https://doi.org/10.1088/0004-637X/764/2/143). arXiv: [1209.0763](https://arxiv.org/abs/1209.0763) [[astro-ph.HE](#)].
- [488] KAI WANG ET AL.:
‘Hadronic origin of prompt high-energy emission of gamma-ray bursts revisited: in the case of a limited maximum proton energy’,
in: *Astrophys. J.* 857.1 (2018), p. 24. DOI: [10.3847/1538-4357/aab667](https://doi.org/10.3847/1538-4357/aab667). arXiv: [1803.04112](https://arxiv.org/abs/1803.04112) [[astro-ph.HE](#)].
- [489] XIANG-GAO WANG ET AL.:
‘How bad or Good are the External Forward Shock Afterglow Models of Gamma-ray Bursts?’,
in: *Astrophys. J. Suppl.* 219.1 (2015), p. 9. DOI: [10.1088/0067-0049/219/1/9](https://doi.org/10.1088/0067-0049/219/1/9). arXiv: [1503.03193](https://arxiv.org/abs/1503.03193) [[astro-ph.HE](#)].
- [490] XIANG-YU WANG and ZI-GAO DAI:
‘Prompt TeV neutrinos from dissipative photospheres of gamma-ray bursts’,
in: *Astrophys. J. Lett.* 691 (2009), pp. L67–L71. DOI: [10.1088/0004-637X/691/2/L67](https://doi.org/10.1088/0004-637X/691/2/L67). arXiv: [0807.0290](https://arxiv.org/abs/0807.0290) [[astro-ph](#)].

- [491] XIANG-YU WANG and RUO-YU LIU:
'Tidal disruption jets of supermassive black holes as hidden sources of cosmic rays: explaining the IceCube TeV-PeV neutrinos',
in: *Phys. Rev. D* 93.8 (2016), p. 083005. DOI: [10.1103/PhysRevD.93.083005](https://doi.org/10.1103/PhysRevD.93.083005). arXiv: [1512.08596](https://arxiv.org/abs/1512.08596) [astro-ph.HE].
- [492] XIAOHU WANG and ABRAHAM LOEB:
'Variability of GRB afterglows due to interstellar turbulence',
in: *Astrophys. J.* 535 (2000), p. 788. DOI: [10.1086/308888](https://doi.org/10.1086/308888). arXiv: [astro-ph/9910477](https://arxiv.org/abs/astro-ph/9910477).
- [493] DONALD C. WARREN ET AL.:
'Synchrotron self-absorption in GRB afterglows: the effects of a thermal electron population',
in: *Mon. Not. Roy. Astron. Soc.* 480.3 (2018), pp. 4060–4068. DOI: [10.1093/mnras/sty2138](https://doi.org/10.1093/mnras/sty2138). arXiv: [1804.06030](https://arxiv.org/abs/1804.06030) [astro-ph.HE].
- [494] E. WAXMAN:
'The Origin of IceCube's Neutrinos: Cosmic Ray Accelerators Embedded in Star Forming Calorimeters',
in: (2017), pp. 33–45. DOI: [10.1142/9789814759410_0003](https://doi.org/10.1142/9789814759410_0003). arXiv: [1511.00815](https://arxiv.org/abs/1511.00815) [astro-ph.HE].
- [495] ELI WAXMAN:
'Cosmological gamma-ray bursts and the highest energy cosmic rays',
in: *Phys. Rev. Lett.* 75 (1995), pp. 386–389. DOI: [10.1103/PhysRevLett.75.386](https://doi.org/10.1103/PhysRevLett.75.386). arXiv: [astro-ph/9505082](https://arxiv.org/abs/astro-ph/9505082).
- [496] ELI WAXMAN:
'Gamma-ray burst afterglow: Confirming the cosmological fireball model',
in: *Astrophys. J. Lett.* 489 (1997), pp. L33–L36. DOI: [10.1086/310960](https://doi.org/10.1086/310960). arXiv: [astro-ph/9705229](https://arxiv.org/abs/astro-ph/9705229).
- [497] ELI WAXMAN:
'GRB afterglow: Supporting the cosmological fireball model, constraining parameters, and making predictions',
in: *Astrophys. J. Lett.* 485 (1997), p. L5. DOI: [10.1086/310809](https://doi.org/10.1086/310809). arXiv: [astro-ph/9704116](https://arxiv.org/abs/astro-ph/9704116).
- [498] ELI WAXMAN:
'High-energy cosmic rays and neutrinos from cosmological gamma-ray burst fireballs',
in: *Phys. Scripta T* 85 (2000). Ed. by L. Bergström, C. Fransson and P. Carlson, pp. 117–126. DOI: [10.1238/Physica.Topical.085a00117](https://doi.org/10.1238/Physica.Topical.085a00117). arXiv: [astro-ph/9911395](https://arxiv.org/abs/astro-ph/9911395).
- [499] ELI WAXMAN and JOHN N. BAHCALL:
'High-energy neutrinos from astrophysical sources: An Upper bound',
in: *Phys. Rev. D* 59 (1999), p. 023002. DOI: [10.1103/PhysRevD.59.023002](https://doi.org/10.1103/PhysRevD.59.023002). arXiv: [hep-ph/9807282](https://arxiv.org/abs/hep-ph/9807282).
- [500] ELI WAXMAN and JOHN N. BAHCALL:
'High-energy neutrinos from cosmological gamma-ray burst fireballs',
in: *Phys. Rev. Lett.* 78 (1997), pp. 2292–2295. DOI: [10.1103/PhysRevLett.78.2292](https://doi.org/10.1103/PhysRevLett.78.2292). arXiv: [astro-ph/9701231](https://arxiv.org/abs/astro-ph/9701231).
- [501] ELI WAXMAN and JOHN N. BAHCALL:
'Neutrino afterglow from gamma-ray bursts: Similar to 10^{18} eV',
in: *Astrophys. J.* 541 (2000), pp. 707–711. DOI: [10.1086/309462](https://doi.org/10.1086/309462). arXiv: [hep-ph/9909286](https://arxiv.org/abs/hep-ph/9909286).

- [502] T. A. WEAVER:
'The structure of supernova shock waves',
in: *Astrophys. J.* 32 (Oct. 1976), pp. 233–282. DOI: [10.1086/190398](https://doi.org/10.1086/190398).
- [503] G. R. WERNER ET AL.:
'The Extent of Power-law Energy Spectra in Collisionless Relativistic Magnetic Reconnection in Pair Plasmas',
in: *Astrophys. J. Lett.* 816.1, L8 (Jan. 2016), p. L8. DOI: [10.3847/2041-8205/816/1/L8](https://doi.org/10.3847/2041-8205/816/1/L8). arXiv: [1409.8262](https://arxiv.org/abs/1409.8262) [[astro-ph.HE](https://arxiv.org/abs/1409.8262)].
- [504] G.R. WERNER ET AL.:
'Non-thermal particle acceleration in collisionless relativistic electron–proton reconnection',
in: *Mon. Not. Roy. Astron. Soc.* 473.4 (2018), pp. 4840–4861. DOI: [10.1093/mnras/stx2530](https://doi.org/10.1093/mnras/stx2530). arXiv: [1612.04493](https://arxiv.org/abs/1612.04493) [[astro-ph.HE](https://arxiv.org/abs/1612.04493)].
- [505] T. WEVERS ET AL.:
'Rapid Accretion State Transitions following the Tidal Disruption Event AT2018fyk',
in: 912.2, 151 (May 2021), p. 151. DOI: [10.3847/1538-4357/abf5e2](https://doi.org/10.3847/1538-4357/abf5e2). arXiv: [2101.04692](https://arxiv.org/abs/2101.04692) [[astro-ph.HE](https://arxiv.org/abs/2101.04692)].
- [506] R. A. M. J. WIJERS and T. J. GALAMA:
'Physical parameters of GRB 970508 and GRB 971214 from their afterglow synchrotron emission',
in: *Astrophys. J.* 523 (1999), pp. 177–186. DOI: [10.1086/307705](https://doi.org/10.1086/307705). arXiv: [astro-ph/9805341](https://arxiv.org/abs/astro-ph/9805341).
- [507] WALTER WINTER and CECILIA LUNARDINI:
'A concordance scenario for the observed neutrino from a tidal disruption event',
in: *Nature Astron.* 5.5 (2021), p. 5. DOI: [10.1038/s41550-021-01343-x](https://doi.org/10.1038/s41550-021-01343-x). arXiv: [2005.06097](https://arxiv.org/abs/2005.06097) [[astro-ph.HE](https://arxiv.org/abs/2005.06097)].
- [508] S. E. WOOSLEY:
'Gamma-ray bursts from stellar mass accretion disks around black holes',
in: *Astrophys. J.* 405 (1993), p. 273. DOI: [10.1086/172359](https://doi.org/10.1086/172359).
- [509] S.E. WOOSLEY and J.S. BLOOM:
'The Supernova Gamma-Ray Burst Connection',
in: *Ann. Rev. Astron. Astrophys.* 44 (2006), pp. 507–556. DOI: [10.1146/annurev.astro.43.072103.150558](https://doi.org/10.1146/annurev.astro.43.072103.150558). arXiv: [astro-ph/0609142](https://arxiv.org/abs/astro-ph/0609142).
- [510] R. L. WORKMAN ET AL.:
'Review of Particle Physics',
in: *PTEP* 2022 (2022), p. 083C01. DOI: [10.1093/ptep/ptac097](https://doi.org/10.1093/ptep/ptac097).
- [511] DI XIAO, ZI-GAO DAI and PETER MÉSZÁROS:
'Prompt Neutrino Emission of Gamma-Ray Bursts in the Dissipative Photospheric Scenario Revisited: Possible Contributions from Cocoon',
in: *Astrophys. J.* 843.1 (2017), p. 17. DOI: [10.3847/1538-4357/aa76e5](https://doi.org/10.3847/1538-4357/aa76e5). arXiv: [1706.01293](https://arxiv.org/abs/1706.01293) [[astro-ph.HE](https://arxiv.org/abs/1706.01293)].
- [512] L. YAN ET AL.:
'Spectroscopic Classifications of Eighteen Superluminous Supernovae from the Zwicky Transient Facility',
in: *Transient Name Server AstroNote* 45 (July 2019), p. 1.

- [513] HOI-FUNG YU ET AL.:
'The Fermi GBM gamma-ray burst time-resolved spectral catalog: brightest bursts in the first four years',
in: *Astron. Astrophys.* 588 (2016), A135. DOI: [10.1051/0004-6361/201527509](https://doi.org/10.1051/0004-6361/201527509). arXiv: [1601.05206](https://arxiv.org/abs/1601.05206) [[astro-ph.HE](#)].
- [514] HOI-FUNG YU, HÜSNE DERELI-BÉGUÉ and FELIX RYDE:
'Bayesian Time-resolved Spectroscopy of GRB Pulses',
in: *Astrophys. J.* 886.1, 20 (Nov. 2019), p. 20. DOI: [10.3847/1538-4357/ab488a](https://doi.org/10.3847/1538-4357/ab488a). arXiv: [1810.07313](https://arxiv.org/abs/1810.07313) [[astro-ph.HE](#)].
- [515] HASAN YÜKSEL ET AL.:
'Revealing the High-Redshift Star Formation Rate with Gamma-Ray Bursts',
in: *Astrophys. J. Lett.* 683 (2008), pp. L5–L8. DOI: [10.1086/591449](https://doi.org/10.1086/591449). arXiv: [0804.4008](https://arxiv.org/abs/0804.4008) [[astro-ph](#)].
- [516] FABIO ZANDANEL ET AL.:
'High-energy gamma-ray and neutrino backgrounds from clusters of galaxies and radio constraints',
in: *Astron. Astrophys.* 578 (2015), A32. DOI: [10.1051/0004-6361/201425249](https://doi.org/10.1051/0004-6361/201425249). arXiv: [1410.8697](https://arxiv.org/abs/1410.8697) [[astro-ph.HE](#)].
- [517] YA. B. ZEL'DOVICH and YU. P. RAIZER:
Physics of shock waves and high-temperature hydrodynamic phenomena,
1967.
- [518] BIN-BIN ZHANG ET AL.:
'Synchrotron Origin of the Typical GRB Band Function—a Case Study of GRB 130606b',
in: *Astrophys. J.* 816.2 (2016), p. 72. DOI: [10.3847/0004-637X/816/2/72](https://doi.org/10.3847/0004-637X/816/2/72). arXiv: [1505.05858](https://arxiv.org/abs/1505.05858) [[astro-ph.HE](#)].
- [519] BING ZHANG:
'Synchrotron radiation in γ -ray burst prompt emission',
in: *Nature Astron.* 4.3 (2020), pp. 210–211. DOI: [10.1038/s41550-020-1041-3](https://doi.org/10.1038/s41550-020-1041-3). arXiv: [2002.09638](https://arxiv.org/abs/2002.09638) [[astro-ph.HE](#)].
- [520] BING ZHANG:
The Physics of Gamma-Ray Bursts,
2018. DOI: [10.1017/9781139226530](https://doi.org/10.1017/9781139226530).
- [521] BING ZHANG and PAWAN KUMAR:
'Model-dependent high-energy neutrino flux from Gamma-Ray Bursts',
in: *Phys. Rev. Lett.* 110.12 (2013), p. 121101. DOI: [10.1103/PhysRevLett.110.121101](https://doi.org/10.1103/PhysRevLett.110.121101). arXiv: [1210.0647](https://arxiv.org/abs/1210.0647) [[astro-ph.HE](#)].
- [522] BING ZHANG and PETER MESZAROS:
'Gamma-ray bursts: Progress, problems & prospects',
in: *Int. J. Mod. Phys. A* 19 (2004), pp. 2385–2472. DOI: [10.1142/S0217751X0401746X](https://doi.org/10.1142/S0217751X0401746X). arXiv: [astro-ph/0311321](https://arxiv.org/abs/astro-ph/0311321).
- [523] BING ZHANG and HUIRONG YAN:
'The Internal-Collision-Induced Magnetic Reconnection and Turbulence (ICMART) Model of Gamma-Ray Bursts',
in: *Astrophys. J.* 726 (2011), p. 90. DOI: [10.1088/0004-637X/726/2/90](https://doi.org/10.1088/0004-637X/726/2/90). arXiv: [1011.1197](https://arxiv.org/abs/1011.1197) [[astro-ph.HE](#)].

- [524] BING ZHANG ET AL.:
'Physical processes shaping GRB x-ray afterglow lightcurves: Theoretical implications from the SWIFT XRT observations',
in: *Astrophys. J.* 642 (2006), pp. 354–370. DOI: [10.1086/500723](https://doi.org/10.1086/500723). arXiv: [astro-ph/0508321](https://arxiv.org/abs/astro-ph/0508321).
- [525] BO ZHANG and BING ZHANG:
'Gamma-Ray Burst Prompt Emission Light Curves and Power Density Spectra in the ICMART Model',
in: *Astrophys. J.* 782 (2014), p. 92. DOI: [10.1088/0004-637X/782/2/92](https://doi.org/10.1088/0004-637X/782/2/92). arXiv: [1312.7701](https://arxiv.org/abs/1312.7701) [[astro-ph.HE](https://arxiv.org/abs/astro-ph.HE)].
- [526] V. N. ZIRAKASHVILI and V. S. PTUSKIN:
'Type II supernovae as sources of high energy astrophysical neutrinos',
in: *Astropart. Phys.* 78 (2016), pp. 28–34. DOI: [10.1016/j.astropartphys.2016.02.004](https://doi.org/10.1016/j.astropartphys.2016.02.004).
arXiv: [1510.08387](https://arxiv.org/abs/1510.08387) [[astro-ph.HE](https://arxiv.org/abs/astro-ph.HE)].
- [527] P. A. ZYLA ET AL.:
'Review of Particle Physics',
in: *PTEP* 2020.8 (2020), p. 083C01. DOI: [10.1093/ptep/ptaa104](https://doi.org/10.1093/ptep/ptaa104).